



Universidade do Minho
Escola de Engenharia

**COMPACTION AND ITS INFLUENCE ON THE STRUCTURAL
BEHAVIOUR OF HIGH SPEED RAILWAYS**

João Paulo Martins

João Paulo Martins

**COMPACTION AND ITS INFLUENCE
ON THE STRUCTURAL BEHAVIOUR
OF HIGH SPEED RAILWAYS**

UMinho | 2011

August 2011





Universidade do Minho
Escola de Engenharia

João Paulo Martins

COMPACTION AND ITS INFLUENCE ON THE STRUCTURAL BEHAVIOUR OF HIGH SPEED RAILWAYS

Doctoral thesis in Civil Engineering

Work performed under the supervision of
Professor António Gomes Correia

August 2011

DECLARATION

Name: João Paulo Martins

E-mail: jpmartins@civil.uminho.pt

Passport number: 11873185

Doctoral thesis title: COMPACTION AND ITS INFLUENCE ON THE STRUCTURAL
BEHAVIOUR OF HIGH SPEED RAILWAYS

Supervisor: Professor António Gomes Correia

Year of conclusion: 2011

Area of knowledge: Civil Engineering

THE INTEGRAL REPRODUCTION OF THIS DISSERTATION IS ONLY AUTHORIZED FOR RESEARCH EFFECTS, AFTER WRITTEN DECLARATION OF THE INTERESTED PARTY, TO WHICH IT PLEDGES TO COMPLY.

University of Minho, August 2011

The thesis was defended at the University of Minho in Guimarães, on October 12, 2011 before the review board composed by:

- **Paulo da Venda Oliveira** - University of Coimbra (*principal examiner*)
- **Jaime Santos** - Technical University of Lisbon (*principal examiner*)
- **Maria Madalena Araújo** - University of Minho (*president of the jury*)
- **Joel Oliveira** - University of Minho (*examiner*)
- **Nuno Araújo** - University of Minho (*examiner*)
- **António Gomes Correia** - University of Minho (*supervisor*)

To all of them, I would like to express my appreciation for their kind and relevant remarks.

If I have seen further
it is by standing on the shoulders of giants
Isaac Newton

Acknowledgment

The author would like to thank all institutions and persons who made this project possible, namely:

- Portuguese Foundation for Science and Technology (FCT) in the form of the PhD grant SFRH/BD/32571/2006 and through project POCI/ECM/61114/2004;
- Prof. António Gomes Correia (University of Minho) for his supervision and support throughout this entire research project;
- University of Minho through the Territory, Environment and Construction Centre (C-TAC) and the Department of Civil Engineering (DEC), for the logistical and human conditions;
- all the technicians in the Civil Engineering Laboratory at University of Minho for their constant help during the laboratory work, in particular to Mr. José Gonçalves and Ricardo Magalhães;
- the technicians in the National Laboratory of Civil Engineering for their constant help during the field work;
- Nuno Araújo, Carlos Palha, Sandra Reis Ferreira, Cristiana Ferreira and José Cunha for their kind support in field and laboratory work;
- all my friends for their constant support and encouragement;
- Gabriela for all she gives to me;
- my parents and sister for their outstanding support, understanding, patience, belief and encouragement.

Abstract

Important aspects that govern railway embankments, namely, high-speed railways are, on one hand, the strict requirements during construction (material quality, state parameters and mechanical properties limits) associated with generally relatively short construction time available and, on the other hand, the strict requirements on residual settlements concerning serviceability conditions, which are inherent to mechanical performance of embankment layers during and after construction. Therefore, performance based tests should play an important role through an integrated design process starting from site investigation, design, construction and maintenance. In this context, full scale trials assume great importance to establish a methodology either on the establishment of compaction conditions and on promoting continuous stiffness evaluation, aiming to meet high quality requirements and reduce construction time. This is developed through this study involving advanced laboratory and field investigations of different materials.

A laboratory test campaign was performed on two materials, a clayey sand and a crushed aggregate employed in field investigation. Void ratio was fixed for each material and molding water content was varied in order to reproduce in situ state conditions. Strength and stiffness were determined by means of triaxial tests. Focus was given to hydro-mechanical behaviour on the very small and large strain domain of clayey sand due to non negligible fine fraction. Results showed marked influence of molding water content on the hydro-mechanical behaviour of both clayey sand and crushed aggregate, yet being stronger on the former material.

Field investigation involved two full scale trials, a railway and a road trial embankments. In the railway trial embankment the same materials studied on the laboratory investigation were employed. Construction of trial layers with different thicknesses (0.22, 0.30, 0.40 and 0.50 m) and different moisture contents (2% dry of optimum, optimum and 2% wet of optimum Modified Proctor) were carried out and state conditions and mechanical properties were evaluated for several energy levels. Focus was given to mechanical evaluation through spot and continuous test methods. Moisture content was found to strongly influences mechanical performance, rather than density, thus reflecting suction effect on mechanical properties. Comparison between laboratory and field results proofs results consistency. Further, continuous mechanical evaluation by means of Por-tancemètre represents a great improvement on quality control/quality assurance (Q_a/Q_c) of compacted layers.

In road trial embankment another two materials were employed, which laboratory investigation was conducted in the aim of another doctoral thesis. Construction of trial layers with different thicknesses (0.30, 0.40 and 0.50 m) but

with similar moisture contents were carried out and, likewise to railway trial embankment, state conditions and mechanical properties were evaluated for several energy levels. Moisture content was found have unnoticeable influence on moduli for the range of moisture content verified in situ. Conversely, dry density seems to influence mechanical properties, as long as moisture content does not vary significantly. Comparison between full scale trial and laboratory results yielded small differences. This results along with the ones obtained from railway trial embankment assumes great importance taking into account that design is based on mechanical properties usually determined from laboratory tests.

Parallel to this study, an experimental program was carried out on road embankment to monitor, on one hand, layer in-ground vibrations during application of impact loads and vibrating loads and, on the other hand, to monitor roller drum roller during compaction seeking to explore the relationship between loads and underlying material mechanical properties. Accelerometers and strain gauges were buried on the capping layer enabling measurement of dynamic response and total strains. In-ground dynamic response reflect a single modulus, though different moduli obtained from dynamic tests performed at layer surface. Further, vertical drum behaviour was found to be sensitive to changes in underlying material stiffness and to be related with in-ground dynamic response.

Keywords: Compaction conditions, moisture content, mechanical behaviour, modulus, stiffness, strength, unsaturated state, full scale trial, in-ground strain and dynamic response.

Sumário

Os aspectos importantes que governam os aterros ferroviários, nomeadamente linhas férreas de alta velocidade, são, por um lado, os elevados requisitos durante a construção (qualidade dos materiais, limites para as condições de estado e para as propriedades mecânicas) associadas a um tempo de construção reduzido e, por outro lado, os elevados requisitos relativos aos assentamentos residuais durante as condições de serviço, que são inerentes ao comportamento mecânico durante e após a construção. Assim, a avaliação mecânica através de ensaios mecanicistas deverá desempenhar um papel preponderante num processo que integra a prospecção, o projecto, a construção e a manutenção. Neste contexto os aterros experimentais assumem grande importância quer na definição das condições de compactação, quer na promoção do controlo de compactação em contínuo visando atingir os elevados requisitos de qualidade e a redução do tempo de construção. Tal é desenvolvido no presente estudo que envolve a investigação avançada em laboratório e em campo de diferentes materiais.

A campanha de laboratório foi realizada sobre dois materiais, uma areia argilosa e um agregado britado, utilizados na investigação de campo. O índice de vazios foi fixado para cada material tendo-se feito variar o teor em água de modo a reproduzir as condições de estado em campo. Os parâmetros de resistência e de rigidez foram determinados através de ensaios triaxiais. Foi dado especial enfoque ao comportamento hidro-mecânico no domínio das muito pequenas e grandes deformações da areia argilosa devido à fracção fina não negligenciável. Os resultados obtidos mostram clara influência do teor em água no comportamento hidro-mecânico de ambos os materiais, sendo essa influência mais evidente na areia argilosa.

O estudo de campo compreendeu dois aterros experimentais, um aterro ferroviário e um aterro rodoviário. Os mesmos materiais estudados em laboratório foram utilizados no aterro ferroviário. Procedeu-se à construção de camadas experimentais com diferentes espessuras (0.22, 0.30, 0.40 and 0.50 m) e diferentes teores em água (2% do lado seco do óptimo, óptimo e 2% do lado húmido do óptimo em relação ao Proctor Modificado) e à avaliação das condições de estado e do comportamento mecânico para vários níveis de energia. Especial enfoque foi dado à avaliação mecânica através de ensaios pontuais e contínuos. Os resultados mostraram grande influência do teor em água, maior do que a influência da densidade, no comportamento mecânico dos materiais o que reflecte o efeito da sucção nas propriedades mecânicas. A comparação entre os resultados de campo e de laboratório confirmou a consistência dos mesmos. Para além disso, concluiu-se que a avaliação mecânica em contínuo por meio da utilização do Portancemètre representa um progresso significativo no controlo/garantia de qualidade das camadas compactadas.

O aterro experimental rodoviário envolveu a utilização de dois materiais, cujo estudo laboratorial foi desenvolvido no âmbito de outra tese doutoral. As camadas experimentais foram construídas com diferentes espessuras (0.30, 0.40 and 0.50 m), mas com teores em água semelhantes e, assim como para o aterro ferroviário, as condições de estado e o comportamento mecânico foram avaliados para vários níveis de energia. Para os teores em água encontrados em campo verificou-se que o teor em água teve pouca influência no módulo das camadas. Pelo contrário, a densidade seca parece influenciar as propriedades mecânicas, desde que não se verifique uma grande variação do teor em água. A comparação dos resultados de campo com os de laboratório mostraram pequenas diferenças. Na linha do concluído para o aterro experimental ferroviário, estes resultados assumem grande importância se se tiver em conta que o projecto tem por base as propriedades mecânicas dos materiais determinadas em laboratório.

Paralelamente a este estudo, no aterro rodoviário realizou-se um programa experimental visando, por um lado, a monitorização de vibrações em profundidade durante a aplicação de cargas de impacto e visando, por outro lado, a monitorização do rolo do cilindro procurando explorar a relação entre as cargas aplicadas e as propriedades mecânicas. Acelerómetros e extensómetros foram instalados em profundidade na camada de leito de pavimento permitindo a medição da resposta dinâmica e das extensões totais. A resposta dinâmica em profundidade reflecte um único módulo, apesar de diferentes módulos obtidos através dos ensaios dinâmicos realizados à superfície. Para além disso, verificou-se que o comportamento do rolo do cilindro é sensível à mudança de rigidez do material e que está relacionado com a resposta dinâmica em profundidade.

Palavras-chave: Condições de compactação, teor em água, comportamento mecânico, módulo, rigidez, resistência, estado não saturado, aterro experimental, resposta dinâmica e deformação em profundidade.

Contents

1	Introduction	1
1.1	Motivation	1
1.2	Objectives	3
1.3	Thesis layout	5
2	Compaction	7
2.1	Introduction	7
2.2	Compaction equipments and technologies	7
2.2.1	Devices embarked on compactors	8
2.2.2	Intelligent compaction	17
2.3	Compaction control	20
2.3.1	Specifications for high speed embankments and rail track layers	22
2.3.2	Static plate loading test (<i>SPLT</i>)	24
2.3.3	New techniques on spot tests method (<i>SSG, FWD, LFWD, SASW</i>)	26
2.3.4	Continuous test method (Portancemètre)	36
2.4	Summary	39
3	The influence of compaction on the hydro–mechanical behaviour	41
3.1	Introduction	41
3.2	Basic concepts of non saturated geomaterials	42
3.2.1	Suction	42
3.2.2	Soil water characteristic curve (<i>SWCC</i>) / Water retention curve (<i>WRC</i>)	45
3.2.3	Stress state variables	48
3.3	Hydro–mechanical behaviour	53
3.3.1	Influence of compaction on saturated geomaterials	54
3.3.2	Influence of compaction on unsaturated geomaterials	60
3.4	Summary	74
4	Experimental program	75
4.1	Introduction	75
4.2	Laboratory investigation	76
4.2.1	Physical characterization	76
4.2.2	Hydro characterization	77
4.2.3	Mechanical characterization	78
4.3	Field investigation: Évora trial railway embankment (<i>ETRE</i>)	85

4.3.1	Materials	86
4.3.2	Experimental plan	86
4.4	Field investigation: Fafe trial road embankment (<i>FTRE</i>)	90
4.4.1	Materials	91
4.4.2	Experimental plan	92
4.4.3	Instrumentation of experimental section	94
4.5	Conclusions	98
5	Laboratory investigation	101
5.1	Introduction	101
5.2	Physical characterization	101
5.3	Hydro characterization	102
5.4	Mechanical characterization	103
5.4.1	Oedometer test	103
5.4.2	Triaxial tests on <i>SC</i> specimens	105
5.4.3	Triaxial tests on <i>CA31.5</i> specimens	114
5.4.4	Triaxial tests with measurements of S-waves velocity	121
5.5	Conclusions	128
6	Field investigation: <i>ETRE</i>	131
6.1	Introduction	131
6.2	State conditions	132
6.3	Moduli from <i>SPLT</i>	137
6.3.1	Comparison of <i>SPLT</i> results following AFNOR standard and using different settlement measuring systems	137
6.3.2	Comparison of E_{V2} modulus following standards: AFNOR NF P94-117-1 (2000) and DIN 18134 (2001)	140
6.4	Moduli obtained from performance related tests	146
6.4.1	<i>LFWD</i> , <i>FWD</i> , <i>SSG</i> and Portancemètre	146
6.4.2	<i>SASW</i>	146
6.5	Correlation between E modulus for several tests	151
6.5.1	<i>SC</i> trial layers	152
6.5.2	<i>CA31.5</i> trial layers	155
6.6	Analysis of full scale trial results and recommendations	156
6.6.1	<i>SC</i> trial layers	156
6.6.2	<i>CA31.5</i> trial layers	161
6.7	Comparison between full scale trial and laboratory results	163
6.8	Conclusions	165
7	Field investigation: <i>FTRE</i>	169
7.1	Introduction	169
7.2	State conditions	170
7.3	Modulus from <i>SPLT</i>	173
7.4	Moduli obtained from performance related tests	174
7.4.1	<i>LFWD</i> , <i>FWD</i> , <i>SSG</i> and Portancemètre	174
7.4.2	<i>SASW</i>	174
7.5	Correlation between E modulus for several tests	182
7.5.1	<i>SP</i> trial and embankment layers	182
7.5.2	<i>ISAC</i> trial and embankment layers	183
7.5.3	<i>CA40</i> base layer	184

7.6	Analysis of full scale trial results and recommendations	185
7.7	Comparison between full scale trial and laboratory results	188
7.8	Field monitoring of roller drum and capping layer vibrations	189
7.8.1	Phase One: Instrumentation	189
7.8.2	Phase One: Test results	190
7.8.3	Phase One: Comparison between tests results	209
7.8.4	Phase Two: Instrumentation	212
7.8.5	Phase Two: Test results	214
7.9	Conclusions	230
8	Conclusions	233
8.1	Conclusions	233
8.1.1	Laboratory investigation	234
8.1.2	Field investigation: Évora trial railway embankment (<i>ETRE</i>)	236
8.1.3	Field investigation: Fafe trial road embankment (<i>FTRE</i>)	238
8.2	Prospective work	241
A	Background on the measurement of stiffness at small strain using dynamic methods	259
A.1	Introduction	259
A.2	Near-field effects	261
A.3	Cross-talk	262
A.4	Sample size effects	263
A.5	Travel distance determination	265
A.6	Travel time determination	266
B	Specification project of <i>SPLT</i>	269
C	<i>ETRE</i> results	271
C.1	State parameters	271
C.2	<i>SPLT</i>	275
C.3	Performance related tests	277
C.3.1	<i>LFWD</i>	277
C.3.2	<i>FWD</i>	278
C.3.3	<i>SSG</i>	278
C.3.4	Portancemètre	279
C.4	Moduli and relative compaction versus water content	280
D	<i>FTRE</i> results	283
D.1	State parameters	283
D.2	Performance related tests	287
D.2.1	<i>LFWD</i>	287
D.2.2	<i>FWD</i>	289
D.2.3	<i>SSG</i>	290
D.2.4	Portancemètre	291
D.3	In-ground accelerations and displacements	293
D.4	In-ground strains	295

List of Figures

2.1	Adjustable excitation direction of a VARIO roller drum and compaction effect (Adam and Kopf, 2000)	8
2.2	Test recordings of vibrations on the roller, a mini roller and geophones (Thurner and Sandström, 2000)	9
2.3	Method to determine CMV involves spectral analysis (right) of two cycles of vertical drum acceleration time history data (left) (Mooney and Adam, 2007)	10
2.4	(a) Compaction meter components; (b) Different means to display the compaction result to the roller operator (Thurner and Sandström, 2000)	12
2.5	One-degree-of-freedom lumped parameter model representation of vibratory compactor (Mooney and Adam, 2007)	12
2.6	Analytical model of vertical vibration of a single drum roller (circular excitation) (Anderegg <i>et al.</i> , 2006)	13
2.7	Illustration of k_s during contact (left) and partial loss of contact behavior (right) (Mooney and Adam, 2007)	14
2.8	Measurement of soil stiffness of homogeneous subsoil (Anderegg and Kaufmann, 2004)	15
2.9	Contact force–drum displacement behaviour (Mooney and Adam, 2007)	15
2.10	Stiffness ($k_B = k_s$) vs. Modulus (Preisig <i>et al.</i> , 2003)	16
2.11	Variation of roller measurement value with soil modulus and relative drum vibration amplitude—results of numerical simulations (Adam and Kopf, 2004)	17
2.12	Operating conditions of a vibratory roller drum (Adam, 1996)	18
2.13	Feedback control system for rollers with data (Anderegg and Kaufmann, 2004)	19
2.14	Hardening response induced by the curved drum (Rinehart and Mooney, 2009)	21
2.15	<i>SPLT</i> following AFNOR NF P94–117–1 (2000) standard	24
2.16	<i>SPLT</i> following DIN 18134 (2001) standard	25
2.17	Humboldt Stiffness Gauge: (a) general aspect; (b) detail of ring shaped foot	26
2.18	Humboldt Stiffness Gauge (Humboldt, 2007)	27
2.19	<i>FWD</i> : (a) general view; (b) detail of geophones and plate	29
2.20	(a) <i>LFWD</i> ; (b) Components of the <i>LFWD</i> (Adam and Adam, 2003)	30
2.21	<i>LFWD</i> data collection screen	31
2.22	(a) P–waves; (b) Rayleigh waves; (c) S–waves; (d) Love Waves	32

2.23	Approximate distribution of vertical particle motions with depth of two surface waves of different wavelengths (Rix and Stokoe, 1989)	33
2.24	Traditional configuration of equipment used in SASW testing with a two-channel recording system (Stokoe <i>et al.</i> , 1994)	34
2.25	(a) Composite experimental dispersion curve from traditional SASW testing at soil site; (b) Comparison between experimental and theoretical dispersion curves for a soil site Stokoe <i>et al.</i> (1994)	35
2.26	Shear wave velocity profiles determined from SASW (using data shown in fig. 2.25) and crosshole tests at the same site Stokoe <i>et al.</i> (1994)	36
2.27	Portancemètre equipment: (a) general aspect; (b) vibrating wheel detail; (c) function schema	38
2.28	Display of the monitor (Quibel, 2006)	39
3.1	Physical model and phenomenon related to capillarity (Fredlund and Rahardjo, 1993)	43
3.2	Capillary tubes showing the air–water interfaces at different radii of curvature (Fredlund and Rahardjo, 1993)	44
3.3	Filter paper method for measuring total and matric suction (Yang <i>et al.</i> , 2008)	45
3.4	Typical WRC (Vanapalli <i>et al.</i> , 1996)	46
3.5	Probable variation of water area in different stages of a WRC (Vanapalli <i>et al.</i> , 1996)	47
3.6	Typical WRCs for four Canadian soils (Vanapalli <i>et al.</i> , 1999) . .	47
3.7	χ variation vs degree of saturation for: (a) a cohesionless silt; (b) compacted soils (Fredlund and Rahardjo, 1993)	49
3.8	Schematic representation of four types of behaviours (Biarez <i>et al.</i> , 1993)	50
3.9	Schematic representation of four types of arrangements (Biarez <i>et al.</i> , 1993)	51
3.10	The stress state variables for unsaturated soil	53
3.11	Initial shear modulus versus mean effective stress (a) Proctor specimens and (b) Harvard specimens; (c) Normalised stiffness coefficient variation with initial molding water content (d’Onofrio and Penna, 2003)	55
3.12	(a) Compaction curves; (b) Relationship between vertical effective stress and small strain Young modulus; (c) Relationship between the small strain stiffness coefficients corrected for void ratio and water content ratio (Santucci di Magistris and Tatsuoka, 2004)	56
3.13	Compressibility parameters (d’Onofrio and Penna, 2003)	57
3.14	Compression curves from Meltramo silty sand: (a) modified Proctor and tamped specimens; (b) modified Proctor, tamped and remoulded specimens (Santucci di Magistris <i>et al.</i> , 1998)	58
3.15	(a) Compaction curves; (b) Peak and ultimate shear strength in the (q, p) plane and ultimate void ratio (Tarantino and Tomblato, 2005)	59

3.16	Water retention curves of a low plasticity soil obtained by drying of compacted samples at different conditions: (a), (b) and (c) initial state; (d) measured water retention curve (Marinho and Stuermer, 2000)	60
3.17	Compaction of soil–water characteristics for specimens compacted at the same initial void ratio and: (a) compacted dry of optimum water content; (b) compacted at optimum water content; (c) compacted wet of optimum water content (Vanapalli <i>et al.</i> , 1999)	61
3.18	Water retention curves for different constant densities of Barcelona low plasticity silty clay (Barrera, 2002)	62
3.19	(a) Static compaction curves for the vertical stresses of 300, 600 and 1200 kPa. The solid square indicates the optimum for the 100 kPa compaction curve; (b) Water retention curves for the respective compaction vertical stresses (Tarantino and Tombolato, 2005)	63
3.20	(a) Normalised Young’s modulus versus total vertical stress for specimens of Perafia sand at different water contents and densities; (b) Interpretation of very small strains triaxial tests using Biarez <i>et al.</i> (1993) micromechanical model for the definition of effective stresses (Fleureau <i>et al.</i> , 2003)	64
3.21	Secant modulus versus total vertical stress for specimens of unbound granular materials with 12% of fines and Plasticity Index of 15% (Caicedo <i>et al.</i> , 2009)	65
3.22	$G_0/G_{0(\text{dry})}$ versus degree of saturation at various void ratios for Ottawa F-125 sand (Qian <i>et al.</i> , 1993)	65
3.23	Initial shear stiffness in controlled–suction RC tests: (a) optimum compacted material; (b) wet of optimum compacted material (Mancuso <i>et al.</i> , 2002)	66
3.24	(a) Dry unit weight and (b) matric suction versus molding water content; Small–strain shear modulus versus (c) matric suction and (d) molding water content for clayey sand (SC), lean clay (CL), and silt (ML) soils (Sawangsurriya <i>et al.</i> , 2008)	67
3.25	(a) Influence of compaction water content on the isotropic compression behaviour: comparison of typical results from series 2 and series 4; (b) Influence of compaction pressure on the isotropic compression behaviour (Sivakumar and Wheeler, 2000)	68
3.26	Results of isotropic compression tests on unsaturated clay compacted at different initial void ratios (Sun <i>et al.</i> , 2007)	69
3.27	Variation of $\lambda_{(s)}$ with suction for: (a) dense samples; (b) loose samples (Estabragh <i>et al.</i> , 2004)	69
3.28	(a) Stress deviator versus axial strain for consolidated undrained tests on unsaturated specimens of Perafito sand; (b) Interpretation of large triaxial tests using Biarez <i>et al.</i> (1993) micromechanical model for the definition of the effective stress. 1: $w = 3.74\%$ ($e = 0.406$), 2: $w = 6.25\%$ ($e = 0.409$), 3: $w = 7.5\%$ ($e = 0.404$), 4: $w = 8\%$ ($e = 0.409$), 5: $w = 9.5\%$ ($e = 0.401$), 6: $w = 10.4\%$ ($e = 0.490$), 7: $w = 14.1\%$ ($e = 0.410$), 8: $w = 14.2\%$ ($e = 0.520$), 9: $w = 16.1\%$ ($e = 0.520$), 10: $w = 17.9\%$ ($e = 0.520$), 11: $w = 18.3\%$ ($e = 0.530$) (Fleureau <i>et al.</i> , 2003)	71

3.29	(a) Shear strength versus degree of saturation for initial void ratio of 0.8; (b) Effect of initial void ratio on unsaturated strength (Maaitah and Mahadin, 2004)	71
3.30	p–q diagram for unsaturated and saturated specimens with void ratio of 0.68 (Maaitah, 2005)	72
3.31	(a) Compaction details for series 1–4 and the curves of standard Proctor compaction and 400 kPa static compaction (Sivakumar and Wheeler, 2000); (b) Critical state data in the plane (q, p) for series 1, 2 and 3 (Wheeler and Sivakumar, 2000)	72
3.32	(a) Critical state line for q and p' under various suctions; (b) Variation of $M(s)$ with suction; (c) Variation of $\mu(s)$ with suction (Estabragh and Javadi, 2008)	73
3.33	Variation of specific volume (v) and mean net stress at critical state condition (Estabragh and Javadi, 2008)	74
4.1	Example of a multistage test result	80
4.2	Holes on stress–path Bishop–Wesley triaxial chamber to incorporate cables: (a) inside view; (b) lateral view	82
4.3	(a) Bottom and (b) top platens with embedded bender–elements (Ferreira <i>et al.</i> , 2010)	82
4.4	Accelerometer and pin (Ferreira <i>et al.</i> , 2010)	83
4.5	Bender elements and accelerometers setup: (a) scheme; (b) view (adopted from Ferreira <i>et al.</i> (2010))	83
4.6	Sample display of acquisition program developed in LabVIEW	84
4.7	<i>ETRE</i> : (a) <i>SC</i> layer; (b) <i>CA31.5</i> material over <i>SC</i> layer; (c) and (d) general overview of <i>SC</i> and <i>CA31.5</i> trial layers	86
4.8	Mesh created for <i>ETRE</i> trial layers with dimensions of $50 \times 6 \text{ m}^2$	87
4.9	Experimental plan adopted on <i>ETRE</i> for layers with dimensions of $50 \times 6 \text{ m}^2$	89
4.10	<i>FTRE</i> : (a) <i>SP</i> material; (b) <i>ISAC</i> material; (c) and (d) general overview of <i>SC</i> and <i>ISAC</i> trial layers	91
4.11	Construction scheme of the <i>FTRE</i>	92
4.12	Mesh created for <i>FTRE</i> trial layers	93
4.13	Construction scheme of the <i>FTRE</i> trial layers	93
4.14	Experimental plan adopted on <i>FTRE</i>	94
4.15	Schematic position of instrumentation zone on <i>FTRE</i> : (a) plant; (b) longitudinal view	97
4.16	Instrumentation with accelerometers and strain gauges during compaction of the capping layer	97
4.17	Instrumentation with accelerometers and strain gauges during compaction of the base layer	98
5.1	Grain–size distributions	102
5.2	Matric suction versus molding water content for <i>SC</i> specimens with the same void ratio ($e = 0.331$)	103
5.3	Oedometer tests results from <i>SC</i> specimens in unsaturated and saturated conditions in: (a) compacted state; (b) loose state	104
5.4	Triaxial tests results at $\sigma_3 = 100 \text{ kPa}$ from <i>SC</i> samples with varying initial molding water contents	106

5.5	Triaxial tests results at $\sigma_3 = 200$ kPa from <i>SC</i> samples with varying initial molding water contents	107
5.6	Triaxial tests results at $\sigma_3 = 300$ kPa from <i>SC</i> samples with varying initial molding water contents	109
5.7	Triaxial test results from <i>SC</i> specimens with varying initial molding water content; (a) peaks and residual deviatoric stress vs. total mean stress; (b) Secant friction angle vs. total mean stress	110
5.8	Specific volume vs. total mean stress obtained from <i>SC</i> triaxial tests: (a) at the end of consolidation at each stage of a multistage test and during consolidation of the single stage test; (b) at peak and critical stage	112
5.9	(a) $E_{\text{sec}}^{\text{nor}}$ at strain levels $\varepsilon = 0.5\%$ and 1.0% vs. σ_1 ; (b) $E_{\text{sec}}^{\text{nor}}$ at strain levels $\varepsilon = 0.5\%$ and 1.0% and stress levels $\sigma_1 = 500$ kPa and 1000 kPa vs. moisture content; (c) Relationship between $E_{\text{sec}}^{\text{nor}}$ at strain levels $\varepsilon = 0.5\%$ and $\varepsilon = 1.0\%$ at stress levels $\sigma_1 = 500$ kPa and 1000 kPa	113
5.10	$E_{\text{sec}}^{\text{nor}} / E_0$ degradation curves corresponding to confining stresses, σ_3 : (a) 100 kPa; (b) 200 kPa; (c) 300 kPa	115
5.11	Triaxial tests results at $\sigma_3 = 100$ kPa from <i>CA31.5</i> samples with varying initial molding water contents	116
5.12	Triaxial tests results at $\sigma_3 = 200$ kPa from <i>CA31.5</i> samples with varying initial molding water contents	117
5.13	Triaxial tests results at $\sigma_3 = 300$ kPa from <i>CA31.5</i> samples with varying initial molding water contents	118
5.14	Triaxial test results from <i>CA31.5</i> specimens with varying initial molding water content; (a) peaks and residual deviatoric stress vs. total mean stress; (b) Secant friction angle vs. total mean stress	119
5.15	Specific volume vs. total mean stress obtained from <i>SB</i> triaxial tests: (a) isotropic, anisotropic at the start of each stage of a multistage test and at peak; (b) w_{OPM} unsaturated specimen on loose state	120
5.16	(a) $E_{\text{sec}}^{\text{nor}}$ at strain levels $\varepsilon = 0.5\%$ and 1.0% vs. σ_1 ; (b) $E_{\text{sec}}^{\text{nor}}$ at strain and stress levels $\varepsilon = 0.5\%$ ($\sigma_1 = 600$ kPa and 1200 kPa) and 1.0% ($\sigma_1 = 1000$ kPa and 2000 kPa) vs. moisture content; (c) Relationship between $E_{\text{sec}}^{\text{nor}}$ at strain levels $\varepsilon = 0.5\%$ and $\varepsilon = 1.0\%$ at stress level $\sigma_1 = 1000$ kPa	122
5.17	Time histories of signals from BE and accelerometers	123
5.18	Deviatoric stress and volumetric strain vs. axial strain obtained from triaxial results at confining stresses of: (a) and (b) 100 kPa; (c) and (d) 200 kPa; (e) and (f) 300 kPa	124
5.19	Evolution of shear moduli with total vertical stress obtained from measurements of S-waves on <i>SC</i> unsaturated samples at: (a) isotropic stress state; (b) anisotropic stress state	125
5.20	Evolution of normalised shear moduli with total vertical stress obtained from measurements of S-waves on <i>SC</i> unsaturated samples at: (a) isotropic stress state; (b) anisotropic stress state . . .	126
5.21	Ratio between average S-waves velocity determined with accelerometers and BE ($V_{\text{Ac}}/V_{\text{BE}}$) and corresponding standard deviation .	127

5.22	Time travel determination with with accelerometers and BE during triaxial test on specimen $w_{OPM+2\%}$ at confining stresses: (a) 100 kPa; (b) 200 kPa	128
6.1	Comparison of state parameters obtained from <i>NM</i> and <i>SCM</i> test methods performed on the same grid: (a) density; (b) volumetric water content	132
6.2	Comparison of average state parameters per layer obtained from <i>NM</i> and <i>SCM</i> test methods: (a) density; (b) volumetric water content	133
6.3	<i>SCM</i> parameters plotted against <i>NM</i> calibrated parameters: (a) density; (b) volumetric water content	133
6.4	State parameters obtained from <i>SCM</i> and <i>NM</i> on <i>SC</i> layers for energy level corresponding to: (a) 4 Passes; (b) 6 Passes; (c) 8 Passes; (d) 10 Passes; (e) 12 Passes	134
6.5	State parameters obtained from <i>SCM</i> and <i>NM</i> on <i>CA31.5</i> layers for energy level corresponding to: (a) 4 Passes; (b) 6 Passes; (c) 8 Passes; (d) 10 Passes; (e) 12 Passes	136
6.6	Measurement of the settlement of the three point measuring system corresponding to <i>SPLT</i> following standard AFNOR carried out on trial layer $0.50 w_{OPM-2\%}$, for 4 Passes of the vibrating roller, on grid: (a) C7 (measurement of the settlement of one support); (b) C3 (measurement of the settlement of one support); (c) C3 (measurement of the settlement of the structure)	138
6.7	Third loading cycle of a <i>SPLT</i> following standard AFNOR carried out on grid A10 of the trial layer $0.40 w_{OPM}$, which energy level corresponds to 12 Passes of the vibrating roller. The one point measuring system was placed in contact with the loading plate approximately 2 cm away from the center	139
6.8	Comparison of E modulus obtained with one point measuring system through the hole in the center of the loading plate and with the corresponding value obtained with the three point measuring system	140
6.9	Comparison of E_{V2} modulus obtained from direct interpretation of <i>SPLT</i> following AFNOR NF P94–117–1 (2000) and DIN 18134 (2001) standards: (a) tests performed in the same grid; (b) average values per layer.	141
6.10	Comparison of E_{V2} modulus obtained from interpretation of <i>SPLT</i> for same normal stress (200 kPa) and same method: (a) tests performed in the same grid; (b) average value per layer.	142
6.11	Coefficient of rigidity I_{rig} determined from numerical analysis	144
6.12	Comparison of E_{V2} modulus obtained from numerical modeling of <i>SPLT</i> for same normal stress (200 kPa) and same method: (a) tests performed in the same grid; (b) average value per layer	144
6.13	Properties and geometry adopted in numerical models for back-analysis of <i>SPLT</i> models following: (a) AFNOR NF P94–117–1 (2000); (b) DIN 18134 (2001) standards	145
6.14	Comparison of E_{V2} modulus obtained from back-analysis	145

6.15	Example of test results (<i>LFWD</i> , <i>SSG</i> and <i>Portancemètre</i>) obtained from layer 0.30 m $w_{OPM-2\%}$ on lane B, for several energy levels	146
6.16	Setup adopted to perform <i>SASW</i> on layer 0.40 w_{OPM} inside grid <i>B6</i>	147
6.17	(a) Waveforms of signals and (b) respective spectrum generated using a light hammer source	147
6.18	Experimental dispersion curve from <i>SASW</i> carried out on layer 0.40 w_{OPM} inside grid <i>B6</i>	148
6.19	Theoretical and experimental composite dispersion curve from <i>SASW</i> carried out on layer 0.40 w_{OPM} inside grid <i>B6</i>	149
6.20	Experimental dispersion curve from <i>SASW</i> carried out on layer 0.40 w_{OPM} inside grid <i>B9</i>	150
6.21	Theoretical and experimental composite dispersion curve from <i>SASW</i> carried out on layer 0.40 w_{OPM} inside grid <i>B9</i>	150
6.22	Plant representation of the output of <i>Portancemètre</i> : (a) values given by the equipment; (b) average values; (c) computed spacial distribution concerning layer 0.30 m $w_{OPM-2\%}$ last energy level (12 passes)	152
6.23	Comparison between E_{Port} and $E_{V2AFNOR}$ average values per energy level	153
6.24	Comparison between E_{Port} and $E_{V2AFNOR}$ for the last energy level (12 passes): (a) tests performed on the same grid; (b) average values grouped into homogeneous areas; (c) average values per layer	154
6.25	Comparison between E_{LFWD} and $E_{V2AFNOR}$: (a) tests performed in the same spot; (b) average values per energy level	154
6.26	Comparison between E_{LFWD} and $E_{V2AFNOR}$ for the last energy level (12 passes): (a) average values grouped into homogeneous areas; (b) average values	155
6.27	Comparison between E_{SSG} and $E_{V2AFNOR}$: (a) average values; (b) average values for the last energy level (12 passes)	155
6.28	0.30 m $w_{OPM-2\%}$ layer moduli E_{Port} , relative compaction and moisture content deviation evolution with number of passes: (a) Moduli and relative compaction; (b) Moduli and moisture content deviation	156
6.29	0.50 m $w_{OPM-2\%}$ layer moduli E_{Port} , relative compaction and moisture content deviation evolution with number of passes: (a) Moduli and relative compaction; (b) Moduli and moisture content deviation	157
6.30	0.40 m w_{OPM} layer moduli E_{Port} , relative compaction and moisture content deviation evolution with number of passes: (a) Moduli and relative compaction; (b) Moduli and moisture content deviation	158
6.31	0.40 m $w_{OPM-2\%}$ layer moduli E_{Port} , relative compaction and moisture content deviation evolution with number of passes: (a) Moduli and relative compaction; (b) Moduli and moisture content deviation	158

6.32	0.40 m $w_{OPM+2\%}$ layer moduli E_{Port} , relative compaction and moisture content deviation evolution with number of passes: (a) Moduli and relative compaction; (b) Moduli and moisture content deviation	159
6.33	E_{Port} modulus and relative compaction (RC) versus moisture content deviation (w) obtained on <i>SC</i> trial layers for energy level corresponding to 12 passes	160
6.34	0.22 m w_{OPM} layer moduli E_{Port} , relative compaction and moisture content deviation evolution with number of passes: (a) Moduli and relative compaction; (b) Moduli and moisture content deviation	161
6.35	0.30 m w_{OPM} layer moduli E_{Port} , relative compaction and moisture content deviation evolution with number of passes: (a) Moduli and relative compaction; (b) Moduli and moisture content deviation	162
6.36	E_{Port} modulus and relative compaction (RC) versus moisture content (w) obtained on <i>CA31.5</i> trial layers for energy level corresponding to 12 passes	162
6.37	Relationship between modulus estimated from laboratory triaxial tests and modulus obtained from <i>SPLT</i> carried out on trial layers for the last energy level	165
7.1	Comparison of state parameters obtained from <i>NM</i> and <i>SCM</i> test methods performed on the same grid: (a) density; (b) volumetric water content	170
7.2	Comparison of average state parameters per layer obtained from <i>NM</i> and <i>SCM</i> test methods: (a) density; (b) volumetric water content	171
7.3	<i>SCM</i> parameters plotted against <i>NM</i> calibrated parameters: (a) density; (b) volumetric water content	171
7.4	State parameters obtained from <i>SCM</i> and <i>NM</i> on <i>SP</i> layers for energy level corresponding to: (a) 4 Passes; (b) 6 Passes; (c) 8 Passes; (d) 10 Passes; (e) 12 Passes; (f) 14 Passes	172
7.5	Setup adopted to perform <i>SASW</i> on <i>SP</i> capping layer inside grid <i>L6</i>	174
7.6	(a) Waveforms of signals and (b) respective spectrum generated using a light hammer source	175
7.7	Experimental dispersion curves from <i>SASW</i> carried out on capping layer inside grid <i>L6</i> using light hammer: (a) first test ; (b) reverse test	175
7.8	Theoretical and experimental composite dispersion curve from <i>SASW</i> carried out on <i>SP</i> capping layer inside grid <i>L6</i> using sledge hammer source	177
7.9	(a) Waveforms of signals and (b) respective spectrum generated using a sledge hammer source	177
7.10	Experimental dispersion curves from <i>SASW</i> carried out on <i>SP</i> capping layer inside grid <i>L6</i> using sledge hammer, corresponding to first test	177
7.11	Waveforms of signals generated using <i>LFWD</i> source and its spectrum	178

7.12	Experimental dispersion curves from <i>SASW</i> carried out on <i>SP</i> capping layer inside grid <i>L6</i> , using <i>LFWD</i> source	178
7.13	Theoretical and experimental composite dispersion curve from <i>SASW</i> carried out on <i>SP</i> capping layer inside grid <i>L6</i> using <i>LFWD</i> source	179
7.14	Waveforms of signals generated using <i>FWD</i> source and its spectrum corresponding to three drop heights	180
7.15	Experimental dispersion curves from <i>SASW</i> carried out on capping layer inside grid <i>L6</i> , using <i>FWD</i> source corresponding to three drops heights: (a) 1 st ; (b) 2 nd ; (c) 3 rd	180
7.16	Theoretical and experimental composite dispersion curve from <i>SASW</i> carried out on capping layer inside grid <i>L6</i> using <i>FWD</i> source	181
7.17	Comparison between moduli obtained from <i>SPLT</i> with Portancemètre and <i>LFWD</i> performed on <i>SP</i> trial layers	183
7.18	Comparison between moduli obtained from <i>SPLT</i> and Portancemètre, <i>SSG</i> and <i>LFWD</i> performed on <i>ISAC</i> trial layers	183
7.19	Comparison of moduli obtained from Portancemètre and: (a) <i>LFWD</i> for average values per energy level; (b) <i>SSG</i> for tests carried out on the same grid and for the last energy level	184
7.20	Trial layer with 0.30 m thickness. Moduli (E_{Port}) and state parameters (relative compaction and moisture content deviation) evolution with number of passes: (a) Moduli and relative compaction; (b) Moduli and moisture content deviation	185
7.21	Trial layer with 0.40 m thickness. Moduli (E_{Port}) and state parameters (relative compaction and moisture content deviation) evolution with number of passes: (a) Moduli and relative compaction; (b) Moduli and moisture content deviation	186
7.22	Trial layer with 0.50 m thickness. Moduli (E_{Port}) and state parameters (relative compaction and moisture content deviation) evolution with number of passes: (a) Moduli and relative compaction; (b) Moduli and moisture content deviation	186
7.23	E_{Port} modulus and relative compaction (RC) versus moisture content (w) obtained on <i>SP</i> trial and embankment layers for the last energy level	187
7.24	Moduli obtained from <i>SPLT</i> performed on on <i>SP</i> and <i>ISAC</i> layers and <i>SSG</i> carried out on <i>SP</i> layers versus moduli obtained from laboratory tests	189
7.25	Average <i>LFWD</i> force–displacement loops from impacts at surface capping layer on sensors vertical alignment at: (a) <i>SP</i> profile; (b) <i>ISAC</i> profile	191
7.26	Strains measurement during <i>LFWD</i> test in: (a) <i>SP</i> profile; (b) <i>ISAC</i> profile	191
7.27	Accelerations time histories from in–ground accelerometers due to <i>LFWD</i> test: (a) <i>SP</i> profile; (b) <i>ISAC</i> profile; and computed displacements time histories: (c) <i>SP</i> profile; (d) <i>ISAC</i> profile . .	192
7.28	Average <i>FWD</i> force–displacement loops from impacts at surface capping layer on sensors vertical alignment at: (a) <i>SP</i> profile; (b) <i>ISAC</i> profile	196

7.29	Strains measurement during <i>FWD</i> test in: (a) <i>SP</i> profile; (b) <i>ISAC</i> profile	196
7.30	Vibrations measurement during <i>FWD</i> test. Computed displacements from in-ground accelerometers in: (a) <i>SP</i> ; (b) <i>ISAC</i> ; Strains from in-ground strain gauges in: (c) <i>SP</i> ; (d) <i>ISAC</i>	198
7.31	Total and cyclic strain data from strain gauges V05 and V04 during pass of Portancemètre in: (a) and (c) <i>SP</i> profile; (b) and (d) <i>ISAC</i> profile	201
7.32	Vibrations measurement during Portancemètre test. Acceleration time histories from in-ground accelerometers in: (a) <i>SP</i> ; (b) <i>ISAC</i> ; Computed displacements in: (c) <i>SP</i> ; (d) <i>ISAC</i>	203
7.33	Accelerometers embarked on roller drum: (a) scheme; (b) instrumentation	204
7.34	Vibration response from in-ground sensors on <i>SP</i> test bed during vibrating roller pass: (a) total strain response; (b) cyclic strain response; (c) acceleration response; (d) approximated displacements	205
7.35	Vibration response on <i>SP</i> test bed during drum vibratory loading: (a) peak acceleration time history; (b) acceleration frequency spectrum; (c) acceleration time history; (d) acceleration time history; (e) approximated displacements	206
7.36	Vibration response on <i>ISAC</i> test bed during drum vibratory loading: (a) peak acceleration time history; (b) acceleration frequency spectrum; (c) and (d) acceleration time history; (f) and (e) approximated displacements	208
7.37	Frequency content of raw drum acceleration data collected from one of the pass of the roller on: (a) <i>CA40</i> ; (b) <i>ISAC</i> base layers .	213
7.38	Time and frequency histories of vertical drum acceleration during successive passes of the roller compacter on the three profiles: (a) <i>ISAC</i> ; (b) <i>ISAC+SP</i> ; (c) <i>CA40+SP</i>	215
7.39	Computed drum displacements for three type of sections: (a) <i>ISAC</i> ; (b) <i>ISAC+SP</i> ; (c) <i>CA40+SP</i>	216
7.40	Average drum acceleration and displacements versus number of passes for three type of sections: (a) <i>ISAC</i> ; (b) <i>ISAC+SP</i> ; (c) <i>CA40+SP</i>	217
7.41	Acceleration time history and computed displacements obtained from in-ground vibrations measured on: (a) and (c) <i>ISAC</i> profile; (b) and (d) <i>CA40+SP</i> profile	222
7.42	In-ground peak acceleration (ac_p) and peak displacement (z_p) evolution with number of roller drum passes: (a) <i>ISAC</i> ; (b) <i>CA40</i>	223
7.43	Total and cyclic strain data from strain gauge: (a) and (b) V08; (c) and (d) V09; (e) and (f) V04	225
7.44	Total (a) and cyclic (b) strain data from strain gauge V06	226
7.45	Total and cyclic strain data from strain gauge: (a) and (b) V01; (c) and (d) V02; (e) and (f) V05	227
7.46	In-ground strains evolution from sensors V04, V08 and V09: (a) peak strains; (b) $\Delta\varepsilon_z/\varepsilon_z$	228
7.47	n-ground strains evolution from sensor V06: (a) peak strains; (b) $\Delta\varepsilon_z/\varepsilon_z$	228
7.48	In-ground strains evolution from sensors V01, V02 and V05: (a) peak strains; (b) $\Delta\varepsilon_z/\varepsilon_z$	229

7.49	In-ground strains evolution during <i>SPLT</i> carried out on: (a) <i>ISAC</i> section; (b) <i>CA40+SP</i> section	229
A.1	(a) Series connected bimorph bender element; (b) parallel connected bimorph bender element	261
A.2	Bender element measurements in different testing setups: (a) no evidence of cross-talk; (b) clear presence of cross-talk in the output signals (Ferreira, 2008)	263
A.3	Time history of received pulse signals for model A (100 × 50 mm) and model B (100 × 75 mm): (a) non-absorbing models <i>A</i> and <i>B</i> , and absorbing model <i>B</i> ; (b) non-absorbing and absorbing model <i>A</i> and reflected signal (Rio, 2006)	265
A.4	Time histories for soil movements 88 mm from bender tip for models with absorbing lateral boundaries: (a) <i>Aa</i> and <i>Ba</i> ; (b) <i>Ana</i> and <i>Bna</i> ; (c) <i>Can</i> and <i>Ca</i> . Spikes indicate theoretical arrival times of bulk P and S waves (Arroyo <i>et al.</i> , 2006)	265
A.5	Multiple-reflection method (Lee and Santamarina, 2005)	267
A.6	Typical S-wave signal within near field: (A) first deflection, (B) first bump maximum, (C) zero after first bump, and (D) major first peak (Lee and Santamarina, 2005)	267
C.1	E_{Port} modulus and relative compaction (RC) versus moisture content deviation (w) obtained on <i>SC</i> trial layers for energy levels corresponding to: (a) 4 passes; (b) 6 passes; (c) 8 passes; (d) 10 passes; (e) 12 passes	280
C.2	E_{Port} modulus and relative compaction (RC) versus moisture content deviation (w) obtained on <i>CA31.5</i> trial layers for energy levels corresponding to: (a) 4 passes; (b) 6 passes; (c) 8 passes; (d) 10 passes; (e) 12 passes	281

List of Tables

2.1	High-speed railway specifications (UIC, 2004; THSRP, 2003) regarding relative compaction and mechanical properties of compacted layers	23
3.1	Calibration curves for Whatman 42 filter paper (Bicalho <i>et al.</i> , 2008)	45
3.2	Possible combinations of stress state variables for an unsaturated soil	52
4.1	Identification and compaction tests performed on <i>SC</i> and <i>CA31.5</i>	76
4.2	Filter paper method performed on <i>SC</i>	78
4.3	Mechanical tests carried out on <i>SC</i> and <i>CA31.5</i>	78
4.4	Oedometer tests performed on <i>SC</i>	79
4.5	Triaxial <i>CD</i> tests performed on <i>SC</i> specimens with 100 mm × 200 mm	80
4.6	Triaxial <i>CD</i> tests performed on <i>CA31.5</i> specimens with 150 mm × 300 mm	81
4.7	Triaxial tests with measurement of S-wave velocity performed on <i>SC</i> specimens with 100 mm × 200 mm	85
4.8	Synthesis of the state conditions and geometric characteristics adopted on the trial embankment	88
4.9	Number of tests conducted on <i>SC</i> trial layers with moisture content $\omega_{opt-2\%}$	89
4.10	Number of tests conducted on <i>SC</i> trial layers with moisture content ω_{opt}	90
4.11	Number of tests conducted on <i>SC</i> trial layers with moisture content $w_{OPM+2\%}$	90
4.12	Number of tests conducted on <i>CA31.5</i> trial layers with moisture content ω_{opt}	90
4.13	Number of tests conducted on <i>SP</i> trial layers	95
4.14	Number of tests conducted on <i>SP</i> embankment and capping layers	95
4.15	Number of tests conducted on <i>CA40</i> base layer	95
4.16	Number of tests conducted on <i>ISAC</i> trial embankment layers . .	96
4.17	Number of tests conducted on <i>ISAC</i> embankment and capping layers	96
4.18	Number of tests conducted on <i>ISAC</i> base layer	96
5.1	Results from identification tests	102
5.2	Coefficients of compressibility (λ_c) and of unloading (λ_u)	103

5.3	Peak and critical state failure envelope parameters M_{peak} , M_{cs} and c and respective internal friction angle (ϕ) obtained from triaxial multistage tests	111
5.4	Isotropic and anisotropic consolidation parameters, Γ and λ , determined from <i>SC</i> triaxial tests	111
5.5	Power law C and n parameters corresponding to regressions on E_{sec}, σ_1 plane determined from <i>SC</i> triaxial tests for $\varepsilon = 0.5\%$ and $\varepsilon = 1.0\%$	114
5.6	Peak and critical state failure envelope parameters M_{peak} , M_{cs} and c and respective ϕ obtained from triaxial multistage tests	119
5.7	Isotropic and anisotropic consolidation parameters, Γ and λ , determined from <i>CA31.5</i> triaxial tests	121
5.8	Power law C and n parameters corresponding to regressions on E_{sec}, σ_1 plane determined from <i>CA31.5</i> triaxial tests for $\varepsilon = 0.5\%$ and $\varepsilon = 1.0\%$	121
5.9	Values of parameters C , n , and coefficient of determination R^2 from regression lines at isotropic stress state	126
5.10	Values of parameters C , n , and coefficient of determination R^2 from regression lines at anisotropic stress state	126
5.11	Values of parameters C , n , and coefficient of determination R^2 from normalised shear modulus ($e = 0.331$) regression lines at isotropic stress state	127
5.12	Values of parameters C , n , and coefficient of determination R^2 from normalised shear modulus ($e = 0.331$) regression lines at anisotropic stress state	127
6.1	State conditions of <i>SC</i> trial layers obtained from <i>SCM</i> and <i>NM</i> after calibration for the last energy level (12 passes)	135
6.2	State conditions of <i>CA31.5</i> trial layers obtained from <i>SCM</i> and <i>NM</i> after calibration for the last energy level (12 passes)	137
6.3	Comparison of the settlements measured with the one point measuring system, through the hole in the center (second loading cycle) or on the loading plate 2 cm away from the center (third loading cycle), and with the three point measuring system	139
6.4	Synthesis of <i>SPLT</i> for the energy level corresponding to 12 Passes of the vibrating roller	141
6.5	Initial and final soil profile for all stages in the inversion procedure regarding <i>SASW</i> carried out on grid <i>B6</i>	148
6.6	Initial and final soil profile in the inversion procedure regarding <i>SASW</i> carried out on grid <i>B6</i> and considering state conditions in grid <i>B7</i>	149
6.7	Initial and final soil profile for all stages in the inversion procedure regarding <i>SASW</i> carried out on grid <i>B9</i>	150
6.8	Initial and final soil profile in the inversion procedure regarding <i>SASW</i> carried out on grid <i>B9</i> and considering state conditions in grid <i>B10</i>	151
6.9	Field and laboratory state conditions and modulus regarding <i>SC</i> geomaterial	163
6.10	State conditions, average E_{v2} modulus and corresponding strain level for <i>SC</i> layers for the last energy level (12 passes)	164

7.1	State conditions of <i>SP</i> trial and embankment layers obtained from <i>NM</i> after calibration for the last energy level at each layer	173
7.2	Average modulus E_{SPLT} obtained from <i>SPLT</i> carried out on trial and base layers, for the last energy levels	173
7.3	Initial and final soil profile for first attempt including all stages in the inversion procedure (light hammer test)	176
7.4	Initial and final soil profile for second attempt including all stages in the inversion procedure (light hammer test)	176
7.5	Initial and final soil profile for first attempt including all stages in the inversion procedure (<i>LFW</i> D test)	179
7.6	Initial and final soil profile for second attempt including all stages in the inversion procedure (<i>LFW</i> D test)	179
7.7	Initial and final soil profile for first attempt including all stages in the inversion procedure (<i>FWD</i> test)	181
7.8	Initial and final soil profile for second attempt including all stages in the inversion procedure (<i>FWD</i> test)	181
7.9	Moduli obtained from <i>SPLT</i> and performance related tests (<i>LFW</i> D, <i>SSG</i> and <i>FWD</i>) carried out on <i>CA40</i> base layer: tests performed on the same grid and average moduli	184
7.10	Field and laboratory state conditions and modulus regarding <i>SP</i> geomaterial	188
7.11	Sensors characteristics used for vibration measurements	190
7.12	Peak in-ground strains measurements obtained from <i>LFW</i> D tests carried out on <i>SP</i> and <i>ISAC</i> profiles	190
7.13	Peak in-ground acceleration measurements and computed peak displacements obtained from <i>LFW</i> D tests carried out on <i>SP</i> and <i>ISAC</i> profiles	193
7.14	In-ground peak displacements computed from accelerometers signals and respective theoretical and estimated strains at capping layer during <i>LFW</i> D tests	194
7.15	Peak in-ground strains measurements obtained from <i>FWD</i> tests carried out on <i>SP</i> and <i>ISAC</i> profiles	197
7.16	Peak in-ground acceleration measurements and computed peak displacements obtained from <i>FWD</i> tests carried out on <i>SP</i> and <i>ISAC</i> profiles	199
7.17	In-ground peak displacements computed from accelerometers signals and respective theoretical and estimated strains at the top of capping layer during <i>FWD</i> tests	199
7.18	In-ground peak displacements computed from accelerometers signals and respective theoretical and estimated strains at the bottom of capping layer during <i>FWD</i> tests	200
7.19	Peak in-ground strains measurements obtained from Portancemètre tests carried out on <i>SP</i> and <i>ISAC</i> profiles	200
7.20	Peak in-ground acceleration measurements and computed peak displacements obtained from Portancemètre tests carried out on <i>SP</i> and <i>ISAC</i> profiles	202
7.21	Sensors characteristics used for vibration measurements	203
7.22	Peak in-ground strains and accelerations measurements and computed displacements obtained during drum pass over <i>SP</i> capping layer	204

7.23	In-ground peak strains, accelerations and computed displacements obtained during performance of different mechanical tests on <i>SP</i> capping layer	210
7.24	In-ground peak strains, accelerations and computed displacements obtained during performance of different mechanical tests on <i>ISAC</i> capping layer	210
7.25	comparison of displacement and strain response stress ratio obtained from <i>LFWD</i> (300 mm loading plate diameter) and <i>FWD</i> (450 mm loading plate diameter)	211
7.26	Sensors characteristics used for vibration measurements	214
7.27	Frequency domain results for vibration on the three profiles	220
C.1	Statistical data obtained from <i>SCM</i> and <i>NM</i> tests carried out on <i>SC</i> trial layer 0.30 m $w_{OPM-2\%}$	271
C.2	Statistical data obtained from <i>SCM</i> and <i>NM</i> tests carried out on <i>SC</i> trial layer 0.40 m $w_{OPM-2\%}$	272
C.3	Statistical data obtained from <i>SCM</i> and <i>NM</i> tests carried out on <i>SC</i> trial layer 0.50 m $w_{OPM-2\%}$	272
C.4	Statistical data obtained from <i>SCM</i> and <i>NM</i> tests carried out on <i>SC</i> trial layer 0.40 m w_{OPM}	272
C.5	Statistical data obtained from <i>SCM</i> and <i>NM</i> tests carried out on <i>SC</i> trial layer 0.40 m $w_{OPM+2\%}$	273
C.6	Statistical data obtained from <i>SCM</i> and <i>NM</i> tests carried out on <i>CA31.5</i> trial layer 0.22 m w_{OPM}	273
C.7	Statistical data obtained from <i>SCM</i> and <i>NM</i> tests carried out on <i>CA31.5</i> trial layer 0.30 m w_{OPM}	274
C.8	Statistical data obtained from <i>SPLT</i> following standards AFNOR NF P94-117-1 (using settlement measuring system in three concentric points on periphery of the loading plate) and DIN 18134 carried out on all trial layers	275
C.9	Statistical data obtained from <i>SPLT</i> following standard AFNOR NF P94-117-1 (using settlement measuring system in the center of the loading plate)	276
C.10	Statistical data obtained from <i>LFWD</i> carried out on all trial layers, for all energy levels	277
C.11	Statistical data obtained from <i>FWD</i> carried out on 0.40 m w_{OPM} , for energy level corresponding to twelve Passes of the vibrating roller	278
C.12	Statistical data obtained from <i>SSG</i> carried out on all trial layers, for all energy levels	278
C.13	Statistical data obtained from Portancemètre carried out on all trial layers, for all energy levels	279
D.1	Statistical data obtained from <i>SCM</i> and <i>NM</i> tests carried out on <i>SP</i> trial layer with 0.30 m thickness	283
D.2	Statistical data obtained from <i>SCM</i> and <i>NM</i> tests carried out on <i>SP</i> trial layer with 0.40 m thickness	283
D.3	Statistical data obtained from <i>NM</i> tests carried out on <i>SP</i> trial layer with 0.50 m thickness	284

D.4	Statistical data obtained from <i>NM</i> tests carried out on <i>SP</i> embankment layers	284
D.5	Statistical data obtained from <i>NM</i> and <i>RBM</i> tests carried out on <i>ASIC</i> trial layer with 0.30 m thickness	285
D.6	Statistical data obtained from <i>NM</i> and <i>RBM</i> tests carried out on <i>ASIC</i> trial layer with 0.40 m thickness	285
D.7	Statistical data obtained from <i>NM</i> and <i>RBM</i> tests carried out on <i>ASIC</i> trial layer with 0.50 m thickness	285
D.8	Statistical data obtained from <i>NM</i> tests carried out on <i>ISAC</i> embankment layers	286
D.9	Statistical data obtained from <i>LFWD</i> carried out on <i>SP</i> trial and embankment layers, for all energy levels and on <i>CA40</i> base layer	287
D.10	Statistical data obtained from <i>LFWD</i> carried out on <i>ISAC</i> trial and embankment layers, for all energy levels	288
D.11	Statistical data obtained from <i>FWD</i> carried out on <i>ISAC</i> capping layer, for the last energy level	289
D.12	Statistical data obtained from <i>FWD</i> carried out on base layer, for the last energy level	289
D.13	Statistical data obtained from <i>SSG</i> carried out on <i>SP</i> trial and embankment layers, for all energy levels	290
D.14	Statistical data obtained from <i>SSG</i> carried out on <i>ISAC</i> trial and embankment layers, for all energy levels	290
D.15	Statistical data obtained from Portancemètre carried out on <i>SP</i> trial and embankment layers, for all energy levels	291
D.16	Statistical data obtained from Portancemètre carried out on <i>ISAC</i> trial and embankment layers, for all energy levels	292
D.17	Statistical data of peak vertical drum acceleration during successive passes of the roller compacter on the three profiles	293
D.18	Statistical data of vertical drum displacement during compaction on the three different sections	294
D.19	Total strain (ε_z) and cyclic portion ($\Delta\varepsilon_z$) due to vibrating roller passes on base layer	295

Glossary

$A_{0.5\Omega}$	acceleration amplitude of the subharmonic component of the vibration
$A_{2\Omega}$	acceleration amplitude of the first harmonic component of the vibration
A_{Ω}	acceleration amplitude of the fundamental component of the vibration
C	constant
C_u	coefficient of uniformity
D_{max}	maximum diameter
F	force
$F(t)$	force time history
FTA	applied force by the vibrating wheel
F_{dr}	force applied by the shaker
F_e	eccentric force of the drum
F_{stat}	static force of the drum
F_s	soil–drum interaction force
I_P	plasticity index
K_{flex}	stiffness of the flexible plate
K_{gr}	stiffness of the ground
L	drum length
M	slope of the projection of the critical state line in (q, p')
R	drum diameter
S_r	Saturation degree
V	velocity of the SSG foot
V_1	velocity at the rigid foot
V_2	velocity at the flexible plate
V_{Ac}	S–waves velocity determined with accelerometers
V_{BE}	S–waves velocity determined with bender elements
V_R	Rayleigh wave velocity
V_p	P–wave velocity
V_s	shear wave velocity
X_1	displacement of the rigid foot
X_2	displacement of the flexible plate
Γ	intercept of critical state line in the plane (v, p') at $p' = 1$ kPa
Ω	circular vibration frequency
χ	fractional cross sectional area of the soil occupied by water
\ddot{z}_d	acceleration of the drum
δ	displacement of the plate

$\delta(t)$	plate deflection time history
δ_c	center deflection of the plate
\dot{u}	estimated velocity
\dot{z}_d	velocity of the drum
γ	Volumetric water content
$\gamma_{max\ field}$	field maximum dry unit weight
$\gamma_{max\ lab}$	laboratory maximum dry unit weight
λ	compressibility index
λ_R	wavelength
λ_c	coefficient of compressibility
λ_u	coefficient of unloading
E_{field}^{nor}	normalised field modulus
E_{field}^{nor}	normalised laboratory modulus
E_0	maximum Young modulus
E_{sec}^{nor}	normalised secant modulus
E_{sec}	secant modulus
E_{vib}	vibration modulus
E	Young's modulus
G_0	maximum shear modulus
S_{air}	air-entry value
WOPM+2%	moisture content 2% wet of optimum Modified Proctor
WOPM-2%	moisture content 2% dry of optimum Modified Proctor
WOPM-4%	moisture content 4% dry of optimum Modified Proctor
WOPM	moisture content equal to optimum Modified Proctor
μ_a	pore air pressure
μ_w	pore water pressure
ν	Poisson's ratio
ω	angular frequency
ϕ	internal friction angle
ψ	total suction
ρ	density
σ	total normal stress
σ'	effective normal stress
$\sigma_{0\ max}$	maximum average normal stress below the plate
σ_3	minor principle stress
σ_{FWD}	stress below the plate of the <i>FWD</i>
σ_{LFWD}	stress below the plate of the <i>LFWD</i>
σ'_v	effective vertical stress
φ	phase angle
a_1	factor of the smooth load settlement curve
a_2	factor of the smooth load settlement curve
ac_{p+}	positive peak acceleration
ac_{p-}	negative peak acceleration
acd_{p+}	Drum peak negative acceleration
acd_{p+}	Drum peak positive acceleration
c	cohesion
c'	effective cohesion
$c_{apparent}$	apparent cohesion
c_f	damping constant of the frame

c_s	soil damping
c_t	suspension damping
d	layer thickness
e	void ratio
e_w	water ratio
f	frequency
$f(e)$	void ratio function
g	gravitational acceleration
g	gravitational constant
k	stiffness computed by <i>SSG</i>
k_f	stiffness of the suspension elements of the drum
k_{plate}	coefficient of stiffness of the plate
k_s	roller-determined stiffness
k_t	suspension stiffness
m_d	mass of the drum
m_e	eccentric rotating mass
$m_{e}r_e$	eccentric moment of unbalanced mass
m_f	mass of the frame
m_{int}	mass of the internal components attached to the rigid foot and of the foot
n	number of test frequencies
p	total mean stress
p'_u	capillary stress
q	deviator stress
r	radius of the plate
s	suction
t	time
v	specific volume
w	filter paper gravimetric water content
w_L	liquid limit
w_P	plastic limit
z_2	settlement of the plate during second load cycle
$z_d(max)$	theoretical maximum drum displacement
z_d	displacement of the drum
z_f	displacement of the frame
I_{rig}	coefficient of rigidity
BBDM	Benkelman Beam Deflection Measurement
CA31.5	crushed aggregate 0/31.5
CA40	crushed aggregate 0/40
CVR	Centre for Waste Valorisation
CV	Coefficient of Variation
ETRE	Évora Trial Railway Embankment
FCT/UNL	New University of Lisbon
FCT	Foundation for Science and Technology
FTRE	Fafe Trial Railway Embankment
FWD	Falling Weight Deflectometer
GW-GM	well-graded gravel with silt and sand
ISAC	Inert Steel Aggregate for Construction
IST	Technical University of Lisbon

<i>LEC-UM</i>	Laboratory of Civil Engineering of University of Minho
<i>LFWD</i>	Light Falling Weight Deflectometer
<i>LNEC</i>	National Laboratory of Civil Engineering
<i>NM</i>	Nuclear Method
<i>RBM</i>	Rubber Balloon Method
<i>REFER</i>	Portuguese National Railways Network
<i>SCM</i>	Sand Cone Method
<i>SC</i>	clayey sand
<i>SN</i>	Portuguese Steel Companies
<i>SP</i>	poor-graded silty sand
<i>SSG</i>	Soil Stiffness Gauge
<i>UM</i>	University of Minho
<i>SASW</i>	Spectral Analysis of Surface Waves
<i>BE</i>	Bender Elements
<i>CCC</i>	Continuous Compaction Control
<i>CCV</i>	Continuous Compaction Value
<i>CETE</i>	Center d'Études Techniques de l'Équipement
<i>CMV</i>	Compaction Meter Value
<i>LabVIEW</i>	Laboratory Virtual Instrumentation Engineering Workbench
<i>OE</i>	Oedometer test
<i>Qc/Qa</i>	Quality control/Quality assurance
<i>RC</i>	Relative Compaction
<i>RMV</i>	Resonance-Meter-Value
<i>SWCC</i>	Soil Water Characteristic Curve
<i>THD</i>	Total Harmonic Distortion
<i>TX</i>	Triaxial test
<i>TXI</i>	Triaxial isotropic test
<i>TXM</i>	Triaxial multistage test
<i>TXS</i>	Triaxial test with measurement of S-waves velocity
<i>VCL</i>	Virgin Compression Line
<i>WRC</i>	Water Retention Curve

Chapter 1

Introduction

1.1 Motivation

The structural behaviour of railways embankments and railtrack layers are strongly influenced by compaction conditions. Usually railways embankments and railtrack layers are constructed on compacted geomaterials that are typically in unsaturated condition during construction and may remain in that condition during the working life of the structure. Several design and maintenance measures are undertaken to maintain unsaturated conditions because they provide favorable engineering materials properties, namely shear strength and deformability.

In practice, routine rail track design is based on rational methods using Young modulus (E) and Poisson's ratio (ν). These parameters are generally determined in terms of total stresses, even though materials used in railways construction are not completely saturated or completely dry. This approach is conservative to varying degrees to that the influence of soil suction is ignored, although it plays a fundamental role on the hydro-mechanical behaviour. In turn, the hydro-mechanical behaviour is influenced by compaction conditions. To this end, the influence of compaction conditions on the hydro-mechanical behaviour assumes great importance.

Traditionally, compaction control is carried out by means of different spot check methods, used systematically or statistically, aimed at determining the geomaterials state parameters (density and moisture content) or layers deformability (E modulus). Even though state parameters of geomaterials are not the most desired engineering properties, it has used widespread for many years because it can be easily determined via weight and volume measurements. The measurement of geomaterial density and moisture content allows the determination of relative compaction and moisture content deviation which are in fact parameters used on compaction control. Although state parameters enable to determine if adequate compaction has been achieved, it does not allow controlling the characteristic values normally considered in design. Therefore, it is current to determine the E modulus, which is an important design parameter for embankments, particularly, to transportation infrastructure. This property is usually evaluated by means of static plate load tests (*SPLT*). However, the current quality control/quality assurance (Q_c/Q_a) methods are time consuming,

labor-intensive and costly. For instance, the determination of density with the water balloon method takes about 45 minutes excluding the time for weighting and drying the sample and the radiometric probe test takes about 5–15 minutes, as a *SPLT* takes at least 30 minutes, besides the need of heavy equipment to guarantee reaction force. The main reason for the adoption of such quality control methods is their relatively simplicity and can be applied to generate data for a statistical evaluation of compaction quality (Lenke *et al.*, 2003).

The strict requirements on quality construction of railway embankments, namely, high-speed railways, demands higher quality compaction control. The reduce construction time, the required high homogeneity of mechanical properties of compacted layers in order to avoid overcompaction and to minimize relative settlements of the embankment platform during serviceability conditions, thus, seeking to minimize the exploration costs, are important aspects that distinguish this structures from conventional earthworks, like road embankments.

Recently, there is a strong trend towards using stiffness and strength to control compaction given the importance of these mechanistic properties in pavement materials evaluation (Briaud, 2001; Loizos *et al.*, 2003; Alshibli *et al.*, 2005; Edil and Sawangsurya, 2005). Mechanistic properties are a measure of quality since non-uniformity of stiffness and/or strength is directly related to progressive failures and life-cycle cost. Moreover, the design method of pavements is based on engineering parameters of materials such as their stiffness and/or strength, which results in a missing link between the design process and construction quality control. As a result, the Q_c/Q_a procedures of construction should be based on a criterion that closely correlates to the performance parameters used in the design.

Increasing demands for better, cheaper and faster compaction control have lead to technology improvements. In this context, devices for field test evaluation of mechanical properties of geomaterials have been recently developed, namely: impact tests (falling weight deflectometer – *FWD* and light falling weight deflectometer – *LFWD*), the soil stiffness gauge (*SSG*) and Spectral Analysis of Surface Waves (*SASW*). These are non-destructive spot tests methods which can be conducted independently and in conjunction with conventional moisture content and density testing improving statistical evaluation and allowing variability reduction, thus substantially enhance construction quality of the entire earthwork. This notwithstanding, these new devices involves different test methods which are not standardised and, therefore, it demands their in situ evaluation.

Compaction is commonly carried out by vibrating rollers which vibration frequency and amplitude is kept constant and the operator chooses the roller speed. Compaction of a certain area is carried out by parallel strips (edge to edge or with some overlapping) covering each strip with a fixed number of passes. However, a certain number of passes and a constant roller speed, vibration frequency and amplitude do not necessarily lead to a homogeneous compaction result on a layer due to variation in material properties, water content of the layer being compacted, and stiffness of the underlying layer. A constant number of passes and constant roller parameters will often leave a certain part of the area insufficiently compacted, another part over-compacted and the rest sufficiently compacted (Briaud and Seo, 2004). Therefore neither proof rolling nor the demand to compact until no further deformation behind the compacting drum will ever be able to meet modern requirements on a homogeneous compaction

result (Thurner and Sandström, 2000).

Though new spot test methods may represent an improvement on Q_c/Q_a , spot test method can never reliably represent the compaction result of the entire area. In addition, some of these test methods requires the delay or stop construction work, because the tests have to be carried out without any disturbing vibrations around the test spot. Regarding high quality projects as high speed railways, where rigorous deformation criteria of the structure soil–railtrack must be satisfied, continuous compaction control (CCC) approach represents a fairly improvement. In this scope, in the early years equipments promoting CCC have been developed, namely, Portancemètre (Quibel, 1999) and devices embarked on the roller drum (Thurner and Sandström, 1980; Adam, 1996; Thurner and Sandström, 2000; Anderegg, 2000; Anderegg and Kaufmann, 2004; Mooney and Rinehart, 2007). Moreover, if a feedback control of one or more of the roller drum vibration parameters (vibration frequency, force amplitude, and forward velocity) is employed, then compaction control could be done by compaction equipment itself and optimization of compaction could be achieved independently of equipment’s operator resulting, in that so called intelligent compaction.

However, the relationship between dynamic loads, namely those applied by dynamic tests (*LFWD*, *FWD* and Portancemètre) and vibratory roller behaviour, and in situ dynamic response is not well understood. A better understanding of the in–ground dynamic behaviour of the soil in response to the loadings imparted by these devices will aid in the development of CCC as well as the refinement and acceptance of rapid spot test devices.

1.2 Objectives

The main objective of this research work is to investigate the influence of compaction on the behaviour of railway embankments and consequently for high quality road embankments. This is seeking through laboratory and field investigations.

Field investigation consists on two full scale trial that have been performed on a railway embankment and another trial has been carried out on a road embankment. The execution of these trials was greatly conditioned by the impossibility to fully perform the initially planned work, in the aim of a cooperation protocol between the National Railway Network and and four national research institutions (University of Minho, *UM*; National Laboratory of Civil Engineering, *LNEC*; New University of Lisbon, *FCT/UNL*; and Technical University of Lisbon, *IST*) to develop the knowledge concerning the methodology for the construction and control of the railway embankments and rail track layers for high speed trains. This was established under the framework of a national research project POCI/ECM/61114/2004, entitled “Interaction soil–rail track for high speed trains”, financed by the Foundation for Science and Technology (*FCT*). In this protocol was planned:

- Execution of a trial embankment to establish a methodology of construction for optimization of embankments performance;
- Construction and observation of two definitive railway embankments, one built according to traditional technologies of construction and control, and

another built according with the new technologies of construction and control. During the construction of definitive embankments instrumentation and monitoring during and post construction would be done. This would allow comparison of performances from the two embankments, as well as eventual comparison with numerical models developed in this context.

In the aim of this protocol it was only possible to perform the trial embankment, which is called hereafter Évora Trial Railway Embankment (*ETRE*).

However, another contract between the Centre for Waste Valorisation (*CVR*) and Portuguese Steel Companies (*SN*), including University of Minho, allows to obtain more knowledge about this subject also under the framework of another National Research program founded by *FCT*. In fact, a trial road embankment was constructed, giving the possibility to carry out different studies using spot and continuous compaction control tests, as well as the instrumentation of the embankment and road layers to measure vibrations and strains induced by the compaction equipment and dynamic tests. Hereafter this trial embankment is referred to as Fafe Trial Road Embankment (*FTRE*).

Field investigation aimed to study the influence of compaction conditions, specifically, water content, compaction energy level and layers thicknesses on the behaviour of compacted layers, particularly, mechanical behaviour. Attempting to get a higher degree of homogeneity in what concerns to state parameters, the water adding procedure employed on earth dams is used on both full scale trials. Furthermore, focus is given to the establishment of a methodology for quality control of compacted layers by using spot methods and continuous approach. In this scope, new devices for field test evaluation of mechanical properties of geomaterials, namely: *LFWD*, *FWD*, *SSG*, *SASW* and Portancemètre, will be evaluated using *SPLT* as a reference test. Correlations between *SPLT* and performance related tests are attempted. In addition, the evolution of modulus, relative compaction and moisture content with the number of passes is investigated in order to understand the influence of state conditions on the mechanical performance of trial layers. Moreover, the homogeneity of either state parameters and mechanical properties will be evaluated for the last energy level and compared with specifications given in literature. Finally, field tests results and laboratory tests results will be compared attempting to establish a link between design mechanical properties usually obtained from laboratory investigation and actual in situ mechanical properties.

Concerning to *ETRE*, two geomaterials employed in railway embankment and railway track layers were studied (clayey sand and crushed aggregate). In addition to aforementioned, the *SPLT* was performed following two commonly used standards (AFNOR NF P94-117-1 (2000) and DIN 18134 (2001)) with the objective to develop a specification of the plate loading test to be used as a reference method. This specification project will be then employed on *FTRE*.

With regards to *FTRE*, it is intended to study compaction conditions, specifically, compaction energy level and layers thicknesses, of two geomaterials traditionally employed in road embankments (poor-graded silty sand and a crushed aggregate) and another resulting from processed steel slag aggregates produced in National Iron and Steel Company (inert steel aggregate for construction – *ISAC*). In addition, on *FTRE* it is intended to investigate the in-ground response of compacted geomaterials during field testing with *SPLT*, *LFWD*, *FWD*, Portancemètre and vibrating roller drum. To this end, in-ground strain

gauges and accelerometers were installed in embankment layers to measure in-situ static and dynamic response. Furthermore, the roller was outfitted with accelerometers to monitor drum acceleration seeking to explore the relationship between roller drum vibration characteristics and underlying soil properties, namely soil stiffness.

The laboratory investigation aims to study the influence of compaction molding water content on the hydro-mechanical behaviour of two geomaterials (clayey sand and a well graded gravel) employed on *ETRE*, reproducing in situ state conditions. The laboratory investigation regarding material employed on *FTRE* was performed in the scope of another doctoral thesis (Reis Ferreira, 2010). Large strain domain will be investigated for both materials, where strength and stiffness parameters will be determined through a multistage procedure and compared to single stage procedure. Specimens will be compacted to the same dry density and with different molding water contents, including the ones employed on field investigation, in order to study the influence of moisture content on strength and stiffness. Focus will be given to clayey sand characterization. Besides large strain tests, also investigation on the very small strain domain of clayey sand will be carry out, where stiffness will be determined by means of seismic wave measurements. A technique employing bender elements in conjunction with accelerometers will be attempted aiming to evaluate the advantages of this procedure on seismic measurements of high stiffness materials. Further, modulus degradation curves will be computed to verify if fits a reference threshold for sands given in literature. In addition, hydro characterization (suction-water content relationship) will be performed in order to highlight the influence of unsaturated condition on the small and large strain mechanical behaviour.

1.3 Thesis layout

The work presented in this thesis has been divided in eight chapters. Following this chapter, Chapter 2, entitled **Compaction**, presents a general overview of compaction equipments and technologies and of compaction control. With respect to former issue, focus is given to devices embarked on compactors and intelligent compaction. Concerning the latter issue, specifications for high speed embankments and rail track layers are addressed and new techniques on spot tests method, namely *SSG*, *FWD*, *LFWD* and *SASW*, as well as continuous test method by means of Portancemètre are highlighted.

Chapter 3, entitled **The influence of compaction on the hydro-mechanical behaviour of geomaterials**, reviews basic concepts on unsaturated geomaterials and describes the influence of compaction conditions on the hydro-mechanical behaviour of either saturated and unsaturated geomaterials. It first starts to present suction phenomena on unsaturated geomaterials and measuring techniques focusing on filter paper method, which was employed in this research work, and to present the soil water characteristic curve (SWCC), also known as soil water retention curve (WRC), which empirically describes the relationship between water content and suction. Then, stress state variables are addressed, where the effective stress approach and independent state variable approach are presented. Finally, the influence of compaction variables, namely, molding water content, compaction energy and compaction method, on the WRC, stiffness, compressibility and strength of either saturated and unsaturated materials are

reviewed.

Chapter 4, entitled **Experimental program**, presents the experimental program adopted, which was developed in three parts, namely, a laboratory investigation and field investigation performed on a railway embankment and another field investigation carried out in a road embankment. Laboratory investigation involves physical, hydro and mechanical characterization of geomaterials employed in field investigations. Laboratory tests are briefly described and tests state conditions are summarized. The field investigation is divided accordingly to the type and location of trial embankments: Évora railway trial embankment (*ETRE*) and Fafe road trial embankment (*FTRE*). The methodology adopted in field investigations is described, namely, materials and experimental plan. Furthermore, regarding *FTRE*, the instrumentation of an experimental section with in-ground accelerometers and strain gauges, as well as the instrumentation of a roller drum with two accelerometers is described.

Chapter 5, entitled **Laboratory investigation**, presents the results obtained from physical, hydro and mechanical characterization of materials employed in field investigations. Main results are presented for the geomaterials studied, yet focus is given to the results on the very small strains.

Chapter 6, entitled **Field investigation: Évora trial railway embankment (*ETRE*)**, deals with the results obtained from in situ tests. Firstly, the state conditions obtained from sand cone method (*SCM*) and nuclear method (*NM*) on each trial layer are presented. Secondly, moduli obtained from *SPLT*, *LFWD*, *SSG*, Portancemètre, *FWD* and *SASW* are presented. Concerning *SPLT*, comparison between moduli obtained from *SPLT* using two measurement devices is carried out. In addition, comparison between moduli obtained from direct interpretation of *SPLT* following AFNOR NF P94-117-1 (2000) and DIN 18134 (2001) standards is carried out, as well as, comparison between moduli obtained from the interpretation of *SPLT* to the same stress and method. Following results presentation, comparison between moduli obtained from different tests is carried out by material type. Then, analysis of the evolution of modulus, relative compaction and moisture content with the number of passes is presented and homogeneity of these parameters are evaluated for the last energy level. Finally, field tests results and laboratory tests results are compared.

Chapter 7, entitled **Field investigation: Fafe trial road embankment (*FTRE*)**, presents the main results obtained from in situ tests. Similarly to previous chapter, the state conditions obtained from *SCM*, *NM* and rubber ballon method (*RBM*) on each trial and embankment layers are presented. Secondly, moduli obtained from *SPLT*, *LFWD*, *SSG*, Portancemètre, *FWD* and *SASW* are presented, following comparison between moduli obtained from different tests is carried out by material type. Then, analysis of the evolution of modulus, relative compaction and moisture content with the number of passes is presented and homogeneity of these parameters is evaluated for the last energy level. Further, field tests results and laboratory tests results are compared. Finally, results from monitoring of roller drum and in-ground vibrations during compaction and application of dynamic loads from *LFWD*, *FWD*, Portancemètre and roller drum are presented.

Chapter 8, entitled **Conclusions**, summarizes the main conclusions gathered throughout this research work. The limitations and obstacles encountered in this research are also revealed, which suggest room for further improvements and developments.

Chapter 2

Compaction

2.1 Introduction

In soil mechanics soil compaction means the mechanical action that might lead to a decrease of void ratio, mainly achieved by the volume reduction of the gas phase. It is generally understood as a quick process, even sudden sometimes, through which it seeks to introduce in the soil marked structural changes in order to create a new type of storage of particles.

In general the performance of a soil, specifically their characteristics, shear strength, deformability and permeability, depend on its void ratio. Thus, the lower the void ratio, the greater is usually its shear strength and less are deformability and its permeability. Exception must be made, however, to “sensitivity” materials, such as clay materials, to which this behaviour does not apply (Guedes de Melo, 1985). Therefore, reducing the soil’s void ratio by compaction, it is possible to improve its performance to future loadings. Compaction is, therefore, a critical element in the construction of transportation infrastructure (highways, railways, airports, etc.) and energy infrastructures (earth dams).

In what follows a brief review of compaction equipments and technologies will be presented focusing on devices embarked on compactors and intelligent compaction. Then, compaction control will be addressed and new techniques on spot tests method, namely soil stiffness gauge (*SSG*), falling weight deflectometer (*FWD*) and light falling weight deflectometer (*LFWD*), and spectral analysis of surface waves (*SASW*), as well as continuous test method by means of Portancemètre will be reviewed in detail.

2.2 Compaction equipments and technologies

Rollers are widely used for compacting soil, fill, and asphalt. The selection of roller depends on characteristics of material to be compacted and machine parameters. Material characteristics are related to layer thickness and material properties like grain size distribution, maximum grain size and grain shape, water content, water and air permeability. The machine parameters include total roller weight and static drum load, static or dynamic compaction, and the diameter and surface shape of the drum (smooth or sheepfoot). In case of

dynamic compaction it must be considered the direction of resulting dynamic contact force, excitation frequency and theoretical drum amplitude.

Traditionally, soil and rock fill materials are compacted with static or vibrating rollers. Rollers with static drums use the effective dead weight of the machine to apply pressure on the surface. Thus, soil particles are pressed together and the void content is reduced. Adequate compaction with static rollers is normally achieved only in the upper layers of the material, i.e., the effective depth of static compaction is limited.

As reported by Adam and Kopf (2000), dynamic rollers make use of a vibrating or oscillating mechanism, which consists of one or more rotating eccentric weights. During dynamic compaction, a combination of dynamic and static load is used. The dynamically excited drum delivers a rapid succession of impacts to the underlying surface where the particles are set in motion by the transmission of compressive and shear waves. These vibrations eliminate periodically the internal friction between particles and facilitate, in combination with the static load, the rearrangement of the particles into positions that result in a lower void ratio and a higher density. Furthermore, the increase in the number of contact points and planes between the grains leads to higher stability, stiffness, and lower long-term settlement behaviour. If dynamic load is applied vertically or horizontally, rollers are denominated as vibratory or oscillatory, respectively. However, by means of two counter-rotating exciting masses, there are roller which enables the application of vertical, inclined and horizontal loads, as is illustrated in Figure 2.1. That is the case of, for example, the VARIO roller developed by BOMAG Company.

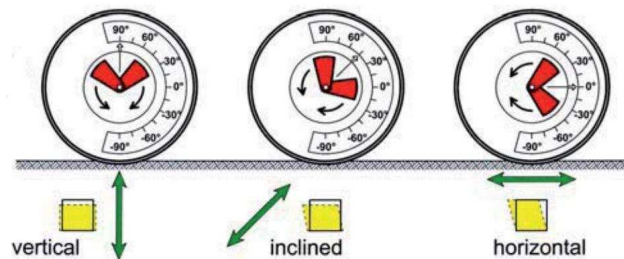


Figure 2.1: Adjustable excitation direction of a VARIO roller drum and compaction effect (Adam and Kopf, 2000)

More recently there has been an increasing interest in vibration-based monitoring of roller compactors to provide continuous assessment of the soil mechanistic properties, namely stiffness and/or modulus, during compaction process. With this aim, devices are embarked on compactors and roller-based measures of soil compaction are determined, e.g. relative indices or soil stiffness. If feedback control is employed on compactors, then so called intelligent compaction is achieved.

2.2.1 Devices embarked on compactors

Thurner and Sandström (2000) reported the early research in Sweden that revealed that motion behaviour of dynamically excited roller drum changed in

dependence of the soil response. A test roller had been equipped with triaxial accelerometers, a mini roller behind the compacting roller was intended to register vibrations passing from the large to the mini roller and triaxial geophones were buried in the ground in order to measure ground vibrations, as shown in Figure 2.2.

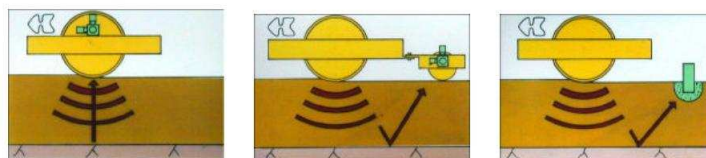


Figure 2.2: Test recordings of vibrations on the roller, a mini roller and geophones (Thurner and Sandström, 2000)

Simultaneous recordings from all sensors were analysed and it was found that the accelerometer on the roller gave significant changes in the time history of the sensor signal. The changes could be related to the increase of the stiffness in the layer, documented by spot tests after each roller pass. The evaluation of these tests led to the development of roller integrated compaction using the roller drum as the measuring tool for instant and continuous compaction control (Thurner and Sandström, 2000). This was the starting point which led roller's constructors to propose devices embarked on compactors with the following purposes:

- provide instantly and continuously relative information to the roller operator, enabling him to evaluate where compaction work is finished, where additional passes are required and what sections cannot be sufficiently compacted with the present roller;
- get an indication concerning the bearing capacity of a layer at the end of compaction.

In 1978, Geodynamik developed and introduced the compaction meter and the compaction meter value (CMV) and many of the roller manufacturers, e.g., Caterpillar, Ingersoll Rand, subsequently adopted the Geodynamik CMV-based system. In the late 1980s, Bomag developed the Omega value and corresponding Terrameter. The Omega value provided a continuous measure of compaction energy. In the late 1990s, Bomag then developed a measurement value E_{vib} which provides a measure of dynamic soil modulus (Kröber and Floss, 2001). Ammann followed suit with the development of a soil stiffness parameter k_s (Anderegg and Kaufmann, 2004).

In the following sections are explained the various roller-determined dynamic measurement values in use today, namely compaction meter value (CMV), Omega value, roller-determined stiffness (k_s) and vibration modulus (E_{vib}).

Compaction Meter Value (CMV)

Compaction meter is a product of the Swedish company Geodynamic AB and the first patent was taken out in 1978. Forssblad (1980) showed that various indices incorporating drum acceleration amplitude and the amplitude of

its harmonics (i.e., multiples of the excitation frequency) could be correlated to soil compaction and underlying stiffness. Adam (1996) showed that the force amplitude “F” of the drum blows is proportional to the first harmonic of the vertical acceleration, and the displacement “s” during the blow can be approximated by the amplitude of the double integral of the fundamental acceleration component of the drum.

In this aim, Thurner and Sandström (1980) proposed the compaction meter value (CMV) following Equation 2.1:

$$\text{CMV} = C \cdot \frac{A_{2\Omega}}{A_{\Omega}} \quad (2.1)$$

where A_{Ω} is the acceleration amplitude of the fundamental component of the vibration; $A_{2\Omega}$ is the acceleration amplitude of the first harmonic component of the vibration, i.e., twice the eccentric excitation frequency (fig. 2.3); C is a constant established during site calibration ($C = 300$ is often used).

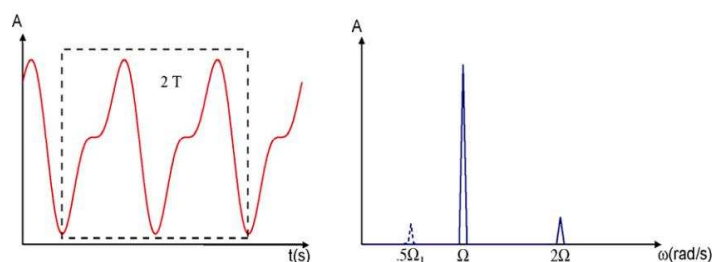


Figure 2.3: Method to determine CMV involves spectral analysis (right) of two cycles of vertical drum acceleration time history data (left) (Mooney and Adam, 2007)

It is known that the ratio of $A_{2\Omega}/A_{\Omega}$ is a measure of nonlinearity (Ewins, 2000; Mooney *et al.*, 2005). Concerning to roller–soil system if a roller with an excitation frequency of 30 Hz produces a 30 Hz drum acceleration response, than in a truly linear system the ratio $A_{2\Omega}/A_{\Omega}$ would be equal to zero. Since the drum acceleration response is distorted and not purely sinusoidal, therefore the roller–soil system is nonlinear. The non linear behaviour of the roller–soil system can be related to non linear elastic–plastic soil behaviour, to partial loss of contact occurs between roller drum and soil and to contact surface varying nonlinearly during each cycle of loading (Adam, 1996). Applying Fourier analysis it can be reproduced a distorted waveform by summing multiples of the excitation frequency. Therefore, the ratio $A_{2\Omega}/A_{\Omega}$ is a measure of the degree of distortion or nonlinearity.

Performing spectral analysis of the measured vertical drum acceleration over two cycles of vibration allow CMV determination (fig. 2.3). The reported CMV is the average of a number of two–cycle calculations. Geodynamik typically averages the values over 0.5 sec; however, this can be modified to meet the manufacturer needs. CMV precision is governed by 1% distortion resolution of the accelerometer. Per Equation 2.1, 1% acceleration distortion equates to $\text{CMV} = 3$ or ± 1.5 . Geodynamik reports less reliability for CMV below 8–10 (Mooney and Adam, 2007).

Former empirical investigations have revealed that the amount of the first harmonic increases with increasing soil stiffness, which means that progress of CMV is significantly influenced by the operating conditions (Adam and Kopf, 2000). Moreover, there is an auxiliary value that can be calculated in order to take into consideration the operating conditions of the drum. This value is measured continuously and presented in a form of a signal called RMV (Resonance–Meter–Value), which is defined by Equation 2.2:

$$\text{RMV} = \frac{A_{0.5\Omega}}{A_{\Omega}} \quad (2.2)$$

where $A_{0.5\Omega}$ is a subharmonic acceleration amplitude caused by jumping, i.e., the drum skips every other cycle.

The loading area from the cylindrical roller drum is a rectangular strip and the size of this area depends on roller parameters like roller size, vibration amplitude and frequency, forward velocity, soil type and stratigraphy underlying the soil being compacted. Thus the relationship between CMV and soil density, stiffness and modulus is empirical and is influenced by these parameters (Sandström and Pettersson, 2004; Mooney *et al.*, 2005). Hence, it is obvious that the actual CMV will vary from roller to roller and that the roller parameters, especially the frequency, have to be kept constant and equal to the parameters used during a calibration (Thurner and Sandström, 2000). Therefore, the use of CMV in continuous compaction control (CCC) requires careful calibration. The associated relationships developed during calibration must be strictly adhered to during subsequent site measurement (Mooney and Adam, 2007).

Several rollers manufactures, like Dynapac, Caterpillar and Ingersoll Rand (via Geodynamik equipment) currently use CMV for roller monitoring. Sakai recently introduced a Continuous Compaction Value (CCV) that, in addition to the fundamental and first harmonic, considers the first subharmonic (0.5Ω) and higher–order harmonics, following Equation 2.3 (Nohse and Kitano, 2002).

$$\text{CCV} = \left[\frac{A_{0.5\Omega} + A_{1.5\Omega} + A_{2.5\Omega} + A_{3\Omega}}{A_{2.5\Omega} + A_{3\Omega}} \right] \times 100 \quad (2.3)$$

Despite the fact that careful calibration should be done, using the roller as the measuring tool has great advantages, such as complete coverage of the area is obtained and that the result is received immediately. Figure 2.4 shows the components of the compaction meter. An accelerometer is attached to the bearing plate of the roller drum in vertical direction. The acceleration signal is analysed in the processor and the result is presented on a dial or display as the CMV.

Omega value

The Omega value is provided by Terrameter system which was developed by Bomag and Kröber (1988). The drum is fitted with a detector unit with two acceleration sensors arranged vertically which pick up the acceleration of the drum. The CCC technique is based on the measure of the energy transmitted to the soil (fig. 2.5). Considering the mass of the drum (m_d), the eccentric rotating mass (m_e), the static force (F_{stat}) and the eccentric force (F_e), the measurement of acceleration of the drum (\ddot{z}_d) and determination of drum velocity (\dot{z}_d) by

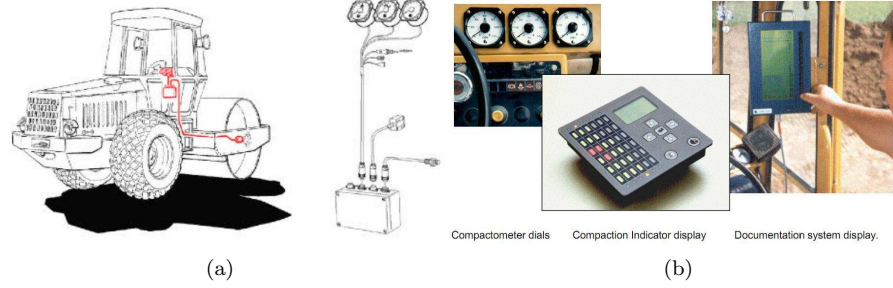


Figure 2.4: (a) Compaction meter components; (b) Different means to display the compaction result to the roller operator (Thurner and Sandström, 2000)

integrating the acceleration components allows the determination of the Omega value (eq. 2.4). This is determined by integrating the transmitted force F_s and drum displacement z_d time history over two consecutive cycles of vibration.

$$\Omega = \int_{2T} (-m_d \ddot{z}_d + (m_d + m_f)g + m_e r_e \Omega^2) z_d dt \quad (2.4)$$

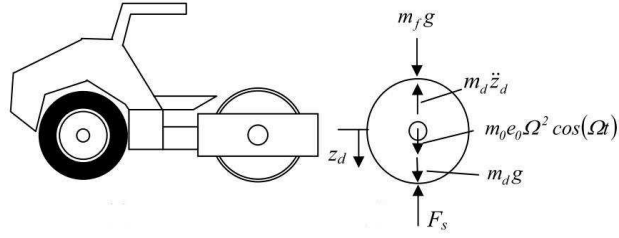


Figure 2.5: One-degree-of-freedom lumped parameter model representation of vibratory compactor (Mooney and Adam, 2007)

In a electronic unit a computer stores the data transmitted by the detector unit and provide to the roller operator in an analogue display the Omega value, while compaction process is in progress. Omega values may range from 0 to 1000, depending on status of compaction or stiffness and, for a certain measuring distance, can be viewed after each pass in a line or bar chart. The measuring system also provides information to roller operator whether further effective compaction passes are possible or not by means of two control lights on the control unit. For this purpose, the mean Omega value of a forward (reverse) pass is compared with the value of the previous forward (reverse) pass. The end of effective compaction work is indicated by a red control light which lights up when falling below a determined difference in values (Floss and Kloubert, 2000).

The Omega value is influenced by machine specific parameters, which are amplitude, frequency and working speed, as well as by soil specific parameters including those that describe stiffness, i.e., the strength and deformation characteristics, namely grain size distribution, plasticity, water content and density.

The influence of subsoil should be considered for layers with less than 1.50 meters (Floss and Kloubert, 2000).

Soil stiffness k_s

In the late 1990s, Ammann introduced a roller-determined soil stiffness parameter, k_s (Anderegg, 1998). A dynamic soil compactor produces nonlinear oscillations whose characteristics may be described analytically (Anderegg, 2000). Accordingly to several authors, Yoo and Selig (1979), Pietzsch and Poppy (1992), Adam (1996), Anderegg and Kaufmann (2004) and Anderegg *et al.* (2006), among others, the vertical kinematics of the soil-drum-frame system can be represented as a lumped parameter model, as illustrated in Figure 2.6.

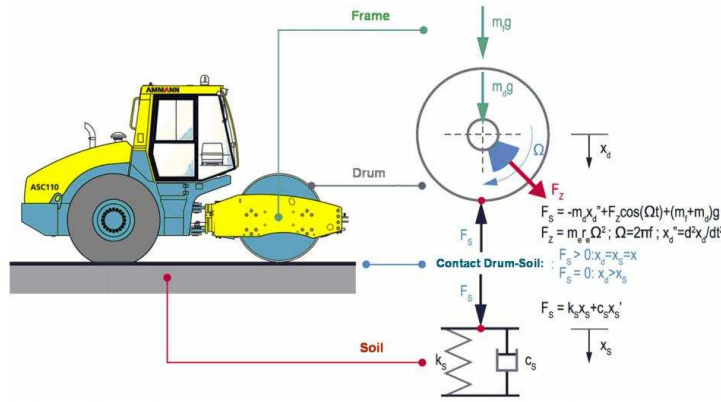


Figure 2.6: Analytical model of vertical vibration of a single drum roller (circular excitation) (Anderegg *et al.*, 2006)

The vibration roller can be subdivided into the frame and the drum. The frame, with mass m_f , consists of the engine, the cabin and the drive which is supported in the drum via elastic suspension elements with stiffness, k_f , and damping constant, c_f . Together with the rubber elements represents a second order lowpass with a natural frequency of 3 to 4 Hz, which dampens excitation frequencies. The drum, with mass, m_d , contains an eccentric rotating unbalanced mass, m_e , which generates the drum vibrations together with the soil at frequency, f . In analytical terms, the steady-state dynamic behaviour of the soil-machine system is defined as in Equations 2.5 and 2.6 (Anderegg and Kaufmann, 2004), where the soil is represented with a Kelvin-Voigt spring-viscous dashpot model.

$$\begin{aligned} F_s &= -m_d \ddot{z}_d + m_e r_e \Omega^2 \cos(\Omega t) + k_t(z_d - z_f) + c_t(\dot{z}_f - \dot{z}_d) + m_f g \\ 0 &= -m_f \ddot{z}_f + k_t(z_d - z_f) + c_t(\dot{z}_f - \dot{z}_d) + m_f g \end{aligned} \quad (2.5)$$

$$\begin{aligned} F_s &= k_s z_d + c_s \dot{z} \text{ if } F_s \geq 0 \\ F_s &= 0 \text{ else} \end{aligned} \quad (2.6)$$

The dot notation signifies the differentiation with respect to time and m_d is drum mass (kg), f is frequency of excitation (Hz), m_f is frame mass (kg),

Ω is circular vibration frequency (Hz), $m_e r_e$ is eccentric moment of unbalanced mass (kg.m), z_d is displacement of drum, k_s is soil stiffness (MN/m), z_f is displacement of frame, c_s is soil damping (MN.s/m), k_t is suspension stiffness (MN/m), c_t is suspension damping (MN.s/m), t is time, and g is gravitational acceleration (9.81 m.s^{-2}).

Anderegg and Kaufmann (2004) proposed an approach wherein the soil stiffness is solved for at the point where the drum is in its down-most position (where $z_d = 0$). This approach reduces the problem to a single variable and allows for a real time solution for k_s . It also assumes that any effect on the drum due to the frame inertia is negligible. Mooney and Rinehart (2007) states that while this assumption is satisfactory for single drum rollers where the ratio of the drum mass to the frame mass is typically between 1.5 and 2, it is less valid for tandem rollers, where the ratio of the drum mass to the frame mass can be lower. The equation for the soil-drum interaction force (F_s) become defined as Equation in 2.7.

$$F_s = -m_d \ddot{z}_d + m_e r_e \Omega^2 \cos(\Omega t) + k_t(z_d - z_f) + m_f g \quad (2.7)$$

The drum inertia force and eccentric force time histories can be determined via measurement of drum acceleration and phase angle φ , i.e., eccentric position. The drum displacement amplitude z_d is determined via spectral decomposition and integration of the measured peak drum accelerations (Anderegg and Kaufmann, 2004). The resulting F_s versus z_d response is graphically illustrated in Figure 2.7 for continuous contact and partial uplift behaviour. Solving the equation of motion for k_s when the drum velocity is zero yields Equation 2.8.

$$k_s = 2\pi^2 f^2 \left[m_d + \frac{m_e r_e \cos(\varphi)}{z_d} \right] \quad (2.8)$$

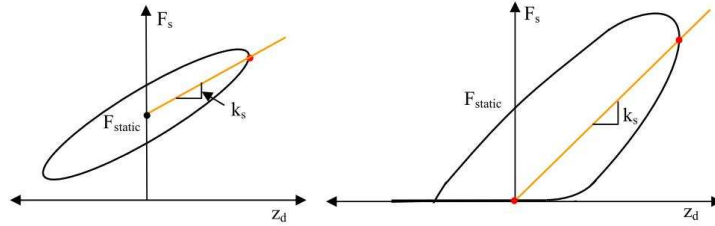


Figure 2.7: Illustration of k_s during contact (left) and partial loss of contact behavior (right) (Mooney and Adam, 2007)

With this approach, the damping, c_s , is eliminated from the calculation, and a quasi-static stiffness, k_s , independent of the exciting frequency, is obtained. Investigations performed by Anderegg and Kaufmann (2004) with a tandem roller vibrating on compacted subgrade with a constant static unbalanced mass, $m_e r_e$, and a variable excitation frequency f from 25 to 50 Hz, showed that the associated stiffness, k_s , is independent of frequency in that frequency range (fig. 2.8). For highest frequencies the system started to become dependent on the machine dynamics, and the measured stiffness values were higher than the static ones because of the wave propagation effects.

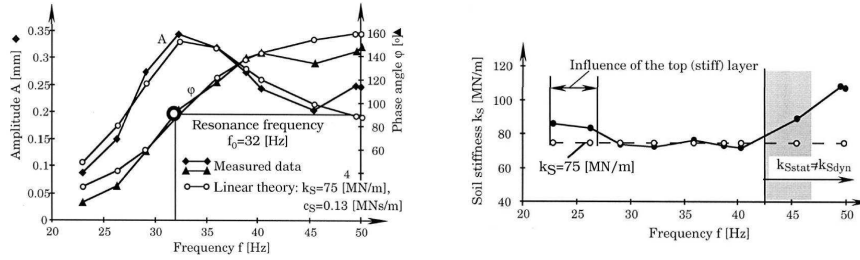


Figure 2.8: Measurement of soil stiffness of homogeneous subsoil (Anderegg and Kaufmann, 2004)

E_{vib} modulus

E_{vib} modulus is the more recent Bomag measurement value (Kröber and Floss, 2001). The principle is identical to the one described above for k_s . A lumped parameter vibration and cylinder on elastic half-space theory is used on its determination. The drum/soil assembly is modeled as shown previously in Figure 2.5. Similarly to Ammann technology, Bomag employs two accelerometers to measure vertical drum acceleration (frame inertia is neglected) which enables to compute drum displacement. Phase angle (φ) is calculated and enables the determination of the contact force F_s per equilibrium of forces. The combination of F_s and z_d data yield contact force–drum deflection curves from which secant stiffness can be extracted, as illustrated in Figure 2.9.

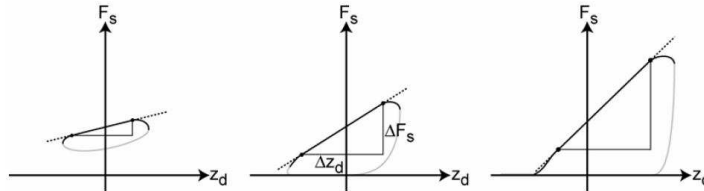


Figure 2.9: Contact force–drum displacement behaviour (Mooney and Adam, 2007)

The relationship between the measured stiffness and vibration modulus E_{vib} , can be established through the application of Hertz and Lundberg's theoretical solutions for a rigid cylinder resting on a homogeneous, isotropic elastic half-space (Lundberg, 1939). Investigations made by Hertz in 1895 and further developments by Lundberg in 1939 gave the relationship between the load on a roller and the imprint area created by the roller. Lundberg's theory is a static solution and relates z_d , F_s , drum length L and diameter R to Poisson's ratio ν and Young's modulus E of the half-space as shown in Equation 2.9.

$$z_d = \frac{2(1-\nu^2)}{\pi E} \frac{F_s}{L} \left(1.8864 + \ln \frac{L}{b} \right) \quad (2.9)$$

$$b = \sqrt{\frac{16R(1-\nu^2)}{\pi E L} F_s}$$

The relationship between the stiffness k_s and the modulus, E , can also be established on an experimental basis by performing the roller tests and plate tests in parallel. Ammann reports on a study from ETH Zurich in Switzerland which was conducted to establish such a relationship (Preisig *et al.*, 2003). Figure 2.10 shows a relationship between the stiffness k_s obtained from the roller and the moduli M_{E1} and M_{E2} from the first load and reload of the plate test. The figure shows a reasonable relationship with some scatter.

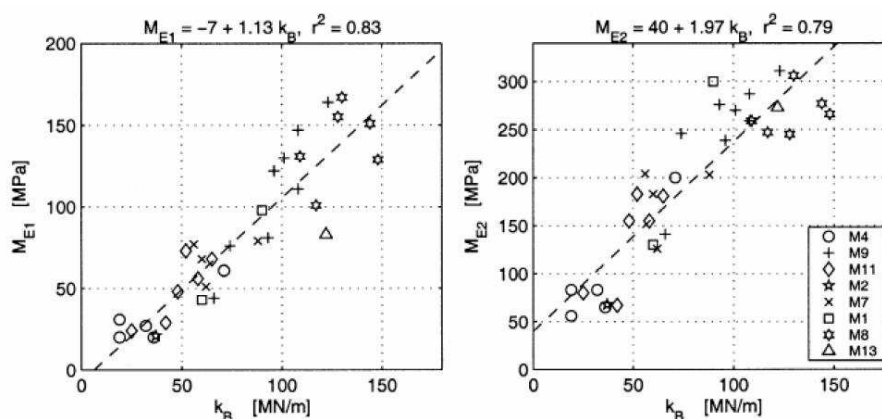


Figure 2.10: Stiffness ($k_B = k_s$) vs. Modulus (Preisig *et al.*, 2003)

Comparison between CMV, Omega value, k_s and E_{vib}

Through numerical simulations of roller-soil behavior using finite element analysis of a roller vibrating on an elastic half-space Adam and Kopf (2004) explored the influence of soil Young's modulus on roller measurement values (E modulus in Figure 2.11). The y-axis in Figure 2.11 depicts the relative drum vibration amplitude, i.e., the ratio of z_d to the theoretical maximum $z_{d(max)}$ given by the ratio between eccentric static moment ($m_{e r_e}$) and mass of the drum (m_d). In addition, zones corresponding to the drum operation under different conditions depending on roller and soil parameters are delimited (Adam, 1996). Five operating conditions specified in Figure 2.12 can occur; definition criteria are the contact condition between drum and soil and the drum motion cycle as a multiple of the excitation cycle.

In Figure 2.11 one can see how relative amplitude and soil modulus influences the behaviour of roller drum during compaction (contact modes). Focusing on continuous contact and partial uplift modes, CMV is very low and constant when the drum is operating in contact mode, regardless of soil modulus. CMV increases as soil modulus increases during partial uplift, thus is sensitive to soil stiffness. However, CMV at a constant soil modulus is amplitude dependent; therefore, a higher eccentric force will yield a greater CMV for the same soil. The amplitude dependence of CMV is more pronounced for softer soils than for stiffer soils. The Omega value was found to be much less sensitive to underlying soil stiffness for constant amplitudes and strongly amplitude dependent.

Parameter k_s was found to increase with soil modulus and is amplitude dependent during partial uplift. It decreases with increasing amplitude during

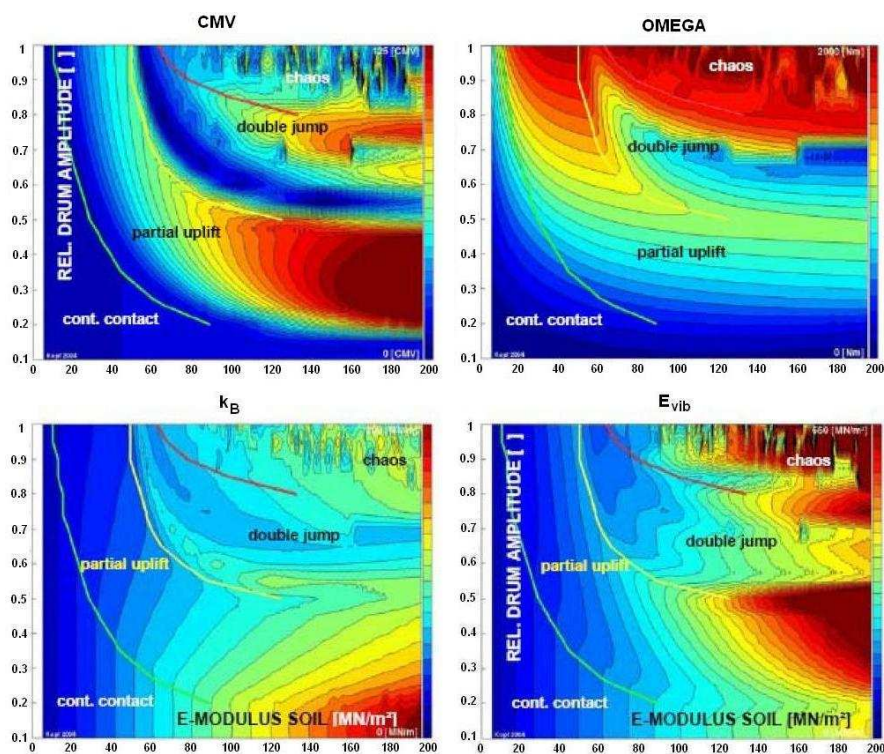


Figure 2.11: Variation of roller measurement value with soil modulus and relative drum vibration amplitude—results of numerical simulations (Adam and Kopf, 2004)

partial uplift, particularly for stiffer soil. The amplitude–dependence of soil stiffness was also demonstrated in field testing by Mooney and Rinehart (2007). Similarly to k_s , E_{vib} is sensitive to changes in soil modulus during continuous contact and partial uplift modes. An increase in soil modulus leads to an increase in E_{vib} . Though E_{vib} exhibits little or no amplitude dependence in continuous contact mode, amplitude dependence increases with increasing amplitude during partial uplift. This amplitude dependence is more pronounced for stiffer soil.

From Figure 2.11 one may conclude that all parameters exhibit amplitude dependence at a constant soil modulus. Mooney and Rinehart (2007) investigated the various roller parameters that determine the soil stiffness, namely drum acceleration and phase lag, as well as the influence of underlying heterogeneity on roller measured soil stiffness. The investigators found that roller determined soil stiffness was strongly dependent on vibration amplitude, and that underlying heterogeneity (e.g., near surface bedrock) presents a significant challenge to the interpretation of data from roller–integrated measurement systems.

2.2.2 Intelligent compaction

As seen in previous section, compaction control could be included in the compaction process through devices embarked on the rollers enabling continuous monitoring and identification of soil properties, i.e. continuous compaction

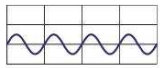
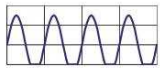
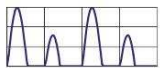
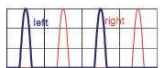
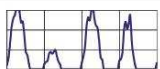
drum motion	Interaction drum-soil	operating condition	soil contact force	application of CCC	soil stiffness	roller speed	drum amplitude
periodic	continuous contact	CONT. CONTACT		yes	low	fast	small
	periodic loss of contact	PARTIAL UPLIFT		yes	↓	↑	↓
		DOUBLE JUMP		yes			
		ROCKING MOTION		no			
chaotic	non-periodic loss of contact	CHAOTIC MOTION		no			

Figure 2.12: Operating conditions of a vibratory roller drum (Adam, 1996)

control (CCC). If, in addition, a feedback control of one or more of the following: vibration frequency, force amplitude, and forward velocity is employed, then compaction control could be done by compaction equipment itself and optimization of compaction could be achieved independently of equipment's operator. This is the basis of intelligent compaction.

Anderegg and Kaufmann (2004) describes the technical conditions required for intelligent compaction, which are shown in Figure 2.13. The vibration behavior of the drum-soil system is measured by using vertically fitted acceleration sensors; the phase lag between the excitation and the displacement of the drum is obtained from the measurement of the point when the exciter unit passes 0 and the point when the measured and doubly integrated acceleration passes 0, that is, the amplitude signal. The roller speed is also measured.

These data are forwarded to the electronic device, where the required variables (e.g., phase angle, soil force, and soil stiffness) are calculated, and the commands to the final controlling elements (differential gear box and hydraulic vibration pump) are generated. When the instructions are executed, the control loop is closed, and the compactor becomes a closed feedback control system that is completely observable and completely controllable. In addition, the control system has an operating panel and a display that shows the machine operator the compaction achieved and the optimum roller speed.

The limit of reasonable use of a vibratory roller is imposed by the nonlinearity behaviour of the drum vibration, which is caused by periodic loss of contact from the soil with the inception of bouncing and rocking. Since nonlinearity is controlled by force, the concept control system is based on restriction of a maximum force. The maximum soil reaction force is controlled to a value that guarantees the smooth entry of power into the soil, depending on the compaction material and the layer thickness. In addition, an analysis of the state of motion ensures that no subharmonic vibrations occur. Expressed in analytical terms, the machine parameters are controlled according to (Anderegg and Kaufmann, 2004):

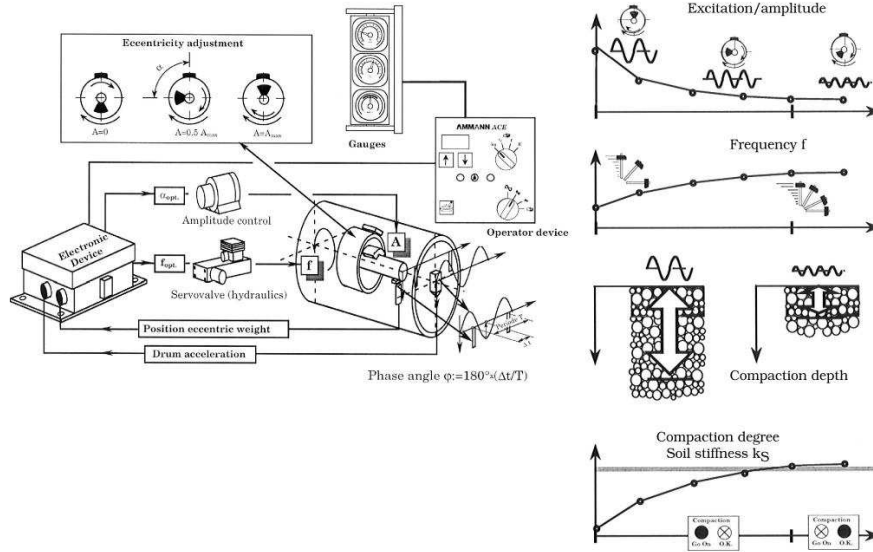


Figure 2.13: Feedback control system for rollers with data (Anderegg and Kaufmann, 2004)

- (i) the excitation frequency Ω in such a way that $\varphi = \varphi_{setpoint}$;
 $140^\circ < \varphi_{setpoint} < 160^\circ$;
- (ii) the eccentric momentum of the unbalanced mass, $m_e r_e$ in such a way that
 $F_{s\ max} = \text{setpoint value}$ ($F_{s\ max}$ as per Equation 2.7);
- (iii) if subharmonic vibrations occur, $m_e r_e$ is reduced immediately;
- (iv) the roller speed is optimal if the impact space is between 2 and 4 cm.

However, roller-measured soil stiffness has been found to vary with excitation force amplitude and frequency (Adam, 1996; Anderegg and Kaufmann, 2004; Mooney and Rinehart, 2007). This behaviour is particularly pertinent regarding intelligent compaction since these parameters are continuously varied in an attempt to promote faster and more uniform compaction. To advance the understanding and capabilities of CCC in vertically homogeneous and layered earth structures as well as the measurement of soil properties during intelligent compaction, the relationship between roller-measured soil stiffness and in situ stress-strain response was explored and characterized by Mooney and Rinehart (2009) and Rinehart and Mooney (2009).

Stress and strain sensors were placed at multiple depths within both vertically homogeneous (clayey sand) and heterogeneous (crushed rock over silt) test beds. Triaxial stress-strain behavior was captured during static and vibratory passes of two commercially available intelligent compactors over a range of typical excitation force frequencies and amplitudes.

Mooney and Rinehart (2009) found roller-measured stiffness to decrease with increasing vibrating force for tests on the vertically homogeneous clayey

sand. This behaviour was attributed to the stress-dependent modulus reduction observed in situ. On the crushed rock over silt layered test bed, roller-measured stiffness increased with increasing vibrating force despite the mild stress-dependent modulus reduction observed in the crushed rock. Authors argues that the ratio of vertical stress in the crushed rock to vertical stress in the underlying silt increased with vibrating force indicate that the crushed rock toked on a greater portion of the load. Because the crushed rock was 4-5 times stiffer than the underlying silt, the composite roller-measured stiffness increases accordingly.

The investigations carried out by Rinehart and Mooney (2009) showed that measured vertical stresses with depth matched well with those estimated using Hertzian cylinder contact theory applied to a homogeneous, linear elastic half space. One unique aspect of curved-drum loading was that the contact area changes as a function of applied force and stiffness of the soil. The contact width was found to strongly influence the resulting vertical stress profiles.

Further, both investigations showed that cyclic strains induced by drum vibration were only 15-25% of those induced by static loading. Authors pointed out this aspect because roller based stiffness measures are based on cyclic drum deformation and the cyclic portion of strain is a reflection of the drum deformation used in the roller-based stiffness calculation. These small magnitudes were attributed to curved drum interaction with the soil and to viscoelasticity. During vibration, the drum/soil contact force equals the static force a cyclic force that is a function of vibrating force and drum inertia. Contact stress and contact area are non linearly related to force and vertical drum deflection, and lead to a hardening type relationship between applied force and drum deflection as depicted in Figure 2.14. The deflections (and in turn strains) due to drum vibration are smaller than the deflections resulting from static loading.

To sum up, roller-measured stiffness and its dependence on vibrating force was found to be influenced by the stress-dependent modulus function of each soil, the varying drum/soil contact area, and by layer characteristics modulus ratio, thickness when layering is present. The interplay between these and other factors (e.g., dynamics, rate dependent response) will dictate the nature of roller-measured stiffness dependence on vibrating force (Mooney and Rinehart, 2009).

2.3 Compaction control

The increasing requirements on quality construction in order to avoid over-compaction and to minimize relative settlements of the embankment platform, as well as to minimize the exploration costs, demands higher quality on soil compaction control. It is meant by compaction control the group of operations taken over compacted layers with the purpose of guarantee that the characteristics assumed in project are being achieved in construction.

In project are considered several parameters values, such as, unit weight, shear strength, deformability and permeability. The compaction control should focus on the distributions of values exhibited by each of these parameters. But happens that the direct and individual control of these parameters requires a lot of work and is time consuming, which is incompatible with the rhythm of construction. Therefore, the control is in general done by an indirect way,

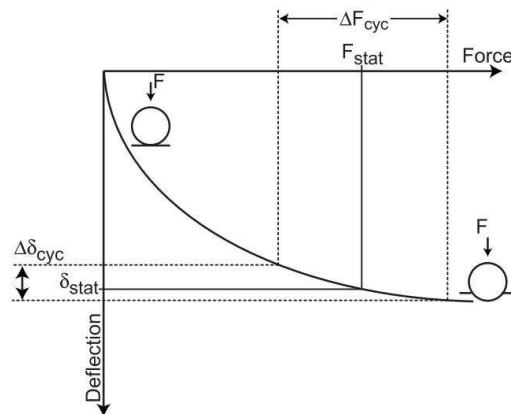


Figure 2.14: Hardening response induced by the curved drum (Rinehart and Mooney, 2009)

through the control of certain characteristics that assure the compaction quality of embankments.

As already mentioned compaction of soil increases its density and produces three important effects: (1) increase in the soil's shear strength, (2) decrease in future settlement of the soil, and (3) decrease in soil's permeability. Thus, soil density is one of the indirect parameters which allow the embankments quality control. Even though soil density is not the most desired engineering property, traditionally it is used by the transportation industry to specify, estimate, measure, and control soil compaction. This practice was adopted many years ago because soil density can be easily determined via weight and volume measurements. The most common methods used for density measurement are sand cone replacement, water balloon and nuclear method.

The measurement of material density allows the determination of relative compaction which is in fact the parameter used on compaction control. In first place, optimum water content and the maximum dry unit weight ($\gamma_{max\ lab}$) are determined in the laboratory by either the standard or modified Proctor test. Then, target values are defined for compacted field dry unit weight ($\gamma_{d\ field}$). Relative compaction (RC) can be expressed as $\gamma_{d\ field}/\gamma_{max\ lab}$. In most specifications for earthwork, the contractor is required to achieve a relative compaction of 90 to 95%.

Although referred compaction control parameters permits to determine if adequate compaction has been achieved, it does not allow controlling all the characteristic values normally considered in project. Therefore, it is current to determine the E modulus, which is an important design parameter for embankments projected, for example, to transportation infrastructure, namely high speed railways.

Further, high quality compaction involves not only a high degree but also a high uniformity of compaction. Experience and long-term monitoring have disclosed that the mechanical behaviour, serviceability index and lifetime of a road or railway depend widely on the compaction degree and homogeneity/uniformity of the multi-layered railway structure. The interactions were investigated intensively already 35 to 30 years ago and resulted in detailed recommendations

(Brandl, 1977), including variation coefficient moduli from plate load tests (one test for $\geq 200 \text{ m}^2$) and for density measurements (replacement method – one test for $\geq 300 \text{ m}^2$, nuclear method – one test for $\geq 150 \text{ m}^2$).

To sum up, traditionally, compaction is controlled by means of different spot test methods, used systematically or statistically, aimed at determining the materials density or the E modulus of the layers in different spots. These current quality control/quality assurance (Qc/Qa) methods are time consuming, labor-intensive and costly. For instance, the determination of density with the water balloon method takes about 45 minutes excluding the time for weighing and drying the sample and the radiometric probe test takes about 5 to 15 minutes, as a plate loading test takes at least 30 minutes, besides the need of heavy equipment to guarantee reaction force. The main reason for the adoption of such quality control methods is their relatively simplicity and can be applied to generate data for a statistical evaluation of compaction quality (Lenke *et al.*, 2003).

Recently, there is a strong trend towards using stiffness and strength to control compaction given the importance of these mechanistic properties in pavement materials evaluation (Briaud, 2001; Loizos *et al.*, 2003; Alshibli *et al.*, 2005; Edil and Sawangsurya, 2005; Gomes Correia *et al.*, 2009a). Mechanistic properties are a measure of quality since non-uniformity of stiffness and/or strength is directly related to progressive failures and life-cycle cost. Moreover, the design method of pavements is based on engineering parameters of materials such as their stiffness and/or strength, which results in a missing link between the design process and construction quality control. As a result, the Qc/Qa procedures of construction should be based on a criterion that closely correlates to the performance parameters used in the design.

Increasing demands for better, cheaper and faster compaction control have lead to technology improvements. In this context, equipments for field test evaluation of mechanical properties of geomaterials have been recently developed, such as, impact tests (Falling Weight Deflectometer – *FWD* and Light Falling Weight Deflectometer – *LFWD*), the Soil Stiffness Gauge (*SSG*), Spectral Analysis of Surface Waves (*SASW*). These are non-destructive spot tests which can be conducted independently and in conjunction with conventional moisture density testing improving statistical evaluation and allowing variability reduction, thus substantially enhance construction quality of the entire earthwork (Edil and Sawangsurya, 2005). Further, equipments enabling continuous evaluation of mechanical properties like Portancemètre had been developed, which represents a great improvement on compaction control. However, these equipments are not normalized and its use demands calibration to reference test given in compaction control specifications (Gomes Correia *et al.*, 2009a). In this scope, in the following section are addressed specifications adopted by countries where high speed railways have been constructed. Further, the aforementioned devices were used in the aim of the present thesis and, therefore, a detail review of each one will be addressed.

2.3.1 Specifications for high speed embankments and rail track layers

There are several aspects that governs high-speed railway embankments and distinguishes from other conventional transportation infrastructure, like road

embankments. High-speed railway embankments demands an infrastructure exhibiting an overall stiffness that limits maximum settlements and minimize relative settlements of the embankment platform during serviceability conditions (Martins *et al.*, 2009), in order to minimize the exploration costs, to avoid high level of discomfort for passengers and reduce induced vibrations on surrounding structures.

These aspects include strict requirements demands of high quality construction of embankment and railtrack layers regarding material quality, state parameters and mechanical properties limits, promoting homogeneity of mechanical behaviour of compacted layers. Requirements increase from bottom to top layers. The embankment layers should provide a stable foundation for the base (subballast) and ballast layers. The range of stiffness of the capping layers is believed to influence ballast, rail and sleeper deterioration, since the influence of the traffic induced stresses extends downwards as much as 5 meters below the bottom of the sleepers. Hence, embankment layers are a very important sub-structure component which as a significant influence on track performance and maintenance. Base layer (subballast) assumes great importance due to several aspects, e.g., to ensure better distribution of loads, to protect the underlying layer against erosion, to avoid seepage into the underlying layer and to prevent the penetration of fine soil material into the track bed, especially to the ballast.

In the scope of the present work focus is given to requirements regarding compaction control, namely, relative compaction and mechanical properties of compacted layers. In Table 2.1 is summarized the requirements regarding compaction control of embankment and railtrack layers in France and Taiwan, given by UIC (2004) and THSRP (2003), respectively.

Table 2.1: High-speed railway specifications (UIC, 2004; THSRP, 2003) regarding relative compaction and mechanical properties of compacted layers

Layer type	THSRP (2003)		UIC (2004)	
	$\gamma_{dOPM} \geq$ [%]	$E_{v2} \geq$ [MPa]	$\gamma_{dOPS} \geq$ [%]	$E_{v2} \geq$ [MPa]
Base	100	120	103	120
Sub-base	95	80	100	80
Embankment	90	45* or 60**	95	45* or 60**

* fine soils; ** sandy and gravel soils;

OPM – Optimum Modified Proctor; OPS – Optimum Standard Proctor

Mechanical properties requirements are similar for all type of layers, whereas specifications only differ on requirements regarding relative compaction. Moreover, it is noteworthy that standards for determination of parameters also differ. Nevertheless, determination of relative compaction is straightforward, while E modulus determination following different standards yield differences either in the procedure and on the interpretation of test results. Accordingly to information from National Railway Network (*REFER*), UIC (2004) is followed regarding compaction control of new high-speed railway lines. This code specifies *SPLT* performance following French standard AFNOR NF P94-117-1 (2000) and German standard DIN 18134 (2001) as reference test for determination of E_{v2} . In this scope, a better insight on these standards will aid on understanding the major aspects that distinguish them.

2.3.2 Static plate loading test (*SPLT*)

The *SPLT* has been used for quality control of pavement structure layers for many years in many European countries. This test method allows the determination of the relationship between load and settlement (load–settlement curve), the aim being to assess the deformation and strength characteristics of soil and to determine the strain modulus.

The test consists of loading a circular plate on the top of the layer to be tested and measuring deflections under load increments. The load is transmitted to the plates by a hydraulic jack, acting against heavy mobile equipment as a reaction force, while the corresponding deflection is measured. French standard AFNOR NF P94–117–1 (2000) and German standard DIN 18134 (2001) are commonly used to perform *SPLT*.

AFNOR NF P94–117–1 (2000)

The test consists in the application, after a pre-load, of two successive loading cycles on a plate with normalized stiffness and diameter. For a 600 mm diameter plate, the first load cycle should correspond to a 0.25 MPa stress under the plate and this stress maintained till the plate's settlement stabilization. Following, the load is release at once. In the second load cycle it should be reach a stress under the plate of 0.20 MPa. The load release should be done only after the plate's settlement stabilization, as the first load cycle (fig. 2.15a). The modulus, E_{V2} , is calculated to the second loading cycle using Boussinesq solution and secant method as in Equation 2.10.

$$E_{V2} = \frac{\pi}{2} \cdot (1 - \nu^2) \cdot \frac{\sigma \cdot r}{z_2} \quad (2.10)$$

where ν is the Poisson's ratio, σ is the normal stress below the plate, r is the radius of the plate and z_2 is the settlement of the plate during second load cycle.

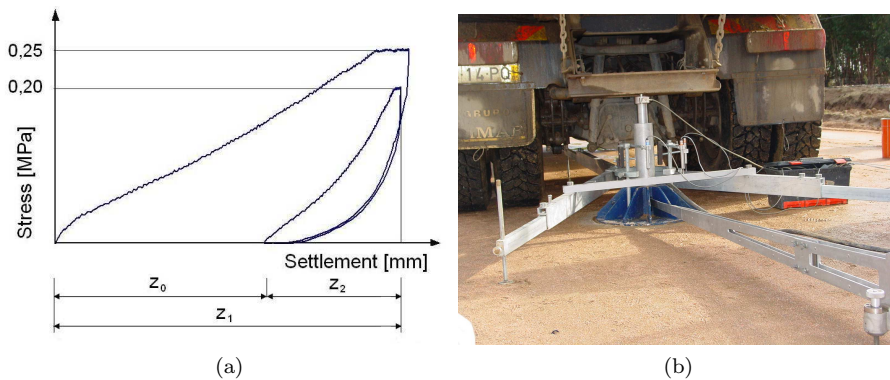


Figure 2.15: *SPLT* following AFNOR NF P94–117–1 (2000) standard

For measuring the settlement of the loading plate two different systems can be used. The first consists in a contact arm assembly which measures the settlement of the center of loading plate. The second consists on the settlement measuring of three concentric points on periphery of the loading plate distanced

of 120° (fig. 2.15b). For both systems, the supports of the measuring devices shall be positioned so stands located 1.5 m from the center of the loading plate.

DIN 18134 (2001)

To determine modulus, E_{V2} , the load shall be applied in not less than six stages, in approximately equal increments, until the required maximum normal stress is reached. Each increase in load (from stage to stage) shall be completed within one minute. The load shall be released in stages, to 50% and 25% of the maximum load and then to the load corresponding to the zero reading. Following that, a further (2nd) loading cycle shall be carried out, in which the load is increased only to the penultimate stage of the first cycle (fig. 2.16a).

A 300, 600 or 762 mm loading plate can be used. To determine the modulus for design calculations the load shall be increased until a settlement of 5, 8 or 13 mm, or a normal stress below the plate of 0.50, 0.25 or 0.20 MPa, respectively, is reached. If the required settlement is reached first, the normal stress measured at this stage shall be taken as maximum stress. In the present work, it was used a plate with 300 mm diameter. The strain modulus, E_{V2} , is calculated to the second loading cycle using the tangent method as in Equation 2.11.

$$E_{V2} = \frac{1.5 \cdot r}{a_1 + a_2 \cdot \sigma_{0max}} \quad (2.11)$$

where r is the radius, σ_{0max} is the maximum average normal stress below the plate and a_1 and a_2 are factors of the smooth load settlement curve corresponding to the second load cycle.

For measuring the settlement of the loading plate a contact arm assembly shall be used and supports shall be located 1.5 m from the center of the loading plate (fig. 2.16b).

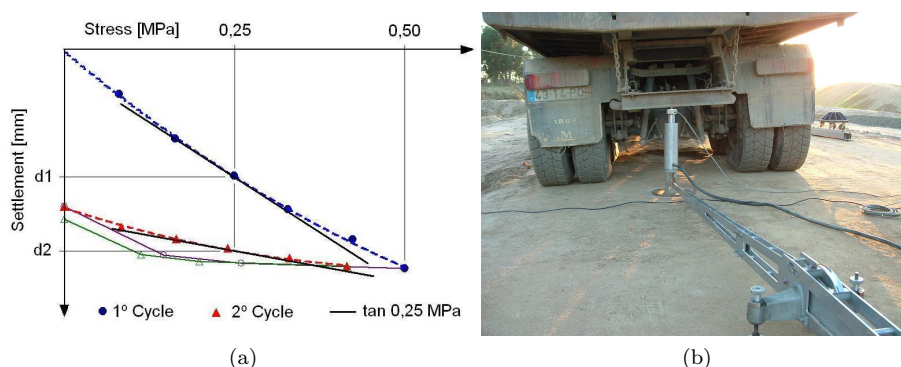


Figure 2.16: *SPLT* following DIN 18134 (2001) standard

2.3.3 New techniques on spot tests method (*SSG*, *FWD*, *LFWD*, *SASW*)

Soil Stiffness Gauge (*SSG*)

The *SSG* is manufactured by Humboldt Manufacturing Company and is a field hand portable instrument that nondestructively measures soil stiffness and soil modulus in a simple and rapid way (fig. 2.17). It is intended for the evaluation of compacted subgrade, subbase and base course layers, including treated materials, for use in roadways and embankments.

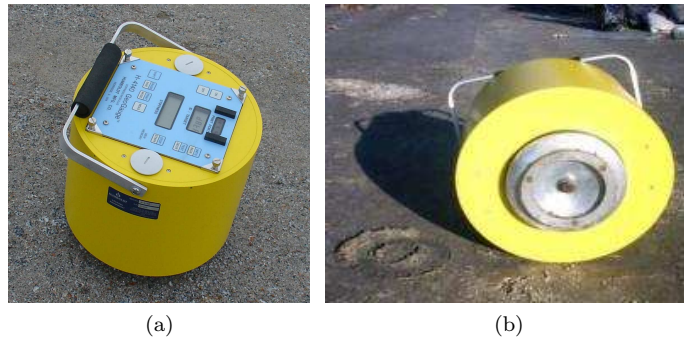


Figure 2.17: Humboldt Stiffness Gauge: (a) general aspect; (b) detail of ring shaped foot

The equipment weighs approximately 10 kg. It has a compact size of 28 cm in diameter by 25.4 cm in height. The device rests on the soil surface via a ring-shaped foot, which has an outside diameter of 114 mm and an inside diameter of 89 mm (fig. 2.17). The foot bears directly on the soil and supports the weight of the *SSG* via several rubber isolators.

A mechanical shaker, which is attached to the foot, excites the footing in the vertical mode from 100 to 196 Hz in 4 Hz increments, producing 25 different frequencies and generating a force of 9 N. The *SSG* has sensors that measure the force, F , and the velocity, V , of the foot (see fig. 2.18). The magnitude of the vertical displacement induced at the soil-ring interface is typically less than 1.27×10^{-6} m, which is measured using velocity sensors. A microprocessor computes the stiffness k (the layer's resistance to deflection) for each of the 25 frequencies, and the average value of the 25 measurements is displayed along with a standard variation.

The force applied by the shaker and transferred to the ground is measured by differential displacement across the internal flexible plate as in Equation 2.12. At the frequencies of operation, the ground-input impedance will be dominantly stiffness controlled (Eq. 2.13). Thus, the ground stiffness is given by Equation 2.14

$$F_{dr} = K_{flex} \cdot (X_2 - X_1) + \omega^2 \cdot m_{int} \cdot X_1 \quad (2.12)$$

$$K_{gr} = \frac{F_{dr}}{X_1} \quad (2.13)$$

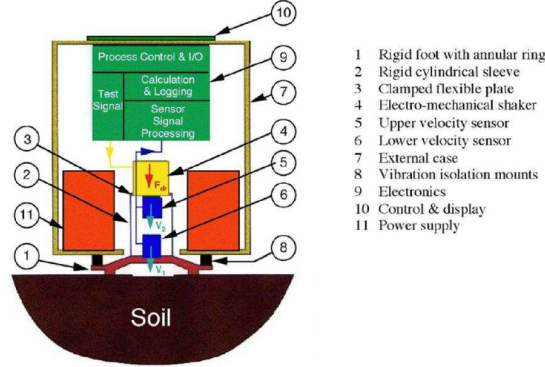


Figure 2.18: Humboldt Stiffness Gauge (Humboldt, 2007)

$$\begin{aligned}
 \bar{K}_{gr} &= K_{flex} \cdot \frac{\sum_1^n \left(\frac{X_2 - X_1}{X_1} \right)}{n} + \frac{\sum_1^n \omega^2}{n} \cdot m_{int} \\
 &= K_{flex} \cdot \frac{\sum_1^n \left(\frac{V_2 - V_1}{V_1} \right)}{n} + \frac{\sum_1^n \omega^2}{n} \cdot m_{int}
 \end{aligned} \tag{2.14}$$

where F_{dr} is the force applied by the shaker; K_{flex} is the stiffness of the flexible plate; X_2 is the displacement at the flexible plate; X_1 is the displacement at the rigid foot; $\omega = 2\pi f$, where f is frequency; m_{int} is the mass of the internal components attached to the rigid foot and of the foot; K_{gr} is the stiffness of the ground, n is the number of test frequencies used in the SSG; V_2 is the velocity at the flexible plate; V_1 is the velocity at the rigid foot.

This approach avoids the need for a non-moving reference for ground displacement and permits the accurate measurement of small displacements. The measured soil stiffness from the SSG can, in turn, be used to calculate the soil modulus of the underlying bound or unbound soil media. The applied force (F) and correspondent deflection (δ) are related with the outside radius of the ring-shaped foot (r), Young's modulus (E) and Poisson's ratio of the tested material through as in Equation 2.15 (Poulos and Davis, 1974).

$$F = \frac{1.77 \cdot r \cdot E}{(1 - \nu^2)} \cdot \delta \tag{2.15}$$

Considering that material's stiffness is given by Equation 2.16, the SSG stiffness k can then be converted to the soil elastic modulus E_{SSG} using the Equation 2.17:

$$k = \frac{F}{\delta} \tag{2.16}$$

$$E_{SSG} = \frac{k \cdot (1 - \nu^2)}{1.77 \cdot r} \tag{2.17}$$

These equations assume that the underlying soil is linear elastic, homogeneous, and isotropic. They also assume an infinite half space. The assumptions

of homogeneity, isotropy, and elasticity are frequently invoked in soil mechanics and pavement design when analyzing soil layers. However, the assumption of an infinite half space is arguably violated when one considers that underlying pavement layers are generally of finite depth (on the order of 20 cm) and are of increasing modulus with depth. Hence, any computation of elastic modulus from the *SSG* measured stiffness must be carefully evaluated (Lenke *et al.*, 2001).

The response is dominated by the stiffness of the underlying soil. The manufacturer specifies a range of stiffness measurement capability from 3 to 70 MN/m, which means an elastic modulus from 25 to 600 MPa. A depth of measurement on the order of twice the foot outside diameter is produced (i.e., 23 cm).

In order to ensure good seating, Humboldt suggests that 60 percent of the *SSG* footprint be clearly visible after removing the *SSG* following a test on natural material. In the case of very rough surfaces, a moist fine sand layer may be placed as a coupling between the *SSG* foot and the soil.

Alshibli *et al.* (2005) conducted a laboratory evaluation on different soil types using both *SSG* and *SPLT* where values for the latter ranged from approximately 0 to 500 MPa. Equation 2.18 describes the regression model obtained.

$$E_{\text{PLT(R)}} = 15.8 \cdot e^{0.011E_{\text{SSG}}} \quad (R^2 = 0.69) \quad (2.18)$$

Falling Weight Deflectometer (*FWD*)

Falling weight deflectometers (*FWDs*) have been in use since the 1980s. These devices are used to measure pavement deflections in response to a stationary dynamic load corresponding to the effect of loading due to standard axle on in-service pavement.

There are several *FWD* manufacturers and, thereby, characteristics may slightly vary. In the scope of this thesis a Dynatest Model 8000E device was used. The *FWD* is mounted on a trailer (fig. 2.19a), that can be towed by most conventional vehicles, where is mounted a load generating and a deflection measurement system. The control/recording system is housed in the towing vehicle.

The load generating system consists of a drop weight mounted on a vertical shaft, which is usually dropped onto a 305 mm or a 450 mm diameter loading plate. Both plates were used in the aim of the present work. The drop weight is hydraulically lifted to predetermined heights ranging from 50 to 510 mm and the applied load ranges from 7 kN to 120 kN depending on the magnitude of the dropping mass and the height of the drop. The impact of the falling weight is capable of producing impact loads approximately halfsinusoidal wave, and a loading time between 25 and 40 ms applies impulse loading to a circular plate. This is in contact with the pavement surface through a 5.6 mm thick rubber buffer (fig. 2.19b), which is usually used to improve the uniformity of loading stress distribution over the whole loading plate area. The applied load is recorded by a load cell.

The deflection measuring system consists of 8 geophones positioned on the pavements/layer surface at fixed distances from the center of the loading plate (fig. 2.19b). These geophones register the velocities due to an applied load and deflections are computed by the software.



Figure 2.19: *FWD*: (a) general view; (b) detail of geophones and plate

The *FWD* is used to establish elastic modulus values for the pavement layers. The principle of the test is the measurement of the deflection bowl produced by dropping a weight onto the pavement.

The analysis of *FWD* results can be carried out in several ways. Back-calculation procedure is widely employed for analyzing deflection data from *FWD* (Lee, 1988). The analysis involves establishing a set of moduli values which would produce deflections to match the displacements recorded. These theoretical deflections are compared with measured deflections and the assumed moduli are then adjusted in an iterative procedure until there is no significant difference between the theoretically calculated and the measured deflections. The moduli determined in this method represent the pavement response to load and can be used to calculate stresses or strains in the pavement structure. Another way consists on the interpretation of the results through spectral analysis of surface waves (Aouad *et al.*, 2007). Then, a static approach can also be used on the interpretation of *FWD* results. The measured center deflection of the plate is combined with the applied load to calculate the stiffness using conventional Boussinesq static analysis. This data is used to estimate the dynamic deformation modulus, E_{FWD} , following Equation 2.19.

$$E_{FWD} = \frac{k_{plate} \cdot (1 - \nu^2) \cdot \sigma \cdot r}{\delta_c} \quad (2.19)$$

where $k_{plate} = \pi/2$ or 2 for rigid and flexible plates, respectively; δ_c is center deflection of the plate; σ is the applied stress; and r is the radius of the plate.

The *FWD* provides periodic non-destructive evaluation of the structural capacity of different pavement sections. Due to its speed, better simulation of traffic loading, and results that can directly be applied in structural design, it has been a good non-destructive test for pavement structure assessment. Although, less experience has been gained with the use of the *FWD* on road bases, subbases and subgrades (Gurp *et al.*, 2000; Abu-Farsakh *et al.*, 2003). Current *FWD* research, suggests that it can be used in quality control during construction of pavement layers (Zaghloul and Saeed, 1996; Rogers *et al.*, 2000). Nevertheless, it faces with some problems, such as tilting of the deflection sensors caused by uneven surface, which in excess of a certain value leads to inaccurate deflection measurements that can not be used in back calculation (Gurp *et al.*, 2000).

Light Falling Weight Deflectometer (*LFWD*)

The *LFWD* is a portable device used to determine the soil's dynamic modulus, E_{LFWD} . It consists of a loading device that produces a defined load pulse, a loading plate and at least one geophone sensor to measure the deflection of the center of the plate. The *LFWD* dynamic modulus (E_{LFWD}) is then calculated from the load pulse and deflection.

The equipment used in this study was a Prima 100 *LFWD* manufactured by Carl Bro Pavement Consultants. It weighs approximately 26 kg and has a 10 kg falling mass that drops on the bearing plate via four rubber buffers. The center geophone sensor measures the deflection caused by the mass impact on the loading plate. During the test, the falling mass impacts the plate, producing a load pulse in the range of 1–15 kN in about 15–20 ms. The diameter of the loading plate used in this study was 300 mm. Alternatively 100 and 200 mm plates are also available.

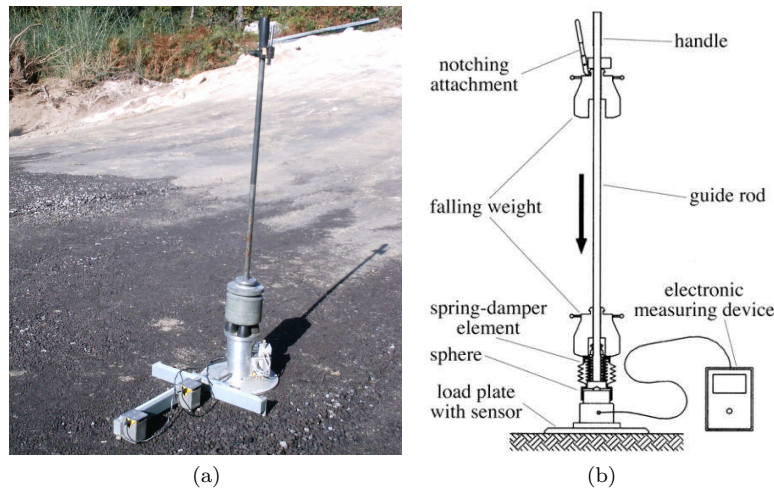


Figure 2.20: (a) *LFWD*; (b) Components of the *LFWD* (Adam and Adam, 2003)

During testing with PRIMA 100, the load is applied to the layer surface via the circular plate. The resulting force and velocity time histories are measured and the corresponding displacement time history is automatically obtained by means of integration (internal to the device) of the velocity record. The equipment is connected to a computer equipped with software for recording, data interpretation and visualization. The output includes respective time histories and peak values of the applied load, $F(t)$, and ensuing deflection, $\delta(t)$, as well as an estimated value of E_{LFWD} . A typical plot of the force and deflection time histories data generated by PRIMA 100 is presented in Figure 2.21. Similarly to *FWD*, the same static approach can be used and Equation 2.19 is employed to the determination of E_{LFWD} .

Fleming *et al.* (2007) point out one particularly important aspect when considering the measurements made is the interpretation of the deflection under load. In general the device software integrates the geophone (velocity transducer) signal to determine the maximum (or peak) deflection value. This has

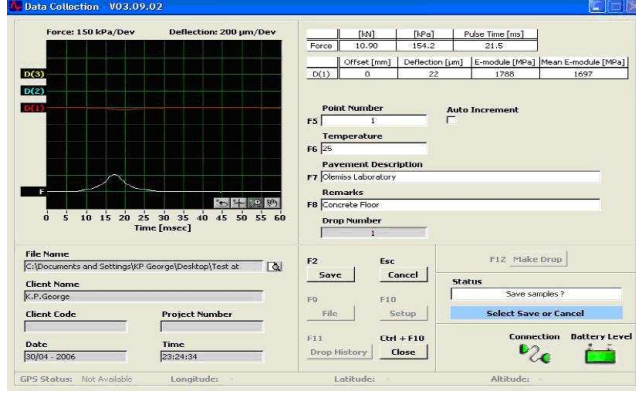


Figure 2.21: LFWD data collection screen

two important ramifications, the first being that under test the peak deflection may not occur at the same instant as the peak load, specifically for lower stiffness materials. The second is that the maximum deflection may include an element of permanent/plastic deflection in addition to recoverable/elastic deflection. This depends upon the “strength” of the materials under test, and the efficacy of the contact between the geophone foot and the material under test. Thus it is apparent that the term “elastic” stiffness should be applied very carefully to this device, and the use of such “elastic” values in elastic pavement analysis needs careful consideration. In their investigations they found significant permanent deflection in loose and partly compacted sand, but no plastic deformation was observed at compacted state.

Several studies have been recently conducted to evaluate LFWD measurements. The SPLT test is standardised and has been used for many years as a useful in situ test to evaluate the strength/stiffness of pavement, thus is considered as a reference test.

Alshibli *et al.* (2005) tested different types of soils with LFWD and SPLT in a laboratory setting to evaluate their relation, where values of the latter ranged approximately from 0 to 700 MPa. The relation given in Equation 2.20 was obtained between E_{FWD} and modulus from the reloading cycle of the SPLT test, $E_{PLT(R)}$.

$$E_{PLT(R)} = 25.25 \cdot e^{0.006E_{FWD}} \quad (R^2 = 0.90) \quad (2.20)$$

Fortunato (2005) performed 36 in situ tests with LFWD (300 mm diameter) and SPLT (600 mm diameter plate) during a geotechnical site investigation work on the platform of the old railway of the Portugal North railway line. These were carried out on different materials. The equipment and standards used were similar to those used in this study. The SPLT values of E_{V2} ranged from 36 to 148 MPa, and relationships between moduli obtained by the two tests were established (Eqs. 2.21 or 2.22).

$$E_{LFWD} = 1.13 \cdot E_{V2}^{0.98} \quad (R^2 = 0.74) \quad (2.21)$$

$$E_{LFWD} = 1.02 \cdot E_{V2} \quad (R^2 = 0.68) \quad (2.22)$$

Spectral Analysis of Surface Waves (SASW)

SASW is a widely used method for in situ testing that have been proposed and developed during the 1980s (Heisey *et al.*, 1982; Nazarian, 1984; Stokoe *et al.*, 1988). It is a seismic method that use the propagation of elastic waves through materials at low deformation level, in the range of 10^{-5} . At this deformation level it is possible to relate deformations and mechanic characteristics of materials using the theory of elasticity in linear system. The shear modulus obtained with these methods are considered as maximum values, G_0 .

There are two categories of seismic wave: volumetric waves and surface waves (fig. 2.22). Volumetric waves are of two types: P-waves and S-waves. P-waves, also known as primary, compressional or longitudinal waves, involve successive compression and rarefaction of the materials through which they pass, i. e., particle moves in the direction of wave propagation (fig. 2.22a). This type of waves can travel through solids and fluids. S-waves, also known as secondary, shear or transverse waves, cause shear deformations as they travel through a material, i. e., particle moves in a plane perpendicular to the direction of wave propagation. The direction of particle movement can be used to divide S-waves into two components. SV-waves whose particle motion lies in a vertical plane, and SH-waves whose particle motion occurs only in a horizontal plane. A given S-wave with arbitrary particle motion can be represented as the vector sum of its SV and SH components. This type of wave can not travel through fluids since they have no shearing stiffness.

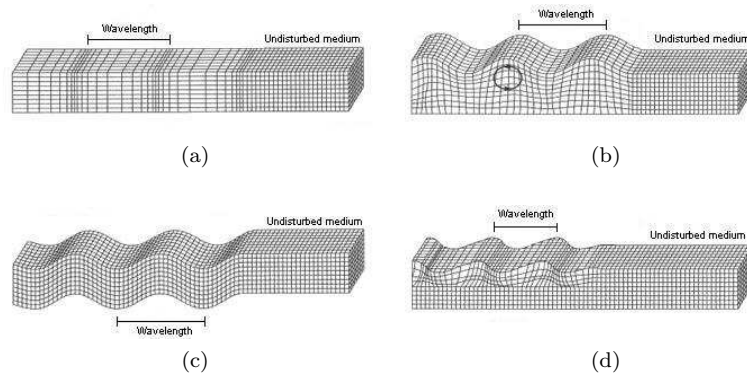


Figure 2.22: (a) P-waves; (b) Rayleigh waves; (c) S-waves; (d) Love Waves

Surface waves results from the interaction between volumetric waves with surface and superficial layers, being created Rayleigh waves and Love waves, which propagation occurs at surface. Rayleigh waves, produced by interaction of P and SV-waves with the surface, involve both vertical and horizontal particle motion, which can be assimilated to water waves occurring in the surface. Particle movement describes ellipses in a vertical plane, where the vertical axle is about one and a half the horizontal axle, which contains the propagation wave direction, with displacement contrary to the propagation wave in the highest point of the ellipses (fig. 2.22b). Love waves result from the interaction of SH-waves with a soft superficial layer than underlying half-space. Particles move horizontally and transversally to direction of propagation (fig. 2.22d).

The basis of the SASW technique is the dispersive property of Rayleigh-type surface waves when propagating in a layered system. Dispersion refers to the variation of Rayleigh wave phase velocity with wavelength (or frequency). Dispersion arises because Rayleigh waves of different wavelengths sample different depths in a material profile as illustrated schematically in Figure 2.23. As wavelength increases, particle motion extends to greater depths in the profile. The velocities of Rayleigh waves, or surface waves, are representative of the material stiffness over depths where there is significant particle motion. For example, the particle motion of a wave that has a wavelength less than the thickness of the top layer is confined to this layer (fig. 2.23). Therefore, the wave velocity is influenced only by the stiffness of the top layer. The velocity of a wave with a wavelength that is longer than the thickness of the top layer, but shorter than the combined thicknesses of the top two layers, is influenced by the properties of only the upper two layers because essentially all motion occurs in these layers. Thus, by using surface waves with a range of wavelengths, it is possible to assess material properties over a range of depths.

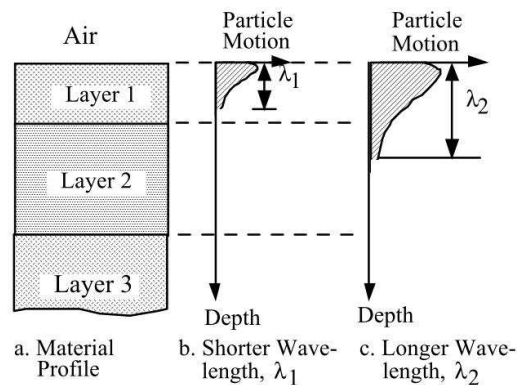


Figure 2.23: Approximate distribution of vertical particle motions with depth of two surface waves of different wavelengths (Rix and Stokoe, 1989)

SASW testing can be synthesised in three different steps that lead to the final result of a stiffness profile for the site: field testing, dispersion curve evaluation and inversion process.

Field testing consists of making field measurements of surface wave phase velocity, V_R , at numerous wavelengths, λ_R . To ensure the adequate application of SASW test it is necessary to take into account the energy source and receivers, considering the desirable frequency range, the space between receivers and the range of exciting frequency for each space adopted.

The energy source that generates surface waves is, normally, mechanical (impact) or electromechanical (continuous) sources that apply dynamical vertical loads to the surface. The impact sources correspond to loads generated by an impulse, as the ones proportioned by hand hammers or weights that falls from a determined high. Normally, as heavy is the impact source, the lower is the generated frequency. However, the same source does not generate the same frequencies in every medium. There are other factors which controls the generated frequency domain, namely the stiffness of the material and the interface between

the source and material to analyse. In general terms, for characterization of superficial layers is used a light hand hammer, being used a heavy one when higher depth is of interest. Regarding continuous sources, electromechanical ones are generally used producing sinusoidal vibrations with a range of frequencies. This allows to control vibration frequency and to set a range of frequencies. Another way to obtain continuous signs is to operate heavy equipment near receivers. The signs produced are random and normally has a sign-to-noise ratio relatively low. At sites where there are no surface area limitations, the primary consideration in selecting an energy source is the required depth of profiling. Deep profiling requires a high-energy, low-frequency wave source, while shallow profiling can be done with a low-energy, high-frequency wave source.

In general, the receivers used in this tests are geophones (velocity transducers) and accelerometers (acceleration transducers), of low frequency and high sensibility, since induced displacements are usually small. The receivers are placed in vertical and aligned relative to energy source. The selection of type of receiver and its spacing depends mostly of the frequency domain used on the test. In order to minimize the effects of proximity of the source, mainly related to body waves and aliasing phenomenon in spectral analysis it is necessary to impose limitations to the distance between energy source and receivers, L , and receivers spacing, d . Tokimatsu *et al.* (1991) proposed the positioning of the receivers in such a way that:

$$L > \frac{\lambda}{4} \quad (2.23)$$

$$\frac{\lambda}{16} \leq d < \lambda \quad (2.24)$$

The general field configuration of the source, receivers, and recording equipment typically used when testing with two receivers is shown in Figure 2.24. The propagation of waves along the surface is monitored with the two receivers placed at distances of d_1 and d_2 from the source. Additionally, distance d_2 is usually kept equal to two times d_1 . Typical receiver spacings for deep profiling are 2, 4, 8, 16, 32 and 64 m. These spacings allow evaluation of most soil profiles to a depth of 50 to 70 m.

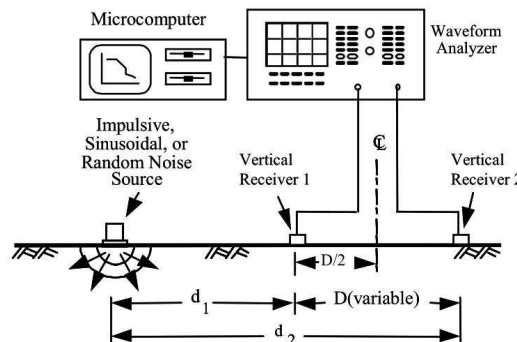


Figure 2.24: Traditional configuration of equipment used in SASW testing with a two-channel recording system (Stokoe *et al.*, 1994)

After the field data are recorded, a dispersion curve is calculated. For testing with multiple receivers, receiver pairs are used to determine the dispersion curve. For each receiver pair, the time histories recorded by the two receivers are transformed to the frequency domain, and the cross power spectrum and coherence function are calculated. It should be noted that all of these frequency domain quantities are calculated in real time by the waveform analyzer. The key data consist of the phase of the cross power spectrum and the coherence function. The coherence function represents a signal-to-noise ratio and is often close to one in the range of acceptable data. The time delay between receivers as a function of frequency, $t(f)$, is calculated from the phase of the cross power spectrum. The surface wave velocity, V_R , is calculated using Equation 2.25. The corresponding wavelength of the surface wave, λ_R , with a given frequency, f , is calculated by Equation 2.26.

$$V_R = \frac{d_2 - d_1}{t(f)} \quad (2.25)$$

$$\lambda_R = \frac{V_R}{f} \quad (2.26)$$

The result of these calculations is a dispersion curve (V_R versus λ_R) for each receiver pair. For the traditional two-channel SASW testing illustrated in Figure 2.24, individual dispersion curves from a group of receiver spacings are assembled together to form the composite dispersion curve for the site. An example of a composite dispersion curve is presented in Figure 2.25 using eight different receiver spacings as noted in the figure. In the scope of the present work experimental dispersion curve was computed using software *SPICE* developed in *KU Leuven* (Schevenels and Geert Degrande, 2009).

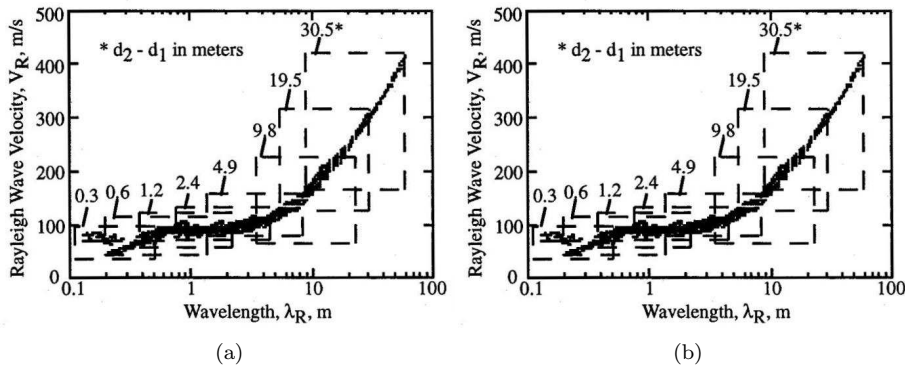


Figure 2.25: (a) Composite experimental dispersion curve from traditional SASW testing at soil site; (b) Comparison between experimental and theoretical dispersion curves for a soil site Stokoe *et al.* (1994)

After a dispersion curve is calculated from the field data, forward modeling is used in the laboratory to evaluate the shear wave velocity profile. Forward modeling is the process of calculating the shear wave velocity profile by a trial-and-error matching of a theoretical dispersion curve with the measured field dispersion curve. In this process, the theoretical dispersion curve is calculated

for an assumed velocity profile. This velocity profile should contain a sufficiently large number of sublayers to define the variation of material properties at the site. The shear wave velocities and thicknesses of the sublayers in the assumed profile are adjusted by trial and error until a satisfactory match between the theoretical and field dispersion curves is obtained. Such a match is illustrated in Figure 2.25b for the smoothed composite dispersion curve developed from the data shown in Figure 2.25a. The resulting shear wave velocity profile is shown in Figure 2.26, along with results from crosshole tests also performed at the site (Stokoe *et al.*, 1994).

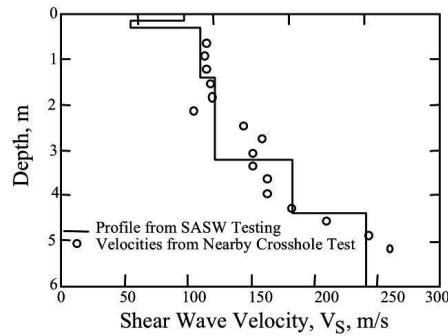


Figure 2.26: Shear wave velocity profiles determined from SASW (using data shown in fig. 2.25) and crosshole tests at the same site Stokoe *et al.* (1994)

According to the theory of elasticity, the relationship between the velocity of shear waves, V_s , and the velocity of Rayleigh waves, V_R , in a uniform is given by Equation 2.27.

$$V_s \leq C \cdot V_R \quad (2.27)$$

The constant C is dependent on the Poisson's ratio. For values of this coefficient of 0.2 and 0.5, C assumes values of 1.09 and 1.05, respectively, which means that the error in evaluating the Poisson's ratio little affect the value of V_s . The value of the shear modulus, G , is determined from values measured of velocity of Rayleigh waves and the density of material, ρ , by the theory of elasticity, given by Equation 2.28. This way it is possible to convert the vertical profile of velocities in a profile of values of shear modulus.

$$G = \rho \cdot V_s^2 \quad (2.28)$$

2.3.4 Continuous test method (Portancemètre)

Hitherto, compaction control has been carried out mainly by means of spot test methods with the purpose to check the density, stiffness or modulus of the compacted layer. Compaction result is checked by means of some spot test method can never reliably represent the compaction result of the entire area, nor contribute to an improvement of the homogeneity of the compaction work. According to national compaction standards in different countries one sample is taken on 2.000 m^3 of compacted soil, which means a relation between sample

volume and compacted volume of 1:1.000.000. Such quality control relation probably is very hard to find elsewhere (Thurner and Sandström, 2000).

Most of spot test methods are time consuming and will in addition delay or stop construction work, because the tests have to be carried out without any disturbing vibrations around the test spot. Moreover, traditionally, soil and rock fill materials are compacted with static or vibrating rollers. As mentioned before, compaction parameters of the roller are chosen by operator and kept constant, which do not necessarily lead to a homogeneous compaction result on a layer. Therefore compaction control by mean of spot test methods will ever be able to meet modern requirements on a homogeneous compaction result (Thurner and Sandström, 2000).

Regarding high quality projects as high speed railways, where rigorous deformation criteria of the structure soil–railtrack must be satisfied, continuous compaction control represents an improvement fairly to compaction control by mean of spot test methods. As has been noted in section 2.2.1, CCC may be achieved by instrumented rollers. However, there is an equipment named, Portancemètre, which operates similarly to instrumented rollers. This equipment performs continuous compaction control by measuring bearing capacity through an instrumented vibrating wheel.

The Portancemètre is an equipment developed by the “Center d’Études Techniques de l’Équipement” (CETE) in France. It measures the bearing capacity of a platform continuously while rolling to a constant speed. The device consists on a narrow vibrating wheel with suitable characteristics towed by a 4x4 vehicle (fig. 2.27). This wheel is set into vibration by way of an eccentric mass activated by a hydraulic engine.

The principle of measure is based on the determination of the curve: force communicated by the vibrating wheel versus deflection, allowing the determination of stiffness of geomaterials and to calculate its modulus. This equipment applies a load, at a 35 Hz frequency, to the soil trough a vibration wheel while rolling to a speed of 1 m/s. The instrumentation installed on the equipment permits to measure the vertical component of acceleration of the vibration and suspended masses, and the vibration frequency and the phase angle between the vibration vertical amplitude and the centrifugal force applied to the wheel (fig. 2.27c). An algorithm associated calculates the vertical force applied to the soil and the corresponding deflection.

The vertical component of the applied force by the vibration wheel (FTA) is calculated by the following expression (Quibel, 1999):

$$FTA = M1 \cdot g + M0 \cdot \Gamma_{V1} + (M1 - M0) \cdot \Gamma_{V2} + m_e \cdot \omega^2 \cdot \cos\varphi \quad (2.29)$$

where $M1 \cdot g$ is the total weight; $M0 \cdot \Gamma_{V1}$ is the inertial force of the vibrating mass with Γ_{V1} being the vertical acceleration measured by means of a single axial accelerometer; $(M1 - M0) \cdot \Gamma_{V2}$ is the inertial force of the frame with Γ_{V2} being the vertical acceleration of the suspended mass; $m_e \cdot \omega^2 \cdot \cos\varphi$ is the vertical component of the centrifugal force produced by the eccentric mass.

The vertical movement of the vibration wheel is determined by a double integration of the signal of the vertical acceleration. The average of the measured values, of the force and deflection, in thirty successive periods, permits to get the



Figure 2.27: Portancemètre equipment: (a) general aspect; (b) vibrating wheel detail; (c) function schema

force–deflection curve of which the upward part is treated by linear regression in the zone 30% to 90% of the vertical maximum force (FTA) applied to determine the stiffness. With a vibration frequency 35 Hz and a travelling speed 1 m/s, the Portancemètre device provides a value of modulus for each meter length (fig. 2.28).

The traveling speed of the whole is measured by means of ultrasonic radar Doppler that also allows to determine the covered distance and therefore to situate the measure in the longitudinal profile.

Some conditions must be guaranteed to allow the application of Portancemètre. Relatively to the layer geometry, the measurements are valid when longitudinal and transversal inclinations are lower than 7 and 5%, respectively. In respect to mechanical properties, loose materials with low shear strength on surface must be considered out of the domain of the equipment. This situation is verified when observed a rut let by the passage of the vibrating wheel with more than 2 cm.

Several tests performed with Portancemètre on structures constructed with different materials (aggregates, soils and treated materials), enabling a variation of the E_{V2} modulus, determined by means of the static plate test (600 mm diameter), from 20 to 500 MPa, showed a very good correlation between measures of stiffness with the Portancemètre and values of modulus determined by dynaplaque 2 or by the classic test (E_{V2}) (Quibel, 1999):

$$E = 5 \cdot k \quad (2.30)$$

E being expressed in MPa and k in kN/mm.

Other experimental results (Quibel, 1999) allow the application domain of the Portancemètre device to be composed by bottom of cuttings, layers and upper parts of embankments and sub-grades, with elastic modulus in the range of 30 to 300 MPa. The material thickness taken in account was about 0.60 m.

Fortunato (2005) conducted two series of *SPLT* (600 mm diameter plate) tests, one of 22 tests and another of 11 tests, and Portancemètre passages on a sub-ballast layer and comparison between moduli was established. From first series the author reported that modulus from 14 *SPLT* tests differed less than 25% from modulus obtained from Portancemètre. Regarding second series, average difference between moduli was found to be 9% with a maximum relative difference not exceeding 27%.

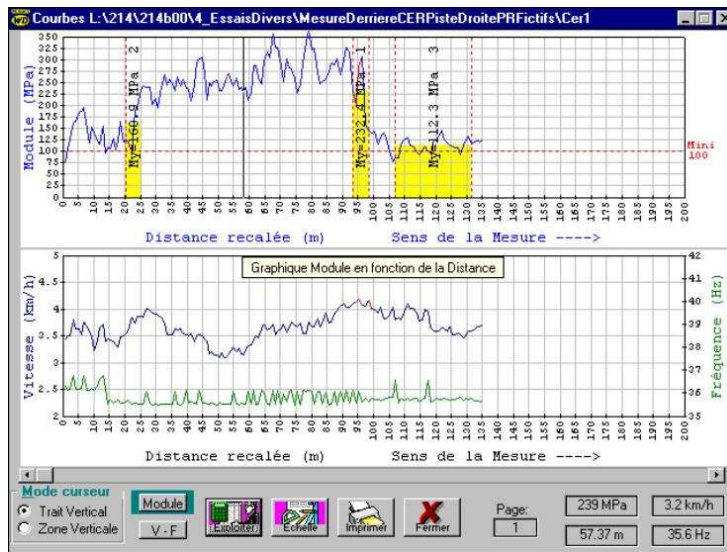


Figure 2.28: Display of the monitor (Quibel, 2006)

2.4 Summary

Compaction has a major influence on mechanical behaviour of compacted geomaterials. Compaction leads to a decrease of void ratio, which, in turn, improves their performance regarding shear strength, deformability and permeability. Hence, compaction assumes a critical role in the construction of transportation infrastructure (highways, railways, airports, etc.) and energy infrastructures (earth dams).

In general, geomaterials are compacted with static or vibrating rollers. Recently there has been an increasing interest in vibration-based monitoring of roller compactors to provide continuous assessment of the soil mechanistic properties, namely stiffness and/or modulus, during compaction process. With this aim, devices are embarked on compactors and roller-based measures of soil compaction are determined, e.g. relative indices or soil stiffness. As so, instantly and continuously relative information allows the roller operator to evaluate where compaction work is finished, where additional passes are required and what sections cannot be sufficiently compacted with the present roller and, on the other hand, allows to get an indication concerning the bearing capacity of a layer at the end of compaction. In this scope, the various roller-determined dynamic measurement values in use today, namely compactor meter value (CMV), Omega value, roller-determined stiffness (k_s) and vibration modulus (E_{vib}) were presented.

If feedback control is employed on compactors, then so called intelligent compaction is achieved. Intelligent compaction technology results from the combination of the absolute measurement technology with a control system that uses the measured information to continuously adapt major control parameters of a vibratory roller, namely, the amplitude, the frequency and the roller velocity, to the required conditions.

The increasing requirements on quality construction in order to avoid over-

compaction and to minimize relative settlements of the embankment platform, as well as to minimize the exploration costs, demands higher quality on soil compaction control.

Recently, there is a strong trend towards using stiffness and strength to control compaction given the importance of these mechanistic properties in pavement materials evaluation (Briaud, 2001; Loizos *et al.*, 2003; Alshibli *et al.*, 2005; Edil and Sawangsurya, 2005). Mechanistic properties are a measure of quality since non-uniformity of stiffness and/or strength is directly related to progressive failures and life-cycle cost. Moreover, the design method of pavements is based on engineering parameters of materials such as their stiffness and/or strength, which results in a missing link between the design process and construction quality control.

Increasing demands for better, cheaper and faster compaction control have lead to technology improvements. In this context, equipments for field test evaluation of mechanical properties of geomaterials have been recently developed, such as, impact tests (Falling Weight Deflectometer – *FWD* and Light Falling Weight Deflectometer – *LFWD*), the Soil Stiffness Gauge (*SSG*), Spectral Analysis of Surface Waves (*SASW*). These are non-destructive spot tests which can be conducted independently and in conjunction with conventional moisture density testing improving statistical evaluation and allowing variability reduction, thus substantially enhance construction quality of the entire earthwork (Edil and Sawangsurya, 2005). These equipments were used in the aim of the present thesis and, therefore, a detail review of each one was addressed in this chapter. Further, equipments enabling continuous evaluation of mechanical properties like Portancemètre had been developed and was also used in the present study. Thus, a detail review was also presented.

Chapter 3

The influence of compaction on the hydro–mechanical behaviour of geomaterials

3.1 Introduction

Compacted geomaterials find their most important applications in geotechnical civil engineering projects. Examples can be found in earth dams and transportation projects, such as road, railways and airport embankments.

Railways embankments and railtrack layers are constructed on compacted geomaterials that are typically in unsaturated condition during construction and may remain in that condition during the working life of the structure. Several design and maintenance measures are undertaken to maintain unsaturated conditions because they provide favorable engineering materials properties, namely shear strength and deformability.

In practice, pavement design is based on rational methods using Young modulus (E) and Poisson's ratio (ν). These parameters are generally determined in terms of total stresses, even though materials used in railways construction are not completely saturated or completely dry. This approach is conservative to varying degrees to that the influence of soil suction is ignored. For this reason, the behaviour of unsaturated materials is of utmost importance.

The mechanical aspects of saturated geomaterials are governed by the Terzaghi's effective stress. When a soil mass is loaded, it deforms and then a counter force is generated so as to balance the load. Although soil consists of a soil skeleton and pore fluid, the latter does not play a principal role in the shear behaviour, that is, the pore fluid does not resist the shear force. The pore water migrates within the soil skeleton subjected to hydraulic boundary conditions. However, on unsaturated geomaterials the pore space is occupied by both air and water, where suction play a fundamental role on the hydro–mechanical aspects. Unsaturated soil behaviour consists of hydraulic part dealing with the suction-saturation relation and a mechanical part dealing with the stress-strain relation. In turn, the hydro–mechanical behaviour is influenced by compaction conditions.

In what follows basic concepts on unsaturated geomaterials will be presented. Then, the influence of compaction conditions on the hydro–mechanical behaviour of either saturated and unsaturated geomaterials will be addressed.

3.2 Basic concepts of non saturated geomaterials

3.2.1 Suction

Soil suction is defined as the potential difference between the soil pore water and water outside the soil pores, per volume of water and is also referred to as free energy state of soil water (Fredlund and Rahardjo, 1993). The free energy of the soil water can be measured in terms of the partial vapor pressure of the soil water (Richards, 1965) and its thermodynamic relationship can be expressed in terms of relative humidity as follows:

$$\psi = -\frac{R \cdot T}{m \cdot g} \cdot \ln\left(\frac{P}{P_0}\right) \quad (3.1)$$

where ψ is soil suction or total suction, R is the universal gas constant, T is the absolute temperature, g is the gravitational constant, P/P_0 is relative humidity in percent where P is the partial pressure of pore water vapor pressure (kPa) and P_0 is the saturation pressure of water vapor over a flat surface of pure water at the same temperature (kPa).

The total suction (free energy) of soil is divided into two components, osmotic and matric suction. Osmotic component is defined as “the equivalent suction derived from the measurement of the partial pressure of the water vapor in equilibrium with a solution identical in composition with the soil water, relative to the partial pressure of water vapor in equilibrium with free pure water” (Fredlund and Rahardjo, 1993). In other words, the osmotic component of soil suction arises from the chemical interactions between dissolved salts and free water (defined as water containing no dissolved solutes).

The second component of soil suction is the matric suction. It is defined as “the equivalent suction derived from the measurement of the partial pressure of the water vapor in equilibrium with the soil water, relative to the partial pressure of the water vapor in equilibrium with a solution identical in composition with the soil water” (Fredlund and Rahardjo, 1993). In unsaturated soil mechanics matric suction is defined as the difference between the pore air pressure and pore water pressure ($\mu_a - \mu_w$). This component is commonly associated with capillary phenomena arising from surface tension of water, which results from intermolecular forces acting on molecules in the contractile skin.

Capillary phenomena is best understood through the classic example of water rising and remaining above the line of atmospheric pressure within a small diameter tube. The surface of the water in the capillary tube is curved and is called a meniscus, as illustrated in Figure 3.1. The height of capillary rise is a function of the tube diameter, contact angle between the tube and wetting liquid. The mathematical relationship is shown below:

$$h_c = \frac{2 \cdot T}{\gamma \cdot r} \cdot \cos\alpha \quad (3.2)$$

where T is the surface tension of the fluid (water for this discussion), r is the radius of the capillary tube, γ is the unit weight of water, and α is the contact angle between the water and capillary tube. Assuming a clean glass tube and pure water (contact angle α becomes 0), equation 3.2 reduces to the following:

$$h_c = \frac{2 \cdot T}{\gamma \cdot r} \quad (3.3)$$

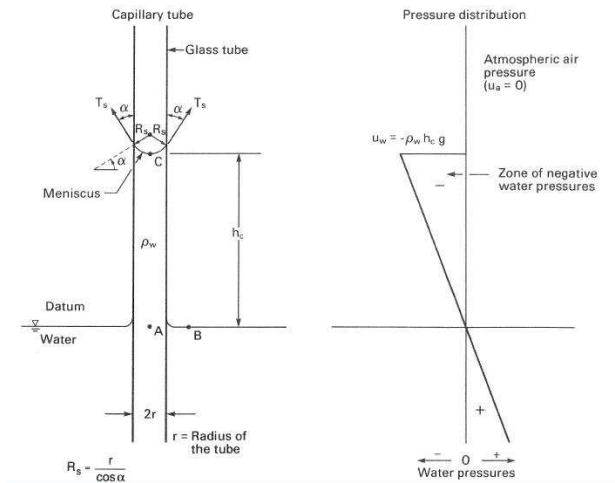


Figure 3.1: Physical model and phenomenon related to capillarity (Fredlund and Rahardjo, 1993)

Setting the hydrostatic equilibrium in the capillary system shown in Figure 3.1, matric suction can be deduced and expressed as follows:

$$(\mu_a - \mu_w) = \frac{2 \cdot T}{r} \cdot \cos(\alpha) \quad (3.4)$$

From Figure 3.2 it can be seen that soil particles similar to the walls of the capillary tube and the surface tension contractile skin (air–water interface) holds both the water intact and the two soil particles together. Considering that the geomaterials pores with small radii act as capillary tubes, Equation 3.3 shows that the smaller the pore radius in the soil, the higher will be matric suction and, therefore, shear strength of unsaturated geomaterials will increase.

In most engineering problems it is primarily the matric suction component which largely governs the behaviour of unsaturated soils (such as mechanical problems) in the lower suction range encountered in most field situations (Vanapalli *et al.*, 1996).

Several measurement techniques are available to measure the suction of a soil sample. A comprehensive description of the experimental techniques commonly used for measuring or controlling soil suctions can be found in Fredlund and Rahardjo (1993). The method selected should depend upon the suction desired. Measurement techniques, such as tensiometers (Delage *et al.*, 2008), psychrometers (Delage *et al.*, 2008), pressure plates (Richards, 1941), and filter paper method (Chandler *et al.*, 1992; Marinho and Oliveira, 2006), are used

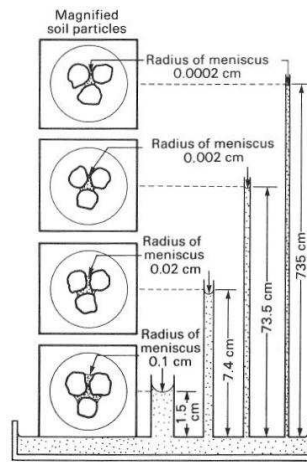


Figure 3.2: Capillary tubes showing the air–water interfaces at different radii of curvature (Fredlund and Rahardjo, 1993)

covering a wide range of suction measurement. Only filter paper method will be described, since it was the only method employed in the aim of this research.

This method was selected because it is capable of measuring a wide range of matric suctions (i.e., from 10 kPa to 10 MPa), it is relatively simple and cost efficient method, and it has been widely used in geotechnical engineering practice (Chandler *et al.*, 1992; Fredlund and Rahardjo, 1993; Likos and Lu, 2002; Marinho and Oliveira, 2006; Bicalho *et al.*, 2008; Yang *et al.*, 2008)

The filter paper method operates on the premise of determining suction of unsaturated soils indirectly by measuring the amount of moisture transferred from soil mass to dry filter papers. It calculates the soil suction indirectly from previous calibration. Basically, the filter paper comes to equilibrium with the soil either through vapour (total suction measurement) or liquid (matric suction measurement) flow. At equilibrium, the filter paper and the soil will have the same suction value. After equilibrium is established between the filter paper and the soil, the gravimetric water content of the filter paper disc is measured. The gravimetric water content of filter paper is then converted to suction using a calibration curve for the type of paper used.

Two filter paper methods exist depending upon if the total or matric suction is to be determined. If total soil suction is desired the non–contact method should be used, while the contact method allows determination of matric suction. Figure 3.3 illustrates the testing setups for total and matric suction measurement. In the contact filter paper technique, water content of an initially dry filter paper increases due to a flow of water in liquid form from the soil to the filter paper until both come into equilibrium. Therefore, a good contact between the filter paper and the soil has to be established. The contact filter paper method becomes inaccurate in high matric suction range since water transport is dominated by vapour transport.

The water content measure is correlated to a calibration curve unique for the filter paper used, and the suction, matric or total, is able to be determined depending upon the calibration curve selected. In the present work ash–less filter papers Whatman 42 was used. In Table 3.1 are listed some published

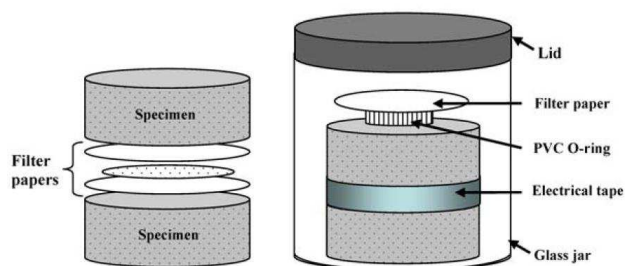


Figure 3.3: Filter paper method for measuring total and matric suction (Yang *et al.*, 2008)

calibration curves for this filter paper (Bicalho *et al.*, 2008). The references correspond to: (1) ASTM D5298 (1992); (2) Hamblin (1981); (3) Fawcett and Collis-George (1967); (4) Chandler and Gutierrez (1986); (5) Chandler *et al.* (1992); (6) Oliveira and Marinho (2006).

Table 3.1: Calibration curves for Whatman 42 filter paper (Bicalho *et al.*, 2008)

Suction	w range [%]	Log_{10} (suction) [kPa]	Reference
Total and Matric	$w < 45.3$	$5.327 - 0.0779 \cdot w$	(1)
	$w > 45.3$	$2.412 - 0.0135 \cdot w$	
Matric		$6.281 - 0.0822 \cdot w$	(2)
Matric		$5.777 - 0.060 \cdot w$	(3)
Matric (*)		$5.85 - 0.0622 \cdot w$	(4)
Matric	$w < 47$	$4.842 - 0.0622 \cdot w$	(5)
	$w > 47$	$6.050 - 2.48 \cdot \text{Log } w$	
Total and Matric	$w < 33$	$4.83 - 0.0839 \cdot w$	(6)
	$w > 33$	$2.57 - 0.0154 \cdot w$	

Note: w = Filter paper gravimetric water content
 (*) suction range (80–6000 kPa)

3.2.2 Soil water characteristic curve (SWCC) / Water retention curve (WRC)

As it was seen on the previous section, behaviour of unsaturated soils depends on the magnitude of suction, which in turn is influenced by soil water content for a given soil. The relationship between water content and suction can be empirically described by the soil water characteristic curve (SWCC) (Fredlund and Rahardjo, 1993; Tinjum *et al.*, 1997; Vanapalli *et al.*, 1999; Marinho and Stuermer, 2000; Bardanis and Kavvas, 2008), also known as soil water retention curve (WRC) (Karube and Kawai, 2001; Aubertin *et al.*, 2003; Nuth and Lalouia, 2008), which is defined as the water storage capacity of a soil at a given soil suction. The water content variable can be a gravimetric water content, w , or a volumetric water content, θ , or degree of saturation, S . A typical WRC is illustrated in Figure 3.4.

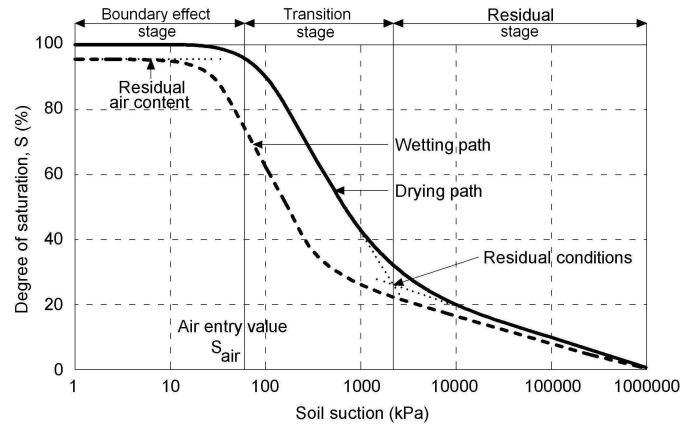


Figure 3.4: Typical WRC (Vanapalli *et al.*, 1996)

The graph consists of two curves: (i) a drying curve and (ii) a wetting curve. The hysteric nature of the curve is due to the complex nature of soil pore structure and can be attributed to the size differences between the primary pores and the interconnecting pore throats, changes in the contact angle during drying and wetting, and trapped air (Fredlund and Rahardjo, 1993; Tinjum *et al.*, 1997).

Vanapalli *et al.* (1999) described the several key features of WRC. One parameter of interest is the air-entry value (S_{air}). Conceptually, the air-entry value represents the differential pressure between the air and water that is required to cause desaturation of the largest pores, i.e., the matric suction value needed to cause water to be drawn from the largest pore space within the soil (Brooks and Corey, 1966; Vanapalli *et al.*, 1999). Further the author identifies several stages of desaturation (see fig. 3.5), namely: the boundary effect stage, the transition stage (i.e., primary and secondary), and the residual stage of unsaturation.

In the boundary effect stage, almost all of the soil pores are filled with water (i.e., the water menisci in contact with the soil particles or aggregates are continuous in this stage). Under these conditions, the single stress state, $(\sigma - \mu_w)$, describes the behaviour of the soil. The soil desaturates at the air-entry suction value in the transition stage. In this stage, the flow of water is in the liquid phase as the applied suction increases and the soil dries rapidly with increasing suction. The connectivity of the water in the voids or pores continues to reduce with increased values of suction, and eventually large increases in suction lead to relatively small changes in the degree of saturation. The residual state of saturation is considered to be the degree of saturation at which the liquid phase becomes discontinuous. Consequently, the residual state of saturation represents the degree of saturation value beyond which it becomes increasingly difficult to remove water from a specimen by drainage. The point at which residual state of saturation is reached is not always clearly defined.

Gupta *et al.* (2007) summaries influencing factors on the WRC. The distinguishing features of the WRC depend on several factors such as soil structure (and aggregation), compaction conditions (i.e., compaction water content, com-

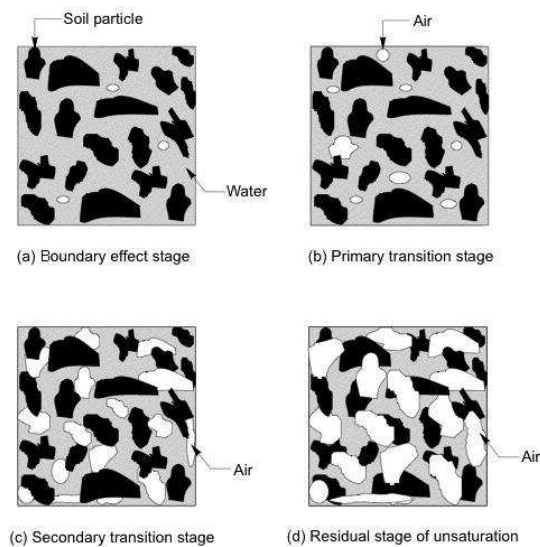


Figure 3.5: Probable variation of water area in different stages of a WRC (Vanapalli *et al.*, 1996)

pactive effort, and method of compaction), dry unit weight (or void ratio), soil type (i.e., mineralogy and texture), and stress history (or stress state). The four most important factors: soil type, compactive effort, compaction water content, and stress history, have the most influence on the nature of the WRC for fine-grained soils. In Figure 3.6 is illustrated the influence of soil type on the shape of the WRC. Soils with smaller pores have higher air-entry value. Soils with a wider range of pore sizes exhibit greater changes in matric suction with water content and thus the slope of the WRC becomes steeper (Hillel, 1980; Fredlund and Rahardjo, 1993; Vanapalli *et al.*, 1999). As will be addressed in next sections, specimens of a particular soil, in spite of having the same texture and mineralogy, can exhibit different WRCs if they are prepared at different compaction conditions.

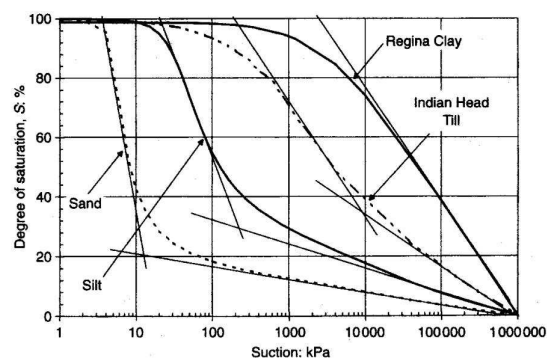


Figure 3.6: Typical WRCs for four Canadian soils (Vanapalli *et al.*, 1999)

3.2.3 Stress state variables

Effective stress approach

Traditional geotechnical engineering studies the behaviour of water or air saturated soils, that is, soils consisting of two phases: solid particles and water or solid particles and air. The principle of effective stress for saturated soil was first stated by Terzaghi (1943) and is commonly expressed in the following form:

$$\sigma' = \sigma - \mu_w \quad (3.5)$$

where σ' is the effective normal stress, σ is the total normal stress and μ_w is the pore water pressure.

Equation 3.5 is a definition of the stress state variable for saturated soils. The mechanical aspects of a saturated soil are governed by the effective stress. In other words, all the measurable effects of a change in stress, such as compression, distortion, and a change in shearing resistance, are exclusively due to changes in the effective stress, σ' . Equation 3.5 was later modified by Bishop *et al.* (1960) to account for the effects of soil suction in unsaturated soils. These authors reasoned that since the unsaturated soil is a three phase system (solid, pore water, and pore air) and water in voids is not continuous, the total stress will be the sum of intergranular stress, the pore air pressure (μ_a), and the pore water pressure (μ_w). They suggested that the effective stress (σ') in unsaturated soils can be expressed as:

$$\sigma' = (\sigma_n - \mu_a) + \chi \cdot (\mu_a - \mu_w) \quad (3.6)$$

where χ is the fractional cross sectional area of the soil occupied by water. For dry soil, χ will be zero and for saturated soil χ will equal to 1.

Later, Bishop and Donald (1961) pointed out that χ value not only depends on the degree of saturation, but is also influenced by soil structure, stress mean value and stress pathway (wetting and drying) leading to a given degree of saturation. Figure 3.7 shows examples of the deviation of χ value from the degree of saturation for two materials. This notwithstanding, efforts were made by Khalili and Khabbaz (1998) in order to develop a unique relation between χ and suction. By the study of shear strength data from several unsaturated soils in the literature, a unique relation between χ and the ratio of suction to air-entry value was showed and can be expressed as:

$$\chi = \left[\frac{(\mu_a - \mu_w)}{(\mu_a - \mu_w)_b} \right]^{-0.55} \quad (3.7)$$

where $(\mu_a - \mu_w)_b$ refers to air entry value.

Later, Khalili *et al.* (2004) proposed an incremental form of effective stress parameter to account for suction effects suggesting that for suctions greater than air entry, χ value varies as outlined in Equation 3.7, but for suction less than air entry, χ value was equal to 1. This concept was tested on shear strength data from the literature having reached good agreement between the measured and predicted values in all cases. As so, the authors concluded that shear strength can be predicted using the effective stress concept.

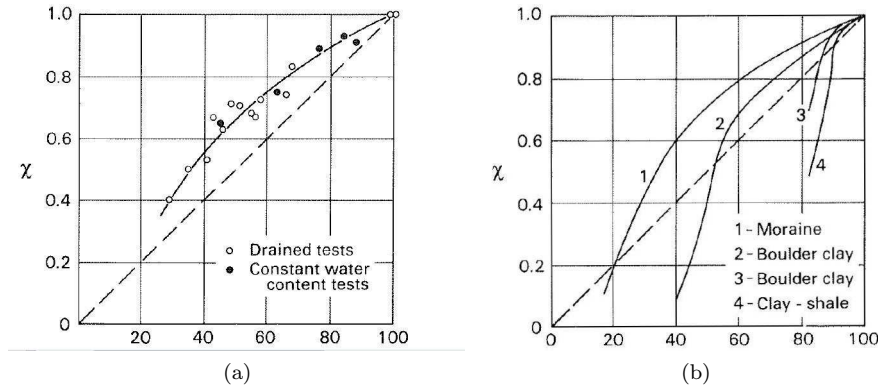


Figure 3.7: χ variation vs degree of saturation for: (a) a cohesionless silt; (b) compacted soils (Fredlund and Rahardjo, 1993)

Biarez *et al.* (1991), Fleureau *et al.* (2001) have shown that an effective stress approach could be used to take into account the effect of negative pore pressure in the interpretation of data in the very small strain domain. Recently, Coussy and Dangla (2002), starting from thermodynamical considerations, confirmed the validity of the effective stress approach from a theoretical point of view as long as the behaviour of the unsaturated soil could be considered as elastic. The authors tried to extend Biot's theory of poroelasticity used in saturated media to model the behaviour of unsaturated soils through an energy approach. This approach yields a consistent general framework to formulate the constitutive relations. Fleureau *et al.* (2003) summarizes this approach which leads to the following expression:

$$\sigma'_{ij} = \sigma_{ij} + p'_u \cdot \delta_{ij} \quad (3.8)$$

where σ_{ij} is the stress tensor and $p'_u \cdot \delta_{ij}$ appears as an isotropic tensor and is termed the capillary stress. Its expression is similar to Equation 3.6 with $\chi = S_w$ (degree of saturation in water), but with an additional term corresponding to the work of the interfaces. Independently from the expression of p'_u , which can be obtained by other methods, this approach validates the effective stress concept when the behaviour of the soil is elastic (Fleureau *et al.*, 2003).

Another approach to define effective stresses starts from the expression of the intergranular forces between two particles in an idealized medium, at the microscopic level, defined as a Micromechanical Model (Biarez *et al.*, 1993). The method consists of calculating the force F_{cap} due to water menisci between two grains of soil, modeled as balls. The balls are supposed to be perfectly water-wettable, gravity is neglected; the menisci are spherical tores, tangent to the particles. The pressure in the air phase is atmospheric ($u_a = 0$). According to the authors, if a partially saturated media consisting of solid grains, air and water is considered, four types of behaviour may be considered according to the hydric state. These types are : discontinuous water phase ($k_w = 0$), discontinuous air phase ($k_a = 0$), discontinuous water and air phase and the particular case of clusters (fig. 3.8). Only the the two first cases were considered.

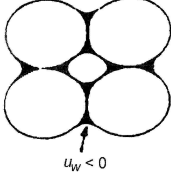
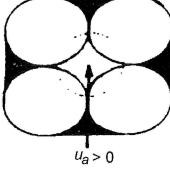
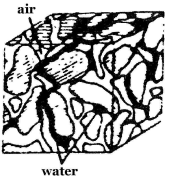

	Case 1	Case 2	Case 3	Case 4
				
k_w	= 0	≠ 0	≠ 0	
k_a	≠ 0	= 0	≠ 0	

Figure 3.8: Schematic representation of four types of behaviours (Biarez *et al.*, 1993)

The first one concerns to low degrees of saturation. In this case water is supposed to be discontinuous ($k_w = 0$) and air continuous, water forms menisci at the contact points between particles; the water pressure inside the menisci is negative ($u_w < u_a$). Experimentally, such conditions are observed for water contents lower than the shrinkage limit. In that case, the intergranular forces due to water are perpendicular to the planes tangent to the particles at the contact points and cannot, therefore, result in a rearrangement of the structure or in a volume change. However, these forces contribute to the strength of the medium. Considering two spheres with the same diameter, the expression of the attraction force resulting from water meniscus (“capillary” force) is:

$$F_{cap}^c = S_{men} \cdot u_c \quad (3.9)$$

where S_{men} , the cross-section area of the meniscus in the plane tangent to the spheres at the contacting point, is directly related to the diameter of the balls and the curvature radii of the meniscus, i.e., to the negative pore water pressure through Laplace’s law, and u_c is the negative pore pressure. The passage from discontinuous to continuous medium is made by considering regular arrangements of balls. Four types of arrangements were considered (fig. 3.9), with densities ranging from 0.83 Mg/m³ (tetrahedric) to 1.81 Mg/m³ (dodecahedric). In a representative elementary volume (*REV*), the capillary stress in a direction is given by:

$$p'_u = \frac{\sum_c F_{cap}^c}{S_{REV}} \quad (3.10)$$

where $\sum_c F_{cap}^c$ is the vectorial sum of the capillary forces acting in this direction and S_{REV} , the cross-section area of the *REV* in the plane normal to this direction. The variations of the capillary stress p'_u with the negative pore water pressure u_c can be derived from the model:

$$p'_u = \frac{\pi \cdot \gamma}{2 \cdot f(e) \cdot R^2} \cdot \left[4R + \frac{3 \cdot (3\gamma - \sqrt{9\gamma^2 + 8\gamma \cdot R \cdot u_c})}{u_c} \right] \quad (3.11)$$

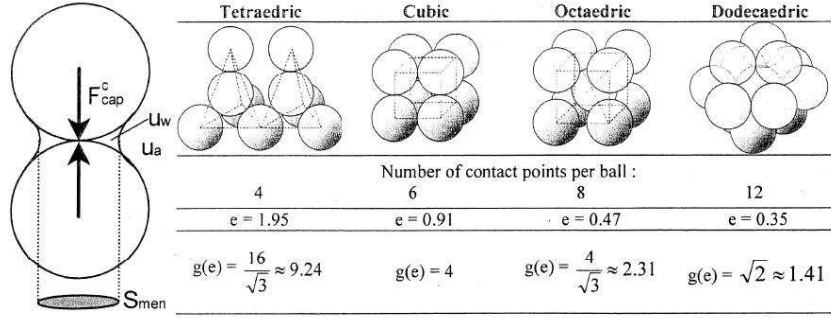


Figure 3.9: Schematic representation of four types of arrangements (Biarez *et al.*, 1993)

where R is the radius of the balls, γ , the surface tension of the liquid. The function of the void ratio, $f(e)$, is derived from a quadratic interpolation between the values of $f(e)$ for the four considered arrangements:

$$f(e) = 0.32e^2 + 4.06e + 0.11 \quad (3.12)$$

When the negative pore water pressure becomes very large, p'_u tends towards a maximum value given by:

$$p'_{u \max} = \frac{2 \cdot \pi \cdot \gamma}{f(e) \cdot R} \quad (3.13)$$

The concept of capillary stress can be extended to real soils, e.g. by deriving the “characteristic dimension” R from the experimental data (Biarez *et al.*, 1993).

Also based on this model, Modaressi *et al.* (1995) proposed another expression (eqs. 3.14 and 3.15) for determination of p'_u .

$$p' = p'_{u \max} \cdot \operatorname{tgh} \left(\frac{u_c}{p'_{u \max}} \right) \quad (3.14)$$

$$p'_{u \max} = \frac{2 \cdot \pi \cdot \gamma}{g(e) \cdot D_{10}} \quad (3.15)$$

As so, for low degrees of saturation effective stress is given by Equation 3.16.

$$\sigma' = \sigma + p'_u \quad (3.16)$$

The second case refers to high degrees of saturation. At this stage the air forms isolated bubbles within the voids ($k_a = 0$). The water phase is continuous and completely wets the grains. As there is no contact between the air bubbles and the solid grains, pore air pressure plays no part in the strength of the medium, but the presence of the bubbles makes it more compressible. In that case, Terzaghi's effective stress concept is valid and p'_u is equal to u_c . As so, the above expression became as follows:

$$\sigma' = \sigma + p'_u = \sigma + u_c \quad (3.17)$$

Many experimental validations of this model have been presented by the authors in the past years that showed, in particular, its ability to model the failure criterion of unsaturated soils.

Independent state variable approach

Another concept to describe unsaturated soil behaviour is the independent state variable approach. Fredlund and Morgenstern (1977) presented a theoretical stress analysis of an unsaturated soil on the basis of multiphase continuum mechanics. The unsaturated soil was considered a four-phase system. The soil particles were assumed to be incompressible and the soil was treated though it were chemically inert. The analysis concluded that stress state of an unsaturated soil can be described by any two of the three possible combinations of stress variables, namely: total normal stress (σ), pore air pressure (μ_a), and pore water pressure (μ_w). Possible combinations are given in Table 3.2.

Table 3.2: Possible combinations of stress state variables for an unsaturated soil

Reference pressure	Stress state variables
Air, μ_a	$(\sigma - \mu_a)$ and $(\mu_a - \mu_w)$
Water, μ_w	$(\sigma - \mu_w)$ and $(\mu_a - \mu_w)$
Total, σ	$(\sigma - \mu_a)$ and $(\sigma - \mu_w)$

These researchers showed that stress state variables, $(\sigma - \mu_a)$ and $(\mu_a - \mu_w)$, were the most advantageous combination because the effects of a change in total normal stress can be separated from the effects caused by a change in the pore-water pressure. The first tensor contains the net normal stress terms and the conventional shear stress components. The second tensor represents the matric suction stress, being an isotropic tensor. The complete form of the stress state for an unsaturated soil can be written as following two independent stress tensors, which are illustrated in Figure 3.10.

$$(\sigma - \mu_a) = \begin{bmatrix} (\sigma_x - \mu_a) & \tau_{yx} & \tau_{zx} \\ \tau_{xy} & (\sigma_y - \mu_a) & \tau_{zy} \\ \tau_{xz} & \tau_{yz} & (\sigma_z - \mu_a) \end{bmatrix} \quad (3.18)$$

and

$$(\mu_a - \mu_w) = \begin{bmatrix} (\mu_a - \mu_w) & 0 & 0 \\ 0 & (\mu_a - \mu_w) & 0 \\ 0 & 0 & (\mu_a - \mu_w) \end{bmatrix} \quad (3.19)$$

Fredlund and Morgenstern (1977) also carried out the null-type test by varying the individual components (σ , μ_a , μ_w) of the stress state variables in a such way that the stress state variables remained constant assuming that this would produce no distortion or volumetric change of the soil. Based on the results of the null tests, the above stress state variables were qualified for describing the mechanical behavior of unsaturated soils.

Accordingly to this approach, a saturated soil can be viewed as a special case of an unsaturated soil. The four phases in an unsaturated soil reduce to

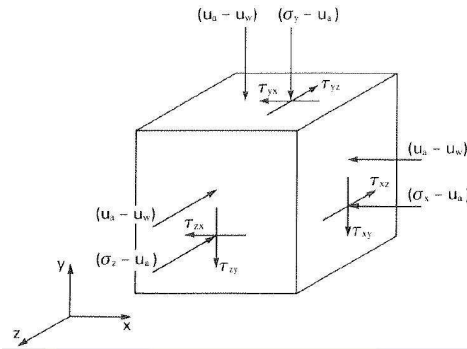


Figure 3.10: The stress state variables for unsaturated soil

two phases for a saturated soil (i.e., soil particles and water). There is also a smooth transition between the stress state for a saturated soil and that of an unsaturated soil. As an unsaturated soil approaches saturation, the degree of saturation, S , approaches 100%. The pore-water pressure, μ_w , approaches the pore-air pressure, μ_a , and the matric suction term, $(\mu_w - \mu_a)$, goes towards zero, disappearing this stress tensor. Only the first stress tensor (Eq. 3.20) is retained for a saturated soil when considering this special case, commonly referred to as effective stress (Terzaghi, 1943).

$$(\sigma - \mu_w) = \begin{bmatrix} (\sigma_x - \mu_w) & \tau_{yx} & \tau_{zx} \\ \tau_{xy} & (\sigma_y - \mu_w) & \tau_{zy} \\ \tau_{xz} & \tau_{yz} & (\sigma_z - \mu_w) \end{bmatrix} \quad (3.20)$$

3.3 Hydro-mechanical behaviour

It is widely recognised that hydro-mechanical behaviour of many geomaterials, in terms of stiffness (Tatsuoka *et al.*, 1997), compressibility and shear strength (Burland, 1990) is significantly affected by structure.

With respect to compacted geomaterials, the compaction conditions, namely molding water content, compaction energy and compaction technique play a fundamental role on the structure of compacted geomaterials, that in turn, strongly affect their hydro-mechanical behaviour. Lambe (1958b) distinguished a flocculated fabric in clay samples compacted dry of optimum and a dispersed fabric in samples compacted wet of optimum. Subsequent inspection by scanning electron microscopy and mercury intrusion porosimetry allowed direct observations of pore size distribution (Barden and Sides, 1971; Delage *et al.*, 1996; Surlol and Lloret, 2007; Romero and Simms, 2008; Koliji *et al.*, 2010). Fine-grained soils compacted dry of optimum generally tend to exhibit a fabric made up of aggregates having a bimodal pore size distribution, whereas samples compacted wet of optimum tend to show a more homogeneous matrix-dominated fabric and single pore size distribution (Barden and Sides, 1971; Delage *et al.*, 1996). Experimental evidence have shown the influence of structure on the hydro-mechanical behaviour of geomaterials (Seed and Chan, 1959; Santucci di Magistris *et al.*, 1998; Sivakumar and Wheeler, 2000; Wheeler and Sivakumar, 2000; d'Onofrio and Penna, 2003; Santucci di Magistris and Tatsuoka, 2004).

With respect to geomaterials in unsaturated state, not only different structures but also suction plays an important role on its hydro-mechanical behaviour. With the purpose to a better understanding of the hydro-behaviour of unsaturated geomaterials, firstly the influence of compaction conditions on the mechanical behaviour (stiffness, compressibility and strength) of saturated geomaterials is reviewed. Then, the influence of compaction conditions on hydro-behaviour of unsaturated geomaterials is addressed.

3.3.1 Influence of compaction on saturated geomaterials

Stiffness

It is known that compaction conditions strongly affect dry density, thus void ratio, which plays a fundamental role on the small strain stiffness of geomaterials. A general expression as proposed by different investigators for the small strain shear modulus (G_0) of geomaterials is of the following form:

$$G_0 = S \cdot f(e) \cdot p'^n \quad (3.21)$$

where S is a non-dimensional material constant reflecting the fabric and structure of the soil, $f(e)$ is the void ratio function and p' is the mean effective principle stress or confining pressure. A number of studies have been conducted to estimate void ratio function (Hardin and Richart, 1963; Lo Presti *et al.*, 1995; Santos, 1999; Hadiwardoyo, 2002). Two types of formulas are used:

$$f(e) = \frac{(B - e)^2}{1 + e} \quad (3.22)$$

$$f(e) = e^{-x} \quad (3.23)$$

Equation 3.22 results from the experimental observation of shear waves in soils (V_s) conducted by Hardin and Richart (1963), whereas Equation 3.23 results from Lo Presti *et al.* (1995) investigations. Santos (1999) and Gupta *et al.* (2007) summarize functions and constants in proposed equations. As a general conclusion, modulus increases with decreasing void ratio. Nevertheless, it is noteworthy that the differences between these reference void ratio functions are more evident at low void ratios.

d'Onofrio and Penna (2003) investigated the influence of compaction conditions on the small strain behaviour of a clayey silt with a clay fraction of about 28%, liquid limit about 50% and plasticity index of 17.8%. Specimens were prepared at the same dry density and water content adopting two different compaction procedures: dynamic (Standard Proctor) and kneading (Harvard) compaction technique. Both Proctor and Harvard specimens were saturated at constant volume prior to undergo the torsional shear and resonant column tests.

The initial shear modulus measured on Proctor and Harvard compacted specimens during isotropic compression phase are plotted respectively in Figure 3.11. The relationship between G_0 and p' was found to be not unique: e.g. G_0 measured at the same mean effective stress, can vary up to 30% for different water content. Data was fitted by power function (Eq. 3.24) with stiffness index, n , slightly varying with water content, ranging between 0.3 and 0.4, regardless of the compaction procedure adopted.

$$\frac{G_0}{p_r'} = S \cdot \left(\frac{p'}{p_r'} \right)^n \quad (3.24)$$

The stiffness coefficient S was found to be substantially affected by both water content and preparation procedure even though when initial shear modulus was normalized by the same void ratio function. The normalised stiffness coefficients, S^* , are plotted in Figure 3.11c against the compaction water content for specimens dynamically compacted (open dots) and by kneading (full dots). The influence of both water content and preparation technique is effective in a limited range around the optimum water content. The authors argue that compaction water content lead to structure of different stiffness in the tested soil while the effect of the preparation technique results in different texture of the soil that, in turn, may yield to a different anisotropy induced in the soils by different compaction method.

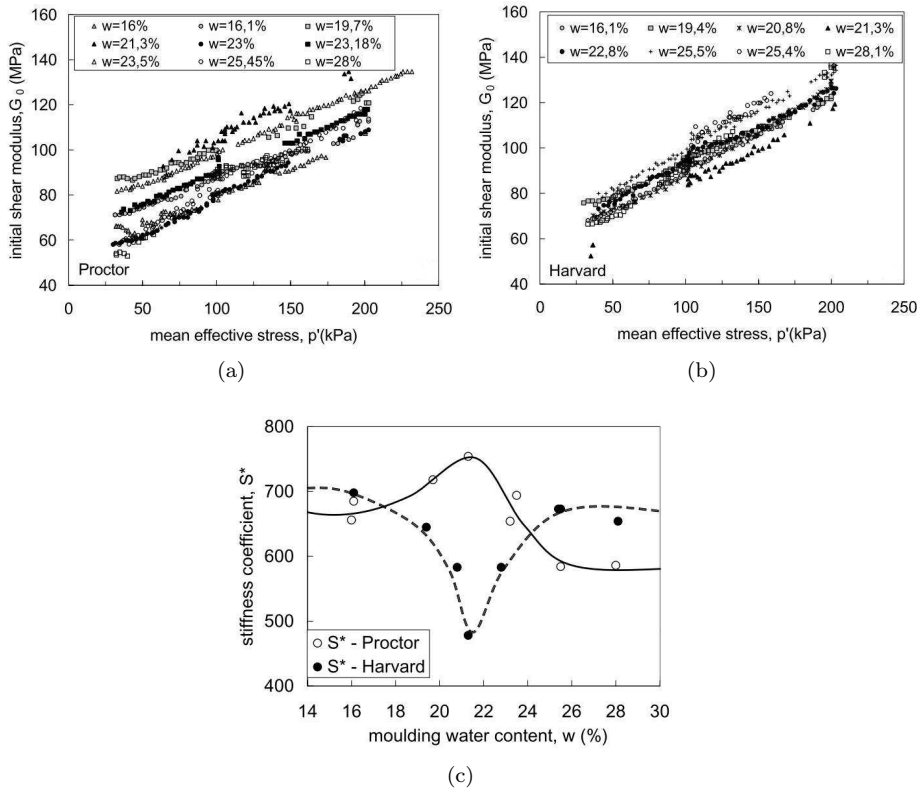


Figure 3.11: Initial shear modulus versus mean effective stress (a) Proctor specimens and (b) Harvard specimens; (c) Normalised stiffness coefficient variation with initial moulding water content (d'Onofrio and Penna, 2003)

Santucci di Magistris and Tatsuoka (2004) carried out a similar investigation on a silty sand (Meltramo silty sand) with D_{max} of 2 mm, C_u of about 400, a clayey fraction of about 16% and w_L of 35% and I_P of 14%. Triaxial compression tests were performed on specimens of Meltramo silty sand compacted

at different molding water contents and with different compaction energy (fig. 3.12a). The relationships between the effective vertical stress (σ'_v) and E_0 modulus are shown in Figure 3.12b including isotropic and anisotropic tests results. The authors reported two trends: (i) at isotropic stress states, the E_0 value increases with increasing σ'_v , but in a different way at anisotropic stress state; (ii) the specimens compacted at the optimum water content have the largest stiffness when compared to the values of the specimens compacted dry and wet of optimum.

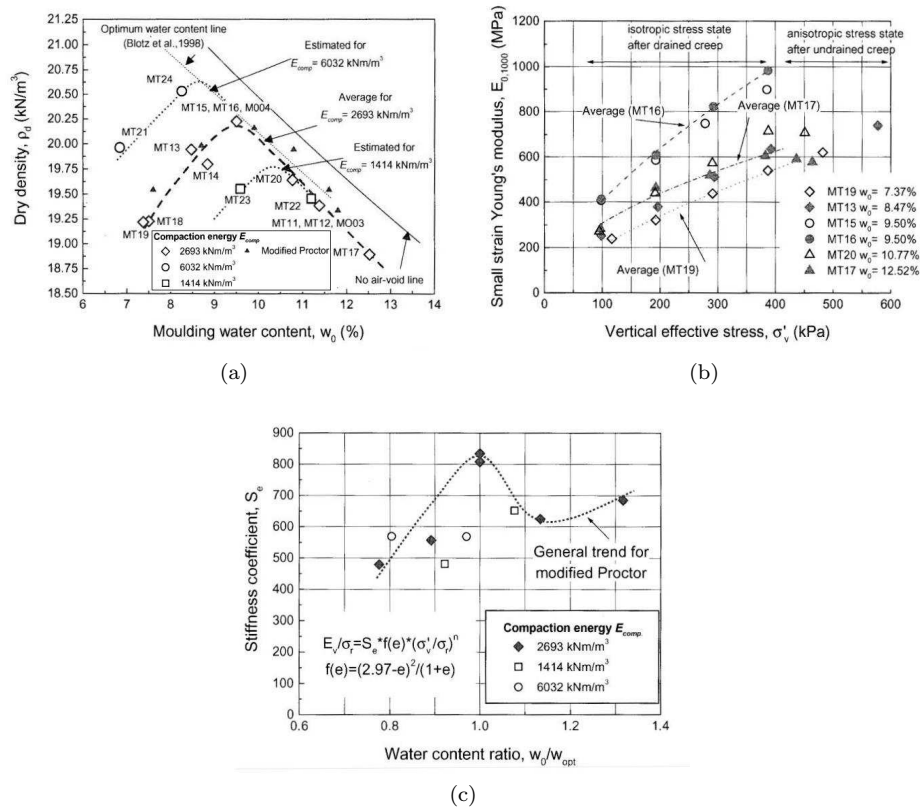


Figure 3.12: (a) Compaction curves; (b) Relationship between vertical effective stress and small strain Young modulus; (c) Relationship between the small strain stiffness coefficients corrected for void ratio and water content ratio (Santucci di Magistris and Tatsuoka, 2004)

A similar method to d'Onofrio and Penna (2003) was used for data interpretation. Data from isotropic stress states was fitted by a power law (Eq. 3.24) and a stiffness index around 0.6 was obtained for the different molding water contents. Then, the power law was normalized by the same void ratio function. The stiffness index, n , was the same and the relationship between stiffness coefficient, S^* and remolding water content is shown in Figure 3.12c. Samples compacted by using modified Proctor energy exhibited a peak value at optimum water content. The authors attributed the variation of S^* to effects of microstructure even though they could not explain why it peaks at optimum water content.

Compressibility

Lambe (1958a) reported that, at relatively low stress levels, clay specimens compacted wet of optimum were more compressible than those compacted dry of optimum, while the reverse was observed at relatively high stresses.

d'Onofrio and Penna (2003) also investigated the compressibility of compacted specimens. The initial water content was found to significantly affect the compressibility of both Harvard and Proctor compacted specimens. The compressibility index (λ) first decreases at increasing moisture content down to a minimum value corresponding to the optimum water content and then increases on the wet side of optimum water contents, as illustrated in Figure 3.13. They state that it appears that compaction at different water content affects the soil constants within isotropic compression line, thus resulting in effectively different materials. From isotropic compression tests on compacted specimens of Meltramo silty sand Santucci di Magistris and Tatsuoka (2004) found a similar trend. From evaluation whether the variation in the λ value with molding water content was due solely to the different compacted densities or effects of microstructure, they concluded that not only dry density, but also the microstructure controls the compression properties.

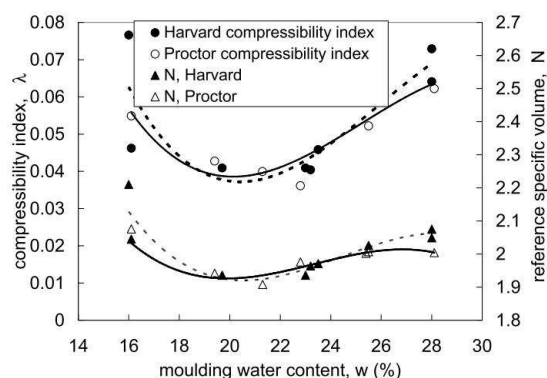


Figure 3.13: Compressibility parameters (d'Onofrio and Penna, 2003)

Santucci di Magistris *et al.* (1998) investigated the influence of compaction conditions on the compressibility of Meltramo silty sand by means of isotropic or K -compression stages in triaxial cell and oedometer tests. Specimens were prepared to different degrees of moisture and density adopting three different methods: (1) modified Proctor compaction; (2) hand-tamping compaction; (3) slurry consolidation. Specimens of Meltramo silty sand were compacted with modified Proctor at optimum and wet of optimum (+2.5%) water content in order to study the influence of water content on the compressibility. It was found higher compressibility from specimen compacted wet of optimum, which agrees with results from d'Onofrio and Penna (2003). In contrast, the same λ was obtained from remoulded specimens with different initial water contents, but the position of the normal consolidation line of the wetter specimen lied higher in the compression plane (v, p').

Further, Santucci di Magistris *et al.* (1998) also conducted isotropic compression tests on compacted specimens (modified Proctor) with slightly different

initial void ratios. Identical λ were obtained (fig. 3.14a).

With respect to compaction method, results obtained by d'Onofrio and Penna (2003) showed that a change from dynamic to kneading compaction has relatively little effect on the compressibility index (see fig. 3.13), but differences were found on the axial and radial deformations measured during isotropic compression stage, where the ratio between axial and radial deformations was always found to be lower than 1 for the dynamic compaction and higher than 1 for the specimens prepared by kneading compaction. Santucci di Magistris *et al.* (1998) found no differences between compressibility index obtained from compacted specimens with modified Proctor and with hand-tamping compaction (fig. 3.14a). Hence, they claim that limited differences in preparation do not seem to affect the compressibility of the studied material, provided that the same initial density is attained through the compaction technique. In contrast, remoulded specimens presented higher λ (fig. 3.14b).

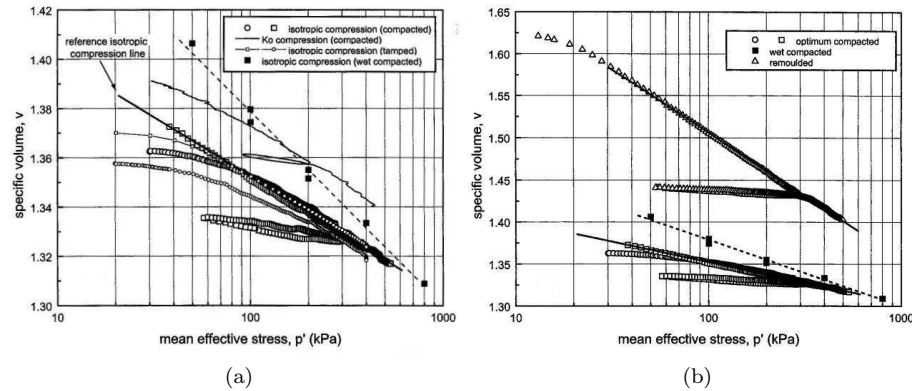


Figure 3.14: Compression curves from Meltramo silty sand: (a) modified Proctor and tamped specimens; (b) modified Proctor, tamped and remoulded specimens (Santucci di Magistris *et al.*, 1998)

Strength

Experimental evidence have shown that compaction conditions may influence the pre-peak stress-strain behaviour (d'Onofrio and Penna, 2003; Santucci di Magistris and Tatsuoka, 2004), but seems to do not influence ultimate shear strength (Seed and Chan, 1959; Santucci di Magistris *et al.*, 1998; Santucci di Magistris and Tatsuoka, 2004; Tarantino and Tombolato, 2005; Oh *et al.*, 2008).

d'Onofrio and Penna (2003) and Santucci di Magistris and Tatsuoka (2004) investigated the pre-peak behaviour and reported similar behaviour to the one verified in the small strain domain. Proctor specimens compacted at optimum water content exhibited higher shear stress rather than specimens compacted at dry and wet of optimum. Santucci di Magistris and Tatsuoka (2004) showed that relationship between the q/p' value at a fixed strain and the dry density becomes less unique as the referred strain becomes smaller, reflecting the pre-peak behaviour at small strains. As the referred strain becomes larger a more unique relationship is obtained rather independent of water content and compaction

energy level.

Experimental data from Santucci di Magistris *et al.* (1998), Tarantino and Tombolato (2005) and Oh *et al.* (2008) evidence that both ultimate shear strength are independent of compaction conditions in the (q, p') and (v, p') space, as illustrated in Figure 3.15. In the light of critical state theory (Wood, 1990), the critical state models for saturated soils are defined in terms of three state variables: mean net effective stress, p' , deviator stress, q , and specific volume, v . At critical state these variables are related through three critical state parameters, M , Γ , and λ and the following equations:

$$q = M \cdot p' \tag{3.25}$$

$$v = \Gamma - \lambda \cdot \ln(p') \tag{3.26}$$

where M is the slope of the projection of the critical state line in (q, p') plane, Γ is the intercept (at $p' = 1$ kPa), and λ is the slope of the projection of the critical state line in $(v, \ln(p'))$ plane.

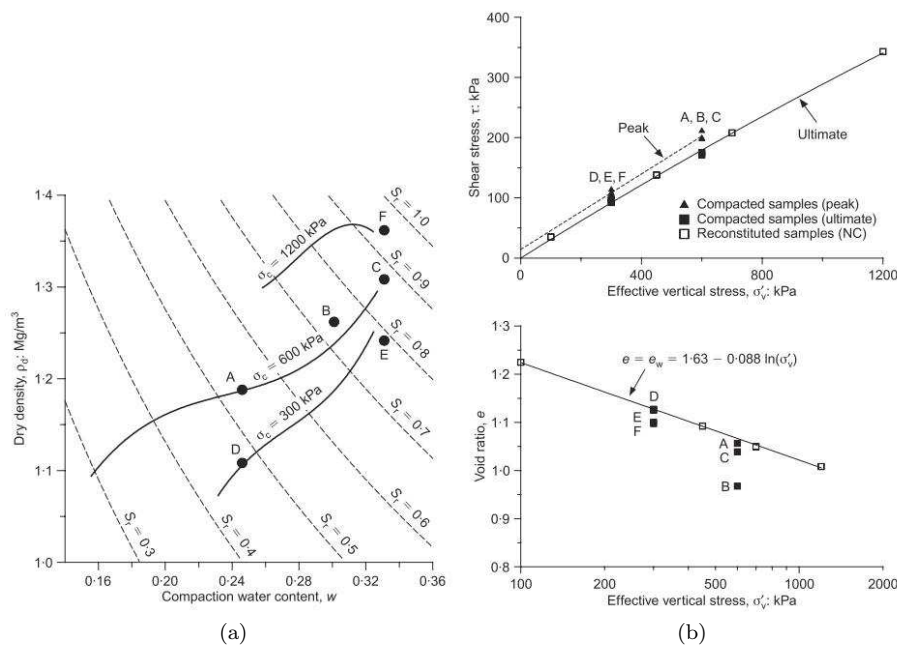


Figure 3.15: (a) Compaction curves; (b) Peak and ultimate shear strength in the (q, p) plane and ultimate void ratio (Tarantino and Tombolato, 2005)

3.3.2 Influence of compaction on unsaturated geomaterials

Water retention curve

Specimens of the same geomaterial, in spite of having same texture and mineralogy, can exhibit different water retention curves if they are prepared at different initial molding water contents. As a result, the hydro-mechanical behaviour will also differ.

Experimental data about the effect of molding water content on the water retention curve is provided by Marinho and Stuermer (2000). They examined the effect of compaction water content on the drying branch of the water retention curve for a residual soil of Gneiss ($LL = 48\%$, $PL = 29\%$ and $\% < 2\mu\text{m} = 45\%$). In Figure 3.16 is shown results from samples compacted at Modified Proctor energy and varying initial water content. Specimens were equilibrated, by drying, to a different water content and water retention curve associated with each specimen was determined.

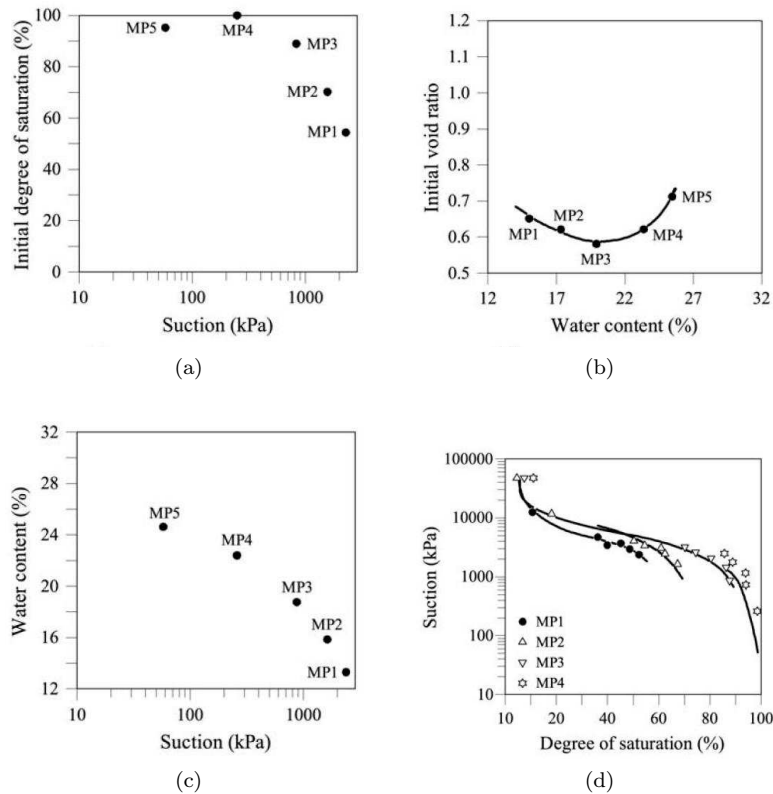


Figure 3.16: Water retention curves of a low plasticity soil obtained by drying of compacted samples at different conditions: (a), (b) and (c) initial state; (d) measured water retention curve (Marinho and Stuermer, 2000)

One note that, though specimens MP2 and MP4 have the same initial dry density, at different compaction water content presented different water retention curves. During the drying process samples compacted near the optimum

water content or below it (MP2) always presented smaller suction than samples compacted at wet of optimum (MP4). For low degrees of saturation curves tend to be similar, irrespective of the original compaction state. The differences reported were attributed to differences in microstructure built into the specimen by the compaction procedure.

Vanapalli *et al.* (1999) investigated the influence of initial water content on the hydraulic behaviour of sandy clay. Specimens were statically compacted to 100 mm in diameter and 21 mm in height in a single layer. A series of tests was carried out on three sets of specimens, each one prepared with the same dry density, i.e., constant void ratio, and with initial water contents ranging from 12.5 and 19.2%, which included dry of optimum, optimum and wet of optimum specimens. The matric suction was determined from individually compacted specimens with a null pressure plate using the axis-translating technique. The results obtained from each specimen allowed to compare the relationship between matric suction versus degree of saturation with the drying water retention curve determined from a single specimen and are shown in Figure 3.17.

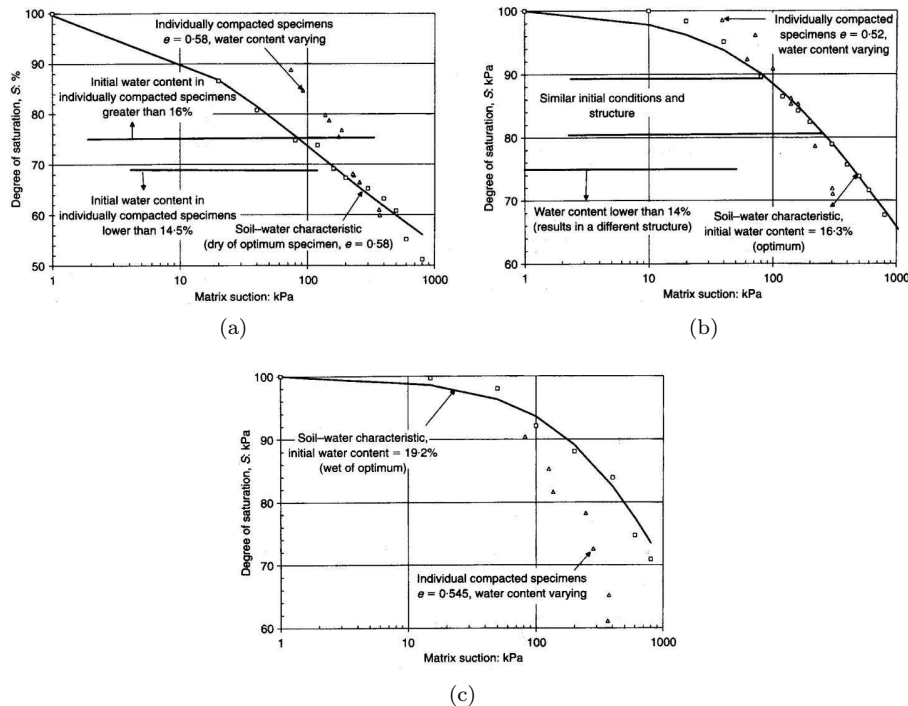


Figure 3.17: Compaction of soil-water characteristics for specimens compacted at the same initial void ratio and: (a) compacted dry of optimum water content; (b) compacted at optimum water content; (c) compacted wet of optimum water content (Vanapalli *et al.*, 1999)

Figures 3.17a, 3.17b and 3.17c shows the best-fit drying water retention curves for specimens with water contents dry of optimum, optimum and wet of optimum, respectively, and results of individuals compacted specimens with the same void ratios and varying water contents. At each set of results, differences between best-fit drying water retention curves and results of individuals

compacted specimens are given to varying initial water contents, which leads to different structures (and aggregation) during compaction. For the range of void ratios studied (0.52–0.58), the authors found a clear relationship between gravimetric water content versus matric suction and concluded that was the initial water content which governed the matric suction of individually compacted specimens.

Different void ratios can be achieved by varying compaction energy. The influence of void ratio on the hydraulic behaviour is given by the variations on the water retention curve due to variations on void ratio. Barrera (2002) investigated the influence of void ratio on water retention curve through measuring suction of compacted specimens at a fixed dry density and varying water contents. Suction was measured in each sample and water retention curve is plotted. If the target dry density is changed a new water retention curve is determined. Figure 3.18 shows the final result for the Barcelona low plasticity silty clay. For a given degree of saturation, increasing the soil density leads to increasing suction. Differences tend to reduce as the soil becomes wetter, but the effect of density is clearly marked.

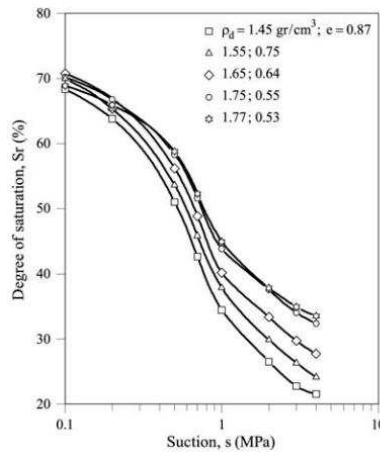


Figure 3.18: Water retention curves for different constant densities of Barcelona low plasticity silty clay (Barrera, 2002)

An alternative procedure to determine the influence of void ratio on the WRC consists on compaction to a given state followed by suitable application of a stress-suction path. Following this procedure Karube and Kawai (2001) and Sun *et al.* (2007) confirmed the above conclusion, i.e., the denser the specimen the higher the degree of saturation at the same imposed suction and the main wetting and drying curves are dependent on the current density.

The influence of both initial water content and compaction energy is evidenced from investigations performed by Vanapalli *et al.* (1999) and Tarantino and Tombolato (2005). In Figure 3.19 is shown moisture density compaction curves for different compaction pressures and respective water retention curves for a speswhite kaolin presented by Tarantino and Tombolato (2005). Though only optimum and wet of optimum seems to be reached only for 1200 kPa compaction vertical stress, it is clear that water retention curves depends on com-

paction pressure. Similar results were obtained from Vanapalli *et al.* (1999). Moreover, it is noteworthy that the air-occlusion suction for the specimens compacted at 1200 kPa vertical stress is very close to the suction of the specimen at the optimum (solid square in fig. 3.19). This result shows that the transition from dry to wet optimum states corresponds to the transition from continuous to discontinuous air phase.

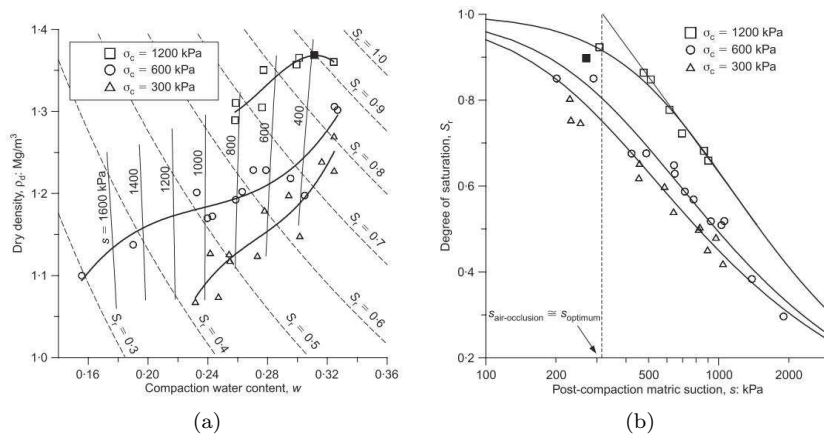


Figure 3.19: (a) Static compaction curves for the vertical stresses of 300, 600 and 1200 kPa. The solid square indicates the optimum for the 100 kPa compaction curve; (b) Water retention curves for the respective compaction vertical stresses (Tarantino and Tombolato, 2005)

Investigations from Huang *et al.* (1998), Gallipoli *et al.* (2003) and Tarantino and Tombolato (2005) confirms that the water retention curves are void ratio dependent and main drying curves and main wetting curves are characterised by two surfaces in the space (s, e, S_r) or (s, e, e_w) , s being suction, S_r being degree of saturation, e being the void ratio and e_w the water ratio (volume of water per volume of solids). Furthermore, Tarantino (2009) concluded that mechanical scanning behaviour investigated in the reconstituted studied materials was also affected by void ratio.

Stiffness

Further, Fleureau *et al.* (2003), Coronado *et al.* (2005), Yang *et al.* (2008) and Caicedo *et al.* (2009) have investigated the influence of water content on the mechanical behaviour.

Fleureau *et al.* (2003) investigated the small strains properties of a residual silty sand (Perafita sand). Several tests performed under several confining stresses and stress deviators and under isotropic stresses allowed to studied the influence of water content on maximum modulus. Measurements were carried out using two different triaxial cells with local strain measurements for tests on large (320 mm high and 160 mm in diameter) and small (140 mm high and 70 mm in diameter) specimens. Specimens were compacted with varying moisture content to the chosen dry density by means of a vibrating hammer. Figure 3.20a shows that, for the unsaturated specimens and for the same void ratio and under the same vertical stress, there is a general increase in the modulus when

the water content decreases, as long as the water content is strictly larger than 0. For the unsaturated specimens, the variations of normalised modulus versus total vertical stress approximately followed a power law, with an exponent $n = 0.35 - 0.45$. On the other hand, the lines for the dry and quasi-saturated specimens were nearly superimposed, with a stiffer slope ($n = 0.68$).

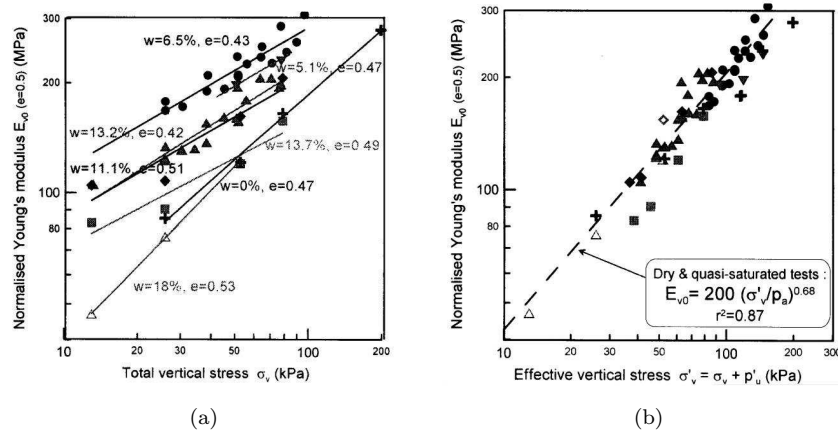


Figure 3.20: (a) Normalised Young's modulus versus total vertical stress for specimens of Perafia sand at different water contents and densities; (b) Interpretation of very small strains triaxial tests using Biarez *et al.* (1993) micromechanical model for the definition of effective stresses (Fleureau *et al.*, 2003)

Further, the interpretation of small strain modulus using Biarez *et al.* (1993) micromechanical model for the definition of effective stresses was attempted. Expressed against the effective stress, all the results were correctly located near the regression line of the dry and quasi-saturated specimens, as illustrated in Figure 3.20b.

Also Coronado *et al.* (2005) and Caicedo *et al.* (2009) found identical trend for unbound granular materials having attributed the increasing modulus with decreasing water content to the increase in capillary forces in the menisci that form between grains. Also here lines corresponding to the evolution of modulus with total vertical stress are more or less parallel for different moisture contents, as illustrated in Figure 3.21.

Qian *et al.* (1993) studied the effects of initial void ratio at compaction on the very small strain shear modulus of sands in resonant column. All the tests were conducted under isotropic stress conditions. Thirteen cohesionless soils were selected for testing to investigate shear modulus under unsaturated conditions. The test sands were prepared by mixing soil and distilled water to a pre-selected degree of saturation. Specimens were then prepared by compacting the soil-water mix to the required void ratio in a metal mould mounted directly on a resonant column device. As illustrated in Figure 3.22, they demonstrated that the value of the maximum shear modulus ratio should be greatest in a soil that has the lowest void ratio, all other factors constant.

The influence of compaction conditions on the small strain modulus was investigated by Mancuso *et al.* (2002) from resonant column tests on Melramo silty sand. Specimens were tested on a controlled-suction resonant column-

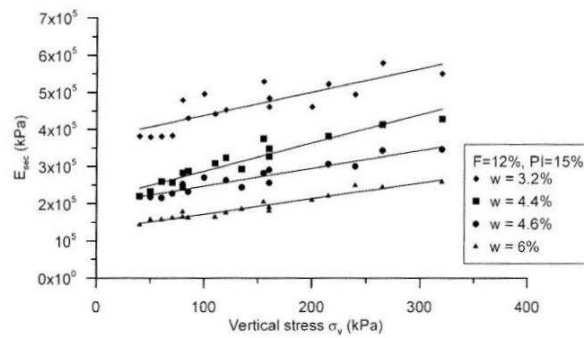


Figure 3.21: Secant modulus versus total vertical stress for specimens of unbound granular materials with 12% of fines and Plasticity Index of 15% (Caicedo *et al.*, 2009)

torsional shear device after compaction by the modified Proctor at the optimum molding water content ($w_{OPM} = 9.8\%$) and on the wet side of the compaction curve ($w_{OPM} + 2.5\%$), resulting an average specific volume of $v = 1.338 \pm 0.009$ and $v = 1.462 \pm 0.004$, respectively. Experimental data showed that the effect of suction on initial shear stiffness is significant, causing an increase in G_{max} ranging from 50 to 85% for the optimum compacted soil and from 40 to 165% for the wet of optimum compacted soil, depending on stress level. Most of the effects were detected for suctions ranging from 0 to about 200 kPa. For values higher than 200 kPa, G_{max} tends toward a threshold that depends on the net stress level. The stiffness versus suction curves showed an S-shaped trend (fig. 3.23) which was explained on the basis of the different ways in which bulk water and menisci water affect soil behavior, and was theoretically justified by distinguishing three different zones on each G_{max} versus suction curve: zone 1 pertaining to suctions lower than the air-entry value of the soil (i.e., bulk-water regulated behavior); zone 2 involving a progressive shift of soil behavior from a bulk-water regulated response to a menisci-water regulated response; and zone 3 where menisci-water effects prevail.

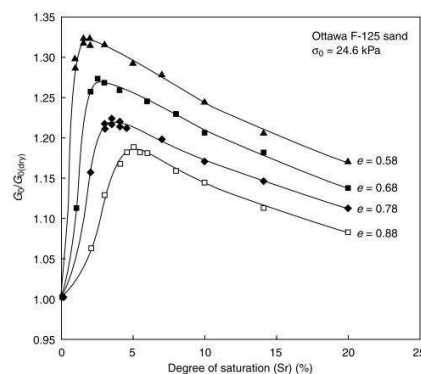


Figure 3.22: $G_0/G_{0(dry)}$ versus degree of saturation at various void ratios for Ottawa F-125 sand (Qian *et al.*, 1993)

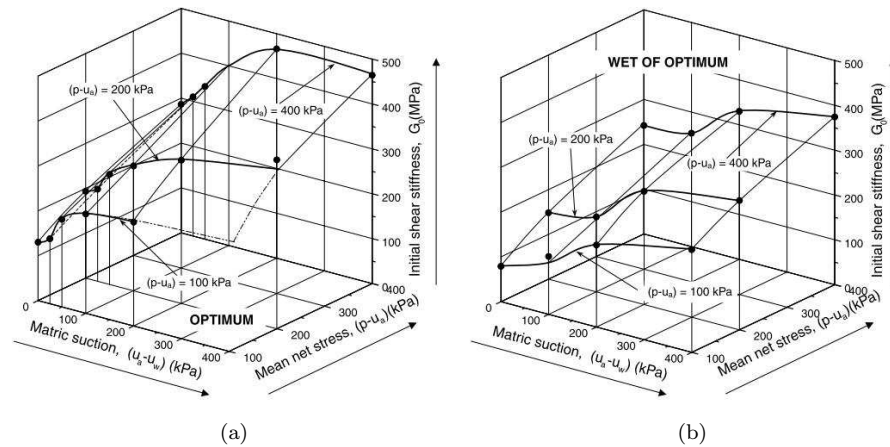


Figure 3.23: Initial shear stiffness in controlled-suction RC tests: (a) optimum compacted material; (b) wet of optimum compacted material (Mancuso *et al.*, 2002)

More recently Sharma and Bukkapatnam (2008) reached a similar trend through a different procedure. A stiffness investigation was carried out on specimens of a clayey silt with 19% clay and 79% silt, compacted at optimum water content 16% and saturated in such a way the dry density of specimens was maintained. Specimens were then subjected to drying by increasing air pressure and stiffness of specimen was obtained from shear wave velocity measurements by means of bender elements. G_0 increases with decreasing degree of saturation, thus increasing matric suction, and S-shape was verified.

The influence of all compaction conditions on the small strain modulus was studied by Sawangsuriya *et al.* (2008). They investigated the relationship of small strain modulus with moisture content for different types of geomaterials, namely a lean clay (CL), a silt (ML) and a clayey sand (SC). Small strain modulus was obtained from shear wave velocity by means of bender elements. Specimens were prepared with standard Proctor effort over a range of molding water contents: 4% and 2% dry of optimum, optimum and 2% and 4% wet of optimum. The variation of shear modulus with matric suction and molding water content is presented in Figure 3.24. In general, the shear modulus increases as matric suction increases and molding water content decreases. They stated that shear modulus of a given compacted soil depends primarily on matric suction and to a lesser degree on molding water content and dry unit weight.

Sawangsuriya *et al.* (2008) also investigated the relationship of small strain modulus with compaction energy, namely, reduced, and enhanced Proctor, which corresponds to 15, 25 and 35 hammer blows per layer. Material studied was a sandy clay (SC). As illustrated in Figure 3.24, the influence of compaction energy on suction is less significant than molding water content. The SC material compacted with standard Proctor effort had higher suction than that compacted with enhanced and reduced Proctor efforts. This notwithstanding, at lower water contents, a higher small stiffness modulus was obtained from specimens compacted by the enhanced Proctor (higher compaction energy). Differences on small strain stiffness tend to vanish at higher molding water contents.

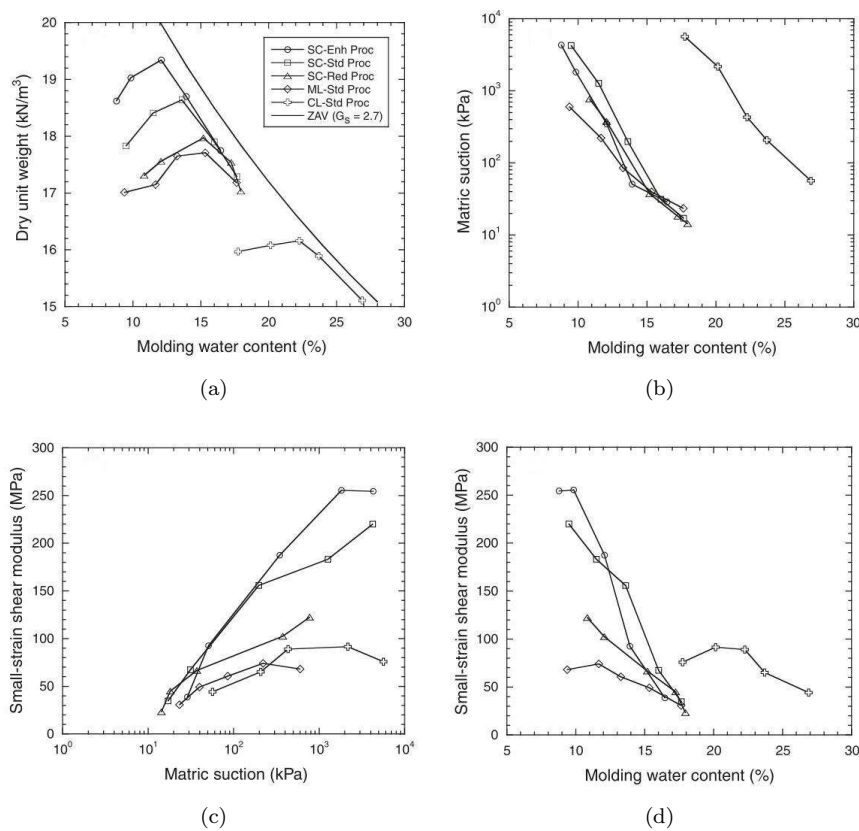


Figure 3.24: (a) Dry unit weight and (b) matric suction versus molding water content; Small-strain shear modulus versus (c) matric suction and (d) molding water content for clayey sand (SC), lean clay (CL), and silt (ML) soils (Sawang-suriya *et al.*, 2008)

Compressibility

Sivakumar and Wheeler (2000) and Wheeler and Sivakumar (2000) conducted an investigation on the influence of compaction condition on the mechanical behaviour of an unsaturated compacted clay. The effect of molding water content and compaction pressure on the compression behaviour were highlighted.

To investigate the influence of molding water content a series of 12 specimens (test series 2) were statically compacted at water content of 25%, corresponding to 4% dry of optimum from standard Proctor compaction. A specific volume of 1.976 ± 0.009 and a degree of saturation of 68.1 ± 0.8 were obtained. Another series of 6 specimens (test series 4) involved static compaction at water content of 28.5% (near the standard Proctor optimum), resulting in similar specific volume, 1.954 ± 0.009 and a degree of saturation of 79.8 ± 0.9 . Controlled-suction triaxial tests were carried out and in Figure 3.25a are presented the results from isotropic consolidation stage for test series 2 and 4. Small differences of the values of specific volume were observed between test series. This notwithstanding, in particular the post-yield data at zero suction show much lower values of specific

volume in series 4 than in series 2. The authors argue that this results are due to the change in compaction water content, rather than to the small difference in initial specific volume achieved by the two methods of compaction because a much larger difference in the compaction-induced specific volume, between other test series, had a lesser effect.

In addition, Sivakumar and Wheeler (2000) and Wheeler and Sivakumar (2000) investigated the influence of void ratio on the mechanical behaviour of unsaturated speswhite kaolin (fig. 3.25b). Controlled-suction triaxial tests were performed on specimens statically compacted at two different compaction pressures, hence different void ratios were obtained at the same water content. The greater compaction pressure employed, hence the lower void ratio, has resulted in additional expansion of the LC yield curve. Moreover, they reported that normal compression lines from samples at higher dry density lie below the corresponding normal compression lines from samples at lower dry density, although the lines from the two series of tests do tend to converge at high values of mean net stress. As so, authors stated that this difference suggests that compaction to a different pressure affects some of the soil constants, thus resulting in effectively a different material.

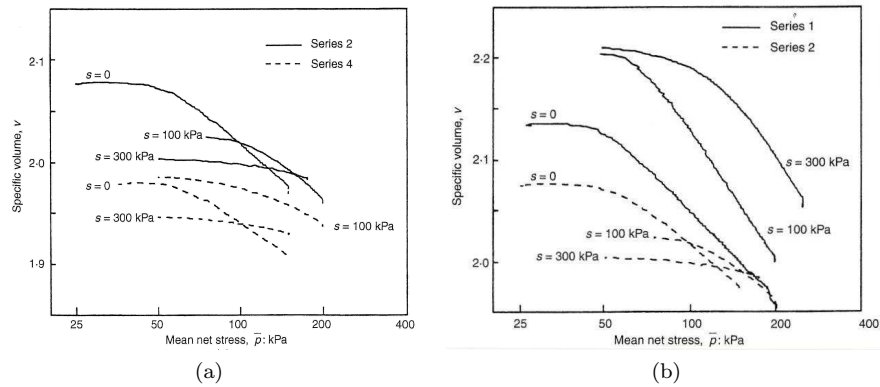


Figure 3.25: (a) Influence of compaction water content on the isotropic compression behaviour: comparison of typical results from series 2 and series 4; (b) Influence of compaction pressure on the isotropic compression behaviour (Sivakumar and Wheeler, 2000)

Also Estabragh *et al.* (2004) and Sun *et al.* (2007) found initial void ratio to influence the collapse behaviour of geomaterials. Figure 3.26 shows the results of isotropic compression tests on compacted specimens at different initial void ratios under suction of 147 kPa. These specimens were prepared by statically compacting samples to different vertical stresses at the same water content of 26%. It can be seen that even under the same imposed suction, a looser specimen has higher compressibility. Moreover, the yield stress increases as the initial void ratio of the compacted specimen decreases, i.e., there is an additional expansion of the LC yield curve as mentioned above.

Following an identical procedure to Sun *et al.* (2007), Estabragh *et al.* (2004) carried out an investigation on an unsaturated compacted silty soil. Isotropic consolidation tests on controlled-suction triaxial apparatus were performed on loose and dense specimens prepared by static compaction at the same water

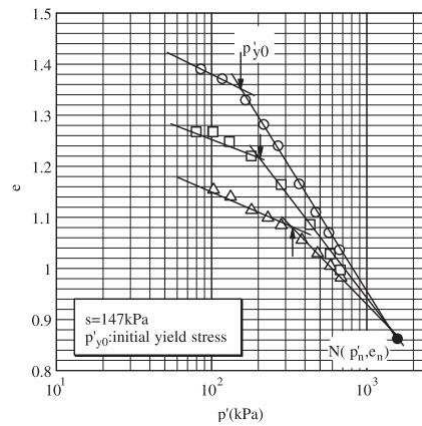


Figure 3.26: Results of isotropic compression tests on unsaturated clay compacted at different initial void ratios (Sun *et al.*, 2007)

content but with two different compaction pressures. They found that compressibility index (λ) for dense (fig. 3.27a) and loose (Fig. 3.27b) samples is a function of suction. The value of λ decreased with increasing suction for suctions greater than 80 and 100 kPa for dense and loose samples, respectively. However, it appeared to decrease sharply as the suction was reduced to zero. This behaviour was not consistent with the model of Alonso *et al.* (1990), who proposed that the slope of isotropic normal consolidation lines λ decreases monotonically with increasing suction from the saturated value, becoming asymptotic at high suctions. Authors argue that it was possible that λ increased with decreasing suction right down to zero suction, and there was then a discontinuity in the value of λ corresponding to the change from unsaturated to saturated conditions. In contrast to conclusions from Sivakumar and Wheeler (2000) and Wheeler and Sivakumar (2000), experimental results for both dense and loose samples show that the normal compression lines for different values of suction diverge with increasing mean net stress, where this divergence was more clear in the case of dense samples.

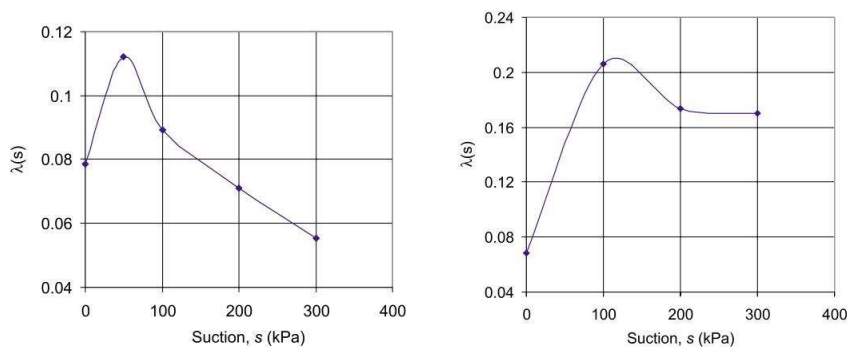


Figure 3.27: Variation of $\lambda_{(s)}$ with suction for: (a) dense samples; (b) loose samples (Estabragh *et al.*, 2004)

Finally, the influence of compaction technique was investigated by Sivakumar and Wheeler (2000) and Wheeler and Sivakumar (2000). The results indicated that a change from static compaction to dynamic compaction (standard Proctor) was found to have had relatively little effect on the soil behaviour.

Mancuso *et al.* (2002) also performed controlled-suction tests on triaxial apparatus to study compressibility of Meltramo silty sand of unsaturated specimens compacted at different molding water contents and dry densities, as previously referred. From experimental data they found that compressibility indices almost double going from optimum to wet of optimum, which denotes the influence of molding water content. Furthermore, compressibility indices significantly decreased with increasing suction. Data showed typical behaviour of fine-grained unsaturated soils (Alonso *et al.*, 1990) in terms of compressibility, in particular the apparent yield points which were fitted by a unique LC locus, as they belong to a single after-compaction yield curve.

Strength

Fleureau *et al.* (2003) conducted consolidated undrained triaxial tests, with measurement of the negative pore water pressure, on specimens compacted with varying initial water content. The test results are shown in Figure 3.28. When the water content increases, there is a progressive change from brittle to plastic behaviour. For water contents lower than 8%, the stress-strain curves present a peak and the specimens seem strongly dilatant. On the other hand, for water contents larger than 16%, perfectly plastic and slightly contractant behaviours were observed. However, in all the tests, the volumetric deformations remained very limited (1 to 1.5%). The authors claimed that in the first case, the negative pore water pressure in the menisci creates strong bonds between the grains, that increase the strength of the material and prevents its deformation. When the water content increases, the grains begin to be surrounded by water, and the behaviour of the soil tends towards that of the saturated soil at the same void ratio.

Moreover, interpretation of the triaxial tests results using Biarez *et al.* (1993) micromechanical model for the definition of the effective stress was attempted. The paths of unsaturated specimens were found to finish near the same maximum strength criterion as the quasi-saturated specimens.

The effect of initial water content on shear strength is clear from results obtained from drained direct shear tests on silty clay presented by Maaitah and Mahadin (2004). In Figure 3.29a are shown the relationships between degrees of saturation and shear strength for three normal stresses. As the degree of saturation increases up to 25% the shear strength increases and then it becomes nearly constant between degree of saturation 25 to 50%. As the saturation increases more than 50% the shear strength decreases. Maaitah (2005) explains this behaviour on the basis of bulk-water regulated behaviour and menisci-water regulated behaviour. The effect of initial void ratio on unsaturated strength was also investigated. As illustrated in Figure 3.29b, to a decrease in void ratio corresponds an increase in shear strength. This is also confirmed by Fleureau *et al.* (2003) results. Differences decreased for low and high degrees of saturation.

Further, Maaitah (2005) analysed some of the results in the light of the critical states (Wood, 1990) and compared with saturated drained tests. The unsaturated critical state lines in the plane (q, p) were found to be parallel to

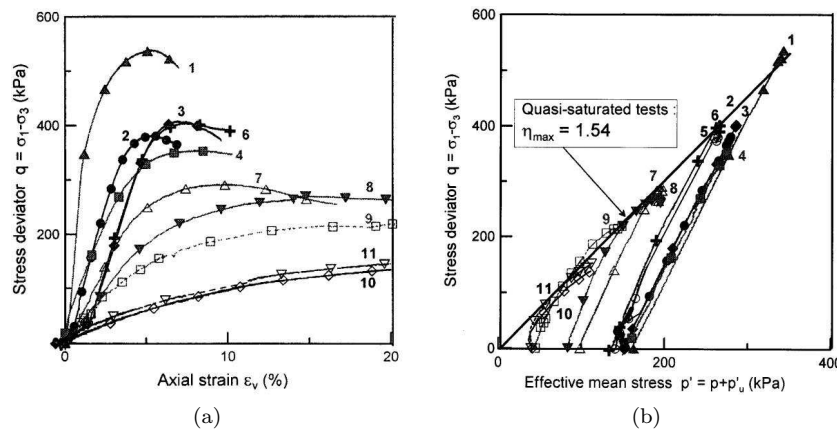


Figure 3.28: (a) Stress deviator versus axial strain for consolidated undrained tests on unsaturated specimens of Perafita sand; (b) Interpretation of large triaxial tests using Biarez *et al.* (1993) micromechanical model for the definition of the effective stress. 1: $w = 3.74\%$ ($e = 0.406$), 2: $w = 6.25\%$ ($e = 0.409$), 3: $w = 7.5\%$ ($e = 0.404$), 4: $w = 8\%$ ($e = 0.409$), 5: $w = 9.5\%$ ($e = 0.401$), 6: $w = 10.4\%$ ($e = 0.490$), 7: $w = 14.1\%$ ($e = 0.410$), 8: $w = 14.2\%$ ($e = 0.520$), 9: $w = 16.1\%$ ($e = 0.520$), 10: $w = 17.9\%$ ($e = 0.520$), 11: $w = 18.3\%$ ($e = 0.530$) (Fleureau *et al.*, 2003)

the saturated lines, as illustrated in Figure 3.30.

Wheeler and Sivakumar (2000) also conducted an investigation on the influence of compaction conditions at the critical states. Four series of samples were prepared by static (series 1, 2 and 4) and dynamic compaction (series 3). The compaction details for series 1–4 are shown in Figure 3.31a.

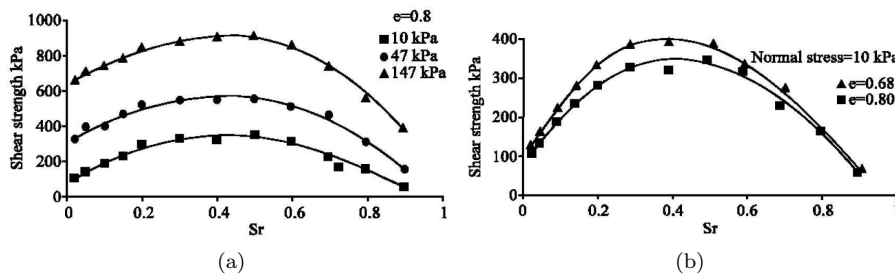


Figure 3.29: (a) Shear strength versus degree of saturation for initial void ratio of 0.8; (b) Effect of initial void ratio on unsaturated strength (Maaitah and Mahadin, 2004)

Controlled-suction triaxial tests were carried out at constant suction. For each value of suction no significant influence of compaction conditions, namely, water content and compaction energy, was observed on the location of the critical state line in the (q, p') plane. At critical states it seems that unsaturated critical state lines are parallel to saturated critical state line in the (q, p') plane (fig. 3.31b) and interception with q is a function of suction according the Equa-

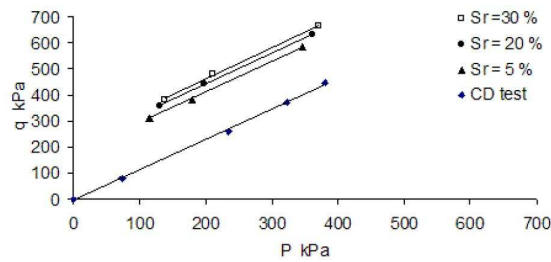


Figure 3.30: p - q diagram for unsaturated and saturated specimens with void ratio of 0.68 (Maaitah, 2005)

tion 3.27. Hence, the angle of internal friction at the critical state appears to be independent of the soil suction. Experimental data from Mancuso *et al.* (2002) and Wang *et al.* (2002) confirms that the slope of critical state line of the unsaturated studied materials at different suctions are parallel on the (q, p') plane to the saturated critical state line for a silty sand and a silty soil, respectively.

$$q(s) = M \cdot p' + \mu(s) \quad (3.27)$$

where M is the slope of of critical state line and $\mu(s)$ is the value given by the interception of critical state line with q .

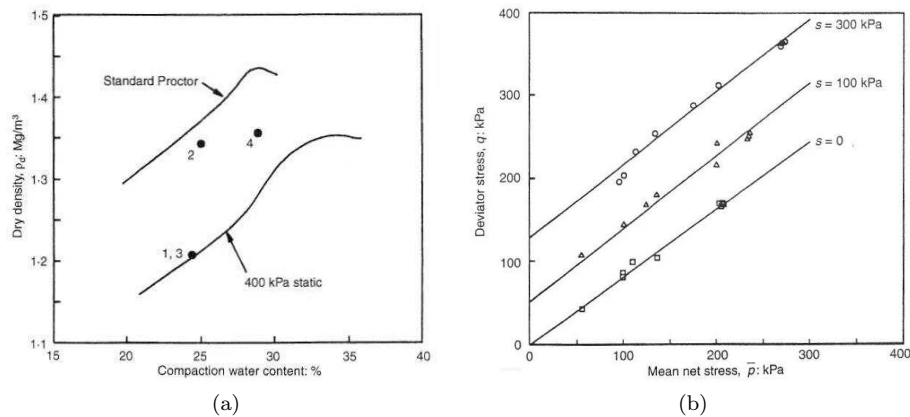


Figure 3.31: (a) Compaction details for series 1–4 and the curves of standard Proctor compaction and 400 kPa static compaction (Sivakumar and Wheeler, 2000); (b) Critical state data in the plane (q, p) for series 1, 2 and 3 (Wheeler and Sivakumar, 2000)

In contrast, Estabragh and Javadi (2008) reported that slope of critical state line in the (q, p) plane is suction dependent and decreases with increasing suction. On the investigation of a silty soil, they found that critical state lines at different suctions are not parallel and, on the conducted experiments, meet each other at a point with a mean net stress of about 950 kN (fig. 3.32a). Figures 3.32b and 3.32c shows the variation of $M(s)$ and $\mu(s)$ with suction. It appears that the value of $M(s)$ decreases with increasing suction, whereas $\mu(s)$ follows

an inverse trend, although not in a linear fashion as assumed by Alonso *et al.* (1990).

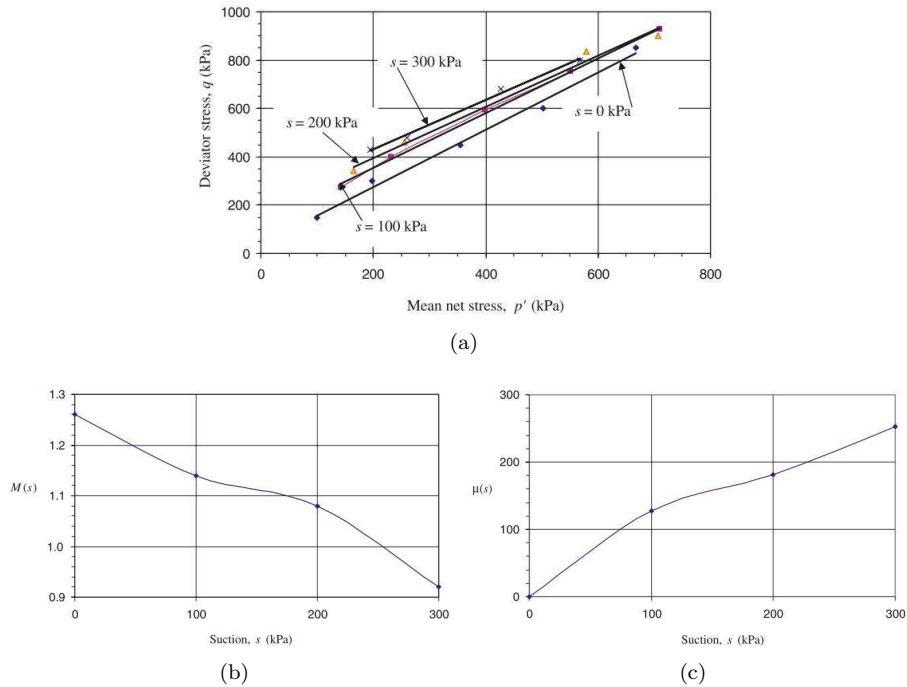


Figure 3.32: (a) Critical state line for q and p' under various suctions; (b) Variation of $M(s)$ with suction; (c) Variation of $\mu(s)$ with suction (Estabragh and Javadi, 2008)

With respect to critical state line in the plane (v, p') , accordingly to Wheeler and Sivakumar (2000), compaction pressure had no apparent effect on the relationship at this plane, suggesting that any differences in initial fabric caused by increased compaction pressure are erased by shearing to a critical state. However, molding water content appears to affect the critical state line at this plane, suggesting that differences in soil fabric produced by compaction at different water contents are not completely erased even by shearing to a critical state. They state that a possible explanation lies in the two levels of soil fabric within samples compacted dry of optimum: the macrostructural arrangement of large clay packets and interpacket voids, and the microstructure within individual packets. The critical states observed in triaxial tests probably correspond to shearing of the macrofabric to a critical state, whereas the relatively strong microfabric of individual clay packets may not reach a critical state, so that the influence of the initial fabric is not completely erased. As so, Equation 3.28 defines the critical state line in the (v, p') .

$$v(s) = \Gamma(s) - \lambda(s) \cdot \ln(p) \quad (3.28)$$

On the other hand, Mancuso *et al.* (2002) and Estabragh and Javadi (2008) reached different results from experimental data. For the studied materials the critical state values of v appear to fall on a unique critical hyperline for each

value of suction and were nearly parallel (fig. 3.33). However, Estabragh and Javadi (2008) reported that the position and the slope of the critical state line at zero suction (saturated condition) were very different to those of the critical state lines for unsaturated soil samples. These trend is also contrary to the model presented by Alonso *et al.* (1990).

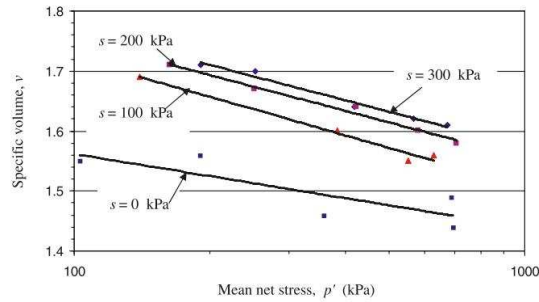


Figure 3.33: Variation of specific volume (v) and mean net stress at critical state condition (Estabragh and Javadi, 2008)

Concerning to the influence of compaction technique, Wheeler and Sivakumar (2000) concluded that a change from static to dynamic compaction, with no change in compaction water content or compaction induced dry density, had no apparent effect on subsequent material behaviour. This was consistent with the fact that there was no influence on behaviour under isotropic stress states.

3.4 Summary

This chapter reviews basic concepts related to the hydro-mechanical behavior of unsaturated geomaterials where suction plays a fundamental role. In turn, suction is influenced by water content whose relationship can be described by the soil water characteristic curve (SWCC), also known as soil water retention curve (WRC). Then is presented the effective stress concept for saturated geomaterials, contrasting with the effective stress concept for unsaturated geomaterials. With regards to unsaturated geomaterials two approaches are commonly used in the literature: effective stress approach and independent state variable approach. In this investigation the effective stress approach was used.

This chapter focus on the influence of compaction conditions (water content, compaction energy and compaction technique) on the hydro-mechanical behaviour of saturated and unsaturated geomaterials is reviewed. It is presented the state of the art on the water retention curve, stiffness, compressibility and strength of unsaturated soils found in published literature about the topics. The hydro-mechanical behaviour of unsaturated geomaterials is not straightforward due to the presence of suction and, even at critical states, the results found on literature are contradictory.

Chapter 4

Experimental program

4.1 Introduction

The experimental program is developed in three parts, namely, a laboratory test campaign, a full scale trial performed on a railway embankment and another trial carried out in a road embankment.

The execution of these trials was greatly conditioned by the impossibility to fully perform the initially planned work, in the aim of a cooperation protocol between the National Railway Network (*REFER*) and four national research institutions (University of Minho, *UM*; National Laboratory of Civil Engineering, *LNEC*; New University of Lisbon, *FCT/UNL*; and Technical University of Lisbon, *IST*) to develop the knowledge concerning the methodology for the construction and control of the railway embankments and rail track layers for high speed trains. This was established under the framework of a national research project POCI/ECM/61114/2004, entitled “Interaction soil–rail track for high speed trains”, financed by the Foundation for Science and Technology (*FCT*). In this protocol was planned:

- Execution of a trial embankment to establish a methodology of construction for optimization of embankments performance;
- Construction and observation of two definitive railway embankments, one built according to traditional technologies of construction and control, and another built according with the new technologies of construction and control. During the construction of definitive embankments instrumentation and monitoring during and post construction would be done. This would allow comparison of performances from the two embankments, as well as eventual comparison with numerical models developed in this context.

In the aim of this protocol it was only possible to perform the trial embankment, which is called hereafter Évora Trial Railway Embankment (*ETRE*).

However, another contract between the Centre for Waste Valorisation (*CVR*) and Portuguese Steel Companies (*SN*), including University of Minho, allows to obtain more knowledge about this subject also under the framework of another National Research program founded by *FCT*. In fact, a trial road embankment was constructed, giving the possibility to carry out different studies using spot

and continuous compaction control tests, as well as the instrumentation of the embankment and road layers to measure vibrations and strains induced by the compaction equipment and load traffic. Hereafter this trial embankment is referred to as Fafe Trial Road Embankment (*FTRE*).

Additionally to the fields tests and monitoring of the embankment trials a laboratory tests program was performed. It was intended to characterize the materials and to support modeling behaviour of materials and the interpretation of field tests in a more phenomenological way.

The experimental program adopted will be described in the following main sections:

- Laboratory investigation;
- Évora trial railway embankment (*ETRE*);
- Fafe trial road embankment (*FTRE*).

4.2 Laboratory investigation

The laboratory investigation involved the study of five materials: Clayey sand (*SC*), Crushed aggregate 0/31.5 (*CA31.5*), Poor-graded silty sand (*SP*), Inert Steel Aggregate for Construction (*ISAC*) and Crushed aggregate 0/40 (*CA40*).

However, in the scope of this thesis only *SC* and *CA31.5* were object of a laboratory investigation, namely, physical, hydro and mechanical characterization. Therefore, a detail description of the tests carried out on these materials will be presented. Concerning the remaining materials, these were studied in the aim of another doctoral thesis (Reis Ferreira, 2010). It is worth to note that these materials were employed in trial embankments.

4.2.1 Physical characterization

SC and *CA31.5* materials were first subject to identification tests, grain size distribution, Atterberg limits, Specific Gravity, Methylene Blue Adsorption method, Sand Equivalent test, and Standard and Modified Proctor tests. A list of tests is presented in Table 4.1.

Table 4.1: Identification and compaction tests performed on *SC* and *CA31.5*

Test	<i>SC</i>	<i>CA31.5</i>
Grain size distribution	×	×
Atterberg limits	×	–
Specific Gravity	×	×
Methylene Blue	×	×
Sand Equivalent	×	×
Standard Proctor	×	–
Modified Proctor	×	×

4.2.2 Hydro characterization

The hydro characterization (suction–water content relationship) was carried out only for *SC* material. State conditions were defined in order to provide information about the influence of the variation of moisture content on the behaviour of studied materials. The specimens were compacted to 97% of the maximum dry density of Modified Proctor, i.e., to the same void ratio, by means of a vibrating hammer, over the range of following molding water contents:

- 4% dry of optimum ($w_{OPM-4\%}$);
- 2% dry of optimum ($w_{OPM-2\%}$);
- optimum (w_{OPM});
- 2% wet of optimum ($w_{OPM+2\%}$).

It is noteworthy that this molding water contents covers the range of the moisture contents employed in field investigation, which will be described in following main sections.

As mentioned in Chapter 3, the filter paper technique was employed to measure matric suction of *SC* specimens. The initial negative pore water pressure (under $\sigma_3 = 0$) was controlled by means of calibrated filter papers Whatman #42, ashless quantitative Type II, with a diameter of 9 cm. In this technique, after compaction, two initially dry filter papers were placed on the top and bottom of the specimens. The outer filter papers were used for suction measurement, while the filter papers in contact with the specimen were used to protect the outer filter papers from soil fouling or contamination. To ensure good contact between the specimen and the filter papers and to make easier to manage the set, specimen and filter papers were sandwiched by acrylic plates and then wrapped up in a plastic foil. After that, the set is placed in a airtight plastic bag and stored inside an temperature controlled cabin. Then, the filter papers and the soil specimen moisture content were allowed to equilibrate.

An equilibrium period of at least 14 days was allowed for the specimens, filter paper, and the air in the sealed container to reach equilibrium. At the end of the equilibration period, the filter papers were removed from the soil specimen, and the wet mass of the outer filter papers were measured with a high precision balance with 0.0001 g accuracy. The measurement process was completed within a few seconds to avoid moisture loss from the filter papers. Subsequently, filter paper and soil were oven-dried at 110°C for 24 hours. The moisture contents of each were individually determined. The equilibrium filter paper water content of the specimen was then converted to matric suction values by calibration curve (Bicalho *et al.*, 2011).

Series of tests were conducted over the range of molding water contents previously defined. At each series corresponding to a given molding water content, three tests were carried out. The state parameters of each test are given in Table 4.2.

The specimen preparation procedure is the same for all samples. Each one is mixed up with the right quantity of water and it is placed in a sealed plastic bag four 24 hours to achieve uniform moisture conditions. After the hydric equilibrium period is reached specimens were compacted with a vibrating hammer in a cylindrical mould with 100 mm in diameter. During compaction process the

Table 4.2: Filter paper method performed on *SC*

	w [%]	e	S [%]
$w_{\text{OPM}-4\%}$	4.6	0.342	35.6
	4.6	0.332	36.7
	4.7	0.329	37.8
$w_{\text{OPM}-2\%}$	6.0	0.329	48.3
	6.9	0.335	47.5
	6.9	0.331	47.2
w_{OPM}	9.3	0.319	77.4
	9.4	0.322	77.4
	9.4	0.334	74.5
$w_{\text{OPM}+2\%}$	11.6	0.321	95.8
	11.9	0.323	97.4
	11.5	0.320	95.3

specimen height was controlled by the time of vibration in order to obtain the fixed dry density. With this purpose, specimens with 100 mm in diameter and 25 mm high were prepared.

4.2.3 Mechanical characterization

Mechanical characterization was carried out on specimens in unsaturated conditions and in the small and large strain domain, involving oedometer tests, triaxial tests and triaxial tests in a stress–path Bishop–Wesley triaxial chamber with measurement of S–waves velocity. In addition, tests in dry or saturated conditions were performed as reference tests. In Table 4.3 are presented the tests performed on *SC* and *CA31.5*.

Table 4.3: Mechanical tests carried out on *SC* and *CA31.5*

Material	Specimens state conditions		Mechanical tests				
	Molding water content	Saturation condition	Type of test				
<i>SC</i>	$w_{\text{OPM}-4\%}$	unsaturated	TXM	–	–	TXS	OE
	$w_{\text{OPM}-2\%}$	unsaturated	TXM	–	–	TXS	OE
	w_{OPM}	unsaturated	TXM	TX	–	TXS	OE
	w_{OPM}	saturated	TXM	TX	–	–	OE
	$w_{\text{OPM}+2\%}$	unsaturated	TXM	–	–	TXS	–
	w_{dry}	unsaturated	TXM	–	–	TXS	–
<i>CA31.5</i>	$w_{\text{OPM}-2\%}$	unsaturated	TXM	–	–	–	–
	w_{OPM}	unsaturated	TXM	–	TXI	–	–
	w_{OPM}	saturated	TXM	–	TXI	–	–
	w_{dry}	unsaturated	TXM	–	–	–	–

Note: TXM – Triaxial multistage test; TX – Triaxial test; TXI – Triaxial isotropic test; TXS – Triaxial tests in a stress–path Bishop–Wesley triaxial chamber with measurement of S–waves velocity; OE – Oedometer test

Oedometer test

In order to study the compressibility of *SC* material under unsaturated and saturated conditions the oedometer test was performed (UNE 103–405–94, 1994). Conventional oedometer equipment and procedures for incremental loading were used. A series of load increments and decrements were applied and the settlement was recorded continuously. The series of load increments and decrements are: 5, 10, 25, 50, 100, 200, 300, 500, 1000, 500, 200, 100 kPa. Previous to the first load increment a preload was applied not exceeding 3 kPa. After the final decrement the final moisture content of the sample was determined.

In Table 4.4 are summarized the conducted tests and respective state parameters. One test with high value of void ratio was performed to determine the intrinsic properties of the soil.

Table 4.4: Oedometer tests performed on *SC*

	w [%]	e	S [%]
WOPM–4%	5.1	0.341	39.6
WOPM–2%	6.6	0.335	51.9
WOPM	8.5	0.322	70.0
WOPM	8.8	0.633	36.8
WOPM _{sat}	8.8	0.339	68.7

The specimens preparation procedure is similar to all the type of tests. However, in this particular case, before material mix up with the right quantity of water, first, it was sieved to avoid the presence of coarse grains (maximum size: 4.75 mm). This was due to the high of the oedometer ring, with dimensions of 19.6 mm high and 70 mm in diameter.

After the hydric equilibrium period, compaction was performed in the same mold used for the preparation of all other specimens, with 100 mm in diameter. The mass of material was placed together with the oedometer ring inside the mold. Once again, the time of vibration was that necessary to obtain the desirable volume. This procedure was adopted since it has the advantage that only the top of the specimen contained in the oedometer ring needs to be trimmed flush.

Triaxial test procedures

Triaxial testing is commonly used to quantify the shear strength of a geo-material, and procedures for such testing are well established. Nevertheless, to obtain maximum information from a limited number of tests and to eliminate the effect of soil variability, a multistage testing procedure was attempted (Ho and Fredlund, 1982; Reis Ferreira, 2010). Thus, triaxial tests were conducted using three stages corresponding to isotropic consolidation stresses of 100, 200 and 300 kPa.

The method consists of applying an isotropic stress of 100 kPa corresponding to the first stage of testing and the sample is allowed to consolidate. Once no further sample volume change can be detected, the sample is in equilibrium with the applied isotropic stress. After consolidation is complete, the minor principle stress (σ_3) is maintained while the sample is loaded at a constant strain rate. A “cyclic loading” procedure was adopted in testing the sample, as illustrated in

Figure 4.1. The deviator stress was applied until it was apparent that the stress was reaching a peak value. At this point, the vertical load was “backed-off” the sample. After that, a new set of stress corresponding to the second stage ($\sigma_3 = 200$ kPa) is applied to the sample, consolidation is again allowed, and the loading process is repeated as before. For the last stage, corresponding to $\sigma_3 = 300$ kPa, the deviator stress is applied until the critical state is reached.

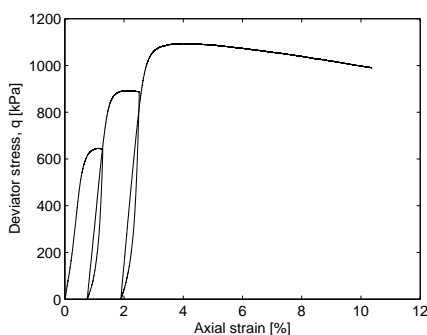


Figure 4.1: Example of a multistage test result

As mentioned before (see Table 4.3), besides unsaturated tests, also dry and saturated triaxial tests were performed as reference tests. In addition, triaxial tests with only one stage, corresponding to $\sigma_3 = 300$ kPa, and isotropic triaxial tests were carried out in order to allow comparison with the last stage of the multistage tests and so, to evaluate if results are influenced by the multistage procedure.

In all triaxial tests, the drainage system remained open. In Tables 4.5 and 4.6 are summarized the triaxial tests conducted on each studied material and respective state parameters.

Table 4.5: Triaxial *CD* tests performed on *SC* specimens with 100 mm \times 200 mm

	w [%]	e	S [%]	Type of test	Minor principle stress, σ_3 [kPa]
W _{OPM-4%}	5.0	0.339	39.1	multistage	100, 200, 300
W _{OPM-2%}	6.9	0.333	55.3	multistage	100, 200, 300
W _{OPM}	9.1	0.342	70.5	multistage	100, 200, 300
W _{OPM iso}	9.8	0.344	75.4	one stage	300
W _{OPM+2%}	10.8	0.336	85.1	multistage	100, 200, 300
W _{dry}	0.0	0.336	0.0	multistage	100, 200, 300
W _{OPM sat}	8.8	0.334	69.9	multistage	100, 200, 300
W _{OPM iso sat}	8.9	0.339	69.5	one stage	300

The specimen preparation procedure is identical for both materials. Each one is mixed up with the right quantity of water and it is placed in a sealed plastic bag four 24 hours to achieve uniform moisture conditions. After that, all specimens are compacted by a vibrating hammer. The time of vibration was that necessary to obtain the fixed dry density.

To perform triaxial tests on *SC*, specimens with 100 mm in diameter and 200 mm high were prepared. After the hydric equilibrium period is reached, in

Table 4.6: Triaxial *CD* tests performed on *CA31.5* specimens with 150 mm × 300 mm

	w [%]	<i>e</i>	<i>S</i> [%]	Type of test	Minor principle stress, σ_3 [kPa]
WOPM-2%	3.8	0.217	47.7	multistage	100, 200, 300
WOPM	5.5	0.226	66.3	multistage	100, 200, 300
W _{dry}	0.0	0.217	0.0	multistage	100, 200, 300
WOPM _{sat}	5.9	0.225	71.0	multistage	100, 200, 300
<i>w</i> _{1% sat}	1.4	0.221	17.8	multistage	100, 200, 300
WOPM _{iso}	5.5	0.226	66.3	isotropic	10, 25, 50, 100, 200, 300, 400
WOPM _{iso sat}	5.9	0.234	68.7	isotropic	10, 25, 50, 100, 200, 300, 400
WOPM _{iso sat}	5.8	0.454	34.9	isotropic	10, 25, 50, 100, 200, 300, 400

order to get the best possible standard homogeneity, compaction was performed in four layers, each one with the same mass of material, in a 100 mm diameter cylindrical mould. For the first layer of 50 mm compression was performed until the desire volume was reached. The other three layers were successively compacted on the top of the previous one using the volume criterion. The interface between the different layers were carefully scarified in order to provide good bonding between them.

The same procedure was adopted for *CA31.5*. However, due to material grain size, specimens with 150 mm in diameter and 300 mm high were prepared. These were compacted in six layers using the same mass of material for each one.

A conventional strain-controlled triaxial press was used to perform triaxial tests. The loading rate of 0.03 mm/min for compression was adopted, which corresponds to 0.015% and 0.010% strain per minute for specimens with 200 mm high and 300 mm high, respectively. The vertical strain was confirmed by means of an external displacement transducer. Conventional triaxial cells were also instrumented with a load cell, located just above the top cap inside the triaxial cell in order to eliminate piston friction effects. Also, two pressure transducers and two volume controllers were used, one to control the pressure-volume of the fluid in the cell and the other to control the pressure-volume of the sample (for saturated tests).

Triaxial tests with measurement of S-waves velocity. Setup and procedures

A series of tests using bender elements and accelerometers was carried out with the purpose to get data in the small strain domain.

Once no chamber was prepared to incorporate bender-extender elements, it was necessary to adapt an existing one. Therefore, the system design was influenced by the characteristics of equipment and sensors available in the Laboratory of Civil Engineering at the University of Minho. For the development of this system, a Bishop-Wesley stress-path chamber was used and adapted to

accommodate the bender–extender elements and the accelerometers.

With regard to bender–extender elements, two bottom and top sensors and one lateral sensor were available. However, only the bottom and top sensors to be installed on the platens were used. New bottom and top platens were designed and manufactured and modifications in stress–path chamber, including drilled holes for cable outlet, were made, as illustrated in Figure 4.2. In Figure 4.3 top and bottom platens are presented with embedded bender–elements. It is worth to note that each platen is composed of two parts. This solution was determined by the fact that the sensors are equipped with original cables and plugs that were not changed in order to preserve the quality of transmitted signals. The bender–extender elements used in this work were manufactured by GDS Instruments (2011) and allow transmission of P–waves and S–waves. However, only measurement of S–waves were performed. This was due to the maximum limit of the acquisition frequency rate allowed by the acquisition equipment used, which does not enable measurement of P–waves.

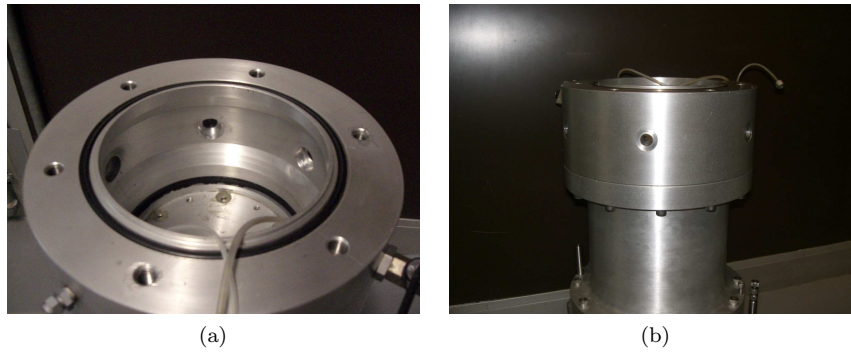


Figure 4.2: Holes on stress–path Bishop–Wesley triaxial chamber to incorporate cables: (a) inside view; (b) lateral view



Figure 4.3: (a) Bottom and (b) top platens with embedded bender–elements (Ferreira *et al.*, 2010)

Concerning to accelerometers, two sensors whose physical characteristics, including the mass and dimension, allow the installation on the side of the sample were available. To measure the soil vibrations on the sides of the specimen it should be guaranteed adequate coupling to the specimen, so that is ensured the

sensors horizontality and stability during measurements. Thus, sensors were fixed to the sides of the specimens at specific points, by means of designed pins screwed to the back of the accelerometers. After specimen placement on the stress–path cell, pins are spiked into the specimen. This involves drilling the membrane and, therefore, careful isolation of the hole must be guaranteed. The accelerometers, from Brüel and Kjær, are piezoelectric sensors type 4513–001, with sensivity of 100 mV/g, measure range of ± 50 g, a frequency range between 1 and 10 kHz, with dimensions of 12.7 mm in diameter and 15.65 mm high and approximately 9 grams in weight (fig. 4.4).



Figure 4.4: Accelerometer and pin (Ferreira *et al.*, 2010)

The final setup is illustrated in Figure 4.5. The conceived testing system comprises a total of four sensors: two bender-extender elements and two accelerometers. The sensor located on the bottom platen is the transmitter BE that sends seismic S–waves, which travel through the specimen, and are received and recorded by the remaining transducers, the receiver BE and the accelerometers.

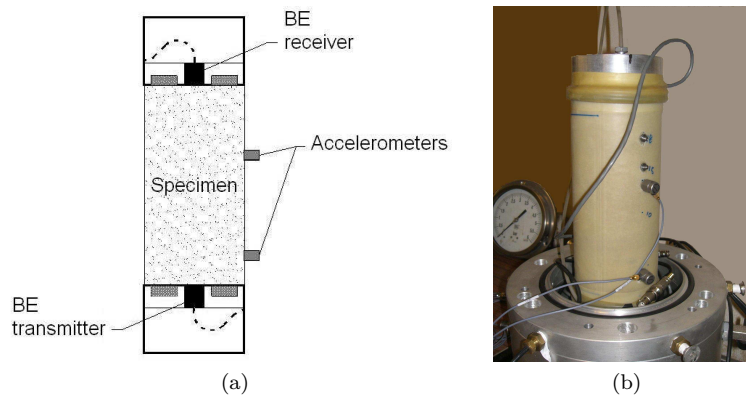


Figure 4.5: Bender elements and accelerometers setup: (a) scheme; (b) view (adopted from Ferreira *et al.* (2010))

The associated electronics equipment consists of two main components: a function generator from Thurlby Thandar Instruments (TG1010A model) and a National Instruments data logger system (SCXI–1600), with 16–bit accelerometer cards (SCXI–1531), connected to a portable computer. The function generator produces the output signal in the form of a sine pulse to a transmitting bender element with the maximum amplitude allowed by the equipment (± 10 V)

in order to enhance the response of the bender element–soil system. Data acquisition was performed at the maximum allowed by equipment (200 kHz), that is to say, a frequency of 50 kHz per channel, which corresponds to a $\Delta t = 0.00002$ s. The portable computer was used to display and collect the signals.

A specific LabVIEW interface was developed for data acquisition and recording. The program operates similarly to an oscilloscope: triggered signals are detected and an average of 16 pulses, which are stacked to improve signal–to–noise ratio, is displayed. In addition, each channel can be individually amplified by a user–defined factor, as shown in Figure 4.6.

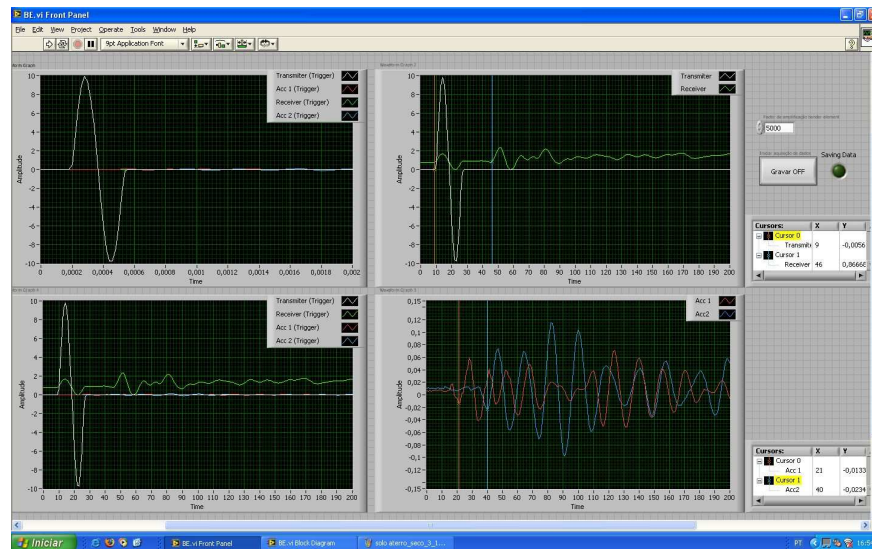


Figure 4.6: Sample display of acquisition program developed in LabVIEW

Triaxial tests with measurement of S–waves velocity were conducted only on *SC* specimens. The test consisted in three phases. Firstly, measurements of S–waves velocity were performed without application of stresses ($\sigma_3 = 0$ kPa) on specimens. Secondly, specimens were submitted to isotropic stresses, namely, 25, 50, 100 kPa, and consolidation was allowed. For each stage measurement of S–waves velocity were conducted. Finally, similarly to triaxial tests, a multistage testing procedure was adopted, using three stages corresponding to isotropic consolidation stresses of 100, 200 and 300 kPa. However, the deviator stress was applied until approximately 30% of the peak value at each stage. This was due to constraints on the air pressure system. Besides unsaturated tests with the previous defined state parameters, also a dry isotropic test was performed. In Table 4.7 is summarized the triaxial tests program with the state parameters for each specimen.

SC specimens dimensions and preparation procedure are similar to the ones previously described for standard triaxial tests. Likewise, the loading rate of 0.03 mm/min for compression was adopted, which corresponds to 0.015% strain per minute. This was possible through the implementation of a control system developed by Araújo (2007).

A load cell located just above the top cap inside the triaxial cell and a pressure transducer to control pressure of the fluid inside the cell were used.

Table 4.7: Triaxial tests with measurement of S-wave velocity performed on *SC* specimens with 100 mm × 200 mm

	w [%]	e	S [%]	Type of test	Minor principle stress, σ_3 [kPa]
$w_{\text{OPM}-4\%}$	4.7	0.331	37.6	isotropic multistage	0, 25, 50, 100 100, 200, 300
$w_{\text{OPM}-2\%}$	6.8	0.333	54.0	isotropic multistage	0, 25, 50, 100 100, 200, 300
w_{OPM}	8.8	0.334	69.9	isotropic multistage	0, 25, 50, 100 100, 200, 300
$w_{\text{OPM}+2\%}$	10.8	0.337	84.9	isotropic multistage	0, 25, 50, 100 100, 200, 300
w_{dry}	0.0	0.332	0.0	isotropic	0,100, 200, 300

No volume controllers were used in this type of test. This was due to the implementation of the accelerometers, which are not prepared to work under water. To this end, air was used instead of water for application of confining pressures. Volume change was estimated from triaxial tests volume change curves.

4.3 Field investigation: Évora trial railway embankment (*ETRE*)

Under the framework of a national research project mentioned previously, a protocol between the Portuguese National Railways Network (*REFER*) and and four national research institutions (*UM*, *LNEC*, *FCT/UNL*, and *IST*) was established, which focused the following main objectives:

- Establishment of a methodology of construction for optimization of embankments performance;
- Development of a specification of the plate loading test to be used as a reference method;
- Methodology for calibration of dynamic plate loading tests, like Falling Weight Deflectometer (*FWD*), Soil Stiffness Gauge (*SSG*), Spectral Analysis Surface Waves (*SASW*) and others;
- Application of continuous compaction control by different tools (like Portancemètre and integrated compaction control) and methodology for calibration;
- Establishment of a methodology for quality control of compacted layers by using spot methods and continuous approach.

To reach the goal, a trial embankment was constructed with the cooperation of *REFER*, *MOTA-ENGIL* and *GEOCONTROLE*. This one took place near the new railway line between “Sines” and “Caia”, in section “Casa Branca – Évora”

at PK 106+800, about 2.5 km from the “Monte das Flores” railway station, and running tests between October and November of 2006.

An experimental program was established consisting on the employment of different materials and on the in situ evaluation of physical and mechanical properties.

4.3.1 Materials

Two type of materials were tested: *SC* for the embankment layers and *CA31.5* for the sub-ballast layer, as shown in Figure 4.7.



Figure 4.7: *ETRE*: (a) *SC* layer; (b) *CA31.5* material over *SC* layer; (c) and (d) general overview of *SC* and *CA31.5* trial layers

4.3.2 Experimental plan

In order to fulfill the main objectives established on the protocol an experimental plan was developed involving optimization of thickness layers constructed over a range of different moisture contents, for different energy levels corresponding to the passes of the compaction equipment. A Caterpillar CS-583D smooth drum vibratory roller was used during investigation, which is classified as V4 accordingly to LCPC/SETRA (1992). For each energy level, the behaviour of trial layers, with different thicknesses and moisture contents, were then evaluated by means of field tests.

Geometry

Trial layers were planned to be constructed with dimensions in plant of 50 m length and 6 m width. Then a mesh was created in order to establish the location to run field tests. This consisted in dividing width into lanes with 2 m (*A*, *B*, *C*) and length into columns with 5 m (1 to 10), thus, resulting grids with dimensions $5 \times 2 \text{ m}^2$. For each grid a set of field tests would be conducted to evaluate physical and mechanical properties of the trial layer, for each energy level applied. In Figure 4.8 is shown the adopted mesh. It should be noted that lanes *A* and *C*, were provided for all types of tests, while lane *B* was only subject to non-destructive tests.

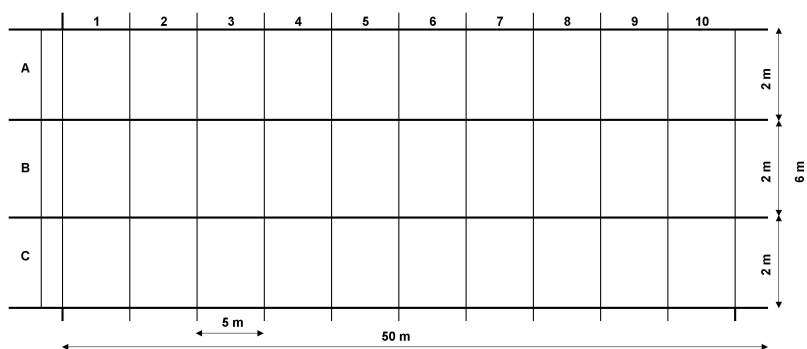


Figure 4.8: Mesh created for *ETRE* trial layers with dimensions of $50 \times 6 \text{ m}^2$

However, due to space and time constraints, not all layers were constructed as initially planned. Some layers were constructed with half of the length (25 m) and/or were constructed over another layers, instead over foundation.

Taking into account the optimization of trial layers thicknesses, these were defined accordingly to the ones commonly used with the studied geomaterials. For *SC* trial layers thicknesses of 0.30, 0.40 and 0.50 m were employed, while for *CA31.5* trial layers thicknesses of 0.22 and 0.30 m were employed.

Moisture conditions of materials

After geometry definition, moisture conditions were established. A range of three different moisture contents were employed on *SC* trial layers: (i) 2% dry of optimum ($w_{\text{OPM}-2\%}$); (ii) optimum (w_{OPM}); (iii) 2% wet of optimum ($w_{\text{OPM}+2\%}$). Concerning to *CA31.5* trial layers only optimum moisture content (w_{OPM}) was employed. Moisture content was established in relation to modified Proctor test for both geomaterials. The geometry and moisture conditions of the trial layers are summarized on Table 4.8.

Concerning to the water application, it is worth noting that the methodology adopted was similar to the one employed on embankment dams. To achieve desirable moisture contents, materials were stacked and water was added. Then materials were mixed up by means of a front shovel.

It should be pointed out that before the construction of the trial layers, superficial soils with poor quality were removed. An excavation of 0.60 m depth was made within an area of approximately 2000 m^2 . In order to promote homogeneity of the support of the trial embankment, foundation with 0.60 m thickness

Table 4.8: Synthesis of the state conditions and geometric characteristics adopted on the trial embankment

Material type	Moisture content, w [%]	Thickness [m]	Dimensions of layers [m ²]	Executed above
SC		0.30	50 × 6	Foundation
	W _{OPM} -2%	0.40	25 × 6	0.30 W _{OPM} -2%
		0.50	50 × 6	Foundation
	W _{OPM}	0.40	50 × 6	Foundation
	W _{OPM} +2%	0.40	50 × 6	0.30 W _{OPM} -2% and 0.40 W _{OPM}
CA31.5	W _{OPM}	0.22	25 × 6	0.50 W _{OPM} -2%
	W _{OPM}	0.30	25 × 6	0.50 W _{OPM} -2%

was compacted in two layers with 0.30 m thickness each, with moisture content in the dry side of the modified Proctor curve. Each layer was compacted with energy level corresponding to twelve passes of the vibrating roller.

Field tests on trial layers

To evaluate the state conditions and mechanical properties of the several layers, for different energy levels, the following fields tests were performed:

- Sand cone method (*SCM*) performed by *LNEC*;
- Nuclear method (*NM*) performed by *LNEC*;
- Static Plate Load Test (*SPLT*) performed by *UM*;
- Soil Stiffness Gauge (*SSG*) performed by *LNEC*;
- Ligth Falling Weight Deflectometer (*LFWD*) performed by *LNEC*;
- Falling Weight Deflectometer (*FWD*) performed by *UM*;
- Spectral Analysis of Surface Waves (*SASW*) performed by *UM*;
- Portancemètre performed by *GEOCONTROLE*.

The *SCM* and *NM* allow determination of state parameters, while the others enable determination of mechanical properties. As stated in Chapter 2, only Portancemètre allows continuous compaction control.

The experimental plan was established according to the mesh previously defined and is illustrated in Figure 4.9. As mentioned previously, some trial layers were constructed with half the length, i.e., 25 m instead of 50 m. In these cases, only half of the experimental plan was carried out. It should be noted that in lanes *A* and *C*, the Portancemètre passes were done after the *SPLT* tests. Each layer was tested for different energy levels corresponding to 4, 6, 8, 10 and 12 passes of the vibrating roller. Exceptions must be made to some tests, which were not performed due to either time and/or weather constraints.

In Tables 4.9 to 4.12 a summary of the number of spot tests conducted is made according to type of geomaterial and moisture content.

	1	2	3	4	5	6	7	8	9	10		
A	LA	SCM-NM-SPLT-LFWD-SSG (4)		SCM-NM-SPLT-LFWD-SSG (8)		SCM-NM-SPLT-LFWD-SSG (8)		SCM-NM-SPLT-LFWD-SSG (8)	SCM-NM-SPLT-LFWD-SSG (8)		SCM-NM-SPLT-LFWD-SSG (4)	PORTANCE METRE
	L1		SCM-NM-SPLT-LFWD-SSG (10)		SCM-NM-SPLT-LFWD-SSG (12)		SCM-NM-SPLT-LFWD-SSG (12)			SCM-NM-SPLT-LFWD-SSG (10)		
B	L2	NM-LFWD-SSG						NM-LFWD-SSG				PORTANCE METRE
	L3			NM-LFWD-SSG						NM-LFWD-SSG		
C	LC	SCM-NM-SPLT-LFWD-SSG (8)	SCM-NM-SPLT-LFWD-SSG (8)	SCM-NM-SPLT-LFWD-SSG (4)				SCM-NM-SPLT-LFWD-SSG (4)		SCM-NM-SPLT-LFWD-SSG (8)	SCM-NM-SPLT-LFWD-SSG (8)	PORTANCE METRE
				SCM-NM-SPLT-LFWD-SSG (10)	SCM-NM-SPLT-LFWD-SSG (12)	SCM-NM-SPLT-LFWD-SSG (10)		SCM-NM-SPLT-LFWD-SSG (12)				

Figure 4.9: Experimental plan adopted on *ETRE* for layers with dimensions of $50 \times 6 \text{ m}^2$

With regards to *SPLT*, whenever the number of tests are presented as, for example, $8 + 5$, it means that were conducted 8 tests following AFNOR standard and 5 tests following DIN standard (recall Chapter 2). Concerning the remaining tests, whenever the number of tests are presented as, for example, $4 + 2^*$, it means that 6 tests were conducted, 2 of which were done at the same spot where *SPLT* were performed.

Table 4.9: Number of tests conducted on *SC* trial layers with moisture content $\omega_{opt-2\%}$

Layer	No. of passes	SCM	NM	SPLT	SSG	LFWD
0.30 m	4	4	10	4	10	8
	6	$4 + 2^*$	7	2	8	8
	8	4	8	4	8	8
	10	4	8	2	8	8
	12	$4 + 2^*$	8	$5 + 5$	8	$8 + 4^*$
0.40 m	4	–	6	–	5	4
	6	–	5	–	5	5
	8	–	5	–	5	5
	10	–	5	–	5	–
	12	$2 + 2^*$	$5 + 3^*$	$5 + 4$	$5 + 4^*$	6^*
0.50 m	4	4	8	4	8	8
	6	4	8	2	8	8
	8	4	9	4	9	3
	10	4	8	2	8	9
	12	4	8	$5 + 5$	8	$7 + 4^*$

Concerning to continuous compaction control by mean of Portancemètre, tests were performed in every layers and for all energy levels corresponding to 4, 6, 8, 10 and 12 passes of the vibrating roller.

Table 4.10: Number of tests conducted on *SC* trial layers with moisture content ω_{opt}

Layer	No. of passes	<i>SCM</i>	<i>NM</i>	<i>SPLT</i>	<i>SSG</i>	<i>LFWD</i>	<i>FWD</i>	<i>SASW</i>
0.40 m	4	1	1	–	8	8	–	–
	6	4	8	–	8	8	–	–
	8	4	8	4	8	8+4*	–	–
	10	4	9	4	8	8+3*	–	–
	12	–	8	8+5	8	8+4*	2	2

Table 4.11: Number of tests conducted on *SC* trial layers with moisture content $w_{OPM+2\%}$

Layer	No. of passes	<i>SCM</i>	<i>NM</i>	<i>SPLT</i>	<i>SSG</i>	<i>LFWD</i>
0.40 m	4	4	8	4	8	7+4*
	6	–	8	–	8	7
	8	4	8	4	8	8
	10	–	8	–	8	8
	12	4+2*	8+3*	5+5	9+4*	8+6*

Table 4.12: Number of tests conducted on *CA31.5* trial layers with moisture content ω_{opt}

Layer	No. of passes	<i>SCM</i>	<i>NM</i>	<i>SPLT</i>	<i>SSG</i>	<i>LFWD</i>
0.22 m	4	6	5	–	5	5
	6	–	5	–	5	5
	8	–	5	–	5	5
	10	–	5	–	5	5
	12	–	5+5*	5+5	5+10*	5
0.30 m	4	6	5	–	5	5
	6	–	5	–	5	5
	8	–	5	–	5	5
	10	–	5	–	5	5
	12	–	5+5*	5+5	5+10*	5

4.4 Field investigation: Fafe trial road embankment (*FTRE*)

In the aim of a national research project POCI/ECM/56952/2004, entitled “Application of waste in transportation infrastructures and geotechnical constructions – Re-use of steel slags” financed by the Foundation for Science and Technology (*FCT*), the Portuguese Steel Companies (*SN*) required Centre for Waste Valorisation (*CVR*) to conduct an experimental field study with the goal to validate/calibrate in situ the results obtained in laboratory for the processed steel slag, actually named Inert Steel Aggregate for Construction (*ISAC*) produced in the Portuguese Steel Companies. The *ISAC* should be used in the base

and sub-base layers, in capping layer and embankment layers.

To reach the goal, *CVR* collaborating with Laboratory of Civil Engineering of University of Minho (*LEC-UM*) and with *LNEC* promoted the construction of a trial road embankment, which took place in the itinerary between “Fafe” and “Cabeceiras de Basto” (E.N. 311), at “Várzea Cova”. Also “Cândido José Rodrigues” (*CJR*) and *GEOCONTROLE* cooperated in the construction and continuous compaction control, respectively. The work and tests run between October and November of 2007.

Likewise in *ETRE*, an experimental plan was established to evaluate physical and mechanical properties of the trial road embankment. Besides behaviour evaluation, vibrations measurements were performed during the execution of road layers.

4.4.1 Materials

The construction plan consisted on the the employment of *ISAC* with the purpose of in situ validation/calibration of results obtained in laboratory for *ISAC* geomaterial. To meet this goal, also traditional materials were employed, namely *SP* and *CA40*, in such a way to allow comparison between *ISAC* and traditional geomaterials. In Figure 4.10 are illustrated the geomaterials employed and a general view of the trial road embankment.



Figure 4.10: *FTRE*: (a) *SP* material; (b) *ISAC* material; (c) and (d) general overview of *SC* and *ISAC* trial layers

4.4.2 Experimental plan

An experimental plan was established in order to fulfill three main objectives: (i) execution of trial layers to optimize thickness layer and energy level corresponding to the passes of the vibrating roller, while state conditions remain constant; (ii) evaluate materials behaviour during execution of trial, embankment and road layers; (iii) measurements of vibrations of the roller drum, as well as vibrations and compression vertical strains of the capping layer due to application of dynamic loads, during and after compaction process. A Hamm 3412 smooth drum vibratory roller was used during investigation, which is classified as V3 accordingly to LCPC/SETRA (1992).

Geometry

The construction plan consisted in three sections, each one with 10 m length, with different configurations adopted regarding the employment of *ISAC* and traditional materials, as illustrated in Figure 4.11. The three configurations were the following:

1. One only employing traditional materials, *SP* on embankment and capping layers and *CA40* on base layer;
2. One employing *SP* on embankment and capping layers and *ISAC* on base layer;
3. One employing *ISAC* on embankment, capping and base layers.

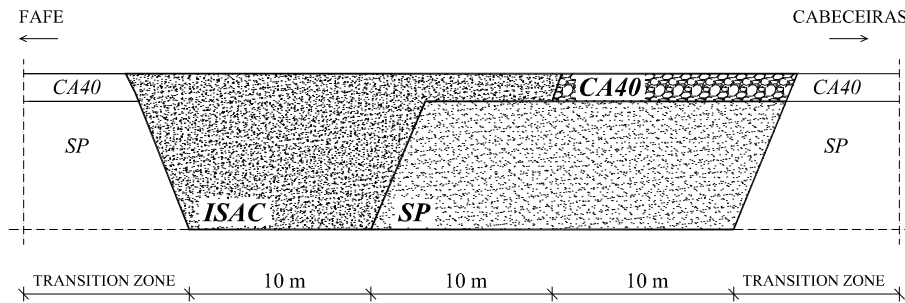
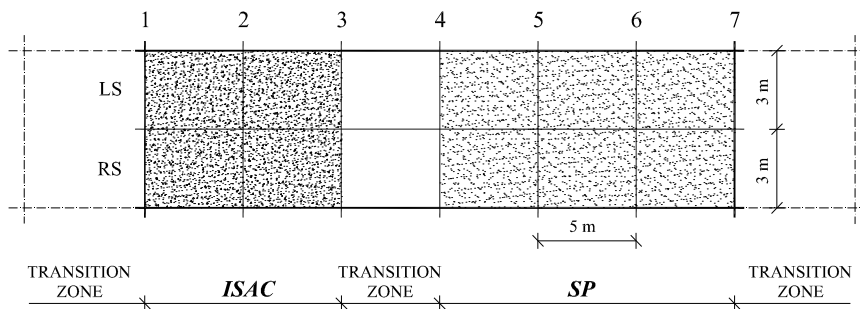


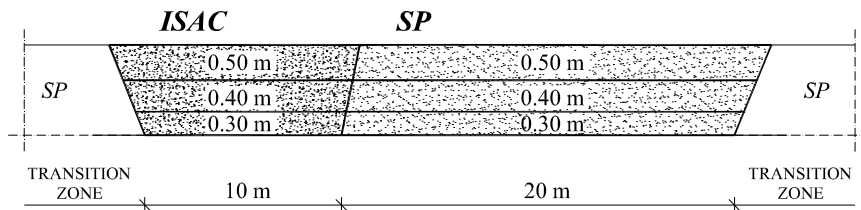
Figure 4.11: Construction scheme of the *FTRE*

All sections had the same width corresponding to the width of the embankment. Similarly to the experimental plan adopted on *ETRE*, a mesh was created in order to establish the location to run field tests. This consisted in dividing each layer into two lanes, named hereafter left side (*LS*) and right side (*RS*), and into columns with 5 m width (0 to 7), as illustrated in Figure 4.12. For each grid a set of field tests would be conducted to evaluate physical and mechanical properties of the trial layer, for each applied energy level.

As mentioned above, the construction process developed in three phases. Firstly, a trial embankment was constructed using *ISAC* and *SP*. In this phase, trial layers with thicknesses 0.30 (1st layer), 0.40 (2nd layer) and 0.50 m (3rd layer) were constructed (fig. 4.13). State conditions and mechanical properties

Figure 4.12: Mesh created for *FTRE* trial layers

were then evaluated for different energy levels corresponding to the passes of the vibrating roller. The main goal was to optimize thickness of the embankment layers and energy level, i.e., the number of passes of the vibrating roller. Secondly, construction of the embankment layers, the capping layer and the base layer were carried out with 0.40 (4th to 7th layer), 0.40 and 0.20 m thicknesses, respectively. Finally, bituminous layers were constructed with a total thickness of 0.14 m.

Figure 4.13: Construction scheme of the *FTRE* trial layers

Moisture contents of materials

For all materials optimum content, in relation to Modified Proctor, was adopted. The water application followed similar procedure to *ETRE*. However, moisture content was corrected on the embankment ever a deviation was verified from *NM* results.

Field tests on trial layers and embankment layers

An experimental plan was established to evaluate the behaviour of trial layers and of the embankment and road layers. The following in situ tests were performed:

- Sand cone method (*SCM*) performed by *LEC-UM*;
- Rubber balloon method (*RBM*) performed by *LNEC*;
- Nuclear method (*NM*) performed by *LEC-UM*;

- Static Plate Load Test (*SPLT*) performed by *LEC-UM*;
- Benkelman beam deflection measurement (*BBDM*) performed by *LEC-UM*;
- Soil Stiffness Gauge (*SSG*) performed by *LNEC*;
- Ligth Falling Weight Deflectometer (*LFWD*) performed by *LNEC*;
- Falling Weight Deflectometer (*FWD*) performed by *LEC-UM*;
- Spectral Analysis of Surface Waves (*SASW*) performed by *LEC-UM*;
- Portancemètre performed by *GEOCONTROLE*.

The experimental plan was established according to the mesh previously defined and is illustrated in Figure 4.14. Concerning to trial layers, each one was tested for different energy levels corresponding to 4, 6, 8, 10, 12 and 14 passes of the vibrating roller. Exceptions must be made to some tests, which were not performed due to either time and/or weather constraints. Regarding the remaining layers, tests were performed for the last energy level.

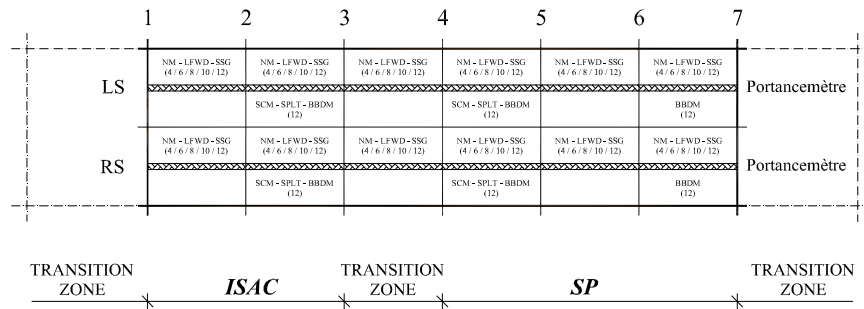


Figure 4.14: Experimental plan adopted on *FTRE*

In Tables 4.13 to 4.18 a summary of the number of spot tests conducted is made for the several layers, according to the type of material.

Likewise to *ETRE*, whenever the number of tests are presented as, for example, $4 + 2^*$, it means that were conducted 6 tests, 2 of which were done at the same spot where *SPLT* were performed.

Concerning to continuous compaction control by mean of Portancemètre, tests were performed in every layers and for all energy levels corresponding to 4, 6, 8, 10 and 12 passes of the vibrating roller.

4.4.3 Instrumentation of experimental section

As stated previously, the instrumentation of the experimental sections aimed the measurement of vibrations of the roller drum, as well as vibrations and compression vertical strains of the capping layer due to application of dynamic loads, during and after compaction process. It was intended to get data in order to investigate the interaction between roller drum and layer to be compacted, as well as to realize the magnitude of strains induced during application of dynamic

Table 4.13: Number of tests conducted on *SP* trial layers

Layer	No. of passes	<i>SCM</i>	<i>NM</i>	<i>SPLT</i>	<i>SSG</i>	<i>LFWD</i>	<i>BBDM</i>
0.30 m	4	2	6	–	6	6	–
(1 st layer)	6	2	6	–	6	6	–
	10	2	6	–	6	6	–
0.40 m	4	2	6	–	6	6	–
(2 nd layer)	6	2	6	–	6	6	–
	8	2	6	–	6	6	–
	10	2	6	–	6	6	–
	12	2	6	2	–	6 + 2*	2
0.50 m	4	–	5	–	3	–	–
(3 rd layer)	6	–	6	–	6	6	–
	10	–	6	–	–	–	–
	12	–	6	–	–	6	–
	14	–	6	–	6	6	–

Table 4.14: Number of tests conducted on *SP* embankment and capping layers

Layer	No. of passes	<i>NM</i>	<i>SSG</i>	<i>LFWD</i>	<i>SASW</i>
0.40 m	8	3	–	6	–
(4 th layer)	10	6	–	–	–
0.40 m	8	–	–	6	–
(5 th layer)	10	6	–	–	–
0.40 m	8	6	–	6	–
(6 th layer)	10	3	–	3	–
0.40 m	8	6	–	6	–
(7 th layer)	8	6	6	6	1
(capping layer)					

Table 4.15: Number of tests conducted on *CA40* base layer

Layer	No. of passes	<i>SPLT</i>	<i>STLT</i>	<i>SSG</i>	<i>LFWD</i>	<i>FWD</i>
Base layer	8	1	2	4	5	6

loads with several equipments, such as, *FWD*, *LFWD*, the Portancemètre and during application of static loads while performing *SPLT*.

In this sense, an experimental plan was developed involving measurements in two sections of the embankment, one executed with *ISAC* material and the other with traditional *SP* material, as illustrated on Figure 4.15.

In order to fulfill these requirements, the instrumentation plan was divided in two setups: one to be employed during compaction of the capping layer and another to be employed during and after compaction process of the base layer. These plans are illustrated in more detail in Figures 4.16 and 4.17.

Table 4.16: Number of tests conducted on *ISAC* trial embankment layers

Layer	No. of passes	<i>RBM</i>	<i>NM</i>	<i>SPLT</i>	<i>SSG</i>	<i>LFWD</i>	<i>BBDM</i>
0.30 m	4	2	4	–	4	4	–
(1 st layer)	6	2	4	–	4	4	–
	10	2	4	–	4	4	–
0.40 m	4	1	4	–	4	4	–
(2 nd layer)	6	2	4	–	4	4	–
	8	2	4	–	4	4	–
	10	–	4	–	4	4	–
	12	1	4	1	–	4 + 2*	2
0.50 m	4	–	3	–	2	–	–
(3 rd layer)	6	–	4	–	4	4	–
	10	–	4	–	–	–	–
	12	–	4	–	–	4	–
	14	–	4	2	4	4 + 1*	–

Table 4.17: Number of tests conducted on *ISAC* embankment and capping layers

Layer	No. of passes	<i>NM</i>	<i>SSG</i>	<i>LFWD</i>	<i>FWD</i>
0.40 m	8	2	–	2	–
(4 th layer)	10	4	–	4	–
0.40 m	8	4	–	2	–
(5 th layer)	10	–	–	4	–
	12	3	–	2	–
0.40 m	10	4	–	4	–
(6 th layer)	12	2	–	2	–
0.40 m	10	4	–	4	–
(7 th layer)					
0.40 m	10	4	2	2	–
(capping layer)	12	4	2	2	2

Table 4.18: Number of tests conducted on *ISAC* base layer

Layer	No. of passes	<i>SPLT</i>	<i>STLT</i>	<i>SSG</i>	<i>LFWD</i>	<i>FWD</i>
Base layer	10	1	4	6	4	4

As can be seen in Figures 4.16 and 4.17, sensors were placed on the same vertical and horizontal alignments, so the results of both sensors can be related. In both setups two type of sensors were used:

- accelerometers for the measurement of vertical vibrations;
- strain gauges for measurement of vertical strains.

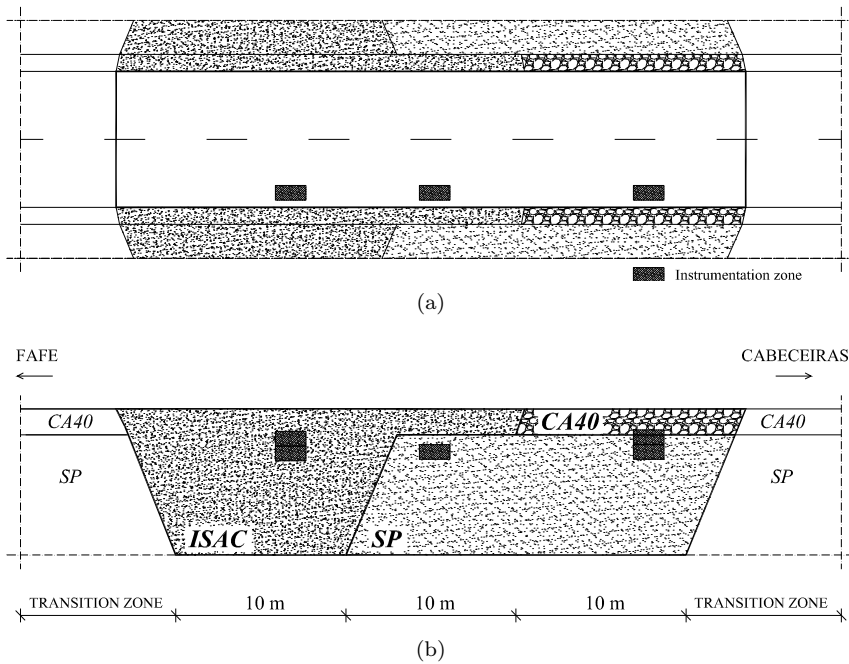


Figure 4.15: Schematic position of instrumentation zone on *FTRE*: (a) plan; (b) longitudinal view

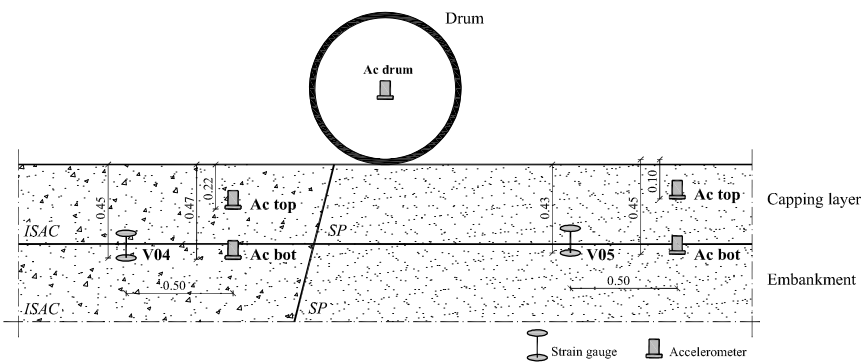


Figure 4.16: Instrumentation with accelerometers and strain gauges during compaction of the capping layer

However, there is a slight difference between the setups adopted. As illustrated in Figure 4.16, during compaction of the capping layer, two accelerometers and one strain gauge placed in depth were used in each section. No strain gauges near surface of the capping layer were used since vibration of the roller could damage these sensors. Instead, one accelerometer was used near surface. At the same time, based on some experiences conducted (Rinehart and Mooney, 2008), two accelerometers were employed on the roller drum to monitor the vibrations experienced by the equipment during compaction, i.e., its

behaviour during compaction process. After compaction, *FWD*, *LFWD* and Portancemètre were carried out on each section enabling the measurement of vibrations and vertical strains induced by each test.

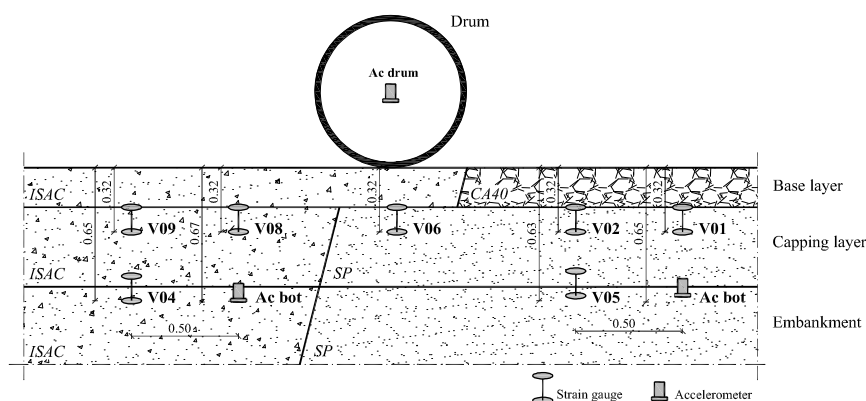


Figure 4.17: Instrumentation with accelerometers and strain gauges during compaction of the base layer

Before the execution of the base layer, the accelerometer near the surface of the capping layer was removed and replaced by two strain gauges. Once the sensors employed in these setup would be unrecoverable, only one accelerometer was used in each section, since these are more expensive. Thereby, the resulting setup in each section consisted in one accelerometer and three strain gauges, as shown in Figure 4.17. Furthermore, two accelerometers were embarked on the roller drum and vibrations were recorded during compaction process. In addition, vertical strains were measured during *SPLT* in each section after compaction.

4.5 Conclusions

In this chapter the experimental program adopted was described. This was developed in three main parts, namely, laboratory investigation, and two field investigations corresponding to Évora trial railway embankment (*ETRE*) and Fafe trial road embankment (*FTRE*).

Regarding laboratory investigation, five geomaterials, which were employed in the field investigation, were studied (clayey sand (*SC*), crushed aggregate (*CA31.5*), poor-graded sand (*SP*), inert steel aggregate for construction *ISAC* and another crushed aggregate (*CA40*)). However, in the scope of this thesis only the first two ones, *SC* and *CA31.5*, were subjected to a laboratory investigation and, therefore, a detail description of the tests carried out on these materials were conducted. Concerning the other materials, these were studied in the aim of a doctoral thesis Reis Ferreira (2010).

Laboratory investigation involved physical, hydro and mechanical characterization. Firstly, physical characterization was carried out. Secondly, hydro characterization was performed by means of filter paper method. In order to provide information about the influence of the variation of moisture content on the behaviour of studied materials, initial state conditions involved series of

tests performed on specimens compacted to 97% of the maximum dry density and over a range of molding water contents: 4% dry of optimum ($w_{OPM-4\%}$), 2% dry of optimum ($w_{OPM-2\%}$), optimum (w_{OPM}) and 2% wet of optimum ($w_{OPM+2\%}$). This range includes the moisture contents employed in field investigation. Finally, mechanical characterization was performed. Tests were carried out in unsaturated, saturated and dry conditions and in the small and large strain domain, which included oedometer tests, triaxial tests and triaxial tests in a stress-path Bishop–Wesley triaxial chamber with measurement of S-waves velocity. These tests were described in detail.

Concerning to field investigation, two trial embankments were conducted: Évora railway trial embankment *ETRE*; and Fafe road trial embankment *FTRE*.

An experimental program for field investigation on *ETRE* was developed involving optimization of thickness layers constructed over a range of different moisture contents, for different energy levels corresponding to the passes of the compaction equipment. *SC* and *CA31.5* were employed on trial embankment. The geometry of the layers were defined and a mesh was created in order to establish the location to run field tests. Thicknesses of 0.30, 0.40 and 0.50 m, and 0.22 and 0.30 m were employed for *SC* and *CA31.5* layers, respectively. Then, moisture conditions of materials were established over a range of three different moisture contents: 2% dry of optimum ($w_{OPM-2\%}$), optimum (w_{OPM}) and 2% wet of optimum ($w_{OPM+2\%}$). However, on *CA31.5* trial layers only optimum moisture content (w_{OPM}), was employed. At last, state conditions and mechanical properties of the several layers were evaluated by means of spot and continuous tests methods. These were conducted for different energy levels.

Similarly, an experimental program were established for field investigation on *FTRE*. *SP*, *CA40* and *ISAC* material were employed. The experimental plan sought three main objectives: (i) execution of trial layers to optimize thickness layer and energy level corresponding to the passes of the vibrating roller, while state conditions remain constant; (ii) evaluate materials behaviour during execution of trial, embankment and road layers; (iii) measurements of vibrations during and post compaction of the capping and base layer. Geometry including layers with 0.30, 0.40 and 0.50 m thickness was defined and a mesh was created to establish the location to run field tests. Only optimum moisture content, (w_{OPM}), was employed. Likewise to *ETRE*, state conditions and mechanical properties of the several layers were evaluated by means of spot and continuous tests methods, which were conducted for different energy levels. Finally, a description of the instrumentation of the capping layer using accelerometers and strain gauges was carried out.

Chapter 5

Laboratory investigation

5.1 Introduction

A laboratory test campaign was carried out on reconstituted samples of two geomaterials, a clayey sand (*SC*) and a crushed aggregate 0/31.5 (*CA31.5*), which, as mentioned previously, were employed in Évora trial railway embankment (*ETRE*). This study aimed to investigate the influence of compaction conditions on the mechanical behaviour of these materials. In this scope, void ratio was fixed corresponding to 97% of the Modified Proctor and moisture content was varied from 4% dry of optimum to 2% wet of optimum for *SC* and from 2% dry of optimum to optimum for *CA31.5*.

In this chapter, the most relevant results provided by the laboratory tests will be presented according to the characterization type, namely, physical, hydro and mechanical and discussed in detail. The tests procedure and specimens state parameters were described in Chapter 4. One should bear in mind that analysis will be performed in total stresses.

5.2 Physical characterization

As mentioned above, two geomaterials were used in this study, a coarse-grained soil, clayey sand (*SC*), and a decomposed granite classified as a well-graded gravel with silt and sand (*GW-GM*), accordingly to the Unified Soil Classification System (ASTM D2487, 2000). For the sake of simplicity, these geomaterials are called herein as *SC* and *CA31.5*, respectively.

The grain-size distribution curves of both materials are plotted in Figure 5.1, whereas in Table 5.1 are given the index properties, namely, Atterberg Limits (NP 143, 1969); Specific Gravity (NP 83, 1965; EN 1097-6, 2000), Methylene Blue (NF P 94-068, 1998; NP EN 933-9, 2002); Sand Equivalent (LNEC E 199, 1967; NP EN 933-8, 2002), and compaction characteristics determined using Modified Proctor (LNEC E 197, 1966; EN 13286-2, 2004).

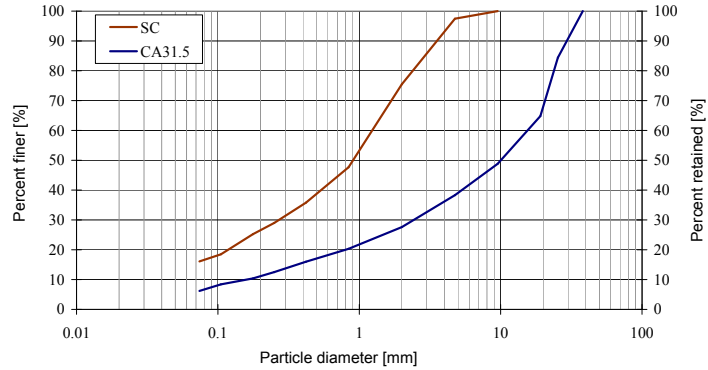


Figure 5.1: Grain-size distributions

Table 5.1: Results from identification tests

Test		Material type	
		SC	CA31.5
Atterberg Limits	w_L	32	–
	w_P	21	–
	I_P	11	–
Specific Gravity		2.65	2.73
Methylene Blue		0.96	1.25
Sand Equivalent		24	38
Modified Proctor	γ_d [kN/m ³]	20.14	22.71
	w [%]	8.6	5.7

5.3 Hydro characterization

As described in Chapter 4, the hydro characterization was carried out only for SC material, using filter paper technique to measure matric suction. In Figure 5.2 is plotted the matric suction versus saturation degree for specimens with similar void ratio, about 0.331. Three tests per saturation degree were carried out in order to verify repeatability. The following calibration equation was used (Chandler *et al.*, 1992):

$$\text{Log}_{10}(\text{suction}) = \begin{cases} 4.842 - 0.0622 \cdot w & \text{if } w < 47, \\ 6.050 - 2.48 \cdot \text{Log}_{10}(w) & \text{if } w > 47 \end{cases} \quad (5.1)$$

The matric suctions obtained for the range of molding water contents from 4% dry of optimum to 3% wet of optimum varied from 215 to 8 kPa, respectively. Matric suction was found to decrease with increasing saturation degree (S_r) accordingly to expression given in Figure 5.2. One note that there is a strong power relation with $R^2 = 0.991$ between matric suction and saturation degree. Regarding to the molding water contents studied, 4% and 2% dry of optimum, optimum and 2% wet of optimum, the corresponding values of matric suction are approximately 170, 51, 21 and 11 kPa, considering void ratio $e = 0.331$.

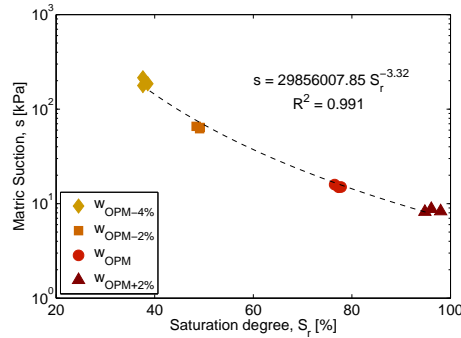


Figure 5.2: Matric suction versus molding water content for *SC* specimens with the same void ratio ($e = 0.331$)

5.4 Mechanical characterization

5.4.1 Oedometer test

A series of one-dimensional consolidation tests under unsaturated and saturated conditions were conducted to study compressibility behaviour of *SC* compacted specimens. As listed in Chapter 4, one saturated and four unsaturated consolidation tests were performed. Figure 5.3a shows three unsaturated tests involving compacted specimens with molding water content corresponding to 4% dry of optimum ($w_{OPM-4\%}$), 2% dry of optimum ($w_{OPM-2\%}$) and optimum (w_{OPM}), and a saturated test with optimum molding water ($w_{OPM_{sat}}$). Unsaturated tests had approximately the same initial void ratio ($e = 0.331$), corresponding to 97% of Modified Proctor, whereas saturated test had a slightly lower initial void ratio ($e = 0.322$). In addition, an unsaturated test in a loose state was carried out in order to obtain the virgin compression line (VCL), and is illustrated in Figure 5.3b. In Table 5.2 are given the coefficients of compressibility (λ_c), considering a regression analysis with the last two points of the loading cycle, and the coefficients of unloading (λ_u) considering all points of the unloading cycle.

Table 5.2: Coefficients of compressibility (λ_c) and of unloading (λ_u)

Specimen	λ_c	λ_u
$W_{OPM-4\%}$	0.0289	0.0032
$W_{OPM-2\%}$	0.0263	0.0030
W_{OPM}	0.0370	0.0034
$W_{OPM_{sat}}$	0.0170	0.0037
W_{OPM} loose	0.0887	0.0043

In Figure 5.3a it can be seen that the curves shapes exhibit non linear behaviour. Despite specimens were submitted to maximum vertical stress of 1000 kPa, one may observe that they did not achieved VCL. More points would be necessary to better define the slope over a total vertical stress of 1000 kPa. This notwithstanding, in the lower stress range, before yielding, the curves shapes are reasonably molding water content independent, which is the same

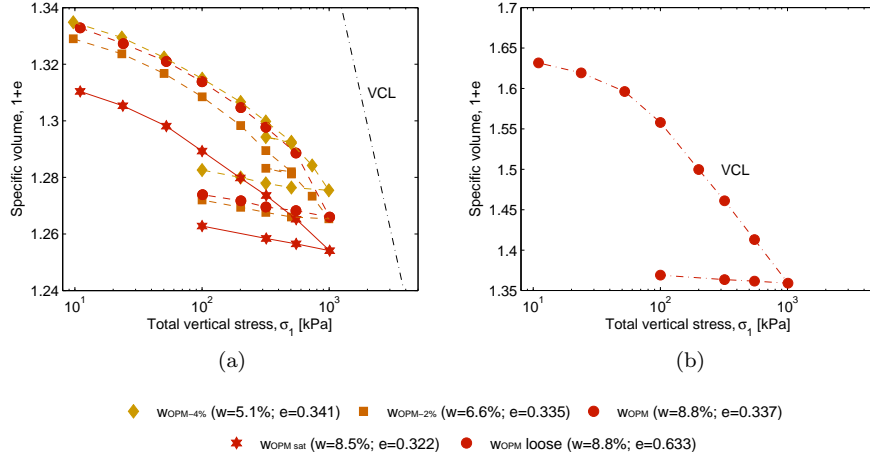


Figure 5.3: Oedometer tests results from *SC* specimens in unsaturated and saturated conditions in: (a) compacted state; (b) loose state

to say suction independent. On the contrary, in the higher stress range after yielding, curves shapes from unsaturated specimens seems to be suction dependent: to lower molding water content corresponds smaller compressibility (λ_c), i.e., there is a decrease of the plastic compressibility with increasing suction. In fact, one can see from Table 5.2 that λ_c are lower for driest specimens. However, specimen $w_{\text{OPM}-2\%}$ presents λ_c slightly lower than corresponding value from $w_{\text{OPM}-4\%}$. This may be attributed to differences on initial void ratio, since initial specific volume of specimen $w_{\text{OPM}-2\%}$ is smaller than the others unsaturated ones, which are close together. This denotes the importance of density at high stress levels, which can be stronger than the suction effect and hide it. Indeed, λ_c obtained from saturated specimen is the lowest, which appears to contradict previous findings since there is any suction contribution. Nevertheless, the initial void ratio from saturated specimen is the lowest which strongly influenced specimen compressibility. As so, as far as plastic compressibility is concerned, the influence of suction and density are similar, since any increase in either of these parameters reduces the compressibility.

The unloading sequences performed at all tests confirm the irreversible nature of the strains. It is interesting noting that λ_u for unsaturated specimens appears to be independent of the suction, since values around 0.0032 were determined. Though specimen in saturated condition had lower initial void ratio, it exhibited similar swelling on the unloading cycle, where a $\lambda_u = 0.0037$ was obtained. The unsaturated specimen in loose state allowed to determine the VCL. A $\lambda_c = 0.0887$ and a $\lambda_u = 0.0043$ were determined. One note that λ_u is slightly higher than values achieved from compacted samples in unsaturated condition.

The data confirm the general findings that an increased suction produces a stiffening of the material with smaller plastic compressibility (Alonso *et al.*, 1990; Cui and Delage, 1996), despite the tight differences observed between unsaturated tests. Saturated test (zero suction) showed the lowest compressibility

which was due to a lower initial void ratio. Further, similar results are produced by variation of suction and density, since any increase in either of these parameters reduces the compressibility. Regarding unloading cycle, it appears that swelling is suction independent for unsaturated specimens.

5.4.2 Triaxial tests on *SC* specimens

Triaxial test results obtained from specimens under various molding water contents, i.e., suction, are presented in Figures 5.4, 5.5 and 5.6, corresponding to confining stresses (σ_3) of 100, 200 and 300 kPa, respectively.

A non linear behaviour is observed where an important strain component is unrecoverable. With decreasing molding water content the shape of the curves gradually changes and the maximum deviatoric stresses increases (figs. 5.4a, 5.5a and 5.6a). An increasingly pronounced maximum is observed at a reducing strain level, illustrating an increasing britleness of the material with decreasing molding water content, i.e., increasing suction. However, as confining stress level increases maximum deviatoric stresses occur at higher strain corresponding to a reduction in britleness behaviour.

The influence of saturation condition on stress–strain curve decreases with increasing confining stress level. For optimum molding water content saturated specimen exhibit slightly lower maximum deviatoric stress at $\sigma_3 = 100$ kPa (fig. 5.4a), whereas at $\sigma_3 = 200$ kPa difference decreases (fig. 5.5a) and for the last stage becomes slightly higher than corresponding value from unsaturated specimen, which was unexpected. This fact is probably due to the multistage test progress. Ho and Fredlund (1982) states that in a multistage test progress the measured peak strength for a certain stage may be smaller than the peak strength for the specimen under the same stress conditions in a single stage test. The strength loss results from structure disturbance from previous stages. With regards to w_{OPM} unsaturated specimen, one can see that specimen experimented great strain during previous stage ($\sigma_3 = 200$ kPa), as illustrated in Figure 5.5a. In fact, at that stage specimen reached deviatoric stress peak at strain about 3%, but specimen was allowed to deform until strain of 4.5%, which probably induced great structure disturbance. As a result, the measured peak strength for the last stage was smaller than would be expected. This behaviour is testified by the results obtained from two additional samples with optimum molding water content. In order to verify the influence of multistage triaxial test procedure, these samples were submitted to saturated and unsaturated triaxial tests ($w_{\text{OPM iso sat}}$ and $w_{\text{OPM iso}}$) in a single stage at $\sigma_3 = 300$ kPa. Stress–strain curves of these two additional tests are plotted in Figure 5.6a. Although greater plastic behaviour from single stage tests are observed, the peak deviatoric stresses from one single stage and multistage saturated tests matches well. Regarding unsaturated tests, peak deviatoric stresses do not agree and value obtained from one single stage test was greater than multistage test. As so, one may conclude that the smaller peak value obtained from multistage test was due structure disturbance experimented at previous stages, namely at stage corresponding to $\sigma_3 = 200$ kPa.

Particular results obtained from w_{dry} and $w_{\text{OPM}+2\%}$ specimen earn to be discussed apart. Dry specimen unexpectedly presented the highest strength, thus a second dry specimen was prepared and tested in order to confirm this result. A stress–strain behaviour on the first stage ($\sigma_3 = 100$ kPa) similar

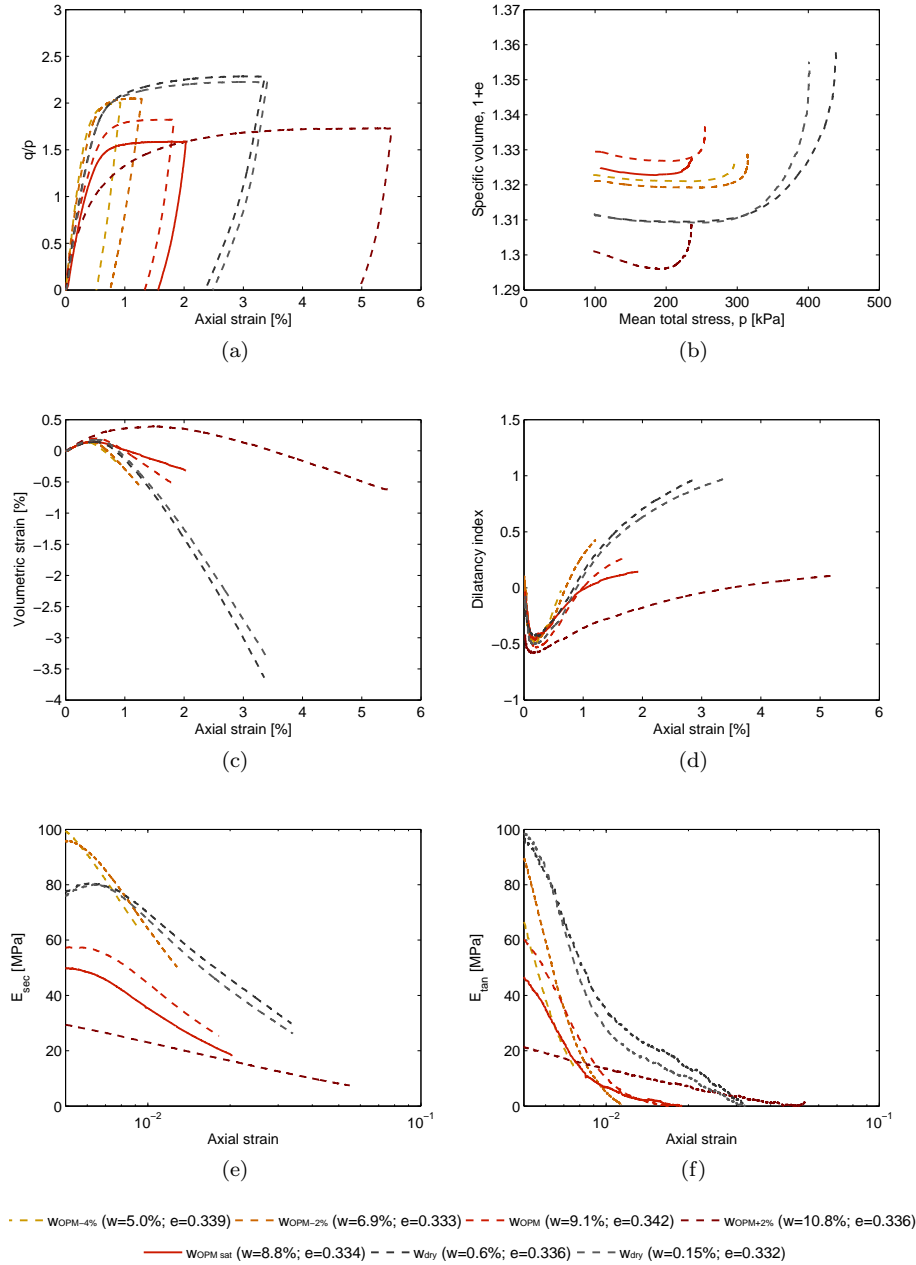


Figure 5.4: Triaxial tests results at $\sigma_3 = 100$ kPa from SC samples with varying initial molding water contents

to the first test was found confirming previous results and, thereby, test was not continued after this stage. It is believed that hygroscopic water between fine grains might contribute to a suction effect which, in turn, contributed to a high peak strength. Hence, triaxial test results from dry specimen should

be treated carefully. With regards to specimen $w_{OPM+2\%}$ a high reduction of specific volume is observed in Figures 5.4b, 5.5b and 5.6b. This behaviour was also unexpected, although no second test was performed in order to confirm the evolution of specific volume during multistage procedure. Therefore, also this results should be treated carefully too.

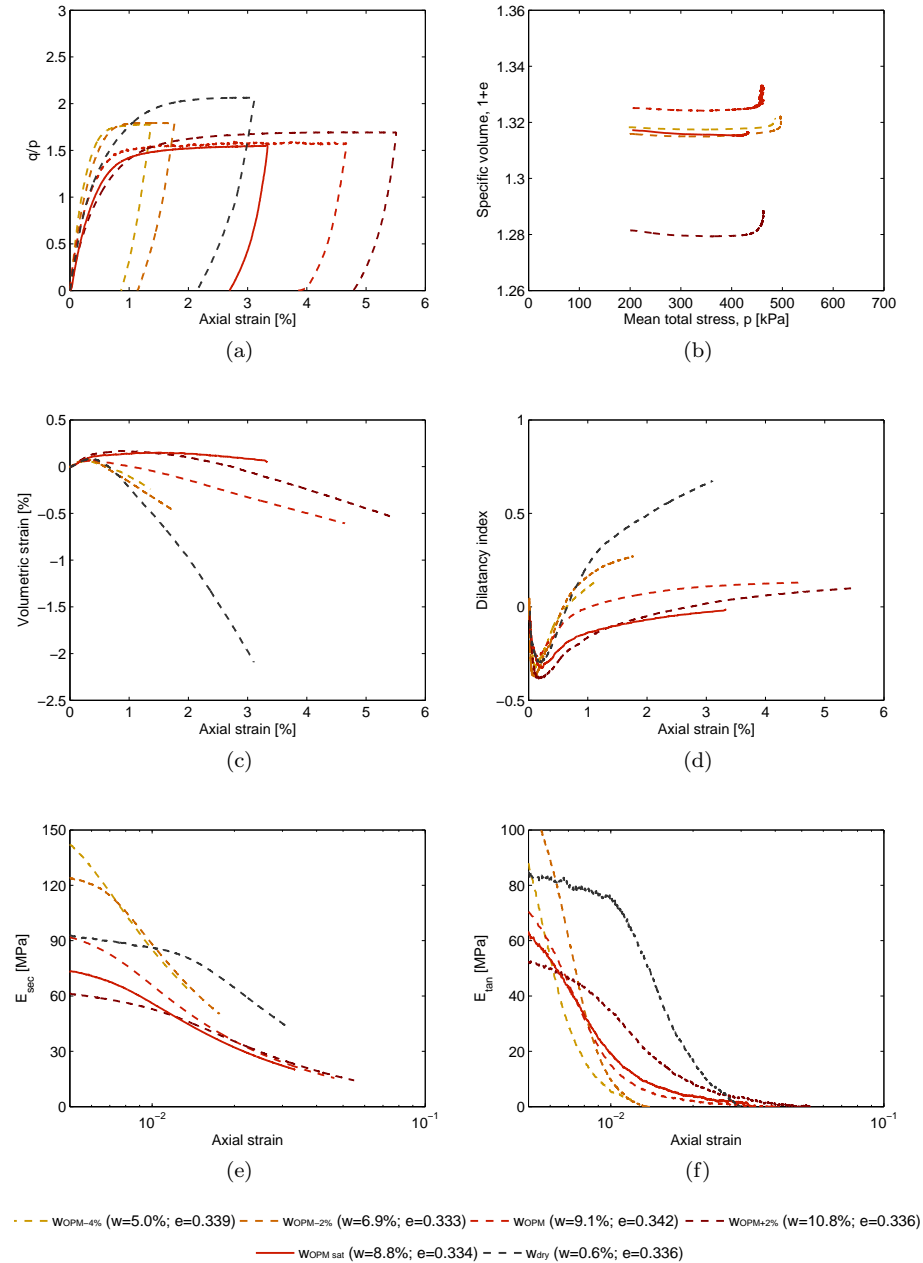


Figure 5.5: Triaxial tests results at $\sigma_3 = 200$ kPa from SC samples with varying initial molding water contents

From volume change curves (figs. 5.4c, 5.5c and 5.6c) one can see contraction followed by dilation, which features granular materials in a dense state. The lower is the molding water content (the higher the suction) the larger is the dilatancy. In fact, for water contents lower than w_{OPM} , specimens seem strongly dilatant, as illustrated in Figures 5.4d, 5.5d and 5.6d. At the lower confining stress level ($\sigma_3 = 100$ kPa) all curves are well ordered and evolve regularly with decreasing water content, i.e., increasing suction. In fact, the negative pore water pressure in the menisci creates strong bonds between the grains, that increase the strength of the material and prevents its deformation. When the water content increases, the grains begin to be surrounded by water and the behaviour of the soil tends towards that of the saturated soil at the same void ratio. Further, at remaining confining stress levels it is noteworthy that specimen $w_{OPM-2\%}$ was slightly dilatant than $w_{OPM-4\%}$. A reduction of contraction and dilatancy is also observed. These facts indicate that, at higher confining stress levels ($\sigma_3 = 200$ kPa and $\sigma_3 = 300$ kPa), confining stress appears to have a major influence on material behaviour than suction.

For the last confining stress level samples were loaded until stabilization of stress-strain and volume change curves were observed, i.e., until critical state was reached. Though critical state was not reached for all samples due to membrane rupture, one can see from Figure 5.6a that all curves tend to the same stress at larger strains, with exception to dry specimen. From volume change curves and dilatancy (figs. 5.6c and 5.6d) critical state seems to have been reached in $w_{OPM_{sat}}$, $w_{OPM_{iso}}$ and $w_{OPM_{iso_{sat}}}$ tests.

Concerning to specimens deformability, in Figures 5.4e and 5.4f, 5.5e and 5.5f and 5.6e and 5.6f one can observe an increasing secant and tangent moduli are associated to decreasing water content. Moreover, moduli increases with increasing confining stress, as would be expected, though relative increase between stages become smaller. Once again, this fact denotes that increasing confining stress appears to reduce suction effect.

In Figure 5.7 are plotted the peak deviatoric stress (q) versus mean total stress (p) obtained from each test, as well as the residual deviatoric stress corresponding to critical states. As would be expected for drained tests on specimens in dense state, yielding first occurs with $q/p > M$. Continued deformation is associated with plastic softening and decrease of stress ratio until a perfectly plastic critical state is reached with $q/p = M$ (Wood, 1990). The peak failure envelope is also represented for each test, which relation can be written as in equations 5.2 and 5.3.

$$q_{peak} = M_{peak} \cdot p + c \quad (5.2)$$

$$q_{cs} = M_{cs} \cdot p \quad (5.3)$$

where M_{peak} and M_{cs} are the slope of the peak and critical state failure envelope, respectively, and c is effective cohesion, c' , or apparent cohesion, $c_{apparent}$. The parameters M_{peak} and M_{cs} are related to the internal friction angle (ϕ) through Equation 5.4.

$$\sin\phi = \frac{3 \cdot M}{6 + M} \quad (5.4)$$

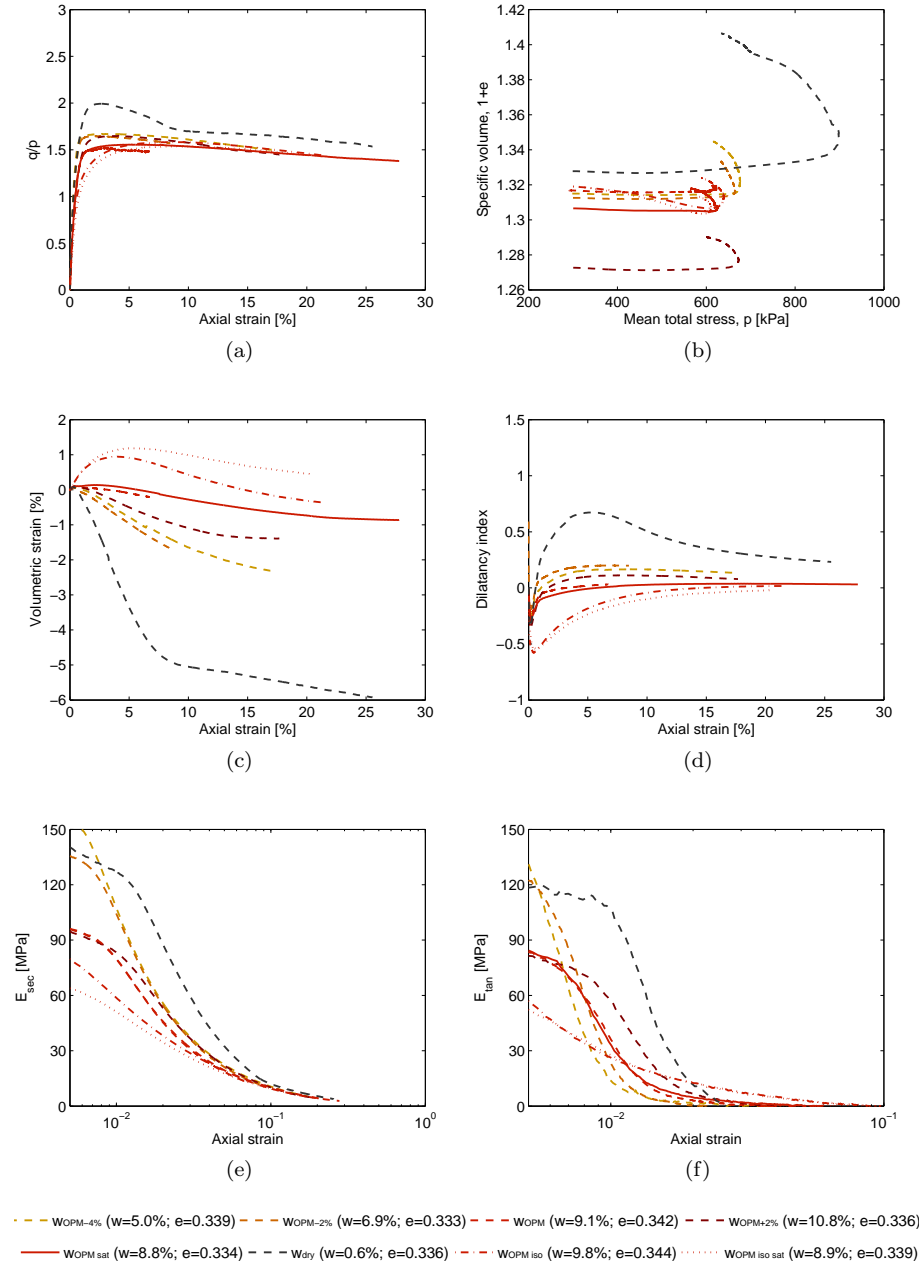


Figure 5.6: Triaxial tests results at $\sigma_3 = 300$ kPa from SC samples with varying initial molding water contents

where M takes the value of M_{peak} and M_{cs} , either internal friction angle, ϕ_{peak} or ϕ_{cs} , is determined, respectively. The average ϕ_{peak} based on data from all multistage and single stage tests are given in Table 5.3, as the ϕ_{cs} .

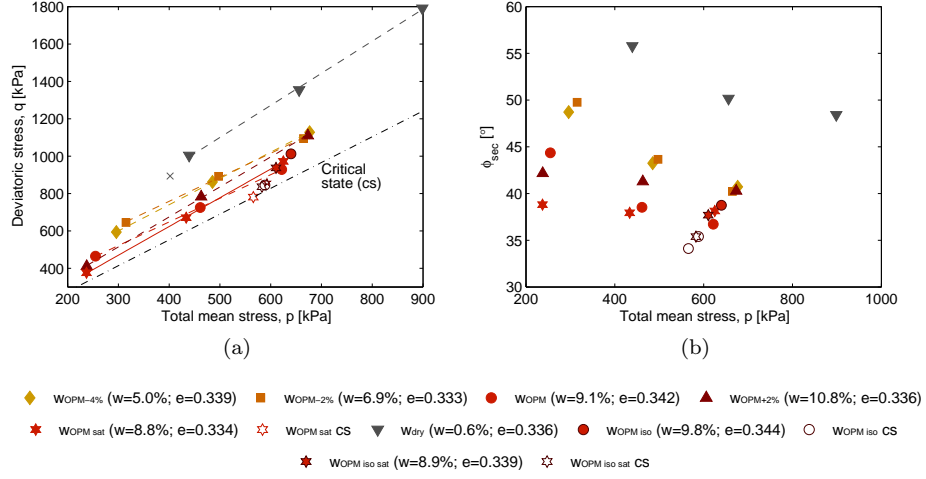


Figure 5.7: Triaxial test results from *SC* specimens with varying initial molding water content; (a) peaks and residual deviatoric stress vs. total mean stress; (b) Secant friction angle vs. total mean stress

One can see that ϕ_{peak} obtained from unsaturated tests ranges between 31.5° and 39.3° , while $\phi_{peak} = 37.7^\circ$ was obtained from optimum saturated test. Thereby, a fairly variation of ϕ_{peak} is observed regarding to unsaturated samples. One should note that the lowest and highest ϕ_{peak} (31.5° and 39.3°), correspond to W_{OPM} and $W_{OPM+2\%}$ tests, respectively. These bound values can be attributed to multistage procedure. As above mentioned, peak results from W_{OPM} specimen were affected by excessive shear strain in the second stage, leading to structure disturbance of specimen as the multistage tests progressed. As a result, the measured peak deviatoric stress for the last stage (i.e., stage $\sigma_3 = 300$ kPa) may actually be smaller than that obtained from a specimen under the same stress conditions, using a single stage test. In fact, this hypothesis was testified with single stage test carried out on $W_{OPM_{iso}}$ unsaturated specimen, as illustrated in Figure 5.7. Hence, if $W_{OPM_{iso}}$ peak value is considered on the determination of ϕ_{peak} , a value of 35° is obtained. In Table 5.3 this hypothesis is identified as W_{OPM}^* . As aforementioned, results from $W_{OPM+2\%}$ specimen should be treated with caution. To sum up, one can conclude that M_{peak} and ϕ_{peak} obtained from unsaturated test results are similar.

A M_{cs} of 1.38 was obtained corresponding to a $\phi_{cs} = 34.1^\circ$. This value is in agree with the range of values given by Bowles (1970) for a silty sand in a dense state. The highest ϕ_{peak} was obtained from dry specimen (w_{dry}), which reflects the higher britleness of specimen in that state condition. The $W_{OPM-4\%}$ and $W_{OPM-2\%}$ tests showed the highest $c_{apparent}$, which seems to reflect the higher suction of these samples. As water content approaches saturated condition, a reduction of $c_{apparent}$ is observed, reflecting a suction decrease.

The evolution of secant friction angle (ϕ_{sec}) with total mean stress is represented in Figure 5.7b. On one hand, one can observe that, for identical total mean stress, ϕ_{sec} increases with decreasing molding water content. On the other hand, for the same specimen, ϕ_{sec} values decrease with increasing mean stress,

Table 5.3: Peak and critical state failure envelope parameters M_{peak} , M_{cs} and c and respective internal friction angle (ϕ) obtained from triaxial multistage tests

Sample	M	c	ϕ [°]
WOPM-4%	1.40	178.8	34.7
WOPM-2%	1.28	244.5	31.9
WOPM	1.26	142.2	31.5
W [*] OPM	1.42	93.0	35.0
WOPM+2%	1.60	33.2	39.3
WOPM _{sat}	1.54	8.90	37.7
W _{dry}	1.72	241.7	41.9
WOPM _{sat} CS	1.38		34.1

where unsaturated specimens with low molding water content present higher reduction of ϕ_{sec} values. This shows the great influence of both molding water content and total mean stress on ϕ_{sec} values. Moreover, at higher total mean stress ϕ_{sec} values get closer and seems to tend to ϕ_{sec} value at critical state, which is consistent with de Beer (1965) investigations on granular materials in a dense state. It should be noted that non linearity of ϕ_{sec} with total mean stress leads to an apparent cohesion in the q, p plane (see Table 5.3) which has only a mathematical meaning resulting from the interception of strength peak envelope on q axis.

The evolution of specific volume with total mean stress (p) at the end of consolidation at each stage of a multistage test and during consolidation of the single stage test are plotted in Figure 5.8. The effect of molding water content on compressibility is investigated. Further, in order to investigate the influence of the anisotropy induced by a multistage test, comparison is made with the results of the isotropic stress applied during consolidation of the single stage test. For each test the isotropic/anisotropic and peak consolidation line are defined by Equation 5.5, where Γ represents the specific volume corresponding to a total mean stress of 1 kPa and λ is the slope. These parameters are summarised in Table 5.4.

$$v = \Gamma + \lambda \cdot \ln(p) \quad (5.5)$$

Table 5.4: Isotropic and anisotropic consolidation parameters, Γ and λ , determined from SC triaxial tests

Sample	Consolidation		Peak	
	λ	Γ	λ_{peak}	Γ_{peak}
WOPM-4%	0.007	1.354	0.005	1.353
WOPM-2%	0.008	1.357	0.014	1.405
WOPM	0.011	1.380	0.019	1.444
WOPM+2%	0.025	1.417	0.031	1.478
WOPM _{sat}	0.017	1.406	0.022	1.452
W _{dry}	-0.015	1.242	0.012	1.426
WOPM _{iso}	0.008	1.367		
WOPM _{iso sat}	0.010	1.377		

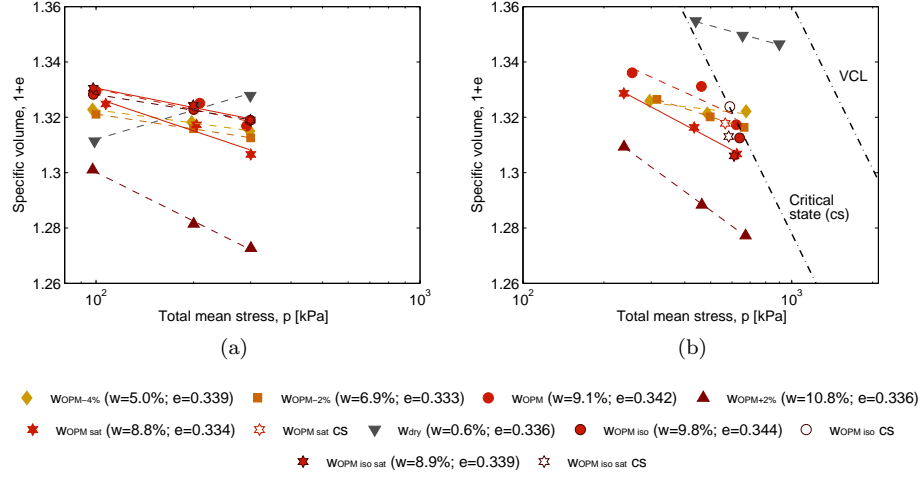


Figure 5.8: Specific volume vs. total mean stress obtained from *SC* triaxial tests: (a) at the end of consolidation at each stage of a multistage test and during consolidation of the single stage test; (b) at peak and critical stage

One note that λ corresponding to unsaturated specimens increases with increasing water content. As so, one may conclude that compressibility increases with increasing molding water content, as previously verified from oedometer tests. Concerning to peak slopes (λ_{peak}) the same trend is observed, reflecting, therefore, the initial molding water content. Moreover, it is interesting noting that λ corresponding to saturated tests are higher than the ones for corresponding unsaturated tests, i.e., compressibility is higher for saturated samples, which denotes the influence of unsaturated conditions. Concerning to results from single and multistage tests, λ for WOPM and WOPM_{iso} unsaturated tests, respectively, are quite similar. In contrast, a greater difference between λ for WOPM_{sat} and WOPM_{iso sat} saturated tests is observed. Regarding the effect of anisotropy induced by multistage triaxial tests these results are inconclusive.

In Figure 5.8b critical state line is also plotted. From theory (Wood, 1990) critical state line lies parallel to VCL obtained from oedometer, yet offset to the left passing through critical state given by triaxial tests. As would be expected all points appears to lie on the left side of critical state line, i.e., in the dry side, which features granular geomaterials in dense state (Wood, 1990). Exception is made to dry specimen.

In order to get a better insight on the influence of compaction conditions on specimens deformability, firstly, E_{sec} is normalized for the same void ratio accordingly to Equation 5.6, where $f(e)$ is a void ratio function given in Equation 5.7 (Hardin and Richart, 1963).

$$E_{sec}^{nor} = E_{sec} \cdot \frac{f(e = 0.331)}{f(e)} \quad (5.6)$$

$$f(e) = \frac{(2.17 - e)^2}{(1 + e)} \quad (5.7)$$

Secondly, in Figure 5.9 $E_{\text{sec}}^{\text{nor}}$ is plotted against axial stress and moisture content. An axial strain of 0.5% and 1.0% were considered taking into account the triaxial tests precision with external measurement. An increasing $E_{\text{sec}}^{\text{nor}}$ with increasing axial stress is observed following a power law accordingly to Equation 5.8, where C is a stiffness coefficient and n is a stiffness index (Hoque and Tatsuoka, 1998; Gomes Correia *et al.*, 2001). In Table 5.5 are summarized the C and n parameters. It should be noted that values gathered from triaxial tests carried in a single stage ($w_{\text{OPM iso}}$ and $w_{\text{OPM iso sat}}$) lie below values obtained from multistage tests. This fact indicates that multistage procedure might influence specimen deformability, as observed previously in Figure 5.6.

$$E_{\text{sec}}^{\text{nor}} = C \cdot \sigma_1^n \quad (5.8)$$

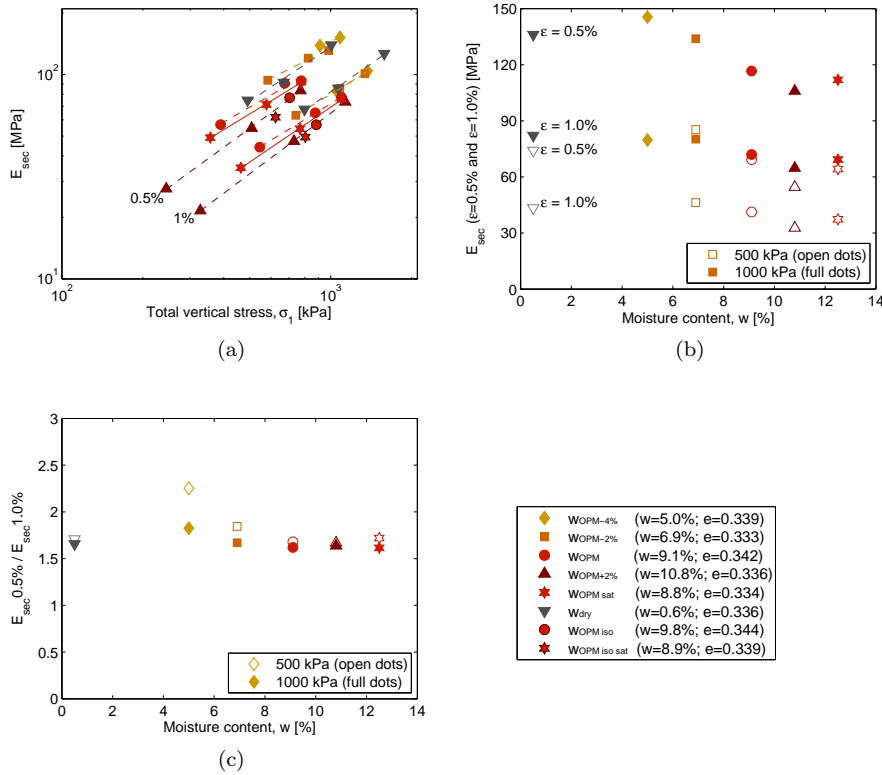


Figure 5.9: (a) $E_{\text{sec}}^{\text{nor}}$ at strain levels $\varepsilon = 0.5\%$ and 1.0% vs. σ_1 ; (b) $E_{\text{sec}}^{\text{nor}}$ at strain levels $\varepsilon = 0.5\%$ and 1.0% and stress levels $\sigma_1 = 500$ kPa and 1000 kPa vs. moisture content; (c) Relationship between $E_{\text{sec}}^{\text{nor}}$ at strain levels $\varepsilon = 0.5\%$ and $\varepsilon = 1.0\%$ at stress levels $\sigma_1 = 500$ kPa and 1000 kPa

Regarding to an axial strain of 0.5% stiffness coefficient (C) denotes a decreasing stiffness of unsaturated specimens with increasing moisture content, therefore reflecting the reduction of suction effect on the deformability of the geomaterial. This trend is shown in Figure 5.9b for $\sigma_1 = 500$ kPa and $\sigma_1 = 1000$ kPa and is consistent with results from similar investigations (Fleureau *et al.*, 2003).

As specimen moisture content approaches saturated condition E_{sec} decreases and appears to remain constant beyond optimum moisture content. The same trend is found concerning to axial strain of 1.0%. However, differences are smaller reflecting the higher degradation of E_{sec} at this strain level. With increasing strain level the stiffness index (n) approaches unity, which value corresponds to perfect plasticity (Biarez *et al.*, 2005).

In Figure 5.9c is shown the relation $E_{\text{sec}0.5\%}/E_{\text{sec}1.0\%}$ for both $\sigma_1 = 500$ kPa and $\sigma_1 = 1000$ kPa. It is noteworthy that relation seems fairly constant as moisture increases beyond optimum value for both stress levels, corresponding to about 1.7, which is quite similar to relation obtained from normalised degradation curve given by Ishibashi and Zhang (1993). In what concerns to specimens with lower moisture content, i.e. higher suction, relation tends to increase and becomes more pronounced for lower stress levels, which is the same to say that as stress level increases there is a reduction of suction effect on deformability.

Table 5.5: Power law C and n parameters corresponding to regressions on E_{sec,σ_1} plane determined from SC triaxial tests for $\varepsilon = 0.5\%$ and $\varepsilon = 1.0\%$

Specimen	$\varepsilon = 0.5\%$		$\varepsilon = 1.0\%$	
	C	n	C	n
WOPM-4%	3.571	0.537	0.241	0.840
WOPM-2%	1.497	0.651	0.332	0.794
WOPM	0.648	0.752	0.279	0.804
WOPM+2%	0.141	0.958	0.072	0.985
WOPM _{sat}	0.440	0.802	0.146	0.892
W _{dry}	0.318	0.877	0.141	0.922

Further, in Figure 5.10 are presented the $E_{\text{sec}}^{\text{nor}}/E_0$ degradation curves for each confining stress stage. In addition, a reference threshold shear strain given by Santos (1999) for sandy soils was converted in a threshold modulus strain and plotted too. This conversion was done considering Poisson ratios of 0.10 and 0.35 corresponding to strain levels of about 10^{-6} and greater than 10^{-2} , respectively. The E_0 values were obtained from unsaturated triaxial tests using bender elements, which results will be presented afterwards. The normalized degradation curves appears to fit reasonably the threshold modulus strain. The influence of moisture content, i.e., suction, on normalized degradation curves confining stress is clearly marked. As confining stress increases, differences between degradation curves become smaller. Therefore, as seen previously, as stress level increases there is a reduction of suction effect on deformability.

5.4.3 Triaxial tests on CA31.5 specimens

Likewise to SC results, in Figures 5.11, 5.12 and 5.13 are presented CA31.5 triaxial tests results at confining stresses (σ_3) of 100, 200 and 300 kPa, respectively, obtained from specimens under different molding water contents, i.e., different suction.

A non linear behaviour is observed for all confining stress stages (figs. 5.11a, 5.12a and 5.13a) where an important strain component is unrecoverable (figs. 5.11a and 5.12a). As would be expected maximum deviatoric stress increases with increasing confining stress and stress-strain curves show maximum devia-

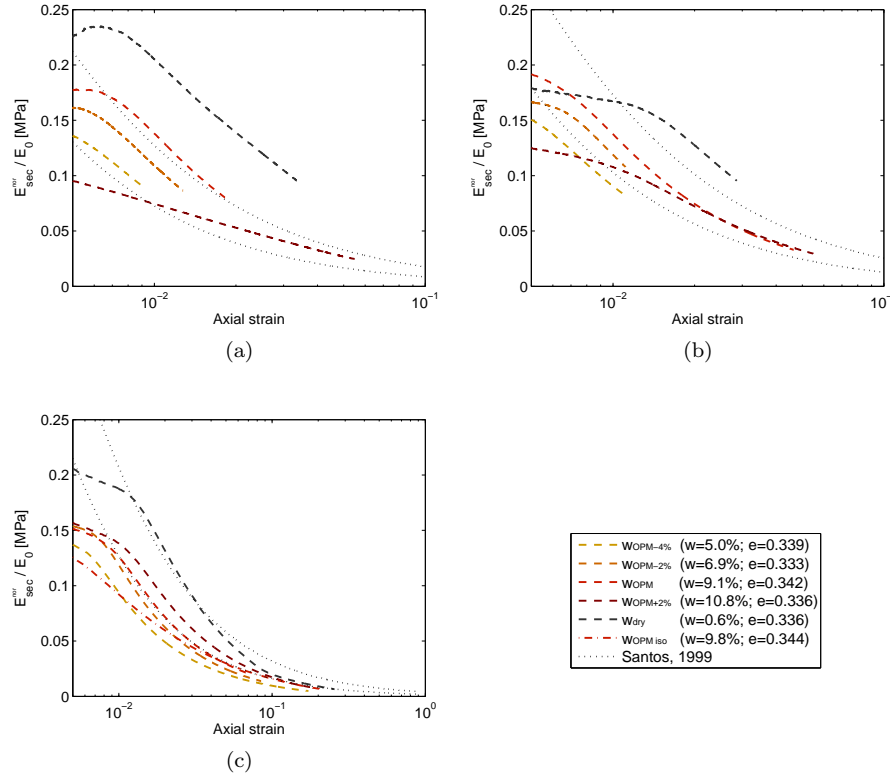


Figure 5.10: $E_{\text{sec}}^{\text{nor}} / E_0$ degradation curves corresponding to confining stresses, σ_3 : (a) 100 kPa; (b) 200 kPa; (c) 300 kPa

toric stress at a reduced strain indicating an increasing britleness behaviour. At the last stage ($\sigma_3 = 300$ kPa) stress–strain curves show peak deviatoric stress for all tests results which features stress–strain behaviour of granular materials at a dense state (5.13a). It is noteworthy that unsaturated sample w_{OPM} presents the highest deviatoric stress at all stages, whereas maximum deviatoric stress reached from unsaturated sample $w_{\text{OPM}-2\%}$ lies between optimum saturated and unsaturated specimens ($w_{\text{OPM sat}}$ and w_{OPM}). Therefore, at the state conditions studied, a higher suction effect seems to not be associated to a lower molding water content as verified previously for *SC* material. This is probably due to the low fine content, which is about 6% (see fig. 5.1).

From volume change curves (figs. 5.11c, 5.12c and 5.13c) contraction following by dilation is observed, which features granular materials in a dense state. Volumetric contraction is appreciably the same for all tests, but is achieved at a reduced strain level with successive stages, thus denoting an increasing britleness, as seen previously from stress–strain behaviour analysis. Unexpectedly, saturated samples showed higher dilatancy than unsaturated ones at stages $\sigma_3 = 100$ and 200 kPa (figs. 5.11d and 5.12d), yet an inverse behaviour is observed at the last stage (fig. 5.13d). As for *SC* material, at the last confining stress level ($\sigma_3 = 300$ kPa) specimens were loaded until stabilization of stress–

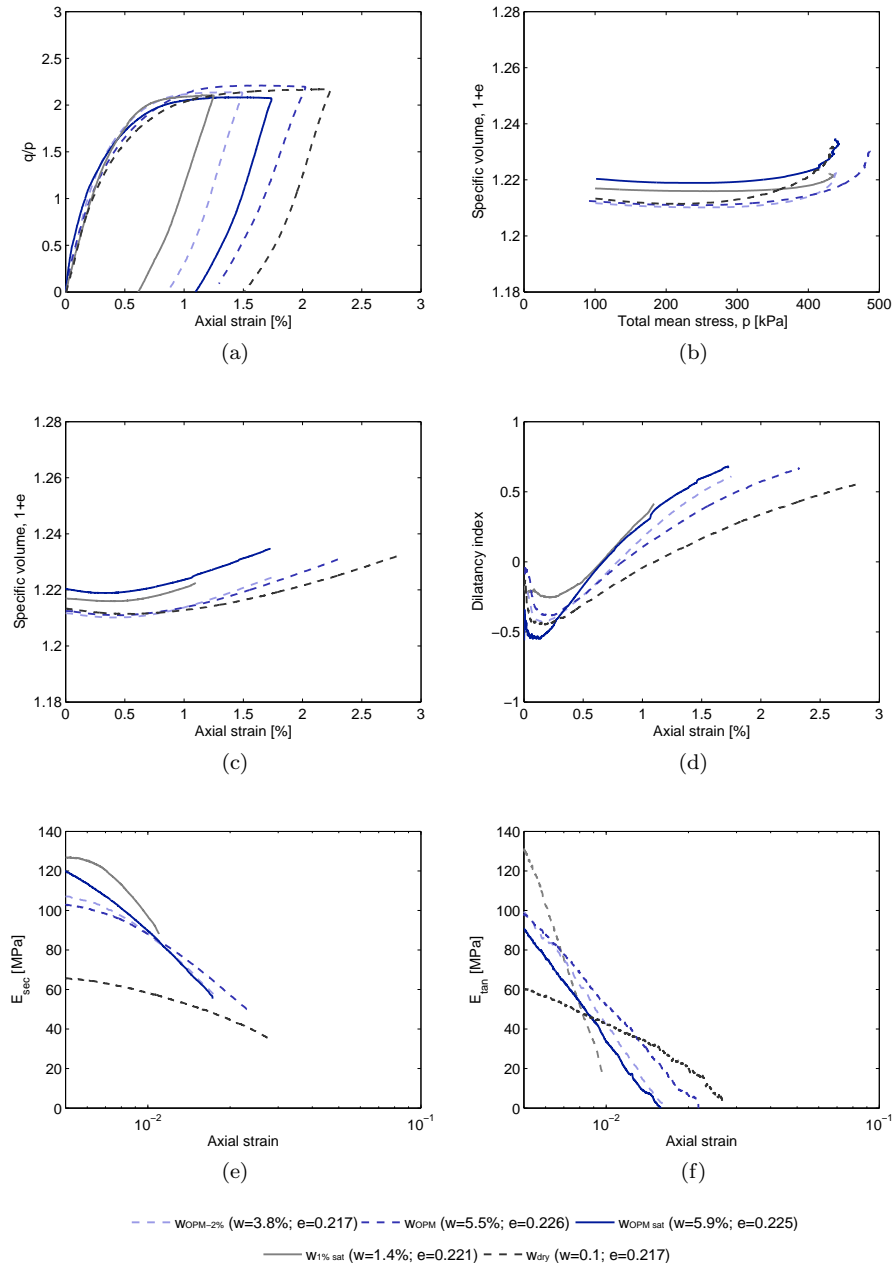


Figure 5.11: Triaxial tests results at $\sigma_3 = 100$ kPa from CA31.5 samples with varying initial molding water contents

strain and volume change curves were observed, i.e., until critical state was reached. Though critical state was not reached for all samples due to membrane rupture, from volume change curves and dilatancy it appears that critical state had been reached in WOPM_{sat} test.

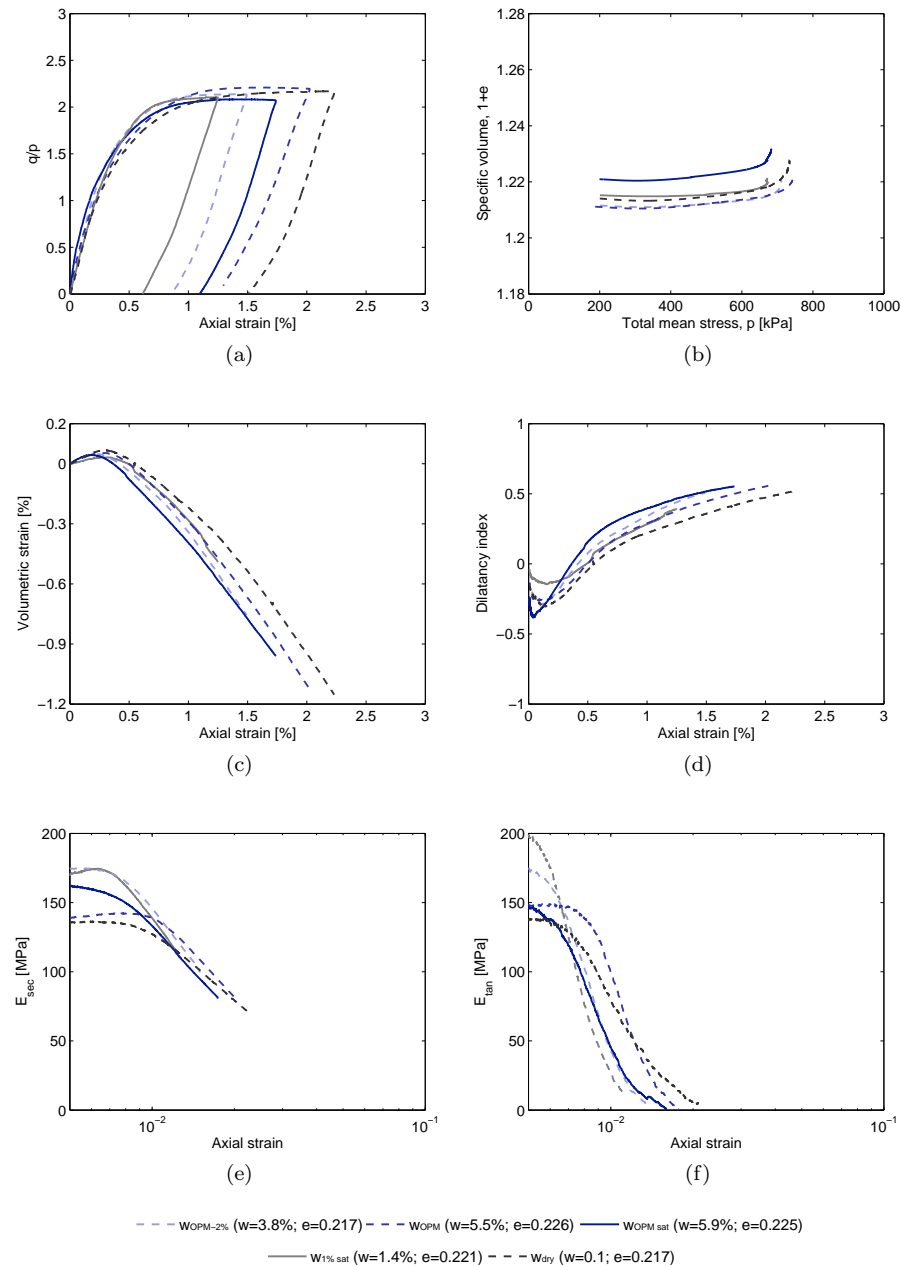


Figure 5.12: Triaxial tests results at $\sigma_3 = 200$ kPa from CA31.5 samples with varying initial molding water contents

Regarding specimens deformability, in Figures 5.11e and 5.11f, 5.12e and 5.12f and 5.13e and 5.13f triaxial results, specifically, secant and tangent moduli are presented. As would be expected, moduli increases with increasing confining stress.

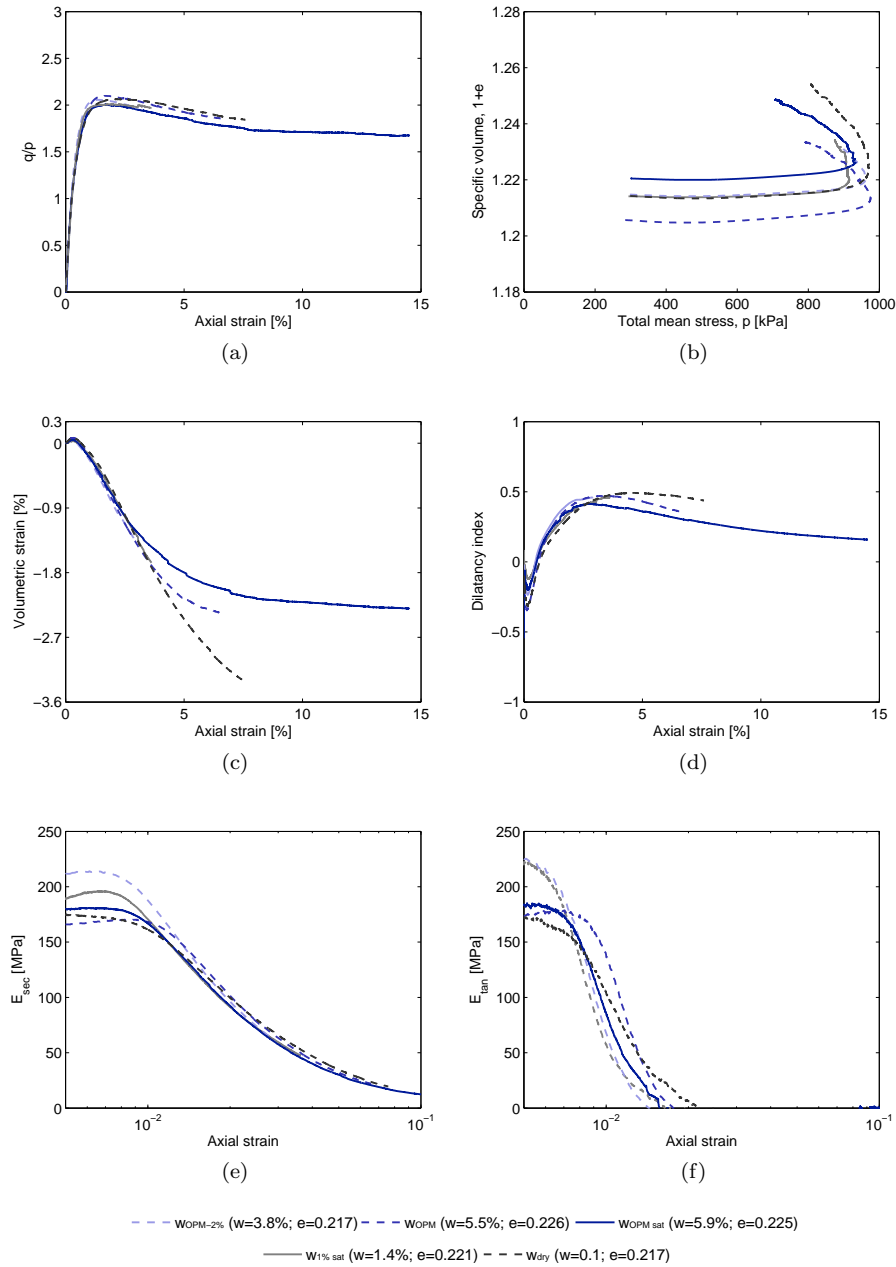


Figure 5.13: Triaxial tests results at $\sigma_3 = 300$ kPa from CA31.5 samples with varying initial molding water contents

In Figure 5.14 are plotted the peaks deviatoric stress (q) versus mean total stress (p) obtained from each triaxial multistage test, as well as the residual deviatoric stress corresponding to critical state obtained from saturated test. The peak failure envelope following relation expressed as in equations 5.2 and

5.3 is also plotted. The parameters M_{peak} and M_{cs} and respective ϕ_{peak} and ϕ_{cs} were determined and are given in Table 5.6.

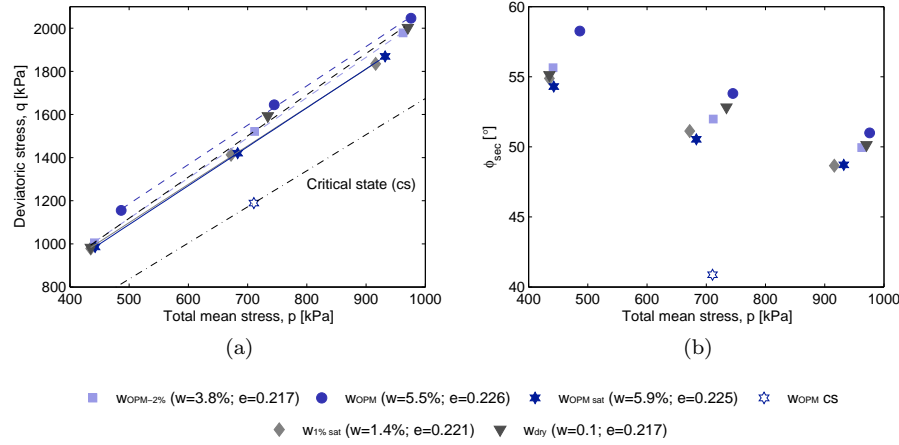


Figure 5.14: Triaxial test results from CA31.5 specimens with varying initial molding water content; (a) peaks and residual deviatoric stress vs. total mean stress; (b) Secant friction angle vs. total mean stress

Table 5.6: Peak and critical state failure envelope parameters M_{peak} , M_{cs} and c and respective ϕ obtained from triaxial multistage tests

Sample	M	c	ϕ [°]
WOPM-2%	1.87	184.7	45.4
WOPM	1.82	273.6	44.4
WOPM _{sat}	1.80	188.5	43.8
W1% _{sat}	1.78	208.7	43.3
W _{dry}	1.91	163.6	46.4
WOPM _{sat} CS	1.67		40.8

Similar peak internal friction angle, ϕ_{peak} , were obtained from WOPM-2% and WOPM unsaturated tests, 45.4 and 44.4°, respectively, which denotes slightly greater strength from driest specimen. Results from saturated specimens (W1%_{sat} and WOPM_{sat}) were found to be identical too, where ϕ_{peak} of 43.8 and 43.3° were obtained. As so, little differences on strength were found whether from saturated or unsaturated specimens and, therefore, one may conclude that suction has little effect on material strength for the studied state conditions. Taking into account the negligible fraction of material passing on sieve no. 200 (about 6%), to some extent, this conclusion would be expected. Moreover, results from saturated specimens (WOPM_{sat} and W1%_{sat}) indicate that fabric did not played a significant role on samples strength. The highest ϕ_{peak} was obtained from W_{dry} specimen, reflecting the higher britleness of specimen in that state condition. Critical states seems to had been reached only in WOPM_{sat} test. A M_{cs} of 1.67 was obtained corresponding to a $\phi_{cs} = 40.8^\circ$.

In Figure 5.7b is presented the secant friction angle (ϕ_{sec}) versus total mean

stress. Likewise to *SC* material, ϕ_{sec} values decrease with increasing total mean stress. However the highest are obtained from w_{OPM} specimen, whereas corresponding values obtained from $w_{OPM-2\%}$ specimen are lower, thereby, confirming conclusions about suction effect reached on previous paragraph. Though saturated specimens were prepared in different manner, they present identical ϕ_{sec} values, which are the lowest.

The evolution of specific volume with total mean stress (p) at the start of each stage is shown in Figure 5.15 in order to investigate the influence of the anisotropy induced by a multistage test. These results are compared with isotropic triaxial tests carried out in order to study compressibility of *CA31.5* material, as listed in Chapter 4. The parameters λ and Γ for each test are given in Table 5.7. One can see that slopes from anisotropic and isotropic compression lines differs significantly. As so, anisotropy induced by multistage triaxial tests seems to be significant. Relation regarding peak values could not be established. It is interesting noting that w_{OPMiso} unsaturated specimen showed greater compressibility than corresponding saturated specimen, though the opposite would be expected. This notwithstanding, differences on slopes are small, thus suction effect appears to have little influence on compressibility. In Figure 5.15b is plotted the specific volume against total mean stress concerning specimen w_{OPMiso} in loose state from which virgin compression line was determined.

In Figure 5.15a critical state line is also plotted. From theory (Wood, 1990) critical state line lies parallel to VCL obtained from isotropic triaxial test, yet offset to the left passing through critical state given by triaxial tests. As would be expected all points lie on the left side of critical state line, i.e., in the dry side, which features granular geomaterials in dense state (Wood, 1990).

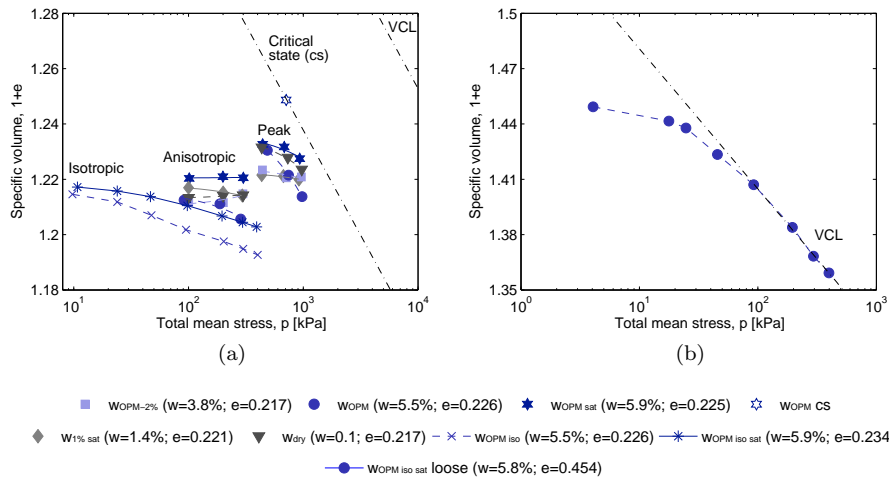


Figure 5.15: Specific volume vs. total mean stress obtained from *SB* triaxial tests: (a) isotropic, anisotropic at the start of each stage of a multistage test and at peak; (b) w_{OPM} unsaturated specimen on loose state

Likewise to *SC* test results analysis, the influence of compaction conditions on specimens deformability is investigated. E_{sec} is normalized for the same void ratio ($e = 0.215$) accordingly to Equation 5.6. In Figure 5.16 E_{sec}^{not} is

Table 5.7: Isotropic and anisotropic consolidation parameters, Γ and λ , determined from *CA31.5* triaxial tests

Sample	Isotropic and Anisotropic		Peak	
	λ	Γ	λ_{peak}	Γ_{peak}
W _O PM-2%	-1.6×10^{-5}	1.210	0.5×10^{-5}	1.225
W _O PM	3.5×10^{-5}	1.216	3.4×10^{-5}	1.247
W _O PM _{sat}	1.1×10^{-5}	1.224	0.2×10^{-5}	1.240
W _{1%} sat	1.4×10^{-5}	1.218	0.3×10^{-5}	1.223
W _{dry}	-0.5×10^{-5}	1.213	1.5×10^{-5}	1.238
W _O PM _{iso}	0.007	1.235		
W _O PM _{iso} sat	0.006	1.237		
W _O PM _{iso} loose sate	0.033	1.557		

plotted against axial stress and moisture content. Once again, an axial strain of 0.5% and 1.0% were considered taking into account the triaxial tests precision with external measurement. An increasing E_{sec}^{nor} with increasing axial stress is observed following a power law accordingly to Equation 5.8. In Table 5.8 are summarized the C and n parameters.

With regards to an axial strain of 0.5%, w_OPM and saturated tests present similar values of C and n , yet stiffness coefficient of unsaturated specimen is slightly lower, thus stiffness is lower. This trend is shown in Figure 5.16b for $\sigma_1 = 600$ kPa and $\sigma_1 = 1200$ kPa. A similar analysis is conducted to an axial strain of 1%, but for stress level domain between $\sigma_1 = 1000$ kPa and $\sigma_1 = 2000$ kPa. Parameters C and n show no significant differences on specimens stiffness, which trend is exhibited in Figure 5.9b. Finally, in Figure 5.9c is shown the relation $E_{sec0.5\%}/E_{sec1.0\%}$ considering $\sigma_1 = 1000$ kPa, where a relation about 1.75 is found. To sum up, suction seems not to play an important role on *CA31.5* material stiffness for the compaction conditions, stress and strain levels considered.

Table 5.8: Power law C and n parameters corresponding to regressions on E_{sec,σ_1} plane determined from *CA31.5* triaxial tests for $\varepsilon = 0.5\%$ and $\varepsilon = 1.0\%$

Specimen	$\varepsilon = 0.5\%$		$\varepsilon = 1.0\%$	
	C	n	C	n
W _O PM-2%	0.295	0.912	0.115	0.963
W _O PM	0.747	0.768	0.165	0.912
W _O PM _{sat}	0.818	0.764	0.159	0.919
W _{1%} sat	0.811	0.766	0.183	0.900
W _{dry}	0.172	0.981	0.085	1.010

5.4.4 Triaxial tests with measurements of S-waves velocity

Another series of triaxial tests on *SC* specimens, under the same water content and void ratio conditions, were carried out in order to obtain the very small strains properties. Characteristics of these tests were presented in pre-

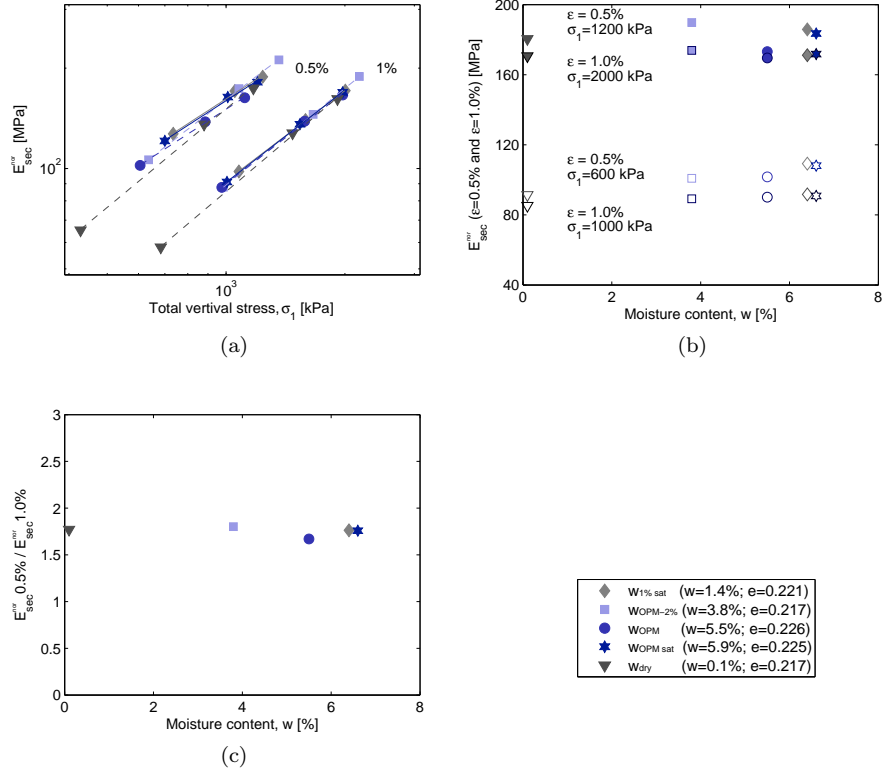


Figure 5.16: (a) E_{sec}^{nor} at strain levels $\varepsilon = 0.5\%$ and 1.0% vs. σ_1 ; (b) E_{sec}^{nor} at strain and stress levels $\varepsilon = 0.5\%$ ($\sigma_1 = 600$ kPa and 1200 kPa) and 1.0% ($\sigma_1 = 1000$ kPa and 2000 kPa) vs. moisture content; (c) Relationship between E_{sec}^{nor} at strain levels $\varepsilon = 0.5\%$ and $\varepsilon = 1.0\%$ at stress level $\sigma_1 = 1000$ kPa

vious chapter. In what follows, a brief description of interpretation of BE and accelerometers signals is made and results obtained from measurements of S-waves velocity with bender elements and accelerometers will be presented.

Interpretation of BE and accelerometers signals

The interpretation of the BE and accelerometers data was performed in time domain. Wave velocities were calculated using the travel length and time measured during the triaxial tests. In Figure 5.17 typical signals of BE and accelerometers are shown. These signals used as example result from a triaxial test carried out on WOPM unsaturated specimen. The identification of the arrival time of the shear waves is not obvious, since they are often advanced by direct and reflected compressional waves (Appendix A). With regards to BE, the first deflection point recorded can be erroneously taken as the first wave arrival, however it is caused by near field effect, hence cannot be considered to correspond to the real shear wave arrival time. The arrival time of shear waves was then assumed to be located in the point of maximum curvature of the recorded response curve, which are marked in Figure 5.17 as point *BE* (in-

put signal) and point BE' (output signal). Note that the polarity of the input and output signals is positive, hence the start of the shear wave is expected to be ascending.

If the same assumption is made for accelerometers signals, the points marked as Ac' (output signals) in Figure 5.17 would correspond to arrival time of shear waves. However, one can observe from Figure 5.17 that arrival time corresponding to signal labeled as $Ac 17.5$ is greater than respective time for BE receiver (point BE'). Recall setup presented on Chapter 4, $Ac 17.5$ is located at smaller vertical distance from source (175 mm) than BE receiver (200 mm). Therefore, arrival time of shear waves should be lower than respective time for BE receiver (point BE'). As so, the first deflection point recorded from accelerometers sensors was considered to correspond to the real shear wave arrival time.

For each test several frequencies ranging between 100 Hz and 10 kHz were tested at each isotropic stage in order to verify the value for which receivers signals amplification was greater. Then, frequency was chosen taking into account the amplification of the receivers signals, as well as conditions to avoid near-field effects (recall section A.2). The time domain interpretation herein used assumes the same travel time for all tested frequencies.

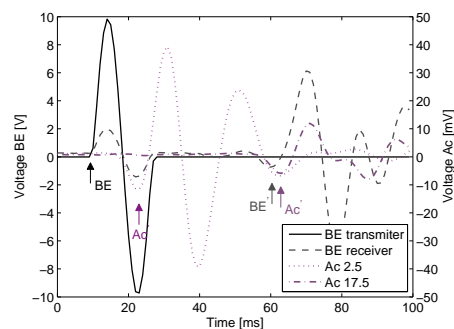


Figure 5.17: Time histories of signals from BE and accelerometers

Experimental results

As described in Chapter 4, specimens were isotropically consolidated and then sheared by the application of large amplitude stress cycles at constant confining stress in a multistage procedure. In Figure 5.18 are illustrated the triaxial results by confining stress.

Measurements of S-waves velocity using BE and accelerometers were conducted during shearing and shear modulus (G_0) was computed. An overview of the global evolution of the shear moduli obtained at isotropic and anisotropic stress states is presented in Figure 5.19. The critical review of literature shows that the shear modulus of unbound granular materials at the very small strain follows a power law accordingly to the Equation 5.9. Further, in Tables 5.9 and 5.10 are given the values of parameters C , n , and coefficient of determination R^2 .

$$G_0 = C \cdot p^n \quad (5.9)$$

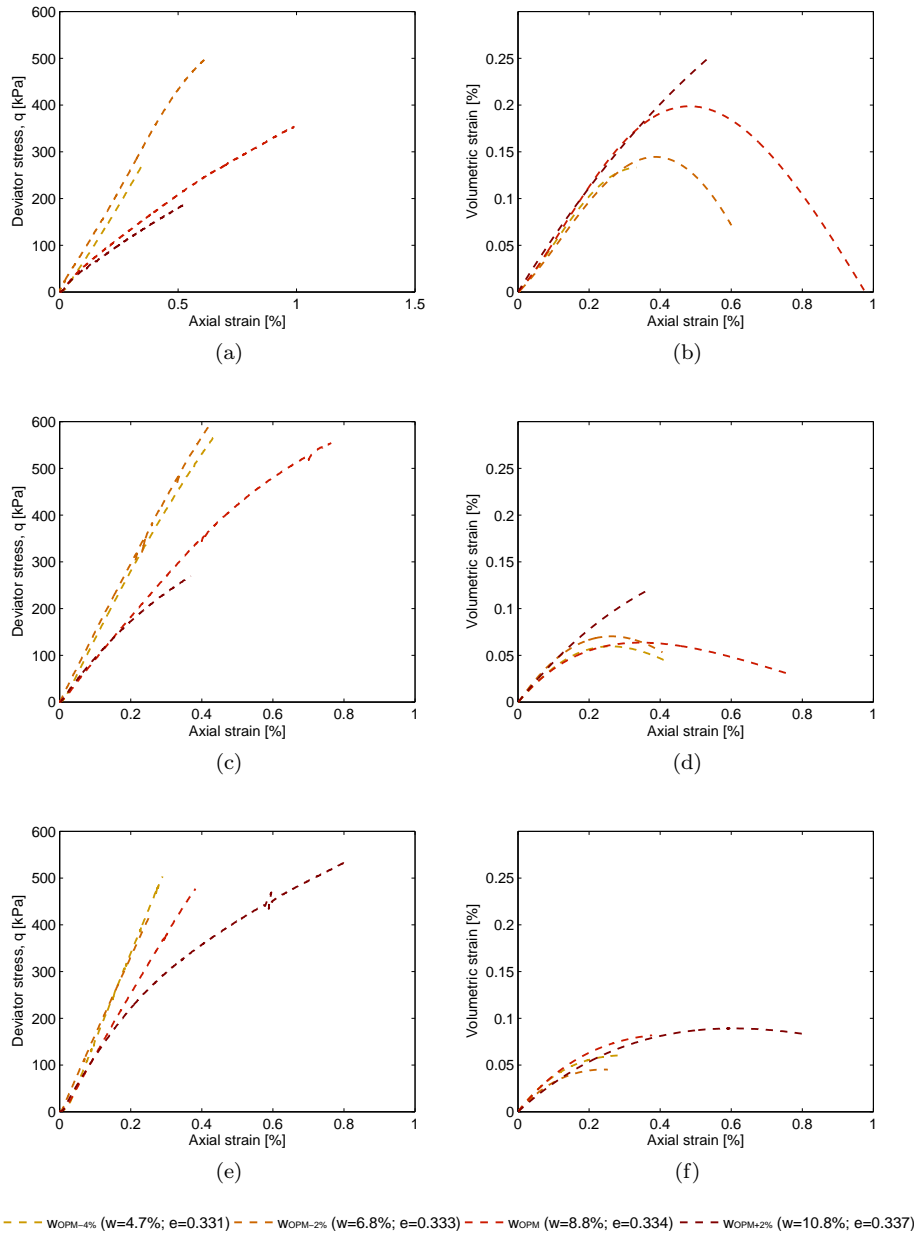


Figure 5.18: Deviatoric stress and volumetric strain vs. axial strain obtained from triaxial results at confining stresses of: (a) and (b) 100 kPa; (c) and (d) 200 kPa; (e) and (f) 300 kPa

The experimental results obtained from isotropic stress states show a good agreement with Equation 5.9, rather than results obtained at anisotropic stress states. With regards to unsaturated specimens at isotropic stress state, the variations of modulus versus total vertical stress follow a power law, with ex-

ponent n increasing from 0.336 to 0.522 and from 0.374 to 0.586 for BE and accelerometers results, respectively, with increasing molding water content, i.e., with decreasing suction. On the contrary, coefficient of stiffness C decreases with increasing molding water content. This trends highlight the increasing stiffness with decreasing moisture content from unsaturated specimens exhibiting, therefore, the influence of suction.

The dry specimen exhibits the stiffer slope ($n = 0.654$ and $n = 0.737$), which is close to the usual values found for dry granular soils (Fleureau *et al.*, 2003). Corresponding shear modulus values are similar to the ones obtained from w_{OPM} unsaturated specimen, which is not fully understood since lower values would be expected. As mentioned earlier for triaxial tests, this fact may be attributed to the influence of hygroscopic water.

Although similar trends for exponent n and coefficient C are verified at anisotropic stress states, slopes (n) and coefficient of stiffness C slightly varied. It appears that induced anisotropy influence shear modulus evolution at very small strains. This notwithstanding, G_0 depends noticeably on total mean stress, being always larger for driest unsaturated specimens. Further it is noteworthy that power laws for driest specimens ($w_{OPM-4\%}$ and $w_{OPM-2\%}$) are more or less parallel. The same happens with quasi-saturated specimens (w_{OPM} and $w_{OPM+2\%}$), yet presenting a stiffer slope and being almost superimposed. Fleureau *et al.* (2003) achieved similar trends regarding “Perafita” sand.

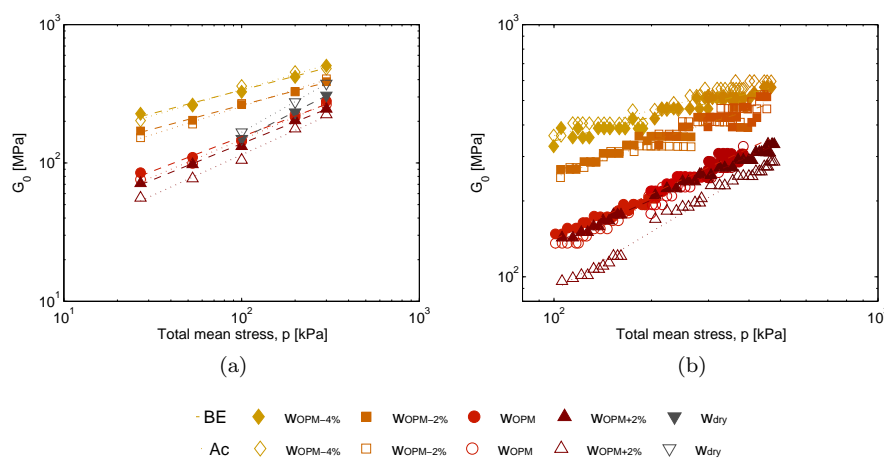


Figure 5.19: Evolution of shear moduli with total vertical stress obtained from measurements of S-waves on SC unsaturated samples at: (a) isotropic stress state; (b) anisotropic stress state

Further, shear modulus was corrected to the same void ratio by using Equation 5.7 proposed by (Hardin and Richart, 1963). In Figure 5.20 are illustrated the data plots regarding moduli normalised. Likewise to previous tables, in Tables 5.11 and 5.12 are given the values of parameters C , n , and coefficient of determination R^2 .

The data plots are quite similar to the ones observed previously (see fig. 5.19 and Tables 5.9 and 5.10). In fact, initial void ratios were similar for all specimens, thus results were likely to not vary noticeably due to moduli nor-

Table 5.9: Values of parameters C , n , and coefficient of determination R^2 from regression lines at isotropic stress state

Sample	Bender Elements			Accelerometers		
	C	n	R^2	C	n	R^2
WOPM-4%	71.6	0.336	0.986	60.6	0.374	0.983
WOPM-2%	53.5	0.345	0.996	39.7	0.405	0.991
WOPM	15.8	0.495	0.990	12.3	0.540	0.993
WOPM+2%	12.4	0.522	0.997	7.7	0.586	0.991
Wdry	7.3	0.654	0.999	5.6	0.737	1.000

Table 5.10: Values of parameters C , n , and coefficient of determination R^2 from regression lines at anisotropic stress state

Sample	Bender Elements			Accelerometers		
	C	n	R^2	C	n	R^2
WOPM-4%	81.6	0.314	0.926	78.6	0.332	0.934
WOPM-2%	41.0	0.402	0.893	30.3	0.456	0.911
WOPM	8.9	0.599	0.976	7.5	0.617	0.975
WOPM+2%	9.9	0.569	0.992	2.6	0.769	0.986

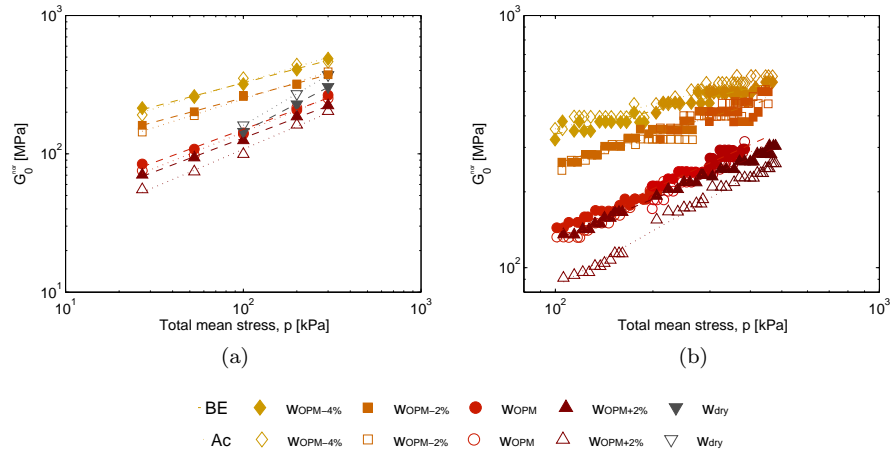


Figure 5.20: Evolution of normalised shear moduli with total vertical stress obtained from measurements of S-waves on SC unsaturated samples at: (a) isotropic stress state; (b) anisotropic stress state

malisation. It can be seen from Tables 5.11 and 5.12 that this analysis leads to identical power laws obtained from previous one. In addition, scatter is not reduced significantly. From results obtained, one may conclude that for the same void ratio and under the same total mean stress, there is a general increase in shear modulus when the water content decreases in the range of 2% wet of optimum and 4% dry of optimum.

Concerning to comparison between results obtained using BE and accelerometers, as observed from Tables 5.9 and 5.10, generally, results obtained from

Table 5.11: Values of parameters C , n , and coefficient of determination R^2 from normalised shear modulus ($e = 0.331$) regression lines at isotropic stress state

Sample	Bender Elements			Accelerometers		
	S	n	R^2	S	n	R^2
W _{OPM} -4%	68.0	0.340	0.994	57.5	0.378	0.978
W _{OPM} -2%	50.8	0.350	0.998	37.7	0.410	0.991
W _{OPM}	16.8	0.476	0.990	13.0	0.521	0.993
W _{OPM} +2%	13.8	0.486	0.997	8.6	0.550	0.990
W _{dry}	6.4	0.677	1.000	4.9	0.760	1.000

Table 5.12: Values of parameters C , n , and coefficient of determination R^2 from normalised shear modulus ($e = 0.331$) regression lines at anisotropic stress state

Sample	Bender Elements			Accelerometers		
	S	n	R^2	S	n	R^2
W _{OPM} -4%	83.2	0.305	0.924	80.2	0.323	0.931
W _{OPM} -2%	43.6	0.386	0.886	32.2	0.440	0.912
W _{OPM}	9.4	0.582	0.979	7.9	0.600	0.970
W _{OPM} +2%	11.0	0.535	0.992	2.9	0.734	0.988

measurements with BE and accelerometers slightly differs. In order to investigate these differences, in Figure 5.21 is illustrated the ratio between average S-waves velocity determined with accelerometers and BE and corresponding standard deviation. With exception to results obtained from w_{OPM}+2% unsaturated specimen, ratio V_{Ac}/V_{BE} was lower than 5%, which denotes good agreement between S-waves velocity determined with both sensors. This difference corresponds to a variation of shear modulus lower than 10%.

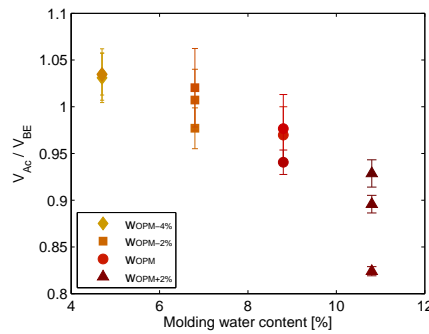


Figure 5.21: Ratio between average S-waves velocity determined with accelerometers and BE (V_{Ac}/V_{BE}) and corresponding standard deviation

For softer specimen (w_{OPM}+2%) one notes a fairly increase on ratio V_{Ac}/V_{BE} ranging from 7 to 18%. One can see that difference decreased with increasing confining stress, which is the same to say as specimens stiffens. Attempting to understand these differences, determination of S-waves velocity earn to be investigated. Hence, in Figure 5.22 are presented examples of travel time determination corresponding to different confining stresses, 100 and 200 kPa. One

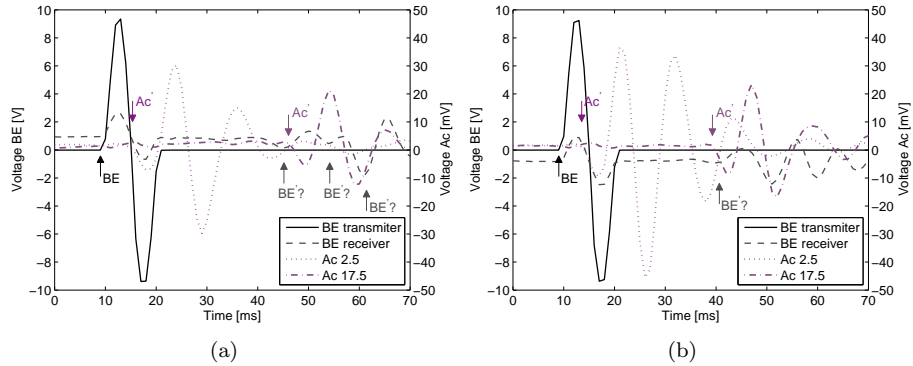


Figure 5.22: Time travel determination with with accelerometers and BE during triaxial test on specimen $w_{OPM+2\%}$ at confining stresses: (a) 100 kPa; (b) 200 kPa

can see from Figure 5.22a that arrival time from both accelerometers is straight, whereas picking BE arrival point is ambiguous. This difficulty, probably due to nearfield effects amplified by a high degree of saturation, led to pick the wrong arrival time, thus to mislead computation of S-wave velocity.

On the other hand, for the remain confining stress stages (200 and 300 kPa), determination of BE arrival time was clear, as illustrated in Figure 5.22b and, thereby, differences became smaller. This is thought to be due to the a decrease on saturation degree, since water expelling through the draining system was observed during test. After test had finished moisture content was determined and this hypothesis was confirmed since a moisture content of 8.9% was found, which is close to the optimum water content. Indeed, computed shear modulus at these stages were quite similar to the corresponding values from w_{OPM} specimen, as seen previously in Figure 5.20b. In conclusion, travel time determination using accelerometers is unambiguous whatever material state condition.

5.5 Conclusions

In this chapter, the most relevant laboratory test results obtained from testing of clayey sand (*SC*) and crushed aggregate (*CA31.5*) materials were presented. Results were divided according to the characterization type, namely, physical, hydro and mechanical characterization. Emphasis was given to mechanical characterization, particularly in what concerns to *SC* material.

Only *SC* was submitted to hydro characterization. The filter paper technique was employed to measure matric suction on specimens compacted with same initial void ratio but varying molding water contents. Matric suction decreased with increasing saturation degree, i.e.e, with increasing molding water content. Tests showed good repeatability and, thereby, filter paper technique proved to be an easy and low cost method to determine water retention curve.

Mechanical characterization involved oedometer test, triaxial tests and triaxial tests with measurement of S-waves velocity. *SC* specimens with varying molding water content both in unsaturated and saturated conditions were sub-

mitted to oedometer tests. In the lower stress range, before yielding, the curves shapes are reasonably molding water content independent, thus suction independent. On the contrary, in the higher stress range after yielding, curves shapes from unsaturated specimens seems to be suction dependent. The data confirm the general findings that an increased suction produces a stiffening of the material with smaller plastic compressibility (Alonso *et al.*, 1990; Cui and Delage, 1996), despite the tight differences observed between unsaturated tests. Saturated test (zero suction) showed the lowest compressibility which was due to a lower initial void ratio. Hence, similar results are produced by variation of suction and density, since any increase in either of these parameters reduces the compressibility. Regarding unloading cycle, it appears that swelling is suction independent for unsaturated specimens.

Both materials were subjected to triaxial tests. As far as what concerns to *SC*, drained saturated and unsaturated multistage triaxial tests were performed on specimens compacted with the same initial void ratio and with molding water contents ranging from 4% dry of optimum to 2% wet of optimum. A strong influence of molding water content on the mechanical behaviour of *SC* material was found, namely regarding strength and deformability parameters, which is attributed to suction effect. However, suction effect decreases with increasing stress and strain levels.

A stress–strain non linear behaviour featuring material in a dense state was observed from all specimens. Specimens with lower molding water content denoted higher britleness behaviour, corresponding higher secant friction angles. However, differences become lower with increasing total mean stress level with specimens with lower molding water content presenting higher reduction of secant friction angles. Moreover, at higher total mean stress ϕ_{sec} values get closer and seems to tend to ϕ_{sec} value at critical state, which is consistent with de Beer (1965) investigations on granular materials in a dense state. Critical state had been reached in unsaturated and saturated tests and a similar ϕ_{cs} was found (34.1°), which means that material behaviour at critical state is independent of initial saturation condition.

Specimens deformability were investigated regarding strain levels 0.5 and 1% and, likewise, identical trends were found. Higher E_{sec} feature specimens compacted dry of optimum. As specimen molding water content approaches saturated condition E_{sec} decreases.. However, differences regarding strain level 1% are smaller reflecting the influence of strain level. In addition, E_{sec} relation for 0.5 and 1% strain level appears to be fairly constant as moisture increases beyond optimum value for both stress levels, corresponding to about 1.7, which is quite similar to relation given by Ishibashi and Zhang (1993). In what concerns to specimens with lower moisture content, i.e, higher suction, relation tends to increase and becomes more pronounced for lower stress levels, which is the same to say that as stress level increases there is a reduction of suction effect on deformability. Further, degradation curves were found to lie between a reference threshold shear strain given by Santos (1999). The influence of moisture content, i.e., suction, on normalized degradation curves confining stress is clearly marked. As confining stress increases, differences between degradation curves become smaller. Therefore, as seen previously, as stress level increases there is a reduction of suction effect on deformability.

Multistage procedure was found to provide good results regarding peak deviatoric stresses, as long as no significant structure disturbance is experimented

at each stage. However, stress–strain curves present higher britleness behaviour rather than triaxial single stage tests. In addition, similar anisotropic and isotropic compression lines regarding w_{OPM} and $w_{OPM_{iso}}$ saturated and unsaturated tests, respectively, were obtained. These results reflect low influence of anisotropy induced by multistage triaxial tests. Further, it was interesting noting that slopes (λ) of unsaturated samples increase with increasing water content, thus confirms a decreasing compressibility, as verified in oedometer tests.

Likewise to *SC* material, also saturated and unsaturated multistage triaxial tests were performed on *CA31.5* specimens compacted with the same initial void ratio and with molding water contents of 2% dry of optimum and optimum, aiming to investigate the influence of molding water content on strength and deformability. In addition, a dry test was carried out.

A stress–strain non linear behaviour featuring material in a dense state was observed from all specimens. Unsaturated specimens denoted higher britleness behaviour, corresponding higher secant friction angles. However, in contrast to *SC* material, specimen with optimum molding water content presented the highest friction angle and saturated specimens the lowest. Once again, differences become lower with increasing total mean stress level and at higher total mean stress ϕ_{sec} values get closer. Critical state had been reached only for saturated tests where a $\phi_{cs} = 40.8^\circ$ was obtained. As so, little differences on samples strength were found whether from saturated or unsaturated samples, which indicates little influence of suction effect on strength in the range of molding water content studied.

The influence of compaction conditions on specimens deformability was investigated regarding strain levels 0.5 and 1%. No significant differences on specimens deformability were found for strain and stress levels evaluated. To this end, suction seems not to play an important role on *CA31.5* material stiffness for the studied compaction conditions. In addition, E_{sec} relation for 0.5 and 1% strain level appears to be fairly constant corresponding to about 1.75, which is quite similar to relation obtained from *SC* material.

The very small strains properties of *SC* were determined from measurements of S–waves velocity with bender elements and accelerometers. Tests were carried out on specimens with the same initial conditions as for triaxial tests. Measurements were performed at isotropic and anisotropic states. Once again, molding water content strongly influences material stiffness at very small strains. Likewise to conventional triaxial tests, stiffness decreased with increasing molding water content exhibiting, thereby, suction effect. Moreover, at lower stress levels differences tend to be higher.

As far as what concerns to comparison between results obtained using BE and accelerometers, generally, results obtained with both sensors slightly differs, with exception to the specimen with higher moisture content. The investigation of travel time determination showed that picking arrival time from both accelerometers is straight, whereas picking BE arrival point is ambiguous. This difficulty, probably due to near–field effects amplified by a high degree of saturation, led to pick the wrong arrival time, thus to mislead computation of S–wave velocity. Therefore, the measurement of S–waves using accelerometers as receivers appears to improve measurements quality in the time domain, particularly concerning quasi–saturated specimens.

Chapter 6

Field investigation: Évora trial railway embankment (*ETRE*)

6.1 Introduction

The current field quality control/quality assurance (Qc/Qa) of road and railway embankments construction requires materials and compacted layers evaluation and comparison with design parameters, that were accessed either by in situ prospection and/or by laboratory tests.

Recently, there is a strong trend towards using stiffness and strength to control compaction rather than index parameters given the importance of these mechanistic properties in pavement materials evaluation (Briaud, 2001; Loizos *et al.*, 2003; Alshibli *et al.*, 2005; Edil and Sawangsurya, 2005). In this scope, the static plate loadind test (*SPLT*) has been used in Portugal as a reference test either for evaluation of layers deformability and as reference test for performance related tests. However, the lack of a national *SPLT* standard for the application on road and railways embankments led constructors to use European standards, specifically, DIN 18134 (2001) and AFNOR NF P94-117-1 (2000). This notwithstanding, these standards differ in the test procedure and method for determination of E modulus. Therefore, evaluation of these standards is required in order to, on one hand, allow comparison of results and definition of standard to be used and, on the other hand, to provide a contribution for the European standardisation of *SPLT*. Further, performance related tests that have been recently developed, namely, impact tests (falling weight deflectometer – *FWD* and light falling weight deflectometer – *LFWD*), the soil stiffness gauge (*SSG*) and spectral analysis of surface waves (*SASW*), and continuous compaction control test methods (Portancemètre), involve different test methods which are not standardised and, therefore, it demands their in situ calibration for different materials and state conditions using *SPLT* as reference test.

A full scale trial was performed on a railway embankment aiming to study the influence of compaction conditions on the mechanical behaviour of compacted layers constructed using two geomaterials, a clayey sand (*SC*) and a

crushed aggregate (*CA31.5*), which were employed in railway embankment and railway track layers, respectively. To this end, *SC* layers were compacted employing different thicknesses (0.30, 0.40 and 0.50 m), and different water contents regarding Modified Proctor (optimum -2%, optimum and optimum +2%), whereas *CA31.5* layers were compacted employing different thicknesses (0.22 and 0.30 m), yet with same water content (optimum Modified Proctor). Index parameters and mechanical properties were then evaluated for several energy levels corresponding to 4, 6, 8, 10 and 12 passes of the vibrating roller.

In this chapter, firstly, index parameters (density, γ , and moisture content, w) obtained from *SCM* and *NM* are presented and directly compared. Secondly, results obtained from *SPLT* following AFNOR NF P94-117-1 (2000) standard and using two different measuring systems are evaluated. Then, comparison with corresponding results obtained from *SPLT* following DIN 18134 (2001) is conducted. Following, *SPLT* is used as reference test and comparison with performance related tests is established. Then analysis of full scale trial results is conducted and recommendations are provided. At last, comparison between field and laboratory results is performed.

6.2 State conditions

The sand cone method (*SCM*) and nuclear method (*NM*) provide state parameters, namely, density (γ) and water content (w). The interpretation of both tests is straight. However, it should be noted that *NM* involved measurements on the same spot at depths of 0, 0.06 and 0.12 m, which were then averaged.

Although *SCM* enable a direct measurement of density and the direct measurement of moisture content through oven drying method (NP 84, 1965), values obtained from *NM* requires calibration with corresponding measures from *SCM* and oven drying method. In order to establish a relationship between test methods, relationship between density (γ) and volumetric water content (θ) is shown in Figures 6.1 and 6.2.

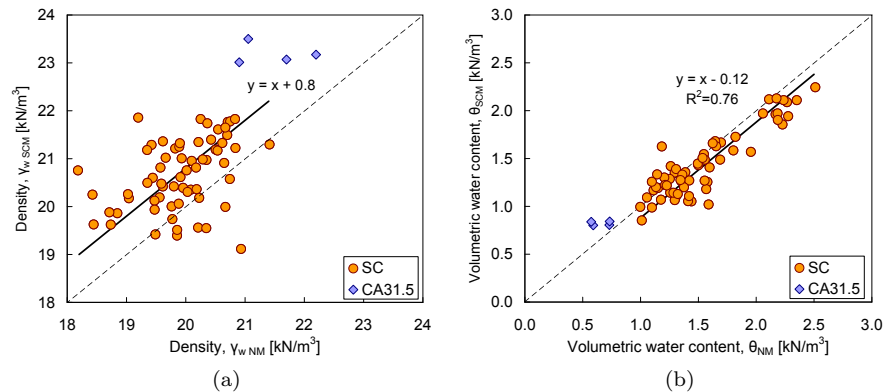


Figure 6.1: Comparison of state parameters obtained from *NM* and *SCM* test methods performed on the same grid: (a) density; (b) volumetric water content

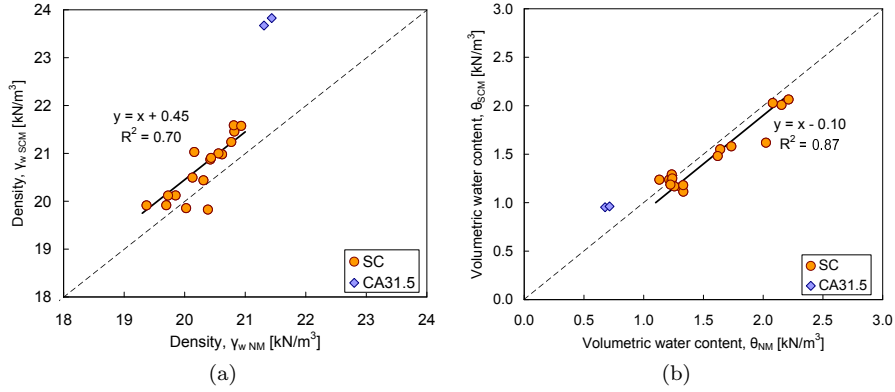


Figure 6.2: Comparison of average state parameters per layer obtained from NM and SCM test methods: (a) density; (b) volumetric water content

Though measures carried out on CA31.5 are plotted no correlation between test methods is established due to lack of results. Thereby, results are corrected accordingly individual relationships between average values.

Firstly, in Figure 6.1 only values obtained from tests carried out on the same grid are included and grid homogeneity is assumed. Even though a poor relationship between density was obtained due to high scatter, values gathered from SCM are slightly higher. On the contrary, a good relationship between volumetric water content was reached, where a R^2 of 0.76 was obtained. Due to high scatter from density results, secondly, a relationship between average values per energy level for each layer was attempted. In Figure 6.2 one can see reasonable and good relationships for density ($R^2 = 0.70$) and volumetric water content ($R^2 = 0.87$), respectively. Hence, values obtained from NM were calibrated accordingly to expressions in Figure 6.2 and will be employed hereafter. The result of calibration is presented in Figure 6.3.

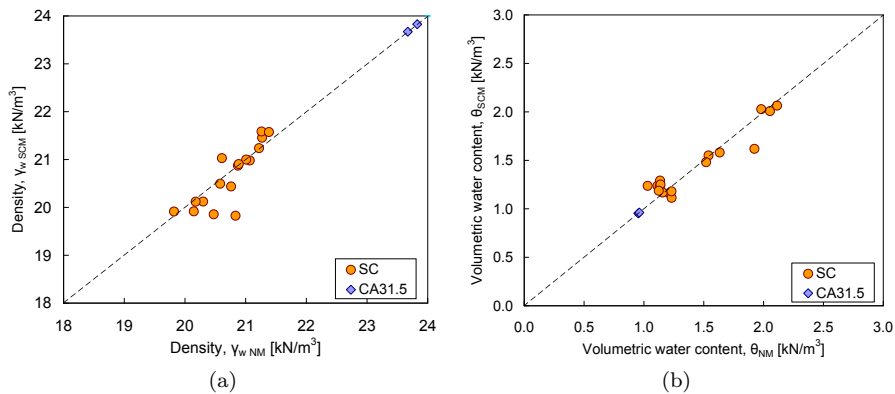


Figure 6.3: SCM parameters plotted against NM calibrated parameters: (a) density; (b) volumetric water content

Following, the state parameters obtained from each test method on SC com-

pacted layers are presented in Figure 6.4 for several energy levels. Due to time constraints and labor intensive *SCM* number of tests are significantly less than *NM* tests.

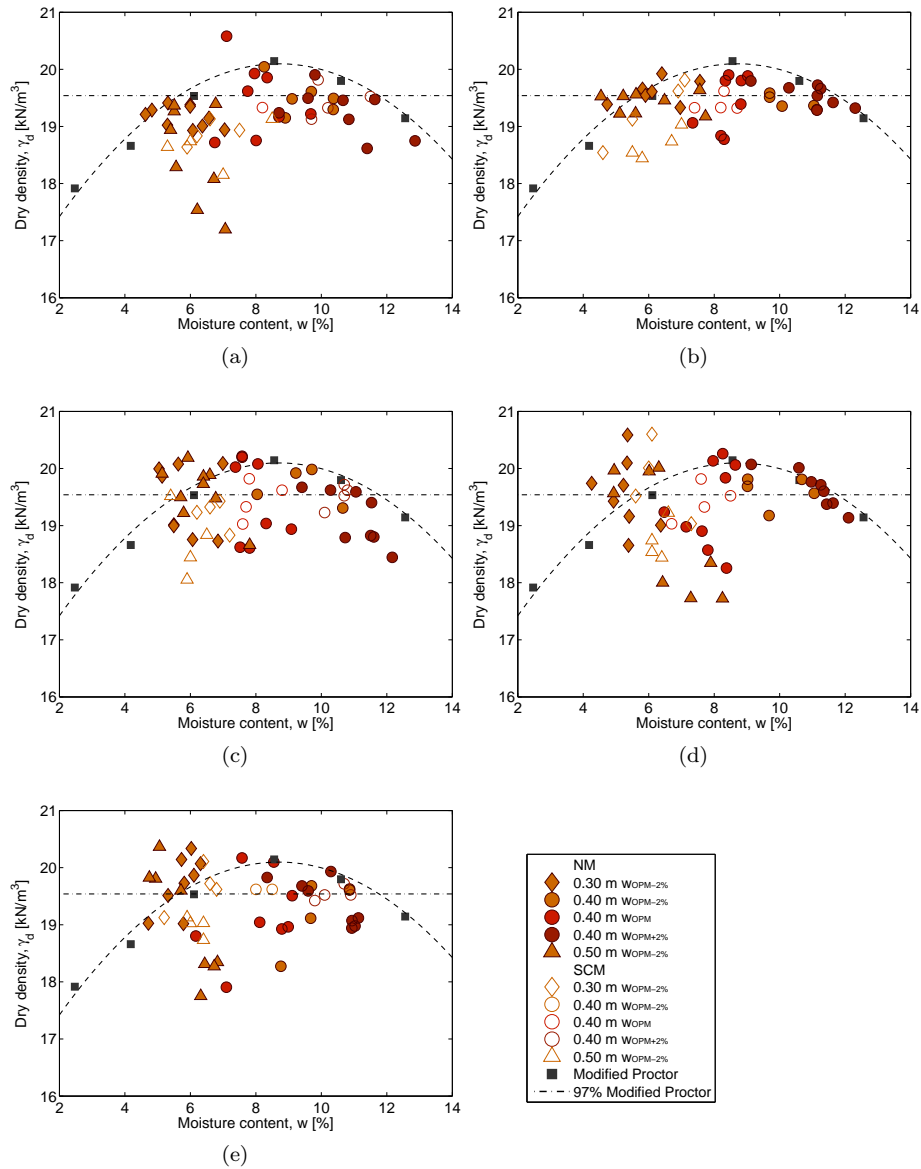


Figure 6.4: State parameters obtained from *SCM* and *NM* on *SC* layers for energy level corresponding to: (a) 4 Passes; (b) 6 Passes; (c) 8 Passes; (d) 10 Passes; (e) 12 Passes

Desirable moisture content was achieved for 0.30 and 0.50 m layers compacted with moisture content 2% dry of optimum. Remaining layers present great scatter despite the fact that material had been subject to a process to make it homogeneous previously to its application, as described in Chapter 4. To

some extent this may be attributed to the weather conditions during these layers construction. Concerning to *SCM* tests results (fig. 6.4), the lowest dry density was obtained on 0.50 m $w_{OPM-2\%}$ layer which lied below the 97% Proctor Modified limit, whereas for the remain layers this limit seems to be achieved at the last energy level (12 passes). With regards to *NM* tests results, high scatter is verified. This notwithstanding, the great number of tests allows to see that there is a gradual shift of optimum moisture content to the left, which means that w_{OPM} decreases with increasing energy level, as would be expected.

In Figure 6.5 data from *SCM* and *NM* tests carried out on *CA31.5* layers are illustrated. Due to time constraints *SCM* was performed only for one energy level. The analysis of *NM* calibrated results for all energy levels demonstrate an increasing γ_d with increasing energy exceeding maximum dry density given by Modified Proctor. Concerning to moisture content, w , an increase about 2% between the first and last energy levels is observed. This probably was due to weather conditions, which were adverse during runing tests on these trial layers. Nevertheless, for the last energy level moisture content is close to optimum value from Modified Proctor.

Since an extensive mechanical characterization was performed for the last energy level (12 passes), focus is given to layers state conditions at this stage. In Tables 6.1 and 6.2 is given statistical data regarding *SC* and *CA31.5* trial layers, respectively. In what concerns to the former layers constructed with 2% dry of optimum, the desirable moisture content was achieved only for layers with 0.30 and 0.50 m thickness, which average value was about 2.5–3% dry of optimum. With regards to dry density a higher average value was reached for layer with 0.30 m thickness, which is close to 98% of Modified Proctor, whereas average dry density for 0.50 m layer was close to 94%. These results denote the influence of layer thickness on dry density regarding compaction equipment used.

Table 6.1: State conditions of *SC* trial layers obtained from *SCM* and *NM* after calibration for the last energy level (12 passes)

	0.30 m	0.50 m	0.40 m		
	$w_{OPM-2\%}$	$w_{OPM-2\%}$	w_{OPM}	$w_{OPM-2\%}$	$w_{OPM+2\%}$
<i>SCM</i> γ_d [kN/m ³]	19.64	18.93		19.62	19.55
<i>SD</i>	0.40	0.17			0.12
<i>CV</i>	2.1	0.9			0.6
w [%]	6.3	6.3		8.3	10.4
<i>SD</i>	0.72	0.23			0.51
<i>CV</i>	11.5	3.7			4.9
<i>NM</i> γ_d [kN/m ³]	19.71	19.03	19.18	19.26	19.39
<i>SD</i>	0.50	0.97	0.74	0.61	0.41
<i>CV</i>	2.5	5.1	3.9	3.1	2.1
w [%]	5.7	5.8	8.0	10.0	10.2
<i>SD</i>	0.50	0.84	1.03	0.90	1.01
<i>CV</i>	8.8	14.4	12.8	9.0	9.8

With regards to layer constructed with moisture content close to optimum and 0.40 m thickness, one can see that the *NM* average value corresponds to 0.5%

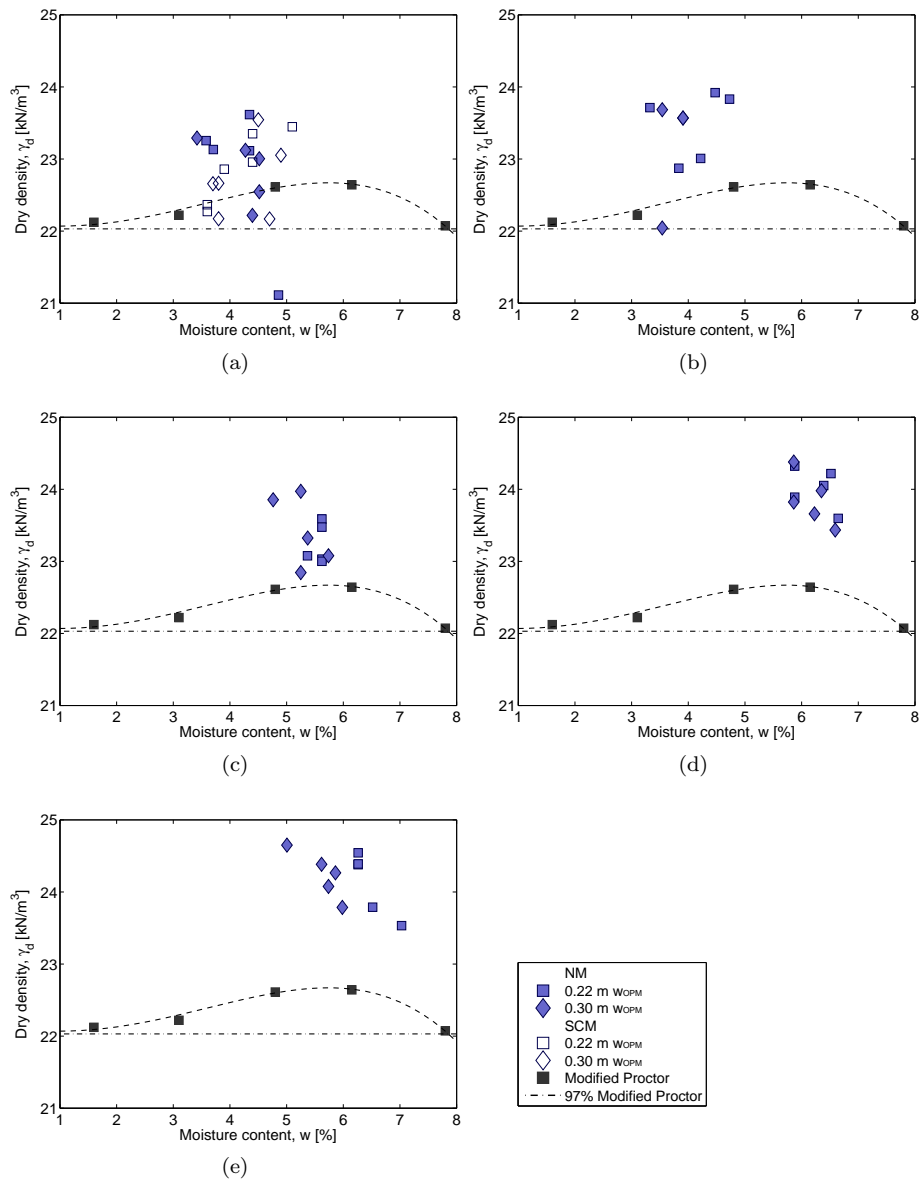


Figure 6.5: State parameters obtained from *SCM* and *NM* on *CA31.5* layers for energy level corresponding to: (a) 4 Passes; (b) 6 Passes; (c) 8 Passes; (d) 10 Passes; (e) 12 Passes

dry of optimum and an average dry density corresponding to 95% of Modified Proctor was achieved for the last energy level.

Concerning to remaining *SC* layers with 0.40 m, though different moisture contents were attempted, 2% dry of optimum and 2% wet of optimum, an identical moisture content was reached on both layers, which was about 1.5% wet of optimum value. Dry density close to 96% of optimum Modified Proctor

was achieved on both layers.

Finally, in what concerns to state conditions of *CA31.5* layers for the last energy level, moisture content around optimum value given by Modified Proctor was achieved for layer with 0.30 m thickness, whereas a moisture content 1% wet of optimum was achieved on layer with 0.22 m thickness. The average dry density was identical for both layers which average value is around 106% of maximum value given by Modified Proctor.

Table 6.2: State conditions of *CA31.5* trial layers obtained from *SCM* and *NM* after calibration for the last energy level (12 passes)

		0.22 m	0.30 m
		WOPM	WOPM
<i>NM</i>	γ_d [kN/m ³]	24.13	24.23
	<i>SD</i>	0.44	0.32
	<i>CV</i>	1.8	1.3
	w [%]	6.5	5.6
	<i>SD</i>	0.33	0.38
	<i>CV</i>	5.2	6.7

To sum up, it appears that the previous stack of material, water adding and mix up by means of a front shovel did not reproduced the desirable moisture content. The adverse weather conditions during running tests may have partially contributed to moisture content mismatch.

6.3 Moduli from *SPLT*

A total of 112 *SPLT* were performed on full scale trial. These were carried out following both AFNOR NF P94-117-1 (2000) and DIN 18134 (2001) standards, corresponding to 78 and 34 tests, respectively, yet the latter were performed only for the last energy level at each layer, as listed in section 4.3. Regarding running tests following AFNOR standard, two settlement measurement systems were used at the same time: one measuring settlement at the center and another measuring settlement in three concentric points on periphery of the loading plate. For this reason, results obtained following AFNOR standard will be differentiated accordingly the settlement measuring system. Only one settlement measurement system measuring at the center of the loading plate was used on tests conducted following DIN standard. Statistical data (average, standard deviation, *SD*, and coefficient of variation, *CV*) obtained from *SPLT* is given in Appendix C. The individual tests results were reported in Gomes Correia *et al.* (2006).

6.3.1 Comparison of *SPLT* results following AFNOR standard and using different settlement measuring systems

The analysis of the *SPLT* results denoted noticeable differences between E_{V2} values obtained with AFNOR standard, using different measuring systems. The detail analysis of tests results at the beginning of the running tests showed

differences in the range of 90% between settlement measurements of the loading plate using the two measuring systems. Thus, the settlement of the supports of the three point measuring system and the settlement of the structure were assessed attempting to justify these differences. However, it was found out insignificant support settlement (δ_s) in such a way to affect the measurement of the settlement of the loading plate (δ_{lp}). These measurements are illustrated in Figure 6.6, which shows a maximum settlement of one support of 0.012 mm ($\frac{\delta_s}{\delta_{lp}} = 1.23\%$).

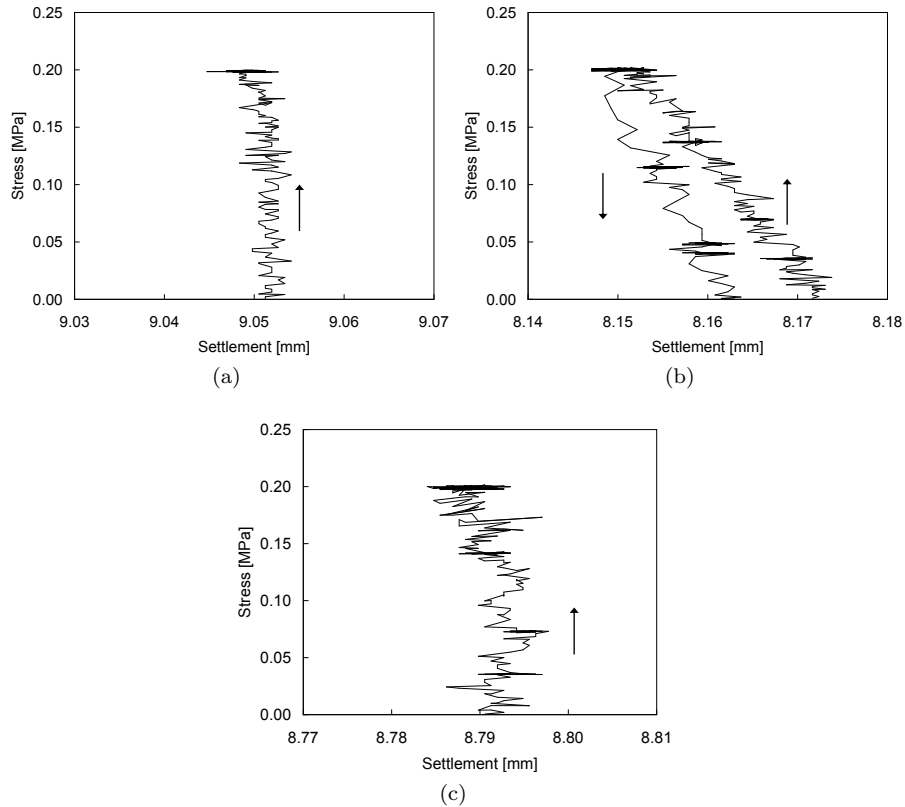


Figure 6.6: Measurement of the settlement of the three point measuring system corresponding to *SPLT* following standard AFNOR carried out on trial layer 0.50 $w_{OPM-2\%}$, for 4 Passes of the vibrating roller, on grid: (a) C7 (measurement of the settlement of one support); (b) C3 (measurement of the settlement of one support); (c) C3 (measurement of the settlement of the structure)

Accordingly to standard AFNOR NF P94-117-1 (2000) the loading plate may contain a hole in its center with 2 cm diameter. The measuring system is placed in such a way that measures the settlement of the material being tested through this hole. Hence, a punching phenomenon caused by the hole was set as hypothesis. In order to investigate this hypothesis, a running test where was verified a significant difference between the two measuring systems (three point and the one point through the hole) was chosen and a third loading cycle was carried out. In this third loading cycle the one point measuring system

was placed in contact with the loading plate approximately 2 cm away from the center. The load–settlement curve is presented in Figure 6.7.

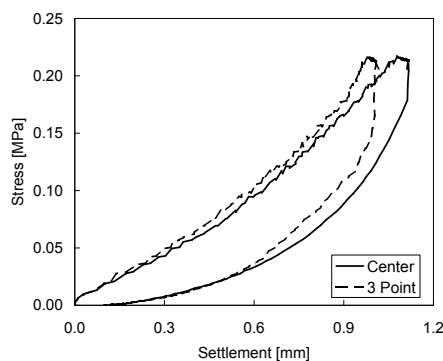


Figure 6.7: Third loading cycle of a *SPLT* following standard AFNOR carried out on grid A10 of the trial layer 0.40 w_{OPM} , which energy level corresponds to 12 Passes of the vibrating roller. The one point measuring system was placed in contact with the loading plate approximately 2 cm away from the center

Assuming a rigid loading plate, the settlement measured with the one point measuring system placed on the loading plate approximately 2 cm away from the center and the three point measuring system should be the same. Though in this case it differs approximately 10% (see Table 6.3), which is thought to be an acceptable difference.

Table 6.3: Comparison of the settlements measured with the one point measuring system, through the hole in the center (second loading cycle) or on the loading plate 2 cm away from the center (third loading cycle), and with the three point measuring system

Loading cycle	One point on the center [mm]		Three Point [mm]	Difference [%]
	Through the hole	On the plate		
2 nd	0.564	–	1.078	91.1
3 rd	–	1.015	1.115	9.9

Furthermore, it should be pointed out the difference between the settlement measured with the three point measuring system between second and third loading cycles that is 3.4%. In the same way, a difference in the same range between settlements measured with the one point measuring system, through the hole in the center (second loading cycle) or on the loading plate 2 cm away from the center (third loading cycle), should be similar. However, a difference of 80% is verified. As a result, measurement through the hole in the center of the loading plate appears to exhibit a punching phenomenon, which might explain the differences mentioned above. Hence, the measurement of the settlement with one point measuring system should be performed on the center of the loading plate instead through the hole in the center in contact with the material being tested.

The analysis of the whole *SPLT* following AFNOR standard, where the two

settlement measuring systems were used at the same time, allows to conclude that E_{V2} modulus obtained with one point measuring system through the hole in the center of the loading plate is approximately 30% higher than the corresponding value obtained with the three point measuring system, as illustrated in Figure 6.8. Therefore, test result using the three point measuring system is considered as the reference value hereafter.

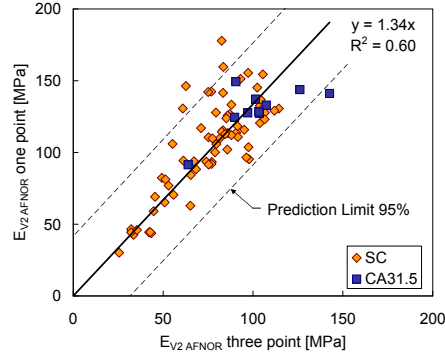


Figure 6.8: Comparison of E modulus obtained with one point measuring system through the hole in the center of the loading plate and with the corresponding value obtained with the three point measuring system

6.3.2 Comparison of E_{V2} modulus following standards: AFNOR NF P94–117–1 (2000) and DIN 18134 (2001)

The *SPLT* has been carried out in most different engineering works, above all following AFNOR NF P94–117–1 (2000) and DIN 18134 (2001) standards. Differences between these standards are twofold: (i) test proceed; (ii) test interpretation, which are reflected on the final elastic modulus obtained. Taking into account the importance that this parameter assumes on quality control of embankments layers, comparison between values obtained following each standard was conducted. With this purpose, experimental plan provided *SPLT* performed following AFNOR NF P94–117–1 (2000) and DIN 18134 (2001) standards on all trial layers for the last energy level, corresponding to 12 passes of the vibrating roller.

For the sake of the interpretation and comparison of *SPLT*, some issues must be pointed out. First, *SPLT* were performed in different grids ($5 \times 2 \text{ m}^2$) on trial layers $0.30 w_{OPM-2\%}$, $0.40 w_{OPM-2\%}$, $0.50 w_{OPM-2\%}$ and $0.40 w_{OPM}$. Second, *SPLT* were conducted in same grids ($5 \times 2 \text{ m}^2$) on remaining trial layers, namely, $0.40 w_{OPM+2\%}$, $0.22 w_{OPM}$ and $0.30 w_{OPM}$. Finally, with exception to tests performed on trial layers $0.50 w_{OPM-2\%}$ and $0.30 w_{OPM-2\%}$, all the other ones were performed in the same day. Table 6.4 sum up these issues.

Comparison of E_{V2} modulus obtained from *SPLT* direct interpretation of standards

Results obtained from *SPLT* carried out in the same grid ($5 \times 2 \text{ m}^2$) were compared assuming homogeneity of state parameters per grid. For this reason,

Table 6.4: Synthesis of *SPLT* for the energy level corresponding to 12 Passes of the vibrating roller

Layer	Number of <i>SPLT</i> following each standard	Performed in the same grid?	Performed in the same day?
0.30 $w_{OPM-2\%}$	5	<i>No</i>	<i>No</i>
0.40 $w_{OPM-2\%}$	5	<i>No</i>	<i>Yes</i>
0.50 $w_{OPM-2\%}$	5	<i>No</i>	<i>No</i>
0.40 w_{OPM}	5	<i>No</i>	<i>Yes</i>
0.40 $w_{OPM+2\%}$	4	<i>Yes</i>	<i>Yes</i>
0.22 w_{OPM}	5	<i>Yes</i>	<i>Yes</i>
0.30 w_{OPM}	5	<i>Yes</i>	<i>Yes</i>

it is believed that correlations presented are independent from state parameters of each layer and, therefore, results from all layers were compared together.

Comparison of E_{V2} modulus obtained from direct interpretation of *SPLT* following both standards is presented in Figure 6.9a. One can see that E_{V2} modulus obtained from direct interpretation of *SPLT* following DIN standard is about 15% higher than corresponding values obtained from *SPLT* following AFNOR standard. An acceptable correlation is verified ($R^2 = 0.69$).

On the assumption of homogeneity of state parameters, comparison between the average values of E_{V2} per layer was carried out. In Figure 6.9b are plotted the E_{V2} average values resulting from direct interpretation of five *SPLT*s following each standard. Average values of E_{V2} obtained from direct interpretation of *SPLT* following DIN standard are 11% higher than the corresponding values obtained following AFNOR standard, which is similar to the one verified for comparison of tests performed in the same grid. Thereby, the assumptions about homogeneity of state parameters per layer are validated by this correlation. Note that a good correlation is verified ($R^2 = 0.83$).

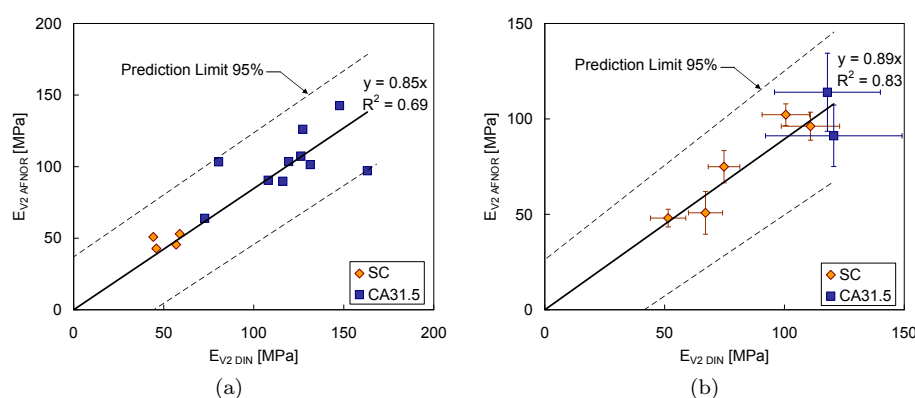


Figure 6.9: Comparison of E_{V2} modulus obtained from direct interpretation of *SPLT* following AFNOR NF P94-117-1 (2000) and DIN 18134 (2001) standards: (a) tests performed in the same grid; (b) average values per layer.

Comparison of E_{V2} modulus obtained from *SPLT* interpretation for the same normal stress and method

As mentioned previously, AFNOR and DIN standards differs on test procedure and on test interpretation. Herein, focus will be given to the latter. Two main differences on the interpretation method must be highlight: (i) the normal stress below the plate for which E_{V2} is calculated; (ii) the method for determination of plate settlement (recall Chapter 2). On one hand, interpretation of *SPLT* following AFNOR standard is performed for a normal stress below the plate of 200 kPa and using secant method for settlement determination. On the other hand, interpretation of *SPLT* following DIN standard is performed for a normal stress below the plate of 250 kPa and using tangent method for settlement determination.

Regarding non-linear stress-strain behaviour of geomaterials, comparison of E_{V2} modulus should be carried for the same normal stress and using same method for settlement determination (secant or tangent). Hence, a normal stress of 200 kPa and secant method was set as reference for the interpretation of *SPLT*s. This option was limited by AFNOR standard procedure which determines a maximum normal stress below the plate of 200 kPa during the second loading cycle and only allows the secant method to be used. In the same manner as previously presented, in Figure 6.10 are plotted the E_{V2} modulus obtained from tests carried out in the same grid and average values per layer. One can see that differences decreases when interpretation for the same normal stress (200 kPa) and same method (secant) is conducted. E_{V2} modulus obtained from tests following DIN procedure are about 10% or 15% lower than corresponding values obtained from tests following AFNOR standard, either when comparison is made between tests done in the same grid (fig. 6.10a) or between average values per layer (fig. 6.10b), respectively. Once again, acceptable and good correlations are testified by values of R^2 equal to 0.68 and 0.81.

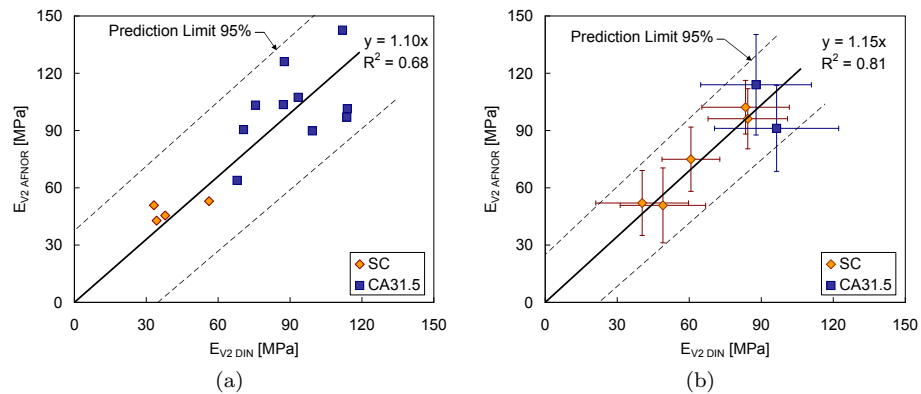


Figure 6.10: Comparison of E_{V2} modulus obtained from interpretation of *SPLT* for same normal stress (200 kPa) and same method: (a) tests performed in the same grid; (b) average value per layer.

In conclusion, from straight interpretation of *SPLT* following both standards or even when interpretation for same normal stress (200 kPa) and same method (secant) is performed, slightly differences are observed. Therefore, for the stud-

ied geomaterials and state parameters, results suggests that test procedure does not have significant influence on value of E_{V2} modulus.

Comparison of E_{V2} modulus obtained from *SPLT* back-analysis

So far *SPLT* have been compared based on straight interpretation of standards or for same normal stress and method. However, it must be pointed out that difference of plate dimension was not considered, which may influence the interpretation undertaken.

As mentioned on Chapter 2, *SPLT* plate with 600 mm in diameter was used for *SPLT* following AFNOR standard, whereas a plate with 300 mm in diameter was used for *SPLT* following DIN standard. It is well recognised that the “pressure bulb” below a circular footing extends to a depth equal to about twice the diameter of the footing. Thus, different “pressure bulbs” are associated to each plate. Consequently, in a multi-layer system E_{V2} modulus per layer must be determined to allow to compare values independently of standard used. Otherwise, only comparison of equivalent E_{V2} modulus is possible. To this end, back-analysis of *SPLT* was carried out. This analysis was based on the Theory of Elasticity and on Boussinesq solution for a rigid circular footing with diameter B loaded by force Q , resting on a linear elastic medium with elastic modulus E and Poisson ratio ν , as expressed in Equation 6.1.

$$s = \frac{Q}{B} \cdot \frac{(1 - \nu^2)}{E} \quad (6.1)$$

Adopting a Poisson ratio, ν , equation 6.1 allows to estimate E modulus. Solving equation 6.1 in order to E modulus the following expression is obtained:

$$E = \frac{\pi}{2} \cdot (1 - \nu^2) \cdot \frac{p \cdot r}{s} \quad (6.2)$$

where p is the stress below the footing and r is the diameter. From previous expression a coefficient of rigidity footing, I_{rig} may be defined as follows:

$$I_{rig} = \frac{\pi}{2} \cdot (1 - \nu^2) \quad (6.3)$$

In order to determine E modulus from back-analysis, a numerical model was implemented using a finite element commercial program (TNO, 2005) and an axisymmetric model was used. The methodology for back-analysis calculations consisted in three phases.

In the first phase rigidity of plates was evaluated. With this purpose, AFNOR and DIN plate (recall Chapter 2) were modeled, the latter considering three thicknesses 21 (plate used in situ tests), 50 and 150 mm. In addition, a uniform load applied directly over foundation was modeled in order to confirm I_{rig} given by analytical expressions (Poulos and Davis, 1974). *SPLT*s were modeled with concentric static linear load applied on plates and a wide range of foundation modulus (0–400 MPa) was considered. A Poisson ratio $\nu = 0.20$ was employed. From the input load and modulus and output settlement the I_{rig} was determined. Results obtained are shown in Figure 6.11. From analysis of Figure 6.11 it can be concluded that AFNOR plate behaves as rigid plate. However, the value of I_{rig} is lower than theoretical value, 1.51. An interesting behaviour regarding DIN plate 21 mm is observed. For low values of E modulus

plate behaves as rigid plate, while for high values of E modulus plate behaves towards flexible plate since I_{rig} becomes closer to the theoretical value for flexible plate, 1.9 (Poulos and Davis, 1974). In order to check minimum thickness for DIN plate to behave as rigid plate, thicknesses equal to 50 and 150 mm were studied. Behaviour as rigid plate was verified for both thicknesses. To sum up, concerning plates used in field tests, both plates behaves as rigid plate within the interval range of interest, i.e., for values of E modulus given by in situ *SPLT*s.

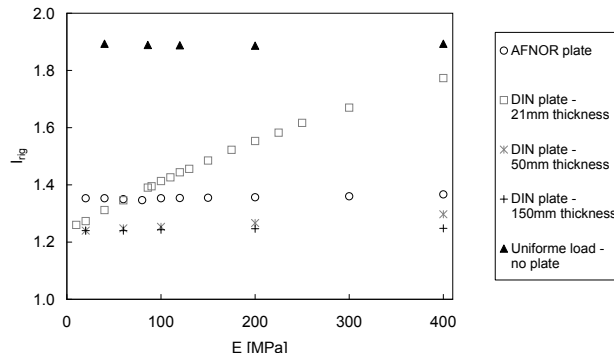


Figure 6.11: Coefficient of rigidity I_{rig} determined from numerical analysis

The second phase consisted on the validation of numerical analysis. With this purpose, numerical modeling of *SPLT* was conducted to verify relationship between E_{V2} given by the interpretation of both standards for the same normal stress, 200 kPa, which results are plotted in Figure 6.12. Relationship between E_{V2} is identical to the one obtained by comparison of interpretation of *SPLT* results for the same stress and method (see fig. 6.10). Although I_{rig} of plates given by numerical models are not the same given by standards, it can be observed negligible influence on relationship established, thus validating numerical modeling.

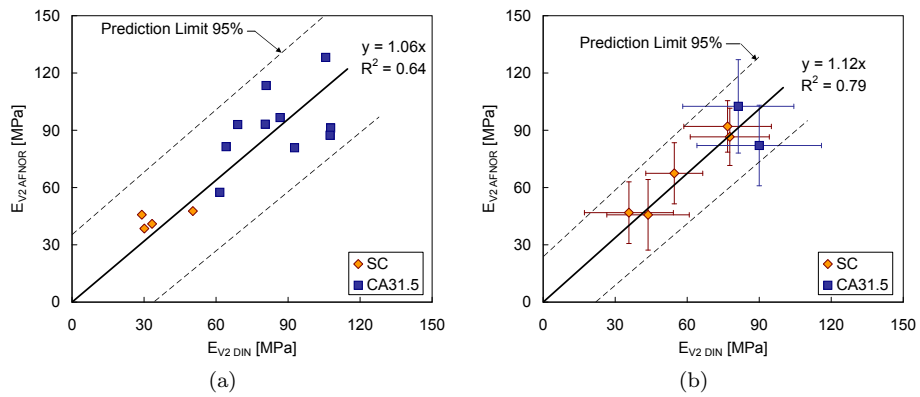


Figure 6.12: Comparison of E_{V2} modulus obtained from numerical modeling of *SPLT* for same normal stress (200 kPa) and same method: (a) tests performed in the same grid; (b) average value per layer

In the third phase back-analysis was conducted. The multi-layered system

adopted is presented in Figure 6.13. Equivalent modulus E_{V_2EQ} was calculated in first place and, further, E_{V_2} modulus of overlying layers were determined in a back-analysis process. The obtained results are shown in Figure 6.14. A relationship close to unit between computed values can be seen. A reasonable correlation is exhibited by a R^2 equal to 0.44. Since a relationship close to unit was obtained, one may conclude that plate diameter had slightly influence on the result of studied cases. Nevertheless, for multi-layered system, comparison of E_{V_2} modulus obtained from *SPLT*s using different plates can only be made by conversion of values for a certain layer with a certain thickness.

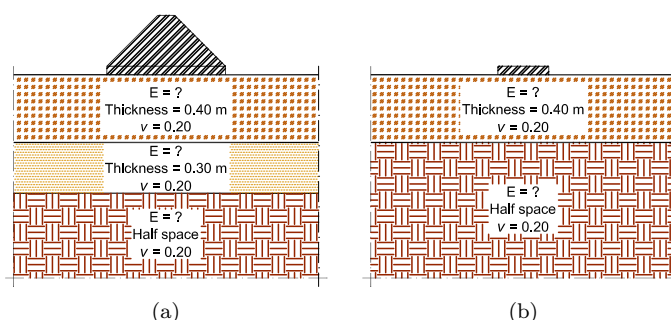


Figure 6.13: Properties and geometry adopted in numerical models for back-analysis of *SPLT* models following: (a) AFNOR NF P94-117-1 (2000); (b) DIN 18134 (2001) standards

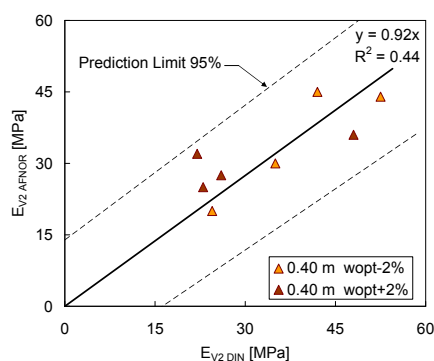


Figure 6.14: Comparison of E_{V_2} modulus obtained from back-analysis

To sum up, comparison between test results following AFNOR and DIN standards should take into account the stress level and method on test interpretation. Furthermore, the plate diameter and plate coefficient of rigidity should be taken into account on determination of equivalent modulus. In addition, *SPLT* carried out accordingly AFNOR NF P94-117-1 (2000) should be carried out using a measuring system that directly measures the plate settlement either using a three point or one point measuring system. These recommendations led to a specification project of *SPLT* (Gomes Correia *et al.*, 2007) which is presented in Appendix B.

6.4 Moduli obtained from performance related tests

6.4.1 *LFWD, FWD, SSG and Portancemètre*

The *LFWD*, *SSG* and Portancemètre devices promptly provide E_{LFWD} , E_{SSG} and E_{Port} moduli, respectively. In Appendix C is given statistical data (average and standard deviation, *SD*, and coefficient of variation, *CV*) obtained with these test methods for each trial layer and for several energy levels. The number of tests enabling statistic treatment by layer and energy level were listed in Chapter 4 and individual tests results were reported in Caldeira (2006).

The *FWD* device provide maximum deflection from which modulus E_{FWD} can be computed promptly too. All tests were conducted starting with one seating load followed by one load drop at four different drop heights, generating this way four different loads, in each station. A load plate with 0.30 m in diameter was used and a flexible load plate was considered. In Appendix C is given statistical data.

It should be bear in mind that Portancemètre is the only continuous test method enabling, therefore, an enhanced characterization of mechanical properties of compacted layers. In fact, while 2 or 4 *LFWD* and *SSG* tests were performed at each lane A, B or C (recall section 4.3), the total length was evaluated with Portancemètre since it gathers one test per meter. This improvement is highlighted in Figure 6.15 showing the evaluation of mechanical properties with the number of passes, corresponding to layer 0.30 m $w_{OPM-2\%}$, lane B.

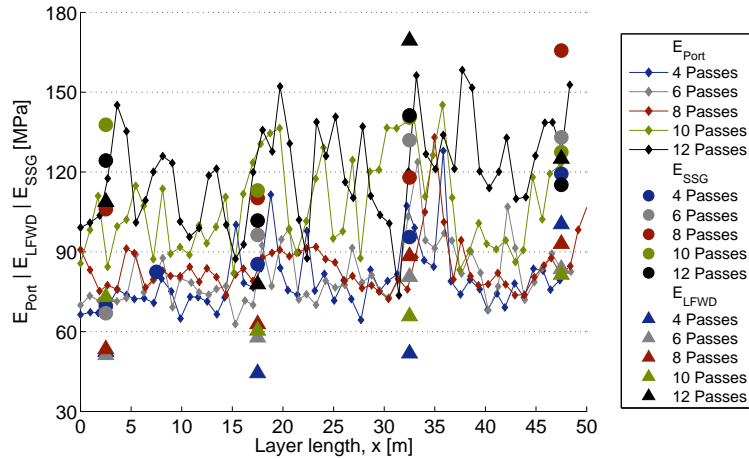


Figure 6.15: Example of test results (*LFWD*, *SSG* and Portancemètre) obtained from layer 0.30 m $w_{OPM-2\%}$ on lane B, for several energy levels

6.4.2 *SASW*

The *SASW* test carried out requires further analysis to provide desirable modulus. In what follows is presented the setup and the interpretation of *SASW* tests carried out on 0.40 w_{OPM} compacted layer.

The setup involved the instrumentation of surface layer with accelerometers placed at equidistant distances. Four vertical receivers (accelerometers) are placed on the ground at an equal distance from a fixed centerline. Because the upper compacted layer of about 0.40 m and foundation layer of about 0.60 m are under consideration, receivers spacing of 1 m is used in this study. The setup adopted is illustrated in Figure 6.16.

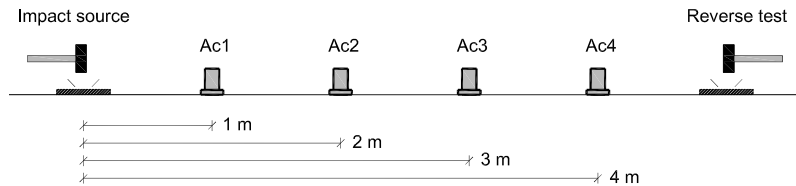


Figure 6.16: Setup adopted to perform SASW on layer 0.40 w_{OPM} inside grid B6

Two tests were performed, one was carried out inside grid 5–6, lane B, whereas another was performed inside grid 8–9, also inside lane B. An impulsive load is applied in line with the receivers at a distance away from the receiver equal to receivers spacing. To improve the signal-to-noise ratio, the impacts are repeated several times (about 20 impacts). A reverse test is also performed with the source in the opposite side of the receiver array, in order to confirm the first test. Active Rayleigh wave data were generated using a light hammer source. The typical waveforms of signals generated using a light hammer source and its spectrum is presented in Figure 6.17. As illustrated in Figure 6.17, these active sources generate high-frequency Rayleigh waves in the range of 10–500 Hz.

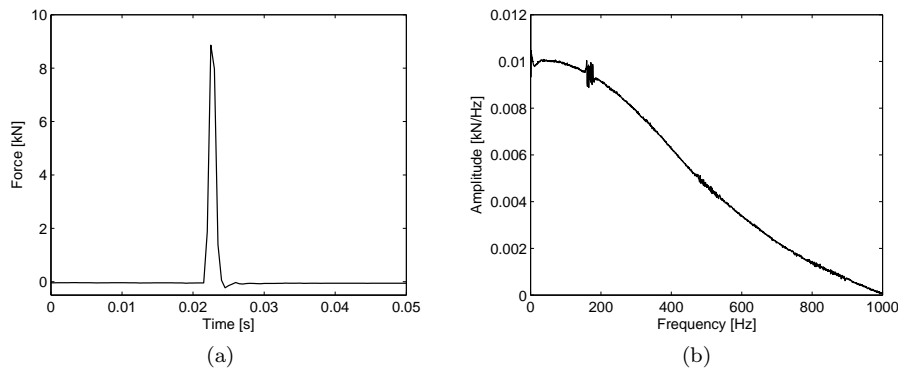


Figure 6.17: (a) Waveforms of signals and (b) respective spectrum generated using a light hammer source

The signals picked up by the receivers are recorded in a laptop by means of an acquisition program developed in LabVIEW. An acquisition system National Instruments SCXI 1600 with accelerometers card 1531, with a maximum sampling rate of 200 kS per second and a resolution of 16 bits was used to collect the signals from both the source and the receiving accelerometers. Data acquisition was performed at a frequency of 2 kHz per channel ($\Delta t = 0.0005$ s).

Results from test inside grid *B6*

Considering each pair of signals, one pair involving receivers 1 and 2 with one meter spacing, and another involving receivers 2 and 4 with two meters spacing, an estimate of the dispersion curve over a certain frequency range is obtained considering filtering criterion, as described in Chapter 2. Assembling the information from the different pairs of receivers the composite dispersion curve is obtained (fig. 6.18). Since the experimental dispersion curve corresponding to the reverberant test spans a short range of frequency, data was discarded. Then a polynomial regression was attempted, however regression showed a low coefficient of determination. Therefore, original data was adopted.

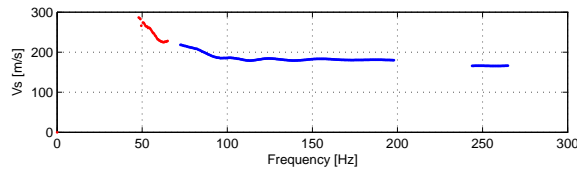


Figure 6.18: Experimental dispersion curve from SASW carried out on layer $0.40 w_{OPM}$ inside grid *B6*

The shear wave profile was computed using an iterative process described previously. The inversion is performed in different stages where a soil profile with an increasing number of layers is used. Table 6.5 gives these values for all stages, as well as the square root of the final value of the objective function.

Table 6.5: Initial and final soil profile for all stages in the inversion procedure regarding SASW carried out on grid *B6*

Stage	Layer	Initial profile			Final profile			$f_{obj}^{1/2}$
		d [m]	V_s [m.s ⁻¹]	γ [kN/m ³]	d [m]	V_s [m.s ⁻¹]	γ [kN/m ³]	
1	1	∞	100	18.64	∞	212	18.64	161
2	1	3.00	212	18.64	1.12	198	18.64	19
	2	∞	212	18.64	∞	427	18.64	
3	1	0.56	198	18.64	0.20	163	18.64	19
	2	0.56	198	18.64	1.18	223	18.64	
	3	∞	427	18.64	∞	478	18.64	
4	1	0.20	163	18.64	0.20	152	18.64	132
	2	0.59	223	18.64	0.30	258	18.64	
	3	0.59	223	18.64	0.80	212	18.64	
	4	∞	478	18.64	∞	454	18.64	

The lowest value of the square root of the objective function was achieved for the shear wave profile corresponding to an earth model with two layers over halfspace (stage 3). From Table 6.5 it can be seen that layers thicknesses mismatch the actual profile, since the trial layer with thickness of 0.40 m lies on a foundation with thickness of 0.60 m.

Then, a new shear wave profile was computed using all data available for the trial layer and foundation layer. To this end, state conditions obtained on

the closest grid (*B7*) were employed. The results found out are given in Table 6.6. Once again the lowest value of $f_{obj}^{1/2}$ was obtained for an earth model with two layers over halfspace, yet is higher than the one obtained in Table 6.5. This notwithstanding, good agreement between theoretical and experimental composite dispersion curves (fig. 6.19) is verified. From the shear wave profile Young modulus can be computed accordingly the following equation 6.4, which results in $E_{SASW} = 185$ MPa.

$$E = \frac{2 \cdot C_s^2 \cdot (1 + \nu)}{\gamma} \quad (6.4)$$

Table 6.6: Initial and final soil profile in the inversion procedure regarding SASW carried out on grid *B6* and considering sate conditions in grid *B7*

Stage	Layer	Initial profile			Final profile			$f_{obj}^{1/2}$
		d [m]	V_s [m.s ⁻¹]	γ [kN/m ³]	d [m]	V_s [m.s ⁻¹]	γ [kN/m ³]	
1	1	0.40	198	21.75	0.40	195	21.75	32
	2	0.60	198	20.60	0.60	200	20.60	
	3	∞	427	18.64	∞	402	18.64	
2	1	0.40	195	21.75	0.40	186	21.75	52
	2	0.60	200	20.60	0.60	230	20.60	
	3	0.60	200	18.64	0.30	209	18.64	
	4	∞	402	18.64	∞	511	18.64	

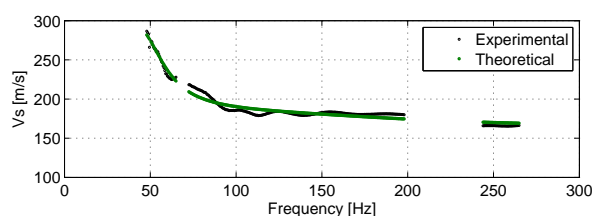


Figure 6.19: Theoretical and experimental composite dispersion curve from SASW carried out on layer 0.40 w_{OPM} inside grid *B6*

Results from test inside grid *B9*

Likewise the previous test, the experimental dispersion curve was computed using the same pairs of signals and filtering criterion and is shown in Figure 6.20. Since the number of points in the composite dispersion curve is not manageable for the successive inversion process, a polynomial regression was adopted.

The same interpretation method was applied. The inversion is performed in different stages where a soil profile with an increasing number of layers is used. Table 6.7 gives these values for all stages, as well as $f_{obj}^{1/2}$.

The lowest value of $f_{obj}^{1/2}$ was achieved for the shear wave profile corresponding to an earth model with three layers over halfspace (stage 4). From Table 6.7 it can be seen that to the first and second layers corresponds thicknesses, d ,

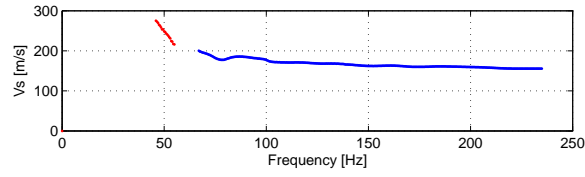


Figure 6.20: Experimental dispersion curve from SASW carried out on layer $0.40 w_{OPM}$ inside grid *B9*

Table 6.7: Initial and final soil profile for all stages in the inversion procedure regarding SASW carried out on grid *B9*

Stage	Layer	Initial profile			Final profile			$f_{obj}^{1/2}$
		d [m]	V_s [m.s ⁻¹]	γ [kN/m ³]	d [m]	V_s [m.s ⁻¹]	γ [kN/m ³]	
1	1	∞	100	18.64	∞	192	18.64	162
2	1	3.00	192	18.64	1.05	181	18.64	95
	2	∞	192	18.64	∞	400	18.64	
3	1	0.52	181	18.64	0.39	169	18.64	28
	2	0.52	181	18.64	1.06	211	18.64	
	3	∞	400	18.64	∞	513	18.64	
4	1	0.39	169	18.64	0.56	173	18.64	22
	2	0.53	211	18.64	0.46	255	18.64	
	3	0.53	211	18.64	0.28	155	18.64	
	4	∞	513	18.64	∞	536	18.64	

of 0.56 m and 0.46 m, thus mismatching the actual field profile. However, it is interesting noting that profile obtained on stage 3 is close to the actual profile, since the trial layer with thickness of 0.40 m lies on a foundation with thickness of 0.60 m.

Then, a new shear wave profile was computed using all data available for the trial layer and foundation layer. To this end, state conditions obtained on the closest grid (*B10*) were employed. The results found out are given in Table 6.20. The value of $f_{obj}^{1/2}$ on stage 2 demonstrates good agreement between theoretical and experimental dispersion curves (fig. 6.21). From the shear wave profile Young modulus was computed resulting in $E_{SASW} = 130$ MPa for the trial layer. This value is significant lower than the one obtained on grid *B6* which reflects the lower density achieved on grid *B9*.

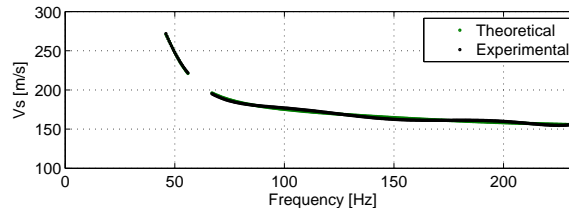


Figure 6.21: Theoretical and experimental composite dispersion curve from SASW carried out on layer $0.40 w_{OPM}$ inside grid *B9*

Table 6.8: Initial and final soil profile in the inversion procedure regarding SASW carried out on grid B9 and considering sate conditions in grid B10

Stage	Layer	Initial profile			Final profile			$f_{obj}^{1/2}$
		d [m]	V_s [m.s ⁻¹]	γ [kN/m ³]	d [m]	V_s [m.s ⁻¹]	γ [kN/m ³]	
1	1	0.40	169	20.54	0.40	178	20.54	96
	2	0.60	211	20.60	0.60	184	20.60	
	3	∞	513	18.64	∞	372	18.64	
2	1	0.40	178	20.54	0.40	169	20.54	25
	2	0.60	184	20.60	0.60	219	20.60	
	3	0.60	184	18.64	0.26	175	18.64	
	4	∞	372	18.64	∞	505	18.64	

6.5 Correlation between E modulus for several tests

As previously described, several tests for determination of E modulus were performed. In this section, correlation between E modulus obtained from *SPLT* test and performance related tests (*LFWD*, *SSG* and *Portancemètre*) will be established. To this end, E_{V2} modulus from *SPLT* using three point measuring system will be set as the reference value, accordingly to conclusions reached on previous sections.

Before the establishment of correlations, it is important to remind that *Portancemètre* is a continuous test, while the others being spot tests, as aforementioned. The output of *Portancemètre* is about one value per meter, which means approximately five values per grid with dimensions $5 \times 2 \text{ m}^2$. Therefore, output was managed in order to enable comparison between values obtained from spot tests. As so, an average value of E_{Port} modulus per grid value was determined. In Figure 6.22 the number of original output given by the equipment, average per grid and computed spacial distribution are illustrated concerning layer 0.30 m $w_{OPM-2\%}$ last energy level.

The methodology employed to the establishment of relationships between *SPLT* and performance related tests was based is the following steps:

- (i) comparison between tests results performed in the same spot for all energy levels;
- (ii) comparison between tests results performed in the same grid for all energy levels;
- (iii) comparison between average values per energy level grouped into homogeneous areas given by *Portancemètre*;
- (iv) comparison between average values per energy level;
- (v) perform previous iterations, yet only considering the last energy level (12 passes).

Ever tests results are unavailable or established relationships at each step show high scatter will not be presented.

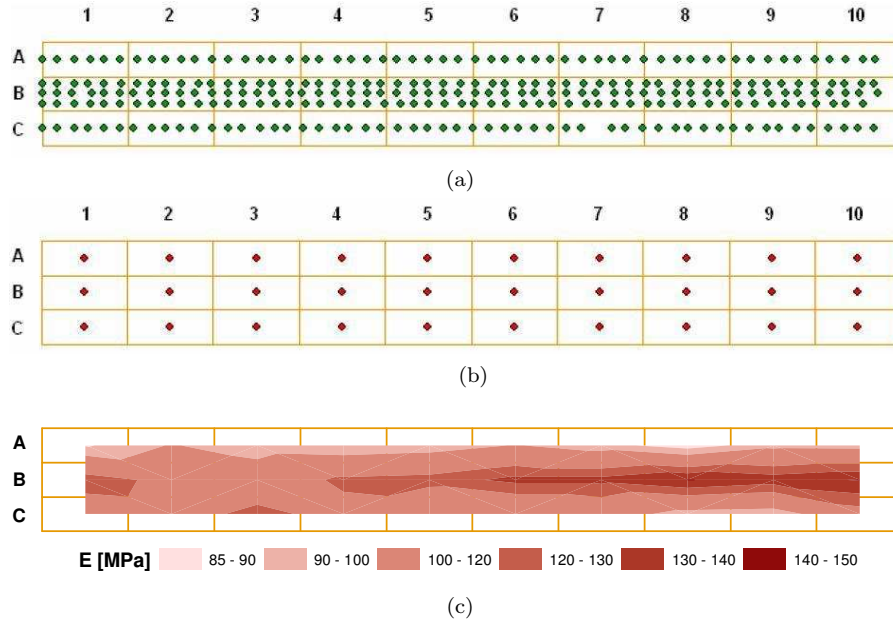


Figure 6.22: Plant representation of the output of Portancemètre: (a) values given by the equipment; (b) average values; (c) computed spacial distribution concerning layer 0.30 m $w_{OPM-2\%}$ last energy level (12 passes)

Owing to the third step, homogeneous areas were defined by averaging Portancemètre modulus in each $5 \times 2 \text{ m}^2$ grid into groups with intervals within the range of 10 MPa. For instance, every grid with an average E_{Port} modulus between 80 and 90 MPa belongs to the same homogeneous area. Spot tests belonging to a given homogeneous area were also grouped together and average was computed. The correlations between Portancemètre results and the other tests were established by comparing the respective average modulus for each homogeneous area. It is worth noting the fact that output values of Portancemètre results from calibration made at the time of the construction of the new Évora railway line. The materials used in the trial embankment were similar to the ones used in the new railway line. Regarding the last step, it is intended to establish relationships between tests carried out for an energy level with low scatter regarding state conditions.

6.5.1 SC trial layers

In first place, relationship between moduli obtained from Portancemètre and *SPLT* is evaluated. Figure 6.23 show reasonable correlation ($R^2 = 0.65$) close to unity between E_{Port} and $E_{V2AFNOR}$ moduli corresponding to average values per energy level (number of passes of the vibrating roller).

A similar trend is given by relationships between tests results for the last energy level, as presented in Figure 6.24, yet modulus obtained from Portancemètre being slightly higher. Poor correlation ($R^2 = 0.42$) is observed from relationship established between tests performed in the the same grid for the last energy level (fig. 6.24a), whereas a reasonable correlation is found from

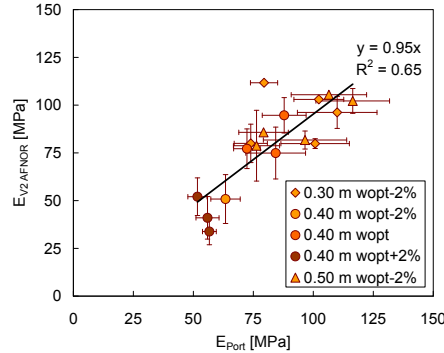


Figure 6.23: Comparison between E_{Port} and $E_{V2AFNOR}$ average values per energy level

comparison between average values grouped into homogeneous areas given by Portancemètre (fig. 6.24b). In contrast, comparison between average values noticeably improves correlation where a $R^2 = 0.97$ is obtained (fig. 6.24c). It is noteworthy that correlations present reduced scatter at the last energy level, which denotes greater homogeneity of mechanical properties. Note that the calibration of Portancemètre is corroborated by this results, despite the fact that Portancemètre modulus being overestimated for values higher than 110 MPa.

In second place, *LFWD* results are compared with reference test *SPLT*. In Figure 6.25a is plotted the $E_{V2AFNOR}$ against E_{LFWD} modulus for tests performed in the same spot and for several energy levels. Despite high scatter ($R^2 = 0.29$), a correlation between moduli close to unity is verified. The evaluation of the relationship between average moduli per energy level show an identical trend, but higher scatter is associated ($R^2 = 0.26$), as illustrated in Figure 6.25b.

Further, in Figure 6.26 is shown the correlations established for the last energy level. Identical trends are verified for both values grouped into homogeneous areas and average values, yet an enhanced correlations are observed, which means reduced scatter at this energy level. Likewise to previous results, it is noteworthy that coefficient of determination is higher regarding average values per energy level ($R^2 = 0.64$). It should be noted that correlation close to unity was obtained.

In third place, relationship between moduli obtained from *SSG* and *SPLT* is shown in Figure 6.27. Although higher scatter is observed for average values per energy level (fig. 6.27a), E_{SSG} modulus is found to be approximately 34% higher than $E_{V2AFNOR}$. An identical trend is obtained from relationship between average values for the last energy level (fig. 6.27b), yet with slightly reduced scatter ($R^2 = 0.41$).

Finally, moduli obtained from *FWD* and *SASW* are analyzed. Concerning the former, since tests were carried out only for layer 0.40m w_{OPM} for the last energy level, average E_{FWD} modulus is compared with corresponding value obtained from reference test. As so, average modulus corresponding to the first drop ($E_{FWD} = 191.9$) is about 2.5 times $E_{V2AFNOR}$. With regards to *SASW*, two tests were performed on trial layer 0.40 w_{OPM} , on grids *B6* and *B9*,

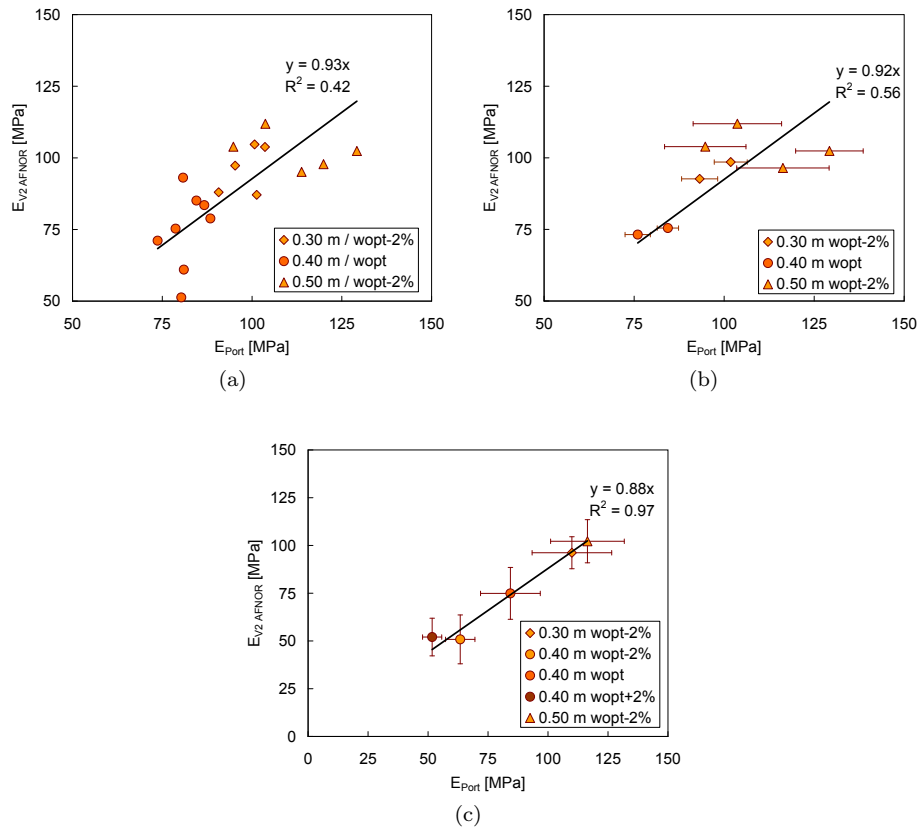


Figure 6.24: Comparison between E_{Port} and E_{V2_AFNOR} for the last energy level (12 passes): (a) tests performed on the same grid; (b) average values grouped into homogeneous areas; (c) average values per layer

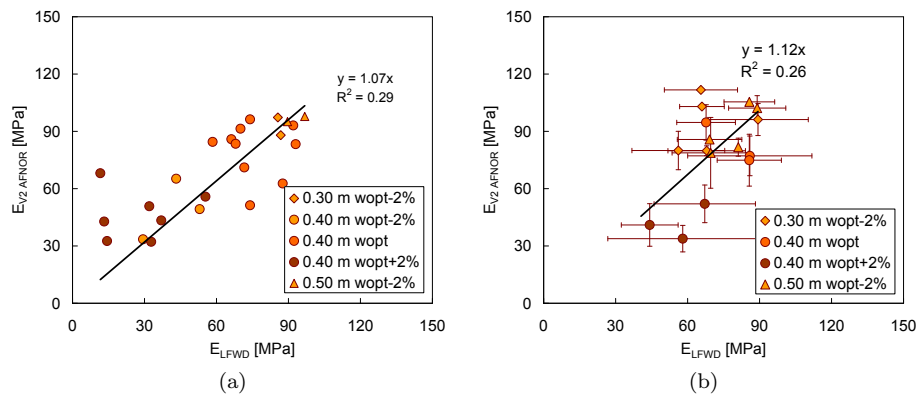


Figure 6.25: Comparison between E_{LFWD} and E_{V2_AFNOR} : (a) tests performed in the same spot; (b) average values per energy level

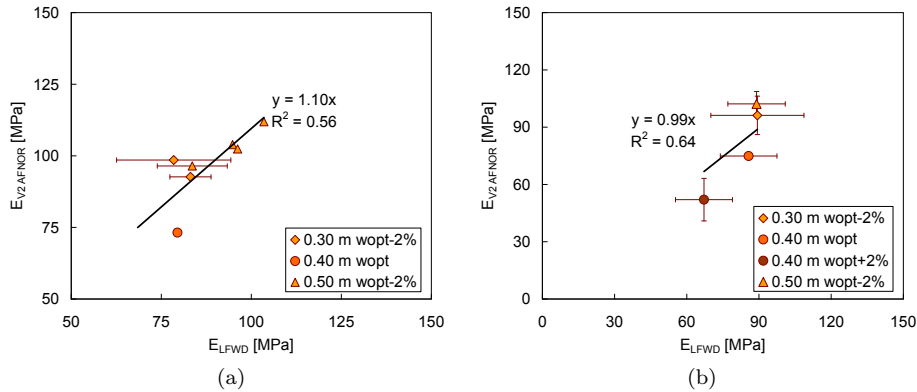


Figure 6.26: Comparison between E_{LFWDD} and $E_{V2AFNOR}$ for the last energy level (12 passes): (a) average values grouped into homogeneous areas; (b) average values

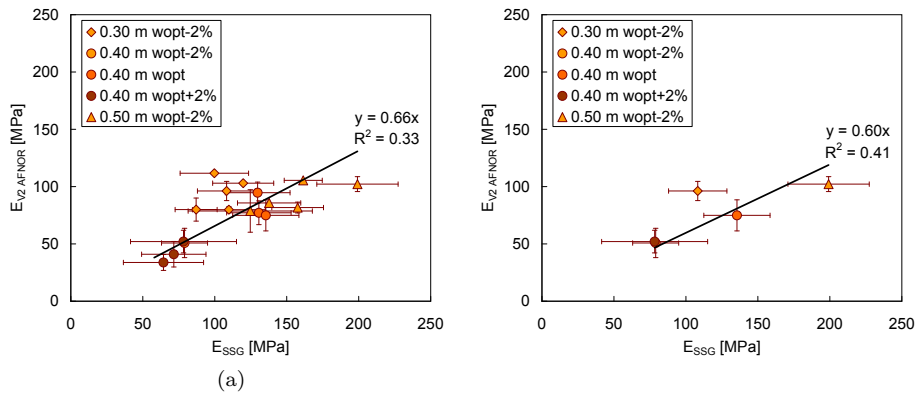


Figure 6.27: Comparison between E_{SSG} and $E_{V2AFNOR}$: (a) average values; (b) average values for the last energy level (12 passes)

which interpretation was conducted on section 6.4.2 and a $E_{SASW} = 185$ MPa and $E_{SASW} = 130$ MPa were obtained, respectively. Since only two tests were conducted and any *SPLT* was conducted on the same grids, E_{SASW} moduli are compared with modulus obtained from Portancemètre for the same grids, 113 and 100 MPa, respectively. E_{SASW} moduli are about 1.6 and 1.3 times greater than average moduli obtained from Portancemètre.

6.5.2 CA31.5 trial layers

Comparison between *SPLT* and performance related test moduli are conducted only for the last energy level, once *SPLT* were carried out only at this stage. Comparison between tests performed in the same spot or in the same grid indicate no correlation between *SPLT* following AFNOR standard and performance related tests. Since only two layers were constructed and regarding previous conclusions, relationship between average values given by *SPLT* following

AFNOR and Portancemètre will be computed individually for each layer. Nevertheless analysis of Portancemètre absolute modulus after calibration should be take with caution due to lack of results.

6.6 Analysis of full scale trial results and recommendations

6.6.1 SC trial layers

The evolution of mechanical properties with increasing energy level and with state conditions will be evaluated herein. To this end, correlations found previously will be employed ever $R^2 > 0.70$, which means only Portancemètre results will be used.

In Figures 6.28 and 6.29 are plotted moduli, obtained from *SPLT* and Portancemètre (after calibration), and state parameters, obtained from *SCM* and *NM* (after calibration), against the number of passes for *SC* layers constructed with moisture content close to 2% dry of optimum. Maximum relative compaction is reached for 12 passes for both layers, yet 0.30 m trial layer presents fairly higher average relative compaction than 0.50 m trial layer.

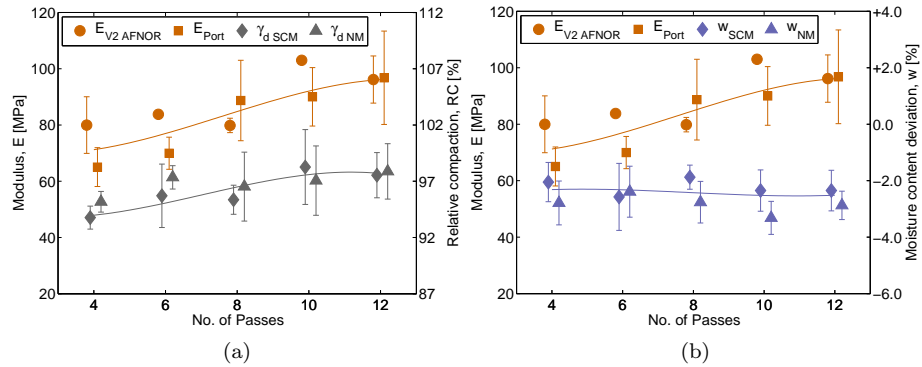


Figure 6.28: 0.30 m $w_{OPM} = 2\%$ layer moduli E_{Port} , relative compaction and moisture content deviation evolution with number of passes: (a) Moduli and relative compaction; (b) Moduli and moisture content deviation

With regards to trial layer with 0.30 m thickness, maximum relative compaction is reached for the last energy level. Focusing on the analysis of moduli and relative compaction, an increase of both parameters with increasing number of passes is verified. On the other hand, in Figure 6.28b one can see that moisture content remains fairly constant. These trends appears to denote the influence of dry density on mechanical performance concerning to the same moisture content. However, analysis of results obtained on trial layer with 0.50 m thickness with similar moisture content is not so straight. In Figure 6.29a one can see that moduli fairly increases with increasing energy level, yet relative compaction slightly varies. As so, in contrast to aforementioned conclusion, unnoticeable influence of dry density on moduli is found. Taking into account dry

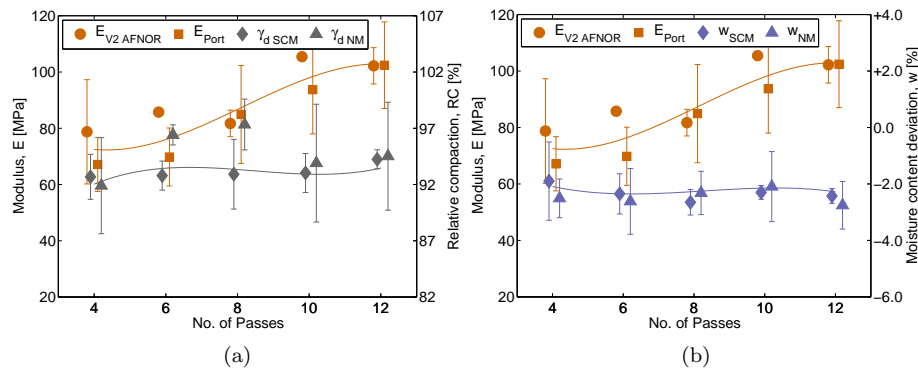


Figure 6.29: 0.50 m $w_{OPM-2\%}$ layer moduli E_{Port} , relative compaction and moisture content deviation evolution with number of passes: (a) Moduli and relative compaction; (b) Moduli and moisture content deviation

density high scatter on trial layer with 0.50 m thickness, results must be treated with caution.

As mentioned previously, moisture content achieved on *SC* layers with 0.40 m thickness were close to 0.5% dry of optimum and 1.5% wet of optimum. In Figures 6.30, 6.31 and 6.32 is presented the evolution of moduli, relative compaction and moisture content deviation with number of passes. Maximum relative compaction is achieved at 8 passes for trial layers 0.40 m, $w_{OPM-2\%}$ and 0.40 m, w_{OPM} , whereas only at 10 passes maximum relative compaction is achieved for trial layer 0.40 m, $w_{OPM+2\%}$. Concerning to 0.40 m trial layer with lower moisture content (fig. 6.30), one can see that state parameters do not vary significantly with increasing energy level, but moduli seems to increase. As so, relationship between moduli and state parameters can not be established. On the contrary, moduli and relative compaction appears to be related on trial layers with moisture content 1.5% wet of optimum, since both parameters increase with increasing energy level, as moisture content remains almost constant. This trend is similar to the one verified for trial layer 0.30 m $w_{OPM-2\%}$.

Further, regarding quality control state parameters and moduli scatter earn to be commented for last energy level (12 passes). Concerning to *SC* layers constructed with 2% dry of optimum, *NM* statistical data for 0.50 m trial layer shows the highest state parameters *CV*, about 14% and 5% regarding moisture content and dry density, respectively. Corresponding values for 0.30 m trial layer are approximately 9% and 3%, being almost half than values regarding 0.50 m trial layer (see Tables C.1 and C.3 in Appendix A). With regards to trial layer 0.40 m w_{OPM} , a *NM* moisture content *CV* about 13% is associated, while dry density presents *CV* close to almost 4%. It is interesting noting that moisture content *CV* is almost the double than dry density *CV* for trial layers compacted dry of optimum. As so, to some extent it appears that state parameters scatter are related. This relation is not observed concerning remaining layers with 0.40 m thickness and compacted wet of optimum. Dry density *CV* of approximately 3% and 2% and moisture content *CV* of about 9% and 10%, respectively, were obtained from *NM* tests carried out on trial layers compacted wet of optimum. To this end, state parameters *CV* lie below the maximum

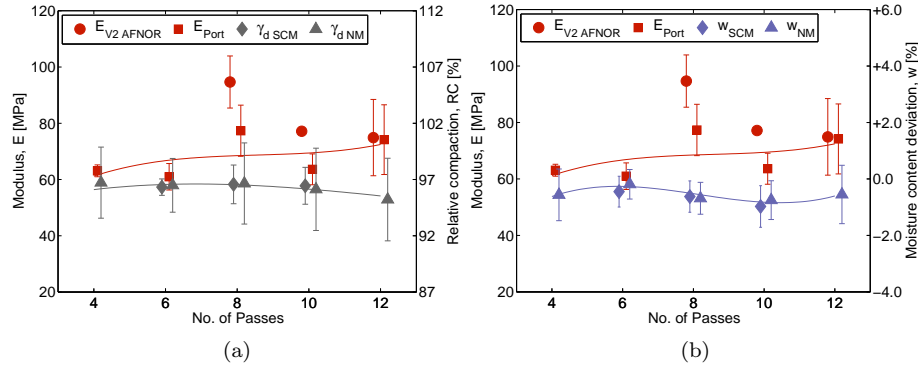


Figure 6.30: 0.40 m w_{OPM} layer moduli E_{Port} , relative compaction and moisture content deviation evolution with number of passes: (a) Moduli and relative compaction; (b) Moduli and moisture content deviation

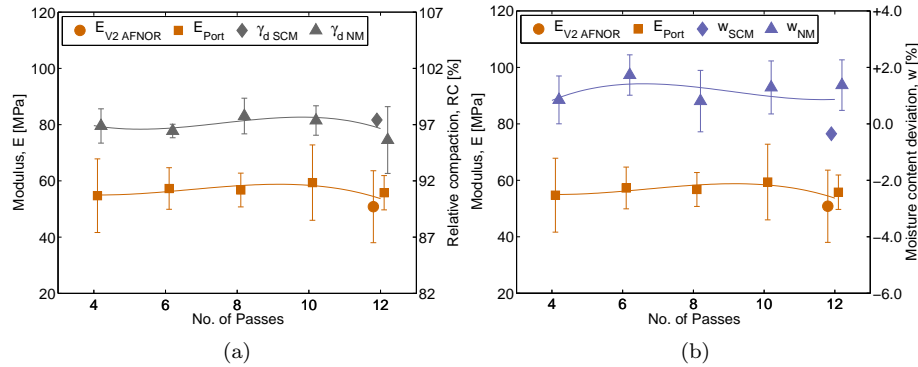


Figure 6.31: 0.40 m $w_{OPM-2\%}$ layer moduli E_{Port} , relative compaction and moisture content deviation evolution with number of passes: (a) Moduli and relative compaction; (b) Moduli and moisture content deviation

values given by Brandl (1977), 5% for dry density determined by means of *NM*, with exception to trial layer 0.50 m $w_{OPM-2\%}$.

The analysis of mechanical properties scatter was based on Portancemètre results (see Table C.13). Trial layers compacted dry of optimum (0.30 m $w_{OPM-2\%}$, 0.50 m $w_{OPM-2\%}$ and 0.40 m w_{OPM}) presented identical modulus *CV* ranging from 13 to 15%, while trial layers with higher moisture content presented lower modulus *CV*, 8 and 10%. As so, moduli *CV* mainly lie below the required maximum given by Brandl (1977), which is 25%. It appears that state parameters and modulus scatter are related, however it should be noted that 0.30 m $w_{OPM-2\%}$ presented higher modulus scatter, though state parameters scatter was the lowest.

Further, the influence of state parameters on mechanical performance is investigated. In Figure 6.33 is plotted moduli and relative compaction against moisture content deviation for the last energy level (12 passes). The results for all passes are presented in Figure C.1 in Appendix C.

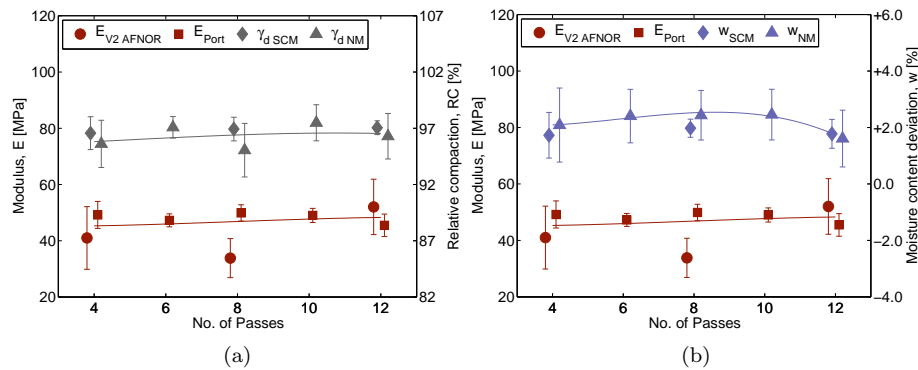


Figure 6.32: 0.40 m $w_{OPM+2\%}$ layer moduli E_{Port} , relative compaction and moisture content deviation evolution with number of passes: (a) Moduli and relative compaction; (b) Moduli and moisture content deviation

As general conclusion for several energy levels, one can verify that moisture content strongly influences mechanical performance of compacted layers, i.e., modulus increases with decreasing moisture content. As shown in Chapter 5 from laboratory campaign, this influence is attributed to suction effect. On the contrary, dry density influence on modulus appears to be unnoticeable. The evolution of modulus and dry density of trial layers with moisture content 3% dry of optimum and 1.5% wet of optimum seems to, at first sight, highlight this conclusion. However, these results should be interpreted taking into account hydro-mechanical behaviour of unsaturated geomaterials. Concerning to trial layers with moisture content 3% dry of optimum, although dry density from 0.30 m trial layer is higher than corresponding value from 0.50 m trial layer, modulus is slightly lower. This phenomena may be due to suction effect. It is known that suction increases with decreasing void ratio and decreasing saturation degree (see fig. 3.18 from Chapter 3). Since moisture content is similar, the increase of suction due to a lower saturation degree (lower dry density) can overlap to the increase of suction due to a lower void ratio (higher dry density). This phenomena should be testified with further laboratory investigation. In what concerns to trial layers with moisture content 1.5% wet of optimum, suction effect is lower and does not seem to explain modulus differences. Instead, it may be due to a higher moisture content CV .

Taking into account the aforementioned issues, it seems that influence of state conditions on mechanical properties of compacted requires analysis considering moisture content and respective suction effect, particularly in what concerns to layers compacted on dry side of compaction curve. With regards to 0.30 m $w_{OPM-2\%}$ and 0.50 m $w_{OPM-2\%}$ layers, similar mechanical properties and moisture content were obtained, but fairly differences on dry density were found. This fact indicates that influence of suction on mechanical properties prevails rather than influence of dry density.

The influence of CV of state parameters on CV modulus is not clear, as seen previously. However, as moisture content of compacted layers approaches optimum value and wet side of compaction curve, modulus CV appears to decrease too. As so, requirements regarding modulus and state parameters

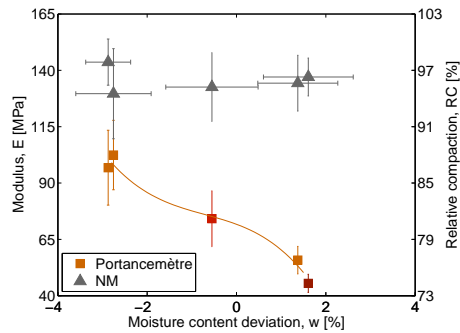


Figure 6.33: E_{Port} modulus and relative compaction (RC) versus moisture content deviation (w) obtained on *SC* trial layers for energy level corresponding to 12 passes

CV of compacted layers should take into account moisture content.

The analysis of results from full scale trial enabled to come to several conclusions. Concerning to state conditions, namely moisture content, desirable moisture content was not achieved for all trial layers and high scatter was verified. As so, the previous stack of material, water adding and mix up by means of a front shovel did not reproduced the desirable homogeneity on moisture content. The adverse weather conditions during running tests may have partially contributed to increase scatter.

The evaluation of mechanical properties by means of *SPLT* following AFNOR NF P94–117–1 (2000) standard and using different measuring systems showed significant differences. A three point measuring system or a one point measuring system on the plate should be used rather than one point measuring point placed on a device that measures layer settlement through a hole on the center of the plate. Further, analysis of *SPLT* following AFNOR NF P94–117–1 (2000) and DIN 18134 (2001) standards showed differences on test procedure and interpretation, which should be taken into account when comparison between test results is proceeded. A direct comparison should be performed for the same stress and method for determination of plate settlement. As mentioned previously, these recommendations led to a specification project of *SPLT* (Gomes Correia *et al.*, 2007) which is presented in Appendix B.

Furthermore, comparison between *SPLT* results and performance related tests allowed to establish correlations and testify equipment calibrations using *SPLT* as reference test. Concerning to *SC* material, a good correlation between *SPLT* following AFNOR standard ($E_{V2\text{AFNOR}}$) and Portancemètre (E_{Port}) moduli was obtained. This results indicate the huge potential of this equipment on continuous stiffness evaluation on earthwork platforms. In contrast, a poor correlation was achieved regarding comparison between *SPLT* following DIN standard ($E_{V2\text{DIN}}$) and Portancemètre (E_{Port}) moduli. This result highlight one advantage of using a plate with larger diameter. A correlation close to unity between *SPLT* based on the AFNOR standard (E_{V2}) and the *LFWD* (E_{LFWD}) moduli was observed, despite data high scatter. The results from this equipment should be treated with caution.

In conclusion, the experiences performed with different equipments to evaluate moduli showed great benefit using Portancemètre, although calibration for

material being tested is required. The quick execution and the immediate layout of the results, which allows quick intervention whenever the deformability conditions are not achieved, are great advantages of this equipment. However, the greatest advantage is to allow continuous evaluation of layers stiffness. Nevertheless, an adequate calibration using *SPLT* is required. With this purpose, it is recommended to conduct calibration during execution of trial embankments.

6.6.2 CA31.5 trial layers

Likewise, in Figures 6.34 and 6.35 are plotted moduli, obtained from *SPLT* and Portancemètre (after calibration), and relative compaction and moisture content deviation, obtained from *SCM* and *NM* (after calibration), against the number of passes for *CA31.5* trial layers. One can see a almost linear increase of relative compaction with energy level, yet moduli do not follow the same trend. On the other hand, moisture content present great variation between energy levels, ranging from 2% dry of optimum to 1% wet of optimum, which may be partially attributed to adverse weather conditions. This notwithstanding, moduli appears to follow moisture content variation for both layers regarding energy levels corresponding to 4 to 10 passes. This trend indicates the great influence of moisture content on mechanical performance rather than dry density. Concerning the last energy level, a significant moduli decrease is verified, though a decrease of moisture content is not observed in the same proportion. It is noteworthy that modulus reaches the highest value close to optimum water content. This behaviour agrees with the one found from laboratory tests (recall Chapter 5), where higher modulus was obtained from specimen with optimum moisture content than modulus obtained from specimen compacted 2% dry of optimum.

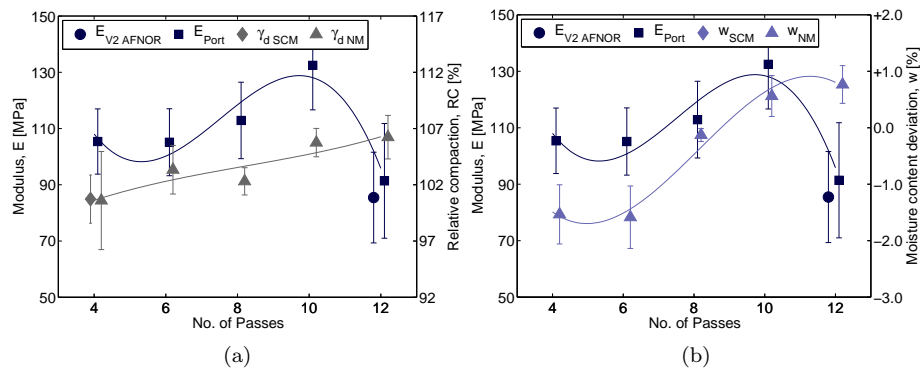


Figure 6.34: 0.22 m w_{OPM} layer moduli E_{Port} , relative compaction and moisture content deviation evolution with number of passes: (a) Moduli and relative compaction; (b) Moduli and moisture content deviation

The influence of moisture constant is illustrated in Figure 6.36 regarding the last energy level (12 passes). The results for all passes are presented in Figure C.2 in Appendix C. Trial layer 0.22 m with higher moisture content (about 1% wet of optimum) presents lower modulus, though both trial layers present similar relative compaction. However, it should be taken into account that a

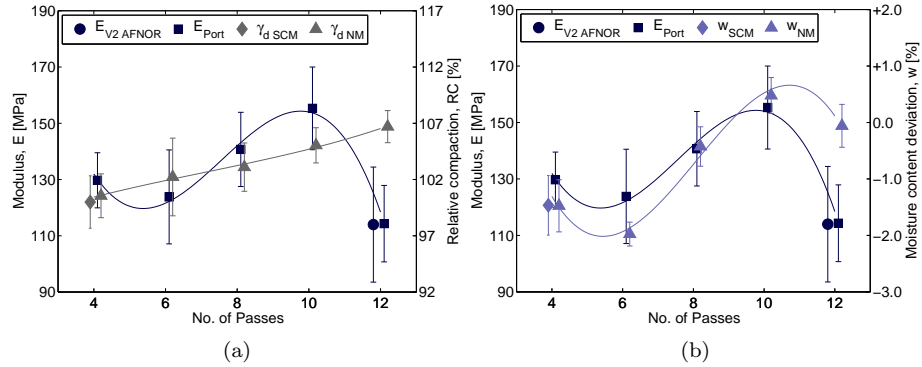


Figure 6.35: 0.30 m w_{OPM} layer moduli E_{Port} , relative compaction and moisture content deviation evolution with number of passes: (a) Moduli and relative compaction; (b) Moduli and moisture content deviation

higher modulus may be associated to higher thickness. A higher number of points would be require to come to reliable conclusions.

Concerning to state parameters CV for the last energy level, dry density CV was about 2% for both layers, which fullfil Brandl (1977) requirements for base layers. Regarding moisture content, CV ranged between 5 and 7%. Concerning modulus CV from Portancemètre, values of 30 and 20% were obtained for the last energy level regarding 0.22 and 0.30 m layers, respectively, which exceed Brandl (1977) requirements for base layers.

Results from *CA31.5* trial layers did not allowed to establish correlations between *SPLT* as reference test and performance related tests. Therefore, equipments calibration for each kind of material is required. In what concerns to the influence of state parameters on mechanical performance, it seems that moisture content has great influence, yet further conclusions requires investigation of trial layers with constant moisture constant, covering a range from 2% dry of optimum to optimum.

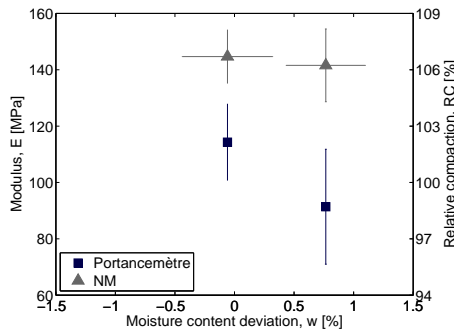


Figure 6.36: E_{Port} modulus and relative compaction (RC) versus moisture content (w) obtained on *CA31.5* trial layers for energy level corresponding to 12 passes

6.7 Comparison between full scale trial and laboratory results

Comparison between moduli obtained from full scale trial and laboratory tests are performed herein. To this end, stress and strain levels on both field and laboratory tests are taken into account, as well as, state conditions.

Firstly, comparison between modulus obtained from *SASW* carried out on 0.40 m w_{OPM} and modulus computed from S-wave measurements on specimen with similar moisture conditions is performed. Methodology for the determination of moduli is based on S-wave propagation through geomaterial, thus involving similar stress and strain levels. Laboratory results obtained on specimen with optimum moisture content (8.8%) were considered since state conditions are the closest to the ones verified on trial layer 0.40 m w_{OPM} . The *SASW* was carried out on grids *B6* and *B9* where $V_s = 195 \text{ m.s}^{-1}$ and $V_s = 169 \text{ m.s}^{-1}$ were obtained, respectively. However, moisture conditions obtained from *NM* carried out on closest grids, *B7* and *B10*, were 7.6% and 8.8%, respectively. Thereby, only the latter is used herein for the sake of comparison. The state conditions and shear modulus determined from field and laboratory tests are summarized in Table 6.9. It is noteworthy that laboratory shear modulus was computed using Equation 5.9 and parameters given in Table 5.9. A total mean stress of 2 kPa corresponding to mean stress at the middle of the layer was considered. In addition, to take into account the great influence of unsaturated condition at this stress level, matric suction computed from expression given in Figure 5.2 was added and a mean stress of 21.8 kPa was obtained. It should be noted that matric suction value is just an approximation since laboratory matric suction versus saturation degree curve was determined considering a void ratio of 0.331, whereas field void ratio is 0.370. This notwithstanding, it is thought to be a good approximation taking into account a high saturation degree (about 70%). Further, shear modulus was corrected for the same void ratio.

Table 6.9: Field and laboratory state conditions and modulus regarding *SC* geomaterial

	Field <i>B10</i>	Laboratory BE Acc	
γ [kN/m ³]	20.64	21.21	
γ_d [kN/m ³]	18.98	19.49	
w [%]	8.8	8.8	
e	0.370	0.331	
	<i>B9</i>		
V_s	169		
G_0	60	73	65
f(e field), f(e lab)	2.37	2.54	
$G_{0 \text{ field}}^{\text{nor}}$ [MPa]	60	68	60

Shear modulus computed from S-wave measurements with bender elements and accelerometers are given in Table 6.9. A perfect match is observed between field shear modulus and shear modulus computed from S-wave measurements with accelerometers. On the other hand, shear modulus computed from S-wave measurements with bender elements is about 13% higher. Nevertheless, a good

relationship between field and laboratory results is found.

Secondly, comparison between modulus obtained from *SPLT* and triaxial tests is conducted. As aforementioned, stress and state conditions should be taken into account, thereby field parameters were gathered from *NM* and *SPLT* results and are summarized in Table 6.10. As described on Chapter 2, E_{V2} modulus following AFNOR standard is computed for a stress level about 200 kPa. Consequently, laboratory secant modulus is estimated for the same stress level and considering the strain level involved in *SPLT* performed at each layer. Triaxial tests did not enable secant modulus for strain levels lower than 0.5%, however modulus degradation curves lie between a reference threshold given by Santos (1999), as illustrated in Figure 5.10 in previous chapter. Hence, secant modulus was computed from Equation 5.8, which parameters are given in Table 5.5, for $\sigma_1 = 200$ kPa and then estimated from the relationship obtained from G/G_0 degradation curves (Ishibashi and Zhang, 1993; Santos, 1999) for the strain levels involved in *SPLT* (ε_{SPLT} in Table 6.10) and 1% (see fig. 5.9). Finally, secant modulus was normalised for field void ratio.

Table 6.10: State conditions, average E_{V2} modulus and corresponding strain level for *SC* layers for the last energy level (12 passes)

	Trial layers				
	0.30 m	0.50 m	0.40 m	0.40 m	0.40 m
	$w_{OPM-2\%}$	$w_{OPM-2\%}$	w_{OPM}	$w_{OPM-2\%}$	$w_{OPM+2\%}$
γ_d	19.54	18.75	19.07	19.48	19.30
w [%]	6.1	6.3	8.0	9.5	9.7
void ratio, e	0.330	0.386	0.363	0.335	0.347
E_{V2}	96.2	102.2	74.9	50.8	52.0
$\varepsilon(\text{field})$	1.0%	0.9%	1.2%	1.8%	1.8%
	Specimens				
	$w_{OPM-2\%}$	$w_{OPM-2\%}$	w_{OPM}	w_{OPM}	w_{OPM}
w [%]	6.9		9.1		
E_{lab}^{nor} ($\sigma_1 = 200$ kPa) [MPa]	100.3	104.8	85.0	62.8	62.8
f(e lab)	2.541	2.541	2.541	2.541	2.541
f(e field)	2.544	2.294	2.395	2.524	2.467
E_{field}^{nor} ($\sigma_1 =$ 200 kPa) [MPa]	100.4	94.6	80.1	62.4	61.0
E_{V2}/E_{field}^{nor}	0.958	1.080	0.935	0.814	0.853

Concerning to layers compacted with moisture content 2% dry of optimum (0.30 m $w_{OPM-2\%}$ and 0.50 m $w_{OPM-2\%}$), average E_{V2} modulus differs less than 8% from modulus determined from triaxial tests on specimen with identical moisture content. However, comparison between average E_{V2} modulus from layers 0.40 m $w_{OPM-2\%}$ and 0.40 m $w_{OPM+2\%}$ and secant modulus determined from specimen with similar moisture content (w_{OPM}) show a difference lower than 18%. Regarding 0.40 m w_{OPM} layer, moisture content is about 1% dry of optimum and specimen with similar moisture content is not available. As so comparison with specimen with optimum moisture content is carried out and a difference of about 7% is found.

These results denotes a reasonable relationship between field and laboratory modulus and assumes great importance taking into account two issues: i) design is based on mechanical properties usually determined from laboratory tests; ii) even though conventional triaxial tests only allow determination of mechanical properties beyond strain level of 1%, for *SC* geomaterial is possible to estimate secant modulus from degradation curves for lower strain levels since degradation curves lie between reference threshold for sands given by Santos (1999).

Finally, the same procedure was adopted in order to establish comparison between E_{SASW} and modulus obtained from conventional triaxial tests. With this purpose, laboratory modulus was computed using Equation 5.8. A total vertical stress of 4 kPa at the middle of the layer was considered and matric suction was added, likewise described previously. Laboratory modulus of 3.6 MPa was obtained, corresponding to a strain level of 1%. From modulus degradation curves obtained in previous chapter (fig. 5.10), modulus reduction at this strain level is about 85%. Thereby, modulus was corrected to take into account the strain level and the same void ratio. As so, laboratory modulus of 22 MPa was achieved, which compares with E_{SASW} equal to 132 MPa. The huge difference found may be due to the estimation of laboratory modulus for a low stress level, which was computed out of the stress interval regarding Equation 5.8.

The relations between laboratory and field modulus found are illustrated in Figure 6.37.

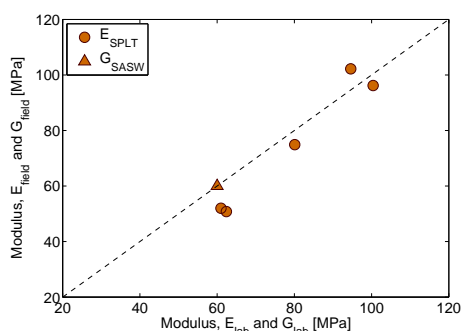


Figure 6.37: Relationship between modulus estimated from laboratory triaxial tests and modulus obtained from *SPLT* carried out on trial layers for the last energy level

6.8 Conclusions

In this chapter the main results obtained on full scale trial were presented. Two type of geomaterials, clayey sand (*SC*) and a crushed aggregate (*CA31.5*), were investigated. To this end, construction of trial layers with different thicknesses (0.22, 0.30, 0.40 and 0.50 m) and different moisture contents (2% dry of optimum, optimum and 2% wet of optimum Modified Proctor) were carried out, as well as evaluation of state conditions and mechanical properties for several energy levels.

State conditions were evaluated by means of sand cone method (*SCM*) and nuclear method (*NM*), the latter requiring calibration. Regarding *SC* trial lay-

ers, moisture content about 3% dry of optimum was achieved on trial layers 0.30 m $w_{OPM-2\%}$ and 0.50 m $w_{OPM-2\%}$, average moisture content 1.5% wet of optimum was achieved on trial layers 0.40 m $w_{OPM-2\%}$ and 0.40 m $w_{OPM+2\%}$, and average moisture content 0.5% dry of optimum was achieved on trial layers 0.40 m w_{OPM} . The adverse weather conditions during construction of trial layers with 0.40 m thickness might have contributed to moisture content mismatch, since favorable weather conditions were verified during construction of trial layers with 0.30 and 0.50 m thickness. Further, statistical data showed higher moisture content coefficient of variation (*CV*) from *SC* trial layers compacted dry of optimum, rather than *SC* trial layers compacted with moisture content wet of optimum. As so, the previous stack of material, water adding and mix up by means of a front shovel did not reproduce the desirable homogeneity on moisture content of trial layers compacted dry of optimum. This notwithstanding, dry density *CV* lie below maximum values given by Brandl (1977), with exception to layer with 0.50 m thickness. Average relative compaction of about 95–96% was obtained from trial layers with 0.40 m thickness, whereas 98 and 94% was obtained from trial layers with 0.30 and 0.50 m thickness, respectively. As so, layer thickness strongly influences relative compaction. To this end, layer with 0.50 m thickness does not fulfill quality control requirements of high quality projects, namely those regarding high speed embankments.

Concerning to *CA31.5* trial layers, moisture content 1% wet of optimum was achieved on layer with 0.22 m thickness, whereas moisture content close to optimum value was achieved on trial layer with 0.30 m thickness. As so, desirable moisture content was achieved only for the latter. Further, it is noteworthy that moisture content strongly varied within increasing energy level. In fact, moisture content obtained from both layers for the first energy level was about 1.5% dry of optimum. Once again, the previous stack of material, water adding and mix up by means of a front shovel did not reproduce the desirable homogeneity on moisture content. However, adverse weather conditions during construction of *CA31.5* trial layers might have contributed to a strong variation of moisture conditions. Nevertheless, for the last energy level both trial layers presented identical moisture content *CV* (5 and 7%), whereas dry density *CV* were less than 2%. Moreover, the same relative compaction was found, about 106%.

Mechanical evaluation was performed by means of static plate loading test (*SPLT*) and performance related tests, namely, impact tests (falling weight deflectometer – *FWD* and light falling weight deflectometer – *LFWD*), the soil stiffness gauge (*SSG*) and spectral analysis of surface waves (*SASW*), and continuous compaction control test method by means of Portancemètre.

With regards to *SPLT*, tests were conducted accordingly standards AFNOR NF P94–117–1 (2000) and DIN 18134 (2001). Further, *SPLT* following AFNOR was carried out using two settlement measuring systems: one measuring settlement on a point at the center of the plate through a hole; another measuring settlement three concentric points on the periphery of the plate. Results from the former measuring systems were found to be more than 30% higher than corresponding values obtained with the latter. Furthermore, analysis of AFNOR and DIN standards showed differences concerning to test procedure and test interpretation. As so, it was demonstrated that values obtained from tests following each standard can only be compared if interpreted for the same stress (200 kPa) and using the same method (secant method). In addition, equivalent modulus should take into account different plates diameter if a multi-layered system

is being tested. Conclusions regarding *SPLT* led to the specification project (Gomes Correia *et al.*, 2007) that is presented in Appendix B.

Further, correlations between performance related tests and *SPLT* moduli were established, where *SPLT* following AFNOR was used as reference test. Good correlation between *SPLT* and Portancemètre moduli was established for *SC* trial layers, the latter being about 10% higher than the former. These results indicate the huge potential of this equipment for the continuous stiffness evaluation on earthwork platforms, being a non destructive method easy to operate enabling quick evaluation of moduli and large number of tests, which allows statistical analysis. Moreover, the instantly layout of moduli enables immediate intervention ever quality control requirements are not achieved. In addition, afterwards treatment of results allows spacial characterization of full area of compacted layer. Thereby, mechanical evaluation by means of Portancemètre represents a great improvement on quality control/quality assurance (Qa/Qc) of compacted layers. Although a correlation close to unity was obtained between *SPLT* and *LFWD* on *SC* trial layers, high scatter led to poor correlation. Thereby, results from this equipment should be treated with caution. No correlation was found between *SPLT* and the others performance related tests. Results from *CA31.5* trial layers did not allowed to establish correlations between *SPLT* as reference test and performance related tests. Therefore, equipments calibration for each kind of material is required.

Then, evaluation of state conditions and mechanical properties with increasing energy level was conducted. In what concerns to *SC* trial layers no clear relationship between dry density and moduli was found. In contrast, moduli was found to decrease with increasing moisture content, as observed from laboratory results from previous chapter, thus reflecting suction effect on mechanical properties. Further, Portancemètre moduli *CV* decreased with increasing moisture content. These results denote the great influence of moisture content either on average moduli and on homogeneity of mechanical performance of layers embankment. With regards to *CA31.5* trial layers, moduli was found to follow moisture content variation concerning energy levels corresponding to 4 to 10 passes. Moduli increased with increasing moisture content, as long as moisture content varies between 2% dry of optimum and optimum value. This trend indicates the great influence of moisture content on mechanical performance rather than dry density. As so, higher requirements regarding compaction control should be considered when compaction is performed with moisture content on the dry side, rather than compaction on the wet side, as long as compacted layers will remain in unsaturated condition. To this end, continuous evaluation of mechanical performance represents a great improvement on compaction control.

Finally, comparison between full scale trial and laboratory results was performed. Shear modulus obtained from *SASW* carried out on trial layer 0.40 m with optimum moisture content was found to be similar to shear modulus given by laboratory tests. Moreover, a maximum difference of 19% between modulus obtained from *SPLT* following AFNOR standard and modulus estimated from triaxial compression tests was found, which assumes great importance taking into account two issues: (i) design is based on mechanical properties usually determined from laboratory tests; (ii) even though conventional triaxial tests only allow determination of mechanical properties beyond strain level of 1%, for *SC* geomaterial is possible to estimate secant modulus from degradation curves

for lower strain levels since degradation curves lie between reference threshold for sands given by Santos (1999).

Chapter 7

Field investigation: Fafe trial road embankment (*FTRE*)

7.1 Introduction

In the aim of a national research project POCI/ECM/56952/2004 with the goal to validate/calibrate in situ the results obtained in laboratory for the processed steel slag (inert steel aggregate for construction, *ISAC*), a trial road embankment was constructed where, besides this non-traditional geomaterial, traditional geomaterials, a poor-graded sand with silt and a well-graded gravel named herein as *SP* and *CA40*, respectively, were employed (Gomes Correia *et al.*, 2009b; Reis Ferreira, 2010). The execution of a trial embankment employing different materials gave the opportunity to carry out different studies, which are twofold: (i) mechanical performance of geomaterials were evaluated by means of static plate loading test (*SPLT*) and performance related tests, falling weight deflectometer (*FWD*) and light falling weight deflectometer (*LFWD*), the soil stiffness gauge (*SSG*), spectral analysis of surface waves (*SASW*) and Portancemètre; (ii) instrumentation of the embankment and road layers enabling the measurement of vibrations and strains induced by the compaction equipment and by performance related tests.

Likewise to Évora trial railway embankment (*ETRE*), the first issue aims to establish correlations between different test methods using *SPLT* as reference test. Taking into account conclusions from previous chapter regarding *SPLT* and the outcome of the specification project presented in Appendix B, *SPLT* were performed following this specification project. To this end, *SP*, *CA40* and *ISAC* trial, embankment and base layers were compacted employing different thicknesses (0.20, 0.30, 0.40 and 0.50 m) and optimum moisture content regarding Modified Proctor. Index parameters and mechanical properties were then evaluated for several energy levels corresponding to 4, 6, 8, 10 and 12 passes of the vibrating roller. A detailed description is given in Chapter 4. As so, firstly index parameters are evaluated by means of sand cone method (*SCM*), rubber balloon method (*RBM*) and nuclear method (*NM*). Secondly, *SPLT* is used

as reference test and correlation with performance related tests is established. Then analysis of full scale trial results is conducted and recommendations are provided. At last, comparison between field and laboratory results is performed.

The second issue deals with vibration measurements of roller drum and layers vibrations during compaction and application of dynamic loads. It is intended to get data in order to investigate the interaction between roller drum and layer to be compacted, as well as to realize the magnitude of strains and accelerations induced during compaction, application of dynamic loads with several equipments, such as, *FWD*, *LFWD*, the Portancemètre and during application of static loads while performing *SPLT*. In this scope, firstly, in-ground strains and acceleration measurements during application of dynamic loads are presented and, secondly, roller drum behaviour and layers in-ground behaviour during compaction process is presented.

7.2 State conditions

In this section *SCM* and *NM* results, namely dry density and moisture content will be presented. The interpretation of both tests is straight. Likewise in previous chapter, since *NM* involves measurements at the same spot at depths of 0, 0.06 and 0.12 m, an average value at each spot was computed. Then, a relationship between density (γ_w) and volumetric water content (θ) between both tests results was attempted for *SP* and *ISAC* materials and is shown in Figures 7.1 and 7.2.

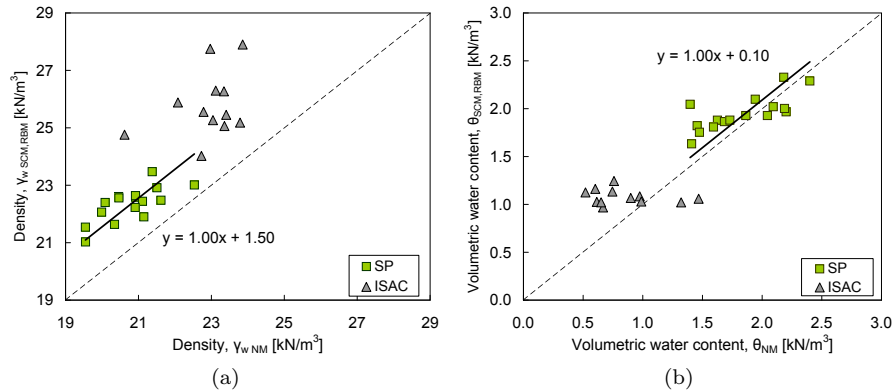


Figure 7.1: Comparison of state parameters obtained from *NM* and *SCM* test methods performed on the same grid: (a) density; (b) volumetric water content

Firstly, in Figure 7.1 only values obtained from tests carried out on the same grid are included and grid homogeneity is assumed. A reasonable relationship between density and volumetric water content was obtained for *SP* material ($R^2=0.53$ and $R^2=0.55$), while a poor relationship was achieved for *ISAC* material. Secondly, a relationship between average values per energy level for each layer was attempted in order to reduce scatter (fig. 7.2). Poor relationships were obtained regarding *ISAC* geomaterial. Therefore, *NM* appears not to be appropriate to evaluate moisture content of *ISAC* geomaterial and, thereby, cal-

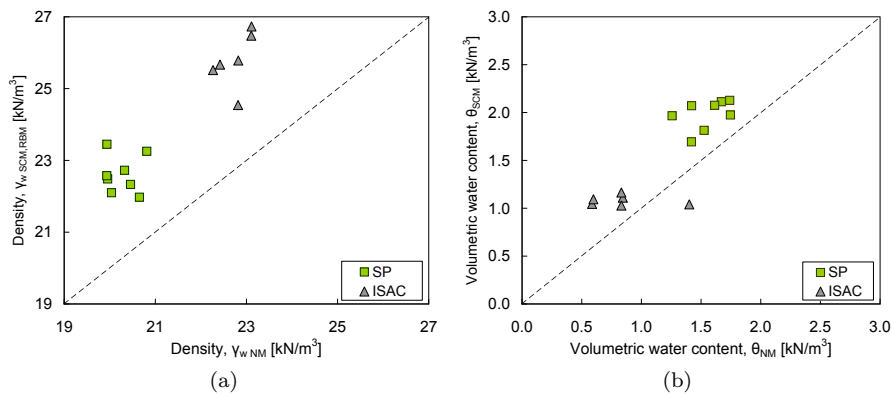


Figure 7.2: Comparison of average state parameters per layer obtained from NM and SCM test methods: (a) density; (b) volumetric water content

ibration was not conducted. On the other hand, calibration of NM carried out on SP was performed using equations given in Figure 7.1. The result of calibration is presented in Figure 7.3, where both average density and volumetric water content obtained from SCM are plotted against the corresponding values obtained from calibration of NM results.

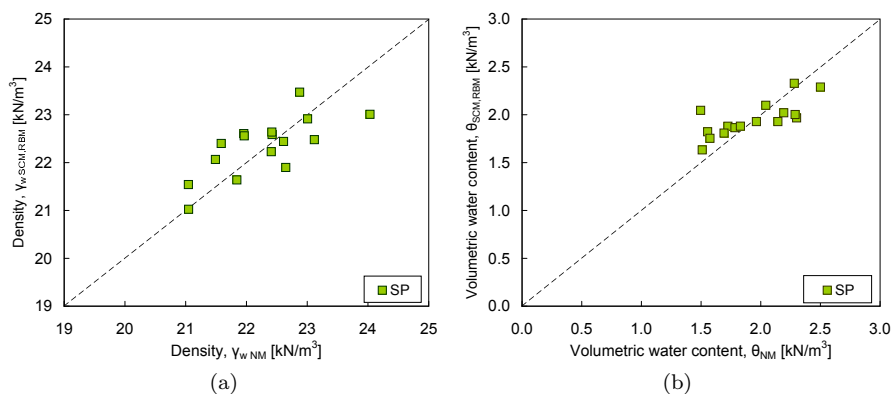


Figure 7.3: SCM parameters plotted against NM calibrated parameters: (a) density; (b) volumetric water content

Following, the state parameters obtained from each test method on SP compacted layers are presented in Figure 7.4 for several energy levels. Due to time constraints and labor intensive SCM number of tests are significantly less than NM tests. Dry density exceeded the maximum value given by Modified Proctor for all layers and energy levels, which may be attributed to a high energy level employed by compaction equipment. In fact, the distribution of points indicate that maximum dry density is achieved at a lower moisture content on the dry side of modified compaction curve which features a higher energy level applied. Trial layers (0.30, 0.40 and 0.50 m w_{OPM}) were compacted with moisture content about 3% to 2% dry of optimum, whereas moisture content ranging between 2%

dry of optimum and optimum value was achieved on embankment layers (4th, 5th, 6th, 7th and 8th layers).

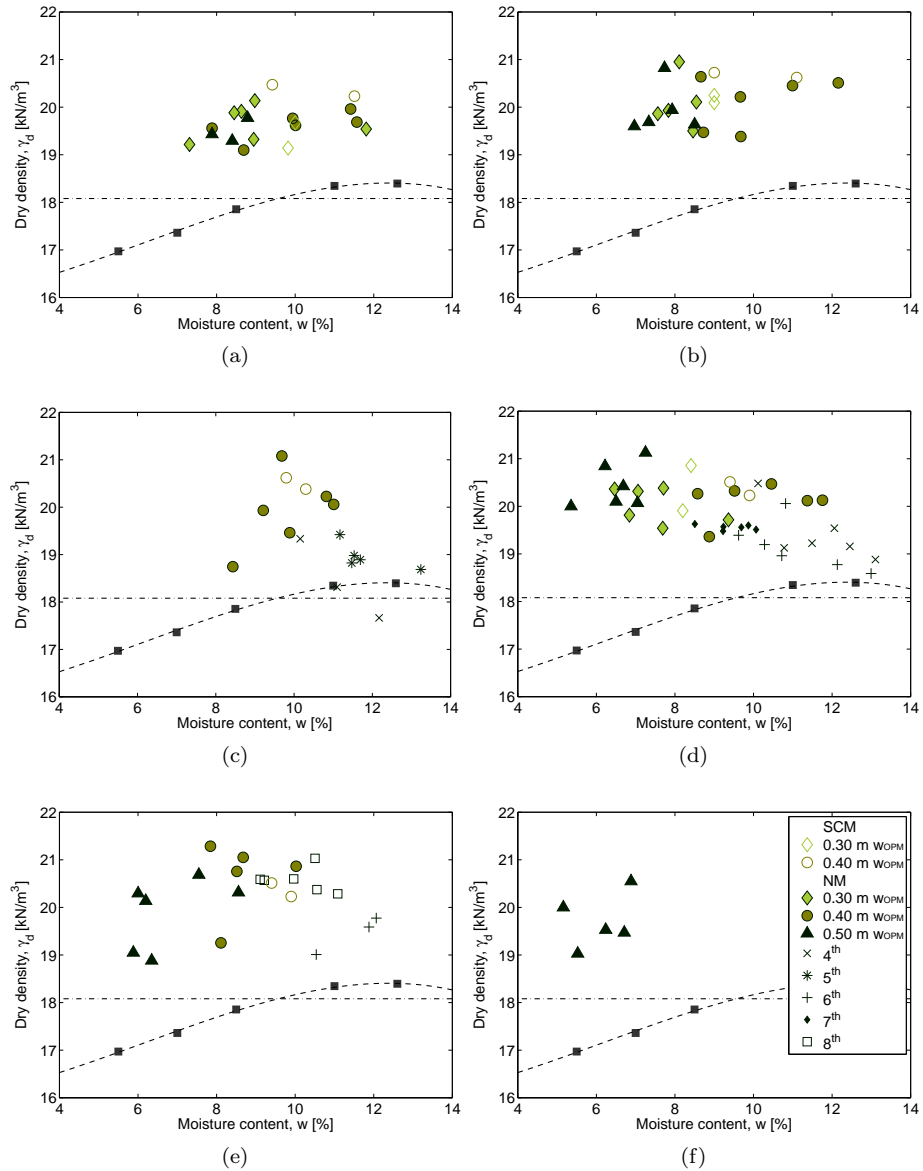


Figure 7.4: State parameters obtained from SCM and NM on SP layers for energy level corresponding to: (a) 4 Passes; (b) 6 Passes; (c) 8 Passes; (d) 10 Passes; (e) 12 Passes; (f) 14 Passes

Since an extensive mechanical characterization was performed for the last energy level, focus is given to layers state conditions at this stage. In Table 7.1 is given respective statistical data regarding SP trial layers and embankment layers. In what concerns to the former layers, moisture content achieved ranged

from 6 to 4% dry of optimum. The highest dry density was obtained from trial layer with 0.40 m thickness, whereas the lowest was achieved on trial layer with 0.50 m thickness even though a higher energy level was applied. These results denote the influence of layer thickness on dry density regarding compaction equipment used. Concerning to embankment layers, all constructed with 0.40 m thickness, average moisture content ranged from 2% dry of optimum to optimum. It is noteworthy that to the lowest dry density achieved in 5th layer corresponds to the higher moisture content.

Table 7.1: State conditions of *SP* trial and embankment layers obtained from *NM* after calibration for the last energy level at each layer

	Trial layers [m]			Embankment layers (0.40 m)				
	0.30	0.40	0.50	4th	5th	6th	7th	8th
No. Passes	10	12	14	10	8	12	10	12
γ_d [kN/m ³]	20.02	20.96	19.84	19.40	18.77	19.46	19.56	20.57
SD	0.37	1.06	0.60	0.57	0.52	0.40	0.05	0.26
CV	1.9	5.0	1.3	2.9	2.8	2.1	0.3	1.3
w [%]	7.5	8.3	5.6	11.7	12.5	11.5	9.4	10.1
SD	1.02	1.12	1.40	1.10	1.90	0.83	0.57	0.79
CV	13.6	13.4	25.1	9.4	15.2	7.2	6.0	7.8

The wetting process employed on *SP* material involved the previous stack of material, water adding and mix up by means of a front shovel and, in addition, moisture content was corrected in situ before compaction process. Still, this procedure did not always met the desirable moisture content.

7.3 Modulus from *SPLT*

In Table 7.2, only average results will be presented since the limited number of tests carried out do not allow to compute other statistical parameters. *SPLT* were carried out following specification project developed by Gomes Correia *et al.* (2007). It is noteworthy that modulus obtained from tests performed on *ISAC* trial and base layer were about 63% and 56% than the corresponding values obtained from *SP* trial layer and base layer, respectively.

Table 7.2: Average modulus E_{SPLT} obtained from *SPLT* carried out on trial and base layers, for the last energy levels

Layer	Material	No. of passes		
		10	12	14
0.40 m	<i>SP</i>	92.8		
	<i>ISAC</i>	151.5		
0.50 m	<i>ISAC</i>	149.4		
Base layer	<i>CA40</i>	119.0		
	<i>ISAC</i>	185.8		

7.4 Moduli obtained from performance related tests

7.4.1 *LFWD*, *FWD*, *SSG* and Portancemètre

Similarly to Chapter 6, statistical data (average and standard deviation, *SD*, and coefficient of variation, *CV*) was computed from moduli obtained from *LFWD*, *SSG* and Portancemètre and data is given in Appendix D for each trial layer and for energy levels evaluated. The number of tests enabling statistic treatment by layer and energy level were listed in Chapter 4.

The *FWD* modulus E_{FWD} was computed and statistical data is also presented in Appendix D. All tests were conducted starting with one seating load followed by one load drop at three different drop heights, generating this way three different loads, in each station. A load plate with 0.45 m in diameter was used and a flexible load plate was considered.

7.4.2 *SASW*

With the aim to perform a *SASW* test, *SP* capping layer was instrumented with accelerometers on the surface. Six vertical receivers (accelerometers) were placed on the ground and offset in incremental distances from a fixed center-line. Because the compacted layers of about 0.40 m are under consideration and taking into account filtering criterion described in Chapter 2, the receivers were offset of 0.40 m, as is illustrated in Figure 7.5. All tests were performed on *SP* capping layer inside grid *L6*.

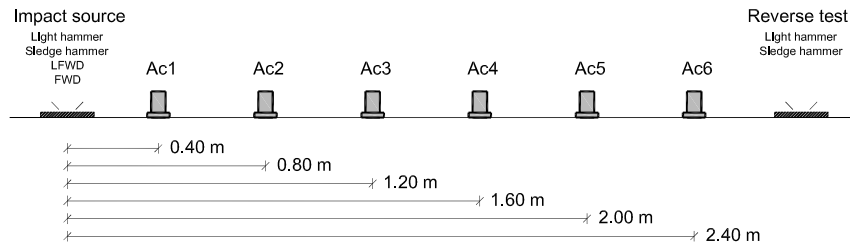


Figure 7.5: Setup adopted to perform *SASW* on *SP* capping layer inside grid *L6*

Several tests were performed applying different impulsive loads in line with the receivers at a distance away from the receiver equal to receivers spacing. Active Rayleigh wave data were generated using a light hammer, a sledge hammer, *LFWD* and *FWD* sources. To improve the signal-to-noise ratio, the impacts are repeated several times. A reverse test is also performed with the source in the opposite side of the receiver array, when a light or sledge hammer source is used, in order to confirm the first test. Satisfactory results were obtained with light hammer, *LFWD* and *FWD* sources.

The acquisition system was described in previous chapter.

Results from test using a light hammer

As illustrated in Figure 7.6, a light hammer source generate high-frequency Rayleigh waves in the range of 10–1500 Hz. This range is higher than the one obtained from SASW tests in *ETRE* (recall section 6.4.2).

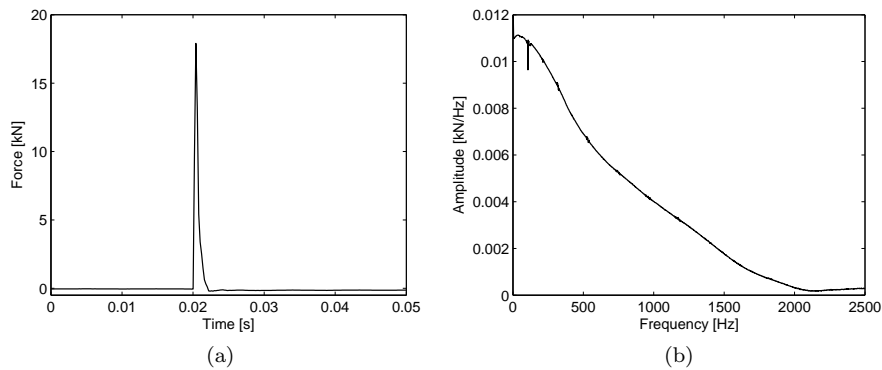


Figure 7.6: (a) Waveforms of signals and (b) respective spectrum generated using a light hammer source

Estimation of the dispersion curve was computed using three pairs of signals, namely, 0.40–0.80 m, 0.80–1.60 m and 1.20–2.40 m, which information was assembled considering filtering criterion, as described in Chapter 2. Experimental dispersion curves corresponding to the first test and the reverse one (fig. 7.7) were then obtained, where only fundamental mode was considered. Figure 7.7 shows that no significant differences are seen between experimental curves obtained with first and reverse test. Therefore only results from first test were analysed. Since the number of points in the composite dispersion curve is not manageable for the successive inversion process, a polynomial regression was adopted.

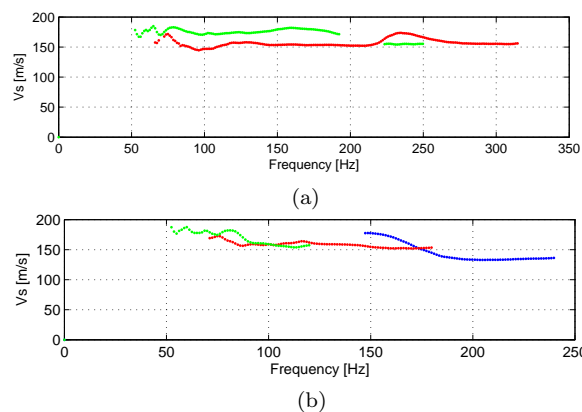


Figure 7.7: Experimental dispersion curves from SASW carried out on capping layer inside grid *L6* using light hammer: (a) first test ; (b) reverse test

The shear wave profile was computed using an iterative process described

previously in Chapter 2. Table 7.3 gives these values for all stages, as well as the square root of the final value of the objective function ($f_{\text{obj}}^{1/2}$). Density equal to 1900 kg/m^3 was assumed at this stage. The lowest value of $f_{\text{obj}}^{1/2}$ was achieved for the shear wave profile corresponding to an earth model with one layer over halfspace. From Table 7.3 it can be seen that a layer with thickness of 0.41 m is identified on the top, which corresponds to the capping layer.

Table 7.3: Initial and final soil profile for first attempt including all stages in the inversion procedure (light hammer test)

Stage	Layer	Initial profile			Final profile			$f_{\text{obj}}^{1/2}$
		d	V_s	γ	d	V_s	γ	
1	1	∞	100	18.64	∞	181	18.64	11.1
2	1	3	181	18.64	0.41	175	18.64	5.4
	2	∞	181	18.64	∞	195	18.64	
3	1	0.45	175	18.64	0.39	175	18.64	7.5
	2	3	195	18.64	1.98	194	18.64	
	3	∞	195	18.64	∞	217	18.64	
4	1	0.39	175	18.64	0.38	175	18.64	11.1
	2	0.99	194	18.64	1.06	194	18.64	
	3	0.99	194	18.64	1.03	197	18.64	
	4	∞	217	18.64	∞	211	18.64	

Then, a new shear wave profile was computed using all data available for the embankment. The results found out are given in Table 7.4. $f_{\text{obj}}^{1/2}$ shows good agreement between theoretical and experimental composite dispersion curves, as illustrated in Figure 7.8. From the shear wave profile Young modulus results were 154 MPa and 188 MPa for the capping layer and embankment layers, respectively.

Table 7.4: Initial and final soil profile for second attempt including all stages in the inversion procedure (light hammer test)

Stage	Layer	Initial profile			Final profile			$f_{\text{obj}}^{1/2}$
		d	V_s	γ	d	V_s	γ	
1	1	0.4	160	22.40	0.4	175	22.40	5.1
	2	2.6	180	21.90	2.6	195	21.90	
	3	∞	217	18.64	∞	269	18.64	

Results from test using a sledge hammer

The typical waveforms of signals generated using a sledge hammer source and respective spectrum is shown in Figure 7.9. This source type generates frequency Rayleigh waves almost in the range of 5–1500 Hz.

Reverse test did not allowed to compute dispersion curve due to the bad coherence between signals from pairs of sensors. With regards to first test, signals from pair formed by sensors positioned at 0.40–0.80 m did not enabled to compute dispersion curve, for the same reason. This was probably due to

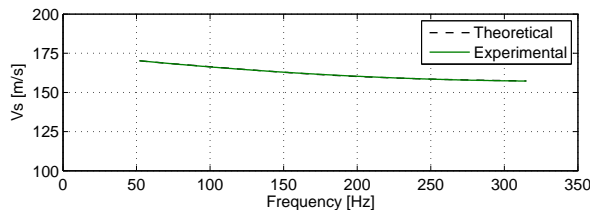


Figure 7.8: Theoretical and experimental composite dispersion curve from SASW carried out on *SP* capping layer inside grid *L6* using sledge hammer source

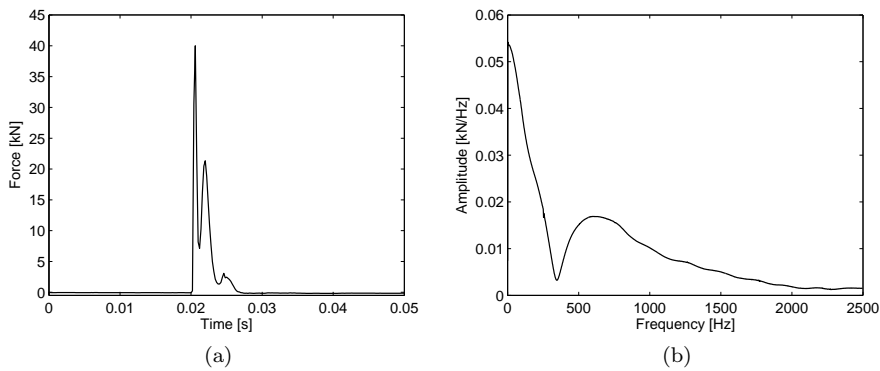


Figure 7.9: (a) Waveforms of signals and (b) respective spectrum generated using a sledge hammer source

the low amplitude of frequency waves over 350 Hz, which did not provided wave lengths lower than the distance between sensors (0.40 m). Therefore, dispersion curve was computed using only two pairs of signals, corresponding to sensors at 0.80–1.60 m and 1.20–2.40 m, and is illustrated in Figure 7.10. One can see that data is scarce, which was probably due to generated short range of frequency waves, and dispersion curves from both pairs of sensors did not matched; thus data was considered to be poor and did not allowed to proceed analysis.

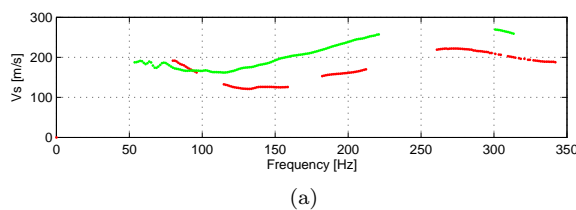


Figure 7.10: Experimental dispersion curves from SASW carried out on *SP* capping layer inside grid *L6* using sledge hammer, corresponding to first test

Results from test using *LFWD*

In Figure 7.11 is illustrated typical waveform of signal generated by *LFWD* equipment, where Rayleigh waves are generated in the range of 0–150 Hz.

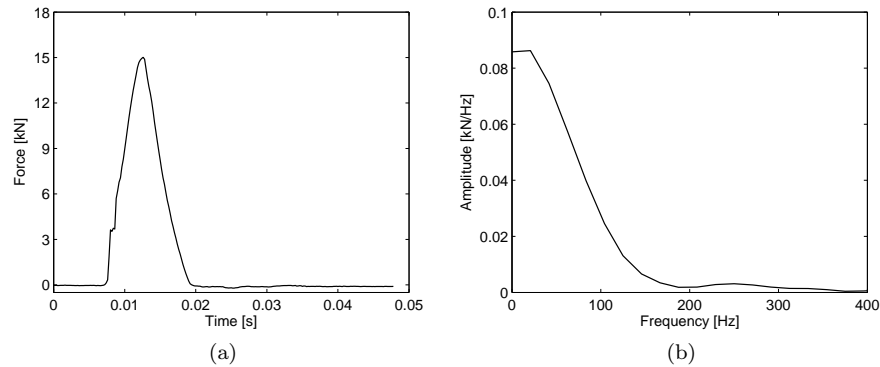


Figure 7.11: Waveforms of signals generated using *LFWD* source and its spectrum

Keeping constant drop height, at least 6 drops were performed in order to compute dispersion curve shown in Figure 7.12. Likewise to the sledge hammer test, the same pairs of signals were used and same filtering criterion applied. Pair 0.40–0.80 m did not allowed to compute dispersion curve due to the bad coherence between signals. Similarly to conclusions for sledge hammer test, frequency waves over 190 Hz practically were not generated, though did not provided wave lengths lower than the distance between sensors (0.40 m). This notwithstanding, good correlation between the other pairs of signal was obtained enabling calculation of dispersion curve.

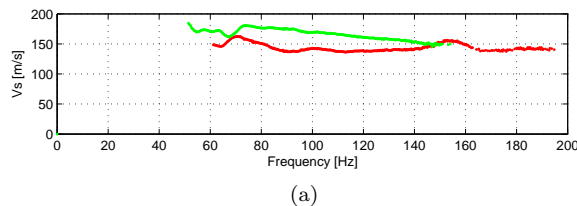


Figure 7.12: Experimental dispersion curves from *SASW* carried out on *SP* capping layer inside grid *L6*, using *LFWD* source

Table 7.5 gives values for all stages of the inversion process, as well as the square root of the final value of the objective function. The lowest value of $f_{obj}^{1/2}$ was achieved for the shear wave profile corresponding to an earth model with two layers over halfspace. As one can see from Table 7.7 the first layer thickness, d , was estimated to be 0.57 m to which corresponds shear wave velocity of $158 \text{ m}\cdot\text{s}^{-1}$.

Then, a new shear wave profile was computed using all data available for the embankment. The results found out are given in Table 7.13. $f_{obj}^{1/2}$ demonstrates

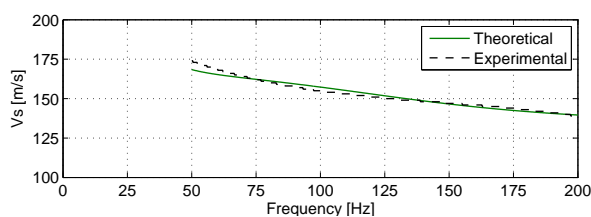
Table 7.5: Initial and final soil profile for first attempt including all stages in the inversion procedure (*LFWD* test)

Stage	Layer	Initial profile			Final profile			$f_{obj}^{1/2}$
		d	V_s	γ	d	V_s	γ	
1	1	∞	100	1900	∞	171	1900	56.4
2	1	3	171	1900	0.57	158	1900	27.1
	2	∞	171	1900	∞	210	1900	
3	1	0.57	158	1900	0.57	158	1900	13.7
	2	3	210	1900	3.57	210	1900	
	3	∞	210	1900	∞	211	1900	
3	1	0.57	158	1900	0.19	130	1900	15.0
	2	1.79	210	1900	1.02	190	1900	
	3	1.79	210	1900	0.42	260	1900	
	4	∞	211	1900	∞	215	1900	

better agreement between theoretical and experimental dispersion curves (fig. 7.13) than the one obtained previously. Young modulus was computed and values of 114 MPa and 200 MPa were found for the capping layer and the embankment layers, respectively.

Table 7.6: Initial and final soil profile for second attempt including all stages in the inversion procedure (*LFWD* test)

Stage	Layer	Initial profile			Final profile			$f_{obj}^{1/2}$
		d	V_s	γ	d	V_s	γ	
1	1	0.40	144	22.40	0.40	151	22.40	8.4
	2	2.60	194	21.90	2.60	202	21.90	
	3	∞	210	18.64	∞	363	18.64	

Figure 7.13: Theoretical and experimental composite dispersion curve from SASW carried out on *SP* capping layer inside grid *L6* using *LFWD* source

Results from test using *FWD*

The typical waveforms of signals generated using a *FWD* equipment source and respective spectrum is presented in Figure 7.14. This source type generates frequency Rayleigh waves almost in the range of 0–100 Hz.

Likewise the previous test, the experimental dispersion curve was computed using the same pairs of signals and filtering criterion. Three tests correspond-

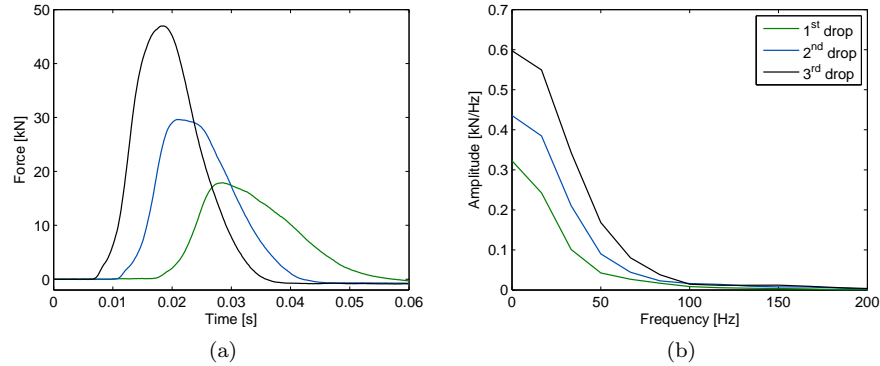


Figure 7.14: Waveforms of signals generated using *FWD* source and its spectrum corresponding to three drop heights

ing to the three drops heights used in the standard *FWD* test carried out in *FTRE* were performed. Each test consisted in at least ten impacts from which experimental dispersion curves were estimated and are shown in Figure 7.15. Once again, only fundamental mode was considered and a polynomial regression was adopted. For the same reasons pointed out previously only two pairs of accelerometers were used to compute dispersion curve.

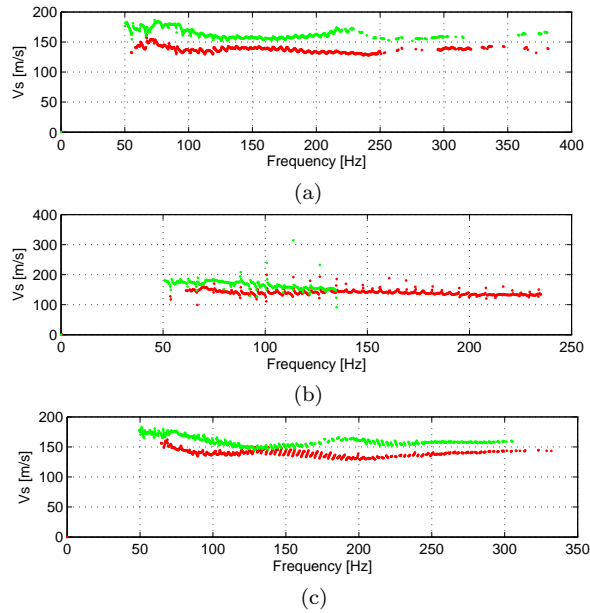


Figure 7.15: Experimental dispersion curves from *SASW* carried out on capping layer inside grid *L6*, using *FWD* source corresponding to three drops heights: (a) 1st; (b) 2nd; (c) 3rd

Table 7.7 gives values for all stages of the inversion process, as well as the square root of the final value of the objective function. The lowest value of $f_{obj}^{1/2}$

was achieved for the shear wave profile corresponding to an earth model with three layers over halfspace. It is noteworthy that at stage 3 the highest value of $f_{\text{obj}}^{1/2}$ was obtained, which was unexpected. Regarding stage 4 the first layer has thickness, d , of 0.21 m, which is about half thickness of the capping layer.

Table 7.7: Initial and final soil profile for first attempt including all stages in the inversion procedure (*FWD* test)

Stage	Layer	Initial profile			Final profile			$f_{\text{obj}}^{1/2}$
		d	V_s	γ	d	V_s	γ	
1	1	∞	100	18.64	∞	164	18.64	60.5
2	1	3	164	18.64	0.35	157	18.64	13.3
	2	∞	164	18.64	∞	183	18.64	
3	1	0.35	157	18.64	0.34	157	18.64	167.6
	2	3	183	18.64	4.28	183	18.64	
	3	∞	183	18.64	∞	268	18.64	
4	1	0.34	157	18.64	0.21	154	18.64	5.2
	2	1.14	183	18.64	0.49	173	18.64	
	3	1.14	183	18.64	2.3	188	18.64	
	4	∞	268	18.64	∞	344	18.64	

Then, a new shear wave profile was computed using all data available for the embankment. The results found out are given in Table 7.16. The value of the square root of the objective function demonstrates good agreement between theoretical and experimental dispersion curves (fig. 7.16). Moreover, $f_{\text{obj}}^{1/2}$ was fairly lower than the one obtained previously on stage 3 regarding an earth model with the same number of layers. Young modulus of 122 MPa and 156 MPa were found, corresponding to the capping layer and embankment layers, respectively.

Table 7.8: Initial and final soil profile for second attempt including all stages in the inversion procedure (*FWD* test)

Stage	Layer	Initial profile			Final profile			$f_{\text{obj}}^{1/2}$
		d	V_s	γ	d	V_s	γ	
1	1	0.4	143	22.40	0.4	156	22.40	26.6
	2	2.6	169	21.90	2.6	178	21.90	
	3	∞	268	18.64	∞	260	18.64	

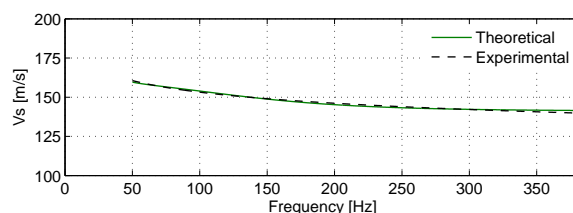


Figure 7.16: Theoretical and experimental composite dispersion curve from SASW carried out on capping layer inside grid *L6* using *FWD* source

7.5 Correlation between E modulus for several tests

Likewise in previous chapter, in what follows, correlation between E modulus obtained from different tests (*SPLT*, *LFWD*, *SSG*, Portancemètre, *FWD* and *SASW*) will be established. To this end, E_{V_2} modulus from *SPLT* will be set as the reference value.

It should be noted that, before the establishment of correlations, being Portancemètre a continuous test, the data given by this equipment was treated in such a way to be possible to compare values with spot tests. In this sense, an average value of E_{Port} modulus per grid was computed, in the same way as in the previous chapter. The methodology employed to the establishment of relationships between *SPLT* and performance related tests was based is the following steps:

- (i) comparison between tests results performed in the same spot for all energy levels;
- (ii) comparison between tests results performed in the same grid for all energy levels;
- (iii) comparison between average values per energy level;
- (iv) perform previous iterations, yet only considering the last energy level.

Due to the small dimensions of the trial, embankment and base layers, it seems to not make sense to group these values into homogeneous, as done for *ETRE*. Once again, ever tests results are unavailable or established relationships at each step show high scatter will not be presented. The results analysis was divided by type of material studied and is presented in the following sub sections.

7.5.1 *SP* trial and embankment layers

In Figure 7.17 is shown the relationship between *SPLT* modulus (E_{V_2}) and Portancemètre and *LFWD* moduli (E_{Port} and E_{LFWD}), despite only two *SPLT* available. Comparison between tests results on the same spot show a E_{V_2} 1.5 times greater than E_{LFWD} . On the other hand, a correlation close to unity observed between E_{Port} and E_{SPLT} moduli, which means moduli given by both test methods are similar. Thus, further relationships were attempted using Portancemètre as reference test, however, high scatter did not allowed the establishment of correlations.

Finally, moduli obtained from *SASW* is analysed. Interpretation of tests performed on capping layer inside grid *L6* resulted in moduli ranging from 135 to 165 MPa. Inside the same grid, *LFWD*, *SSG* and Portancemètre were carried out and moduli equal to 57, 112 and 83 MPa were obtained respectively. When these results are compared with *SASW*, significant differences are achieved. *SASW* modulus is approximately 160, 35 and 80% higher than *LFWD*, *SSG* and Portancemètre moduli. These differences are probably related with two fundamental aspects, namely, stress and deformation level applied by each test method. *LFWD* and Portancemètre applies higher stress and deformation levels than *SSG*, thus attempting on non linear behaviour of *SP* material it results in

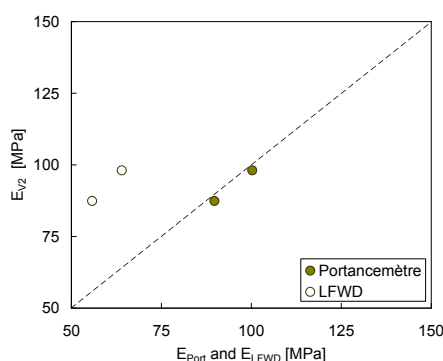


Figure 7.17: Comparison between moduli obtained from *SPLT* with Portancemètre and *LFWD* performed on *SP* trial layers

lower moduli. On the other hand, *SSG* applies lower stress levels and, therefore, correlation between E_{SSG} and *SASW* modulus is the closest one.

7.5.2 ISAC trial and embankment layers

Likewise to *SP* material, correlations between moduli were carried out. Firstly, in Figure 7.18 E_{V2} modulus is plotted against E_{Port} , E_{LFWD} and E_{SSG} moduli. E_{SPLT} modulus is higher, approximately 44%, than the corresponding values obtained with Portancemètre (E_{Port}), despite lack of results to allow sustainable conclusions. For this reason, it seems that calibration of Portancemètre was not suitable for this type of material. Concerning moduli obtained from *LFWD* and *SSG* tests, these are fairly lower than the ones obtained from *SPLT*. As one can see, E_{V2} is about two times E_{LFWD} and more than two times E_{SSG} .

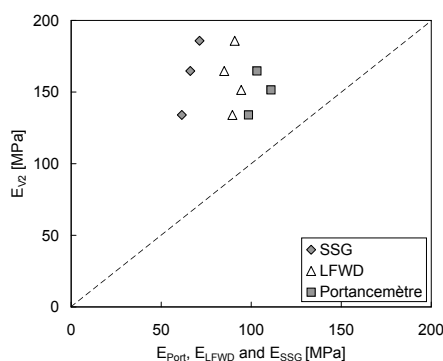


Figure 7.18: Comparison between moduli obtained from *SPLT* and Portancemètre, *SSG* and *LFWD* performed on *ISAC* trial layers

Owing to the lack of *SPLT* results and likewise to *SP* material, Portancemètre was used as reference test. In Figure 7.19, moduli given by Portancemètre, *LFWD* and *SSG* are compared. In Figure 7.19a correlation between E_{Port} and E_{LFWD} moduli is established for average values per layer and energy level, where

poor correlation is verified ($R^2 = 0.41$). Nevertheless, E_{Port} appears to be about 18% higher than E_{LFWD} . Also poor correlation ($R^2 = 0.38$) was found for comparison between E_{Port} and E_{SSG} , regarding moduli obtained on the same grid and for the last energy level. E_{Port} is about 47% higher than E_{SSG} .

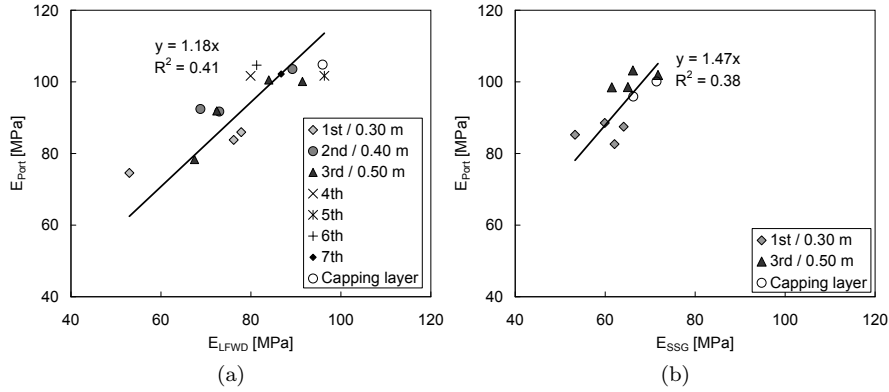


Figure 7.19: Comparison of moduli obtained from Portancemètre and: (a) *LFWD* for average values per energy level; (b) *SSG* for tests carried out on the same grid and for the last energy level

7.5.3 CA40 base layer

Concerning *SPLT*, only one test was carried out on this type of material, which E_{SPLT} result was 119 MPa. Nevertheless, comparison with the corresponding values E_{LFWD} , E_{FWD} and E_{SSG} obtained from tests performed inside the same grid is conducted in Table 7.9. In addition, also average values are given. It should be noting that *FWD* modulus was gathered from second drop weight with corresponding stress below the plate of 193 kPa, which is closer to the 200 kPa applied on *SPLT*.

Table 7.9: Moduli obtained from *SPLT* and performance related tests (*LFWD*, *SSG* and *FWD*) carried out on *CA40* base layer: tests performed on the same grid and average moduli

	E_{V2}	E_{LFWD}	$\frac{E_{\text{LFWD}}}{E_{V2}}$	E_{SSG}	$\frac{E_{\text{SSG}}}{E_{V2}}$	E_{FWD}	$\frac{E_{\text{FWD}}}{E_{V2}}$
E [MPa]	119.0	144.6	1.21	111.6	0.94	90.5	0.76
Average [MPa]		120.3	1.01	119.6	1.01	90.2	0.76

One can see that average E_{LFWD} and E_{SSG} are almost the same as E_{V2} , though moduli obtained in the same grid differed 21% and 6%, respectively. On the other hand, E_{FWD} either obtained from *FWD* carried out on the same grid or average value was about 24% lower than E_{V2} .

7.6 Analysis of full scale trial results and recommendations

The evolution of mechanical properties of trial layers with increasing energy level and with state conditions will be evaluated herein. Taking into account poor correlations found previously, only Portancemètre results will be used.

In Figures 7.20, 7.21 and 7.22 are plotted moduli obtained from Portancemètre, and state parameters, obtained from *SCM* and *NM* (after calibration), against the number of passes. The maximum relative compaction is achieved for 6 passes for trial layers with 0.30 and 0.50 m, yet, concerning to the latter, maximum moduli is only achieved for 12 passes. With regards to trial layer with 0.40 m thickness, both maximum relative compaction and moduli are achieved for 12 passes of the vibrating roller.

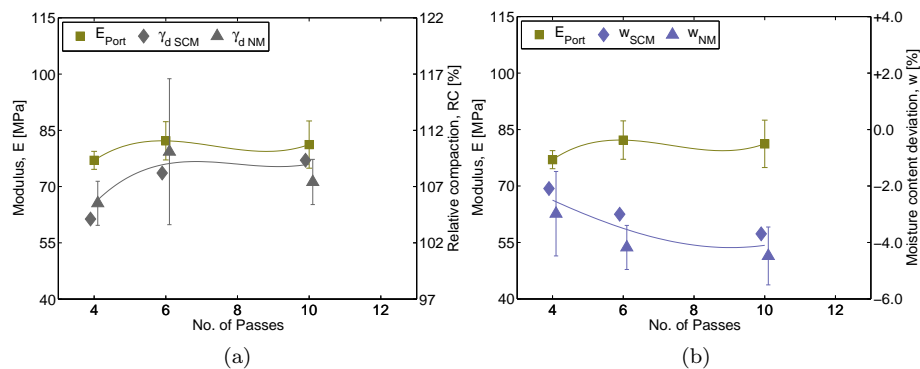


Figure 7.20: Trial layer with 0.30 m thickness. Moduli (E_{Port}) and state parameters (relative compaction and moisture content deviation) evolution with number of passes: (a) Moduli and relative compaction; (b) Moduli and moisture content deviation

Focusing on the analysis of moduli and relative compaction regarding all trial layers, it seems that dry density has great influence on mechanical properties. Moduli seems to follow dry density trends, i.e., increases with increasing dry density and vice-versa. This trend is similar to the one verified for *ETRE* on *SC* trial layers (recall section 6.6).

Further, the influence of state parameters on mechanical performance is investigated. To this end, in Figure 7.23 is plotted moduli and relative compaction against moisture content deviation for the last energy level for trial and embankment layers.

One can see a wide range of state parameters. Moisture content deviation ranged from 6% dry of optimum to optimum, whereas relative compaction varied between 102% and 113%. However, modulus appears to not vary significantly with moisture content. For example, relative compaction corresponding to moisture content deviation about 4%, 2% and 0.5% dry of optimum is quite similar, yet modulus is identical for the limits moisture contents and lower corresponding to 2.5% dry of optimum. Thereby, moisture content appears have unnoticeable influence on mechanical properties for the moisture content range

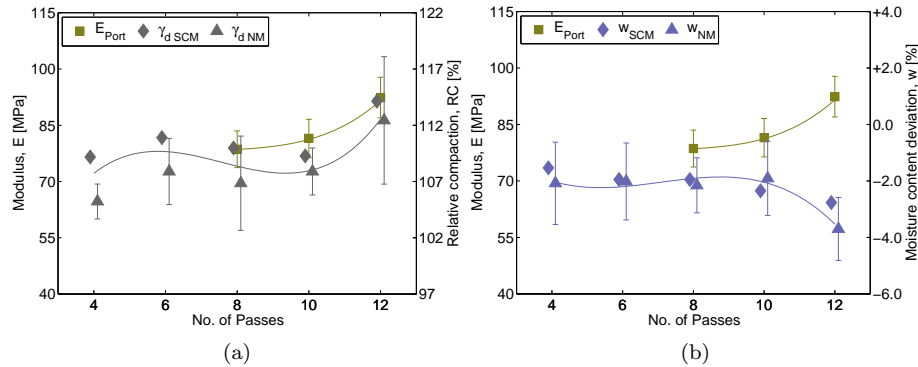


Figure 7.21: Trial layer with 0.40 m thickness. Moduli (E_{Port}) and state parameters (relative compaction and moisture content deviation) evolution with number of passes: (a) Moduli and relative compaction; (b) Moduli and moisture content deviation

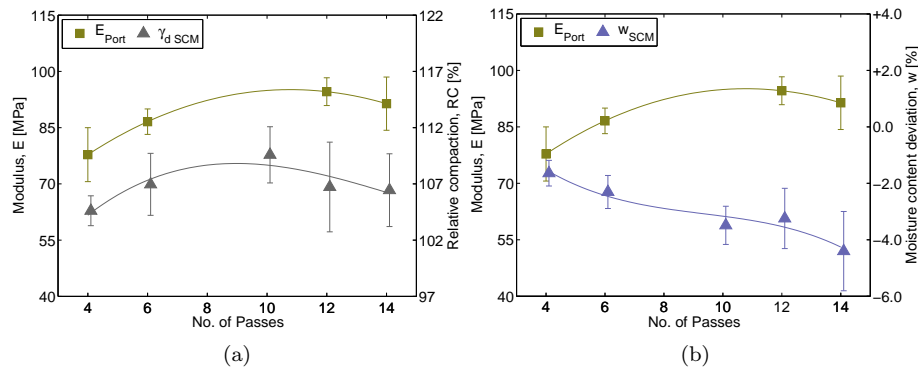


Figure 7.22: Trial layer with 0.50 m thickness. Moduli (E_{Port}) and state parameters (relative compaction and moisture content deviation) evolution with number of passes: (a) Moduli and relative compaction; (b) Moduli and moisture content deviation

investigated. In contrast, relative compaction appears to influence mechanical properties. Grouping results by similar moisture content deviation, namely, about 4%, 2% and 1%, one can observe that modulus increase with increasing relative compaction, i.e. dry density. An investigation of hydro-mechanical behaviour of *SP* material is required in order to justify these conclusions.

Further, regarding quality control state parameters and moduli scatter earn to be commented for last energy level. Concerning to *SP* trial layers the highest dry density *CV* was obtained from *NM* carried out on layer with 0.40 m thickness, about 5%, whereas trial layers with 0.30 and 0.50 m thickness presented *CV* lower than 2%. Owing to embankment layers, a dry density *CV* lower than 3% was achieved. As so, state parameters *CV* lie below the maximum values given by Brandl (1977), 5% for dry density determined by means of *NM*. Owing to moisture content, a *CV* varying between 6% and 25% was verified, where the

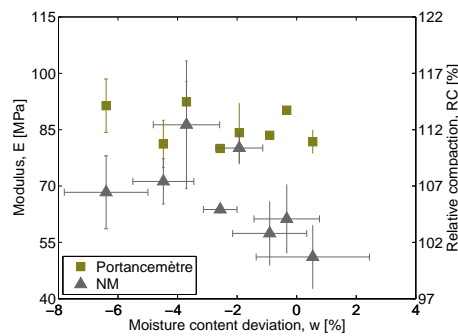


Figure 7.23: E_{Port} modulus and relative compaction (RC) versus moisture content (w) obtained on *SP* trial and embankment layers for the last energy level

highest value was obtained in 0.40 m trial layer and the lowest obtained in 7th embankment layer.

The analysis of mechanical properties scatter was based on Portancemètre results (see Table D.15). Trial layers presented identical modulus *CV* ranging from 6 to 8%, while embankment layers presented modulus *CV* ranging from 4 to 9%. As so, moduli *CV* mainly lie below the required maximum given by Brandl (1977), which is 25%. No relation between state parameters and modulus scatter was found.

The analysis of results from full scale trial allowed to conclude that the wetting process employed on *SP* did not produced desirable moisture content. Process involved the previous stack of material, water adding and mix up by means of a front shovel and, in addition, moisture content was corrected in situ before compaction process. Still, this procedure did not always met the desirable moisture content. Further, *NM* appear not to be appropriate for determination of state parameters of *ISAC* material.

Concerning to mechanical evaluation, the reduced number of *SPLT* did not allowed the establishment of reliable correlations with performance related tests. Nevertheless, a correlation close to unity was observed between *SPLT* and Portancemètre for tests carried out on *SP*, whereas on *ISAC* *SPLT* modulus was found to be approximately 1.45 times modulus obtained from Portancemètre. These results shows that an adequate calibration using *SPLT* is required. Therefore, it is recommended to conduct calibration during execution of trial embankments. This notwithstanding, the quick execution and the immediate layout of the results allowed quick intervention whenever the deformability conditions were not achieved, which highlights the great advantage of this equipment, besides being a continuous method.

Poor correlations with other performance related tests, namely *LFWD* and *SSG*, using Portancemètre as reference test were obtained due to high scatter. Therefore, the results from these equipments should be treated with caution.

7.7 Comparison between full scale trial and laboratory results

Likewise to previous chapter, comparison between moduli obtained from full scale trial and laboratory tests are performed herein. To this end, stress and strain levels on both field and laboratory tests are taken into account, as well as, state conditions.

Firstly, comparison between modulus obtained from *SASW* carried out on capping layer and modulus obtained from triaxial tests carried out in the aim of a doctoral thesis (Reis Ferreira, 2010). The variation of secant modulus versus total vertical stress considering a strain level of 4×10^{-5} is given by Equation 7.1.

$$E_{\text{sec}} = 211 \cdot \left(\frac{\sigma_1}{p_a} \right)^{0.64} \quad (7.1)$$

To take into account in situ stress and strain levels laboratory modulus was determined for a total vertical stress of 4.5 kPa, corresponding to an average vertical stress at the middle of the capping layer with 0.40 m thickness. Since suction data is not available regarding *SP* material, a matric suction level similar to the one determined from *SC* material was adopted, about 20 kPa, in order to take into account unsaturated condition. As so, a laboratory modulus of 86 MPa was obtained and then corrected for the same in situ void ratio. With regards to strain level, no correction was conducted since there are no available laboratory results regarding in situ strain level involved in *SASW* test (1×10^{-6}). Nevertheless, accordingly Ishibashi and Zhang (1993) degradation curves there is no significant modulus reduction these strain levels. The state conditions and modulus determined from field and laboratory tests are summarized in Table 7.10.

Table 7.10: Field and laboratory state conditions and modulus regarding *SP* geomaterial

	<i>SASW</i> on <i>L6</i>			Laboratory
	Light hammer	<i>LFWD</i>	<i>FWD</i>	
γ [kN/m ³]		22.40		20.65
γ_d [kN/m ³]		20.33		18.44
w [%]		10.2		12
<i>e</i>		0.279		0.411
V_s	175	151	156	
G_0	70	52	56	
E_0 ($\nu = 0.10$)	154	115	122	86
f(e field), f(e lab)		2.80		2.19
$E_{0\text{field}}^{\text{nor}}$ [MPa]	154	115	122	109

The only laboratory results available were obtained on specimen with optimum moisture content (12%), whereas in situ moisture content is about 2% dry of optimum. From Table 6.9 one can see that field modulus is about 5% to 50% higher than laboratory modulus. However, these results should be treated with caution due to simplifications adopted.

Comparison between *SPLT* and laboratory results was conducted by Reis Ferreira (2010) using the same procedure described previously. However, a stress level of 200 kPa and a strain level of 1×10^{-3} were considered. Laboratory modulus was found to be about 10% to 27% greater than modulus obtained from *SPLT* on *SP* layers and ranged from 3% to 26% higher than modulus obtained from *SPLT* on *ISAC* layers. In the same manner, also modulus obtained from *SSG* was compared with laboratory results. Once again, laboratory results were found to be about 13% higher than *SSG* modulus. In Figure 7.24 moduli obtained from laboratory tests are plotted against moduli obtained from field tests.

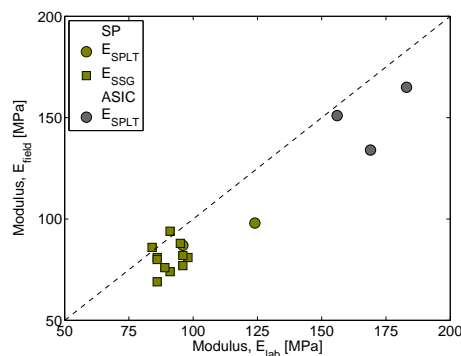


Figure 7.24: Moduli obtained from *SPLT* performed on on *SP* and *ISAC* layers and *SSG* carried out on *SP* layers versus moduli obtained from laboratory tests

7.8 Field monitoring of roller drum and capping layer vibrations during compaction and application of dynamic loads

As described in Chapter 4, field monitoring of vibrations (vertical strains and vertical accelerations) was conducted in two phases. Phase One measurements were carried out on capping layer in materials *ISAC* and *SP* during dynamic tests, namely, *LFWD*, *FWD*, Portancemètre and during roller drum vibration. Phase Two involved measurements of roller drum vibrations, as well as capping layer vibrations during compaction of base layer.

7.8.1 Phase One: Instrumentation

The instrumentation in this phase involved strain gauges and accelerometers. It is important noting that while the former reflects both static and dynamic response, the latter only reflects dynamic response.

The setup adopted is illustrated in Figure 4.16a, in Chapter 4. One strain gauge was buried in the capping layer of *SP* profile at depth 0.43 m, while another strain gauge was buried in the capping layer of *ISAC* profile at depth 0.45 m. Though the sensors depth were slightly different for the two profiles, they are close enough to elicit comparison. It should be noted that these sensors

were not calibrated previously to its in-ground placement, thus values presented hereafter are direct values given by sensors. In addition, two uniaxial accelerometers were buried in the top and bottom of the capping layer. For *SP* profile, the top and bottom accelerometers were placed at depth $z = 0.10$ m and $z = 0.45$ m, whereas for *ISAC* profile sensors were placed $z = 0.22$ m and $z = 0.47$ m. As so, bottom accelerometers also allows comparison, despite differences in depth, while top accelerometers do not allow direct comparison. The characteristics of these accelerometers are given in Table 7.11.

Table 7.11: Sensors characteristics used for vibration measurements

Designation	Type	Sensibility [V/g]	Measurement range [g]	Frequency range [Hz]
in-ground accelerometers	PCB 623B13	1	± 5	0.5 to 1000

7.8.2 Phase One: Test results

LFWD

For both profiles, *ISAC* and *SP*, two *LFWD* tests were performed at surface capping layer, one at strain gauges vertical alignment and another at accelerometers vertical alignment, thereby enabling the evaluation of vertical in-ground strains and in-ground accelerations. Each *LFWD* test consisted in at least six impacts and a plate with 300 mm diameter was used.

The force versus displacement loops corresponding to one impact at each vertical alignment on both profiles are plotted in Figure 7.25. An average $F_{\text{peak}} = 15$ kN loading was measured for *LFWD* performed in the *SP* profile, while an average $F_{\text{peak}} = 15.5$ kN loading was measured for tests performed in *ISAC* profile, corresponding to average stress below the plate of 212 and 219 kPa, respectively. It is interesting noting that significant differences between plate displacements are observed, mainly those corresponding to *LFWD* tests performed in *ISAC* material, though spot tests were spaced of 0.50 m.

Figure 7.26 illustrates the strain measurement during *LFWD* testing on both profiles. In Table 7.12 is summarized data obtained from *LFWD* carried out at strain gauges vertical alignment and respective in-ground peak strains measurements. Identical peak strains were measured in *SP* and *ISAC* profile (356×10^{-6} and 361×10^{-6} , respectively) reflecting similar modulus obtained from tests interpretation. Moreover, strain response stress ratio is approximately 1.67 for both profiles. Despite different materials being tested, identical stress strain behaviour is found from profiles at strain gauges vertical alignments.

Table 7.12: Peak in-ground strains measurements obtained from *LFWD* tests carried out on *SP* and *ISAC* profiles

Material profile	Measurement depth	Stress below the plate [kPa]	E_{LFWD} [MPa]	Peak strain [$\times 10^{-6}$]
<i>SP</i>	0.43 m	212	62	356
<i>ISAC</i>	0.45 m	215	60	361

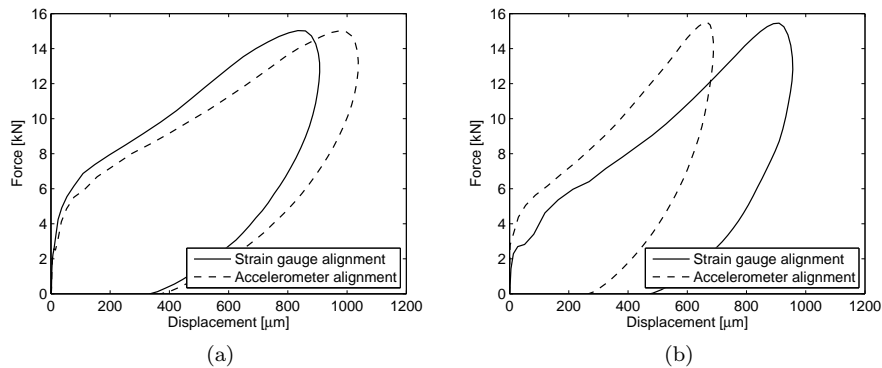


Figure 7.25: Average *LFWD* force–displacement loops from impacts at surface capping layer on sensors vertical alignment at: (a) *SP* profile; (b) *ISAC* profile

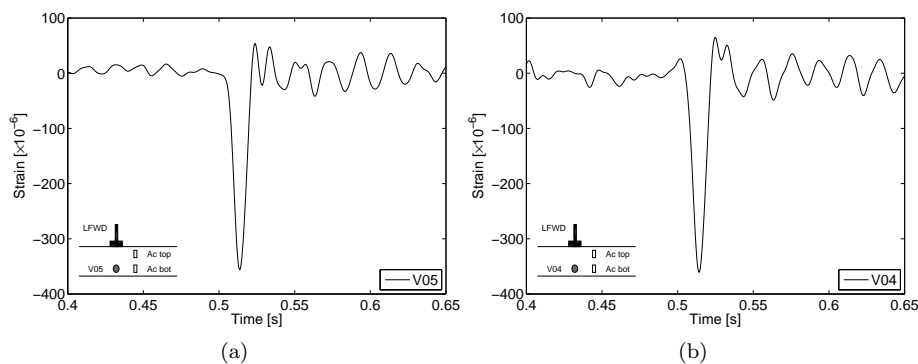


Figure 7.26: Strains measurement during *LFWD* test in: (a) *SP* profile; (b) *ISAC* profile

The acceleration time histories are presented in Figures 7.27a and 7.27b and peak acceleration data is given in Table 7.13. The acceleration data from top accelerometer in *SP* profile is not provided because exceeded the measurement range of the sensor, which means acceleration peak was higher than 49.1 m/s^2 . This was probably due to the lower depth of top accelerometer in *SP* profile ($z = 0.10 \text{ m}$) than in *ISAC* profile ($z = 0.22 \text{ m}$). One can see that peak from top accelerometer lags peak from bottom accelerometer due to wave propagation through profile. Further, in order to estimate displacements double integration on frequency domain was conducted on accelerometers data (see figs. 7.27c and 7.27d) and computed peak displacements are given in Table 7.13. Negative values represent downward displacement.

One can see that both acceleration and displacement peaks decrease with increasing depth. It is noteworthy at higher depth (0.43 and 0.45 m) the amplitude of upward acceleration exceeded the downward acceleration in *SP* profile and was the same in *ISAC* profile, whereas at $z = 0.22 \text{ m}$ in *ISAC* profile downward acceleration exceeded the upward acceleration. Acceleration data from

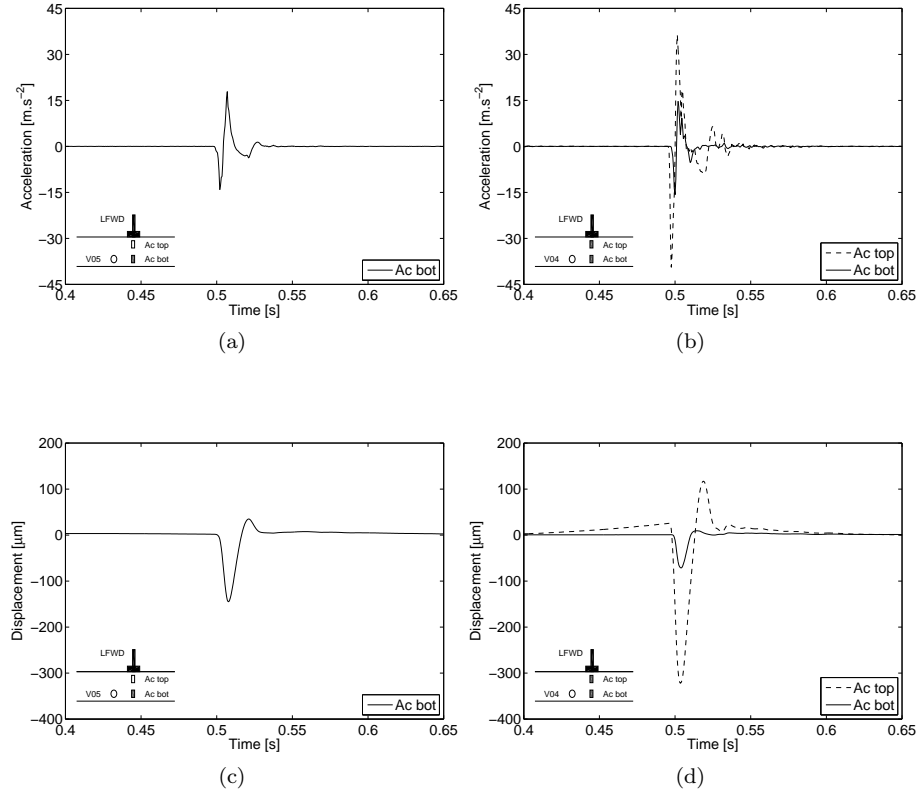


Figure 7.27: Accelerations time histories from in-ground accelerometers due to *LFWD* test: (a) *SP* profile; (b) *ISAC* profile; and computed displacements time histories: (c) *SP* profile; (d) *ISAC* profile

SP profile presented the greater difference between ac_{p+}^{SP} and ac_{p-}^{SP} . Concerning displacements on *ISAC* profile, a reduction about 78% between peak negative displacements from top and bottom sensors is verified.

Comparison between in-ground peak displacements from both profiles shows that computed displacements at higher depth in *SP* profile is almost two times the corresponding observed on *ISAC* profile, indicating thereby greater stiffness from *ISAC* profile. In fact, a higher E_{LFWD} was obtained on *ISAC* profile which is consistent with estimated displacements. However, computed displacements differ by a factor of about 2.1, yet moduli only differ about 1.6, despite applied stress almost the same. Aiming to understand these differences, theoretical modulus, stress and strain were computed from static loading theory applied to a homogeneous, isotropic, linear elastic half-space. Accordingly to Achenbach (1999) cited by Mooney and Miller (2009) elastic theory considering static loading can be used for dynamic loading when the time for stress waves through the volume of soil involved is much less than the duration of the load pulse. For *LFWD* testing on *ISAC* and *SP* materials, shear wave velocities of about 90 m.s^{-1} and 170 m.s^{-1} , respectively, were estimated from time

Table 7.13: Peak in-ground acceleration measurements and computed peak displacements obtained from *LFWD* tests carried out on *SP* and *ISAC* profiles

Material profile	Measure- ment depth [m]	Stress below the plate [kPa]	E_{LFWD} [MPa]	Peak accele- ration [m.s ⁻²]		Peak displace- ment [mm]
				ac_{p+}	ac_{p-}	
<i>SP</i>	0.45	212	54	18	14	0.145
<i>ISAC</i>	0.22	215	84	37	39	0.319
	0.47			15	15	0.069

lag between *LFWD* sensors located at 300 and 600 mm far from the center of the plate. Assuming a effective depth of $1.5D$, travel times of 5.0 and 2.6 ms are about three to five times less than the load pulse duration (approximately 13.5 ms). Therefore, static analysis using measured dynamic force provides a reasonable approximation to which the dynamic stress measurements can be compared. Through equations 7.2, 7.3 and 7.4, theoretical stress and strain response beneath the center of a circular plate can be determined (Timoshenko and Goodier, 1951), where σ_z , σ_r and σ_θ are vertical, radial and tangential stresses, ε_z is vertical strain, z is depth, E is Young modulus and ν is Poisson ratio which is assumed to be 0.35 and R is the radius.

$$\sigma_z = \int_0^{2\pi} \int_0^R \frac{3 \cdot q(r)}{2 \cdot \pi} \frac{z^3 \cdot r}{(r^2 + z^2)^{5/2}} dr d\alpha \quad (7.2)$$

$$\sigma_{r(r=0)} = \sigma_{\theta(r=0)} = \int_0^{2\pi} \int_0^R \frac{r \cdot q(r)}{4 \cdot \pi} \left[\frac{3 \cdot z \cdot r^2}{(r^2 + z^2)^{5/2}} - \frac{z \cdot (1 - 2 \cdot \nu)}{(r^2 + z^2)^{3/2}} \right] dr d\alpha \quad (7.3)$$

$$\varepsilon_z = \frac{1}{E} [\sigma_z - \nu \cdot (\sigma_r + \sigma_\theta)] \quad (7.4)$$

From static loading theory (equations 7.2, 7.3 and 7.4), relations between moduli and strains, thus, displacements, should be similar. Therefore, on one hand, E_{LFWD} obtained from *SP* profile may be underestimated or, on the other hand, E_{LFWD} obtained from *ISAC* profile may be overestimated.

To this end, observed differences can be explained by different contact stress distributions between the plate and *ISAC* or *SP* materials. Moduli calculus was carried out considering uniform contact stress distribution corresponding to flexible plate. However, elastic half-space theory predicts inverse parabolic distribution if a rigid plate is considered, although a parabolic stress distribution may be considered depending on material type being tested (Terzaghi, 1943). The author suggested inverse parabolic distribution on cohesive soil and parabolic distribution on granular soil. Indeed, *ISAC* material is a granular material where suction does not play significant role, thereby parabolic stress distribution seems to be more suitable. As so, modulus and in-ground strains were computed considering uniform and parabolic stress distribution given by equations 7.5 and 7.6, respectively (Mooney and Miller, 2009). Results are summarized in Table 7.14.

$$q(r) = \frac{\sigma \cdot R}{2 \cdot (R^2 - r^2)^{0.5}} \quad (7.5)$$

$$q(r) = \frac{2 \cdot (R^2 - r^2) \cdot \sigma}{R^2} \quad (7.6)$$

A $E_{LFWD} = 112$ MPa is obtained on *ISAC* material, corresponding to approximately 2.1 times E_{LFWD} obtained from *SP*, which is similar to the obtained displacement relation. Further, relation between theoretical strains considering parabolic contact stress for *ISAC* and uniform contact stress for *SP* is approximately 2.2. Therefore, it seems that parabolic contact stress distribution is more suitable to *LFWD* tests performed in *ISAC* material when compared to *LFWD* results obtained from *SP* material considering uniform stress distribution below the plate.

Table 7.14: In-ground peak displacements computed from accelerometers signals and respective theoretical and estimated strains at capping layer during *LFWD* tests

Section	<i>ISAC</i>		<i>SP</i>
Accelerometer	Ac top	Ac bot	Ac bot
Depth [m]	0.22	0.47	0.45
σ below the plate [MPa]	215		212
Peak displacement, u (μm)	319	69	145
Peak velocity, \dot{u} [$\times 10^{-3} \text{m.s}^{-1}$]	91	27	35
	Uniform stress distribution		
E_{LFWD} [MPa]	84		54
Theoretical strain [$\times 10^{-6}$]	1086	353	584
Estimated V_s [m.s^{-1}]	110	110	89
Estimated V_p [m.s^{-1}]	230	230	184
Estimated strain, $\frac{\dot{u}}{V_p}$ [$\times 10^{-6}$]	394	117	190
	Parabolic stress distribution		
E_{LFWD} [MPa]	112		
Theoretical strain [$\times 10^{-6}$]	969	270	
Estimated V_s [m.s^{-1}]	128	128	89
Estimated V_p [m.s^{-1}]	266	266	184
Estimated strain, $\frac{\dot{u}}{V_p}$ [$\times 10^{-6}$]	341	101	190

Vibration induced strain levels were also evaluated and are given in Table 7.14. Assuming elastic plane wave propagation (reasonable for vertical wave propagation along test vertical alignment), peak axial strain levels were estimated from the relationship between estimated velocity and compressional wave velocity ($\frac{\dot{u}}{V_p}$) derived from the specific and characteristic impedance in combination with Hooke's law. Estimated velocity (\dot{u}) is computed by integration of acceleration signal, whereas compressional wave velocity (V_p) is estimated from equations 7.7 and 7.8. A $\nu = 0.35$ is used throughout. Axial strain levels were in the range of 10^{-6} at sensors depth. Vibration induced strain levels reflects dynamic portion of strain response and represents approximately 25–27% of total strain resulting from static response plus dynamic portion.

$$E = 2 \cdot \rho \cdot V_s^2 \cdot (1 + \nu) \quad (7.7)$$

$$\nu = \frac{0.5 \cdot \left(\frac{V_p}{V_s}\right)^2 - 1}{\left(\frac{V_p}{V_s}\right)^2 - 1} \quad (7.8)$$

To sum up, strains measurements from both profiles (356 and 361×10^{-6}) and corresponding moduli (60 and 62 MPa) appears to be consistent since relations between measures are similar. In contrast, though computed displacements from acceleration data (145 and $69 \mu\text{m}$) and corresponding moduli (54 and 84 MPa) appears to be consistent, respective relations between measures, 2.1 and 1.6 , indicate that modulus obtained on *ISAC* may be underestimated. Considering parabolic stress distribution below the plate, relation between moduli is found to be 2.2 . Therefore, it seems that parabolic stress distribution is more appropriate for *ISAC* material when presenting high stiffness.

FWD

The procedure adopted for *FWD* tests was the same described earlier for *LFWD*. *FWD* tests were performed at surface capping layer at the vertical alignment of strain sensors and accelerometers in both profiles. Tests were carried out using a circular loading plate with a diameter of 450 mm and consisted in impact loads from three drop heights. Only one impact by each drop height was performed. It should be noted that *FWD* test in *SP* profile was performed after *LFWD* test, while *FWD* in *ISAC* profile test was carried out after roller drum stationary vibration.

Figure 7.28 shows the force versus displacement data gathered by the equipment. Three force levels of approximately 20 , 30 and 47 kN are generated. Good agreement between plate displacements from both tests performed on *SP* is verified. In contrast, plate displacements measured during tests on *ISAC* material differs significantly. In fact, plate displacements obtained from *FWD* carried out at strain vertical alignment are almost twice the corresponding value obtained from *FWD* carried out at accelerometer vertical alignment. This result was unexpected since tests were spaced of 0.50 m. This may be attributed to additional compaction during drum tests, since they were performed before *FWD* tests. Plate displacements obtained from *FWD* on *ISAC* profile are about a half and a third of plate displacements measured on *SP* material, which denotes lower deformability from *ISAC* material. Further, it is noteworthy that *ISAC* material presents almost no viscosity.

Figure 7.29 illustrates the strain time histories during *FWD* testing on *ISAC* and *SP* profiles. In Table 7.15 is summarized data obtained from these tests. In both profiles strains increased with increasing stress applied by *FWD* device corresponding to higher drop heights. Unexpectedly strains obtained from *ISAC* profile are greater than obtained from *SP* profile, since *ISAC* profile was supposed to have greater stiffness. In fact, *FWD* moduli obtained in *ISAC* profile were almost two times the ones obtained in *SP* profile. Theoretical strains were computed from static loading theory in order to understand these results. Load pulse duration was about 33 ms, whereas the calculated travel times are 4.0 to 7.5 ms, corresponding to four to seven times less, thereby, static loading theory can be applied. Loading stresses were similar in both tests, thus, through the equations 7.2, 7.3 and 7.4, lower strains levels are expected for profile with

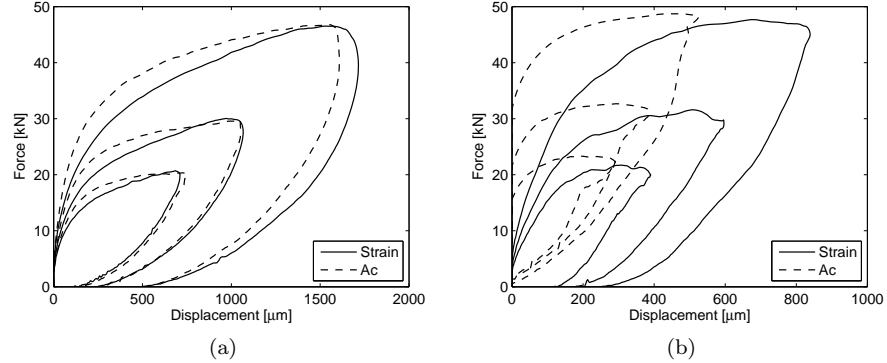


Figure 7.28: Average *FWD* force–displacement loops from impacts at surface capping layer on sensors vertical alignment at: (a) *SP* profile; (b) *ISAC* profile

higher modulus. However, the inverse behaviour was found. Though *ISAC* profile presented higher modulus, higher strains were measured. This behaviour is not consistent with theory and reasonable explanation was not found.

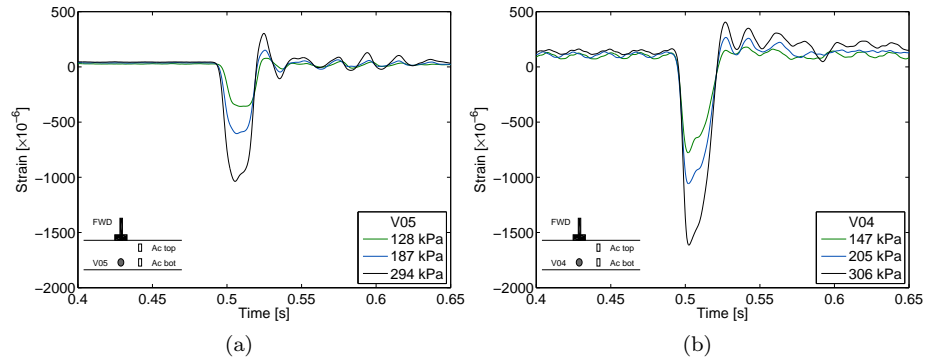


Figure 7.29: Strains measurement during *FWD* test in: (a) *SP* profile; (b) *ISAC* profile

The strain response stress ratio ($\varepsilon_{z=0.43/0.45}/\sigma$) due to all loadings was computed in order to eliminate response stress dependence. Values 3.16, 3.50 and 3.70 were found from *SP* profile, whereas 6.41, 5.92 and 5.85 were obtained from *ISAC* profile. As one can see, values for *SP* material seems to indicate that strain response at $z = 0.43$ m is dependent on stress applied, where an increase on stress applied results in strain softening response. This finding demonstrates non linear behaviour of *SP* material at the evaluated depth range for in situ state conditions and stress levels applied. Regarding *ISAC* material, though strain response seems to be non linear too, a hardening response is observed. These softening and hardening response of *SP* and *ISAC* material, respectively, may be explained from the stress dependency of soil stiffness. It is well documented

Table 7.15: Peak in-ground strains measurements obtained from *FWD* tests carried out on *SP* and *ISAC* profiles

Material profile	Measurement depth [m]	Stress below the plate [kPa]	E_{FWD} [MPa]	Peak strain [$\times 10^{-6}$]
<i>SP</i>	0.43	129	72	408
		187	60	655
		294	67	1087
<i>ISAC</i>	0.45	137	138	878
		199	132	1178
		300	141	1755

that soil stiffness increases with increasing confining stress and decreases with increasing shear stress. Within each impact due to falling weight, the shear stress and confining stress increases. From the previous results it seems that the decrease of stiffness due to increasing shear stress overlaps the increasing confining stress effect for *SP* material, resulting in a softening response with increasing stress. On the contrary, for *ISAC* material, the confining stress effect seems to superimpose to the increase of shear stress, leading to a hardening effect.

Owing to *FWD* tests carried out at accelerometers vertical alignment, acceleration time histories and computed displacements are illustrated in Figure 7.30. Also here acceleration and displacement data are not provided ever acceleration exceeded the measurement range of the sensor. In Table 7.16 is given acceleration and displacement peak data.

One can see that acceleration and displacement peaks increase with increasing applied stress and decrease with increasing depth. Acceleration peaks obtained from in-ground accelerometers in *SP* profile were higher than the ones obtained from in-ground accelerometers in *ISAC*. In *SP* profile, ac_{p-}^{SP} exceeded ac_{p+}^{SP} at both depths and the difference between peaks increased with increasing drop height. Conversely, in *ISAC* profile ac_{p+}^{ISAC} exceeded ac_{p-}^{ISAC} at both sensors, with exception to result from accelerometer at $z = 0.45$ m corresponding to the 3rd drop height. Nevertheless, difference between peaks decreased with increasing drop height. Likewise to acceleration data from *LFWD* tests, one can see that peak from top accelerometer lags peak from bottom accelerometer due to wave propagation through profile.

A reduction of about 53% between top and bottom (0.22 m and 0.47 m) peak displacements is obtained in *ISAC* profile for all stress levels. With regards to *SP* profile, results available denotes a reduction of 66% between displacements obtained at $z = 0.10$ m and $z = 0.45$ m. Comparison between displacements from both profiles denote a different trend from strain results. Displacements on *SP* at $z = 0.45$ m ranged between 1.9 to 2.6 times the correspondent observed on *ISAC* at $z = 0.47$ m, despite stress applied by equipment does not differ significantly. These results indicate higher stiffness from *ISAC* profile, which is testified by higher moduli, about three times greater than corresponding moduli from *SP* profile.

Taking into account conclusions regarding stress distribution below *LFWD* plate in previous section, the relations between displacements and moduli due to *FWD* tests were investigated too. In Tables 7.17 and 7.18 are given the

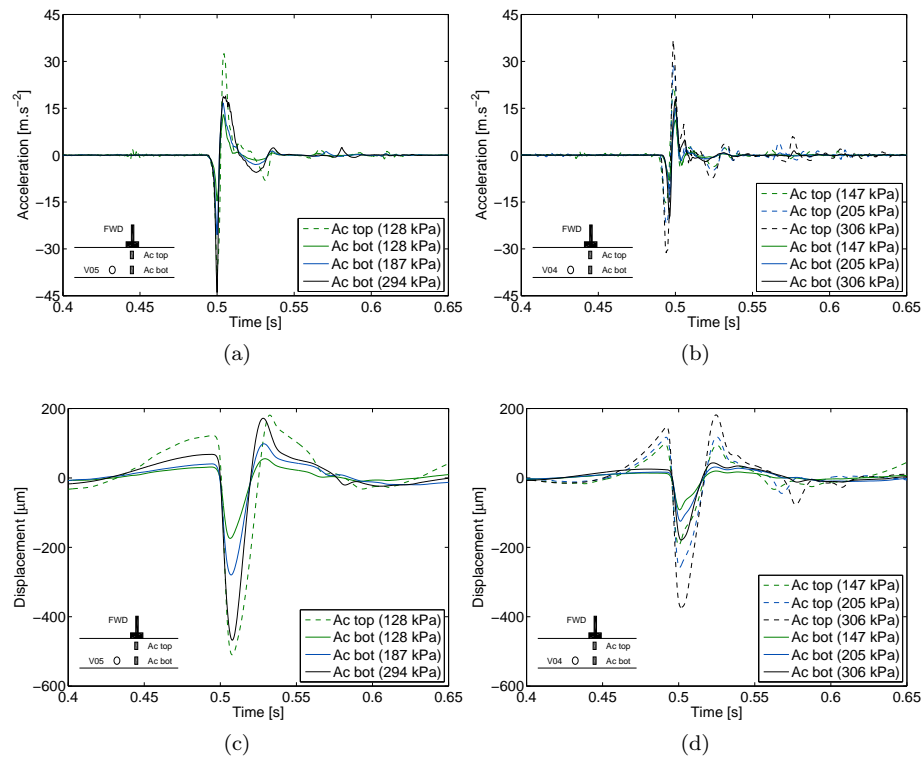


Figure 7.30: Vibrations measurement during *FWD* test. Computed displacements from in-ground accelerometers in: (a) *SP*; (b) *ISAC*; Strains from in-ground strain gauges in: (c) *SP*; (d) *ISAC*

results from this iteration. If a parabolic stress distribution is considered relation between moduli increases to 3.9, 4.0 and 4.3, which is greater than the ones found for uniform stress distribution. As so, different relations are found regarding displacements and moduli gathered from both profiles.

In Tables 7.17 and 7.18 is also given vibration induced strain levels. Once again, axial strain levels were in the range of 10^{-6} at sensors depth. The dynamic portion was estimated and values of approximately 25–29% of total strain were found. Note that this values are similar to the ones found from *LFWD* results.

Portancemètre

Strains and acceleration recorded during the pass of Portancemètre are presented in Figures 7.31 and 7.32. As described in Chapter 2, Portancemètre operates at typical speed of 1.0 m/s and excitation frequency of 35 Hz. Data was referenced to each in-ground sensor. The abscissa reflects the position of the Portancemètre, which is traveling left to right, thus, negative x indicate that Portancemètre is approaching the sensors while positive x indicate that Portancemètre is moving away from the sensors. The $x = 0$ position means that Portancemètre is in the vertical alignment of the sensor. While acceleration measurements reflects only cyclic forces generated by the vibrating wheel,

Table 7.16: Peak in-ground acceleration measurements and computed peak displacements obtained from *FWD* tests carried out on *SP* and *ISAC* profiles

Material profile	Measurement depth [m]	Stress below the plate [kPa]	E_{FWD} [MPa]	Peak acceleration [m.s ⁻²]		Peak displacement [mm]
				ac_{p+}	ac_{p-}	
<i>SP</i>	0.1	129	67	34	37	0.507
		129	67	13	14	0.173
	0.45	187	70	17	25	0.278
		294	72	20	43	0.463
<i>ISAC</i>	0.22	147	199	22	15	0.193
		205	209	30	21	0.258
		306	230	38	30	0.361
	0.47	147	199	11	8	0.091
		205	209	15	12	0.124
		306	230	18	20	0.175

Table 7.17: In-ground peak displacements computed from accelerometers signals and respective theoretical and estimated strains at the top of capping layer during *FWD* tests

Section	<i>SP</i>		<i>ISAC</i>	
Depth [m]	0.10		0.22	
Drop	1 st	1 st	2 nd	3 rd
σ below the plate [MPa]	128	147	205	306
Displacement, u [μm]	507	193	258	361
Velocity, \dot{u} [$\times 10^{-3}\text{m.s}^{-1}$]	121	58	78	109
	Uniform stress distribution			
E_{FWD} [MPa]	67	199	209	230
Theoretical strain [$\times 10^{-6}$]	1770	447	592	803
Estimated V_s [m.s ⁻¹]	99	170	174	183
Estimated V_p [m.s ⁻¹]	206	354	363	380
Estimated strain, $\frac{\dot{u}}{V_p}$ [$\times 10^{-6}$]	589	165	215	286
	Parabolic stress distribution			
E_{FWD} [MPa]		265	279	307
Theoretical strain [$\times 10^{-6}$]		468	619	841
Estimated V_s [m.s ⁻¹]		196	201	211
Estimated V_p [m.s ⁻¹]		409	419	440
Estimated strain, $\frac{\dot{u}}{V_p}$ [$\times 10^{-6}$]		143	186	248

Table 7.18: In-ground peak displacements computed from accelerometers signals and respective theoretical and estimated strains at the bottom of capping layer during *FWD* tests

Section	<i>SP</i>			<i>ISAC</i>		
Depth [m]	0.45			0.47		
Drop	1 st	2 nd	3 rd	1 st	2 nd	3 rd
σ below the plate [MPa]	128	187	294	147	205	306
Displacement, u [μm]	173	278	463	91	124	175
Velocity, \dot{u} [$\times 10^{-3}\text{m.s}^{-1}$]	42	63	96	25	35	50
Uniform stress distribution						
E_{FWD} [MPa]	67	70	72	199	209	230
Theoretical strain [$\times 10^{-6}$]	534	748	1141	197	261	355
Estimated V_s [m.s^{-1}]	99	101	102	170	174	183
Estimated V_p [m.s^{-1}]	206	210	213	354	363	380
Estimated strain, $\frac{\dot{u}}{V_p}$ [$\times 10^{-6}$]	204	301	452	70	96	131
Parabolic stress distribution						
E_{FWD} [MPa]				265	279	307
Theoretical strain [$\times 10^{-6}$]				161	213	289
Estimated V_s [m.s^{-1}]				196	201	211
Estimated V_p [m.s^{-1}]				409	419	440
Estimated strain, $\frac{\dot{u}}{V_p}$ [$\times 10^{-6}$]				61	83	113

strain measurements reflect both the static weight of the equipment and the cyclic forces. The effects of overburden and previous tests have been removed so the strain measurements presented here are due to the Portancemètre alone, i.e., strains at the beginning are equal to zero.

Figure 7.31 illustrate total strains measurements during Portancemètre pass on *SP* and *ISAC* profiles and respective cyclic portion. Peak strains are summarized in Table 7.19. Both total and cyclic strains in *ISAC* profile were about twice than those obtained in *SP* profile. This behaviour was unexpected since Portancemètre performed in each profile showed greater deformability of *SP* profile. The ratio between cyclic and total strains were similar, about 30%.

Table 7.19: Peak in-ground strains measurements obtained from Portancemètre tests carried out on *SP* and *ISAC* profiles

Material profile	Measurement depth [m]		E_{Port} [MPa]	Peak strain [$\times 10^{-6}$]
<i>SP</i>	0.43	Total	84	1107
		Cyclic		335
<i>ISAC</i>	0.45	Total	102	2104
		Cyclic		690

It is worth noting that in *ISAC* profile, material immediately in front of the vibrating wheel experiences vertical extension, whereas in *SP* material this behaviour is unnoticeable. This phenomenon was also observed by Mooney and Rinehart (2009) in a gravelly sand test bed (30% gravel, 10% fines) and almost unnoticeable in a more fine-grained material. The authors refer to it as a *bow*

wave phenomenon which is due to the traveling nature of the vibrating loading. Further, Figure 7.31 reveals no plastic strain resulting from Portancemètre test on *ISAC* profile, whereas on *SP* profile small plastic strain was observed. At strain sensors depth the width of the zone of material influenced by the equipment is about 0.80–0.90 m at *ISAC* profile and 0.90–1.0 m at *SP* profile.

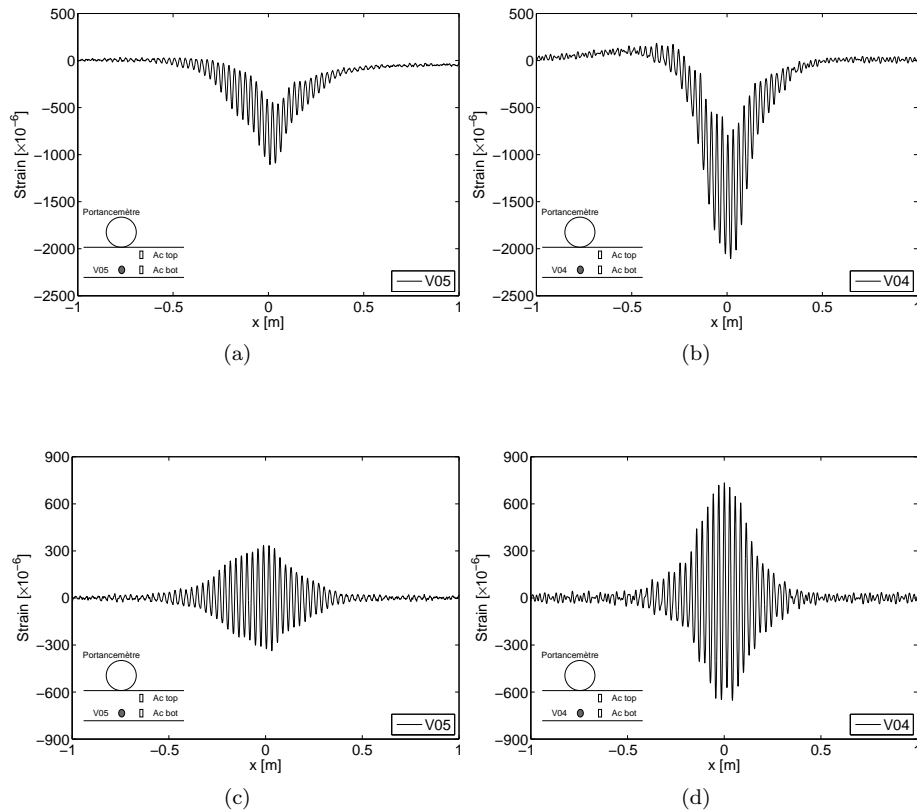


Figure 7.31: Total and cyclic strain data from strain gauges V05 and V04 during pass of Portancemètre in: (a) and (c) *SP* profile; (b) and (d) *ISAC* profile

Concerning to dynamic response given by acceleration time histories, acceleration peak decreases with depth, as illustrated in Figures 7.32a and 7.32b. Moreover, ac_{p+} exceeded ac_{p-} at both sensors located at top of capping layer. Differences between peaks decreased for bottom accelerometers, being almost the same. Double integration on frequency domain was conducted on data gathered from the accelerometers in order to compute the approximated displacements (see figs. 7.32c and 7.32d). Negative values represent downward displacement. In Table 7.20 is given peak accelerations and displacements.

As observed previously for acceleration data, displacements are higher near the point of load application and decrease as depth increases. A reduction of 70% and 75% between top and bottom peak displacements is verified, corresponding to *SP* and *ISAC* profiles, respectively. Further, displacements at $z = 0.45$ m in

Table 7.20: Peak in-ground acceleration measurements and computed peak displacements obtained from Portancemètre tests carried out on *SP* and *ISAC* profiles

Material profile	Measure-ment depth [m]	E_{Port} [MPa]	Peak accele-ration [m.s ⁻²]		Peak displace-ment [mm]
			ac_{p+}	ac_{p-}	
<i>SP</i>	0.10	84	21	13	0.281
	0.45		5	4	0.085
<i>ISAC</i>	0.22	102	17	13	0.199
	0.47		4	4	0.049

SP profile is about 1.7 times the corresponding displacement obtained on *ISAC* profile. This relation appears to reflect moduli obtained on both profiles, E_{Port} from *ISAC* profile being about 1.2 times E_{Port} from *SP* profile. Regarding to displacements at depth $z = 0.10$ m, displacements obtained in *SP* profile are greater 1.3 times than the ones obtained in *ISAC* profile at $z = 0.22$ m. This trend is contrary to the observed through strain data.

It is interesting noting that displacement computed from bottom accelerometer on *SP* slightly decreased when Portancemètre loading is on vertical alignment of accelerometers. Displacements increased as Portancemètre approached, peaks at approximately 0.15 m away from sensor, slightly decreased to a local minimum when the roller was just above the sensor, increased as Portancemètre was moving away, peaks again at approximately 0.15 m away from the sensor, and decreased beyond this point. Beneath loading shear stress and strain are theoretically zero or very small compared with normal stresses and strains (Johnson, 1987). Hence, it seems that strains induced by Portancemètre at depth $z = 0.45$ m when was approaching and moving away from the sensor results from shear and normal strains acting together.

Roller drum

Vibrations measurements induced by vibratory roller were also carried out on both *SP* and *ISAC* profiles. A Hamm 3412 smooth drum vibratory roller was used during investigation. The total weight of the compactor is 12200 kg, with the static weight under the front drum and rear tires equal to 6705 kg and 5495 kg, respectively. The drum is 1.504 m in diameter and 2.140 m in width and houses an eccentric mass configuration that provides circular excitation at frequencies of 30 and 40 Hz. Manually set eccentric configurations provide eccentric static moments ranging between 256 and 215 kN and nominal amplitudes between 1.91 and 0.90 mm, respectively. The drum-frame connection configuration is different on the right and left sides and access to a non-rotating mount was only possible on the left side (see fig. 7.33).

Besides in-ground instrumentation, one accelerometer was embarked on the roller in order to monitor its behaviour during vibrations measurements at this stage. This was embarked on the non-rotating mount on the left side where access was available. Taking into account the asymmetry of the drum, another accelerometer was placed on the top and at the middle of the drum in order to investigate the influence of sensor location. This was carried out during drum

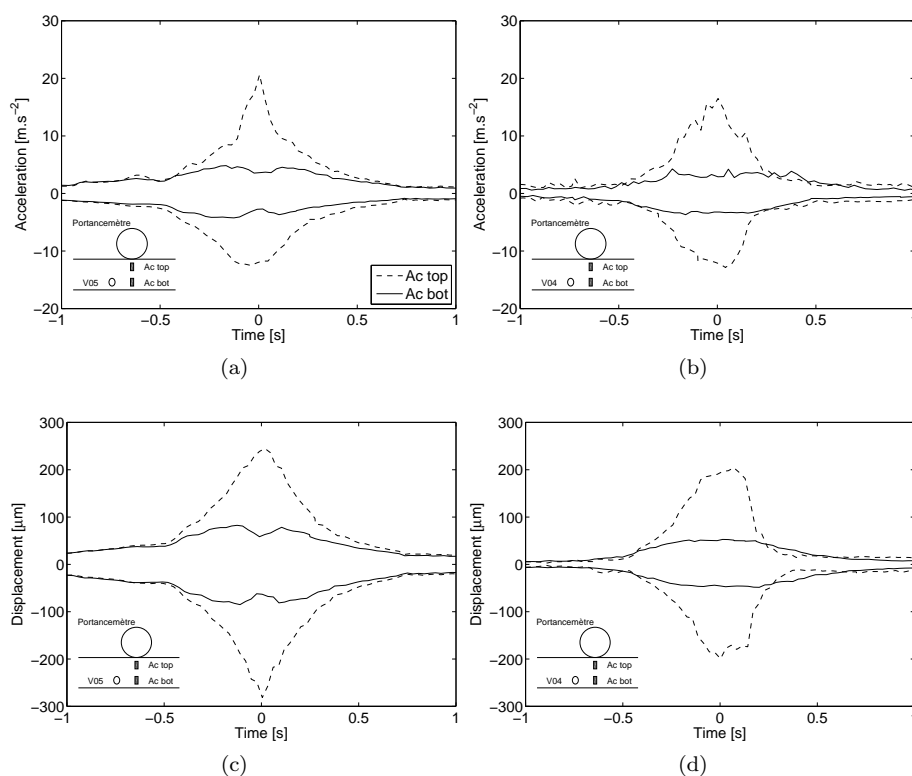


Figure 7.32: Vibrations measurement during Portancemètre test. Acceleration time histories from in-ground accelerometers in: (a) *SP*; (b) *ISAC*; Computed displacements in: (c) *SP*; (d) *ISAC*

vibration on *ISAC* profile. The characteristics of these accelerometers are given in Table 7.21.

Table 7.21: Sensors characteristics used for vibration measurements

Designation	Type	Sensibility [V/g]	Measurement range [g]	Frequency range [Hz]
Roller accelerometers	Vibra Metrics 1018	0.1	± 500	3 to 10000

Two types of tests were performed on *SP* test bed. Firstly, measurements of in-ground vibrations were carried out during the pass of the vibrating roller. Drum vibration was not monitored during this test. Secondly, the roller was set in place in order to the drum apply vibratory load above accelerometers and remained stationary during vibration. The drum was allowed to apply vibratory loading during at least 4 seconds. The eccentric configuration was set in order to provide the lower eccentric static moment at the beginning of record. Then, eccentric static moment was manually increased by the operator until roller drum become to translate laterally. Therefore, for the sake of comparison of

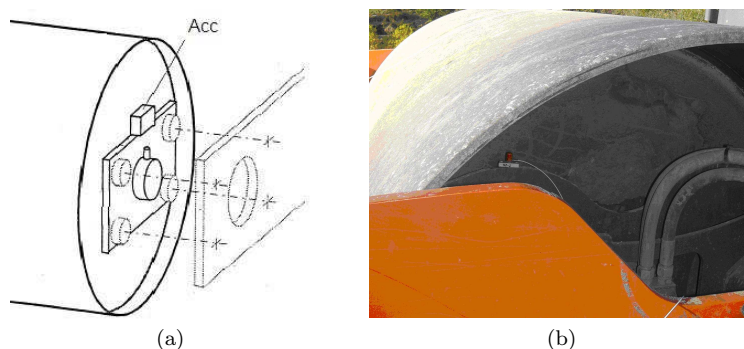


Figure 7.33: Accelerometers embarked on roller drum: (a) scheme; (b) instrumentation

tests conducted in each profile, it should be bear in mind that each test did not had the same eccentric static moment time history.

In Figure 7.34 is shown the in-ground total and cyclic strain response, as well as, the acceleration and approximated displacements response during vibrating roller pass. In Table 7.22 peak data is summarized. Likewise to Portancemètre results, the effects of overburden and previous tests have been also removed. Again, data was referenced to each in-ground sensor and abscissa reflects the position of the roller drum. From strain response (figs. 7.34a and 7.34b) one can see that cyclic response represents 98% of total strain response, which indicates that drum remained in contact with the material during compaction. No plastic strain was observed after roller pass. At sensor depth ($z = 0.43$ m) the width of the zone of material influenced by the roller is about 0.70–0.80 m.

Table 7.22: Peak in-ground strains and accelerations measurements and computed displacements obtained during drum pass over *SP* capping layer

Meas- urement depth [m]	Peak strain [$\times 10^{-6}$]	Peak acceleration [$\text{m}\cdot\text{s}^{-2}$]		Peak dis- placement [mm]
		ac_{p+}	ac_{p-}	
0.43	Total	1903		
	Cyclic	1873		
0.10		32	49	1.100
0.45		21	18	0.700

Owing to dynamic response given by acceleration histories (fig. 7.34c), acceleration peak decreases with depth. A greater difference between positive and negative peaks acceleration was observed for sensor near surface, where negative peak is greater than positive peak. On the contrary, positive peak acceleration given by bottom sensor is greater than negative peak. This fact denotes high non linear behaviour (Mooney *et al.*, 2005). Note that results show lower difference between negative and positive peaks, which tends to linear behaviour response. Approximated displacements were computed through double integration on frequency domain and are illustrated in Figure 7.34d. As observed previously for acceleration data, displacements are higher near the point of load application

and decrease as depth increases. A reduction of 60% between top and bottom displacement is verified.

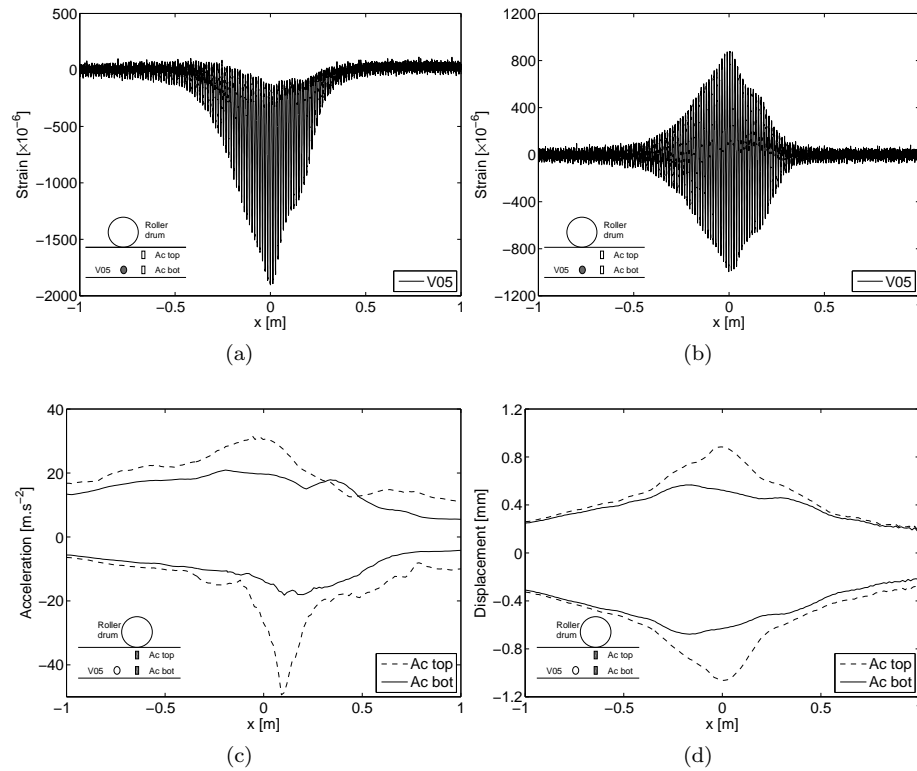


Figure 7.34: Vibration response from in-ground sensors on *SP* test bed during vibrating roller pass: (a) total strain response; (b) cyclic strain response; (c) acceleration response; (d) approximated displacements

The time and frequency content of acceleration responses on *SP* test bed due to drum stationary vibratory loading are presented in Figure 7.35, as well as approximated displacements, which were determined from acceleration data through double integration in the frequency domain. From the time history acceleration data, peak values were gleaned for upward and downward in vertical direction and are presented in Figure 7.35a. Following a positive down sign convention, peak positive acceleration is downward and occurs when the drum is in the highest point in its trajectory. Conversely, peak negative acceleration is upward and occurs when the drum is at its lowest point.

Focusing on frequency content, one can see that excitation frequency is about 19 Hz. The analysis of the drum acceleration time history presented in Figures 7.35c and 7.35d corroborates the results in frequency domain. Indeed, 19 Hz is about half of the operation frequency of the roller, which ranges between 30 and 40 Hz. As so, drum operating in periodic loss of contact, specifically, operating in double jump (Adam, 1996), was set as hypothesis. However, it is worth noting that frequency content covers low to high eccentric static moments. Although double jump operating mode is rather probable for high eccentric static

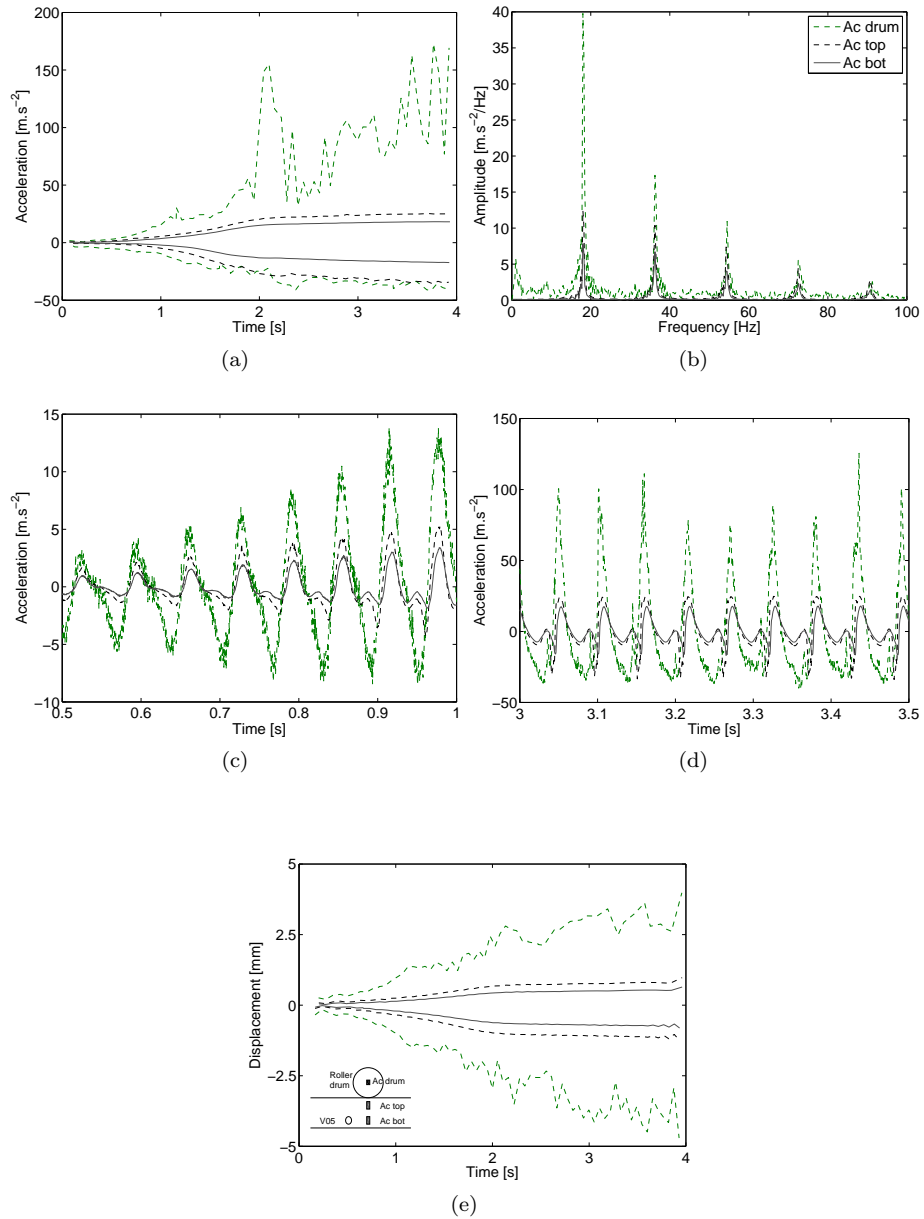


Figure 7.35: Vibration response on *SP* test bed during drum vibratory loading: (a) peak acceleration time history; (b) acceleration frequency spectrum; (c) acceleration time history; (d) acceleration time history; (e) approximated displacements

moments, for low eccentric static moments, probability is lower. Nevertheless, continuous compaction control still may be applied in double jump operating mode (Adam, 1996). Taking into account the strain results during roller pass, it is believed that roller drum was in contact with the ground during vibration.

Another explanation might be an improperly operation of the excitation system. These hypothesis could not be confirmed since the roller was no longer available at the time of this analysis.

Owing to the acceleration time history on *SP* profile illustrated in Figure 7.35a, acceleration peak decreases with depth. Differences between peak positive (acd_{p+}) and negative accelerations (acd_{p-}) of the accelerometer embarked on the roller drum yields non linear behaviour of the coupled drum–soil system. Note that acd_{p-} exceeds acd_{p+} for lower eccentric static moments, while the opposite is observed for greater eccentric static moments. The nonlinearity of the coupled roller drum–soil system media distorts the output of a sinusoidal input forcing function. The distortion is manifested in harmonic content within drum vibration response spectra (Ewins, 2000; Mooney *et al.*, 2005), as can be observed from frequency content in Figure 7.35b.

Another behavioural characteristic from acceleration time history is worth noting. Beyond the 3 seconds, the acd_{p-} remains almost constant, despite increasing eccentric static moment. On the contrary, acd_{p+} fairly increased. Thus, surface deformation seems to remain almost constant, despite increasing vibration force. This is confirmed by the approximated displacements determined in frequency domain which remain almost constant beyond 3 seconds, as can be seen in Figure 7.35e.

Regarding in–ground accelerometers, differences between acd_{p+} and acd_{p-} of the top accelerometer ($z = 0.10$ m) are noticeable for higher eccentric static moment and remained almost constant beyond 2.5 seconds. No significant differences were seen for lower eccentric static moments (fig. 7.35c). On the other hand, acd_{p-} (32 m.s^{-2}) exceeds acd_{p+} (24 m.s^{-2}) in 33% for higher eccentric static moments (fig. 7.35d). This seems to indicate non linear behaviour at $z = 0.10$ m for lower vibrations forces, while increasing vibration forces yields increasing non linear behaviour. Concerning to acceleration at $z = 0.45$ m, differences between acd_{p+} and acd_{p-} are unnoticeable during increasing of eccentric static moment, which seems to reflect linear behaviour. Along with the other sensors, peak accelerations from accelerometer at $z = 0.45$ m remain constant for higher eccentric static moment.

These findings indicate non linear behaviour below the drum for the applied eccentric static moments during vibration on *SP* test bed. Further, non linear behaviour at depth $z = 0.10$ m for higher vibration forces is observed, while at depth $z = 0.45$ m linear behaviour seems to be present for the applied eccentric static moments. In addition, for greater eccentric static moments, drum peak negative acceleration and in–ground peak acceleration remained almost constant, i.e., deformation remained almost constant (see fig. 7.35e). This indicates non linear relationship between vibration force applied by the drum and deformation below the drum and in depth.

For *ISAC* profile only stationary vibration test was performed. Time and frequency content of acceleration responses due to drum vibratory loading are presented in Figure 7.36, as well as approximated displacements computed from acceleration data. The frequency content of the drum acceleration presented in Figure 7.36b given by either accelerometer on the left side of the drum or the accelerometer placed on the top at the middle shows a peak amplitude about 19 Hz indicating that drum was operating at this frequency. The acceleration time history illustrated in Figure 7.36e confirms this finding.

Concerning to the drum acceleration measurement, Figure 7.36a presents

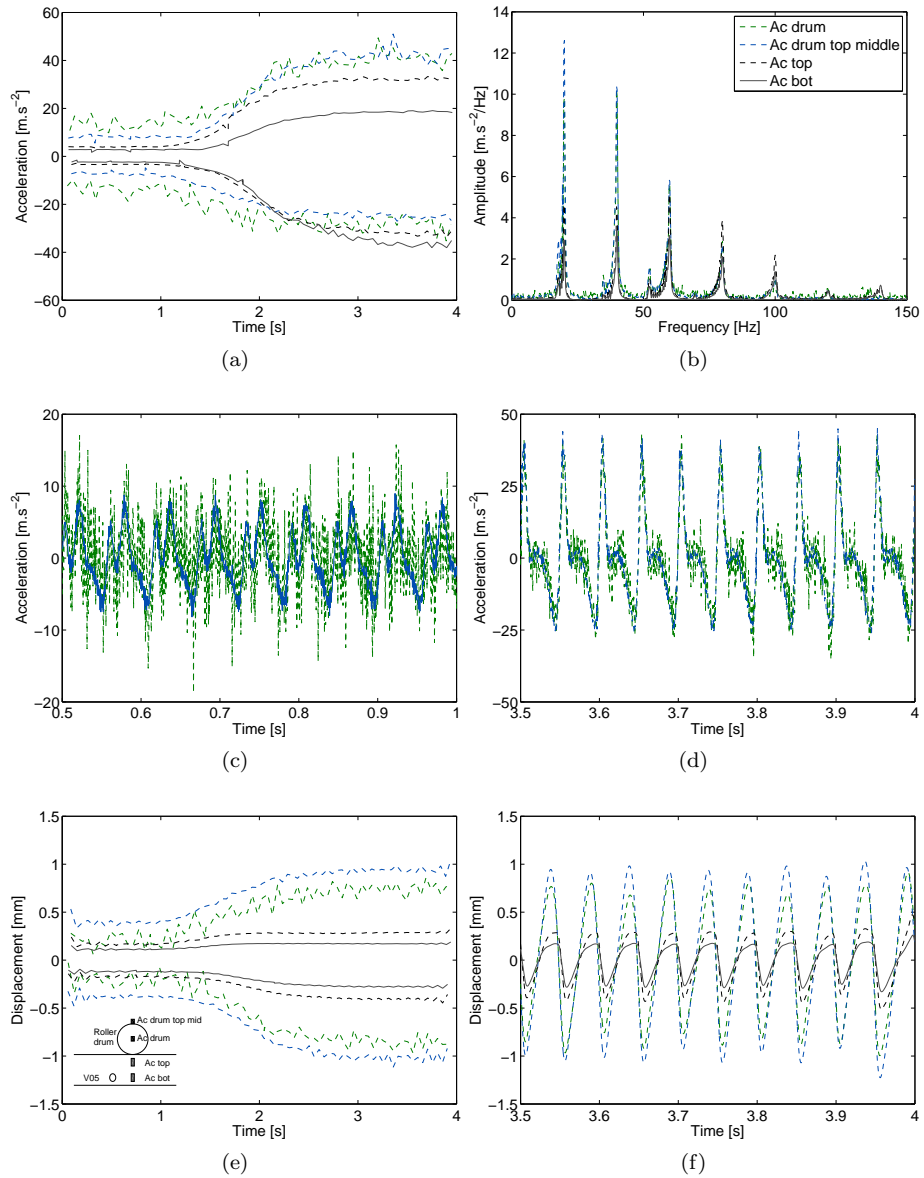


Figure 7.36: Vibration response on *ISAC* test bed during drum vibratory loading: (a) peak acceleration time history; (b) acceleration frequency spectrum; (c) and (d) acceleration time history; (f) and (e) approximated displacements

peak accelerations given by accelerometers placed on the left side of the drum and at the top at the middle of the drum. One can see that acceleration from both sensors slightly differs. Acceleration given by accelerometer located at the left side is greater than acceleration given by the sensor located at the top at the middle of the drum for lower eccentric static moments and tends to be almost the same for higher eccentric static moments. Since the acceleration level during

tests carried out on *ISAC* afterwards were close to the values reached for higher eccentric static moments in this measurement, the location of the accelerometer has almost no influence on acceleration results. However, from computed displacements illustrated in Figure 7.36e, one can see that displacement determined from accelerometer located on the left side of the drum is about 85% of the displacement exhibited on the top and at the middle of the drum. It is worth noting that signal from accelerometers placed on the left side of the drum on the non-rotation mount showed higher noise levels, as can be confirmed from drum acceleration time and frequency content in Figures 7.36b and 7.36d.

In contrast to the observed in measurements carried out in *SP* test bed for lower eccentric static moments, differences between acd_{p+} and acd_{p-} given by sensors embarked on the roller drum were unnoticeable till acceleration level about $\pm 20 \text{ m.s}^{-2}$, yielding, therefore, linear behaviour of the coupled drum-soil system. In Figure 7.36a can be seen that beyond this point, as acceleration level increases acd_{p+} becomes greater than acd_{p-} indicating non linear behaviour.

Acceleration measurements in depth at *ISAC* test bed showed a different trend from the results seen previously in *SP* test bed. Although for lower eccentric static moments acceleration peak decreases with depth, as expected, for greater eccentric static moments acd_{p+} follow the same trend, while acd_{p-} slightly increased with depth, as illustrated in Figure 7.36a. Regarding sensor located at $z = 0.22 \text{ m}$, differences between acd_{p+} and acd_{p-} were significant. On the other hand, despite no significant differences between peak accelerations given by accelerometer at $z = 0.45 \text{ m}$ were seen for the lowest eccentric static moments, acd_{p-} become greater with increasing eccentric static moment. This notwithstanding, the approximated computed displacements followed the normal trend, since a decreased with increasing depth is observed in Figure 7.36e. In fact, for the greatest eccentric static moment applied, approximated displacement at depths $z = 0.22 \text{ m}$ and $z = 0.45 \text{ m}$ were approximately 0.40 and 0.28 mm, corresponding to 47% and 33% of the surface displacement determined from accelerometer on left side of the drum (0.85 mm), as shown in Figure 7.36f, and a reduction of 30% between in-ground displacements.

From results obtained at *ISAC* test bed, differences between peak accelerations obtained with accelerometers located on the drum and at depth $z = 0.22 \text{ m}$ indicate non linear behaviour when applied eccentric static moments similar to the compaction process. On the contrary, results obtained from accelerometer located at $z = 0.45 \text{ m}$ indicate linear behaviour.

7.8.3 Phase One: Comparison between tests results

In Tables 7.23 and 7.24 are summarized data gathered during performance of different mechanical tests by material type, *SP* and *ISAC*, attempting to establish relation between in-ground measurements. Due to different loading nature, comparison will be conducted accordingly loading type, namely, impact loads (*LFWD* and *FWD*) and vibrating loads (Portancemètre and roller drum). Nevertheless, strain measurements from both profiles allow to conclude that tests are ordered by increasing induced strains, which seems to indicate that roller drum has the higher depth influence, whereas *LFWD* has the lowest.

Moreover, in-ground displacements obtained from acceleration measurements were consistent with profiles stiffness. Higher in-ground displacements were found regarding *SP* profile than in *ISAC* profile, which is consistent with lower

modulus obtained in the former than the latter. Hence, in-ground dynamic response reflect moduli obtained from dynamic tests performed at layer surface.

Table 7.23: In-ground peak strains, accelerations and computed displacements obtained during performance of different mechanical tests on *SP* capping layer

Tests	Displacement (accelerometers)			Strain gauges	
	$z = 0.10$ m [mm]	$z = 0.43$ m [mm]	E [MPa]	$z = 0.45$ m [$\times 10^{-6}$]	E [MPa]
<i>LFWD</i> *	212 kPa		54	356	62
<i>FWD</i> **	129 kPa	0.507	67	408	72
	187 kPa		70	655	70
	294 kPa		72	1087	67
Portan- cemètre	Total		84	1107	84
	Cyclic	0.281	0.085	670	
Roller drum	Total			1903	
	Cyclic	1.100	0.700	1873	

* Plate with 0.30 m diameter

** Plate with 0.45 m diameter

Table 7.24: In-ground peak strains, accelerations and computed displacements obtained during performance of different mechanical tests on *ISAC* capping layer

Tests	Displacement (accelerometers)			Strain gauges		
	$z = 0.22$ m [mm]	$z = 0.45$ m [mm]	E [MPa]	$z = 0.47$ m [$\times 10^{-6}$]	E [MPa]	
<i>LFWD</i> *	215 kPa	0.319	0.069	84	361	60
<i>FWD</i> **	147 kPa	0.193	0.091	199	878	138
	205 kPa	0.258	0.124	209	1178	132
	306 kPa	0.361	0.175	230	1755	141
Portan- cemètre	Total			102	2104	102
	Cyclic	0.199	0.049		1380	

* Plate with 0.30 m diameter

** Plate with 0.45 m diameter

Comparison between *LFWD* and *FWD* results

Prior to results analysis it should be noted that tests on *SP* profile were carried out ordered in the following way: *LFWD*, *FWD*, Portancemètre and roller drum. In contrast, tests on *ISAC* profile were carried out by the following order: *LFWD*, Portancemètre, roller drum and *FWD*.

Focusing on *SP* profile, it is noteworthy that moduli obtained from *LFWD* on strain and accelerometers vertical alignments spaced of 0.50 m are similar, as moduli obtained from *FWD* are similar too. To this end mechanical properties of this profile may be considered homogeneous. This conclusion is corroborated by relations between in-ground measurements given in Table 7.25. Displacement response stress ratio (\dot{u}/σ) and strain response stress ratio (ε/σ) were computed in order to eliminate response stress dependence.

Table 7.25: comparison of displacement and strain response stress ratio obtained from *LFWD* (300 mm loading plate diameter) and *FWD* (450 mm loading plate diameter)

Section	Sensor depth [m]	\dot{u}/σ		$\frac{\dot{u}/\sigma_{FWD}}{\dot{u}/\sigma_{LFWD}}$	ε/σ		$\frac{\varepsilon/\sigma_{FWD}}{\varepsilon/\sigma_{LFWD}}$
		<i>LFWD</i>	<i>FWD</i>		<i>LFWD</i>	<i>FWD</i>	
<i>SP</i>	0.43		1.35			3.16	
	and	0.68	1.49	2.19	1.68	3.50	2.08
<i>ISAC</i>	0.45		1.57			3.70	
	0.22		1.41				
		1.48	1.30	0.88			
			1.20				
	0.45		0.66			6.41	
	and	0.32	0.62	1.94	1.66	5.92	3.57
	0.47		0.58			5.85	

One can see that both \dot{u}/σ and ε/σ obtained at $z = 0.43$ m from *FWD* test is about twice (2.19 and 2.08) the corresponding value obtained from *LFWD* test. These relations are close to that predicted from homogeneous, isotropic, linear elastic theory considering a single modulus, which led to a $\frac{\varepsilon/\sigma_{FWD}}{\varepsilon/\sigma_{LFWD}}$ of 1.80. Nevertheless, relations between in-ground strains and displacements are similar showing, thereby, measurements consistency with both type of sensors. Further, one can see that both in-ground strains and displacements at bottom of the layer are higher due to *FWD* test, even though lower stress levels are applied concerning first and second drop heights. These results denote the greater depth influence from plate with high diameter. Indeed, taking into account homogeneous profile and considering a single modulus, theoretical approach (equations 7.2, 7.3 and 7.4) corroborate these results. To this end, even though moduli obtained from *LFWD* and *FWD* carried out on *SP* profile differs, in-ground measurements with both strain gauges and accelerometers show consistency with theoretical approach considering a single modulus. As so, this results highlight the importance of tests methods calibration to a reference test.

With regards to *ISAC* profile the same analysis was attempted. However, significant *LFWD* and *FWD* moduli is verified for both vertical alignments. This is probably due to roller drum stationary vibration which was carried out between *LFWD* and *FWD* tests and may have induced significant differences on profile mechanical behaviour. Moreover, even though tests were conducted on spots spaced 0.50 m, moduli noticeably differs and, thereby, homogeneity can not be assumed. To this end, theoretical approach was conducted using moduli obtained from each test.

At *ISAC* section \dot{u}/σ obtained at $z = 0.22$ m from both tests were similar, only differing about 12%, yet higher values were obtained for *LFWD* test. The relation given by theoretical approach reveals a difference of about 40%. This notwithstanding, these results shows consistency. At bottom of the capping layer ($z = 0.45$ and 0.47 m) a $\frac{\dot{u}/\sigma_{FWD}}{\dot{u}/\sigma_{LFWD}}$ close to 2 was found. However, theoretical values revealed a relation close to 0.80. Moreover, at the same depth ε/σ_{FWD} was over three times greater than $\varepsilon/\sigma_{LFWD}$, while theoretical approach shows a relation of 0.80. These results are not consistent with static linear elastic theory.

As so, results from *ISAC* profile showed inconsistency with theoretical approach, which might be due to significant mechanical properties changes induced by stationary vibrating.

Comparison between Portancemètre and roller drum results

Strain measurements and computed displacements during roller drum and Portancemètre passes are directly compared only for *SP* profile, since measurements during roller drum pass on *ISAC* profile are not available.

Regarding strain response at bottom of *SP* capping layer, total peak strain induced by Portancemètre is about 58% of corresponding value induced by roller drum, whereas cyclic strain induced from the former represents 36% of the latter. These results demonstrates either greater depth of influence and greater stress applied by the roller drum. Further, it is interesting to note that at strain sensors depth the width of the zone of material influenced by Portancemètre is about 0.90–1.0 m, whereas the width of the zone of material influenced by the roller drum is on the order of 0.70–0.80 m.

Concerning to approximated vertical displacements higher differences are verified. At the top of capping layer ($z = 0.10$ m) peak negative displacements induced by Portancemètre were found to be 25% of displacements induced by roller drum, while at bottom of capping layer ($z = 0.45$ m) Portancemètre induced displacements are only 12% of the ones induced by roller drum. A similar dynamic in-ground response is found at higher depth. Since roller drum and Portancemètre wheel dynamic behaviour reflects dynamic in-ground response, this fact might indicate a good correlation between mechanical properties determined from instrumented rollers and Portancemètre. It is noteworthy that this relation is one third of the one found from strain results.

Though peak accelerations are not presented in Tables 7.23 and 7.24, comparison between measurements during vibration pass of both equipments are compared too. From top accelerometer ($z = 0.10$ m) peak negative and positive acceleration levels corresponding to Portancemètre pass were 13 and 20 m.s^{-2} , respectively, whereas values corresponding to roller drum pass were 49 and 32 m.s^{-2} . From bottom accelerometer ($z = 0.45$ m) peak negative and positive acceleration levels corresponding to Portancemètre pass were 4 and 5 m.s^{-2} , respectively, whereas values corresponding to roller drum pass were 18 and 21 m.s^{-2} . It is noteworthy that positive peak value is greater than negative peak value during Portancemètre pass, while the opposite is verified during roller drum pass. In contrast, at $z = 0.45$ m positive peak values are greater than negative peak values during both equipment passes. These features indicate different type of responses to vibrating load at $z = 0.10$ m and $z = 0.45$ m, which is probably due to stress-strain levels induced by each equipment. At greater depth differences between peak values decrease which might be associated to a stress-strain behaviour close to linear. The greater differences observed at lower depth are related to nonlinear stress-strain behaviour. Indeed, from strains measurement, roller drum seems to induce higher stresses.

7.8.4 Phase Two: Instrumentation

The setup adopted in this phase is illustrated in Figure 4.16b of Chapter 4. Either in-ground strain gauges and accelerometers placed at bottom of the

capping layer (at depth 0.45 m in Phase One) were left in same position, while the accelerometers in the top of the capping layer were replaced by new strain gauges. As so, the same setup was implemented for both *ISAC* and *CA40+SP* profiles, where two strain gauges were placed at 0.32 m from the surface of the base layer and another strain gauge and one accelerometer were located at 0.65 m depth. In addition, another strain gauge was buried in the capping layer belonging to profile *ISAC+SP* at 0.32 m depth from the surface of base layer. This operation was carried out after material placement and before roller passes.

Besides in-ground instrumentation, one accelerometer was embarked on the roller on the non rotating mount on the left side, in order to monitor its behaviour during compaction. However, high noise level was detected on the acceleration signal during pass 1. The author became aware of this problem and it was found to be due to a wire problem. Therefore, data from roller drum during this pass was discarded. In order to prevent malfunction of one sensor, two accelerometers (Ac drum 1 and Ac drum 2) were embarked on the drum during further passes (2 to 10). Frequency domain features were determined from the vibration histories of both accelerometers. Frequency content of the raw acceleration data of the drum collected from one of the passage of the roller is shown in Figure 7.37. From these figures some issues earn to be comment.

One can see from frequency content that accelerometer Ac drum 2 only shows peak magnitude for frequencies of interest, specifically the drum frequency and its harmonics. On the other hand, frequency content of accelerometer Ac drum 1 shows high magnitude for low frequencies, between 0 and 10 Hz. Due to the high noise level on raw data from accelerometer Ac drum 1, hereafter drum acceleration is referred as data gathered from accelerometer Ac drum 2. In addition, it can be seen that the drum excitation frequency is approximately 19 Hz, similarly to the verified in previous tests with the roller. This issue was reported in the previous section.

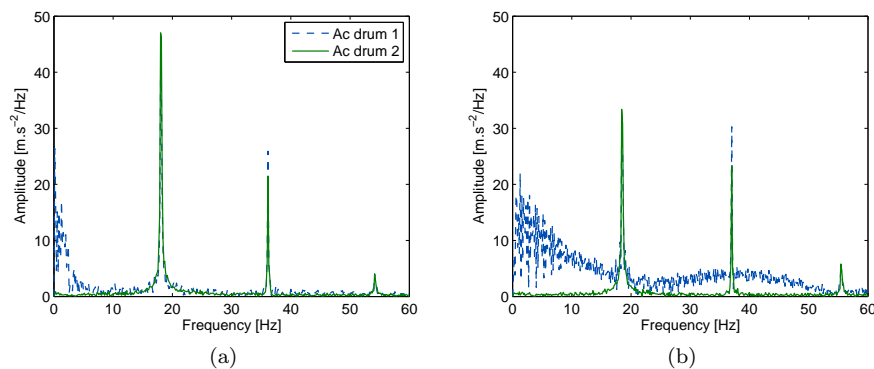


Figure 7.37: Frequency content of raw drum acceleration data collected from one of the pass of the roller on: (a) *CA40*; (b) *ISAC* base layers

The characteristics of either accelerometers embarked on the drum and in-ground accelerometers are given in Table 7.26. The characteristics of the drum vibratory roller were described in previous section.

Table 7.26: Sensors characteristics used for vibration measurements

Designation	Type	Sensibility [V/g]	Measurement range [g]	Frequency range [Hz]
in-ground accelerometers	PCB 623B13	1	± 5	0.5 to 1000
Roller accelerometers	Vibra Metrics 1018	0.1	± 500	3 to 10000

7.8.5 Phase Two: Test results

Drum vertical acceleration measurements

Drum vibration data as recorded continuously during compaction process on all three profiles in order to do not interfere with construction methodology. Data was gathered during 1, 2, 4, 6, 8 and 10 passes of vibrating roller. However, due to wire problems with accelerometer embarked on drum during pass 1 of the vibrating roller, as reported previously, only data from vibrating roller passes 2 to 10 will be presented.

Taking into account that roller had no positioning system and roller velocity was not recorded, in-ground sensors were used as reference to positioning the roller drum. In this way, roller velocity was estimated from time lag between the drum and wheels of the roller passing over strain gauges at each profile. Then, data was referenced to the middle of each set of in-ground sensors. Thus, data to be presented corresponds to the traveled distance by the roller over each set of in-ground sensors, i.e., over each different profile.

Time and frequency domain features were determined from the vibration histories. The abscissa in following time history figures reflects the position of the drum relative to in-ground sensors location. The roller is traveling left to right, thus, negative x indicate that the drum is approaching the sensors. The drum is directly above the middle of the set of sensors at $x = 0$ and positive x indicate that drum is moving away from the sensors.

Computed velocities show that instrumented vibratory roller was driven over base layer at varying speeds 0.18 to 0.30 m.s⁻¹. Peak vertical drum acceleration amplitudes measured at the three profiles (*ISAC*, *ISAC+SP* and *CA40+SP*) during each pass ranged from 15 to 30 m.s⁻² and are shown in Figure 7.38. Note that these acceleration levels are in the range of the ones given by Mooney *et al.* (2005) and Mooney and Rinehart (2007). As mentioned previously, double integration on frequency domain was conducted on data gathered from the accelerometers in order to compute the approximated displacements. In Figure 7.39 computed peak vertical displacements from accelerometer embarked on the drum are illustrated for the three profiles. Statistical data (average, standard deviation and coefficient of variation) regarding peak accelerations and displacements is given in Tables D.17 and D.18 in Appendix D.

Both drum acceleration and displacement decreases with increasing number of passes, as shown in Figure 7.40. Since, peak negative acceleration occurs when the drum is at the bottom in its trajectory, i.e., during rebound from the ground, hereafter peak negative vertical drum acceleration (acd_p^-) will be used as reference. Time domain analysis showed that as base layer was transformed from its placed state (near Pass 2) to a compacted state (Pass 10), average

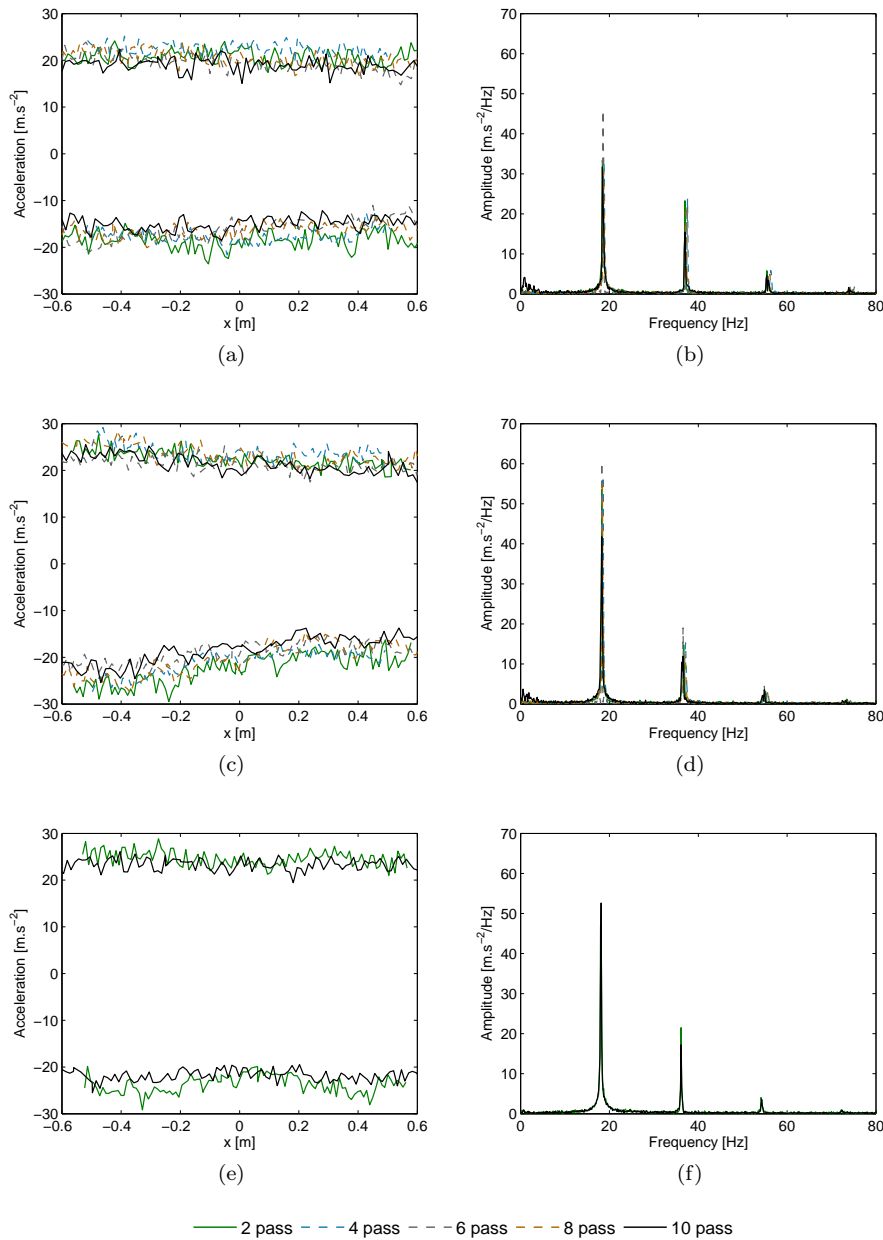


Figure 7.38: Time and frequency histories of vertical drum acceleration during successive passes of the roller compactor on the three profiles: (a) *ISAC*; (b) *ISAC+SP*; (c) *CA40+SP*

acd_p^- decreased about 19% on *ISAC* and *ISAC+SP* profiles and about 8% on *CA40+SP* profile. The same trend was found from computed displacements, however, reduction levels were about 14, 6 and 5%, respectively. Further, it is noteworthy that coefficient of variation (*CV*) slightly decreased from Pass 2 to

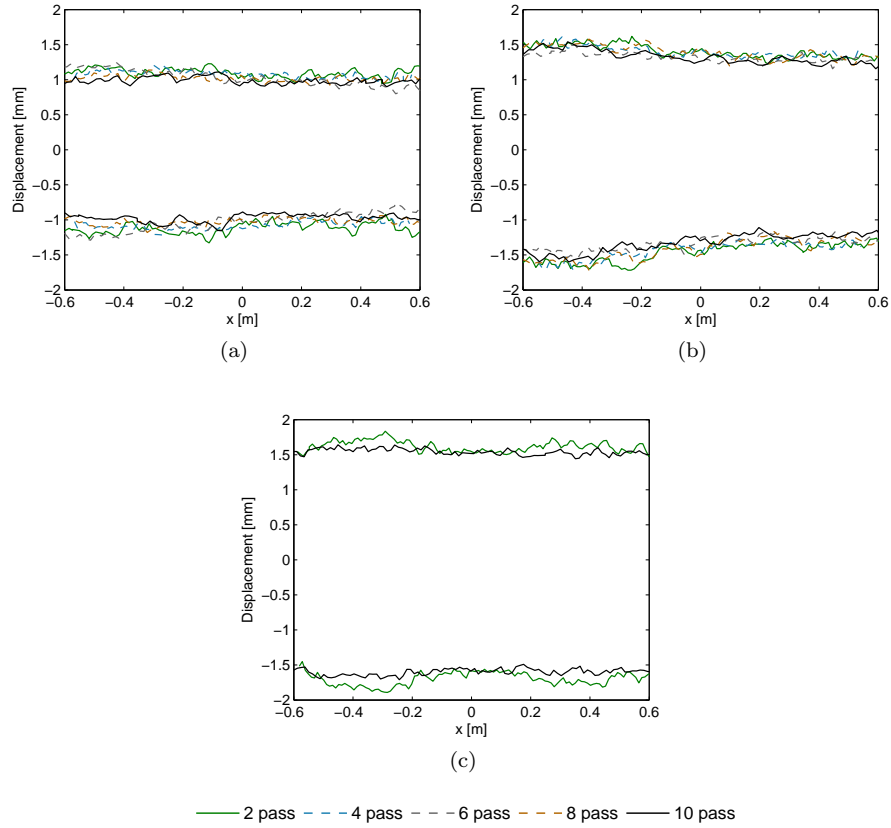


Figure 7.39: Computed drum displacements for three type of sections: (a) *ISAC*; (b) *ISAC+SP*; (c) *CA40+SP*

Pass 10 for all profiles, which means homogeneity was improved.

In addition, different drum behaviour is found in Figures 7.38 and 7.39 according to the type of material being compacted, which means drum vertical movement is found to be sensitive to changes in underlying materials stiffness. Comparison between vibration characteristics on different profiles showed the lowest average acd_p^- on *ISAC* profile, while the greatest drum accelerations were observed on *CA40+SP* profile. Concerning to vibration results for the last pass of vibrating roller (10 Pass), average acd_p^- on *ISAC* profile was 15 m.s^{-2} and increased 22 and 46% for *ISAC+SP* and *CA40+SP* profiles, respectively. Vertical drum displacements during compaction of *ISAC* profile is about $\pm 1 \text{ mm}$, while increases approximately 30 and 50%, up to ± 1.3 and $\pm 1.5 \text{ mm}$, during compaction of profiles *ISAC+SP* and *CA40+SP*, respectively.

The decrease of both peak drum accelerations and displacements verified either towards increasing number of passes and with different underlying materials can be related with stiffness. It is known that materials stiffens with number of passes of the roller. In fact, moduli obtained from *SPLT* carried out for 10 passes were the highest on *ISAC* profile. Moreover, moduli obtained from *SPLT* performed in *ISAC* section ($E_{\text{SPLT}} = 185 \text{ MPa}$) is approximately 50% greater

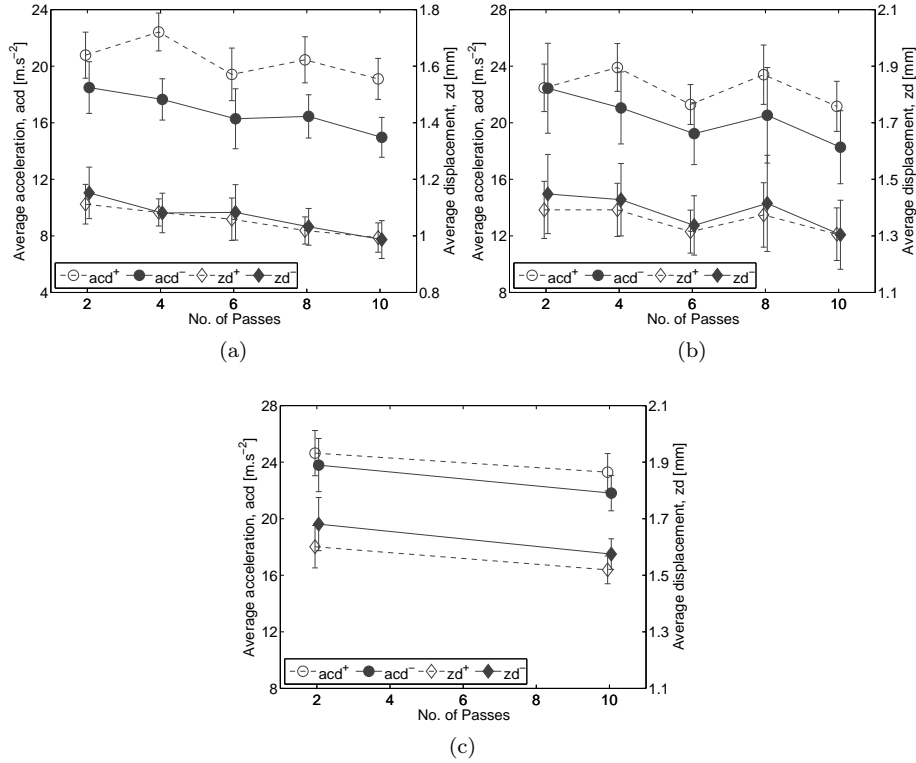


Figure 7.40: Average drum acceleration and displacements versus number of passes for three type of sections: (a) *ISAC*; (b) *ISAC+SP*; (c) *CA40+SP*

than the correspondent value obtained on *CA40+SP* profile ($E_{SPLT} = 119$ MPa). This relation (50%) is quite similar to the one verified between average acd_p^- and zd_p^- , about 46% and 50%, respectively. As so, one may conclude that peak drum accelerations decreased with increasing stiffness.

In the same manner, also moduli obtained from *FWD* carried out were investigated. *FWD* results on *ISAC* section are higher than the corresponding values obtained on the other sections. Indeed, average E_{FWD} in *ISAC* profile regarding to 1st, 2nd and 3rd drop heights is, respectively, 73, 82 and 100% greater than the corresponding values obtained from *ISAC+SP* profile, and 54, 64 and 78% greater than the corresponding values obtained from *CA40+SP* profile. However, comparison between average acd_p^- measured on *ISAC+SP* and *CA40+SP* profiles and *FWD* moduli did not showed the same trend. Average acd_p^- , corresponding to 10 passes, measured in *CA40+SP* profile was 19% greater than the average peak acceleration measured in *ISAC+SP* profile, yet E_{FWD} obtained from tests performed on *CA40+SP* profile were 10–13% greater than the E_{FWD} obtained on *ISAC+SP* profile, which is not consistent with the previous findings.

However, *FWD* moduli obtained from test campaigns carried out on these profiles after placing betuminous layers revealed consistently identical or greater stiffness of *ISAC+SP* profile than in *CA40+SP* profile (Reis Ferreira, 2010). It

is worth noting that the same type of bituminous material was placed over base layer. To this end, these profiles only differ on base layer material. Therefore, it is believed that differences on *FWD* results are influenced mainly by base layer and, consequently, reflect the greater stiffness of the *ISAC* base layer. These last results are consistent with acceleration measurements.

In order to investigate this phenomena acceleration measurements were investigated. Though *CV* for *ISAC+SP* (14.1%) was much greater than the corresponding value obtained for *CA40+SP* (5.7%), it does not seem sufficient to explain the contradicting trends found. On the other hand, stress dependency of *ISAC* material stiffness may explain it. Material stiffness increases with increasing confining stress and decreases with increasing shear stress. Within an impact loading, the shear stress increases and the confining stress increases too due to lateral confinement. Stresses induced by roller drum may be substantially greater than the stress applied by *FWD*. To this end, the increase of stiffness due to an increase of confining stress seems to come over the decrease in stiffness due to an increase of shear stress. Thus, vibration history of the drum reflects higher stiffness of *ISAC+SP* profile. Regarding *FWD* results obtained from tests carried out on bituminous layers, it seems that the effect of confining stress induced by bituminous layers leads to an increasing stiffness of *ISAC* material in base layer.

The previous results demonstrated that vibration characteristics exhibited sensitivity to changes in underlying material properties due to compaction process. Drum peak vertical acceleration and displacement decreased as underlying material stiffens. This type of drum behaviour was observed by Scullion *et al.* (2006) and Mooney and Rinehart (2007) when drum is operating at excitation frequencies lower than the natural frequency of drum-soil system. The frequency content illustrated in Figure 7.38 indicated that roller drum was operating at frequency about 19 Hz. Therefore, the natural frequency of drum-soil system is believed to be higher.

Focusing on acceleration measurements, the acceleration levels measured at any time during compaction reflect machine vibration upon a complex body of involved soil that is stressed by the vibrating drum at a given time and location. The involved soil ahead of the drum is less dense than the involved soil behind the drum. Hence, the drum vibration characteristics during any pass reflect machine vibration on soil that varies from loose state ahead of the roller to compacted state behind the drum. Either from Figure 7.38 and Table D.17 one can see that peak positive drum acceleration significantly exceeds peak negative drum acceleration at all profiles and during all passes of the roller. The overage ranged between 12–28% for *ISAC* profile, 0–16% for *ISAC+SP* profile and 4–7% for *CA40+SP* profile. Also note that differences tend to be higher with increasing number of passes, although a clear trend could not be observed. Difference between positive and negative drum acceleration seems to be dependent on the changes of underlying materials. Mooney *et al.* (2005) found that acceleration amplitudes were close to symmetric in vertical direction during stationary vibration on a fairly linear elastic underlying medium, whereas drum acceleration amplitudes on non linear underlying medium were up to 18% greater in the negative vertical acceleration than the positive one. This difference is also a measure of system nonlinearity due to numerous aspects, e.g., inelastic soil behaviour, machine nonlinearity, curved drum acting on the soil surface and possible drum decoupling from the soil (Adam, 1996; Anderegg

and Kaufmann, 2004; Mooney *et al.*, 2005; van Susante and Mooney, 2008).

The harmonic content on frequency history also confirmed the non linear behaviour of soil–drum system. Mooney *et al.* (2005) investigated harmonic content as a measure of system nonlinearity. The harmonic components normalized by the fundamental component H_{f_i}/H_{f_1} and the total harmonic distortion (THD), both as percentages, were determined for tests carried out with instrumented roller over four materials with different stiffnesses, as mentioned earlier. The THD provided a measure of collective harmonic content and is expressed as follows:

$$\text{THD} = \frac{\sqrt{H_{f_2}^2 + H_{f_3}^2 + \dots + H_{f_N}^2}}{H_{f_1}} \times 100 \quad (7.9)$$

The authors verified that the normalized frequency components and the THD were small (less than 1%) during vibration on rubber tires, which was supposed to be a fairly linear elastic underlying medium; the majority of the distortion was manifested in the first harmonic for all test beds. Moreover, normalized frequency components and THD increased with underlying material stiffness and was found to exhibit much greater sensitivity to changes in underlying material stiffness than drum acceleration amplitude. A similar investigation was conducted with regards to three profiles and results are presented on Table 7.27.

The THD essentially reflects the ratio H_{f_2}/H_{f_1} , since values of H_{f_3} and H_{f_4} were much smaller than H_{f_2} . THD varied from 41 to 74% during compaction on *ISAC*, 23 to 30% on *ISAC+SP* and 33 to 46% on *CA40+SP* profiles. The high values of THD reflects high non linear behaviour of soil–drum system. Compaction over *ISAC* profile exhibited greater nonlinearity which is consistent with the ratio between average peak positive and negative drum acceleration given in Table D.17. However, it seems that there is no linear relation between these two parameters within the number of passes of the vibrating roller. Regarding *ISAC+SP*, THD values are the lowest, while average peak positive and negative drum acceleration ranges from 0 up to 16%. This interval includes the ratio for *CA40+SP* profile (4–7%). This probably due to the greater scatter on acceleration data measured during compaction of *ISAC+SP* profile that is reflected in a higher *CV*.

It is worth noting that magnitude of THD measured during vibration on *ISAC* was about 55% greater than magnitude of THD measured during vibration on *CA40+SP*, whereas it ranged between 26 to 225% in relation to *ISAC+SP* profile. Taking into account previous conclusions, it seems that THD was sensitive to changes in underlying material and increased with increased stiffness. The THD relation between *ISAC* and *CA40+SP* profiles of 55% is consistent with the relation between modulus given by *SPLT* performed on both profiles. However, a close look to THD variation within the number of passes in each profile did not showed a clear trend. When comparison between passes 2 and 10 is established, one can see that THD decreased for *ISAC* and *CA40+SP* profiles, while the opposite was observed for *ISAC+SP* profile. This trend was against the established relation between THD and stiffness. Therefore, it seems that THD is not sufficient feature to be used as indicator of varying stiffness.

Table 7.27: Frequency domain results for vibration on the three profiles

Section		No. of Passes				
		2	4	6	8	10
<i>ISAC</i>	Freq [Hz]	18.6	18.9	18.7	18.9	18.6
	H_1 [m.s ⁻² /Hz]	33	34	46	30	32
	H_2 [m.s ⁻² /Hz]	23	24	18	22	16
	H_3 [m.s ⁻² /Hz]	6	6	5	5	5
	H_4 [m.s ⁻² /Hz]	1	2	2	1	2
	H_2/H_1 [%]	70	70	39	72	49
	H_3/H_1 [%]	17	17	11	16	14
	H_4/H_1 [%]	4	5	4	5	5
	THD [%]	72	72	41	74	51
<i>ISAC + SP</i>	Freq [Hz]	18.4	18.7	18.4	18.6	18.4
	H_1 [m.s ⁻² /Hz]	53	57	60	55	42
	H_2 [m.s ⁻² /Hz]	15	15	19	12	12
	H_3 [m.s ⁻² /Hz]	3	3	5	3	4
	H_4 [m.s ⁻² /Hz]	1	1	1	1	1
	H_2/H_1 [%]	28	27	32	22	28
	H_3/H_1 [%]	6	6	8	6	8
	H_4/H_1 [%]	2	1	2	1	2
	THD [%]	29	27	32	23	30
<i>CA40 + SP</i>	Freq [Hz]	18.1				18.3
	H_1 [m.s ⁻² /Hz]	47				52
	H_2 [m.s ⁻² /Hz]	21				17
	H_3 [m.s ⁻² /Hz]	4				4
	H_4 [m.s ⁻² /Hz]	1				1
	H_2/H_1 [%]	45				33
	H_3/H_1 [%]	9				7
	H_4/H_1 [%]	2				2
	THD [%]	46				33

In-ground acceleration measurements

In-ground acceleration measurements were carried out during roller drum operation over all profiles. Data was gathered during 1, 2, 4, 6, 8 and 10 passes of the vibrating roller on base layer. Similarly to previous analysis, time domain features were determined from the vibration histories. Then, data gleaned from in-ground accelerometers was computed in order to obtain displacements. It should be highlighted that vibrations measurements reflects only the cyclic response induced by the roller drum.

Vibration data from accelerometers was referenced to each in-ground sensors, which means that abscissa x reflects the position of the drum relative to the in-ground sensor location. Negative x indicate that the drum is approaching the sensors while positive x indicate that drum is moving away from the sensors. The $x = 0$ position means that the roller drum was in the vertical alignment of the sensor. It should be noted that the roller is traveling left to right, except for pass 1 in which roller traveled in the opposite way. Peak amplitudes time history of in-ground accelerations measured on *ISAC* and *CA40+SP* profiles are plotted in Figure 7.41 ever results were available. Peak positive and negative values due to vibration above accelerometers are plotted in Figure 7.42 along with computed displacements.

A noticeable decrease of in-ground peak accelerations and displacements between 1 and 10 passes of vibrating roller is observed in both profiles (fig. 7.42). Peak accelerations (ac_p^+ and ac_p^-) decreased 21 and 42%, respectively, in *ISAC* profile, whereas in *CA40+SP* profile a corresponding reduction of 32 and 47% is verified. Regarding peak displacements (z_p^+ and z_p^-) in *ISAC* profile, a decrease of 37% is obtained from both positive and negative displacements, whereas in *CA40+SP* profile a reduction of 27 and 32% is verified, respectively. Accordingly to previous conclusions from drum behaviour, stiffness increases with increasing number of passes of the vibrating roller. To this end, one may conclude that both in-ground accelerations and displacements at 0.65 m depth decreases as base layer stiffens. In fact, both parameters obtained from *CA40+SP* were more than twice the corresponding value for *ISAC* profile (fig. 7.42), which denotes greater stiffness from *ISAC* profile. These results are consistent with the ones obtained on previous sections.

It is noteworthy that a greater decrease of in-ground accelerations and displacements is observed between passes 1 and 2 for both profiles, which denotes a great improvement in profile mechanical properties between passes 1 and 2. Concerning *ISAC* profile, beyond pass 2 an increase of both parameters is observed during pass 4, while from pass 6 to 10 an unclear trend is observed. Nevertheless, between passes 2 and 10 peak positive in-ground accelerations and displacements fairly increased, whereas, negative in-ground accelerations and displacements remained almost the same. Owing to *CA40+SP* one can observe that all parameters decreased between pass 2 and 10.

Focusing on acceleration measurements, it is interesting noting that average ac_p^- exceeded average ac_p^+ in *ISAC* profile, except to pass 10. The ratio between these parameters was about 23% for pass 1 and decreased to -10% for pass 10, which means that acd_p^+ exceeded acd_p^- . From vibration measurements during roller stationary vibrating loading presented earlier, one can see that for the same level of drum vibration (ac_p^+ about 20 m.s⁻²; ac_p^- about 15 m.s⁻²) peak positive exceeding peak negative acceleration features in-ground vibra-

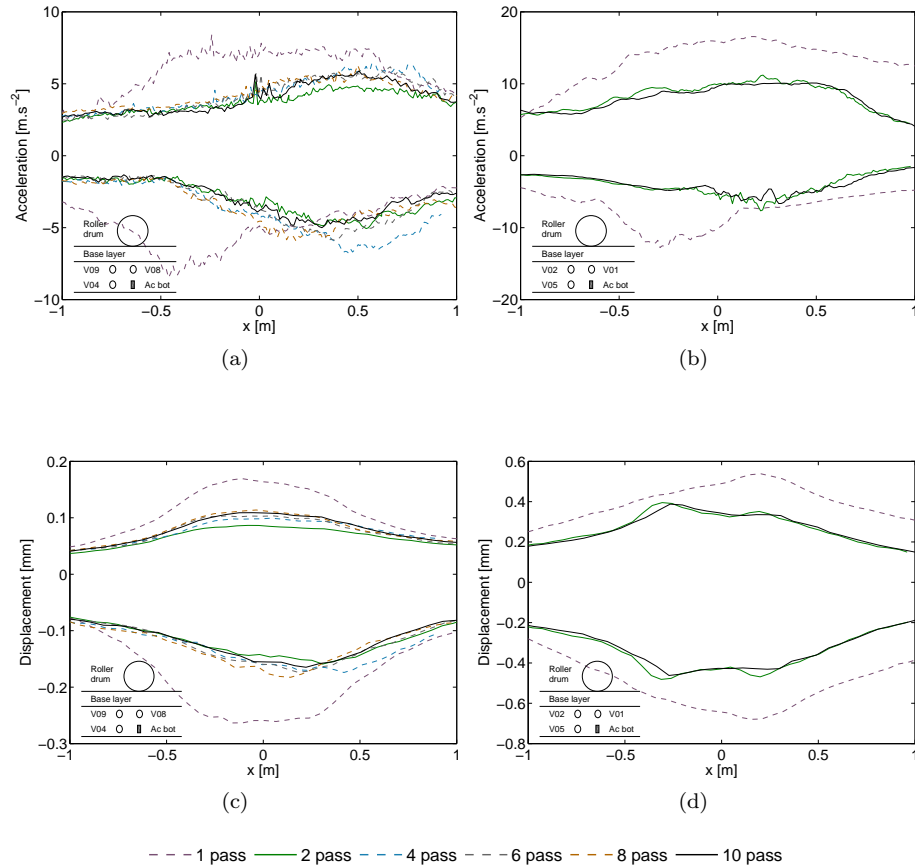


Figure 7.41: Acceleration time history and computed displacements obtained from in-ground vibrations measured on: (a) and (c) *ISAC* profile; (b) and (d) *CA40+SP* profile

tion at $z = 0.22$ m, while the opposite was observed for in-ground vibration at $z = 0.45$ m, where stress level is lower. Given these facts, it seems that for lower stresses ac_p^- exceeds ac_p^+ , whereas for higher stresses the opposite is verified. Hence, by applying this finding to the results of in-ground vibrations during *ISAC* base layer compaction, one may conclude that stress level at $z = 0.65$ m increased with increasing number of passes of the vibration roller and, consequently, with increasing *ISAC* profile stiffness. This may be explained by drum-material contact width during successive passes of vibrating roller. As profile stiffens the contact width narrows and, therefore, applied stress increases leading to an increase stress in depth.

From in-ground accelerations measured on *CA40+SP* profile a different trend was verified. ac_p^+ exceeded ac_p^- for passes 1, 2 and 10 with corresponding ratios of 15, 38 and 34%, respectively. From vibration measurements during roller stationary vibrating loading presented earlier, one can see from both accelerometers that ac_p^- exceeded ac_p^+ during low eccentric static moments, i.e., lower stresses, while the opposite was observed for high eccentric static mo-

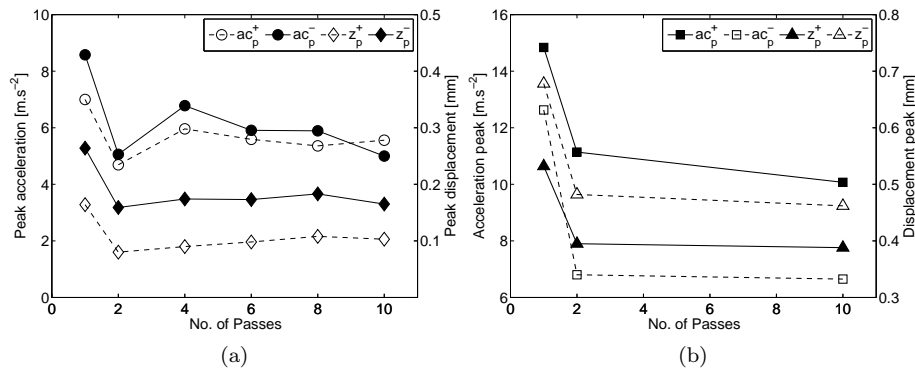


Figure 7.42: In-ground peak acceleration (ac_p) and peak displacement (z_p) evolution with number of roller drum passes: (a) ISAC; (b) CA40

ments, i.e., higher stresses. Thus, by applying this finding to the results of in-ground vibrations during CA40 base layer compaction, one may conclude that stress level at $z = 0.65$ m increased within passes 1 and 2 and slightly decreased between passes 2 and 10. Recalling previous section, drum roller response indicated that stiffness increased between passes 2 and 10. Given these opposite trends, it seems that stiffness increase of profile was due mainly to CA40 base layer.

Another interesting feature is that maximum ac_p^- occurred when roller was about 0.50 m away from sensor regarding pass 1. This distance decreased to approximately half distance to pass 2 and remained constant for the other passes, which seems to be relate to increasing stiffness of the profile. Note that due to the roller being traveling in opposite direction during pass 1, the evolution of in-ground vibration is fairly symmetric to the other lines. In the same way, negative displacements are highest when drum roller was about 0.30 m away from the sensor and slightly decreased when the roller drum moved towards the sensor. A fairly symmetric behaviour was observed when the roller drum moved away from the sensor (fig. 7.41d). Regarding ISAC profile, although maximum peak negative displacements were observed when the roller drum was above sensor during pass 1, for the other passes peak negative displacement was observed when the roller drum was approximately 0.25 m away from the sensor and when the roller drum was moving away from the sensor. The phenomena was also observed from strain data and will be discussed later.

In-ground strain measurements

Strain measurements carried out during 1, 2, 4, 6, 8 and 10 passes of the vibrating roller on base layer are presented in Figures 7.43, 7.44 and 7.45, corresponding to ISAC, ISAC+SP and CA40+SP profiles. It is important to bear in mind that strain response reflects the response due to both static weight of the drum and cyclic forces generated by the vibrating drum. Further, it should be noted that the effects of of overburden and previous passes have been removed so strains are due to the roller drum only, which means all passes start with zero strain. Likewise to acceleration data, strain data was referenced to each

in-ground sensors, which means that abscissa x reflects the position of the drum relative to the in-ground sensor location.

In Table D.19 is given total strain (ε_z) and cyclic portion ($\Delta\varepsilon_z$) due to vibrating roller passes on base layer, as well as the ratio $\Delta\varepsilon_z/\varepsilon_z$. Note that for strain gauge V08, placed in *ISAC* section, only data from passes 2 and 4 are presented, since sensor become inoperative beyond this point. Regarding strains measurements on *CA40+SP* profile (strain gauges V01, V02 and V05) only data from passes 1, 2 and 10 are available. This was due to problems in the acquisition system during remaining passes.

In-ground peak strains and ratio $\Delta\varepsilon_z/\varepsilon_z$ at roller drum position $x = 0$ were evaluated with number of passes and are plotted in Figures 7.46, 7.47 and 7.48. Data analysis shows that evolution of peak total strain and ratio $\Delta\varepsilon_z/\varepsilon_z$ is inverse.

A clear trend is observed from strain data obtained in *ISAC* section, where peak total strain increases with increasing number of passes, which means with increasing stiffness of the material being compacted (fig. 7.46a). As mentioned earlier, this behaviour may be attributed to the narrow contact width of the drum-material. Though sensors V08 and V09 were at same depth, measured ε_z maximum values ranged from 2500 to 4500×10^{-6} and from 1 to 2200×10^{-6} , respectively. As so, ε_z given by strain gauge V08 was about twice the ε_z given by strain gauge V09 (see figs. 7.43a and 7.43b). This may be due to improper installation of the sensor V08, for example, disturbance of material around the sensor during placement which was left in a loose state. This notwithstanding, the same trend is verified from both sensors V08 and V09. With regards to strain gauge V04 at $z = 0.65$ m, ε_z values ranged from 500 to 1100×10^{-6} , which were approximately half than the ones obtained from strain gauge V09. Recall both sensors were placed in the same vertical alignment.

Conversely, ratio $\Delta\varepsilon_z/\varepsilon_z$ was found to decrease within the number of passes, as illustrated in Figure 7.46b. Actually, $\Delta\varepsilon_z$ for strain gauges V04 and V09 decreased 43 and 45%, respectively, between passes 1 and 10, yet great reduction was observed between pass 1 and 2. Since this parameter reflects only the cyclic portion of strain measurements, comparison with in depth acceleration measurements shows that this trend is consistent with the one found from accelerometers data at the same depth (fig. 7.42a). Note that the ratio ranged over 6–18%. The small magnitude of $\Delta\varepsilon_z$ compared to ε_z was also found by Rinehart and Mooney (2009) and result from curved drum-material interaction and material viscoelasticity. During vibration, the applied force equals the static force \pm a cyclic force depending on eccentric static moment of the roller drum. Contact stress and contact width are nonlinearly related to force and vertical drum deflection, and leads to a hardening type relationship between applied force and drum deflection (see Figure 2.14 in Chapter 2). The deflections (and in turn strains) due to drum vibration are relatively small compared to deflections resulting from static loading. Further, one can see from Table D.19 that $\Delta\varepsilon_z$ from V09 and V08 were similar, varying around 120×10^{-6} , which corresponds to an order of magnitude less than ε_z . $\Delta\varepsilon_z$ from V04 varied around 80×10^{-6} , corresponding to less than half the value obtained from sensors V08 and V09.

The strains plot from strain gauge V06 (fig. 7.44) placed at 0.32 m depth in *ISAC+SP* section illustrate differences from the previous section. From pass 1 to 2 ε_z decreased, increased between passes 2 and 6 and decreased again till last

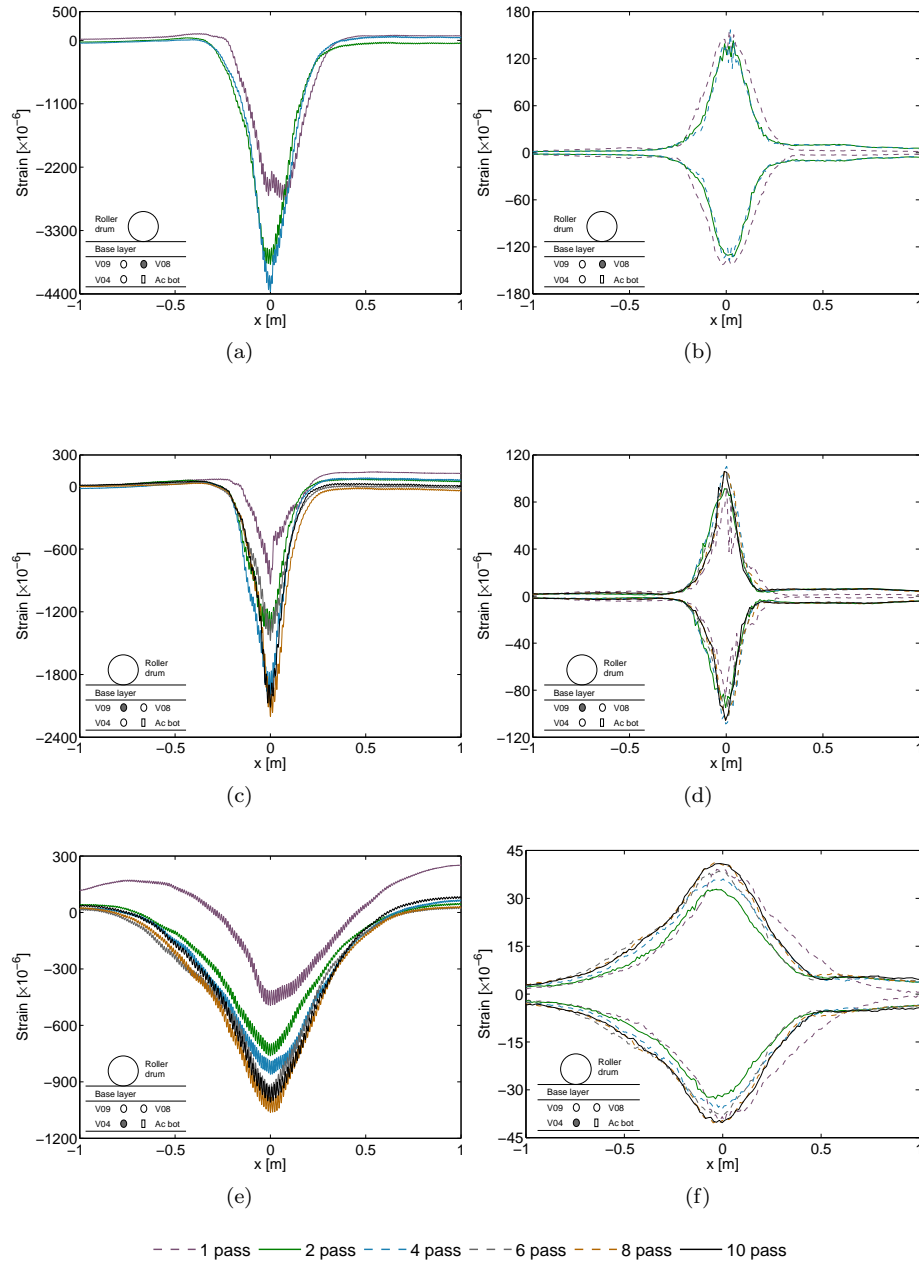


Figure 7.43: Total and cyclic strain data from strain gauge: (a) and (b) V08; (c) and (d) V09; (e) and (f) V04

pass (fig. 7.47a). Although these variations, ε_z decreased about 66% between passes 1 and 10. This finding is consistent with the stress reducing effect of an overlying stiff layer (Burmister, 1958). In fact, as previously found, *ISAC*

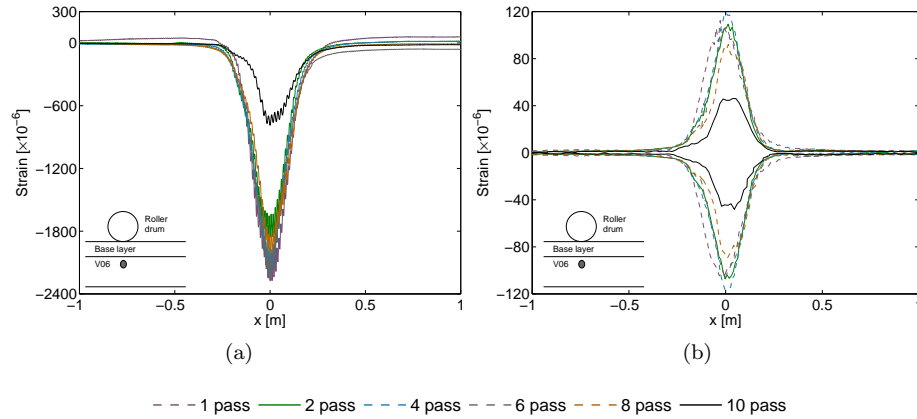


Figure 7.44: Total (a) and cyclic (b) strain data from strain gauge V06

material stiffness is greatly improved in compacted state, inducing a significant reduction of stress at *SP* capping layer, which stiffness is lower, thus explaining the significant reduction on total strains. On the contrary, the ratio $\Delta\varepsilon_z/\varepsilon_z$ increased approximately 32% (fig. 7.47b). Note that this trend is contrary to the one verified in *ISAC* profile.

With regards to *CA40+SP* section, a different trend from previous sections is found. Strain data obtained from sensors placed at $z = 0.32$ m, V01 and V02, evolves in different ways, as one can see in Figure 7.48a. As so, the outcome is inconclusive. In contrast, a clear trend is verified from total strain concerning to strain gauge V05 placed at depth $z = 0.65$ m (fig. 7.48a). Total strain decreased with increasing number of passes. As aforementioned, this finding is consistent with the stress reducing effect of an overlying stiff layer (Burmister, 1958). Similarly to reported on analysis of data from *ISAC* section, strains given by sensors V01 and V02, placed at same depth, are quite different too. ε_z measured ranged from 300 to 400×10^{-6} for the former and from 800 to 1300×10^{-6} for the latter. Regarding strain sensor V05, one can see that ε_z ranged from 500 to 700×10^{-6} , which strains are about half the ones from strain gauge V09 placed in the same vertical alignment.

Owing to the cyclic portion, once again one can see from Figure 7.48b that only strain gauge V05 presents a clear trend, where $\Delta\varepsilon_z$ increases with increasing number of passes. However, this trend is contrary to the one observed from acceleration data (fig. 7.42b). $\Delta\varepsilon_z$ from V01 and V02 is an order of magnitude less than ε_z . $\Delta\varepsilon_z$ from V01 ranged from 40 to 70×10^{-6} and 130 to 170×10^{-6} from V02. Although sensors were placed at the same depth a significant difference on $\Delta\varepsilon_z$ from V01 and V02 is noticeable. Concerning to V05, $\Delta\varepsilon_z$ varied about 40×10^{-6} . The ratio $\Delta\varepsilon_z/\varepsilon_z$ ranges over 11–17%, which are consistent with values obtained for the other profiles.

Focusing on total strain history it is noteworthy that the widening with depth of the zone of material influenced by the roller, which is on the order of 0.50 – 0.60 m, 0.35 – 0.45 m and 0.40 – 0.50 m at $z = 0.32$ m corresponding to *ISAC*, *ISAC+SP* and *CA40+SP* section, respectively, and widens to about 1.40 – 1.60 m and 1.00 – 1.10 m at $z = 0.65$ m, concerning to *ISAC* and *CA40+SP* sections.

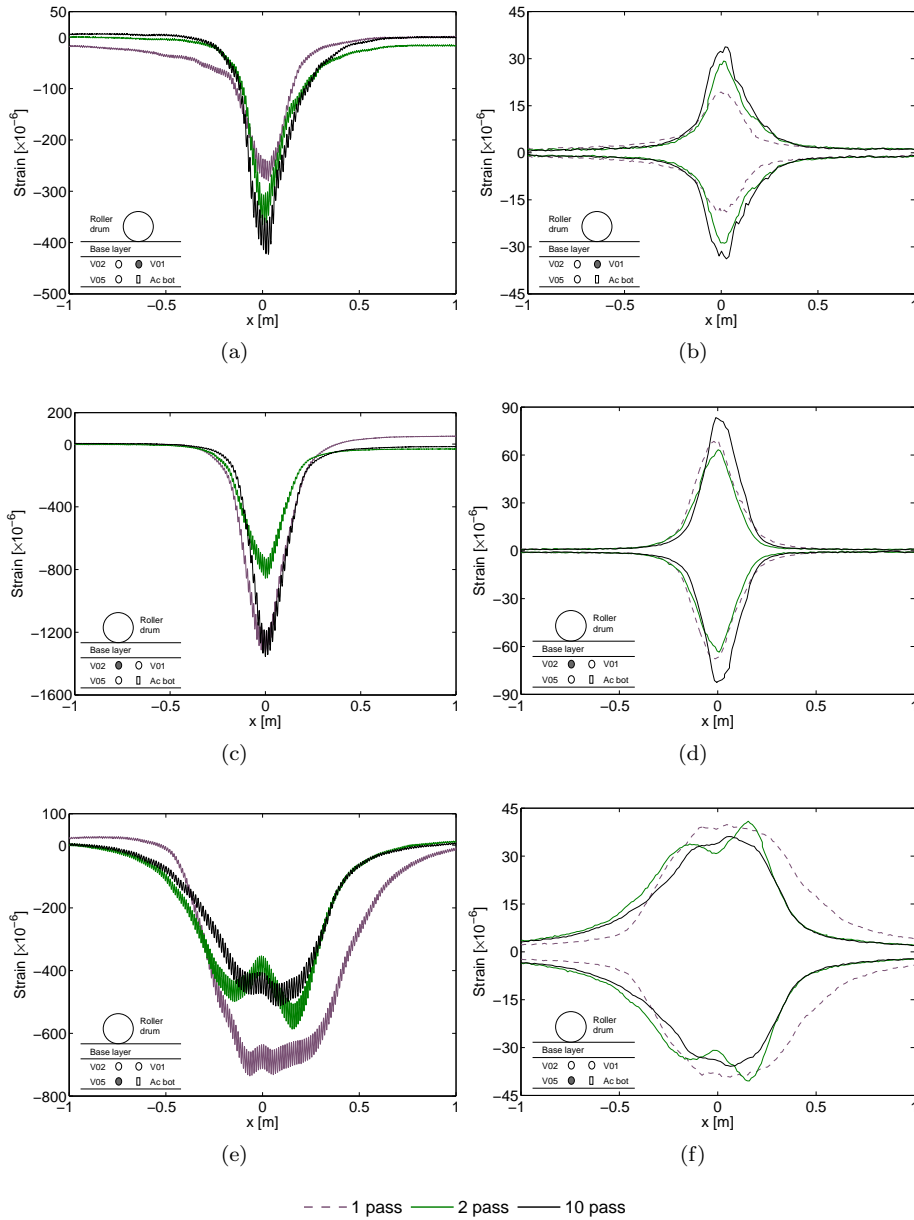


Figure 7.45: Total and cyclic strain data from strain gauge: (a) and (b) V01; (c) and (d) V02; (e) and (f) V05

This results shows that a given roller-measured stiffness value is representative of soil about 0.25–0.30m in the front of and behind the center of the drum near surface. Through the measurement of depth stress and strain Mooney and Rinehart (2009) reached a similar value on their research.

Hence, area of influence of *SPLT* performed with loading plate of 600 mm in

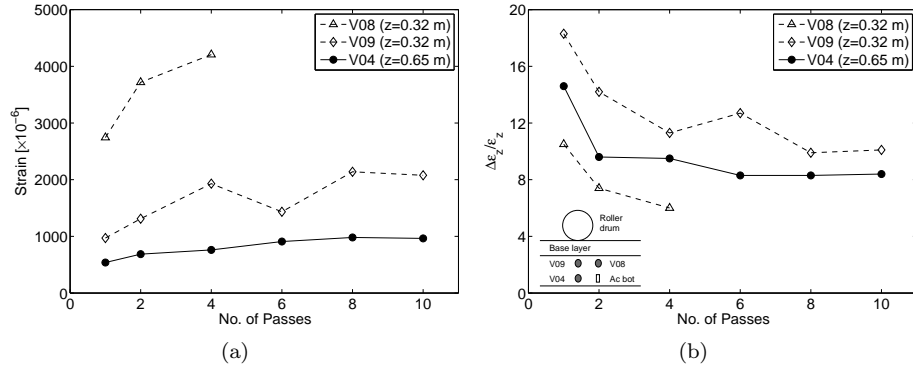


Figure 7.46: In-ground strains evolution from sensors V04, V08 and V09: (a) peak strains; (b) $\Delta \varepsilon_z / \varepsilon_z$

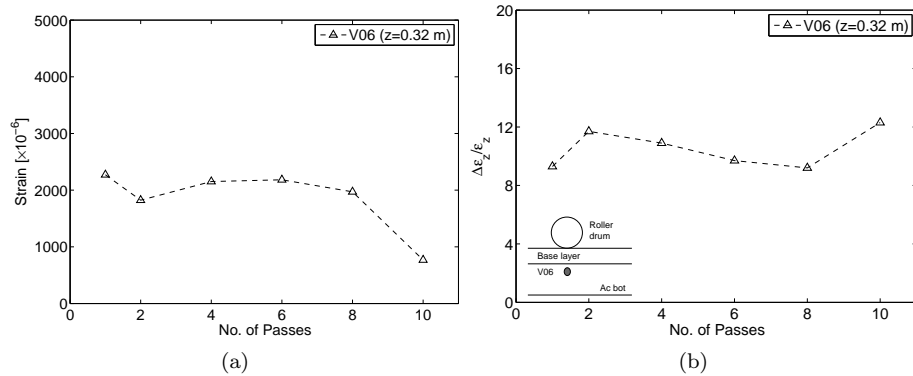


Figure 7.47: In-ground strains evolution from sensor V06: (a) peak strains; (b) $\Delta \varepsilon_z / \varepsilon_z$

diameter is similar to the area of influence of roller drum, which may explain the obtained correlation between *SPLT* results and roller drum behaviour (see previous section). Therefore, area of influence assumes great importance when performing correlations of roller-measured stiffness to spot tests results as is commonly performed in CCC (Mooney and Rinehart, 2009). Further, in order to investigate depth of influence from both roller drum and *SPLT*, *SPLT* was performed over strain sensors V09 and V04 at *ISAC* section and over strain sensors V02 and V05 at *CA40+SP* section after 10 passes of the roller drum. In Figure 7.49 are shown the in-ground strains evolution at depths $z = 0.32$ and $z = 0.65$ m with applied stresses below the plate. Bold line refers to in-ground response during the second load cycle from which modulus is calculated.

Regarding *ISAC* section (fig. 7.49a), nonlinear behaviour was observed from strain gauge V09 at depth $z = 0.32$ m, while at depth $z = 0.65$ m linear behaviour was verified. In second load cycle relative strains of 878×10^{-6} and 810×10^{-6} were measured, respectively, which contrast from total strains in-

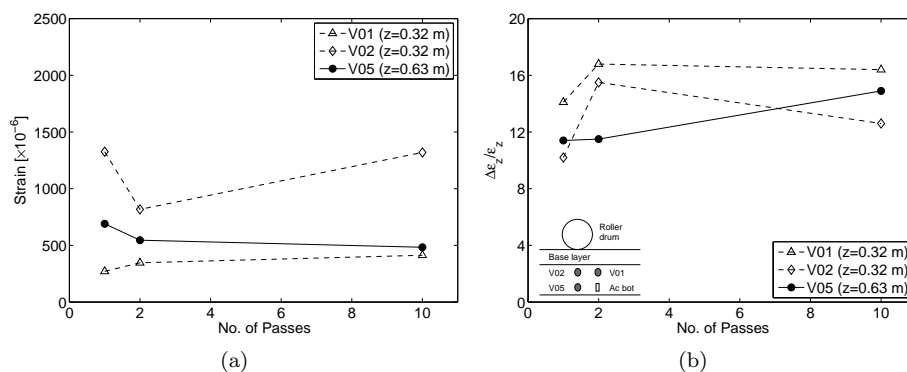


Figure 7.48: In-ground strains evolution from sensors V01, V02 and V05: (a) peak strains; (b) $\Delta \epsilon_z / \epsilon_z$

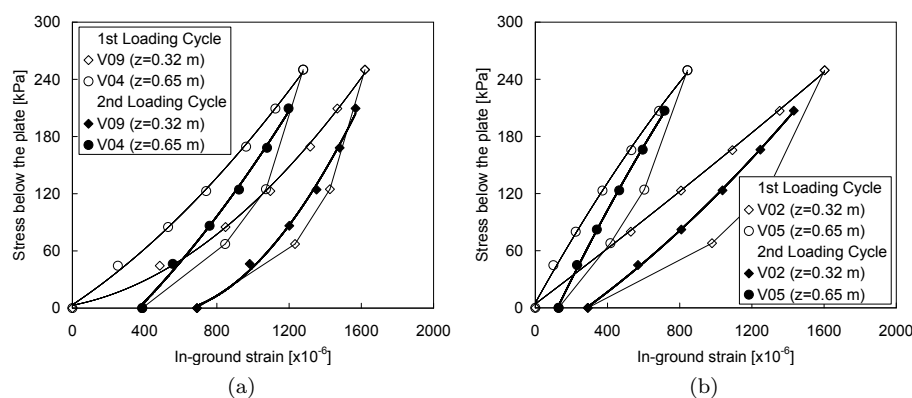


Figure 7.49: In-ground strains evolution during *SPLT* carried out on: (a) *ISAC* section; (b) *CA40+SP* section

duced by roller drum during pass 10 (2078×10^{-6} and 938×10^{-6}). Though strains at $z = 0.32$ m induced by roller drum and *SPLT* differs significantly, at greater depth ($z = 0.65$ m) strain levels are quite similar.

In what concerns to *SPLT* carried out on *CA40+SP* section (fig. 7.49b), a hardening response was observed from strain gauge V02 at depth $z = 0.32$ m, while at depth $z = 0.65$ m strain gauge V05 exhibited softening response during second loading cycle. This notwithstanding, response may be considered as fairly linear. In second load cycle relative strains of 1112×10^{-6} and 568×10^{-6} were measured, respectively, which seems to match total strains induced by roller drum during pass 10, 1320×10^{-6} and 483×10^{-6} . This findings demonstrated close strain responses between load applied by the roller and *SPLT*, thus, are of great importance for the establishment of correlations with roller drum behaviour. It is noteworthy that strain at the bottom of the capping layer is two times less than at the top of the same layer. This difference is consistent

with the stress reducing effect of an overlying stiff layer (Burmister, 1958).

Further, one can see that material immediately in front of the drum experiences vertical extension during pass 1, which is due to the traveling nature of the roller (Adam, 1996).

Finally, it is interesting noting the development of both ε_z and $\Delta\varepsilon_z$ from sensor V05. These values increased as the roller drum approached, peaks at approximately at $x = 0.05$ to 0.15 m, and slightly decreased to a local minimum when the roller was just above the sensor at $x = 0$. As the roller moved away, ε_z and $\Delta\varepsilon_z$ increased, peaks at approximately at $x = 0.05$ to 0.15 m and decreased beyond this point. Beneath the drum ($x = 0$) shear stress and strain are theoretically zero or very small compared with normal stresses and strains (Johnson, 1987; Hirikawa *et al.*, 2000). Hence, peak strains are due to normal and shear stresses induced by the roller, which effect is greater approximately at $x = \pm 0.05$ to 0.15 m away from vertical alignment of the sensor. The same behaviour was found from acceleration data and is identical to the one observed during Portancemètre pass on capping layer of *SP* profile at depth $z = 0.45$ m.

7.9 Conclusions

In this chapter, results obtained from several in situ tests performed on trial, embankment and base layers were presented. Three types of materials were studied, namely, poor-graded sand with silt (*SP*) employed in trial and embankment layers, inert steel aggregate for construction (*ISAC*) employed in trial, embankment and base layers and a well-graded gravel (*CA40*) employed in base layers.

Firstly, state conditions obtained from sand cone method (*SCM*), rubber balloon method (*RBM*) and nuclear method (*NM*) were presented. *NM* was found to be inappropriate to determine state conditions of *ISAC* layers. Moisture content of *SP* trial layers ranged over 3–4% dry of optimum, whereas embankment layers varied between 1 and 3% dry of optimum. The wetting process employed on *SP* material which involved the previous stack of material, water adding and mix up by means of a front shovel and, in addition, moisture content was corrected in situ before compaction process, did not reproduced desirable moisture conditions. Moreover, density slightly decreased with increasing moisture content. The highest moisture content coefficient of variation (*CV*) was obtained from trial layer with 0.50 m thickness, which denotes the influence of layer thickness on moisture content homogeneity. Nevertheless, dry density *CV* was less than 3% for all layers, which lie below limit given by Brandl (1977).

Secondly, correlations between moduli obtained from light falling weight deflectometer (*LFWD*), soil stiffness gauge (*SSG*), falling weight deflectometer (*FWD*), spectral analysis of surface waves (*SASW*) and Portancemètre using static plate loading test (*SPLT*) as reference test were attempted. Concerning to *SP* material, though the data is limited, a general relationship between *SPLT* (E_{V2}) and Portancemètre (E_{Port}) moduli close to unity was found. This means that results given by these tests are approximately the same validating the calibration method used and indicate the huge potential of this equipment for the continuous stiffness evaluation on earthwork platforms. Recall conclusion from *SC* material on *ETRE* was similar. The *SPLT* results were then compared with *LFWD* results, but a difference of approximately 55% was found. Since corre-

lation between Portancemètre and *SPLT* is close to unity, the former was used as reference test to confirm this difference. Comparison between Portancemètre with *LFWD* was then found to be around 40%. This conclusion differs from the obtained in previous chapter to *SC* material. Thus, more results would be required in order to study the application of *LFWD* to this type of material. The relation of Portancemètre to the *SSG* (E_{SSG}) moduli yielded data with large scatter, although the moduli obtained with both equipments was approximately the same. Likewise conclusions in previous chapter, the results from *LFWD* and *SSG* equipment should be treated with caution.

With regards to *ISAC* material different conclusions were obtained regarding to the ones described in previous paragraph. Moduli given by *SPLT* (E_{V2}) and Portancemètre (E_{Port}) differ approximately 45%. Correlation between *LFWD* and Portancemètre moduli was close to unity (only differs 12%), while between *SSG* and Portancemètre moduli differs 30%. This shows the necessity of equipments calibration for each kind of material. Though it seems possible to establish correlations between moduli of in situ performance-based tests methods, material type and state conditions should be taken into account on this evaluation. Concerning to *CA40+SP* profile due to lack of results no sustainable conclusions were obtained.

SASW were carried out using different sources types, namely light hammer, sledge hammer and *LFWD* and *FWD* equipments. Sledge hammer source was found not appropriated to the setup employed. On the contrary, good results were obtained using light hammer source, as well as results obtained using *LFWD* and *FWD* as sources demonstrated that these equipments can be used for seismic surface analysis. This findings assume great importance, specially in the case of *FWD* since equipment has already mounted a deflection measuring system consisting of 8 geophones positioned along 3 meters from the center of the source (loading plate). Besides traditional back-analysis or even static loading approach for the interpretation of *FWD* test, data gathered from these sensors can be used to perform surface seismic analysis. This interpretation would allow, on one hand, to confirm traditional back-analysis regarding the number of layers and, on the other hand, the extraction of low strain modulus.

Then, analysis of moduli and state conditions was conducted. Moisture content was found have unnoticeable influence on moduli for the range of moisture content studied, 1 to 4% dry of optimum. Conversely, dry density seems to influence mechanical properties. Moduli increased with increasing dry density, as long as moisture content do not vary significantly.

Comparison between full scale trial and laboratory results yielded differences lower than 27%, laboratory moduli being higher than field moduli. This results assumes great importance taking into account that design is based on mechanical properties usually determined from laboratory tests.

Further, an experimental program was carried out to monitor drum roller and layer vibrations in two phases. Phase One aimed vibrations measurement of the capping layer during tests, namely, *LFWD*, *FWD*, Portancemètre and roller drum. Accelerometers and strain gauges were buried on the capping layer enabling measurement of dynamic response and total strains. *ISAC* and *SP* materials were tested in this phase.

Strain measurements from *SP* and *ISAC* profiles during aforementioned tests indicate different depths of influence, which can be ordered in increasing way: *LFWD*, *FWD*, Portancemètre and roller drum. However, strain measurements

did not always reflected moduli obtained from performance related tests. In fact, higher strains were obtained from in-ground measurements in *ISAC* profile that was found to had higher stiffness. These results were unexpected and theoretical approach regarding *LFWD* and *FWD* tests was unable to explain these results. On the contrary, in-ground displacements obtained from acceleration measurements were consistent with profiles stiffness. Higher in-ground displacements were found regarding *SP* profile than in *ISAC* profile, which is consistent with lower modulus obtained in the former than the latter. Hence, in-ground dynamic response reflect moduli obtained from dynamic tests performed at layer surface.

Owing to impact loads from *LFWD* and *FWD* on *SP* profile, in-ground strains and displacements were consistent with theoretical approach considering a single modulus, yet modulus obtained from both tests differed. These results highlight the importance of test methods calibration using a reference test and allowed to conclude higher depth of influence from plate with higher diameter. Results obtained from *ISAC* profile did not confirmed these conclusions, which might be attributed to stationary drum tests between impact tests which induced significant differences on profile mechanical homogeneity.

Concerning to vibration loads induced by Portancemètre and roller drum on *SP* profile, displacements at lower depth differed about 25%, whereas at higher depth differed only 12%. The analysis of acceleration data denote non linear behaviour at lower depth, while behaviour close to linear appears to prevail at higher depth. As so, a similar dynamic in-ground response is found at higher depth. Since roller drum and Portancemètre wheel dynamic behaviour reflects dynamic in-ground response, this fact might indicate a good correlation between mechanical properties determined from instrumented rollers and Portancemètre.

Phase Two involved vibrations measurement of roller drum and vibrations of capping layer during compaction of base layer. Three different profiles were tested, namely, one formed only by *ISAC* material, and the others formed by *ISAC* and *CA40* materials resting on *SP* capping layer. Two accelerometers were embarked on the drum and acceleration signals were then computed in order to obtain roller vertical movement during compaction. At the same time, capping layer was instrumented with in-ground accelerometers and strain gauges in order to get information of vibrations in depth. Vertical drum acceleration and displacement were found to be sensitive to changes in underlying soil stiffness. Both decreased with increasing soil stiffness for an excitation frequency of about 19 Hz, which features drum vibration below the natural frequency of test bed. Further, good correlation was found between drum vibration and *SPLT* modulus obtained from *ISAC* and *CA40+SP* profiles. In addition, at 0.65 m depth strain levels induced by *SPLT* were similar to the ones induced by roller drum, denotes identical depth of influence. These findings shows that *SPLT* modulus reflect drum behaviour and, therefore, should be used as reference test.

Concerning in-ground vibrations measurements, similar trend to drum behaviour was found, i.e., accelerations and computed displacements decreased within number of passes on both profiles, thus with increasing stiffness. Therefore, in-ground dynamic response measured by means of in-ground accelerometers denotes close relation to drum behaviour, as was concluded from Phase One. On the other hand, results from in-ground strains were inconclusive.

Chapter 8

Conclusions

8.1 Conclusions

Several aspects that governs high-speed railway embankments, which distinguishes from other conventional transportation infrastructure, like road embankments, were identified. High-speed railway embankments demands an infrastructure exhibiting an overall stiffness that limits maximum settlements and minimize relative settlements of the embankment platform during serviceability conditions, in order to minimize the exploration costs, to avoid high level of discomfort for passengers and reduce induced vibrations on surrounding structures.

These aspects include strict requirements demands of high quality construction of embankment and railtrack layers regarding material quality, state parameters and mechanical properties limits, promoting homogeneity of mechanical behaviour of compacted layers. As mentioned in Chapter 2 requirements increase from bottom to top layers. The embankment layers should provide a stable foundation for the base (subballast) and ballast layers. The range of stiffness of the capping layers is believed to influence ballast, rail and sleeper deterioration, since the influence of the traffic induced stresses extends downwards as much as 5 meters below the bottom of the sleepers. Hence, embankment layers are a very important substructure component which as a significant influence on track performance and maintenance. Base layer (subballast) assumes great importance due to several aspects, e.g. to ensure better distribution of loads, to protect the underlying layer against erosion, to avoid seepage into the underlying layer and to prevent the penetration of fine soil material into the track bed, especially to the ballast.

Furthermore, strict requirements on quality construction demands higher quality on materials compaction control. From the literature review, it was concluded that there is a strong trend towards using performance based properties like stiffness and strength to assess layer compaction (Briaud, 2001; Loizos *et al.*, 2003; Alshibli *et al.*, 2005; Edil and Sawangsurya, 2005). These properties are a measure of quality since non-uniformity of stiffness and/or strength is directly related to progressive failures and life-cycle cost. Moreover, the design method of layer systems is based on engineering parameters of materials such as their stiffness and/or strength, which results in a missing link between the

design process and construction quality assessment.

Increasing demands for better, cheaper and faster compaction assessment have led to technology improvements. In this context, equipments for field test evaluation of mechanical properties of geomaterials have been recently developed, such as, impact tests (Falling Weight Deflectometer – *FWD* and Light Falling Weight Deflectometer – *LFWD*), the Soil Stiffness Gauge (*SSG*), Spectral Analysis of Surface Waves (*SASW*). These are non-destructive spot tests which can be conducted independently and in conjunction with conventional moisture density testing improving statistical evaluation and allowing variability reduction, thus substantially enhance construction quality of the entire earthwork (Edil and Sawangsurya, 2005). Moreover, equipments enabling continuous evaluation of layer stiffness, like Portancemètre, had been developed which represents a great improvement on platform quality. However, these equipments are not standardized and requires comparison to the reference test given on specifications, usually static plate load test (*SPLT*) following either AFNOR NF P94–117–1 (2000) or DIN 18134 (2001) before CEN standards will be available.

Moreover, railway embankments and railtrack layers are constructed on compacted geomaterials that are typically in unsaturated condition during construction and may remain in that condition during the working life of the structure. Several design and maintenance measures are undertaken to maintain unsaturated conditions because they provide favorable engineering materials properties, namely strength and stiffness. The literature review showed that compaction conditions (moisture content, compaction energy and compaction technique) strongly influence the hydro-mechanical behaviour of unsaturated geomaterials, namely, strength and stiffness, due to suction effect. However, the hydro-mechanical behaviour of unsaturated geomaterials is not straightforward due to the presence of suction and, even at critical states, the results found on literature are contradictory. Therefore, a better understanding of the hydro-mechanical behaviour of compacted layers requires both laboratory and field investigations.

In the scope of the present work laboratory and field evaluation of influence of compaction conditions on the hydro-mechanical behaviour of different geomaterials was carried out. In what follows the main achievements will be pointed out.

8.1.1 Laboratory investigation

Throughout a laboratory investigation the influence of compaction conditions, namely, molding water content, on hydro-mechanical behaviour of geomaterials was evaluated. Emphasis was given to mechanical characterization, particularly regarding to clayey sand (*SC*) material, since it has a non negligible fine fraction. The same procedure was employed on all tests to study both materials. Specimens were compacted with the same initial void ratio but with different molding water contents and tested in unsaturated condition. Further also saturated and dry tests were carried out.

The hydro-characterization of *SC* material was carried out by means of filter paper technique. Tests showed good repeatability and, thereby, filter paper technique proved to be an easy and low cost method to determine water retention curve. Molding water content was found to strongly influences matrix

suction that, in turn, play an important role on the mechanical behaviour of *SC* material. Compressibility of *SC* specimens was found to be suction independent in the lower stress range, before yielding. On the contrary, in the higher stress range after yielding, curves shapes from unsaturated specimens seems to be suction dependent: the higher the suction, the lower is the compressibility. This was confirmed by isotropic compressibility of unsaturated samples which increased with increasing water content. As so, an increasing suction produces a stiffening of the material with smaller plastic compressibility. However, during unloading sequences, compressibility appeared to be suction independent for the compacted unsaturated specimens. The data confirm the general findings that an increased suction produces a stiffening of the material with smaller plastic compressibility (Alonso *et al.*, 1990; Cui and Delage, 1996), despite the tight differences observed between unsaturated tests.

As far as what concerns to *SC*, a strong influence of molding water content on the mechanical behaviour was found at both large and very small strain domain, namely regarding strength and stiffness parameters, which is attributed to suction effect. Strength and stiffness increases with decreasing molding water content, i.e. with increasing suction. However, for the same state conditions, strength and stiffness was found to decrease with increasing stress and strain levels, which is due to a reduction of suction effect. In what concerns to strength, these trends agrees with the ones found by Estabragh *et al.* (2004) and differs from Alonso *et al.* (1990). Stress–strain curves featuring materials in a dense state were obtained. Critical state had been reached in unsaturated and saturated tests and a similar internal friction angle at critical state (ϕ_{cs}) was found, thus material behaviour at critical state is independent of initial saturation condition. Concerning to stiffness, similar trends were found by Fleureau *et al.* (2003). It is noteworthy that stiffness degradation curves were found to lie between a reference threshold shear strain given by Santos (1999). As so, the material characterization on the very small and large strain domain enabled to estimate stiffness for any strain domain.

A stress–strain non linear behaviour featuring material in a dense state was also observed from crushed aggregate (*CA31.5*) specimens. However, slight influence of molding water content on the mechanical behaviour was found at large strain domain, which indicates little influence of suction effect on strength and stiffness in the range of molding water content studied. This is probably due to a negligible fine fraction. Unsaturated specimens denoted higher britleness behaviour, corresponding higher secant friction angles. However, in contrast to *SC* material, specimen with optimum molding water content presented the highest friction angle and saturated specimens the lowest. Once again, differences become lower with increasing total mean stress level. Critical state had been reached only for saturated test. Concerning to stiffness, no significant differences on specimens stiffness were found for strain and stress levels evaluated. To this end, suction seems not to play an important role on *CA31.5* material stiffness for the studied compaction conditions.

Further, multistage procedure was found to provide good results regarding peak deviatoric stresses, as long as no significant structure disturbance is experimented at each stage. However, stress–strain curves present higher britleness behaviour rather than triaxial single stage tests.

Finally, as far as what concerns to tests on the very strain domain a setup using bender elements and accelerometers was attempted. Comparison between

results obtained using BE and accelerometers showed that, generally, results obtained with both sensors slightly differs, with exception to the specimen with higher moisture content where significant differences were found. The investigation of travel time determination showed that picking arrival time from both accelerometers is straight, whereas picking bender elements arrival point is ambiguous. This difficulty, probably due to near-field effects amplified by a high degree of saturation, led to pick the wrong arrival time, thus to mislead computation of S-wave velocity. Therefore, the measurement of S-waves using accelerometers as receivers appears to improve measurements quality in the time domain, particularly concerning quasi-saturated specimens.

8.1.2 Field investigation: Évora trial railway embankment (*ETRE*)

A full scale trial was carried out involving two type of geomaterials, *SC* and *CA31.5*. Trial layers with different thicknesses (0.22, 0.30, 0.40 and 0.50 m) and different moisture contents (2% dry of optimum, optimum and 2% wet of optimum Modified Proctor) were constructed. Then, evaluation of state conditions and mechanical properties for several energy levels were carried out and statistical data was computed.

State conditions were evaluated by means of sand cone method (*SCM*) and nuclear method (*NM*), the latter requiring calibration. Regarding *SC* trial layers, average moisture content of trial layers ranged from 3% dry of optimum to 1.5% wet of optimum, which reflects a deviation from previously planned. Further, statistical data showed higher moisture content coefficient of variation (*CV*) from *SC* trial layers compacted dry of optimum, rather than *SC* trial layers compacted with moisture content wet of optimum. Concerning to *CA31.5* trial layers, moisture content 1% wet of optimum was achieved on layer with 0.22 m thickness, whereas moisture content close to optimum value was achieved on trial layer with 0.30 m thickness. Moreover, moisture content strongly varied within increasing energy level. In fact, moisture content obtained from both layers for the first energy level was about 1.5% dry of optimum.

As so, the previous stack of material, water adding and mix up by means of a front shovel did not reproduced the desirable moisture contents nor even the desirable homogeneity. It should be noted that the adverse weather conditions during construction of some trial layers might had contributed to these results. This notwithstanding, dry density *CV* lie below maximum values given by Brandl (1977), with exception to *SC* trial layer with 0.50 m thickness. To this end, layer with 0.50 m thickness does not fulfill quality control requirements of high quality projects, namely those regarding high speed embankments. Further, layer thickness was found to influence relative compaction of *SC* trial layers for the compaction equipment and energy levels studied. Relative compaction decreased with increasing layer thickness.

Mechanical evaluation was carried out by means of static plate load test (*SPLT*) and performance related tests, namely, Soil Stiffness Gauge (*SSG*), light falling weight deflectometer (*LFWD*), falling weight deflectometer (*FWD*), spectral analysis of surface waves (*SASW*) and Portancemètre.

Focus was given to the evaluation of mechanical properties by means of *SPLT* which were performed following two commonly used standards, AFNOR NF P94-117-1 (2000) and DIN 18134 (2001). *SPLT* following AFNOR was

carried out using two settlement measuring systems: one measuring settlement on a point at the center of the plate through a hole; another measuring settlement three concentric points on the periphery of the plate. Results from the former measuring systems were found to be more than 30% higher than corresponding values obtained with the latter. Therefore, measuring settlement on a point at the center of the plate through a hole is not recommended. Furthermore, analysis of both standards was performed and differences concerning to test proceed and test interpretation was found. Comparison between results obtained from direct interpretation of *SPLT*s following AFNOR NF P94-117-1 (2000) and DIN 18134 (2001) standards showed a difference between moduli of approximately 10%, where values obtained from DIN standard were the highest. However, differences between standards regarding stress level and method of interpretation were observed. Thus, interpretation for same stress level (200 kPa) and method (secant method) was conducted. In this case modulus given by tests performed following DIN standard were 15% lower than the ones achieved by tests performed following AFNOR standard. In addition, equivalent modulus should take into account different plates diameter if a multi-layered system is being tested. Conclusions regarding *SPLT* led to the specification project (Gomes Correia *et al.*, 2007) that is presented in Appendix B.

The analysis of the results from several tests methods to evaluate moduli allowed to establish correlations and testify equipment calibrations using *SPLT* as reference test. Good correlation between *SPLT* and Portancemètre moduli was established for *SC* trial layers, the latter being about 10% higher than the former. Although a correlation close to unity was obtained between *SPLT* and *LFWD* on *SC* trial layers, high scatter led to poor correlation. Thereby, results from this equipment should be treated with caution. No correlation was found between *SPLT* and the others performance related tests. Results from *CA31.5* trial layers did not allowed to establish correlations between *SPLT* as reference test and performance related tests. Therefore, equipments calibration for each kind of material is required.

These results indicate the huge potential of Portancemètre for the continuous stiffness evaluation on earthwork platforms, being a non destructive method easy to operate enabling quick evaluation of moduli and large number of tests, which allows statistical analysis. Moreover, the instantly layout of moduli enables immediate intervention ever quality control requirements are not achieved. In addition, afterwards treatment of results allows spacial characterization of full area of compacted layer. Thereby, mechanical evaluation by means of Portancemètre represents a great improvement on quality control/quality assurance (Q_a/Q_c) of compacted layers.

Then, the influence of state conditions on the mechanical properties was evaluated. In what concerns to *SC* trial layers no moduli was found to decrease with increasing moisture content confirming, thus reflecting suction effect on mechanical properties. Indeed, this trend is consistent with laboratory results. Further, Portancemètre moduli *CV* decreased with increasing moisture content. These results denote the great influence of moisture content either on average moduli and on homogeneity of mechanical performance of layers embankment. No clear relationship between dry density and moduli was found. With regards to *CA31.5* trial layers, moduli was found to follow moisture content variation. Moduli increased with increasing moisture content, as long as moisture content varies between about 2% dry of optimum and optimum value. This trend indi-

cates the great influence of moisture content on mechanical performance rather than dry density. It is noteworthy that the highest modulus was obtained for moisture content close to optimum value, which is consistent with results from laboratory results once again.

To sum up, great influence of moisture content was found either on average moduli and homogeneity rather than density. As so, higher requirements regarding compaction control should be considered regarding moisture content rather than dry density, particularly when compaction is performed with moisture content on the dry side as long as compacted layers will remain in unsaturated condition. Further, since mechanical properties reflect moisture conditions, continuous evaluation of mechanical performance represents a great improvement on compaction control. This fact highlights the great benefit using continuous compaction control devices like Portancemètre.

Finally, comparison between full scale trial and laboratory results was performed. A perfect match between shear modulus obtained from *SASW* and shear modulus given by laboratory tests was found. In addition, a maximum difference of 19% between modulus obtained from *SPLT* following AFNOR standard and modulus estimated from triaxial compression tests was found. These findings assumes great importance taking into account two issues: (i) design is based on mechanical properties usually determined from laboratory tests; (ii) even though conventional triaxial tests only allow determination of mechanical properties beyond strain level of 1%, for *SC* geomaterial is possible to estimate secant modulus from degradation curves for lower strain levels since degradation curves lie between reference threshold for sands given by Santos (1999).

8.1.3 Field investigation: Fafe trial road embankment (*FTRE*)

Another full scale trial was performed. Three types of materials were studied, namely, poor-graded sand (*SP*) used in trial and embankment layers, inert steel aggregate for construction (*ISAC*) used in trial, embankment and base layers and crushed aggregate (*CA40*) used in base layers. However, only *SP* and *ISAC* were used in trial layers, which were constructed at optimum water content with varying thicknesses compacted with different energy levels. Likewise in *ETRE*, a full scale trial was carried out involving state conditions and mechanical properties evaluation.

State conditions were obtained from *SCM*, rubber balloon method (*RBM*) and *NM* tests, the last requiring calibration. *NM* was found to be inappropriate to determine state conditions of *ISAC* layers.

Moisture content of *SP* trial layers ranged over 3–4% dry of optimum, whereas embankment layers varied between 1 and 3% dry of optimum. The wetting process employed on *SP* material which involved the previous stack of material, water adding and mix up by means of a front shovel and, in addition, in situ moisture content correction before compaction process, did not reproduced desirable moisture conditions close to optimum. The highest moisture content *CV* was obtained from trial layer with 0.50 m thickness, which denotes the influence of layer thickness on moisture content homogeneity. Nevertheless, dry density *CV* was less than 3% for all layers, which lie below limit given by Brandl (1977).

Focus was given to the analysis of the results from tests methods to evaluate moduli. Correlations between moduli obtained from *LFWD*, *SSG*, *FWD*, *SASW*

and Portancemètre using *SPLT* as reference test were attempted. Concerning to *SP* material, though the data is limited, a general relationship between *SPLT* modulus (E_{V2}) and Portancemètre (E_{Port}) moduli close to unity was found once again. This means that results given by these tests are approximately the same validating the calibration method used. Correlation between *SPLT* and other performance related tests showed differences higher than 55%. As so, due to lack of results of *SPLT*, Portancemètre was used as reference test to confirm correlations based on a greater number of points. However, high scatter did not enable sustainable conclusions. As mentioned previously, the results from *LFWD* and *SSG* equipment should be treated with caution.

With regards to *ISAC* material different conclusions were obtained. Moduli given by *SPLT* (E_{V2}) and Portancemètre (E_{Port}) differed approximately 45%. Once more, due to lack of *SPLT* tests, Portancemètre was used as reference test. Correlation between *LFWD* and ‘Portancemètre’ moduli was close to unity (only differs 12%), while between *SSG* and Portancemètre moduli differs 30%, yet high scatter was observed. Concerning to *CA40+SP* profile due to lack of results no sustainable conclusions were obtained. This shows the necessity of equipments calibration for each kind of material. Though it seems possible to establish correlations between moduli of in situ performance-based tests methods, material type and state conditions should be taken into account on this evaluation.

SASW were carried out on *SP* embankment layer using different sources types, namely light hammer, sledge hammer and *LFWD* and *FWD* equipments. Good results were obtained using light hammer source, *LFWD* and *FWD* as sources. This findings assume great importance, specially in the case of *FWD* since equipment has already mounted a deflection measuring system consisting of 8 geophones positioned along 3 meters from the center of the source (loading plate). Besides traditional back-analysis or even static loading approach for the interpretation of *FWD* test, data gathered from these sensors can be used to perform surface seismic analysis. This interpretation would allow, on one hand to confirm traditional back-analysis regarding the number of layers and, on the other hand, the extraction of modulus on the very small strain domain.

Then, analysis of moduli and state conditions was conducted. In contrast to conclusions obtained from *ETRE*, moisture content was found have unnoticeable influence on moduli for the range of moisture content studied, 1 to 4% dry of optimum. Conversely, dry density seems to influence mechanical properties. Moduli increased with increasing dry density, as long as moisture content do not vary significantly. However, no relation between dry density *CV* and modulus *CV* was found.

Comparison between full scale trial and laboratory results yielded differences lower than 27%, laboratory moduli being higher than field moduli. This results assumes great importance taking into account that design is based on mechanical properties usually determined from laboratory tests.

Further, an experimental program was carried out to monitor drum roller and layer vibrations in two phases. Phase One aimed vibrations measurement of the capping layer during tests, namely, *LFWD*, *FWD*, Portancemètre and roller drum. Accelerometers and strain gauges were buried on the capping layer enabling measurement of dynamic response and total strains. *ISAC* and *SP* materials were tested in this phase.

Stain measurements from *SP* and *ISAC* profiles during aforementioned tests

indicate different depths of influence, which can be ordered in increasing way: *LFWD*, *FWD*, Portancemètre and roller drum. However, strain measurements did not always reflected moduli obtained from performance related tests, since higher strains were obtained from in-ground measurements in *ISAC* profile that was found to had higher stiffness. On the contrary, in-ground displacements obtained from acceleration measurements were consistent with profiles stiffness. Higher in-ground displacements were found regarding *SP* profile than in *ISAC* profile, which is consistent with lower modulus obtained in the former than the latter. Hence, in-ground dynamic response was found to reflect moduli obtained from dynamic tests performed at layer surface.

Comparison between in-ground strains and displacements during impact loads *LFWD* and *FWD* on *SP* profile, showed consistency with theoretical approach considering a single modulus, yet modulus obtained from both tests differed. These results highlight the importance of test methods calibration using a reference test. Moreover, it allowed to conclude higher depth of influence from plate with higher diameter. Results obtained from *ISAC* profile did not confirmed these conclusions, which might be attributed to stationary drum tests between impact tests which induced significant differences on profile mechanical homogeneity.

Analysis of in-ground accelerations during Portancemètre and roller drum passes on *SP* profile exhibited non linear behaviour at depth of 0.10 m, while behaviour close to linear appears to prevail at depth of 0.45 m. Moreover, quite similar in-ground vibrations were found at higher depth, which denotes similar dynamic in-ground response. Since roller drum and Portancemètre wheel dynamic behaviour reflects dynamic in-ground response, this fact might indicate a good correlation between mechanical properties determined from instrumented rollers and Portancemètre.

Owing to the roller drum behaviour monitoring during stationary vibration tests, comparison between drum acceleration given by both sensors (one located at the top and middle of the drum and another located at the left side of the non-rotating mount) slightly differed for low eccentric static moments and was almost the same for higher static moments. Acceleration measured at the top middle of the drum was greater and signal noise level was lower. Approximated displacements obtained from sensor on the left side were 85% lower than the ones obtained from sensor at the top middle. Since continuous compaction control (CCC) based on roller drum measurements uses displacements obtained from computed acceleration signals, this difference should be taking into account on stiffness determination.

Phase Two involved vibrations measurement of roller drum and vibrations of capping layer during compaction of base layer. Vertical drum acceleration and displacement were found to be sensitive to changes in underlying soil stiffness. Both decreased with increasing soil stiffness for an excitation frequency of about 19 Hz, which features drum vibration below the natural frequency of test bed. Further, good correlation was found between drum vibration and *SPLT* modulus obtained from *ISAC* and *CA40+SP* profiles. In addition, at 0.65 m depth strain levels induced by *SPLT* were similar to the ones induced by roller drum, denotes identical depth of influence. These findings shows that *SPLT* modulus is related to drum behaviour and, therefore, should be used as reference test.

Concerning in-ground vibrations measurements, similar trend to drum behaviour was found, i.e., accelerations and computed displacements decreased

within number of passes on both profiles, that is the same to say with increasing stiffness. Therefore, in-ground dynamic response measured by means of in-ground accelerometers denotes close relation to drum behaviour, as was concluded from Phase One. On the other hand, results from in-ground strains were inconclusive.

8.2 Prospective work

As future work hydro-mechanical behaviour of *SC* geomaterial in unsaturated condition should be investigated using suction measurement apparatus in order to get a better insight on the interpretation of both laboratory and field results. On one hand, it would allow effective stress analysis and validate matric suction obtained from filter paper method and, on the other hand, to validate theoretical effective stress approaches.

Taking into account the apparent influence of dry density on the mechanical behaviour of *SP* material for slight variations of moisture content, a laboratory campaign is required in order to confirm this behaviour.

The measurement of S-waves velocity by means of bender elements and accelerometers requires calibration using materials with well known properties. Further, interpretation technique of accelerometers signal in the frequency domain is necessary in order to compare with results obtained from time domain.

Regarding mechanical evaluation by means of field tests, full scale trials employing different materials would be useful in order to establish correlations between mechanical tests. Further, it allows to get state parameters and mechanical properties variation, which information is of great interest on the behaviour analysis and design involving reliable analysis.

In addition, full scale trials should be performed coupled with “intelligent rollers” promoting and validating this technology (Parente, 2010). Moreover, investigations using in-ground sensors (strain gauges, cell pressures and accelerometers) should be carried out. Vibration characteristics of the roller drum should be continuously monitored enabling the loading action of the drum to be characterized. This information would be then used to develop numerical models of the interaction roller drum-material behaviour during compaction process.

The *FWD* appears to be a promising device to evaluate modulus in the very small strain domain, besides large strain domain. This equipment applies impact loads and has already mounted a deflection measuring system consisting of 8 geophones positioned along 3 meters from the center of the source (loading plate). As so, besides traditional back-analysis or even static loading approach for the interpretation of *FWD* test, data gathered from these sensors could be used to perform seismic analysis of surface waves. This interpretation would allow the extraction of low strain modulus. This would represent a great benefit on the mechanical evaluation of road and railway platforms.

Bibliography

- Abu-Farsakh, M. Y., Alshibli, K., Nazzal, M. and Seyman, E. "Assessment of in situ test technology for construction control of base courses and embankments. Report No. FHWA/LA.04/385." Technical report, Louisiana Transportation Research Center, Louisiana, USA (2003).
- Achenbach. *Wave propagation in elastic solids*. Elsevier Science, Amsterdam, The Netherlands (1999).
- Adam, C. and Adam, D. "Modelling of the dynamic load plate test with the light falling weight device." *Asian Journal of Civil Engineering (Building and Housing)*, 4: 73–89 (2003).
- Adam, D. *Flächendeckende dynamische Verdichtungskontrolle (FDVK) mit Vibrationswalzen*. Ph.D. thesis, Technical University of Vienna (1996).
- Adam, D. and Kopf, F. "Sophisticated compaction technologies and continuous compaction control." *Compaction of Soils and Granular Materials. Gomes Correia & Quibel (eds.), Presses Ponts et Chaussées, Paris, France*, 207–220 (2000).
- Adam, D. and Kopf, F. "Operational devices for compaction optimization and quality control (continuous compaction control & light falling weight device)." *Proc. International Seminar on Geotechnics in Pavement and Railway Design and Construction, Athens, Greece*, 97–106 (2004).
- AFNOR NF P94–117–1. "Sols: reconnaissance et essais. Portance des plates-formes. Partie 1: Module sous chargement statique à la plaque (E_{v2})." *Association Française de Normalisation* (2000).
- Alonso, E., Gens, A. and Josa, A. "A constitutive model for partially saturated soils." *Géotechnique*, 3(40): 405–430 (1990).
- Alshibli, K. A., Abu-Farsakh, M. and Seyman, E. "Laboratory evaluation of the geogauge and light falling weight deflectometer as construction control tools." *Journal of Materials in Civil Engineering, ASCE, September/October*, 560–569 (2005).
- Anderegg, R. *Nichtlineare Schwingungen bei dynamischen Bodenverdichtern*. Ph.D. thesis, Fortschritt-Berichte VDI Reihe 4: Bauingenieurwesen Nr. 146. Düsseldorf. In German (1998).

- Anderegg, R. “Ace ammann compaction expert - automatic control of the compaction.” *Compaction of Soils and Granular Materials. Gomes Correia & Quibel (eds.), Presses Ponts et Chaussées, Paris, France*, 229–236 (2000).
- Anderegg, R. and Kaufmann, K. “Intelligent compaction with vibratory rollers: Feedback control systems in automatic compaction and compaction control.” *Transportation Research Record. 1868*, 124–134 (2004).
- Anderegg, R., von Felten, D. and Kaufmann, K. “Compaction monitoring using intelligent soil compactors.” *Proc. GeoCongress 2006: Geotechnical Engineering in the Information Technology Age, February, Atlanta* (2006).
- Aouad, M., Stokoe, K. and Joh, S.-H. “Estimating subgrade stiffness and bedrock depth: Combined Falling Weight Deflectometer and simplified Spectral Analysis of Surface Waves Measurements.” *Transportation Research Record: Journal of the Transportation Research Board*, 40–48 (2007).
- Araújo, N. *Desenvolvimento de equipamento triaxial de precisão para a obtenção do limite elástico de geomateriais*. Provas de Aptidão Pedagógica e Capacidade Científica, Universidade do Minho, Setembro, Guimarães (2007).
- Arroyo, M. *Pulse tests in soil samples*. Ph.D. thesis, University of Bristol, UK (2001).
- Arroyo, M., Medina, L. and Muir Wood, D. “Numerical modelling of scale effects in bender-based pulse tests.” NUMOG VIII, Pande, G.N. and Pietruszczak, S. (eds): 589–594 (2002).
- Arroyo, M., Muir Wood, D. and Greening, P. “Source near-field effects and pulse tests in soil samples.” *Géotechnique*, 53(3)(3): 337–345 (2003).
- Arroyo, M., Muir Wood, D., Greening, P. D., Medina, L. and Rio, J. “Effects of sample size on bender-based axial g_0 measurements.” *Géotechnique*, 56(1): 39–52 (2006).
- Arulnathan, R., Boulanger, R. and Riemer, M. “Analysis of bender element tests.” *Geotechnical Testing Journal*, 21(2): 120–131 (1998).
- ASTM D2487. “Standard practice for classification of soils for engineering purposes (Unified Soil Classification System).” *ASTM International* (2000).
- ASTM D5298. “Standard test method for measurement of soil potential (suction) using filter paper.” *Annual Book of ASTM Standards*, 15.09 (1992).
- Aubertin, M., Mbonimpa, M., Bussière, B. and Chapuis, R. P. “A model to predict the water retention curve from basic geotechnical properties.” *Canadian Geotechnical Journal*, 40(6): 1104–1122 (2003).
- Bardanis, M. and Kavvadas, M. “Soil–water characteristic curves and void ratio changes relative to suction for soils from greece.” *Unsaturated Soils: Advances in Geo-Engineering Toll et al. (eds). Taylor & Francis Group, London, ISBN 978-0-415-47692-8*, 263–269 (2008).

- Barden, L. and Sides, G. "Engineering behavior and structure of compacted clay." *Journal of Soil Mechanics and Foundations Division, ASCE*, 96(4): 1171–1197 (1971).
- Barrera, M. *Estudio experimental del comportamiento hidro-mecánico de suelos colapsables*. Ph.D. thesis, E.T.S de Ingenieros de Caminos, Canales & Puertos de Barcelona (2002).
- Biarez, J., Fleureau, J. M. and Kheirbek-Saoud, S. "Validité de $\sigma' - \mu_w$ dans un sol compacté." In "Proc. 10th European Conference on SMFE, Firenze," (1991).
- Biarez, J., Fleureau, J. M. and Taibi, S. "Mechanical constitutive model for unsaturated granular media made up by spheres." In Thornton (editor), "Proc. 2nd Int. Conf. on Micromechanics of Granular Media. Birmingham (ed. by Thornton), Balkema, Rotterdam, 51–58," 51–58. Balkema, Rotterdam (1993).
- Biarez, J., Gomes Correia, A. and Lopez-Caballero, F. "From very small strains to failure." *Deformation characteristics of geomaterials. Di Benedetto et. al (eds)*, 125–141 (2005).
- Bicalho, K., Marinho, F., Fleureau, J.-M. and Gomes Correia, A. "Evaluation of filter paper calibrations for indirect determination of soil suctions of unsaturated soils." *Unsaturated Soils - Alonso & Gens (eds) ©2011 Taylor & Francis Group, London, ISBN 978-0-415-60428-4*, 609–613 (2011).
- Bicalho, K., Marinho, F. A., Gomes Correia, A., Ferreira, S. and Fleureau, J. "Effect of the filter paper calibration on the soil–water retention curve of an unsaturated compacted silt sand." *XI Congresso Nacional de Geotecnia, Coimbra, Portugal. CD-ROM* (2008).
- Bishop, A. and Donald, I. "The experimental study of partly saturated soil in the triaxial apparatus." In "Proceedings of the 5th International conference of soil mechanics and foundation engineering," volume 1, 13–22 (1961). Paris.
- Bishop, A. W., Alpan, I., Blight, G. and Donald, I. "Factors controlling the strength of partly saturated cohesive soils." In "Proc. ASCE Conf. on Shear Strength of Cohesive soils," 503–532. Boulder (1960).
- Blewett, J., Blewett, I. and Woodward, P. "Phase and amplitude responses associated with the measurement of shear–wave velocity in sand by bender elements." *Canadian Geotechnical Journal*, 37: 1348–1357 (2000).
- Bowles, J. E. *Engineering properties of soils and their measurements*. McGraw–Hill, New York (1970).
- Brandl, H. *Unbound courses in road engineering – Compaction, grain crushing, frost resistance, bearing behaviour, design, quality requirements, quality assurance and control (in German)*. Vienna: Federal Ministry of Public Works and Technology (1977).
- Briaud, J. and Seo, J. "Intelligent compaction: Overview and research needs." Technical report, Texas A&M University (2004).

- Briaud, J. L. "Introduction to soil moduli." *Geotechnical News, BiTech Publishers, Richmond, B.C., Canada.*, 19.02 (2001).
- Brignoli, E., Gotti, M. and Stokoe, K. "Measurement of shear waves in laboratory specimens by means of piezoelectric transducers." *Geotechnical Testing Journal*, 19(4): 384–397 (1996).
- Brocanelli, D. and Rinaldi, V. "Measurement of low strain material damping and wave velocity with bender elements in the frequency domain." *Canadian Geotechnical Journal*, 35: 1032–1040 (1998).
- Brooks, R. H. and Corey, A. T. "Properties of porous media affecting fluid flow." *Journal of the Irrigation and Drainage Division. ASCE*, 92(2): 61–88 (1966).
- Burland, J. "On the compressibility and shear strength of natural clays." *Géotechnique*, 40(3): 327–378 (1990).
- Burmister, D. "Evaluation of pavement systems of the WASHO road testing layered system methods." *Highway Research Board, Washington, D.C.*, 26–54 (1958).
- Caicedo, B., Coronado, O., Fleureau, J. and Gomes Correia, A. "Resilient behaviour of non standard unbound granular materials." *Road Materials and Pavement Design*, 10(2): 287–312 (2009).
- Caldeira, L. "Linha ferroviária Casa Branca – Évora. Resultados dos ensaios realizados no aterro experimental." Technical report, LNEC (2006).
- Chandler, R. J., Crilley, M. S. and Montgomery-Smith, G. "A low-cost method of assessing clay desiccation for low-rise buildings." In "Institute of Civil Engineering," volume 92, 82–89 (1992).
- Chandler, R. J. and Gutierrez, C. I. "The filter paper method of suction measurement." *Géotechnique*, 2: 265–268 (1986).
- Coronado, O., Fleureau, J., Gomes Correia, A. and Caicedo, B. "Influence of suction on the properties of two granular road materials." *International Conference on the Bearing Capacity of Roads, Railways and Airfields, Trondheim, Norway* (2005).
- Coussy, O. and Dangla, P. "Approche énergétique du comportement des sols non saturés." *Mécanique des sols non saturés. (eds. by Coussy, O. and Fleureau, J. M.), Hermès, Paris*, 137–174 (2002).
- Cui, Y. and Delage, P. "Yielding and plastic behaviour of an unsaturated compacted silt." *Géotechnique*, 46(2): 291–311 (1996).
- de Beer, E. "Influence of the mean normal stress on the shearing strength of sand." *Proceedings of the 6th International Conference on Soil Mechanics and Foundation Engineering. Montreal.*, 1: 165–169 (1965).
- Delage, P., Audiguier, M., Cui, Y. and Howat, M. "Microstructure of a compacted silt." *Canadian Geotechnical Journal*, 33(1): 150–158 (1996).

- Delage, P., Romero, E. and Tarantino, A. "Recent developments in the techniques of controlling and measuring suction in unsaturated soils." *Unsaturated Soils: Advances in Geo-Engineering Toll et al. (eds). Taylor & Francis Group, London, ISBN 978-0-415-47692-8*, 33–52 (2008).
- DIN 18134. "Determining the deformation and strength characteristics of soil by plate loading test." *Deutsches Institut für Normung* (2001).
- d'Onofrio, A. and Penna, A. "Influence of compaction variables on the small strain behaviour of a clayey silt." In "Deformation Characteristics of Geomaterials, Di Benedetto et al. (eds), Swets & Zeitlinger, Lisse," (2003).
- Dyvik, R. and Madshus, C. "Laboratory measurements of g_{max} using bender elements." In "ASCE convention: Advances in the art of testing soils under cyclic conditions, Detroit, Michigan," (1985).
- Edil, T. and Sawangsurya, A. "Earthwork quality control using soil stiffness." *Proceedings of the 16th International Conference on Soil Mechanics and Geotechnical Engineering, Osaka, Japan* (2005).
- EN 1097-6. "Test for mechanical and physical properties of aggregates – Part 6: Determination of particle density and water absorption." *European Committee for Standardization* (2000).
- EN 13286-2. "Unbound and hydraulically bound mixtures – Part 2: Test methods for the determination of the laboratory reference density and water content – Proctor compaction." *European Committee for Standardization* (2004).
- Estabragh, A. and Javadi, A. "Critical state for overconsolidated unsaturated silty soil." *Canadian Geotechnical Journal*, 45: 408–420 (2008).
- Estabragh, A., Javadi, A. and Boot, J. "Effect of compaction pressure on consolidation behaviour of unsaturated silty soil." *Canadian Geotechnical Journal*, 41: 540–550 (2004).
- Ewins, D. J. *Modal testing : theory, practice and application*. Research Studies Press, Baldock, Hertfordshire, UK (2000).
- Fam, M. and Santamarina, J. C. "Study of geoprocesses with complementary mechanical and electromagnetic wave measurements in an oedometer." *Geotechnical Testing Journal*, 18(3): 307–314 (1995).
- Fawcett, R. G. and Collis-George, N. "A filter paper method for determining the moisture characteristics of soil." *Australian Journal of Experimental Agriculture and Animal Husbandry*, 7: 162–167 (1967).
- Ferreira, C. "Bender element tests measurements using time and frequency domain techniques." In "3rd International Symposium on Deformation Characteristics of Geomaterials. Lyon, France," (2003).
- Ferreira, C. *The Use of Seismic Wave Velocities in the Measurement of Stiffness of a Residual Soil*. Ph.D. thesis, Faculty of Engineering of the University of Porto (2008).

- Ferreira, C., Martins, J. P. and Gomes Correia, A. “Setup of bender–extender elements and accelerometers in a triaxial stress–path cell (in portuguese).” *12 Congresso Nacional de Geotecnia. In CD-Rom*, 247–256 (2010).
- Fleming, P., Frost, M. and Lambert, J. “A review of the lightweight deflectionometer (LWD) for routine insitu assessment of pavement material stiffness.” *TRB 2007 Annual Meeting* (2007).
- Fleureau, J. M., Dufour-Laridan, E. and Gomes Correia, A. “Influence of compaction and loading conditions on the dynamic properties of a silty sand.” In “Proc. 4th Int. Conf. on Recent Advances in Geotechnical Earthquake Engineering and Soil Dynamics, San Diego,” (2001).
- Fleureau, J. M., Hadiwardoyo, S. and Gomes Correia, A. “Generalised effective stress analysis of strength and small strains behaviour of a silty sand, from dry to saturated state.” *Soils and Foundations*, 43(4): 21–33 (2003).
- Floss, R. and Kloubert, H. J. “Newest developments in compaction technology.” *Compaction of Soils and Granular Materials. Gomes Correia & Quibel (eds.), Presses Ponts et Chaussées, Paris, France*, 247–261 (2000).
- Forssblad, L. “Compaction meter on vibrating rollers for improved compaction control.” *Proc. Intl Conf. on Compaction, Paris*, 2: 541–546 (1980).
- Fortunato, E. *Renewal of railways platforms. Studies about bearing capacity*. Ph.D. thesis, University of Oporto, Porto, Portugal (in portuguese) (2005).
- Fredlund, D. and Morgenstern, N. “Stress state variable for unsaturated soils.” *Journal of Geotechnical Engineering Division, ASCE*, 103(103): 447–466 (1977).
- Fredlund, D. G. and Rahardjo, H. *Soil mechanics for unsaturated soils*. John Wiley & Sons, Inc. (1993).
- Gajo, A., Fedel, A. and Mongiovi, L. “Experimental analysis of the effects of fluid-solid coupling on the velocity of elastic waves in saturated porous media.” *Géotechnique*, 47(5): 993–1008 (1997).
- Gallipoli, D., Wheeler, S. J. and Karstunen, M. “Modelling the variation of degree of saturation in a deformable unsaturated soil.” *Géotechnique*, 53(1): 105–112 (2003).
- GDS Instruments. “Bender elements datasheet.” (2011). (last accessed at February 2011).
- Gomes Correia, A., Anh Dan, L. Q., Shinoda, M., Tatsuoka, F. and Koseki, J. “Small strain stiffness under different isotropic and anisotropic stress conditions of two granular granite materials.” In “In Shibuya et al. (ed.), Advanced laboratory stress–strain testing of geomaterials, Balkema: Rotterdam,” (2001).
- Gomes Correia, A., Araújo, N., Martins, J. and Cunha, J. “Ensaio de carga com placa realizados no aterro experimental da linha de Évora.” Technical report, University of Minho (2006).

- Gomes Correia, A., Martins, J., Caldeira, L., Maranha das Neves, E. and Delgado, J. “Comparison of in situ performance-based tests methods to evaluate moduli of railway embankments.” *8th International Conference on the Bearing Capacity of Roads, Railways and Airfields, Illinois*, 2: 1331–1340 (2009a).
- Gomes Correia, A., Martins, J. and Cunha, J. “Projecto de especificação do ensaio de carga estático com placa.” Technical report, University of Minho (2007).
- Gomes Correia, A., Reis Ferreira, S., Roque, A. and Cavalheiro, A. “Processed portuguese stell slag - A new geomaterial.” *8th International Conference on the Bearing Capacity of Roads, Railways and Airfields, Illinois*, 1: 197–204 (2009b).
- Goto, S., Tatsuoka, F., Shibuya, S., Kim, Y. and Sato, T. “A simple gauge for local small strain measurements in the laboratory.” *Soils and foundations*, 31: 169–180 (1991).
- Greening, P. and Nash, D. “Frequency domain determination of g_0 using bender elements.” *ASTM Geotechnical Testing Journal*, 27: 1–7 (2004).
- Guedes de Melo, F. *Compactação de aterros de barragens de terra*. Laboratório Nacional de Engenharia Civil, Lisboa, Portugal. (1985).
- Gupta, S., Ranaivoson, A., Edil, T., Benson, C. and Sawangsuriya, A. “Pavement design using unsaturated soil technology.” Technical report, Minnesota Department of Transportation (2007).
- Gurp, C., Groenendijk, J. and Beuving, E. “Experience with various types of foundation tests.” *Proceedings of the Fifth International Conference on Unbound Aggregate in Roads, Nottingham, United Kingdom* (2000).
- Hadiwardoyo, S. *Characterization of granular materials from very small to large strains*. Ph.D. thesis, Ecole Centrale Paris (2002).
- Hamblin, A. P. “Filter paper method for routine measurement of field water potential.” *Journal of Hydrology*, 53(3–4): 355–360 (1981).
- Hardin, B. O. and Richart, F. J. “Elastic wave velocities in granular soils.” *Journal of the Soil Mechanics and Foundations Division, ASCE*, 89(SM1): 33–65 (1963).
- Heisey, J. S., Stokoe, K. H. I. and Meyer, A. “Moduli of pavement systems from spectral analysis of surface waves.” *Transportation Research Record. No 852*, 22–31 (1982).
- Hillel, D. *Fundamentals of soil physics*. Academic Press, Inc., San Diego, CA. (1980).
- Hirikawa, D., Tatsuoka, F. and Kawasaki, H. “Stress distribution in sand subjected to roller compaction.” *Compaction of Soils and Granular Materials. Gomes Correia & Quibel (eds.), Presses Ponts et Chaussées, Paris, France*, 65–78 (2000).

- Ho, D. Y. F. and Fredlund, D. G. "A multistage triaxial test for unsaturated soils." *Geotechnical Testing Journal*, 5: 18–25 (1982).
- Hoque, E., Sato, T. and Tatsuoka, F. "Performance evaluation of Idts for use in triaxial tests." *Geotechnical Testing Journal*, 20: 149–167 (1997).
- Hoque, E. and Tatsuoka, F. "Anisotropy in the elastic deformations of materials." *Soils and Foundations*, 38(1): 163–179 (1998).
- Huang, S., Barbour, S. L. and Fredlund, D. "Development and verification of a coefficient of permeability function for a deformable unsaturated soil." *Canadian Geotechnical Journal*, 35: 411–425 (1998).
- Humboldt, M. C. *GeoGaugeTM. User guide. Model: H-4140* (2007).
- Ishibashi, I. and Zhang, X. "Unified dynamic shear moduli and damping ratios of sand and clay." *Soils and Foundations, JSSMFE*, 33(1): 182–191 (1993).
- Ishihara, K. *Soil behaviour in earthquake geotechnics*. Oxford University Press Inc. (1996).
- Johnson, K. *Contact mechanics*. Cambridge University Press, Cambridge, U.K. (1987).
- Jovicic, V. "Conditions for rigorous bender element test in triaxial cell." In "International Symposium on Deformation Characteristics of Geomaterials. Lyon, France.", (2003).
- Jovicic, V., Coop, M. and Simic, M. "Objective criteria for determining g_{max} from bender element tests." *Géotechnique*, 46(2): 357–362 (1996).
- Karube, D. and Kawai, K. "The role of pore water in the mechanical behavior of unsaturated soils." *Geotechnical and Geological Engineering*, 19: 211–241 (2001).
- Khalili, N., Geiser, F. and Blight, G. E. "Effective stress in unsaturated soils: Review with new evidence." *International Journal of Geomechanics*, 4(2): 115–126 (2004).
- Khalili, N. and Khabbaz, M. H. "A unique relationship for χ for the determination of the shear strength of unsaturated soils." *Géotechnique*, 48(5): 681–687 (1998).
- Koliji, A., Vulliet, L. and Laloui, L. "Structural characterization of unsaturated aggregated soil." *Canadian Geotechnical Journal*, 47(3): 297–311 (2010).
- Kröber, W. *Untersuchung der dynamischen Vorgänge bei der Vibrationsverdichtung von Böden*. Ph.D. thesis, Schriftenreihe, Heft 11, Lehrstuhl und Prüfamnt für Grundbau, Bodenmechanik und Felsmechanik der Technischen Universität München. In German. (1988).
- Kröber, W. and Floss, W., R. and Wallrath. "Dynamic soil stiffness as quality criterion for soil compaction." *Geotechnics for Roads, Rail Tracks and Earth Structures*, A.A. Balkema Publishers, Lisse / Abingdon / Exton (Pa) / Tokyo (2001).

- Kuwano, R., Wicaksono, R. and Mulmi, S. “Small strain stiffness of coarse granular materials measured by wave propagation.” *4th International Symposium on Deformation Characteristics of Geomaterials, Burns, S.E.; Mayne, P. W. and Santamarina, J.C. (eds) IOS Press, Amsterdam, Georgia Institute of Technology, Atlanta, Georgia, USA* (2008).
- Lambe, T. “The engineering behaviour of compacted clay.” *Journal of Soil Mechanics and Foundations Division, ASCE*, 84(2): 1–35 (1958a).
- Lambe, T. “The structure of compacted clay.” *Journal of Soil Mechanics and Foundations Division, ASCE*, 84(2): 1–34 (1958b).
- LCPC/SETRA. “Realisation des remblais et des couches de forme. Guide technique.” *Laboratoire Central des Ponts et Chaussées* (1992).
- Lee, J. S. and Santamarina, J. C. “Bender elements: Performance and signal interpretation.” *Journal of Geotechnical and Geoenvironmental Engineering*, 131(9): 1063–1070 (2005).
- Lee, S. *Backcalculation of Pavement Moduli by Use of Pavement Surface Deflections*. Ph.D. thesis, University of Washington, Seattle, Washington (1988).
- Lenke, L., McKeen, R. and Grush, M. “Laboratory evaluation of the geogauge for compaction control.” *TRB 2003 Annual Meeting, CD-ROM* (2003).
- Lenke, L. R., Gordon McKeen, R. and Grush, M. “Evaluation of a mechanical stiffness gauge for compaction control of granular media.” Technical report, Research Bureau New Mexico State Highway & Transportation Department, New Mexico, USA (2001).
- Likos, W. and Lu, N. “Filter paper technique for measurement total soil suction.” *Journal of the Transportation Research Board, No. 1786, TRB, Washington, D.C.*, 1120–1128 (2002).
- LNEC E 197. “Ensaio de compactação.” *Laboratório Nacional de Engenharia Civil* (1966).
- LNEC E 199. “Ensaio de equivalente de areia.” *Laboratório Nacional de Engenharia Civil* (1967).
- Lo Presti, D., Pallara, O. and Puci, I. “A modified commercial triaxial testing system for small strain measurements: Preliminary results on pisa clay.” *Geotechnical Testing Journal*, 18: 15–31 (1995).
- Loizos, A., Boukoulas, G. and A., K. “Dynamic stiffness modulus for pavement subgrade evaluation.” *Journal of Transportation Engineering, ASCE, July/August*, 434–443 (2003).
- Lundberg, G. “Elastische berührung zweier halbräume.” *Forschung auf dem Gebiete des Ingenieurwesens, Göteborg. In German*, 201–211 (1939).
- Maahtah, O. “Experimental verification of a theoretical model for the shear strength of unsaturated soil.” *Electronic Journal of Geotechnical Engineering*, 10(C): 1–9 (2005).

- Maaitah, O. and Mahadin, S. "Variation on shear strength of unsaturated subgrade causes roads cracks." *Journal of Applied Sciences*, 4(3): 335–339 (2004).
- Mancuso, C., Vassallo, R. and dOnofrio, A. "Small strain behavior of a silty sand in controlled–suction resonant column–torsional shear tests." *Canadian Geotechnical Journal*, 39: 22–31 (2002).
- Marinho, F. A. M. and Oliveira, O. M. "The filter paper method revised." *ASTM Geotechnical Testing Journal*, 29(3): 250–258 (2006).
- Marinho, F. A. M. and Stuermer, M. M. "The influence of the compaction energy on the SWCC of a residual soil." In "Geo–Denver 2000. Advances in Unsaturated Geotechnics," (2000).
- Martins, J., Gomes Correia, A., Ramos, L., Marcelino, J., Caldeira, L. and Delgado, J. "Measurement of vibrations induced by high–speed trains." *8th International Conference on the Bearing Capacity of Roads, Railways and Airfields, Illinois*, 2: 1311–1319 (2009).
- Modaressi, A., Abou Bekr, N. and Fry, J. J. "Unified approach to model partially saturated and saturated soil." In *Proc. I International Conference on Unsaturated Soils. Unsat'95. Unsaturated soils. Alonso & Delage Eds. Presses de l'École National des Ponts et Chaussées, Paris*, 3: 1495–1502 (1995).
- Mooney, M. A. and Adam, D. "Vibratory roller integrated measurement of earthwork compaction: An overview." *FMGM 2007: Seventh International Symposium on Field Measurements in Geomechanics, ASCE* (2007).
- Mooney, M. A., Gorman, P. B. and Gonzalez, J. N. "Vibration–based health monitoring of earth structures." *Structural Health Monitoring*, 4(2): 137–152 (2005).
- Mooney, M. A. and Miller, K. "Analysis of lightweight deflectometer test based on in situ stress and strain response." *Journal of Geoenvironmental Engineering*, 135(2): 199–208 (2009).
- Mooney, M. A. and Rinehart, R. V. "Field monitoring of roller vibration during compaction of subgrade soil." *Journal of Geotechnical Geoenvironmental Engineering, ASCE*, 257–265 (2007).
- Mooney, M. A. and Rinehart, R. V. "In–situ soil response to vibratory loading and its relationship to roller–measured soil stiffness." *Journal of Geotechnical and Geoenvironmental Engineering, ASCE*, 135(8): 1022–1031 (2009).
- Nazarian, S. *In situ determination of elastic moduli of soil deposits and pavement systems by Spectral–Analysis–of–Surface–Waves method*. Ph.D. thesis, University of Texas, Austin (1984).
- NF P 94–068. "Soils: investigation and testing. Measuring of the methylene blue adsorption capacity of a rocky soil. Determination of the methylene blue of a soil by means of the stain test." (1998).

- Nohse, Y. and Kitano, M. “Development of a new type of single drum vibratory roller.” *Proc. 14th International Conference of the International Society for Terrain-Vehicle Systems, Vicksburg, MS USA October 20-24* (2002).
- NP EN 933-8. “Ensaio das propriedades geométricas dos agregados. Parte 8: Determinação do teor de finos. Ensaio do equivalente de areia.” *Instituto Português da Qualidade* (2002).
- NP EN 933-9. “Ensaio das propriedades geométricas dos agregados. Parte 8: Determinação do teor de finos. Ensaio do azul de metileno.” *Instituto Português da Qualidade* (2002).
- NP 143. “Determinação dos limites de consistência em solos.” *IGPAI - Repartição e Normalização* (1969).
- NP 83. “Determinação da densidade das partículas.” *IGPAI - Repartição e Normalização* (1965).
- NP 84. “Solos. Determinação do teor em água.” *IGPAI - Repartição e Normalização* (1965).
- Nuth, M. and Lalouia, L. “Advances in modelling hysteretic water retention curve in deformable soils.” *Computers and Geotechnics*, 35(6): 835-844 (2008).
- Oh, W., Garga, V. and Vanapalli, S. “Shear strength characteristics of statically compacted unsaturated kaolin.” *Canadian Geotechnical Journal*, 45: 910-922 (2008).
- Oliveira, O. M. and Marinho, F. A. M. “Evaluation of filter paper calibration.” *UNSAT 2006* (2006).
- Parente, M. *Gestão da compactação*. Master’s thesis, University of Minho (2010).
- Pennington, D. *The anisotropic small strain stiffness of Cambridge Gault clay*. Ph.D. thesis, Department of Civil Engineering, Univ. Bristol (1999).
- Pennington, D. S., Nash, D. F. T. and Lings, M. L. “Horizontally mounted bender elements for measuring anisotropic shear moduli in triaxial clay specimens.” *Geotechnical Testing Journal*, 24(2): 133-144 (2001).
- Pietzsch, D. and Poppy, W. “Simulation of soil compaction with vibratory rollers.” *Journal of Terramechanics*, 6: 585-597 (1992).
- Poulos, H. and Davis, E. *Elastic Solutions for Soil and Rock Mechanics*. John Wiley & Sons, New York, NY (1974).
- Preisig, M., Caprez, M. and Amann, P. “Validieren von methoden der flachendecken dynamischen verdichtungskontrolle (FDVK).” Technical report, Ammann (2003).
- Qian, X., Gray, D. and Woods, R. “Voids and granulometry: effects on shear modulus of unsaturated sands.” *Journal of Geotechnical Engineering, ASCE*, 119(2): 295-314 (1993).

- Quibel, A. “New in situ devices to evaluate bearing capacity and compaction of unbound granular materials.” *Unbound Granular Materials. Laboratory Testing, In-situ Testing and Modelling*. Gomes Correia A. (ed.), Technical University of Lisbon, 141–151 (1999).
- Quibel, A. “Adapted “Portancemetre” for track structure stiffness measurement on existing tracks.” Technical Report TIP5-CT-2006-031415, LCPC and CETE Normandie-Centre (2006).
- Reis Ferreira, S. M. *Comportamento Mecânico e Ambiental de Materiais Granulares. Aplicação às Escórias de Aciaria Nacionais*. Ph.D. thesis, University of Minho (2010).
- Richards, G. “Measurement of the free energy of soil moisture by the psychrometric technique using thermistors.” *Moisture equilibria and moisture changes in soils beneath covered areas, A Symp, in Print*. Australia: Butterworths, 39–46 (1965).
- Richards, L. “A pressure– membrane extraction apparatus for soil solution.” *Soil Science*, 51: 377–386 (1941).
- Rinehart, R. V. and Mooney, M. A. “Instrumentation of a roller compactor to monitor vibration behavior during earthwork compaction.” *Automation in construction*, 17: 144–150 (2008).
- Rinehart, R. V. and Mooney, M. A. “Measurement of roller compactor induced triaxial soil stresses and strains.” *Geotechnical Testing Journal*, 32(4) (2009).
- Rio, J. *Advances in laboratory geophysics using bender elements*. Ph.D. thesis, University College London, University of London (2006).
- Rix, G. and Stokoe, K. I. “Stiffness profiling of pavement subgrades.” *Transportation Research Record*, 1235: 1–9 (1989).
- Rogers, C., Fleming, P. and Frost, M. W. “Stiffness behavior of trial road foundations.” *Proceedings of the Fifth International Conference on Unbound Aggregate In Roads, Nottingham, United Kingdom* (2000).
- Romero, E. and Simms, P. “Microstructure investigation in unsaturated soils: A review with special attention to contribution of mercury intrusion porosimetry and environmental scanning electron microscopy.” *Journal of Geotechnical and Geological Engineering*, 26: 705–727 (2008).
- Sánchez-Salineró, I., Roesset, J. M. and Stokoe, I., K.H. “Analytical studies of body wave propagation and attenuation.” Technical report, No GR86–15, Civil Engineering Department, University of Texas at Austin (1986).
- Sandström, A. and Pettersson, C. “Intelligent systems for Qa/Qc in soil compaction.” *Proc. of the TRB 2004 Annual Meeting* (2004).
- Santamarina, J. C., Klein, K. A. and Fam, M. A. *Soils and Waves – Particulate materials behavior, characterization and process monitoring*. John Wiley & Sons, New York (2001).

- Santos, J. A. *Caracterização de solos através de ensaios dinâmicos e cíclicos de toro. Aplicação ao estudo do comportamento de estacas sob acções horizontais estáticas e dinâmicas.* Ph.D. thesis, Instituto Superior Técnico (1999).
- Santucci di Magistris, F., Silvestri, F. and Vinale, F. “The influence of compaction on the mechanical behaviour of a silty sand.” *Soils and Foundations*, 38(4): 41–56 (1998).
- Santucci di Magistris, F. and Tatsuoka, F. “Effect of moulding water content on the stress–strain behaviour of a compacted silty sand.” *Soils and Foundations*, 44(2): 85–101 (2004).
- Sawangsurriya, A., Edil, T. and Bosscher, P. “Modulus-suction-moisture relationship for compacted soils.” *Canadian Geotechnical Journal*, 45: 973–983 (2008).
- Schevenels, M. and Geert Degrande, S. “EDT: An ElastoDynamics Toolbox for MATLAB.” *Computers & Geosciences*, 35: 1752–1754 (2009).
- Scullion, T., Sebesta, S., Rich, D. and Liu, W. “Field evaluation of new technologies for measuring pavement quality.” Technical report, Texas University (2006).
- Seed, H. and Chan, C. “Structure and strength characteristics of compacted clays.” *Journal of the SMFD, ASCE*, 85(SM1): 87–128 (1959).
- Sharma, R. and Bukkapatnam, A. “An investigation of unsaturated soil stiffness.” In “The 12th International Conference of International Association of Computer Methods and Advances in Geomechanics,” (2008).
- Sivakumar, V. and Wheeler, S. “Influence of compaction procedure on the mechanical behaviour of an unsaturated compacted clay. part 1: Wetting and isotropic compression.” *Géotechnique*, 50(4): 359–368 (2000).
- Stokoe, K., Wright, S., Bay, J. and Roesset, J. “Characterization of geotechnical sites by SASW method.” *Technical Review: Geophysical Characterization of Sites, ISSMFE Technical Committee 10, R.D. Woods (ed.), Oxford Publishers, New Delhi* (1994).
- Stokoe, K. I., Nazarian, S., Rix, G., Sanchez-Salinero, I., Sheu, J. and Mok, Y. “In situ seismic testing of hard-to-sample soils by surface wave method.” *Earthquake Engineering and Soil Dynamics II – Recent Advances in Ground-Motion Evaluation, ASCE*, 264–277 (1988).
- Sun, D. A., Sheng, D. C., Cui, H. B. and Sloan, S. W. “A density–dependent elastoplastic hydro–mechanical model for unsaturated compacted soils.” *Int. J. Numer. Anal. Meth. Geomech.*, 31: 1257–1279 (2007).
- Suriol, J. and Lloret, A. “Cambios en la estructura de suelos compactados frente a humedecimiento & secado.” *Ingeniería Civil*, 147: 67–76 (2007).
- Tarantino, A. “A water retention model for deformable soils.” *Géotechnique*, 59(9): 751–762 (2009).

- Tarantino, A. and Tombolato, S. “Coupling of hydraulic and mechanical behaviour in unsaturated compacted clay.” *Géotechnique*, 55(4): 307–317 (2005).
- Tatsuoka, F., Jardine, R., Lo Presti, D., Di Benedetto, H. and Kodaka, T. “Characterising the pre-failure deformation properties of geomaterials.” *Proc. XIV Int. Conf. on SMGE. Hamburg 1977. Balkema, Rotterdam*, 4: 2129–2164 (1997).
- Terzaghi, K. *Theoretical Soil Mechanics*. New York. John Wiley and Sons (1943).
- Theron, M., Clayton, C. R. I. and Best, A. I. “Interpretation of side-mounted bender element results using phase shift and group velocity.” *ISLyon03: International symposium on deformation behaviour of geomaterials (eds H. Di Benedetto, T. Doanh, H. Geoffroy and C. Sauzeat)*, 127–132, Balkema, Rotterdam (2003).
- THSRP. *Taiwan High Speed Railway Project. Design specification*, volume 9 (2003).
- Turner, H. and Sandström, A. “A new device for instant compaction control.” *Proceedings of International Conference on Compaction, Paris*, 2: 611–614 (1980).
- Turner, H. F. and Sandström, A. J. “Continuous compaction control, CCC.” *Compaction of soils and granular materials. Gomes Correia & Quibel (eds.)*, Presses Ponts et Chaussées, Paris, France, 237–246 (2000).
- Timoshenko, S. and Goodier, J. N. *Theory of elasticity*. McGraw–Hill, New York (1951).
- Tinjum, J. M., Benson, C. H. and Lisa, R. B. “Soil-water characteristic curves for compacted clays.” *Journal of Geotechnical and Geoenvironmental Engineering*, 1060–1069 (1997).
- TNO. *Diana 9*. <http://tnodiana.com/> (2005).
- Tokimatsu, F., Kuwayama, S., Tamura, S. and Miyadera, Y. “ v_s determination from steady state rayleigh wave method.” *Soils and Foundations*, 32(2): 153–163 (1991).
- UIC. “Ouvrages en terre et couches d’assise ferroviaires.” *Code UIC 719R, 2^{ème} édition* (2004).
- UNE 103–405–94. “Consolidación unidimensional de una muestra de terreno.” *Asociación Española de Normalización y Certificación (AENOR)* (1994).
- van Susante, P. J. and Mooney, M. A. “Capturing nonlinear roller compactor behavior through lumped parameter modeling.” *Journal of Engineering Mechanics*, 134(8): 684–693 (2008).
- Vanapalli, S. K., Fredlund, D. G., D.E., P. and Clifton, A. “Model for the prediction of shear strength with respect to soil suction.” *Canadian Geotechnical Journal*, 33: 379–392 (1996).

- Vanapalli, S. K., Fredlund, D. G., and Pufahl, D. E. “The influence of soil structure and stress history on the soil–water characteristics of a compacted till.” *Géotechnique*, 49(2): 143–159 (1999).
- Viana da Fonseca, A., Ferreira, C. and Fahey, M. “A framework for interpretation of bender element tests, combining time–domain and frequency–domain methods.” *Geotechnical Testing Journal*, 32 (2): 1–17 (2009).
- Viggiani, G. and Atkinson, J. “Interpretation of bender element tests.” *Géotechnique*, 45(1): 149–154 (1995).
- Wang, Q., Pufal, D. and Fredlund, D. “A study of critical state on an unsaturated silty soil.” *Canadian Geotechnical Journal*, 39: 213–218 (2002).
- Wheeler, S. and Sivakumar, V. “Influence of compaction procedure on the mechanical behaviour of an unsaturated compacted clay. part 2: Shearing and constitutive modelling.” *Géotechnique*, 50(4): 369–378 (2000).
- Wood, D. M. *Soil behaviour and critical state soil mechanics*. Cambridge University Press (1990).
- Yang, S., Lin, H., Kung, J. and Liao, J. “Shear wave velocity and suction of unsaturated soil using bender element and filter paper method.” *Journal of GeoEngineering*, 3(2): 67–74 (2008).
- Yoo, T.-S. and Selig, E. “Dynamics of vibratory–roller compaction.” *Journal of the Geotechnical Engineering Division, ASCE*, 1211–1231 (1979).
- Zaghloul, S. and Saeed, N. “The use of the falling weight defelectometer in asphalt pavement quality control, quality management of hot-mix asphalt.” *ASTM STP 1299, D.S. Decker (ed.), American Society for Testing and Materials, West Conshohocken, PA* (1996).

Appendix A

Background on the measurement of stiffness at small strain using dynamic methods

A.1 Introduction

The basic principles and methods for determining soil stiffness at very small strain rely on wave propagation phenomena in a linear elastic medium (Ishihara, 1996). If an oscillating loading is applied to a homogeneous unbounded elastic space, two types of waves will emanate from the loading: volumetric waves and surface waves.

From the two types of volumetric waves generated from an energy source, the one of most interest in this study is the shear wave. Since the pore fluid does not have shear stiffness, only the soil skeleton propagates S -waves. As a result, the shear modulus G of a material is related to the velocity of a shear wave through it by:

$$G = \rho \cdot V_s^2 \quad (\text{A.1})$$

where ρ is the density.

For an isotropic elastic soil the effective stress elastic parameters are related by:

$$E = 2 \cdot G \cdot (1 + \nu) \quad (\text{A.2})$$

On contrast, P -waves can be propagated also by the pore fluid. Therefore, in saturated, unconsolidated materials, P -wave velocities are often controlled by the bulk stiffness of water.

There are several ways to obtain the shear modulus either in the field or in laboratories in the small strain domain. In situ methods to determine shear modulus are generally described as a part of geophysical surveying, they all have

the principle of sending waves through the ground and recording them in different points, and the wave distortion and speed are interpreted to give information about the soil from which they pass. There are many methods available to create artificial waves like the Cross-Hole (*CH*) and Down-Hole (*DH*) methods, the seismic cone penetration test (*SCPT*) and the spectral analysis of surface waves (*SASW*).

Measurement of soil stiffness in laboratory throughout the small strain (about 10^{-5} up to 10^{-3}) can be made using local gauges attached directly to the specimen (Goto *et al.*, 1991; Hoque *et al.*, 1997), while throughout very small strain range (strains below 10^{-5}) can be made using dynamic methods, such as resonant column and bender element method (Santos, 1999; Ferreira, 2008). Since bender elements were used in laboratory tests, only bender element method will be focused.

A bender element is a piece of piezo-ceramic elements which distort or bends if a voltage across it is changed or, if bent by an external force, the voltage across it changes. The transducers are made of bimorphs in which two sheets of piezo-electric material are fused together. When a voltage is applied to it, depending on the materials polarity, it will either contract or expand, and similarly when it expands or contracts it produces a voltage. Therefore if a voltage is applied to both sides of the bender element, one side will lengthen while the other will shorten. This in turn will cause the bender element to flex in one direction, and then in the opposite direction when the voltage is reversed as shown in Figure A.1.

Bender elements may be assembled to operate in two different ways: parallel or series (fig. A.1). In parallel bimorphs, the electrodes are on the outside of each plate, but these are connected together to the same terminal and the central conductor is connected to the other terminal. The plates are polarized in the same direction in this case. In series bimorphs the electrodes on the outside of each plate are connected to a voltage source and the plates are polarised in opposite direction. They develop twice the voltage of those connected in parallel for the same driving force and they provide only half the displacement of parallel elements for the same applied voltage. To this end, a suitable setting should use a parallel bender element as the source and a series bimorph as the receiver.

Bender elements are usually set into the top and bottom platens of a triaxial or oedometer cell and penetrate into the specimen a small distance. Mounted as cantilever beams, one element is vibrated by changing the voltage across it. The motion of the bender element initiates a shear wave to propagate through the soil specimen. When the shear wave reaches bender element some distance away, it causes it to flex and thus producing a voltage between the electrodes. The input voltage (created using a function generator) and the received signal are monitored using a digital oscilloscope, allowing the travel time to be determined. Then, velocity can be computed using following Equation:

$$V = \frac{L}{t} \quad (\text{A.3})$$

where V is the wave velocity, L is the distance between the tips of source and receiver bender elements, and t is the travel time. The dynamic elastic shear (G) and Young (E) moduli can then be determined through equations A.1 and

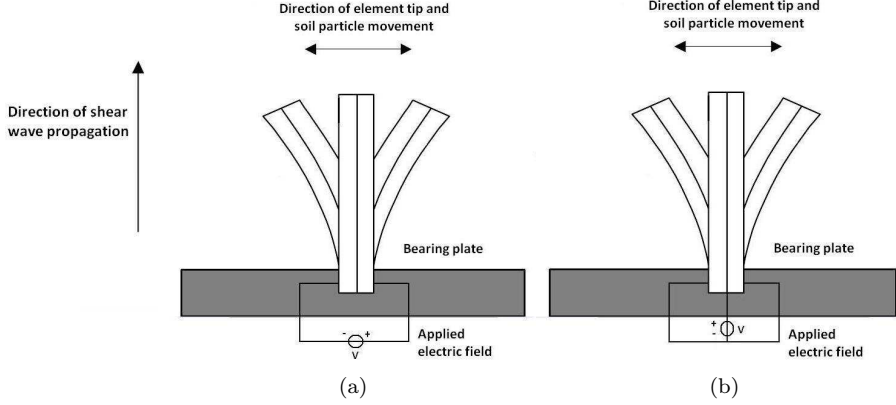


Figure A.1: (a) Series connected bimorph bender element; (b) parallel connected bimorph bender element

A.2.

Although in principle the use of bender elements appears to be straight forward, in practice their use can lead to ambiguous and uncertain results. This has led to a great deal of research focused on the principles and assumptions underlying their use. The convenience of bender element tests is limited by subjectivity associated with identifying wave travel time and uncertainties surrounding the validity of some interpretation methods. Doubts exist regarding the influence of transducer support conditions on the characteristics of transmitted waves and the importance of reflected components on received waveforms (Dyvik and Madshus, 1985; Brignoli *et al.*, 1996; Viggiani and Atkinson, 1995). The received signals can be distorted by near field effects, cross-talking and sample size effects.

A.2 Near-field effects

The first deflection of the signal may not correspond to the arrival of the shear wave but to the arrival of the so-called near-field component which travels with the velocity of a compression wave (Sánchez-Salinero *et al.*, 1986).

Theoretical studies on three-dimensional transmission of waves through an infinite elastic body have been performed and described in detail by Sánchez-Salinero *et al.* (1986). They presented fundamental equation solution for shear waves which are composed of three terms. In a simplified form shear wave components can be generally represented as:

$$S = S_{far-field, traveling at V_s} + S_{near-field, traveling at V_s} + S_{near-field, traveling at V_p} \quad (A.4)$$

In simplified terms, two of the components of a shear wave propagate at the shear wave velocity V_s , while the other component propagates at the compression wave velocity V_p . The terminology “far-field” and “near-field” denote different attenuations with distance. The near-field components attenuate much

faster than the far-field so, although their contribution is important very near to the source, it rapidly decreases with distance from the source. Analytical studies of this phenomenon can be found in Arroyo *et al.* (2003) and Rio (2006).

From the previous can be concluded that these near-field effects may mask the arrival of the shear wave when the receiver is located at a near distance from the source, adding difficulties when choosing the arrival point. Near-field effects in bender element tests have been recognized by many researchers (Viggiani and Atkinson, 1995; Brignoli *et al.*, 1996; Jovicic *et al.*, 1996). From their experimental observations was showed that the near-field effect could be reduced by increasing the frequency of the transmitted signal in such a way that at least two wavelengths should travel in the length of the specimen. This limit is represented by the following expression:

$$N = R_d = \frac{L}{\lambda} = \frac{L \cdot f}{V_s} \geq 2 \quad (\text{A.5})$$

On the contrary, others have found it difficult to ever obtain a clear shear wave arrival (Gajo *et al.*, 1997; Pennington, 1999). These apparent problems and the need for a definitive, objective criterion for determining shear wave travel time from any type of input signal led Arroyo *et al.* (2003) to look in more detail at the often quoted Sanchez-Salinerro solution. According to their analysis, acceptable results are found if phase or group velocity is measured at more than about 1.6 normalized distances (or travel lengths) from the source. The frequency adjustment to limit near-field influence has been translated into the following expression:

$$f_{lim} = \frac{V_s}{\lambda} > \frac{V_s}{1.6 \cdot L} \quad (\text{A.6})$$

A.3 Cross-talk

Cross-talk is associated to electromagnetic coupling between source and receiver bender elements. This phenomena manifests as an output signal with an early component that is quasismultaneous with the input signal (Santamarina *et al.*, 2001), as can be observed in Figure A.2. This cross-talk can be very important in conductive soils, such as saturated soils.

Lee and Santamarina (2005) conducted an experimental study to explore cross-talk associated with the different wiring of the transducers, either in series or in parallel-type bender elements. This problem can be overcome by properly grounding the bender element and the use of parallel to series bender element combination (Lee and Santamarina, 2005). Brocanelli and Rinaldi (1998) improved received signal by coating the bender element with conductive silver paint over the insulating epoxy resin and grounding it. Through a process of trial and error, by handling the different elements of the circuit, Rio (2006) concluded that cross-talk phenomena can occur at different points of the circuit. The physical proximity of the plugs in the electronics equipments and the lack of grounding of the testing apparatus are some of the aspects that may contribute to the presence of crosstalk.

Since it may sometimes be impossible to eliminate this phenomena, measures should be taken to improve received signal. High magnitude of the output signal results on a high signal-to-noise ratio, which enables to minimize cross-talk.

the soil specimen is surrounded by water, oil or air, while in the second case soil specimen is contained in a steel ring. Consequently, sample geometric properties will determine the influence of reflection of wave components in bender element tests. This is the same to say that so-called sample size effects will depend on the particular test configuration.

Usually bender elements are incorporated into the upper and lower load platens of triaxial and oedometer apparatus. In most cases, therefore, bender tests proceed as a pulse transmission test along the sample axial direction. Arroyo (2001) examined in depth the problem of sample size effects in cylindrical specimens in this configuration. Two different phenomena may play a role here: those linked to end reflections from the loading platens, and those due to reflections from the lateral sample boundaries. According to Arroyo *et al.* (2006), whereas the first may be incorporated with relative ease into an elastodynamic model of the soil transmission subsystem, the second are harder to deal with, particularly when compounded with end reflections.

In this sense Arroyo *et al.* (2006) and Rio (2006) showed how sample size of cylindrical specimen due to lateral boundary reflection affects the results of bender element test by the 3D numerical simulation. In order to establish an analogy between boundary conditions and laboratory setups, the authors studied two cases that can be translated into two opposite types of lateral boundary conditions: reflecting and absorbing boundaries. In general, the higher the impedance of the confining media relative to that of the soil, the higher the proportion of energy reflected back into the sample. This means that oedometer tests with metallic boundaries will be very close to the perfectly reflecting case; the same will apply for dry soil and triaxial conditions. The case of saturated soil and triaxial conditions is less clear-cut, and probably intermediate between the perfectly absorbing and perfectly reflecting conditions. These authors show clearly the influence of the reflected wave components in the received signals.

Rio (2006) shows the simulation results for a standard triaxial specimen (model A of 100×50 mm, with a slenderness of 2) and for a specimen model B (100×75 mm), for the cases of reflecting (non-absorbing) and absorbing boundaries (see fig. A.3). For the absorbing case, first arrival occurs at the expected instant with less distortion than non-absorbing case, where first arrival does not occur as expected and larger distortions of response can be observed. The author also shows that response of the non-absorbing model results from the overlap of responses for non-absorbing and absorbing conditions. This proves the importance of wave reflection caused by sample geometry and boundary conditions, which are complex issues, especially for the interpretation of BE results in the time domain (Ferreira, 2008).

Arroyo *et al.* (2006) also simulated cylindrical specimens with different slendernesses and absorbing and non-absorbing boundaries conditions. Figure A.4a presents the same representative section for the *Ba* (200×50 mm) and *Aa* (100×50 mm) models with absorbing lateral boundaries. The time histories are very similar. The same happens for the *Bna* and *Ana* models with non-absorbing lateral boundaries, as shown by the sections in Figure A.4b. Joint consideration of these figures shows the striking differences in the wave shapes induced when the nature of the lateral boundaries is changed. The sections in Figure A.4c show that there was indeed no appreciable difference between models *Ca* and *Cna* (model with dimensions 100×400 mm): the lateral boundaries are so distant that they have negligible influence on the propagating motion.

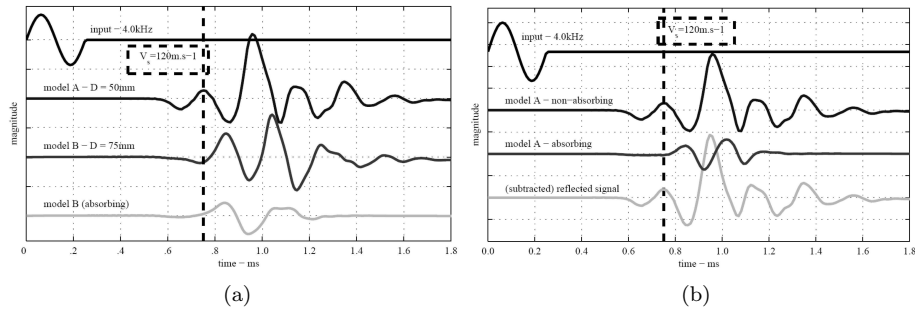


Figure A.3: Time history of received pulse signals for model A (100×50 mm) and model B (100×75 mm): (a) non-absorbing models A and B, and absorbing model B; (b) non-absorbing and absorbing model A and reflected signal (Rio, 2006)

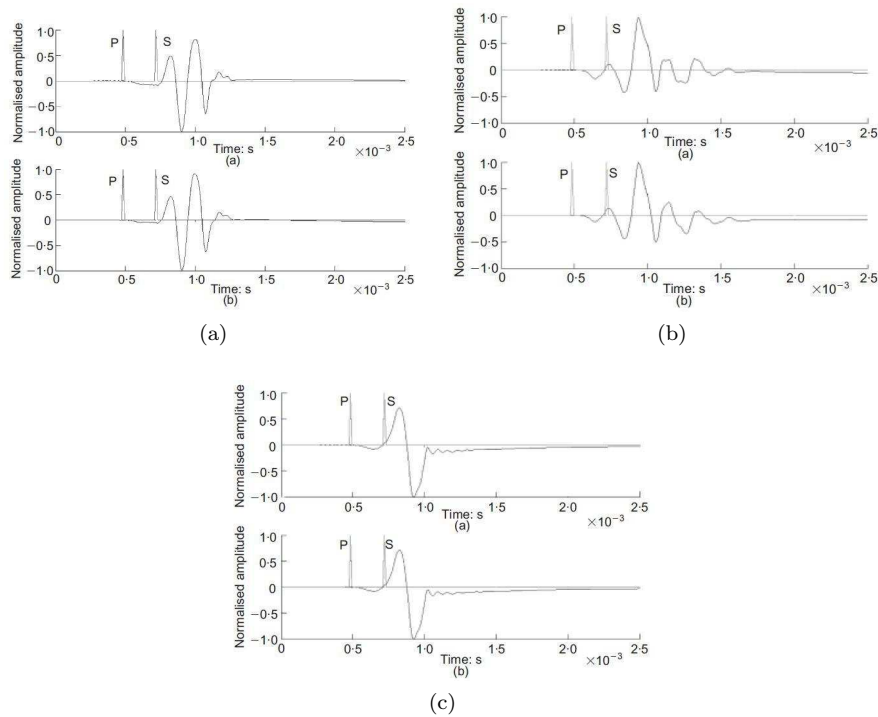


Figure A.4: Time histories for soil movements 88 mm from bender tip for models with absorbing lateral boundaries: (a) *Aa* and *Ba*; (b) *Ana* and *Bna*; (c) *Can* and *Ca*. Spikes indicate theoretical arrival times of bulk P and S waves (Arroyo *et al.*, 2006)

A.5 Travel distance determination

The main task when using bender elements is to calculate the shear wave velocity. Once the travel time between the transmitting and receiving bender

element has been measured, it should be a simple matter to calculate the shear wave velocity, following Equation A.3, which means by dividing the travel distance by the travel time. However, there are several difficulties for travel length and travel time determination.

The tip-to-tip distance is the most commonly assumed by a variety of authors (Dyvik and Madshus, 1985; Viggiani and Atkinson, 1995; Brignoli *et al.*, 1996; Pennington *et al.*, 2001), although not always justified. It corresponds to the minimum distance between transducer tips. This assumption is supported by data gathered with bender elements and resonant column tests by Dyvik and Madshus (1985). They observed that the results from the bender element test fitted best the resonant column results for travel distances measured tip-to-tip. Viggiani and Atkinson (1995) conducted laboratory tests on samples with different heights. For different confining pressures the sample length was plotted against the travel time. The chosen linear relationship between the results from different samples, at similar stress states, indicate the correct travel distance to be the tip-to-tip distance. Brignoli *et al.* (1996) performed tests with bender elements as well as with shear-plates on samples with different heights, also coming to the conclusion that the correct travel distance must be measured between tip-to-tip.

Alternatives to the tip-to-tip travel distance are proposed by some authors. Fam and Santamarina (1995) used the distance between mid-embedded height but did not justify it. Rio (2006) conducted a series of bender element tests on artificial polyurethane samples, covering a large range of sample heights, travel distances and relative embedment heights. The results indicated that the wave travel distance should be measured not between transducers tip-to-tip but between about 60% of the transducers embedment height, coinciding with the estimated centres of dynamic pressure exerted by the transmitter bender element on the sample. Arulnathan *et al.* (1998) states that the travel time can be also measured by comparison of the first and the second arrival of the wave in the output signal using the second arrival method. This is possible due to reflection at the ends of the specimen. Lee and Santamarina (2005) uses multiple reflections method where the S-wave reflections from end plates are enhanced by maximizing the soil-plate impedance mismatch. The authors state that this method solves uncertainty not only in travel time but also in travel distance: as shown in Figure A.5, the travel distance between the first and the second event is always the twice the plate-to-plate distance given by the following expression.

$$d_{pp} = 2(L + 2L_b) \quad (\text{A.7})$$

The tip-to-tip distance has been herein adopted. During the course of a test, the deformation experienced by the specimen was taken into account, and included in the computation of travel length.

A.6 Travel time determination

The determination of the travel time is more controversial. Determination of travel times of elastic waves from bender elements for calculus of the shear wave velocity of laboratory soil specimens may be done using time domain techniques and frequency domain techniques (Dyvik and Madshus, 1985; Brignoli *et al.*,

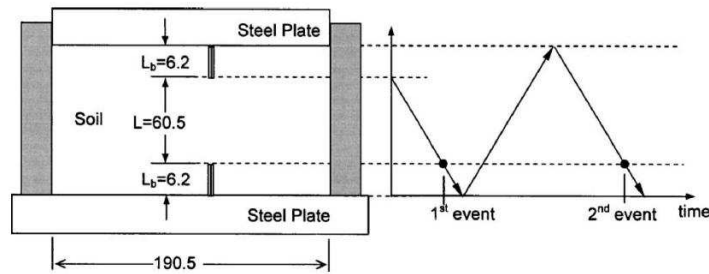


Figure A.5: Multiple-reflection method (Lee and Santamarina, 2005)

1996; Ferreira, 2003). Jovicic (2003) claims that the measurement should be taken in the time domain preferably directly from the screen because automatic interpretation of arrival times using numerical processing (frequency domain) usually does not consider changes in boundary conditions during the course of a test. In contrast, Ferreira (2003) indicates that time domain techniques seem to overestimate shear wave velocity and G_0 .

Regarding time domain technique, this method of interpretation assumes plane wave-fronts and the absence of any reflected or refracted waves (Arulnathan *et al.*, 1998). A typical output signal gathered from a step input signal is presented in A.6.

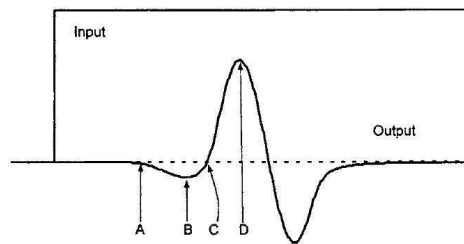


Figure A.6: Typical S-wave signal within near field: (A) first deflection, (B) first bump maximum, (C) zero after first bump, and (D) major first peak (Lee and Santamarina, 2005)

Identifying at which point the shear wave arrives (A , B , C or D) is open to user interpretation. The problem arises due to a phenomena described previously, such as near field and sample size effects. Suggested criteria and recommendations vary depending on installation, application, and input signal (Dyvik and Madshus, 1985; Fam and Santamarina, 1995; Viggiani and Atkinson, 1995; Jovicic *et al.*, 1996; Lee and Santamarina, 2005; Arroyo *et al.*, 2006). Although point A indicates the very first deflection of the shear wave, it has contrary polarity. As mentioned above, this phenomenon is assigned to dispersion, either by near-field effects or wave reflections at the boundary conditions. Hence, this point does not correspond to the first arrival of the shear wave. The first arrival of the shear wave is most likely located between points B and C . Point B is located at the first trough of the wave, at the start of the main sinusoidal cycle, while point C is located where the main cycle crosses zero, as depicted in the

figure by the zero intercept dashed line. Herein point B adopted as the arrival time.

Alternative methods in time domain technique were explored by Arulnathan *et al.* (1998) and Lee and Santamarina (2005) based on second arrival of the output. As mentioned previously, this is possible due to reflection at the ends of the specimen. However, second arrival of the wave is often undetected in the signal, since it contains less energy than the first arrival. That is the case of standard triaxial tests with high specimens due to large travel distances. In this research specimens of 200 mm high were used and, therefore, this method was not applied.

Alternative signal processing procedures have been explored to avoid “picking” a travel time, including cross correlation and frequency domain analyses. For further details one should consult Ferreira (2008).

As has been noted, time domain techniques are generally simple and straightforward, as the travel time can be directly defined from the measurement of the time interval between characteristic points in the transmitted and received wave traces. However, the input signal is given by the function generator and may not exactly correspond to the input bender element signal (Lee and Santamarina, 2005). Besides, near-field and sample size effects contributes to distortion of the output signal and leads to misinterpretation. On the other hand, frequency domain techniques tend to be more elaborate, as these are supported by signal processing and spectrum analyses tools, and enable automated data acquisition and processing. However, computed signals are not of “same nature”, which also may lead to misinterpretation.

In this sense, Ferreira (2008) found that the exclusive use of either method proved to be unreliable. Therefore, a practical framework for bender element testing was recently proposed by Viana da Fonseca *et al.* (2009), combining two distinct interpretation methods, in the time and the frequency domain, as a means to effectively reduced the uncertainty and subjectivity often associated with bender elements testing and obtain the most reliable value for the travel time.

The issues highlighted above can be overcome if two sensors acting as receivers are used. Ferreira *et al.* (2010) proposed the instrumentation of specimens with two accelerometers in combination with bender elements. In this setup, the signal produced by the bender element transmitter is acquired by the bender element receiver and by the two accelerometers. The advantages of this setup are twofold: i) the interpretation of the acceleration measurements can be directly made both in the time and in the frequency domain, since the signals are of the same nature; ii) these measurements can be used to verify the bender element signals, and thus minimize the subjectivity of the interpretation of bender element results.

Appendix B

Specification project of *SPLT*

STATIC PLATE LOAD TEST

DETERMINING THE DEFORMATION MODULUS BY THE STATIC PLATE LOAD TEST (E_{v2})

Contents	Page
1. SCOPE	2
2. NORMATIVE REFERENCES	2
3. SYMBOLS AND ABBREVIATIONS.....	2
4. TEST PRINCIPLE	3
5. APPARATUS	3
5.1. REACTION LOADING SYSTEM	3
5.2. LOADING PLATE	4
5.3. COMMAND AND MEASURING DEVICE OF LOAD APPLIED TO THE PLATE.....	4
5.4. SETTLEMENT MEASURING DEVICE	5
5.5. AUXILIAR EQUIPMENT	5
6. TEST PROCEDURE	6
6.1. TEST SETUP	6
6.2. PRELOADING.....	6
6.3. LOADING AND UNLOADING	6
7. RESULTS	7
8. TEST REPORT	10

1. SCOPE

With the present specification project is intended to describe the plate load test principle, equipment, procedures and results interpretation from static loading on a rigid plate. This test enable the determination of modulus known as “deformation modulus under static plate loading” of platforms.

This test is intended for use in earthworks and infrastructures of roads, railways and airports, where maximum material dimension under the plate do not exceed $\frac{1}{4}$ plate diameter.

This specification project specifies a method which permits the relationship between load and settlement to be determined, the aim being to assess the deformation characteristics of geomaterials and determine strain modulus. The maximum modulus value to be measured with this test is 250 MPa. The deformation modulus under static plate loading does not features the relative compaction of platforms.

2. NORMATIVE REFERENCES

NF P94-117-1, Sols: reconnaissance et essais. Portance des plates-formes. Partie 1: Module sous chargement statique à la plaque (E_{v2}).

DIN 18134, Determining the deformation and strength characteristics of soil by the plate loading test.

3. SYMBOLS AND ABBREVIATIONS

D_{max} is the maximum dimension of geomaterials particles given in millimeters;

E_{v2} is the deformation modulus under static plate loading evaluated on the second loading cycle and is given in MPa;

ν is the geomaterial Poisson coefficient taking 0,25 value in the lack of information;

σ_0 is the average stress under the plate, given in MPa;

d is the plate diameter, given in millimeters;

z is the plate maximum settlement during the second load cycle, given in millimeters.

4. TEST PRINCIPLE

After choosing test site, two successive loading cycles are applied to material, accordingly normalized procedures, through a plate with diameter and stiffness normalized.

The first loading cycle is applied in successive increments and then load is released in stages. The procedure is repeated for a second loading cycle. For each stage, the average normal stress under the plate, σ_0 , is plotted against plate settlement and the a load-settlement curve is obtained.

The deformation modulus under static plate loading, E_{v2} , expresses material deformation characteristics and is computed from the second loading cycle of the load-settlement curve.

5. APPARATUS

The following equipment is required:

- reaction loading system;
- plate loading apparatus;
- command and measurement device of load applied to the plate;
- settlement measurement device.

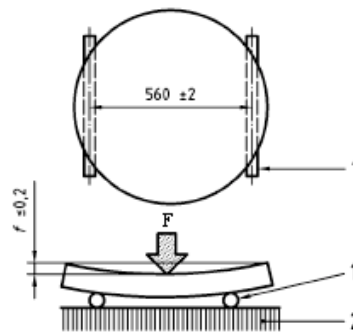
5.1. REACTION LOADING SYSTEM

The reaction loading cycle shall produce a reaction load which is at least 10% greater than the maximum test load required. The reaction loading system supports should be at least 1,20 m far away from the center of the loading plate.

5.2. LOADING PLATE

The loading plate diameter is $600 \text{ mm} \pm 2 \text{ mm}$, for tests on materials which maximum particle dimension not exceeding $\frac{1}{4}$ of loading plate diameter.

The loading plate stiffness shall be in such a way that under a applied force, F , equal to $10 \pm 0,5 \text{ kN}$ at its center, deflection, f , between plate center and plate edge measured accordingly Figure 1, does not exceed $0,2 \text{ mm}$.



1 – Steel cylinder

diameter: $20 \text{ mm} \pm 1$

length: $600 \text{ mm} \pm 5$

2 – Solid with stiffness similar to a concrete block with approximate dimensions::

$L = c = 1 \text{ m}$ e $h = 0,5 \text{ m}$

Roughness tolerance of superior face: $\pm 1 \text{ mm}$

Figura 1 – Scheme for loading plate stiffness verification.

Also a loading plate with diameter $300 \text{ mm} \pm 0,5 \text{ mm}$ can be used. A minimum thickness of $50 \text{ mm} \pm 0,2 \text{ mm}$ is required to guarantee stiffness condition of loading plate.

5.3. COMMAND AND MEASURING DEVICE OF LOAD APPLIED TO THE PLATE

The device shall allow a normal load to be applied to the plate inducing a normal stress under the plate of $0,25 \text{ MPa}$, for plate with 600 mm diameter, and $0,50 \text{ MPa}$, for plate with 300 mm diameter. Suitable means shall be provided to prevent buckling of elements and guarantee vertical forces. Loading speed shall satisfy conditions given in section 6.2.

Device shall also enable measurement of loads applied to the plate as described in section 6.2 and, if required, shall allow load sustain during settlement stabilization.

The load on the plate shall be measured by means of a strain gauge with a limit of error of 1% and resolution of the gauge shall be at least 0,0001 MPa for 600 mm loading plate and at least 0,001 MPa for 300 mm loading plate.

5.4. SETTLEMENT MEASURING DEVICE

The resolution of settlement measuring device shall be at least 0,01 mm and shall enable measurements at least 10 mm.

The following measuring systems can be used:

- one point measuring system located less than 20 mm of the center of the plate;
- three points measuring system located concentrically on the periphery of the loading plate at $120^\circ \pm 10^\circ$ and at same distance, a , from the center of the loading plate ($a \pm 5$ mm).

The supports of the measuring systems shall be located at 1,50 m far away from the center of the plate and from supports of the reaction loading system.

5.5. AUXILIAR EQUIPMENT

The following auxiliar equipment is required:

- spade;
- rule to level with, at least, 0,8 m length;
- bucket with, at least, 20 liters of clean sand 0/2 mm;
- trowel;
- hand brush;
- protection element against weather conditions if measuring device used is sensible to meteorological agents.

6. TEST PROCEDURE

6.1. TEST SETUP

Record measurement point coordinates. Test area with 0,7 m x 0,7 m shall be levelled with rule. A clean sand layer shall be put on the test area and spread and levelled with trowel in such a way to achieve a thin layer.

The loading plate shall lie in the center of this surface in full contact with the material being tested. This may be achieved by rotating the plate back and forth in angles of 30 to 45°.

The loading device shall be placed centrally on the loading plate beneath the reaction loading system and measuring device shall be placed accordingly the requirements given in sections 5.3 and 5.4.

If necessary protection element against weather conditions shall be installed.

6.2. PRELOADING

Prior to starting the test, the strain gauge and the dial gauge or displacement transducer shall be set to zero and the plate preloaded for about 30 seconds. The load applied shall correspond to a normal stress of 0,01 MPa 600 mm plate. The reading of the gauge or transducer at this load shall be taken as zero reading.

6.3. LOADING AND UNLOADING

The load shall be applied in not less than six stages, in approximately equal increments, until the required maximum normal stress is reached. Each increase in load (from stage to stage) shall be completed within one minute. The load shall be released in stages, to 50% and 25% of the maximum load and then to the load corresponding to the zero reading. Following that, a further (2nd) loading cycle shall be carried out, in which the load is to be increased only to the penultimate stage of the first cycle (see Figure 2).

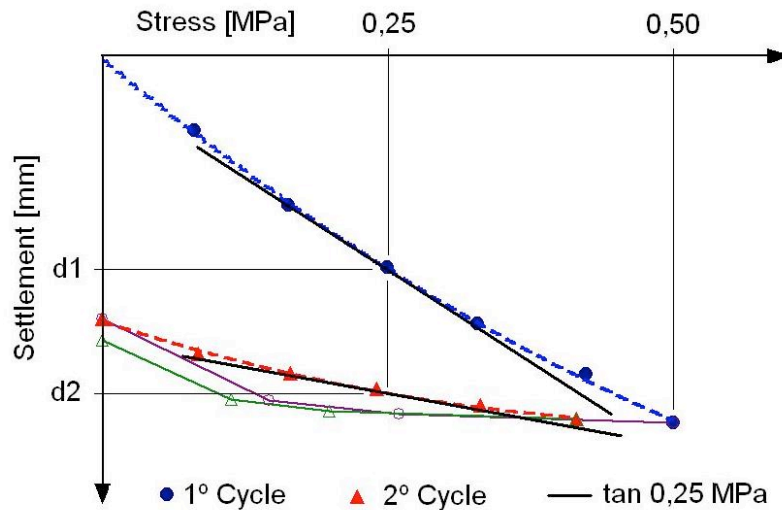


Figure 2 – Load-settlement curve for determination of deformation modulus, E_{v2} .

When testing soil, the time interval between the application of each load increment shall be two minutes, the load being held constant during this period.

If a test proceeds in an unexpected manner (e.g. if the loading plate tips or sinks rapidly), the soil at the test site shall be dug up to a depth equal to the plate diameter. If stones are encountered, or if the soil is of less than stiff consistency, this shall be recorded.

If, during the loading cycle, a higher load than intended is inadvertently applied, this load shall be maintained and a note made in the records.

NOTE: In order to check the results obtained from the second loading cycle, a third cycle may be carried out to the same maximum load, this being applied immediately after the second loading stage, without any further intermediate stages.

7. RESULTS

The deformation modulus, E_{v2} (secant modulus), shall be calculated using Boussinesq equation:

$$E_{v2} = \frac{\pi}{4} \cdot (1 - \nu^2) \cdot \frac{p \cdot d}{z}$$

where:

z represents plate settlement on the second loading cycle, expressed in millimeters;
 ν , p , d are, respectively, coefficient of Poisson, average stress under the plate, expressed in MPa and plate diameter, expressed in millimeters.

The plate settlement, z , shall be based on smooth load-settlement curve by adjustment of a second degree polynomial. To this end, settlement, z , on the plate center shall be calculated using following equation:

$$z = a_0 + a_1 \cdot \sigma_0 + a_2 \cdot \sigma_0^2$$

where:

σ_0 is the average stress under the plate, in MPa;
 a_0 , a_1 , a_2 are factors in mm, mm/MPa and mm/MPa².

Factors a_0 , a_1 , a_2 are obtained from adjustment of a second degree polynomial to the load-settlement curve, not being considered the initial value (zero).

As so, the deformation modulus, Ev_2 (secant modulus), shall be calculated using following equation:

$$Ev_2 = \frac{\pi}{4} \cdot (1 - \nu^2) \cdot \frac{p \cdot d}{a_1 \cdot \sigma_0 + a_2 \cdot \sigma_0^2}$$

Ev_2 shall be calculated for a stress under the plate of 0,20 MPa. However, the evaluation of this parameter can be performed for any stress level of the second loading cycle.

In the next tables is given an exemple of measured values during a test and the results interpretation for evaluation of deformation modulus, Ev_2 .

Table 1 – Measured values obtained from the first loading cycle.

Loading stage	Load (kN)	Stress σ_0 (MPa)	z (mm)
0	0,00	0,000	0,00
1	11,78	0,042	0,60
2	23,56	0,083	1,20
3	35,34	0,125	1,70
4	47,12	0,167	2,14
5	58,90	0,208	2,52
6	70,68	0,250	2,90
7	35,24	0,125	2,77
8	17,62	0,062	2,55
9	0,00	0,000	1,71

Table 2 – Measured values obtained from second loading cycle.

Loading stage	Load (kN)	Stress σ_0 (MPa)	z (mm)
10	0,00	0,000	1,71
11	11,78	0,042	2,06
12	23,56	0,083	2,34
13	35,34	0,125	2,58
14	47,12	0,167	2,80
15	58,90	0,208	2,96
16	24,36	0,086	2,78
17	12,18	0,043	2,49
18	0,00	0,000	2,01

Table 3 – Results interpretation

Parameter	2 nd loading cycle
σ_{0max} (MPa)	0,208
a_0 (mm)	1,716
a_1 (mm/MPa)	8,505
a_2 (mm/MPa)	-12,117
$E\nu_2 = \frac{\pi}{4} \cdot (1 - \nu^2) \cdot \frac{p \cdot d}{a_1 \cdot \sigma_0 + a_2 \cdot \sigma_0^2}$	72,6

8. TEST REPORT

The test report shall include the following information:

- reference to the entity who performed the test;
- reference to test technical specification;
- earthwork identification;
- test date;
- test location;
- value of “deformation modulus under static plate loading (E_{v2})”;
- observations, namely unexpected circumstance which did not allowed strict requirements fulfillment given in the present document, for example: weather conditions, D_{max} value, unlevelled platform.

ACKNOWLEDGEMENT

The present specification project was performed in the aim of a cooperation protocol between the National Railway Network and and four national research institutions (University of Minho, UM; National Laboratory of Civil Engineering, LNEC; New University of Lisbon, FCT/UNL; and Technical University of Lisbon, IST) to develop the knowledge concerning the methodology for the construction and control of the railway embankments and rail track layers for high speed trains. This was established under the framework of a national research project POCI/ECM/61114/2004, entitled “Interaction soil–rail track for high speed trains”, financed by the Foundation for Science and Technology (FCT).

Appendix C

ETRE results

C.1 State parameters

Table C.1: Statistical data obtained from *SCM* and *NM* tests carried out on *SC* trial layer 0.30 m $w_{OPM-2\%}$

Tests		No. of Passes				
		4	6	8	10	12
<i>SCM</i>	Average γ_d [kN/m ³]	19.62	20.03	19.95	20.57	20.41
	<i>SD</i>	0.21	0.59	0.27	0.70	0.42
	<i>CV</i>	1.1	3.0	1.3	3.4	2.1
	Average w (%)	6.6	6.0	6.7	6.3	6.3
	<i>SD</i>	0.70	1.19	0.43	0.73	0.72
	<i>CV</i>	10.6	19.7	6.4	11.7	11.5
<i>NM</i>	Average γ_d [kN/m ³]	18.91	19.46	19.23	19.32	19.55
	<i>SD</i>	0.20	0.28	0.73	0.73	0.61
	<i>CV</i>	1.1	1.1	3.8	3.8	3.1
	Average w [%]	6.2	6.5	6.2	5.7	6.1
	<i>SD</i>	0.64	0.72	0.62	0.51	0.37
	<i>CV</i>	10.3	10.3	10.0	8.8	6.0

Table C.2: Statistical data obtained from *SCM* and *NM* tests carried out on *SC* trial layer 0.40 m $w_{OPM-2\%}$

		No. of Passes				
		4	6	8	10	12
<i>SCM</i>	Average γ_d [kN/m ³]					20.39
	Average w [%]					8.25
<i>NM</i>	Average γ_d [kN/m ³]	19.57	19.52	19.78	19.71	19.30
	<i>SD</i>	0.34	0.11	0.37	0.32	0.77
	<i>CV</i>	1.8	0.6	1.9	1.6	4.0
	Average w [%]	9.1	9.8	9.0	9.4	9.5
	<i>SD</i>	0.69	0.58	0.87	0.74	0.62
	<i>CV</i>	7.6	5.9	9.7	7.9	6.5

Table C.3: Statistical data obtained from *SCM* and *NM* tests carried out on *SC* trial layer 0.50 m $w_{OPM-2\%}$

		No. of Passes				
		4	6	8	10	12
<i>SCM</i>	Average γ_d [kN/m ³]	19.39	19.42	19.44	19.47	19.67
	<i>SD</i>	0.42	0.27	0.65	0.36	0.18
	<i>CV</i>	2.2	1.4	3.4	1.9	0.9
	Average w [%]	6.7	6.3	6.0	6.3	6.3
	<i>SD</i>	1.39	0.71	0.45	0.24	0.23
	<i>CV</i>	20.7	11.4	7.6	3.9	3.7
<i>NM</i>	Average γ_d [kN/m ³]	18.14	19.22	19.46	18.65	18.75
	<i>SD</i>	1.00	0.22	0.51	1.20	1.10
	<i>CV</i>	5.5	1.2	2.6	5.5	5.9
	Average w [%]	6.5	6.3	6.5	6.8	6.3
	<i>SD</i>	0.64	0.94	0.66	1.13	0.81
	<i>CV</i>	9.8	14.9	10.1	9.8	12.9

Table C.4: Statistical data obtained from *SCM* and *NM* tests carried out on *SC* trial layer 0.40 m w_{OPM}

		No. of Passes				
		4	6	8	10	12
<i>SCM</i>	Average γ_d [kN/m ³]	20.08	20.16	20.21	20.18	
	<i>SD</i>		0.15	0.36	0.34	
	<i>CV</i>		0.8	1.8	1.7	
	Average w [%]	8.2	8.2	8.0	7.6	
	<i>SD</i>		0.54	0.56	0.74	
	<i>CV</i>		6.7	7.0	9.7	
<i>NM</i>	Average γ_d [kN/m ³]	19.43	19.40	19.40	19.28	19.07
	<i>SD</i>	0.75	0.60	0.86	0.90	0.91
	<i>CV</i>	3.9	3.1	4.4	4.7	4.8
	Average w [%]	8.0	8.3	7.9	7.8	8.0
	<i>SD</i>	0.75	0.38	0.50	0.53	0.79
	<i>CV</i>	9.4	4.6	6.3	6.7	9.9

Table C.5: Statistical data obtained from *SCM* and *NM* tests carried out on *SC* trial layer 0.40 m $w_{OPM+2\%}$

		No. of Passes				
		4	6	8	10	12
<i>SCM</i>	Average γ_d [kN/m ³]	20.21		20.29		20.31
	<i>SD</i>	0.30		0.22		0.13
	<i>CV</i>	1.5		1.1		0.6
	Average w [%]	10.3		10.6		10.4
	<i>SD</i>	0.81		0.32		0.51
	<i>CV</i>	7.8		3.0		4.9
<i>NM</i>	Average γ_d [kN/m ³]	19.34	19.72	19.23	19.82	19.47
	<i>SD</i>	0.47	0.19	0.54	0.34	0.44
	<i>CV</i>	2.4	1.0	2.8	1.7	2.2
	Average w [%]	10.1	10.3	10.4	10.3	9.7
	<i>SD</i>	1.07	0.76	0.75	0.75	0.84
	<i>CV</i>	10.6	7.4	7.2	7.2	8.7

Table C.6: Statistical data obtained from *SCM* and *NM* tests carried out on *CA31.5* trial layer 0.22 m w_{OPM}

		No. of Passes				
		4	6	8	10	12
<i>SCM</i>	Average γ_d [kN/m ³]	23.77				
	<i>SD</i>	0.51				
	<i>CV</i>	2.1				
	Average w [%]	4.2				
	<i>SD</i>	0.58				
	<i>CV</i>	14.0				
<i>NM</i>	Average γ_d [kN/m ³]	22.85	23.47	23.23	24.02	24.13
	<i>SD</i>	0.99	0.49	0.28	0.29	0.44
	<i>CV</i>	4.3	2.1	1.2	1.2	1.8
	Average w [%]	4.2	4.1	5.6	6.3	6.5
	<i>SD</i>	0.52	0.55	0.11	0.36	0.33
	<i>CV</i>	12.6	13.4	2.1	5.8	5.2

Table C.7: Statistical data obtained from *SCM* and *NM* tests carried out on *CA31.5* trial layer 0.30 m w_{OPM}

		No. of Passes				
		4	6	8	10	12
<i>SCM</i>	Average γ_d [kN/m ³]	23.60				
	<i>SD</i>	0.55				
	<i>CV</i>	2.3				
	Average w [%]	4.2				
	<i>SD</i>	0.53				
	<i>CV</i>	12.5				
<i>NM</i>	Average γ_d [kN/m ³]	22.84	23.22	23.41	23.85	24.23
	<i>SD</i>	0.44	0.78	0.49	0.36	0.32
	<i>CV</i>	1.9	3.4	2.1	1.5	1.3
	Average w [%]	4.2	3.7	5.3	6.2	5.6
	<i>SD</i>	0.46	0.21	0.35	0.32	0.38
	<i>CV</i>	10.9	5.7	6.6	5.2	6.7

C.2 *SPLT*

Table C.8: Statistical data obtained from *SPLT* following standards AFNOR NF P94-117-1 (using settlement measuring system in three concentric points on periphery of the loading plate) and DIN 18134 carried out on all trial layers

Trial layer	Modulus [MPa]	AFNOR					DIN
		4	6	8	10	12	12
0.30 m $w_{OPM-2\%}$	E_{V2}	80.0	111.7	79.9	103.0	96.2	110.9
	SD	10.1		2.6		8.4	13.9
	CV	12.6		3.2		8.7	12.5
0.40 m $w_{OPM-2\%}$	E_{V2}					50.8	68.4
	SD					12.8	8.7
	CV					25.2	12.7
0.50 m $w_{OPM-2\%}$	E_{V2}	78.8	85.8	81.7	105.5	102.2	100.6
	SD	18.5		4.7		6.5	11.3
	CV	23.5		5.8		6.3	11.2
0.40 m w_{OPM}	E_{V2}			94.7	77.2	74.9	74.8
	SD			9.3	10.4	13.6	7.5
	CV			9.8	13.5	18.1	10.1
0.40 m $w_{OPM+2\%}$	E_{V2}	41.0		33.8		52.0	45.9
	SD	11.1		6.9		9.9	14.1
	CV	27.2		20.5		18.9	30.7
0.22 m w_{OPM}	E_{V2}					91.2	120.6
	SD					16.1	32.5
	CV					17.7	27.0
0.30 m w_{OPM}	E_{V2}					114.0	117.9
	SD					20.5	25.2
	CV					18.0	21.4

Table C.9: Statistical data obtained from *SPLT* following standard AFNOR NF P94-117-1 (using settlement measuring system in the center of the loading plate)

Trial layer	Modulus [MPa]	No. of Passes				
		4	6	8	10	12
0.30 m $w_{OPM-2\%}$	E_{V2}	103.6	111.7	110.6	120.7	135.5
	SD	11.4		14.6	14.0	11.4
	CV	11.0		13.2	11.6	8.4
0.40 m $w_{OPM-2\%}$	E_{V2}					68.2
	SD					20.3
	CV					29.7
0.50 m $w_{OPM-2\%}$	E_{V2}	106.1	98.7	109.1	132.3	121.2
	SD	32.4		6.3		18.3
	CV	30.6		5.8		15.1
0.40 m w_{OPM}	E_{V2}			112.7	139.0	138.3
	SD			11.6	9.1	24.0
	CV			10.3	6.5	17.4
0.40 m $w_{OPM+2\%}$	E_{V2}	51.5		41.2		61.3
	SD	12.7		7.4		13.4
	CV	24.8		18.0		21.8
0.22 m w_{OPM}	E_{V2}					121.6
	SD					17.5
	CV					14.4
0.30 m w_{OPM}	E_{V2}					139.1
	SD					8.5
	CV					6.1

C.3 Performance related tests

C.3.1 LFWD

Table C.10: Statistical data obtained from LFWD carried out on all trial layers, for all energy levels

Trial layer	Modulus [MPa]	No. of Passes				
		4	6	8	10	12
0.30 m w _{OPM-2%}	E _{LFWD}	56.1	65.6	68.0	66.0	99.4
	SD	19.3	15.3	16.2	9.3	34.3
	CV	34.5	23.3	23.8	14.1	34.5
0.40 m w _{OPM-2%}	E _{LFWD}	68.6	51.36	67.7		
	SD	33.9	16.5	43.0		
	CV	49.5	32.2	63.4		
0.50 m w _{OPM-2%}	E _{LFWD}	69.6	69.2	81.1	85.7	74.2
	SD	16.1	13.4		10.6	37.9
	CV	23.1	19.4		12.3	51.1
0.40 m w _{OPM}	E _{LFWD}	65.7	66.8	67.7	85.9	126.1
	SD	11.8	13.5	12.2	25.9	47.4
	CV	17.9	20.2	18.1	30.1	37.6
0.40 m w _{OPM+2%}	E _{LFWD}	44.2	40.6	58.0	54.9	67.2
	SD	11.8	19.7	31.2	24.5	21.1
	CV	26.8	48.6	53.9	44.7	31.5
0.22 m w _{OPM}	E _{LFWD}	88.6	95.3	101.7	70.5	80.3
	SD	18.4	12.5	14.0	27.6	20.8
	CV	20.8	13.1	13.7	39.2	25.8
0.30 m w _{OPM}	E _{LFWD}	78.1	89.1	72.2	84.3	80.3
	SD	17.5	16.2	7.2	15.0	20.8
	CV	22.4	18.1	10.0	17.8	25.8

C.3.2 FWD

Table C.11: Statistical data obtained from *FWD* carried out on 0.40 m w_{OPM} , for energy level corresponding to twelve Passes of the vibrating roller

Drops	1 st	2 nd	3 rd	4 th
Average σ [kPa]	435.3	650.6	993.1	1251.3
<i>SD</i>	7.1	7.9	12.1	11.5
<i>CV</i>	1.6	1.2	1.2	0.9
Average E_{FWD} [MPa]	191.9	220.2	221.5	233.7
<i>SD</i>	33.8	29.6	25.9	35.1
<i>CV</i>	17.6	13.5	11.7	15.0

C.3.3 SSG

Table C.12: Statistical data obtained from *SSG* carried out on all trial layers, for all energy levels

Trial layer	Modulus [MPa]	No. of Passes				
		4	6	8	10	12
0.30 m $w_{OPM-2\%}$	E_{SSG}	87.0	99.7	109.8	119.7	108.2
	<i>SD</i>	14.6	23.8	25.3	21.2	20.2
	<i>CV</i>	16.8	23.9	23.1	17.7	18.7
0.40 m $w_{OPM-2\%}$	E_{SSG}	65.0	57.9	75.0	85.1	79.0
	<i>SD</i>	26.3	21.1	30.9	18.7	16.0
	<i>CV</i>	40.5	36.4	41.1	21.9	20.2
0.50 m $w_{OPM-2\%}$	E_{SSG}	124.7	137.8	157.6	161.5	199.1
	<i>SD</i>	43.1	22.0	18.0	13.2	28.2
	<i>CV</i>	34.6	16.0	11.4	8.2	14.2
0.40 m w_{OPM}	E_{SSG}	111.6	119.9	129.8	130.6	135.5
	<i>SD</i>	18.8	28.2	22.5	22.4	23.0
	<i>CV</i>	16.9	23.5	17.3	17.1	17.0
0.40 m $w_{OPM+2\%}$	E_{SSG}	71.5	79.5	64.4	65.1	78.3
	<i>SD</i>	22.4	23.0	27.9	25.6	36.8
	<i>CV</i>	31.3	29.0	43.3	39.3	47.0
0.22 m w_{OPM}	E_{SSG}	71.3	68.7	67.5	48.0	66.5
	<i>SD</i>	11.4	7.6	10.2	19.3	1.1
	<i>CV</i>	15.9	11.1	15.2	40.1	1.6
0.30 m w_{OPM}	E_{SSG}	72.0	76.2	68.5	70.1	76.0
	<i>SD</i>	6.2	11.9	6.8	10.9	8.4
	<i>CV</i>	8.6	15.6	10.0	15.5	11.0

C.3.4 Portancemètre

Table C.13: Statistical data obtained from Portancemètre carried out on all trial layers, for all energy levels

Trial layer	Modulus [MPa]	No. of Passes				
		4	6	8	10	12
0.30 m $w_{OPM-2\%}$	E_{Port}	73.9	79.5	100.8	102.3	110.0
	SD	6.9	5.7	14.3	10.4	16.6
	CV	9.4	7.1	14.2	10.1	15.1
0.40 m $w_{OPM-2\%}$	E_{Port}	62.2	65.1	64.5	67.5	63.4
	SD	13.1	7.4	6.0	13.4	6.1
	CV	21.0	11.4	9.3	19.9	9.7
0.50 m $w_{OPM-2\%}$	E_{Port}	76.3	79.3	96.5	106.5	116.4
	SD	9.6	10.3	17.4	15.7	15.4
	CV	12.6	13.0	18.0	14.8	13.2
0.40 m w_{OPM}	E_{Port}	71.7	69.3	87.9	72.3	84.3
	SD	2.1	4.7	9.1	5.5	12.4
	CV	2.9	6.7	10.4	7.7	14.8
0.40 m $w_{OPM+2\%}$	E_{Port}	55.9	53.7	56.7	55.7	51.7
	SD	4.8	2.3	2.9	2.5	4.0
	CV	8.6	4.2	5.1	4.4	7.7
0.22 m w_{OPM}	E_{Port}	77.5	77.3	83.0	97.4	67.2
	SD	11.6	11.9	13.6	15.8	20.4
	CV	14.9	15.3	16.4	16.2	30.3
0.30 m w_{OPM}	E_{Port}	79.1	75.5	85.8	94.7	69.7
	SD	9.8	16.7	13.2	14.7	13.6
	CV	12.4	22.1	15.4	15.5	19.5

C.4 Moduli and relative compaction versus water content

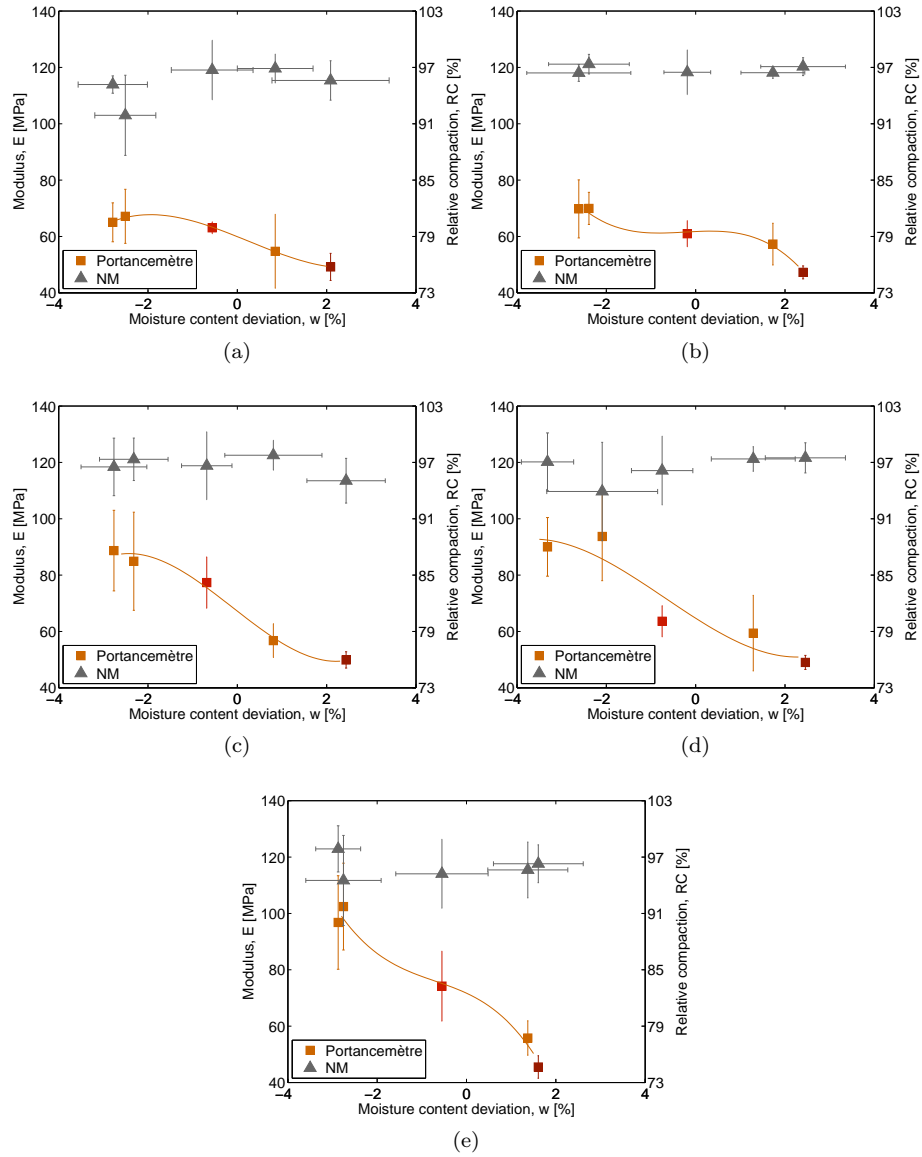


Figure C.1: E_{Port} modulus and relative compaction (RC) versus moisture content deviation (w) obtained on *SC* trial layers for energy levels corresponding to: (a) 4 passes; (b) 6 passes; (c) 8 passes; (d) 10 passes; (e) 12 passes

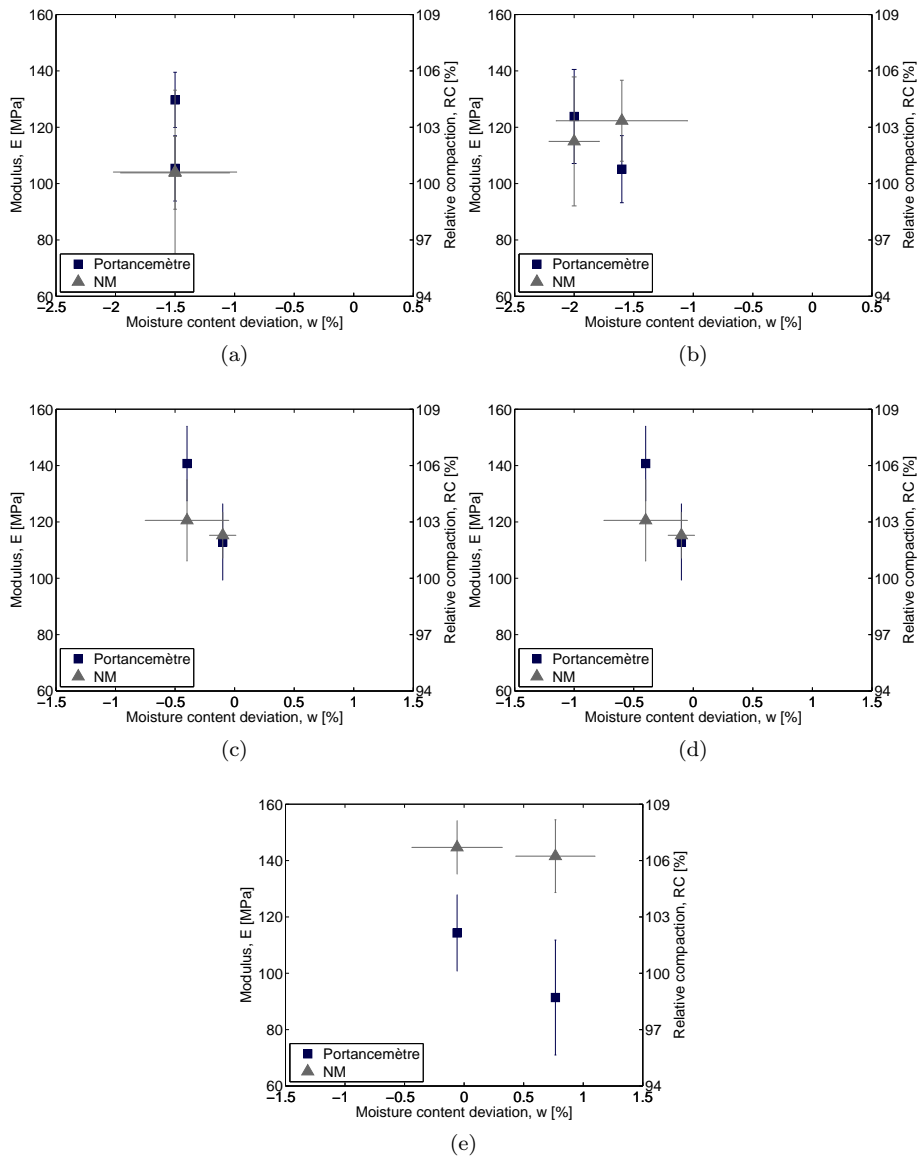


Figure C.2: E_{Port} modulus and relative compaction (RC) versus moisture content deviation (w) obtained on CA31.5 trial layers for energy levels corresponding to: (a) 4 passes; (b) 6 passes; (c) 8 passes; (d) 10 passes; (e) 12 passes

Appendix D

FTRE results

D.1 State parameters

Table D.1: Statistical data obtained from *SCM* and *NM* tests carried out on *SP* trial layer with 0.30 m thickness

		No. of Passes		
		4	6	10
<i>SCM</i>	Average γ_d [kN/m ³]	21.34	20.16	20.40
	Average w [%]	9.9	9.0	8.3
<i>NM</i>	Average γ_d [kN/m ³]	19.95	20.40	20.11
	<i>SD</i>	0.21	0.66	0.20
	<i>CV</i>	1.1	3.2	1.0
	Average w [%]	9.5	8.9	8.8
	<i>SD</i>	0.58	0.41	0.42
	<i>CV</i>	6.1	4.6	4.8

Table D.2: Statistical data obtained from *SCM* and *NM* tests carried out on *SP* trial layer with 0.40 m thickness

		No. of Passes				
		4	6	8	10	12
<i>SCM</i>	Average γ_d [kg/m ³]	20.36	20.65	20.50	20.36	21.29
	Average w [%]	10.5	10.1	10.1	9.7	9.2
<i>NM</i>	Average γ_d [kg/m ³]	19.95	20.23	20.11	20.23	20.66
	<i>SD</i>	0.19	0.33	0.45	0.23	0.58
	<i>CV</i>	1.0	1.6	2.3	1.1	2.8
	Average w [%]	9.8	9.8	9.8	9.8	9.1
	<i>SD</i>	0.55	0.52	0.35	0.51	0.50
	<i>CV</i>	5.6	5.3	3.6	5.2	5.5

Table D.3: Statistical data obtained from *NM* tests carried out on *SP* trial layer with 0.50 m thickness

		No. of Passes				
		4	6	10	12	14
<i>NM</i>	Average γ_d [kg/m ³]	19.84	20.07	20.31	20.02	19.95
	<i>SD</i>	0.15	0.29	0.27	0.43	0.33
	<i>CV</i>	0.7	1.4	1.3	2.2	0.7
	Average w [%]	9.2	8.9	8.4	8.5	8.1
	<i>SD</i>	0.16	0.23	0.25	0.39	0.59
	<i>CV</i>	1.8	2.6	3.0	4.6	7.3

Table D.4: Statistical data obtained from *NM* tests carried out on *SP* embankment layers

Layer		No. of Passes		
		8	10	12
<i>4th</i>	Average γ_d [kN/m ³]	19.31	19.87	
	<i>SD</i>	0.45	0.30	
	<i>CV</i>	2.3	1.5	
	Average w [%]	10.4	10.5	
	<i>SD</i>	0.44	0.45	
	<i>CV</i>	4.2	4.3	
<i>5th</i>	Average γ_d [kN/m ³]	19.54		
	<i>SD</i>	0.25		
	<i>CV</i>	1.3		
	Average w [%]	10.9		
	<i>SD</i>	0.74		
	<i>CV</i>	6.8		
<i>6th</i>	Average γ_d [kN/m ³]		19.72	19.90
	<i>SD</i>		0.28	0.25
	<i>CV</i>		1.4	1.2
	Average w [%]		10.3	10.4
	<i>SD</i>		0.50	0.30
	<i>CV</i>		4.8	2.8
<i>7th</i>	Average γ_d [kN/m ³]		19.90	
	<i>SD</i>		0.03	
	<i>CV</i>		0.1	
	Average w [%]		9.6	
	<i>SD</i>		0.22	
	<i>CV</i>		2.3	
<i>8th</i>	Average γ_d [kN/m ³]			20.49
	<i>SD</i>			0.14
	<i>CV</i>			0.7
	Average w [%]			9.8
	<i>SD</i>			0.32
	<i>CV</i>			3.2

Table D.5: Statistical data obtained from *NM* and *RBM* tests carried out on *ASIC* trial layer with 0.30 m thickness

		No. of Passes		
		4	6	10
<i>RBM</i>	Average γ_d [kN/m ³]	24.67	23.49	24.57
	Average w [%]	4.5	4.5	4.5
<i>NM</i>	Average γ_d [kN/m ³]	21.98	22.23	21.82
	<i>SD</i>	0.40	0.41	0.66
	<i>CV</i>	1.8	1.9	3.0
	Average w [%]	4.4	3.1	3.1
	<i>SD</i>	0.8	0.4	0.1
	<i>CV</i>	17.2	13.3	2.6

Table D.6: Statistical data obtained from *NM* and *RBM* tests carried out on *ASIC* trial layer with 0.40 m thickness

		No. of Passes				
		4	6	8	10	12
<i>RBM</i>	Average γ_d [kN/m ³]	25.31	25.70	24.48		
	Average w [%]	4.6	4	4.25		
<i>NM</i>	Average γ_d [kN/m ³]	22.27	22.28	20.87	20.60	20.45
	<i>SD</i>	0.69	0.68	1.10	0.50	0.77
	<i>CV</i>	3.1	3.1	5.3	2.4	3.7
	Average w [%]	4.4	4.7	7.2	8.0	7.5
	<i>SD</i>	0.5	0.6	0.4	0.5	1.1
	<i>CV</i>	10.3	11.7	5.6	6.9	15.3

Table D.7: Statistical data obtained from *NM* and *RBM* tests carried out on *ASIC* trial layer with 0.50 m thickness

		No. of Passes				
		4	6	8	12	14
<i>RBM</i>	Average γ_d [kN/m ³]					25.80
	Average w [%]					3.3
<i>NM</i>	Average γ_d [kN/m ³]	23.51	24.39	24.88	24.33	25.25
	<i>SD</i>		0.60	0.11	0.56	
	<i>CV</i>		2.5	0.4	2.3	
	Average w [%]	0.7	0.7	0.5	0.3	0.4
	<i>SD</i>		0.1	0.1	0.2	
	<i>CV</i>		7.9	19.8	43.9	

Table D.8: Statistical data obtained from *NM* tests carried out on *ISAC* embankment layers

Layer		No. of Passes		
		8	10	12
4 th	Average γ_d [kN/m ³]	23.17	24.45	
	<i>SD</i>		0.79	
	<i>CV</i>		3.2	
	Average w [%]	0.9	0.9	
	<i>SD</i>		0.05	
	<i>CV</i>		5.1	
5 th	Average γ_d [kN/m ³]	24.16		23.57
	<i>SD</i>	0.37		
	<i>CV</i>	1.5		
	Average w [%]	1.5		1.3
	<i>SD</i>	0.26		
	<i>CV</i>	17.2		
6 th	Average γ_d [kN/m ³]		24.77	24.85
	<i>SD</i>		1.00	
	<i>CV</i>		4.0	
	Average w [%]		1.7	1.6
	<i>SD</i>		0.40	
	<i>CV</i>		23.4	
7 th	Average γ_d [kN/m ³]		24.58	
	<i>SD</i>		0.62	
	<i>CV</i>		2.5	
	Average w [%]		0.9	
	<i>SD</i>		0.24	
	<i>CV</i>		27.2	
8 th	Average γ_d [kN/m ³]			25.04
	<i>SD</i>			0.92
	<i>CV</i>			3.7
	Average w [%]			1.0
	<i>SD</i>			0.57
	<i>CV</i>			56.3

D.2 Performance related tests

D.2.1 LFWD

Table D.9: Statistical data obtained from *LFWD* carried out on *SP* trial and embankment layers, for all energy levels and on *CA40* base layer

Layer	Modulus [MPa]	No. of passages					
		4	6	8	10	12	14
0.30 m	ELFWD	41.5	54.5		47.6		
	SD	5.0	8.5		7.9		
	CV	12.1	15.5		16.7		
0.40 m	ELFWD	49.4	53.5	42.2	45.9	70.6	
	SD	11.4	16.3	3.0	4.9	23.5	
	CV	23.0	30.5	7.2	10.6	33.4	
0.50 m	ELFWD	46.9	51.3			61.1	51.5
	SD		8.2			13.1	8.1
	CV		15.9			21.4	15.8
4 th	ELFWD			66.6			
	SD			14.1			
	CV			21.2			
5 th	ELFWD			53.5			
	SD			7.5			
	CV			14.0			
6 th	ELFWD			50.0	77.6		
	SD			11.6			
	CV			23.2			
7 th	ELFWD			47.2			
	SD			4.5			
	CV			9.5			
Capping layer	ELFWD			50.4			
	SD			8.6			
	CV			17.1			
Base layer	ELFWD				120.3		
	SD				21.5		
	CV				17.9		

Table D.10: Statistical data obtained from *LFWD* carried out on *ISAC* trial and embankment layers, for all energy levels

Layer	Modulus [MPa]	No. of passages					
		4	6	8	10	12	14
0.30 m	E_{LFWD}	53.0	76.2		77.9		
	SD	5.5	10.6		12.1		
	CV	10.4	14.0		15.6		
0.40 m	E_{LFWD}	63.3	64.0	68.8	73.0	89.2	
	SD	14.0	7.1	9.3	9.8	13.2	
	CV	22.2	11.1	13.5	13.5	14.8	
0.50 m	E_{LFWD}	67.5	72.4			91.5	84.0
	SD		5.7			19.2	5.6
	CV		7.9			21.0	6.7
4 th	E_{LFWD}			70.0	79.9		
	SD				3.6		
	CV				4.6		
5 th	E_{LFWD}			73.7	96.3		
	SD			7.1	8.0		
	CV				8.3		
6 th	E_{LFWD}			78.4	81.3		
	SD				6.6		
	CV				8.1		
7 th	E_{LFWD}				86.7		
	SD				7.7		
	CV				8.9		
Capping layer	E_{LFWD}					95.9	
Base layer	E_{LFWD}				116.1		
	SD				23.0		
	CV				19.8		

D.2.2 FWD

Table D.11: Statistical data obtained from *FWD* carried out on *ISAC* capping layer, for the last energy level

	Drops		
	1 st	2 nd	3 rd
σ [kPa]	131.8	193.0	298.5
E_{FWD} [MPa]	96.8	104.2	119.5

Table D.12: Statistical data obtained from *FWD* carried out on base layer, for the last energy level

Profile		Drops		
		1 st	2 nd	3 rd
<i>ISAC</i>	σ [kPa]	126.8	184.0	284.6
	<i>SD</i>	2.7	3.3	5.6
	<i>CV</i>	2.1	1.8	2.0
	Average E_{FWD} [MPa]	138.7	148.3	167.4
	<i>SD</i>	44.9	49.6	49.4
	<i>CV</i>	32.3	33.5	29.5
<i>ISAC + SP</i>	σ [kPa]	124.0	178.9	276.2
	<i>SD</i>	2.2	5.2	1.4
	<i>CV</i>	1.8	2.9	0.5
	Average E_{FWD} [MPa]	80.0	81.4	83.7
	<i>SD</i>	8.3	7.1	7.7
	<i>CV</i>	10.3	8.7	9.2
<i>CA40 + SP</i>	σ [kPa]	120.3	175.7	281.3
	Average E_{FWD} [MPa]	89.8	90.2	94.3

D.2.3 SSG

Table D.13: Statistical data obtained from SSG carried out on SP trial and embankment layers, for all energy levels

Layer	Modulus [MPa]	No. of passages				
		4	6	8	10	14
0.30 m	E _{SSG}	70.9	77.3		77.7	
	SD	8.0	10.7		6.9	
	CV	11.2	13.9		8.9	
0.40 m	E _{SSG}	64.7	76.1	74.2	85.1	
	SD	10.3	13.0	8.0	13.3	
	CV	15.9	17.1	10.8	15.6	
0.50 m	E _{SSG}	82.6	86.4			73.9
	SD		14.5			14.4
	CV		16.8			19.4
Capping layer	E _{SSG}			103.9		
	SD			7.2		
	CV			6.9		

Table D.14: Statistical data obtained from SSG carried out on ISAC trial and embankment layers, for all energy levels

Layer	Modulus [MPa]	No. of passages					
		4	6	8	10	12	14
0.30 m	E _{SSG}	54.1	59.9		59.8		
	SD	3.5	4.1		4.7		
	CV	6.5	6.9		7.8		
0.40 m	E _{SSG}	53.8	56.3	66.6	61.7		
	SD	9.9	2.8	10.6	6.8		
	CV	18.3	4.9	15.9	11.0		
0.50 m	E _{SSG}	71.1	58.6				66.1
	SD		5.8				4.3
	CV		9.9				6.4
Capping layer	E _{SSG}					68.8	
Base layer	E _{SSG}				70.1		
	SD				4.6		
	CV				7.6		

D.2.4 Portancemètre

Table D.15: Statistical data obtained from Portancemètre carried out on *SP* trial and embankment layers, for all energy levels

Layer	Modulus [MPa]	No. of passages					
		4	6	8	10	12	14
0.30 m	E_{Port}	77.0	82.2		81.2		
	SD	2.4	5.1		6.3		
	CV	3.1	6.2		7.7		
0.40 m	E_{Port}			78.6	81.5	92.4	
	SD			4.9	5.1	5.4	
	CV			6.2	6.2	5.8	
0.50 m	E_{Port}	77.8	86.6			94.6	91.4
	SD	7.2	3.4			3.7	7.1
	CV	9.2	3.9			3.9	7.8
4 th	E_{Port}			85.6	90.2		
	SD			6.3			
	CV			7.4			
5 th	E_{Port}			81.8			
	SD			3.1			
	CV			3.8			
6 th	E_{Port}				83.5		
7 th	E_{Port}			78.9	80.0		
	SD			2.7			
	CV			3.5			
Capping layer	E_{Port}			79.5	84.2		
	SD			5.9	7.7		
	CV			7.4	9.2		

Table D.16: Statistical data obtained from Portancemètre carried out on *ISAC* trial and embankment layers, for all energy levels

Layer	Modulus [MPa]	No. of passages					
		4	6	8	10	12	14
0.30 m	E _{Port}	74.6	83.8		86.0		
	<i>SD</i>	2.7	5.7		2.6		
	<i>CV</i>	3.6	6.8		3.1		
0.40 m	E _{Port}			92.4	91.7	103.6	
	<i>SD</i>			7.8	4.1	6.5	
	<i>CV</i>			8.4	4.5	6.3	
0.50 m	E _{Port}	78.3	91.9			100.1	100.5
	<i>SD</i>	3.3	1.9			2.2	2.4
	<i>CV</i>	4.2	2.1			2.2	2.4
4 th	E _{Port}				101.7	109.3	
	<i>SD</i>				3.1		
	<i>CV</i>				3.1		
5 th	E _{Port}				101.7	105.8	
	<i>SD</i>				2.9		
	<i>CV</i>				2.8		
6 th	E _{Port}				104.7	106.3	
	<i>SD</i>				4.7		
	<i>CV</i>				4.5		
7 th	E _{Port}				102.9	107.9	
	<i>SD</i>				4.2		
	<i>CV</i>				4.0		
Capping layer	E _{Port}				103.8	104.8	102.4
	<i>SD</i>				2.7	8.1	
	<i>CV</i>				2.6	7.7	

D.3 In-ground accelerations and displacements

Table D.17: Statistical data of peak vertical drum acceleration during successive passes of the roller compacter on the three profiles

Section	Average (m.s ⁻²)	Number of Passes					Pass 10/2 [%]
		2	4	6	8	10	
<i>ISAC</i>	<i>acd</i> ⁺	20.78	22.42	19.42	20.45	19.10	8.1
	<i>SD</i>	1.63	1.34	1.86	1.63	1.45	
	<i>CV</i>	7.8	6.0	9.6	7.9	7.6	
	<i>acd</i> ⁻	18.49	17.65	16.28	16.45	14.97	19.0
	<i>SD</i>	1.83	1.46	2.12	1.53	1.41	
	<i>CV</i>	9.9	8.3	13.0	9.3	9.4	
	<i>acd</i> ⁺ / <i>acd</i> ⁻	1.12	1.27	1.19	1.24	1.28	
<i>ISAC + SP</i>	<i>acd</i> ⁺	22.47	23.91	21.29	23.40	21.16	5.8
	<i>SD</i>	1.68	1.69	1.41	2.10	1.77	
	<i>CV</i>	7.5	7.1	6.6	9.0	8.4	
	<i>acd</i> ⁻	22.44	21.05	19.23	20.53	18.27	18.6
	<i>SD</i>	3.18	2.55	2.19	3.38	2.58	
	<i>CV</i>	14.2	12.1	11.4	16.5	14.1	
	<i>acd</i> ⁺ / <i>acd</i> ⁻	1.00	1.14	1.11	1.14	1.16	
<i>CA40 + SP</i>	<i>acd</i> ⁺	24.64				23.29	5.5
	<i>SD</i>	1.60				1.32	
	<i>CV</i>	6.5				5.6	
	<i>acd</i> ⁻	23.79				21.81	8.3
	<i>SD</i>	1.88				1.25	
	<i>CV</i>	7.9				5.7	
	<i>acd</i> ⁺ / <i>acd</i> ⁻	1.04				1.07	

Table D.18: Statistical data of vertical drum displacement during compaction on the three different sections

Section	Average [mm]	Number of Passes				
		2	4	6	8	10
<i>ISAC</i>	zd^+	1.112	1.083	1.059	1.019	0.994
	<i>SD</i>	0.070	0.048	0.075	0.048	0.052
	<i>CV</i>	6.3	4.4	7.1	4.7	5.2
	zd^-	1.152	1.081	1.083	1.032	0.987
	<i>SD</i>	0.091	0.070	0.098	0.065	0.067
	<i>CV</i>	7.9	6.5	9.1	6.3	6.8
<i>ISAC + SP</i>	zd^+	1.392	1.392	1.315	1.374	1.306
	<i>SD</i>	0.101	0.094	0.076	0.114	0.093
	<i>CV</i>	7.3	6.8	5.8	8.3	7.1
	zd^-	1.448	1.428	1.337	1.415	1.304
	<i>SD</i>	0.140	0.128	0.105	0.170	0.122
	<i>CV</i>	9.7	9.0	7.8	12.0	9.4
<i>CA40 + SP</i>	zd^+	1.601				1.519
	<i>SD</i>	0.075				0.049
	<i>CV</i>	4.7				3.2
	zd^-	1.681				1.575
	<i>SD</i>	0.094				0.054
	<i>CV</i>	5.6				3.4

D.4 In-ground strains

Table D.19: Total strain (ε_z) and cyclic portion ($\Delta\varepsilon_z$) due to vibrating roller passes on base layer

Section	Sensor	Strain [$\times 10^{-6}$]	Number of Passes					
			1	2	4	6	8	10
<i>ISAC</i>	V08	ε_z	2744	3719	4207			
		$\Delta\varepsilon_z$	288	276	253			
		$\Delta\varepsilon_z/\varepsilon_z$ [%]	10.5	7.4	6.0			
	V09	ε_z	970	1312	1930	1433	2139	2078
		$\Delta\varepsilon_z$	178	186	219	182	211	211
		$\Delta\varepsilon_z/\varepsilon_z$ [%]	18.3	14.2	11.3	12.7	9.9	10.1
	V04	ε_z	539	686	760	908	981	964
		$\Delta\varepsilon_z$	79	66	72	76	81	81
		$\Delta\varepsilon_z/\varepsilon_z$ [%]	14.6	9.6	9.5	8.3	8.3	8.4
<i>ISAC</i> <i>+SP</i>	V06	ε_z	2272	1823	2153	2183	1971	768
		$\Delta\varepsilon_z$	212	213	236	212	182	94
		$\Delta\varepsilon_z/\varepsilon_z$ [%]	9.3	11.7	10.9	9.7	9.2	12.3
<i>CA40</i> <i>+SP</i>	V01	ε_z	270	346				412
		$\Delta\varepsilon_z$	38	58				68
		$\Delta\varepsilon_z/\varepsilon_z$ [%]	14.1	16.8				16.4
	V02	ε_z	1326	817				1320
		$\Delta\varepsilon_z$	135	127				166
		$\Delta\varepsilon_z/\varepsilon_z$ [%]	10.2	15.5				12.6
	V05	ε_z	690	546				483
		$\Delta\varepsilon_z$	79	63				72
		$\Delta\varepsilon_z/\varepsilon_z$ [%]	11.4	11.5				14.9

